

The background of the cover features a teal header and a white background with intricate blue line art of ocean waves. The waves are depicted with concentric, swirling lines that create a sense of movement and depth. The teal header contains the main title in white, bold, sans-serif capital letters. Below the header, a dark grey band contains the editor and publisher information in white, sans-serif capital letters. The bottom of the cover is white, with the Frontiers Research Topics logo and name at the very bottom.

EMERGING TECHNOLOGIES WITH HIGH IMPACT FOR OCEAN SCIENCES, ECOSYSTEM MANAGEMENT, AND ENVIRONMENTAL CONSERVATION

EDITED BY: Oscar Pizarro and Leonard Pace
PUBLISHED IN: Frontiers in Marine Science



frontiers

Frontiers eBook Copyright Statement

The copyright in the text of individual articles in this eBook is the property of their respective authors or their respective institutions or funders. The copyright in graphics and images within each article may be subject to copyright of other parties. In both cases this is subject to a license granted to Frontiers.

The compilation of articles constituting this eBook is the property of Frontiers.

Each article within this eBook, and the eBook itself, are published under the most recent version of the Creative Commons CC-BY licence.

The version current at the date of publication of this eBook is CC-BY 4.0. If the CC-BY licence is updated, the licence granted by Frontiers is automatically updated to the new version.

When exercising any right under the CC-BY licence, Frontiers must be attributed as the original publisher of the article or eBook, as applicable.

Authors have the responsibility of ensuring that any graphics or other materials which are the property of others may be included in the CC-BY licence, but this should be checked before relying on the CC-BY licence to reproduce those materials. Any copyright notices relating to those materials must be complied with.

Copyright and source acknowledgement notices may not be removed and must be displayed in any copy, derivative work or partial copy which includes the elements in question.

All copyright, and all rights therein, are protected by national and international copyright laws. The above represents a summary only. For further information please read Frontiers' Conditions for Website Use and Copyright Statement, and the applicable CC-BY licence.

ISSN 1664-8714

ISBN 978-2-88971-084-3

DOI 10.3389/978-2-88971-084-3

About Frontiers

Frontiers is more than just an open-access publisher of scholarly articles: it is a pioneering approach to the world of academia, radically improving the way scholarly research is managed. The grand vision of Frontiers is a world where all people have an equal opportunity to seek, share and generate knowledge. Frontiers provides immediate and permanent online open access to all its publications, but this alone is not enough to realize our grand goals.

Frontiers Journal Series

The Frontiers Journal Series is a multi-tier and interdisciplinary set of open-access, online journals, promising a paradigm shift from the current review, selection and dissemination processes in academic publishing. All Frontiers journals are driven by researchers for researchers; therefore, they constitute a service to the scholarly community. At the same time, the Frontiers Journal Series operates on a revolutionary invention, the tiered publishing system, initially addressing specific communities of scholars, and gradually climbing up to broader public understanding, thus serving the interests of the lay society, too.

Dedication to Quality

Each Frontiers article is a landmark of the highest quality, thanks to genuinely collaborative interactions between authors and review editors, who include some of the world's best academicians. Research must be certified by peers before entering a stream of knowledge that may eventually reach the public - and shape society; therefore, Frontiers only applies the most rigorous and unbiased reviews.

Frontiers revolutionizes research publishing by freely delivering the most outstanding research, evaluated with no bias from both the academic and social point of view. By applying the most advanced information technologies, Frontiers is catapulting scholarly publishing into a new generation.

What are Frontiers Research Topics?

Frontiers Research Topics are very popular trademarks of the Frontiers Journals Series: they are collections of at least ten articles, all centered on a particular subject. With their unique mix of varied contributions from Original Research to Review Articles, Frontiers Research Topics unify the most influential researchers, the latest key findings and historical advances in a hot research area! Find out more on how to host your own Frontiers Research Topic or contribute to one as an author by contacting the Frontiers Editorial Office: frontiersin.org/about/contact

EMERGING TECHNOLOGIES WITH HIGH IMPACT FOR OCEAN SCIENCES, ECOSYSTEM MANAGEMENT, AND ENVIRONMENTAL CONSERVATION

Topic Editors:

Oscar Pizarro, The University of Sydney, Australia

Leonard Pace, Schmidt Ocean Institute, United States

Citation: Pizarro, O., Pace, L., eds. (2021). Emerging Technologies With High Impact for Ocean Sciences, Ecosystem Management, and Environmental Conservation. Lausanne: Frontiers Media SA. doi: 10.3389/978-2-88971-084-3

Table of Contents

- 05 Editorial: Emerging Technologies With High Impact for Ocean Sciences, Ecosystem Management, and Environmental Conservation**
Oscar Pizarro and Leonard Pace
- 07 Leveraging Automated Image Analysis Tools to Transform Our Capacity to Assess Status and Trends of Coral Reefs**
Ivor D. Williams, Courtney S. Couch, Oscar Beijbom, Thomas A. Oliver, Bernardo Vargas-Angel, Brett D. Schumacher and Russell E. Brainard
- 21 Targeted Sampling by Autonomous Underwater Vehicles**
Yanwu Zhang, John P. Ryan, Brian Kieft, Brett W. Hobson, Robert S. McEwen, Michael A. Godin, Julio B. Harvey, Benedetto Barone, James G. Bellingham, James M. Birch, Christopher A. Scholin and Francisco P. Chavez
- 33 Mapping Fish Chorus Distributions in Southern California Using an Autonomous Wave Glider**
Camille M. L. S. Pagniello, Megan A. Cimino and Eric Terrill
- 42 Next-Generation Optical Sensing Technologies for Exploring Ocean Worlds—NASA FluidCam, MiDAR, and NeMO-Net**
Ved Chirayath and Alan Li
- 66 Development of Surface Drifting Buoys for Fiducial Reference Measurements of Sea-Surface Temperature**
Marc Le Menn, Paul Poli, Arnaud David, Jérôme Sagot, Marc Lucas, Anne O'Carroll, Mathieu Belbeoch and Kai Herklotz
- 78 Wave Measurements From Radar Tide Gauges**
Laura A. Fiorentino, Robert Heitsenrether and Warren Krug
- 92 Coastal Harmful Algae Bloom Monitoring via a Sustainable, Sail-Powered Mobile Platform**
Jordon S. Beckler, Ethan Arutunian, Tim Moore, Bob Currier, Eric Milbrandt and Scott Duncan
- 106 Virtual Reality and Oceanography: Overview, Applications, and Perspective**
Noah L. Walcutt, Benjamin Knörlein, Tom Sgouros, Ivona Cetinić and Melissa M. Omand
- 117 The Development and Validation of a Profiling Glider Deep ISFET-Based pH Sensor for High Resolution Observations of Coastal and Ocean Acidification**
Grace K. Saba, Elizabeth Wright-Fairbanks, Baoshan Chen, Wei-Jun Cai, Andrew H. Barnard, Clayton P. Jones, Charles W. Branham, Kui Wang and Travis Miles
- 134 SHiPCC—A Sea-going High-Performance Compute Cluster for Image Analysis**
Timm Schoening
- 140 Emerging Technologies and Coral Reef Conservation: Opportunities, Challenges, and Moving Forward**
Elizabeth M. P. Madin, Emily S. Darling and Marah J. Hardt

- 147** *Fish Spawning Aggregations Dynamics as Inferred From a Novel, Persistent Presence Robotic Approach*
Laurent M. Chérubin, Fraser Dalgleish, Ali Khaleel Ibrahim, Michelle Schärer-Umpierre, Richard S. Nemeth, Anthony Matthews and Richard Appeldoorn
- 166** *Using Ship-Deployed High-Endurance Unmanned Aerial Vehicles for the Study of Ocean Surface and Atmospheric Boundary Layer Processes*
Christopher J. Zappa, Scott M. Brown, Nathan J. M. Laxague, Tejendra Dhakal, Ryan A. Harris, Aaron M. Farber and Ajit Subramaniam
- 183** *Remote Sensing of Natural Waters Using a Multichannel, Lidar-Compatible Raman Spectrometer and Blue Excitation*
Andréa de Lima Ribeiro and Helen Pask
- 195** *Oceanids C2: An Integrated Command, Control, and Data Infrastructure for the Over-the-Horizon Operation of Marine Autonomous Systems*
Catherine A. Harris, Alvaro Lorenzo-Lopez, Owain Jones, Justin J. H. Buck, Alexandra Kokkinaki, Stephen Loch, Thomas Gardner and Alexander B. Phillips
- 215** *Multi-Decadal Humpback Whale Migratory Route Fidelity Despite Oceanographic and Geomagnetic Change*
Travis W. Horton, Alexandre N. Zerbini, Artur Andriolo, Daniel Danilewicz and Federico Sucunza



Editorial: Emerging Technologies With High Impact for Ocean Sciences, Ecosystem Management, and Environmental Conservation

Oscar Pizarro¹ and Leonard Pace^{2*}

¹ Australian Centre for Field Robotics, The University of Sydney, Sydney, NSW, Australia, ² Schmidt Ocean Institute, Palo Alto, CA, United States

Keywords: technology, ocean science, ocean observation, ecosystem management, conservation

Editorial on the Research Topic

Emerging Technologies With High Impact for Ocean Sciences, Ecosystem Management, and Environmental Conservation

Earth's oceans are essential for sustaining life as we know it. It's difficult to overstate their value, we rely on our oceans to maintain the planet habitable by regulating its climate and atmospheric composition. We also feed ourselves directly or indirectly through fishing and aquaculture, move vast amounts of energy, raw materials and goods across the globe on ships, enjoy recreation and sports on beaches and on (and under) waves. Our oceans, unfortunately, also continue to act as the final resting place for much of our waste.

While humanity no longer sees them as a boundless resource to use and abuse, our understanding of the oceans and our ability to manage and conserve marine ecosystems are challenged by their very scale and dynamic nature. The IPCC Special Report on the Ocean and Cryosphere in a Changing Climate highlights increasing observational capacity as a solution for providing the data to improve understanding and modeling of the gaps in knowledge of climate feedbacks in biological systems, and the capacity and limits of biological adaptation for many ecosystems (Bindoff et al., 2019). Many of the observational tools in use today are not reliable for long-term unattended use at sea or cost-efficient enough for scalable deployment. While modern systems capture a wealth of information; i.e., satellites providing constant high resolution coverage at the surface but unable to penetrate depths, the Argo network collecting vast temporal data but providing only point scale data per float, autonomous systems providing high resolution data capture over increasing scales but requiring maintenance for biofouling and system wear, there is ample room for enhancement. Improved scientific understanding and technological innovation offer opportunities to deliver quality marine observations at optimal resolution and coverage, analyze them at scale, and apply the resulting insights to inform timely ecosystem management, conservation, restoration, and marine science.

This Research Topic showcases examples of innovation in scalable, practical, and cost-efficient ocean observation techniques that enable transformative improvement in the understanding of the oceanic processes and marine ecosystems, such as low cost robotic marine survey platforms and workflows, Chérubin et al., intelligent sensing technologies and methodologies, Zhang et al., resource-efficient planning and execution of marine survey and monitoring, Zappa et al., effective observational practices and methodologies that are easy to use and transfer to broad user communities with reduced expertise and training requirements, Williams et al., intelligent and intuitive data analytical tools and services, Schoening, and other related innovations with high impact potential for ocean sciences, ecosystem management, and environmental conservation.

OPEN ACCESS

Edited and reviewed by:

Oscar Schofield,
Rutgers, The State University of New
Jersey, United States

*Correspondence:

Leonard Pace
lp@schmidt-ocean.org

Specialty section:

This article was submitted to
Ocean Observation,
a section of the journal
Frontiers in Marine Science

Received: 24 February 2021

Accepted: 26 March 2021

Published: 24 May 2021

Citation:

Pizarro O and Pace L (2021) Editorial:
Emerging Technologies With High
Impact for Ocean Sciences,
Ecosystem Management, and
Environmental Conservation.
Front. Mar. Sci. 8:671877.
doi: 10.3389/fmars.2021.671877

Together, these advances and insights represent real progress and reasons for optimism in the development of better tools and approaches in support of marine science and conservation. Contributions like the ones highlighted here and ones yet to come increase the odds that we will address some of the many environmental challenges along the way to a sustainable global civilization.

REFERENCES

Bindoff, N. L., Cheung, W. W. L., Kairo, J. G., Arístegui, J., Guinder, V. A., Hallberg, R., et al. (2019). "Changing ocean, marine ecosystems, and dependent communities," in *IPCC Special Report on the Ocean and Cryosphere in a Changing Climate*, eds H.-O. Pörtner, D. C. Roberts, V. Masson-Delmotte, P. Zhai, M. Tignor, E. Poloczanska, K. Mintenbeck, A. Alegria, M. Nicolai, A. Okem, J. Petzold, B. Rama, and N. M. Weyer (in press).

AUTHOR CONTRIBUTIONS

LP and OP contributed to the drafting and completion of the editorial. OP wrote the first draft of the manuscript. LP edited and made additions to sections of the editorial. Both authors contributed to editorial revision, read, and approved the submitted version.

Conflict of Interest: The authors declare that the research was conducted in the absence of any commercial or financial relationships that could be construed as a potential conflict of interest.

Copyright © 2021 Pizarro and Pace. This is an open-access article distributed under the terms of the Creative Commons Attribution License (CC BY). The use, distribution or reproduction in other forums is permitted, provided the original author(s) and the copyright owner(s) are credited and that the original publication in this journal is cited, in accordance with accepted academic practice. No use, distribution or reproduction is permitted which does not comply with these terms.



Leveraging Automated Image Analysis Tools to Transform Our Capacity to Assess Status and Trends of Coral Reefs

Ivor D. Williams^{1*}, Courtney S. Couch^{1,2}, Oscar Beijbom^{3,4}, Thomas A. Oliver¹, Bernardo Vargas-Angel^{1,2}, Brett D. Schumacher⁵ and Russell E. Brainard¹

¹ Ecosystem Sciences Division, Pacific Islands Fisheries Science Center, National Oceanic and Atmospheric Administration (NOAA), Honolulu, HI, United States, ² Joint Institute for Marine and Atmospheric Research, University of Hawai'i at Mānoa, Honolulu, HI, United States, ³ Global Change Institute, The University of Queensland, St Lucia, QLD, Australia, ⁴ Berkeley Artificial Intelligence Research, University of California, Berkeley, Berkeley, CA, United States, ⁵ Sustainable Fisheries Division, Pacific Islands Regional Office, National Oceanic and Atmospheric Administration, Honolulu, HI, United States

OPEN ACCESS

Edited by:

Victor Zykov,
Schmidt Ocean Institute,
United States

Reviewed by:

Thomas Mock,
University of East Anglia,
United Kingdom
Gregory P. Asner,
Arizona State University, United States

*Correspondence:

Ivor D. Williams
ivor.williams@noaa.gov

Specialty section:

This article was submitted to
Ocean Observation,
a section of the journal
Frontiers in Marine Science

Received: 25 August 2018

Accepted: 10 April 2019

Published: 30 April 2019

Citation:

Williams ID, Couch CS, Beijbom O, Oliver TA, Vargas-Angel B, Schumacher BD and Brainard RE (2019) Leveraging Automated Image Analysis Tools to Transform Our Capacity to Assess Status and Trends of Coral Reefs. *Front. Mar. Sci.* 6:222. doi: 10.3389/fmars.2019.00222

Digital photography is widely used by coral reef monitoring programs to assess benthic status and trends. In addition to creating a permanent archive, photographic surveys can be rapidly conducted, which is important in environments where bottom-time is frequently limiting. However, substantial effort is required to manually analyze benthic images; which is expensive and leads to lags before data are available. Using previously analyzed imagery from NOAA's Pacific Reef Assessment and Monitoring Program, we assessed the capacity of a trained and widely used machine-learning image analysis tool – CoralNet coralnet.ucsd.edu – to generate fully-automated benthic cover estimates for the main Hawaiian Islands (MHI) and American Samoa. CoralNet was able to generate estimates of site-level coral cover for both regions that were highly comparable to those generated by human analysts (Pearson's $r > 0.97$, and with bias of 1% or less). CoralNet was generally effective at estimating cover of common coral genera (Pearson's $r > 0.92$ and with bias of 2% or less in 6 of 7 cases), but performance was mixed for other groups including algal categories, although generally better for American Samoa than MHI. CoralNet performance was improved by simplifying the classification scheme from genus to functional group and by training within habitat types, i.e., separately for coral-rich, pavement, boulder, or "other" habitats. The close match between human-generated and CoralNet-generated estimates of coral cover pooled to the scale of island and year demonstrates that CoralNet is capable of generating data suitable for assessing spatial and temporal patterns. The imagery we used was gathered from sites randomly located in <30 m hard-bottom at multiple islands and habitat-types per region, suggesting our results are likely to be widely applicable. As image acquisition is relatively straightforward, the capacity of fully-automated image analysis tools to minimize the need for resource intensive human analysts opens possibilities for enormous increases in the quantity and consistency of coral reef benthic data that could become available to researchers and managers.

Keywords: coral reef, image analysis, machine learning, CoralNet, Hawaii, American Samoa, benthic monitoring

INTRODUCTION

The scale and severity of threats to coral reefs have increased substantially in recent years (Burke et al., 2011; De'ath et al., 2012; Hughes et al., 2018a). Local stressors, such as land-based pollution, crown-of-thorns seastar predation, disease outbreaks, over-exploitation, and destructive fishing practices have caused significant localized reef decline (Edinger et al., 1998; Fabricius, 2005; Miller et al., 2009). Additionally, coral reefs have recently experienced consecutive years of thermal stress and mass coral bleaching resulting in widespread coral mortality (Heron et al., 2016; Couch et al., 2017; Hughes et al., 2018a,b). Given the speed of change and the increasing severity of threats, scientists and managers need the capability to rapidly assess coral reef status, ideally over large areas, and to quantify change. In addition, broad-scale data on benthos are critical to understanding drivers of change and identifying management responses that promote or undermine coral reef resilience, i.e., the ability to resist or recover from stressors (Maynard et al., 2010; McClanahan et al., 2012).

While a variety of metrics are used to assess coral reef status and trends, the majority of coral reef surveys and monitoring programs gather information on percent cover of benthic organisms, particularly coral cover (De'ath et al., 2012; Johansson et al., 2013). During the last 30 years, many benthic monitoring programs have transitioned from *in situ* measurements of benthic cover to some form of photographic survey, such as photo-transects and video surveys. These approaches not only create a permanent archive suitable for subsequent analysis, but also tend to greatly reduce in-water survey time, which is frequently constraining for underwater visual surveys. In combination with photographic surveys, utilization of towed divers, diver propulsion systems, and autonomous underwater vehicles can facilitate considerable expansion of spatial coverage (Armstrong et al., 2006; Williams et al., 2010; González-Rivero et al., 2014). However, the concomitant post-survey burden associated with extracting data from the acquired imagery is a major drawback of photographic survey approaches. Images gathered from those types of surveys have typically been manually analyzed using point annotation software, such as Coral Point Count with Excel extensions (CPCe), photoQuad, pointCount99, PhotoGrid, or Biigle (Porter et al., 2001; Kohler and Gill, 2006; Trygonis and Sini, 2012; Langenkämper et al., 2017). As manual annotation of imagery is time-consuming and thus expensive, this not only limits the amount of survey data that can feasibly be analyzed, but can also lead to significant lags before survey results become available. Additionally, variability in performance among human analysts, which can be non-trivial for some groups of benthos, is a potential source of bias (Beijbom et al., 2015; González-Rivero et al., 2016).

Recent advances in automated image analysis suggest that there is scope for a substantial portion of the image-analysis workload to be automated using machine-learning tools. During the last decade, several programs have been developed to automate point classification of benthic imagery (Marcos et al., 2005; Stokes and Deane, 2009; Shihavuddin et al., 2013; Beijbom et al., 2015). The most widely used of those, at least for coral reef

surveys, is CoralNet¹, which includes an online repository, a tool that allows the user to manually-annotate imagery and machine-learning algorithms to fully- or partially-automate classification of benthic imagery once sufficient data are available to train the system (Beijbom et al., 2015).

In the first (alpha) version of CoralNet, image features based on texture and color were extracted from imagery and then classified by a Support Vector Machine (Beijbom et al., 2015). The performance of that version was assessed by comparing automatically generated benthic point data against data generated by a number of human annotators. Compared to human analysts, the accuracy of automatically generated benthic point data varied considerably among different benthic categories – with 62% accuracy for coral and 28–48% for algal groups: macroalgae, turf, and crustose coralline algae (CCA). This was significantly lower than the accuracy of human annotators when compared to the same annotators' previous annotations, and in comparison to other human annotators analyzing the same sets of imagery. In late 2016, an updated (beta) version of CoralNet was released. This version relies on Deep Learning, which has replaced hand-crafted features for almost all computer vision tasks and revolutionized the field (LeCun et al., 2015). In the beta version of CoralNet, accuracy (i.e., agreement with reference annotations) of the automated classifier “robot” increased to 80% for corals and 48–66% for algal groups, such as macroalgae, turf, and CCA. Those levels of accuracy are comparable to what are typically achieved by different human analysts manually annotating the same points (Beijbom unpubl. data).

However, despite improved classification in the beta version, and widespread usage of CoralNet as an image analysis and archiving tool, few users utilize any level of automation in CoralNet analysis. Specifically, as of July 2018, CoralNet users had uploaded 822 data sets consisting of over 700,000 images to CoralNet, but few users make use of any form of automation, and half of those that do only permit CoralNet to annotate points when the “robot” (i.e., automated-analysis algorithm) is at least 90% certain of a classification.

Here, we aim to build on previous studies of CoralNet by assessing and refining its use in its current (beta) form as an automated analysis tool for a large-scale survey and monitoring program. The data and imagery we use come from NOAA's Pacific Reef Assessment and Monitoring Program (Pacific RAMP) which has surveyed coral reefs at approximately 40 islands and atolls across the US-affiliated Pacific since the early 2000s. For that program, survey sites are randomly located in diverse hard bottom habitats and water depths around multiple islands in each region and, therefore, span wide ranges of habitat structure, exposure, and light availability – factors which affect benthic assemblage structure as well as color and organism morphology, thus adding complexity to automated classification (Glynn, 1976; Dollar, 1982; Salih et al., 2000). Specifically, we utilize previously human-analyzed imagery from two regions – American Samoa and Hawaii – to train CoralNet systems and test the ability of the resulting trained robots to: (1) fully-automatically generate estimates of benthic cover for different functional groups and

¹coralnet.ucsd.edu

coral genera; (2) compare fully-automatically generated site- and island-scale estimates of cover against those generated by human analysts for different habitat types and regions; and (3) assess the impacts of using different benthic classification schemes of varying complexity.

MATERIALS AND METHODS

Source of Benthic Imagery, Survey Methods and Design

The imagery and benthic data used in this study were gathered by NOAA's Pacific Islands Ecosystem Sciences Division (ESD) for the Pacific RAMP, which is part of the US National Coral Reef Monitoring Program (NCRMP) (NOAA Coral Program, 2014). In its current form, Pacific RAMP visits and surveys regions and islands once or twice every 3 years. During each survey visit, sites around each island are randomly located within three depth strata comprising all hard bottom habitats in <30 m of water, with primary focus on fore reef habitats. Back reef and lagoon habitats are also surveyed, but much less intensively. Survey sites encompass substantial variability in habitat type (including rock/boulder, and pavement habitats), reef condition, benthic assemblages, and coral cover (ranging from 0 to >70% in each region), as well as in environmental factors that influence image quality, such as water depth and turbidity.

Survey data and imagery used in this study come from two regions: the main Hawaiian Islands (MHI) and American Samoa (Figure 1), those being regions with relatively low and relatively high coral diversity, respectively. MHI imagery was gathered between 2010 and 2015, and American Samoa sites from 2015. The number of sites per island and year are shown in Table 1.

At each site, a total of 30 benthic images were captured along 1 or 2 transect lines with a total combined length of 30 m (1 photograph per meter). Photos were taken with digital cameras, maintained at a standard height above the substrate using a 1-m PVC monopod. No artificial lighting was used; instead cameras were manually white balanced by divers immediately before they began the photo-transect. Details of cameras and settings are provided in Supplementary Table S1. More detail on survey design and methods are available elsewhere (Heenan et al., 2017; Swanson et al., 2018).

Previous Annotation of Imagery by Human Analysts

Benthic images used in this study had been previously annotated by human analysts, all of whom were trained in identification of benthic organisms and had passed a data quality test. Analysts identified benthic organisms under 10 randomly-located points per image (totaling 300 points per site). Coral Point Count with Excel extensions (Kohler and Gill, 2006) (CPCe) was used to analyze MHI imagery from 2010 and 2012, and CoralNet for all other images (Lozada-Misa et al., 2017). Images annotated with CoralNet used the "ORIGINAL" classification scheme (Supplementary Table S2), which required analysts to identify corals to genus or a combination of genus and growth form for

select genera (*Montipora*, *Pavona*, and *Porites*), macroalgae to genus, and other benthic features to functional group or higher-level taxonomic grouping (e.g., "sand," "sponge," "turf algae") (Lozada-Misa et al., 2017). Images analyzed with CPCe were analyzed using similar schemes, but with corals only identified to growth-form for 2010 imagery. Imagery was arbitrarily assigned to different human analysts within a pool of trained analysts – 11 for MHI, and 8 for American Samoa.

Training and Testing CoralNet

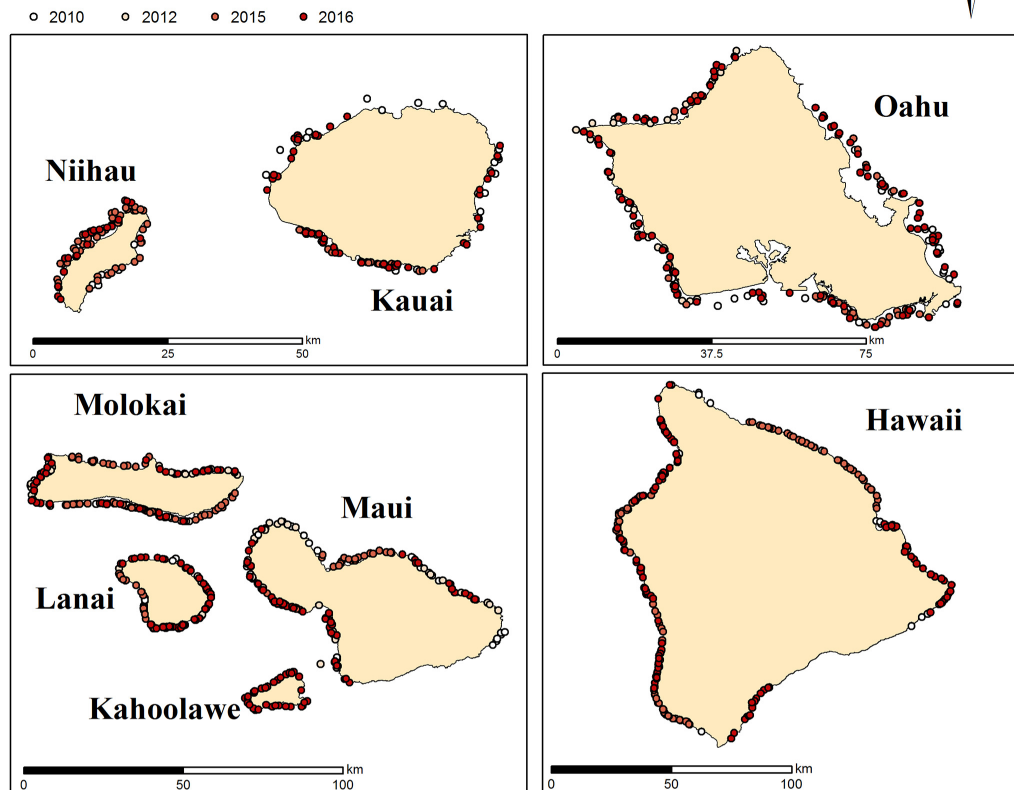
Although CoralNet can be used solely as a tool for manual annotation imagery, its greater potential comes from its machine-learning capabilities, which allow trained CoralNet systems to automatically annotate additional imagery (Beijbom et al., 2015). For this study, we used data from imagery that had previously been manually-annotated in CoralNet to generate training and test sets in order to assess the ability of CoralNet (beta) to automatically estimate benthic cover.

CoralNet allows users to organize images into "sources" (i.e., a set of images and an associated benthic classification scheme). Sources are defined at the discretion of the user, but would typically be based on geography, habitat, depth zone, or other characteristic that would lead users to group a set of images together and apply a common benthic classification scheme. ESD created region-specific sources – e.g., one for MHI and another for American Samoa. A key consideration when defining a source is that the CoralNet machine-learning algorithm operates within a source. Thus, identification of a point as being of the coral genus *Pocillopora* in the MHI source would contribute to the training of the MHI "robot," but it would not at all affect the training of robots in other sources.

We created two sources for this analysis: one for American Samoa, using imagery from 468 sites, and one for MHI, with imagery from 913 sites. All the American Samoa imagery and 598 of the MHI images had been previously manually analyzed in CoralNet (Table 1). Those existing manual annotations formed the basis of our training sets, i.e., they were used to train CoralNet "robots" in our new sources. As noted above, the other MHI images (from 2010 and 2012) had not been analyzed using CoralNet and had used slightly different classification schemes. Therefore, data from those images could not be included in the training sets. We nevertheless included those images in the MHI source so we could compare functional-group cover (e.g., "coral," "turf") generated from those images by trained CoralNet systems against values from the earlier manual annotation.

We downloaded and uploaded point annotations to and from CoralNet in "annotation files," which included the filename, *x-y* coordinates within image, annotation-value (i.e., classification of each point), and annotator-identifier for each of the 10 points on each image. From the original CoralNet human-analyst annotations, we generated paired training sets, retaining the original annotations for one half of the training imagery, and setting annotations for the other points to blanks. Having paired training sets allowed us to successively train CoralNet on one half of the previously analyzed imagery within a source and then let CoralNet automatically annotate the remaining imagery. As the CoralNet robot was initialized

Main Hawaiian Islands



American Samoa

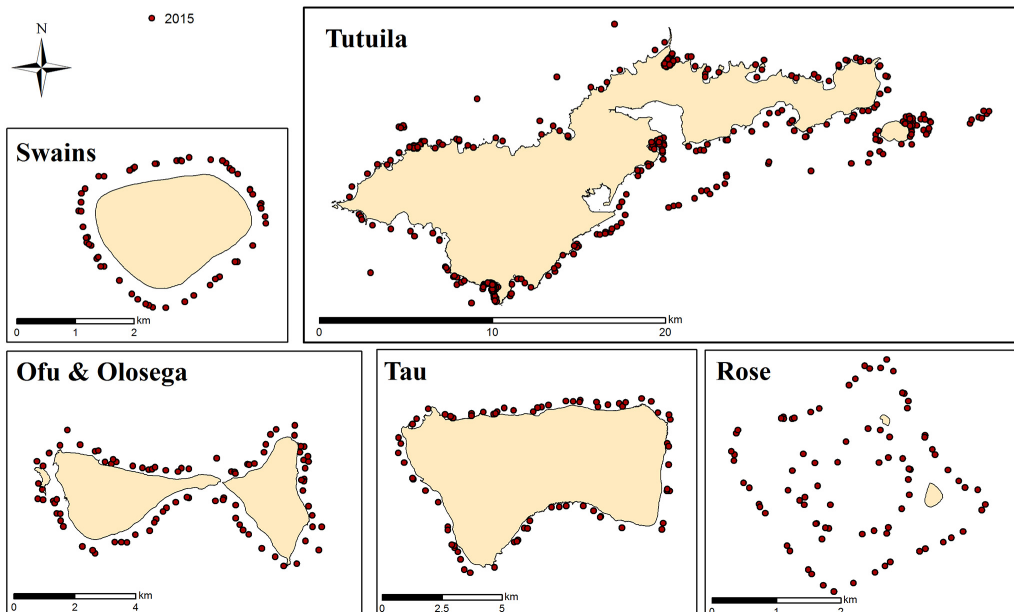


FIGURE 1 | Survey sites in MHI and American Samoa. Each dot represents a survey site. At each site, 30 planar benthic photographs were taken by survey divers from ~1 m above the substrate.

between each run, we were able to combine the automatically-annotated data from the two runs in each pair to generate a complete set of fully-automated annotations for a source. Importantly, this meant that CoralNet robots were never trained on the points that they subsequently automatically annotated. As each training set included half of the suitable images, the full American Samoa training set included annotations from 70,200 points (half of 468 sites \times 30 images \times 10 points), and each full MHI training set included annotations from 89,700 points.

For each source, we trained and tested CoralNet for three variations of the classification scheme, (**Supplementary Table S2**): the relatively complex “ORIGINAL” scheme, which has the finest resolution of classification, with 85 distinct benthic classes (65 used for MHI); the SIMPLER scheme, in which corals and macroalgae were pooled to a smaller number of classes (32 in American Samoa, 31 in MHI), based on growth form for corals and division for macroalgae (e.g., red, green, brown algae), but with some common and relatively distinct genera retained (among corals: *Porites*, *Pocillopora*, *Montipora* in MHI; those plus *Acropora* in Samoa; and, among macroalgae: *Halimeda* in American Samoa); and “BASE” (14 classes), in which benthos was pooled to functional group – e.g., “all coral”; “all macroalgae.”

As there was great variability among sites in habitat types within our broad survey domains, particularly in MHI, we trained and tested the MHI BASE scheme separately within four habitat types which had been recorded at the time of the surveys, using an explicit classification scheme (Ayotte et al., 2015). Those habitat types were: “aggregate reef,” which are continuous and generally structurally-complex habitats with conspicuous cover of corals; “pavement,” which are relatively flat habitats with low and patchy coral cover; “rock-boulder,” which are complex, frequently basalt habitats with highly variable coral cover, and for all “other” habitats. There were respectively 188, 167, 159, and 84 sites within each of those habitat types that were used for training. The great majority of American Samoa sites were classified as aggregate reef;

therefore, there was no clear reason to filter those by habitat. Instead, images from American Samoa were separately trained and tested with the BASE classification for each of the five islands (**Table 1**).

Data Synthesis and Analysis

Manually-annotated (“human-analyst”) and fully machine-annotated (“CoralNet”) point data were pooled to site-level percent cover estimates. Bland-Altman plots (Bland and Altman, 1986) were used to compare and visualize the human-analyst and CoralNet estimates of benthic cover. Specifically, those show site-level differences between the two estimates plotted against the site-level mean of the two methods. To quantify the performance of different schemes, we calculated the mean and standard deviation of site-level differences in cover between the two types of annotation.

In order to compare human-analyst and CoralNet performance at scales that are likely more relevant to many monitoring programs, site-level data were pooled by island and year (henceforth “island-year”) using a standard approach to generate higher-level data from the stratified-random design, i.e., mean and variance per strata were weighted by the size of the strata to generate island-scale values (Heenan et al., 2017). The extent and significance of the differences in cover for all possible island-year pairs were calculated and compared between the two annotation methods. By doing so, we assessed whether we would draw different conclusions about spatial and temporal patterns among island-years from CoralNet and human-analyst cover estimates. Specifically, for the MHI, we had data from 4 to 8 islands in each of the 4 years (**Table 1**) – leading to 325 pairwise island-year combinations (e.g., between Oahu 2012 and Oahu 2015; or between Oahu 2012 and Maui 2015). For American Samoa, there were only data from five islands in a single year, and thus 10 possible island-year pairs. For each method, the mean and standard error of difference in cover between all possible island-year pairs were calculated as follows (with “ISL1” and “ISL2” being the two island and year combinations in a pair):

$$\text{Mean of difference} = \text{absolute}(\text{Mean}_{\text{ISL1}} - \text{Mean}_{\text{ISL2}})$$

$$\text{Standard error (SE) of difference} = \sqrt{(\text{SE}_{\text{ISL1}}^2 + \text{SE}_{\text{ISL2}}^2)}$$

We converted standard error of difference to 95% confidence intervals using the *t*-distribution for the degrees of freedom of the island-year pair ($N_{\text{ISL1}} + N_{\text{ISL2}} - 2$). We considered 95% confidence interval of difference not overlapping zero as evidence of significant difference at alpha of 0.05.

Finally, in order to visualize the impact of training set size on site-level consistency between annotations methods, we calculated the mean difference between human-analyst and CoralNet cover estimates for all test runs and plotted that against the size of the test run training set (i.e., how many annotated points were included in that training set). Human-analyst

TABLE 1 | Number of survey sites per island per year.

Main Hawaiian Islands	2010	2012	2015	2016
Hawaii	37	–	82	79
Kauai	20	–	17	44
Lanai	14	27	11	33
Maui	30	43	27	41
Molokai	9	48	38	32
Niihau	16	–	42	15
Oahu	36	35	32	77
Kahoolawe	–	–	–	28
American Samoa			2015	
Ofu and Olosega			81	
Rose			49	
Swains			47	
Tau			64	
Tutuila			227	

and CoralNet data used in this study are provided in the **Supplementary Materials**.

RESULTS

Site-Scale Coral Cover Estimates

For both MHI and American Samoa sites, human-analyst, and CoralNet coral cover estimates were strongly correlated (Pearson's $r > 0.97$) for all training schemes. However, in both regions, statistical fits were better, i.e., differences between annotation methods were reduced and fit closer to 1:1 line in the more simplified training schemes (**Figure 2**). For MHI sites, the best fit was for the “BASE-HABITAT” training scheme, i.e., using the BASE classification with sites trained and automatically

annotated separately for each habitat type, for which the mean of CoralNet minus human-analyst coral cover estimates was $-0.6 \pm 3.4\%$ (mean \pm standard deviation, **Figure 2**). Among those MHI habitat types, the fit between human-analyst and CoralNet coral cover estimates was notably better for aggregate reef sites than for sites in other habitat types (**Figure 3**). For American Samoa sites, the best fit was for the BASE scheme – benthos classified to broad functional groups for which the mean difference between CoralNet and human-analyst site level estimates was $1.0 \pm 2.7\%$. Separately training and automatically analyzing American Samoa sites by island (“BASE-ISLAND” scheme) marginally worsened the fit.

The capacity of CoralNet to generate estimates of cover of common coral genera varied between regions and among genera (**Figure 4**). For MHI sites, relative to human-analysts, CoralNet

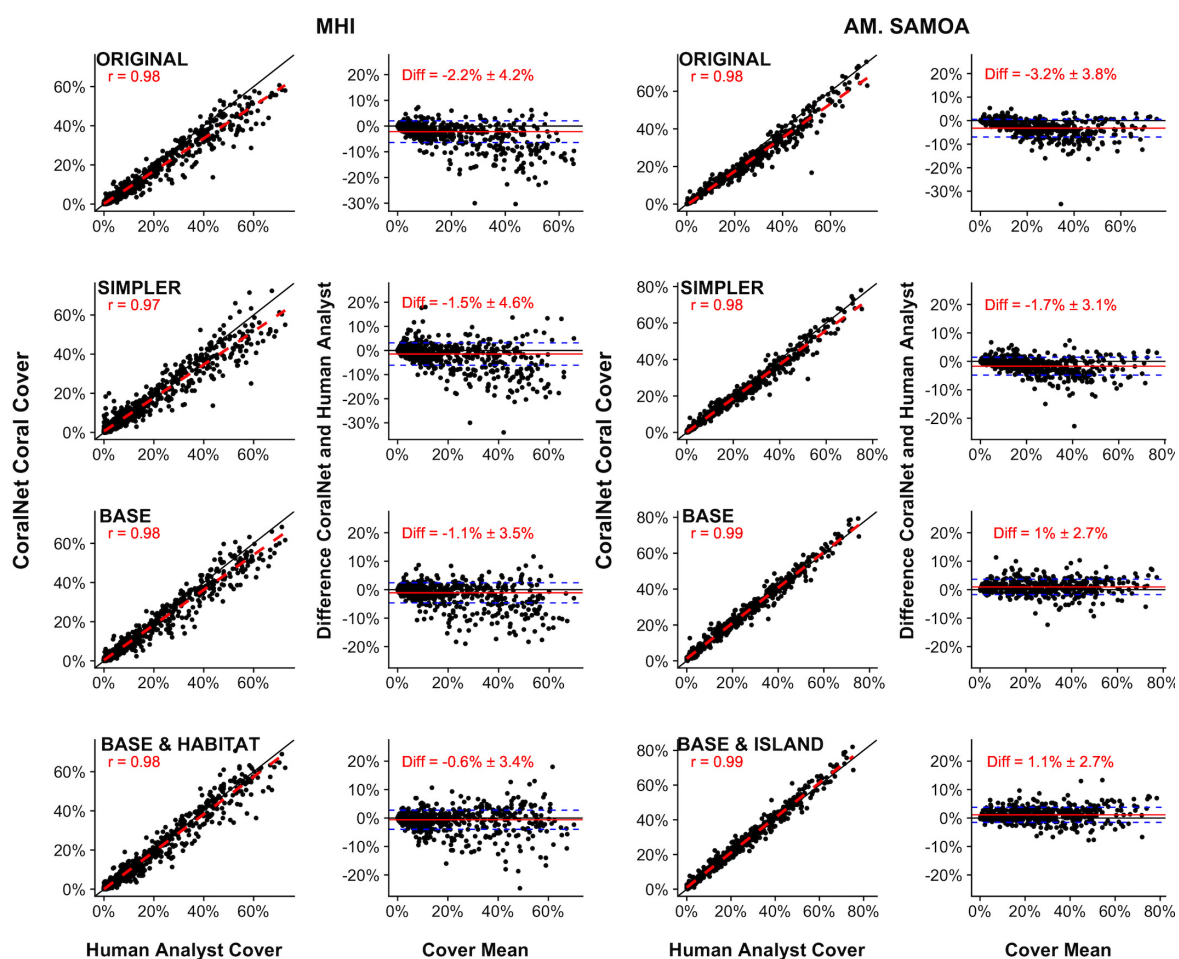


FIGURE 2 | Site-level coral cover by human analysts and CoralNet for different classification and training schemes. For each pair of figures, each point in the left-hand figures is a single site; the solid black line is the 1:1 line, the dashed red line is a linear fit of the point data, and “ r ” value shown is Pearson’s correlation. Each point in the right-hand figures is the difference between CoralNet and human-analyst cover estimates at a site, plotted against the mean of cover from the two annotation methods. The red horizontal line is the mean of the site-level difference in cover; and the blue dashed lines represent mean ± 1 standard deviation (SD). Training schemes are defined in **Supplementary Table S2**, but go from most complex (“ORIGINAL,” in which corals and macroalgae are generally identified to genus and below) to most simplified (“BASE,” in which benthos is analyzed to functional group only). The bottom row represents schemes in which CoralNet was trained using the BASE classification but with sites filtered by habitat type for MHI (“BASE-HABITAT”) and by island for American Samoa (“BASE-ISLAND”) (**Supplementary Table S2**). Total number of sites is 598 for MHI, and 468 for American Samoa. Correlations are significant ($p < 0.0001$) in all cases.

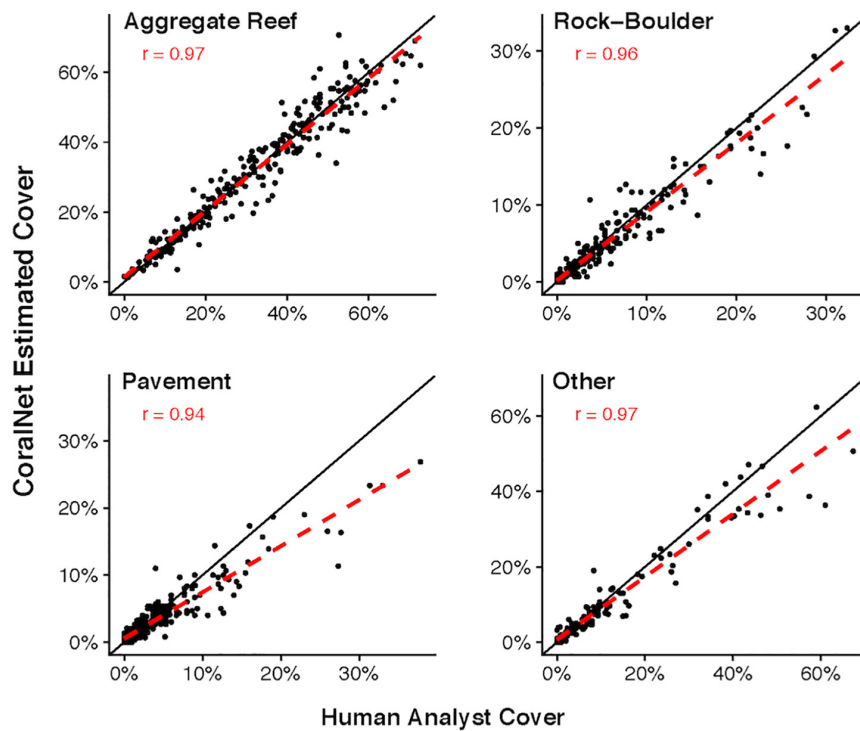


FIGURE 3 | MHI Site-level coral cover by human analysts and CoralNet within different habitat types. Each point represents a single site; the solid black line is the 1:1 line, and the dashed red line is a linear fit of the point data. Results are for CoralNet trained using the “BASE” classification (**Supplementary Table S2**). “*r*” values are Pearson’s correlation coefficients. Number of sites per habitat type are: 188 for aggregate reef; 167 for pavement; 159 for rock-boulder; and 84 for other habitats. Correlations are significant ($p < 0.0001$) in all cases.

generated similar estimates of *Porites* cover (Pearson’s $r = 0.98$, difference: $0.1 \pm 2.2\%$), tended to underestimate *Montipora* cover (Pearson’s $r = 0.92$, difference: $-1.7 \pm 5.7\%$), and was least well correlated with *Pocillopora* (Pearson’s $r = 0.81$, difference: $-0.1 \pm 1.1\%$). In contrast, for the four genera we assessed at American Samoa sites, CoralNet, and human-analyst cover estimates were strongly correlated (Pearson’s $r > 0.95$) and otherwise in relatively good agreement – the highest difference between CoralNet and human-analyst cover was $1.1 \pm 2.7\%$ for *Montipora*.

Site-Scale Estimates of Other Benthos

CoralNet performance for other broad benthic categories: macroalgae, CCA, sand/sediment, and turf, varied considerably between regions (**Figure 5**). For MHI sites, CoralNet tended to substantially overestimate turf cover (difference: $10.9 \pm 10.0\%$), the dominant component of benthos at many MHI sites, and underestimate other categories compared with human analysts (**Figure 5**). In contrast, CoralNet and human-analyst cover estimates of those groups were fairly consistent for American Samoa sites, particularly for CCA, which was abundant in that region (**Figure 5**). Relative to human-analysts, CoralNet also tended to overestimate turf cover at American Samoa sites, but to a much lower degree than in the MHI (difference: $6.2 \pm 5.7\%$, **Figure 5**). At American Samoan sites, CoralNet generated cover estimates for a number of algal sub-groupings that were similar to

those generated by human-analysts, including *Halimeda*, “other green macroalga” (Pearson’s $r > 0.96$ and relatively unbiased for both, **Supplementary Figure S1**), and encrusting macroalgae (e.g., *Peyssonnelia*, and encrusting growth forms of genera, such as *Lobophora*).

Comparisons Between CoralNet and Human-Analyst Pooled Coral Cover Estimates

The high degree of consistency between human-analysts and CoralNet in MHI site level coral cover, resulted in a mean difference between annotation methods of $0.8\% (\pm 0.7\% \text{ SD})$ when data were pooled by island and year (**Figure 6**). Of the 26 MHI island-years from which we have data, CoralNet and human-analyst coral cover estimates only twice differed by $> 2.5\%$ – for Oahu and Lanai, both in 2010. Coral cover estimates were relatively good at Niihau (which had low coral cover) and Hawaii Island, which had had average cover of 14.6% , but for which the difference between annotation methods was $< 0.3\%$ in all years (**Figure 6**). Concordance between annotation methods was lower at Oahu and Kauai, both of which had moderate to low coral cover – i.e., means of around $5\text{--}7\%$ – but where the difference between annotation methods was consistently $\sim 2\%$ in each year (**Figure 6**). Notably, for all island-year combinations, the differences between CoralNet and human-analyst estimates

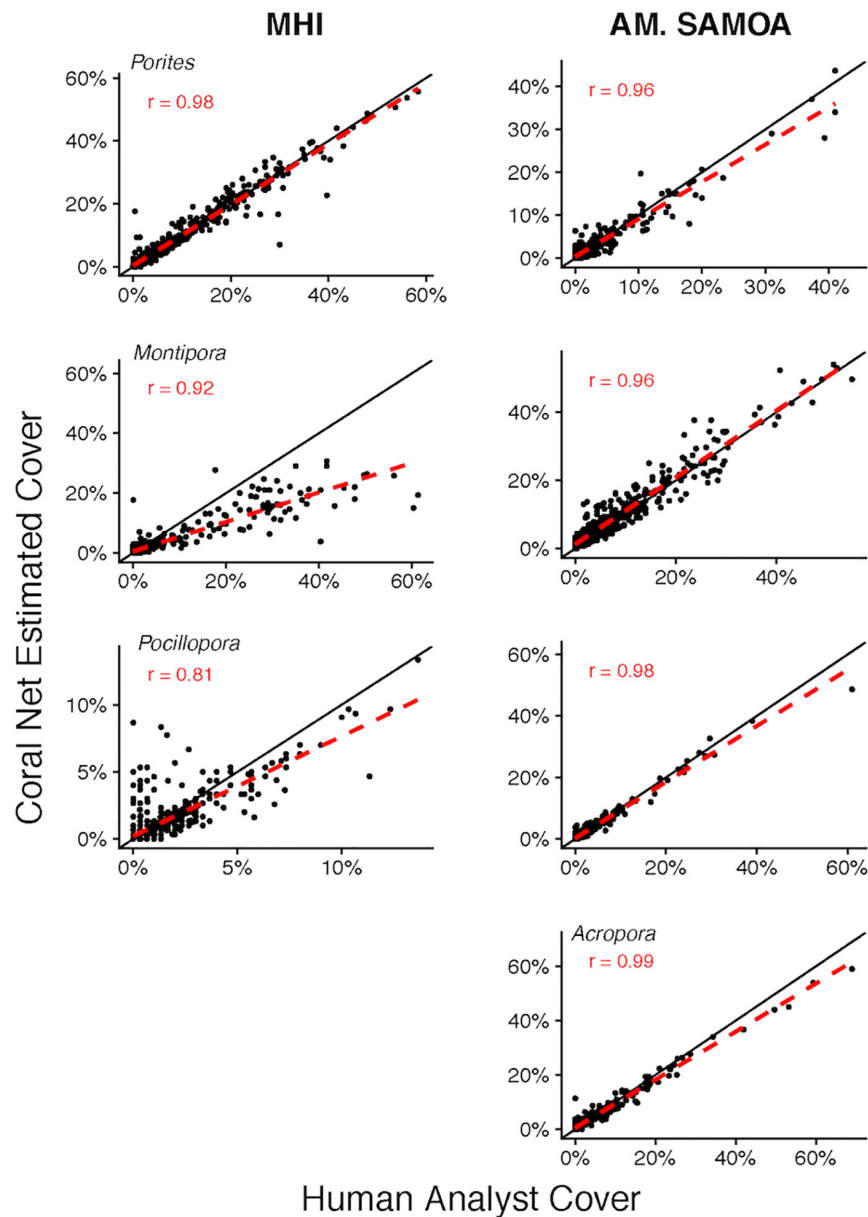


FIGURE 4 | Site-level coral cover of common genera by human analyst and CoralNet. Figures in the left column are for MHI sites, and in the right column for American Samoa. Each point represents a single site; the solid black line is the 1:1 line, and the dashed red line is a linear fit of the point data. *Acropora* were not recorded at MHI sites. CoralNet was trained using the “SIMPLER” classifications (**Supplementary Table S2**). “*r*” values are Pearson’s correlation coefficients. Total number of sites is 598 for MHI, and 468 for American Samoa. Correlations are significant ($p < 0.0001$) in all cases.

of coral cover (i.e., methodological differences) were relatively small compared to the uncertainty in the island-year estimate per method (i.e., the variability among sites within the island-year). Specifically, there was a substantial degree of overlap between CoralNet and human-analyst error bars for each island-year (**Figure 6**). Differences in relative performance of CoralNet compared to human-analysts may have been in part due to variation in the dominant coral genera at each island, as CoralNet island-year estimates were clearly better for *Porites* than for *Montipora* (**Supplementary Figure S2**).

CoralNet estimates of coral cover at American Samoa were higher than human-analyst estimates at all five islands. Differences in island-scale mean were $<1\%$ at Ofu and Olosega, Tau, and Tutuila, but 4.1% at Swains (**Figure 7**). The relatively poor performance of CoralNet at Swains may have been related to CoralNet underestimating both *Montipora* (the most abundant genus at Swains) and *Acropora* (**Supplementary Figure S3**). CoralNet estimates of algal cover at American Samoa were relatively good for data

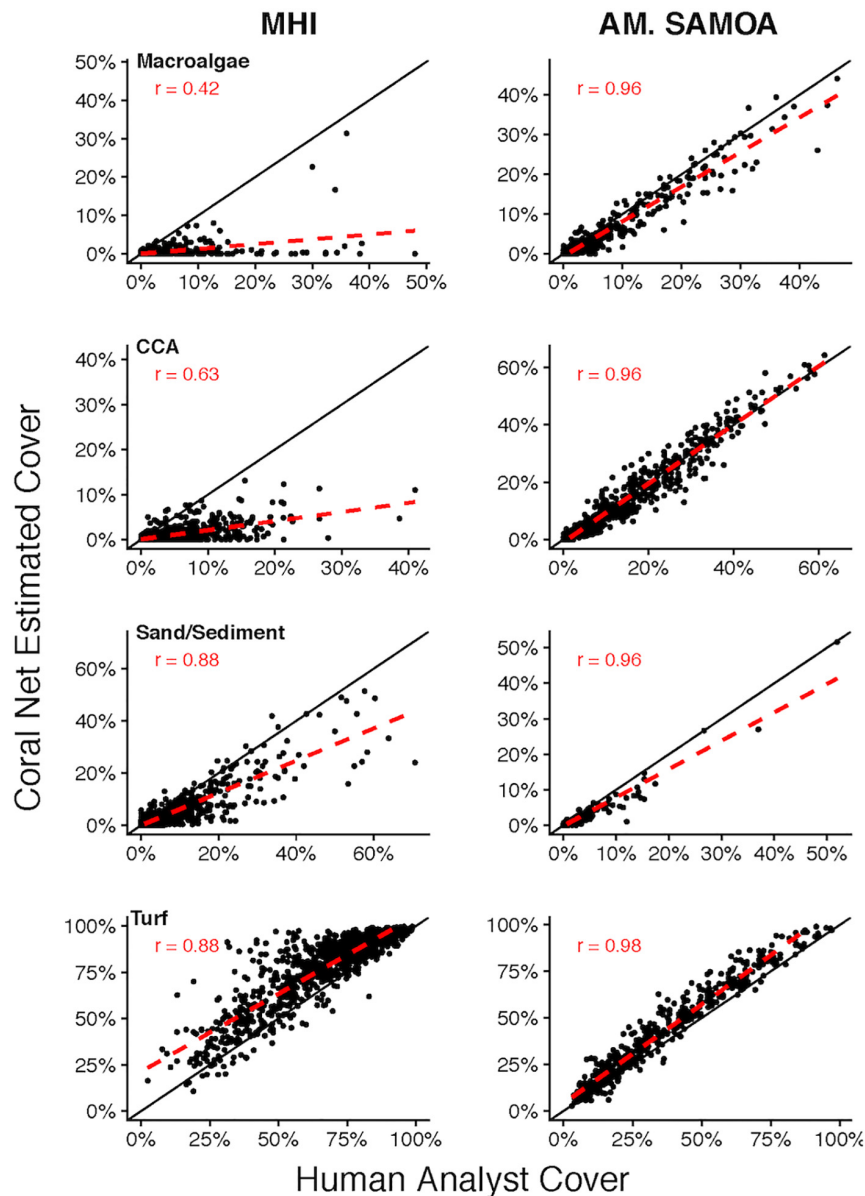


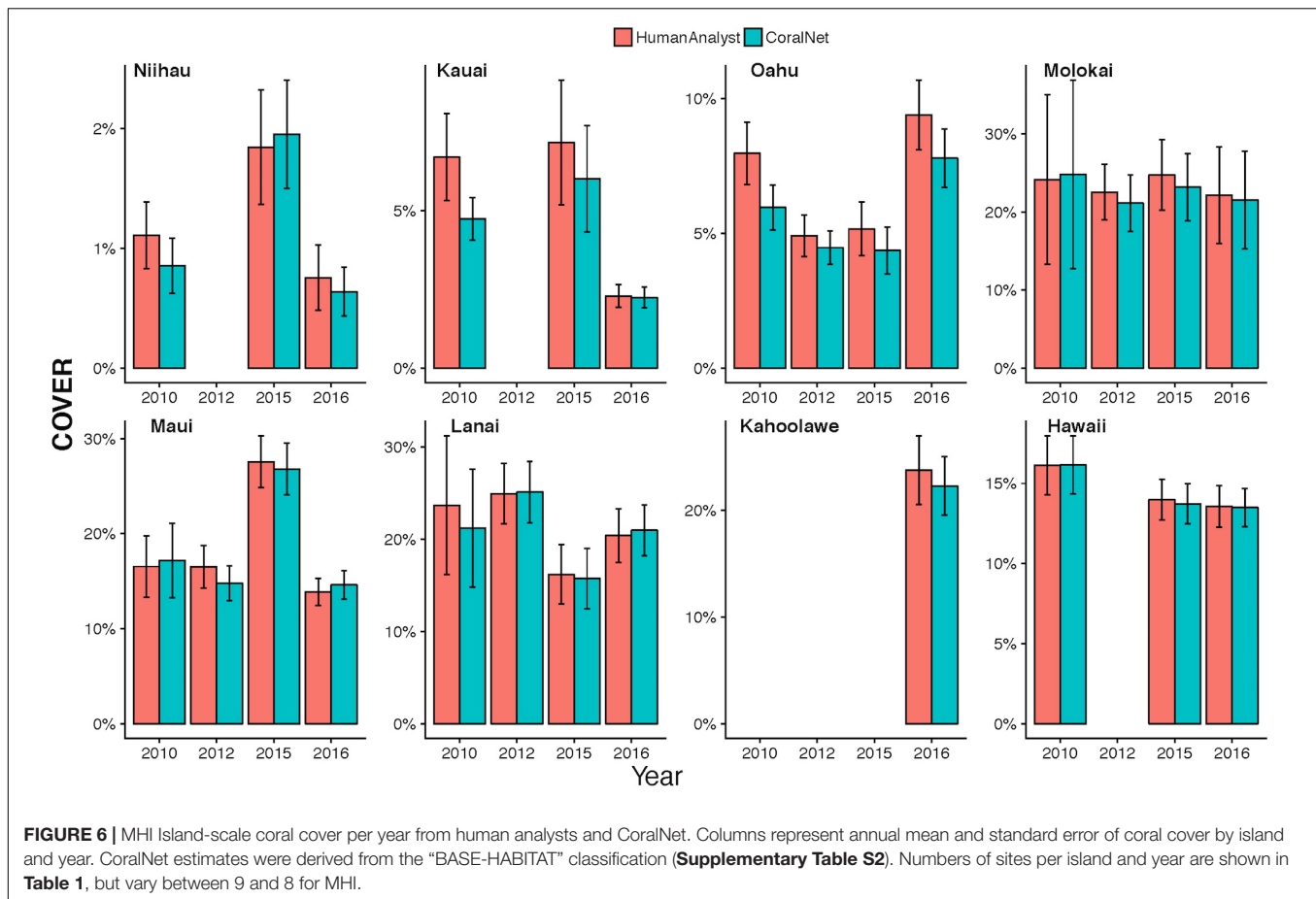
FIGURE 5 | Site-level coral cover of non-coral functional groups by human analyst and CoralNet. Figures on the left-hand side show MHI site data, and those on the right represent American Samoa sites. Each point denotes a single site; the solid black line is the 1:1 line, and the dashed red line is a linear fit of the point data. MHI CoralNet estimates were derived from the “BASE-HABITAT” classification. American Samoa CoralNet estimates were derived from the “BASE” classification (Supplementary Table S2). “*r*” values are Pearson’s correlation coefficients. Total number of sites is 598 for MHI, and 468 for American Samoa. Correlations are significant ($p < 0.0001$) in all cases.

pooled to island-scale, particularly for CCA and Halimeda (Supplementary Figure S4).

Relative Performance of CoralNet and Human-Analyst Data at Quantifying Differences Coral Cover in Space and Time

CoralNet performed similarly to human analysts when quantifying the magnitude and statistical significance of

differences in coral cover between island-year pairs. For both regions, there was close to 1:1 agreement between CoralNet and human-analyst estimates of difference in coral cover between island-years (Figure 8), indicating that CoralNet estimates were unbiased compared to those derived from human-analyst data. Also, of the 10 possible paired comparisons among islands in American Samoa, the same six pairs were consistently considered significantly different, whether CoralNet or human-analyst cover estimates were used (Figure 8). For the MHI, CoralNet, and human-analyst estimates yielded the same statistical result for



95% (310 of 325) of island-year pairs (**Figure 8**). In cases where the statistical outcome was different, that result was due to small differences in confidence intervals – e.g., results were marginally significant for human-analysts and marginally non-significant for CoralNet. There was also very little difference in the precision of human-analyst and CoralNet estimates of scales of differences between island-year pairs. Among MHI island-year pairs, CoralNet confidence intervals of difference were on average 95% of human-analyst confidence intervals; and for American Samoa island pairs, CoralNet confidence intervals were 104% of those from human-analyst estimates.

Impact of Training Set Size on Site Level Error

For the MHI BASE-HABITAT and American Samoa BASE-ISLAND training runs, mean site-level coral cover error (i.e., the mean difference between human-analyst and CoralNet site level cover) ranged from $1.1 \pm 1.4\%$ (mean \pm SD) at MHI rock-boulder sites, to $3.9 \pm 2.7\%$ at Swains (**Supplementary Figure S5**). For those training sets, which were the smallest sets used in each region, there was no evident association between mean error and the size of training set (which ranged from 7,050 previously annotated points at Swains to 34,050 at Tutuila, **Supplementary Figure S5**).

DISCUSSION

Our results demonstrate the potential to use fully-automated image analysis tools to quantify spatial and temporal differences in coral reef benthic cover. The imagery used in this study came from sites randomly located across all hard-bottom, <30 m fore reef habitats around five islands in American Samoa and eight islands in the MHI. Despite the broad geographic scope of our surveys, which encompass diverse coral communities, habitats, and ambient conditions – including light and turbidity – CoralNet systems were capable of generating estimates of coral cover that were highly comparable to those produced by human analysts. Our results therefore highlight the feasibility of developing a regional-scale automated image-analysis capability for key benthic features that could support multiple research and monitoring needs to increase the amount of data available to inform coral reef management.

An important step to improving comparability of CoralNet and human-analyst benthic cover estimates was to assess a range of classification schemes from relatively simple to relatively complex. CoralNet tended to underestimate coral cover relative to human analysts by an average of approximately 2–3% per site in the more complex classification schemes, but the bias was reduced to around 1% or less for the simplest schemes – in which all corals were grouped into a single category. We also found that

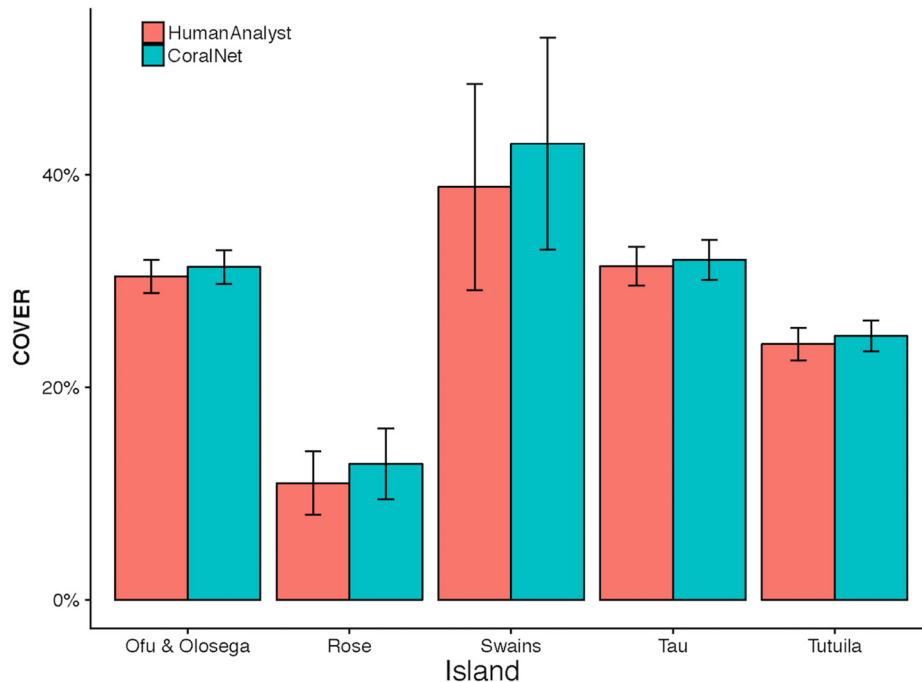


FIGURE 7 | American Samoa island-scale coral cover from human analysts and CoralNet. Coral cover mean and standard error is shown for each island. CoralNet estimates are for the “BASE” classification (**Supplementary Table S2**). Numbers of sites per island are shown in **Table 1**, but vary between 47 and 227 for American Samoa.

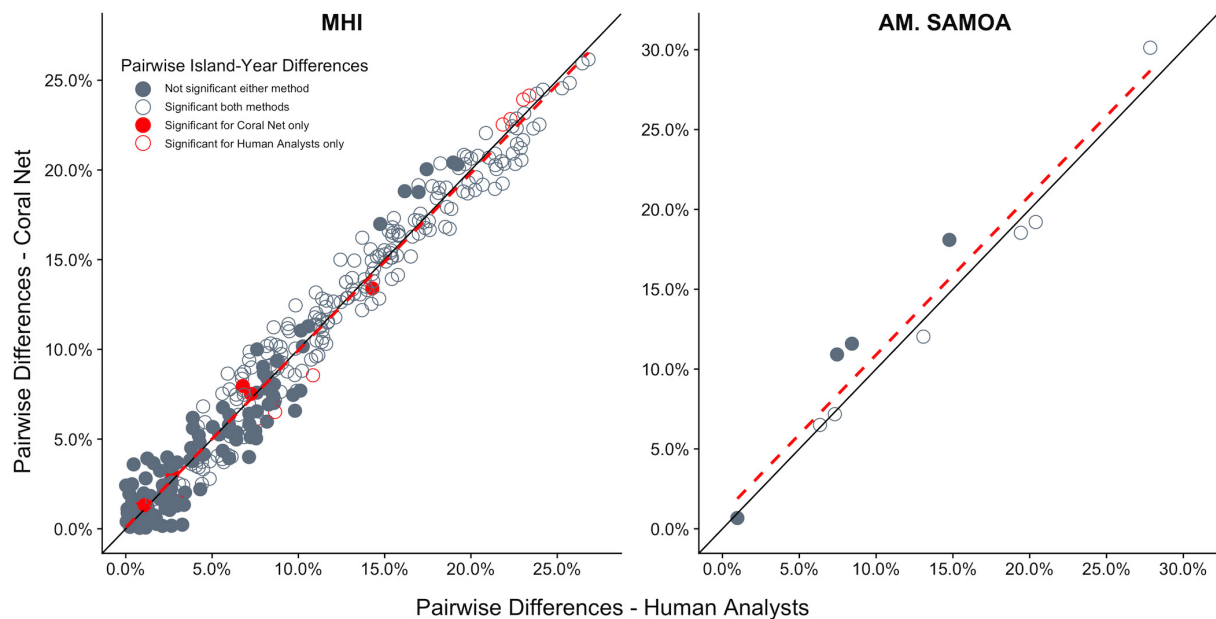


FIGURE 8 | Difference in cover between all island-year pairs for human-analyst and CoralNet. Each point represents one island-year pair (325 pairs in MHI, 10 for American Samoa). The black solid-line represent the 1:1 – i.e., difference in cover between island-years was identical for the two methods. The red hatched line is a linear fit of the points. Points shown in dark gray are cases where human-analyst and CoralNet produced the same statistical result. The 15 red points in MHI are cases where there was a difference in statistical outcome depending on the annotation method used. Solid circles represent island-year pairs for which human-analyst cover estimates did not significantly differ, and empty circles where the difference was significant.

training robots with imagery from a single comparable habitat improved performance. Estimates with known and relatively consistent bias can still be useful, as it is possible to adjust for that. Nevertheless, it seems desirable to reduce the scale of those differences where possible. Our study does not prove that simple schemes should generally be expected to improve CoralNet performance, but it does indicate that testing a range of classification schemes is likely necessary to maximize the utility of the CoralNet system for any particular research question and situation.

Although we compare CoralNet data against human-analyst data, we do not intend to imply that human-analyst data perfectly represents benthic cover. In fact, differences in performance among even experienced analysts tend to be of a similar scale to that which we found between CoralNet and overall human-analysts for the best performing classification schemes, i.e., ~1% difference in coral cover estimates per site and considerably higher for some other benthic groups (Beijbom et al., 2015; González-Rivero et al., 2016). Arguably, as well as reducing the resources required to conduct analysis, one of the key benefits of using automated analysis tools such as CoralNet is that analyst performance will be consistent across the entire image dataset, and thus patterns in space and time do not risk being confounded or obscured by differences in analyst performance. Our study clearly demonstrates the potential to use CoralNet in this way – as CoralNet performed nearly identically to our pool of human analysts when quantifying the scale and statistical significance of differences in coral cover between island-year pairs. Using a large pool of trained and experienced analysts, as we do, is one way to reduce human-analyst bias between survey periods and locations. However, that is not always possible, and automated analysis is likely to be particularly useful for survey programs that rely on a small number of analysts, or where there is high turnover of analysts – as both of those increase scope for inconsistent analyst performance to lead to bias.

Even with the large training sets available to us, automated classification was strongly dissimilar to human-annotations for some common groups, such as most algal categories in MHI. Previous studies using Support Vector Machines have tended to show relatively poor analysis performance, both automated and manual, for algal groups (Beijbom et al., 2015; González-Rivero et al., 2016). Turf is a particularly challenging group (Beijbom et al., 2015; González-Rivero et al., 2016), as there is inherently great variability within that category, from nearly bare and heavily cropped substrate to relatively thick turf mats along with substantial differences in color and texture of different nominally “turf” patches. High variability within and among human analysts leads to a high degree of error in human-analyst estimates, as well as inconsistent training of the automated classifier, both of which likely contributed to the relatively high degree of difference between human-analyst and CoralNet estimates for some of these categories. Notably, for American Samoa, but not MHI, there was strong agreement between CoralNet and human-analysts for CCA. This may partly have been due to much greater abundance of CCA in American Samoa (mean cover ~18% across all sites) than in MHI (~4%), but may also have been due to substantial differences in CCA appearance

between regions. In American Samoa, CCA forms distinct, conspicuous and often brightly-colored patches, whereas, in the MHI, CCA patches are typically small and less-distinct within a mosaic of other algal and benthic groups.

Certainly, the high degree of variability in algal morphology is likely to present challenges for both human and automated image analysis, which highlights the need for careful consideration of the objectives of automated analysis. Even when it is not possible to adequately train an automated analyst for all categories of interest, there is likely still considerable scope for using automation to reduce human-analyst workload. For example, running CoralNet in alleviation mode involves CoralNet providing classification suggestions together with a measure of confidence allowing human analysts to accept or modify those suggestions (Beijbom et al., 2015).

The ability to train automatic annotators capable of robustly quantifying coral cover from essentially all shallow water reefs within two disparate regions highlights the scope for automated image analysis to greatly increase the quantity of benthic data that can be feasibly and cost-effectively generated by monitoring programs. Even with a human-assisted workflow, the image analysis bottleneck and associated costs could be greatly reduced, thereby allowing for more imagery to be collected from more sites. Such an approach would improve data quality – by increasing representativeness of data or by increasing precision and therefore statistical power. The greatest potential gains might come from fully-automated image analysis combined with use of autonomous platform technologies to increase the amount and scale of image acquisition (Griffin et al., 2017; Manderson et al., 2017).

Given the evident capacity of automated analysis technology to generate high quality benthic data, it may be desirable to develop image-analysis tools suitable for much wider use. For example, citizen scientists could take advantage of trained and proven automated analysis robots from their region. Users of those systems could thereby rapidly convert imagery into data useful for their own purposes and potentially contribute to regional data pools. That would presumably require some degree of standardization – e.g., in image resolution, photograph orientation, and image footprint. Collectively, this could lead to large, highly-comparable datasets suitable for purposes such as landscape ecology, habitat mapping, and marine spatial planning (González-Rivero et al., 2016).

Automated image analysis technology is likely to greatly improve in coming years, perhaps in part through accounting for 3-dimensional structure of benthic features, as can be derived from structure-for-motion photogrammetry (Burns et al., 2015; Edwards et al., 2017). However, it is clear that automated analysis tools, such as CoralNet, are already capable of generating benthic cover estimates comparable to those derived from human analysts, and suitable for many purposes. The capacity to rapidly convert large quantities of geo-referenced imagery into robust cover data has the potential to transform what can be achieved by coral reef monitoring and survey programs, particularly if integrated with advances in automated image acquisition. Fully realizing those benefits will require standardization of analysis methodologies, image acquisition, and classification schemes,

and a commitment to increased sharing of data and imagery (Durden et al., 2017). Doing so will greatly increase the utility of resulting data for a wide range of conservation, management, and research purposes.

AUTHOR CONTRIBUTIONS

IW, CC, BV-A, TO, and BS conceived the research question. IW, CC, and OB analyzed the data. IW and CC wrote the manuscript with considerable help from all the authors. All the authors provided critical feedback and helped with interpreting the results.

FUNDING

This project was funded by NOAA's Coral Reef Conservation Program (<http://coralreef.noaa.gov>), NOAA's Pacific Islands Fisheries Science Center, and the NMFS Automated Image Analysis Strategic Initiative. The findings and conclusion in this manuscript are those of the authors and do not necessarily represent the views of NOAA. The use of trade, firm, or

corporation names in this publication is for the convenience of the reader and does not constitute an official endorsement or approval of any product or service to the exclusion of others that may be suitable.

ACKNOWLEDGMENTS

We thank the members of Ecosystem Science Division's fish and benthic survey team and partners for their tireless efforts in collecting data around American Samoa and the main Hawaiian Islands, as well as the dedicated officers and crews of the NOAA Ships *Hi'alakai* and *Oscar Elton Sette* for providing safe and productive platforms for our research teams. We also thank Paula Ayotte for GIS support with this project.

SUPPLEMENTARY MATERIAL

The Supplementary Material for this article can be found online at: <https://www.frontiersin.org/articles/10.3389/fmars.2019.00222/full#supplementary-material>

REFERENCES

- Armstrong, R. A., Singh, H., Torres, J., Nemeth, R. S., Can, A., Roman, C., et al. (2006). Characterizing the deep insular shelf coral reef habitat of the hind bank marine conservation district (US Virgin Islands) using the seabed autonomous underwater vehicle. *Cont. Shelf Res.* 26, 194–205. doi: 10.1016/j.csr.2005.10.004
- Ayotte, P., McCoy, K., Heenan, A., Williams, I., and Zamzow, J. (2015). *Coral Reef Ecosystem Division Standard Operating Procedures: Data Collection for RAPID Ecological Assessment Fish Surveys*. Available at: http://www.pifsc.noaa.gov/library/pubs/admin/PIFSC_Admin_Rep_15-07.pdf. (accessed December 2011).
- Beijbom, O., Edmunds, P. J., Roelfsema, C., Smith, J., Kline, D. I., Neal, B. P., et al. (2015). Towards automated annotation of benthic survey images: variability of human experts and operational modes of automation. *PLoS One* 10:e0130312. doi: 10.1371/journal.pone.0130312
- Bland, J. M., and Altman, D. G. (1986). Statistical methods for assessing agreement between two methods of clinical measurement. *Lancet* 1, 307–310. doi: 10.1016/s0140-6736(86)90837-8
- Burke, L., Reyter, K., Spalding, M., and Perry, A. (2011). *Reefs at Risk: Revisted*. Washington, DC: World Resources Institute.
- Burns, J., Delparte, D., Gates, R., and Takabayashi, M. (2015). Integrating structure-from-motion photogrammetry with geospatial software as a novel technique for quantifying 3D ecological characteristics of coral reefs. *PeerJ* 3:e1077. doi: 10.7717/peerj.1077
- Coral, N. O. A. A., and Program. (2014). *NOAA Coral Reef Conservation Program. National Coral Reef Monitoring Program. Silver*. Available at: http://docs.lib.noaa.gov/noaa_documents/NOS/CRCP/noaa_crmp_national_coral_reef_monitoring_plan_2014.pdf (accessed March 18, 2015).
- Couch, C. S., Burns, J. H. R., Liu, G., Steward, K., Gutlay, T. N., Kenyon, J., et al. (2017). Mass coral bleaching due to unprecedented marine heatwave in papahānaumokuākea marine national monument (Northwestern Hawaiian Islands). *PLoS One* 12:e0185121. doi: 10.1371/journal.pone.0185121
- De'ath, G., Fabricius, K. E., Sweatman, H., and Puotinen, M. (2012). The 27-year decline of coral cover on the great barrier reef and its causes. *Proc. Natl. Acad. Sci. U.S.A.* 109, 17995–17999. doi: 10.1073/pnas.1208909109
- Dollar, S. J. (1982). Wave stress and coral community structure in hawaii. *Coral Reefs* 1, 71–81. doi: 10.1007/BF00301688
- Durden, J. M., Luo, J. Y., Alexander, H., Flanagan, A. M., and Grossmann, L. (2017). Integrating “big data” into aquatic ecology: challenges and opportunities. *Limnol. Oceanogr. Bull.* 26, 101–108. doi: 10.1002/lob.10213
- Edinger, E. N., Jompa, J., Limmon, G. V., Widjatmoko, W., and Risk, M. J. (1998). Reef degradation and coral biodiversity in Indonesia: effects of land-based pollution, destructive fishing practices and changes over time. *Mar. Pollut. Bull.* 36, 617–630. doi: 10.1016/s0025-326x(98)00047-2
- Edwards, C. B., Eynaud, Y., Williams, G. J., Pedersen, N. E., Zgliczynski, B. J., Gleason, A. C. R., et al. (2017). Large-area imaging reveals biologically driven non-random spatial patterns of corals at a remote reef. *Coral Reefs* 36, 1291–1305. doi: 10.1007/s00338-017-1624-3
- Fabricius, K. E. (2005). Effects of terrestrial runoff on the ecology of corals and coral reefs: review and synthesis. *Mar. Pollut. Bull.* 50, 125–146. doi: 10.1016/j.marpolbul.2004.11.028
- Glynn, P. W. (1976). Some physical and biological determinants of coral community structure in the eastern pacific. *Ecol. Monogr.* 46, 431–456. doi: 10.2307/1942565
- González-Rivero, M., Beijbom, O., Rodríguez-Ramírez, A., Holtrop, T., González-Marrero, Y., Ganase, A., et al. (2016). Scaling up ecological measurements of coral reefs using semi-automated field image collection and analysis. *Remote Sens.* 8:30. doi: 10.3390/rs8010030
- González-Rivero, M., Bongaerts, P., Beijbom, O., Pizarro, O., Friedman, A., Rodríguez-Ramírez, A., et al. (2014). The catlin seaview survey - kilometre-scale seascape assessment, and monitoring of coral reef ecosystems. *Aquat. Conserv. Mar. Freshw. Ecosyst.* 24, 184–198. doi: 10.1002/aqc.2505
- Griffin, K. J., Hedge, L. H., González-Rivero, M., Hoegh-Guldberg, O. I., and Johnston, E. L. (2017). An evaluation of semi-automated methods for collecting ecosystem-level data in temperate marine systems. *Ecol. Evol.* 7, 4640–4650. doi: 10.1002/ece3.3041
- Heenan, A., Williams, I. D., Acoba, T., DesRochers, A., Kosaki, R. K., Kanemura, T., et al. (2017). Long-term monitoring of coral reef fish assemblages in the western central pacific. *Sci. Data* 4:170176. doi: 10.1038/sdata.2017.176
- Heron, S. F., Maynard, J. A., van Hooidonk, R., and Eakin, C. M. (2016). Warming trends and bleaching stress of the world's coral reefs 1985–2012. *Sci. Rep.* 6:38402. doi: 10.1038/srep38402
- Hughes, T. P., Anderson, K. D., Connolly, S. R., Heron, S. F., Kerry, J. T., Lough, J. M., et al. (2018a). Spatial and temporal patterns of mass bleaching of corals in the anthropocene. *Science* 359, 80–83. doi: 10.1126/science.aan8048
- Hughes, T. P., Kerry, J. T., Baird, A. H., Connolly, S. R., Dietzel, A., Eakin, C. M., et al. (2018b). Global warming transforms coral reef assemblages. *Nature* 556, 492–496. doi: 10.1038/s41586-018-0041-2

- Johansson, C. L., van de Leemput, I. A., Depczynski, M., Hoey, A. S., and Bellwood, D. R. (2013). Key herbivores reveal limited functional redundancy on inshore coral reefs. *Coral Reefs* 32, 963–972. doi: 10.1007/s00338-013-1044-y
- Kohler, K. E., and Gill, S. M. (2006). Coral point count with excel extensions (CPCe): a visual basic program for the determination of coral and substrate coverage using random point count methodology. *Comput. Geosci.* 32, 1259–1269. doi: 10.1016/j.cageo.2005.11.009
- Langenkämper, D., Zuurwilt, M., Schoening, T., and Nattkemper, T. W. (2017). BIIGLE 2.0 - browsing and annotating large marine image collections. *Front. Mar. Sci.* 4:83. doi: 10.3389/fmars.2017.00083
- LeCun, Y., Bengio, Y., and Hinton, G. (2015). Deep learning. *Nature* 521, 436–444. doi: 10.1038/nature14539
- Lozada-Misa, P., Schumacher, B. D., and Vargas-Angel, B. (2017). *Analysis of Benthic Survey Images Via Coralnet: A Summary of Standard Operating Procedures and Guidelines*. Administrative Report No. H-17-02. Honolulu, HI: Joint Institute for Marine and Atmospheric Research University.
- Manderson, T., Li, J., Dudek, N., Meger, D., and Dudek, G. (2017). Robotic coral reef health assessment using automated image analysis. *J. Field Robot.* 34, 170–187. doi: 10.1002/rob.21698
- Marcos, M. S. A., Soriano, M., and Saloma, C. (2005). Classification of coral reef images from underwater video using neural networks. *Opt. Express* 13, 8766–8771.
- Maynard, J. A., Marshall, P. A., Johnson, J. E., and Harman, S. (2010). Building resilience into practical conservation: identifying local management responses to global climate change in the southern great barrier reef. *Coral Reefs* 29, 381–391. doi: 10.1007/s00338-010-0603-8
- McClanahan, T. R., Donner, S. D., Maynard, J. A., MacNeil, M. A., Graham, N. A. J., Maina, J., et al. (2012). Prioritizing key resilience indicators to support coral reef management in a changing climate. *PLoS One* 7:e42884. doi: 10.1371/journal.pone.0042884
- Miller, J., Muller, E., Rogers, C., Waara, R., Atkinson, A., Whelan, K. R. T., et al. (2009). Coral disease following massive bleaching in 2005 causes 60% decline in coral cover on reefs in the us virgin Islands. *Coral Reefs* 28, 925–937. doi: 10.1007/s00338-009-0531-7
- Porter, J., Kosmynin, V., Patterson, K., Porter, K., Jaap, W., Wheaton, J., et al. (2001). “Detection of coral reef change by the florida keys coral reef monitoring project,” in *The Everglades, Florida Bay, and Coral Reefs of the Florida Keys* eds J. W. Porter and K. G. Porter (Boca Raton, FL: CRC Press), doi: 10.1201/9781420039412-32
- Salih, A., Larkum, A., Cox, G., Kühl, M., and Hoegh-Guldberg, O. (2000). Fluorescent pigments in corals are photoprotective. *Nature* 408, 850–853. doi: 10.1038/35048564
- Shihavuddin, A. S. M., Gracias, N., Garcia, R., Gleason, A., and Gintert, B. (2013). Image-based coral reef classification and thematic mapping. *Remote Sens.* 5, 1809–1841. doi: 10.3390/rs5041809
- Stokes, M. D., and Deane, G. B. (2009). Automated processing of coral reef benthic images. *Limnol. Oceanogr. Methods* 7, 157–168. doi: 10.4319/lom.2009.7.157
- Swanson, D., Bailey, H., Schumacher, B., Ferguson, M., and Vargas-Angel, B. (2018). *Ecosystem Sciences Division Standard Operating Procedures: Data Collection for Rapid Ecological Assessment Benthic Surveys*. Honolulu, HI: Pacific Islands Fisheries Science Center.
- Trygonis, V., and Sini, M. (2012). Photoquad: a dedicated seabed image processing software, and a comparative error analysis of four photoquadrat methods. *J. Exp. Mar. Bio. Ecol.* 42, 99–108. doi: 10.1016/j.jembe.2012.04.018
- Williams, S. B., Pizarro, O., Webster, J. M., Beaman, R. J., Mahon, I., Johnson-Roberson, M., et al. (2010). Autonomous underwater vehicle-assisted surveying of drowned reefs on the shelf edge of the great barrier reef, Australia. *J. Field Robot.* 27, 675–697. doi: 10.1002/rob.20356

Conflict of Interest Statement: OB created and continues to maintain and manage the CoralNet system. However, CoralNet is free to use and is in no way a commercial enterprise.

The remaining authors declare that the research was conducted in the absence of any commercial or financial relationships that could be construed as a potential conflict of interest.

Copyright © 2019 Williams, Couch, Beijbom, Oliver, Vargas-Angel, Schumacher and Brainard. This is an open-access article distributed under the terms of the Creative Commons Attribution License (CC BY). The use, distribution or reproduction in other forums is permitted, provided the original author(s) and the copyright owner(s) are credited and that the original publication in this journal is cited, in accordance with accepted academic practice. No use, distribution or reproduction is permitted which does not comply with these terms.



Targeted Sampling by Autonomous Underwater Vehicles

Yanwu Zhang^{1*}, John P. Ryan¹, Brian Kieft¹, Brett W. Hobson¹, Robert S. McEwen¹, Michael A. Godin², Julio B. Harvey³, Benedetto Barone⁴, James G. Bellingham⁵, James M. Birch¹, Christopher A. Scholin¹ and Francisco P. Chavez¹

¹ Monterey Bay Aquarium Research Institute, Moss Landing, CA, United States, ² IntuAware, Northampton, MA, United States, ³ Department of Molecular, Cell, and Developmental Biology, University of California, Santa Cruz, Santa Cruz, CA, United States, ⁴ Department of Oceanography, University of Hawaii at Manoa, Honolulu, HI, United States, ⁵ Department of Applied Ocean Physics and Engineering, Woods Hole Oceanographic Institution, Woods Hole, MA, United States

OPEN ACCESS

Edited by:

Leonard Pace,
Schmidt Ocean Institute,
United States

Reviewed by:

Xing Liu,
Zhejiang University of Technology,
China

Alessandro Ridolfi,
University of Florence, Italy
Alexander LeBaron Forrest,
University of California, Davis,
United States

*Correspondence:

Yanwu Zhang
yzhang@mbari.org

Specialty section:

This article was submitted to
Ocean Observation,
a section of the journal
Frontiers in Marine Science

Received: 08 January 2019

Accepted: 04 July 2019

Published: 14 August 2019

Citation:

Zhang Y, Ryan JP, Kieft B,
Hobson BW, McEwen RS, Godin MA,
Harvey JB, Barone B, Bellingham JG,
Birch JM, Scholin CA and Chavez FP
(2019) Targeted Sampling by
Autonomous Underwater Vehicles.
Front. Mar. Sci. 6:415.
doi: 10.3389/fmars.2019.00415

In the vast ocean, many ecologically important phenomena are temporally episodic, localized in space, and move according to local currents. To effectively study these complex and evolving phenomena, methods that enable autonomous platforms to detect and respond to targeted phenomena are required. Such capabilities allow for directed sensing and water sample acquisition in the most relevant and informative locations, as compared against static grid surveys. To meet this need, we have designed algorithms for autonomous underwater vehicles that detect oceanic features in real time and direct vehicle and sampling behaviors as dictated by research objectives. These methods have successfully been applied in a series of field programs to study a range of phenomena such as harmful algal blooms, coastal upwelling fronts, and microbial processes in open-ocean eddies. In this review we highlight these applications and discuss future directions.

Keywords: targeted sampling, autonomous underwater vehicle (AUV), Environmental Sample Processor (ESP), phytoplankton patch, upwelling front, open-ocean eddy

1. INTRODUCTION

Traditional ship-based methods for detecting and sampling dynamic ocean features are often laborious and difficult, and long-term tracking of such features using ships is practically impossible. Consequently, there is a growing effort toward enabling autonomous underwater vehicles (AUVs) to autonomously find, track, and sample ephemeral oceanographic features. Several studies (Cruz and Matos, 2010a,b; Petillo et al., 2010; Cazenave et al., 2011; Zhang et al., 2012a) have used AUVs to detect and track the thermocline based on temperature gradients in the vertical dimension. In Petillo and Schmidt (2014), two AUVs collaboratively surveyed internal waves by using adaptive thermocline tracking and vehicle-to-vehicle track-and-trail behaviors via acoustic communications. AUVs were also used to locate seafloor hydrothermal vents (German et al., 2008; Paduan et al., 2018), trace chemical plumes (Farrell et al., 2005; Kukulya et al., 2018), and survey oil plumes emanating from a damaged wellhead (Camilli et al., 2010; Zhang et al., 2011). The AUV detected the plume based on a proxy signal (e.g., optical backscatter signal for hydrothermal vent plumes) and followed a tracking strategy to trace the plume source and map the plume field. In addition to using a suite of physical, chemical, and bulk biological sensors, some AUVs are now equipped with water samplers to take advantage of the vehicle's mobility to collect material while underway (Camilli et al., 2010; Ryan et al., 2010a; Govindarajan et al., 2015; Pargett et al., 2015; Wulff et al., 2016; Billings et al., 2017; Scholin et al., 2017).

In parallel with AUV hardware developments, a long-sought goal is to develop onboard intelligence that allows the AUV to autonomously assess prevailing conditions and determine when and where to focus survey observations and water sample collections. We call this “targeted sampling”—the use of AUVs to detect specific oceanic features based on real-time analysis of sensor data, and to respond to detection through vehicle path adaptation and water sample acquisition. Different from pre-programmed missions, the AUV adapts behavior in real time to track, map, and sample the target. Scientific insights into particular ocean phenomena are used to derive AUV algorithms for executing targeted sampling while taking advantage of the vehicle’s flexible behaviors and growing endurance. In section 2, we present methodology and results from four field experiments that are representative of these growing capabilities. We conclude and propose future work in section 3.

2. AUV TARGETED SAMPLING METHODS AND FIELD EXPERIMENTS

The design principle underlying targeted sampling methods is to combine oceanographic knowledge of ocean phenomena of interest, and AUV capabilities that enable effective observational studies of the targeted feature. This combination, implemented by onboard signal processing, permits studies of the targeted feature at temporal and spatial resolutions not previously possible. Example field experiments highlighted here represent the studies of two coastal ocean phenomena—harmful algal blooms (HABs) and frontal systems, and one open-ocean phenomenon—the deep chlorophyll maximum (DCM) layer.

2.1. Capturing Peak Samples in a Phytoplankton Patch

Phytoplankton distributions in the ocean are patchy, and this patchiness has consequences for many ecosystem processes including primary production, the survival and growth of zooplankton and fish larvae, and the development of HABs (Lasker, 1975; Cowles et al., 1998; McManus et al., 2008; Ryan et al., 2008, 2010c; Sullivan et al., 2010). A common manifestation of patchiness is the formation of a vertically limited layer of maximum plankton abundance within the water column. In coastal ecosystems these layers can have small vertical scales, with a thickness ranging from < 1 m to a few meters (Cowles et al., 1998; McManus et al., 2008; Ryan et al., 2010c). To study the planktonic community in layers, it is critical to acquire water samples within the areas of high abundance and vertically within the layer as it fluctuates in space and time.

Traditionally, Niskin bottles are lowered from the ship deck to take water samples. Locating a phytoplankton layer requires a human operator to inspect the cast profiles of chlorophyll fluorescence and manually determine triggering depths. This process is difficult to sustain for extensive surveys of mesoscale (~ 100 km) features, and the 1-m vertical scale of the bottle makes it difficult to localize sample acquisition within phytoplankton layers having small (< 1 m) vertical scales. To advance capabilities for high-resolution mapping and

sampling of these features, we enabled an AUV to autonomously find the phytoplankton layer within vehicle profiles of high-resolution surveys and trigger water sampling precisely in the layer. Our Dorado AUV is equipped with 20 (previously 10) syringe-like water samplers, called “gulgurs” (Ryan et al., 2010a, bottom photo in **Figure 1**). Once triggered, each gulper acquires a 1.5-l water sample in 1–2 s. A HOBI Labs HydroScat-2 sensor measures chlorophyll fluorescence at 700 nm wavelength and optical backscatter at 420 and 700 nm wavelengths. Consistency of gulper triggering within the phytoplankton layer is essential to successful sampling. We designed a peak-capture algorithm to meet this challenge.

In any real-time gradient-based peak detection algorithm, a detection delay is unavoidable—the peak is detected only when it has just passed. Such a delay is especially problematic for a thin layer because a small delay will miss the peak. To overcome this peak-detection delay problem, our algorithm (Zhang et al., 2010) takes advantage of the AUV’s yo-yo trajectory (in the vertical dimension), as illustrated in **Figure 1**. In one yo-yo cycle, e.g., an ascent profile followed by a descent profile, the vehicle crosses the layer twice, measuring a fluorescence peak at each crossing. At two consecutive crossings separated by a short distance ($< \text{several hundred meters}$), the two peaks are expected to have similar signal levels. On the vehicle’s first crossing (on the ascent profile), peak detection (by tracking the fluorescence signal’s slope) comes with a delay, but a sliding window saves the true peak value. On the second crossing (on the descent profile), water sampling is triggered the moment the fluorescence measurement reaches the saved peak value, resulting in sample capture right on the peak. If the second peak is slightly lower than the first (i.e., the saved signal peak level), no triggering will occur. This actually serves our objective of sampling only high peaks. Conversely, if the second peak is slightly higher than the first, sampling will be triggered at a signal level slightly before (hence slightly lower than) the second peak, yet already at a high near-peak level. The algorithm keeps track of the fluorescence background level and the baseline of the peaks in real time to ensure that peak detection is tuned to ambient conditions. The algorithm cross-checks for concurrent high values of optical backscatter to ensure that sampling targets true peaks of planktonic particles and not physiologically-controlled variations in fluorescence.

This peak-capture algorithm has been running on the Dorado AUV in a series of field programs since 2009. In the spring of 2015, Monterey Bay, CA experienced the most toxic HAB event ever recorded in this region (Ryan et al., 2017), caused by diatoms of the genus *Pseudo-nitzschia*. Two AUV missions (during upwelling relaxation and intensification, respectively) on a transect in the southern bay are shown in **Figure 2**. The AUV ran on a yo-yo trajectory between 2-m depth and the shallower of 75-m depth and 10-m altitude above the seabed. The depth of the HAB biomass maximum varied between near surface and 30-m depth. In this study, two 2nd-generation Environmental Sample Processors (2G-ESPs) (Scholin, 2013; Scholin et al., 2017) were moored at fixed depths of 4 and 6 m in the southern and northern bay, respectively. The ESP measurements provided key information for planning AUV deployments, but they missed HAB peaks when the local biomass was deeper

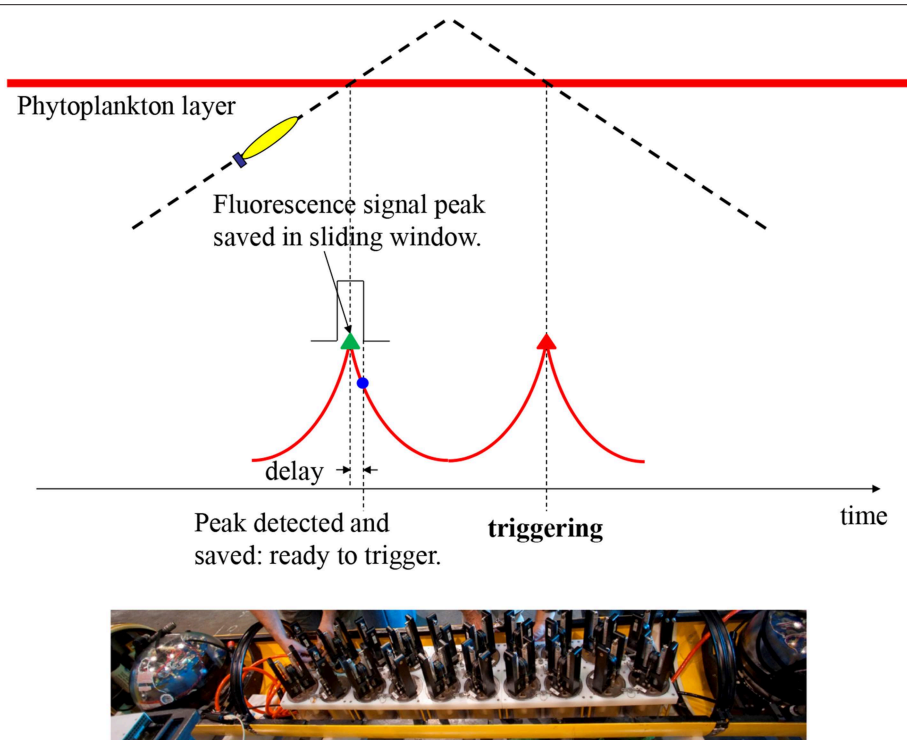


FIGURE 1 | Illustration of the AUV algorithm for capturing peak samples in a phytoplankton patch. On the AUV's yo-yo trajectory through a phytoplankton layer, the vehicle detects the peak chlorophyll fluorescence (with delay) on the first crossing, and saves the peak signal level. On the second crossing, the AUV triggers sampling at the saved peak fluorescence level with no delay. The bottom photo (courtesy of Todd Walsh) shows 20 “gulper” samplers installed in the midsection of a Dorado-class AUV.

than the sample intake of the moored ESPs. In contrast, the Dorado AUV mobility and the peak-capture algorithm enabled consistent sampling within the maximum HAB biomass, as shown in **Figure 2B**. Analyses of the gulper water samples showed very high concentrations of *Pseudo-nitzschia* (**Figure 2A**) and particulate domoic acid (pDA) (**Figure 2B**), the biotoxin within their cells.

Whether a patch is near the surface, in a subsurface layer, or near the seabed, the peak-capture algorithm is effective because it applies signal processing in the time domain throughout the full depth range of AUV profiles. For example, studies of larval ecology employing this algorithm in Monterey Bay in October 2009 detected the highest larval abundances in a dense phytoplankton patch that was subducted to the seabed within an upwelling front (Ryan et al., 2014). A ship-based survey would not have targeted near-seabed waters or provided the high-resolution data required to detect the patch within the small-scale front. In contrast, the AUV resolved the physical-biological interaction and precisely targeted the feature of interest.

2.2. Classifying and Sampling Distinct Water Types Across a Coastal Upwelling Front

Coastal upwelling is a wind-driven physical process that brings cooler, saltier, and usually nutrient-rich deep water upward to replace warmer, fresher, nutrient-depleted surface water.

In addition to bringing up nutrients to support primary production, upwelling generates dynamic fronts that influence marine ecology in a variety of ways (Barber and Smith, 1981). Fronts occur frequently in the major eastern boundary upwelling systems of the northeastern and southeastern Atlantic and Pacific (Smith, 1981). In Monterey Bay, when a northwesterly wind persists along the coast, upwelling develops at Point Año Nuevo, and the cold upwelling filaments spread southeastward across the mouth of the bay, as shown in the satellite sea surface temperature (SST) images (**Figure 3**). In the northern bay, however, the water column typically remains stratified (warm at surface and cold at depth) because that region is sheltered from upwelling-inducing wind by the Santa Cruz mountains, and sheltered from the upwelling filaments by the coastal recess, thus forming an “upwelling shadow” (Graham et al., 1992; Graham and Largier, 1997). The boundary between the stratified, biologically enriched water of the upwelling shadow, and the unstratified, biologically impoverished water transported southeastward from the Point Año Nuevo upwelling center, is called the “upwelling front.” Upwelling fronts support enriched phytoplankton and zooplankton populations, as well as physical processes that can locally enhance plankton aggregation and nutrient supply (Woodson et al., 2009; Ryan et al., 2010b,c, 2014; Harvey et al., 2012), thus playing an important role in structuring ocean ecosystems. Detection and sampling of upwelling fronts is important for ecological studies of coastal upwelling systems (Zhang et al., 2015).

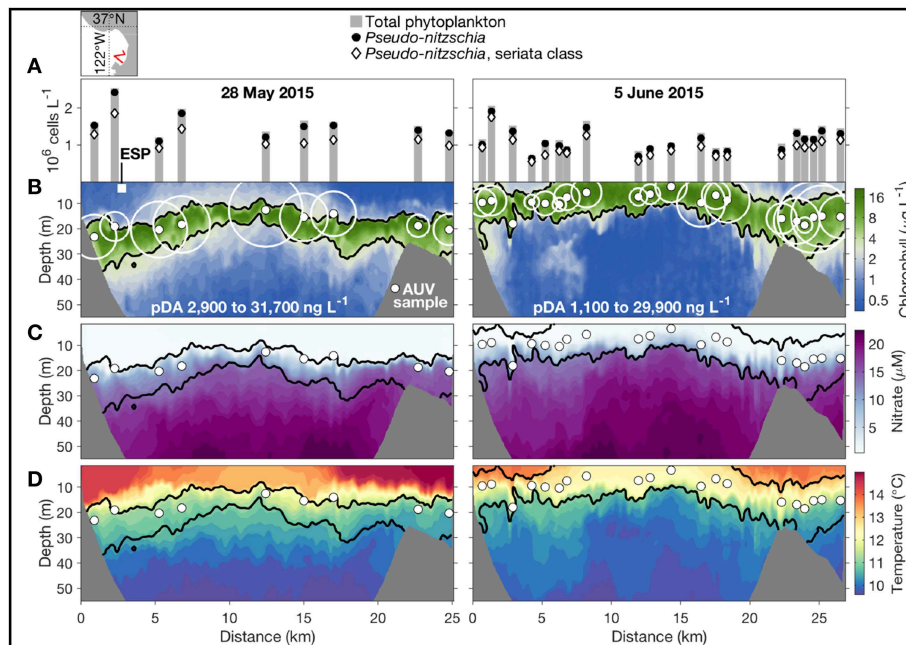


FIGURE 2 | In May–June 2015, the Dorado AUV acquired water samples precisely from the HAB layer in two missions on a transect in the southern Monterey Bay, during upwelling relaxation (left) and intensification (right). The AUV transect's location is shown in the upper-left map. The AUV started from the southeast end of the transect. **(A)** Cell counts from microscopy, shown directly above the sample locations (indicated by the small solid white circles in **B–D**). **(B–D)** Chlorophyll concentration, nitrate concentration, and temperature along the AUV transect. In **(B)**, the pDA concentration of each sample is represented by the size of the open white circle, and the range of pDA in each transect is noted. The position and depth of the moored 2G-ESP is indicated by the white square in **(B)**. Adapted from Ryan et al. (2017) with permission.

Upwelling fronts move due to variations in wind and ocean circulation, as shown in **Figure 3**. These fronts are also associated with strong physical and biological gradients that occur on small spatial scales. These attributes of fronts present challenges to effective observation and sampling. Traditional ship-based methods are incapable of autonomously detecting and sampling fronts. Further, they are laborious and costly¹. The physical process of upwelling offers an excellent classifier for distinguishing upwelling from stratified water columns: the former is much more homogeneous vertically than the latter. An AUV yo-yo trajectory provides a convenient way to measure water column vertical homogeneity. Hence we developed an AUV algorithm to autonomously distinguish between upwelling and stratified water columns based on vertical temperature homogeneity, and to accurately locate an upwelling front based on the horizontal gradient of vertical temperature homogeneity (Zhang et al., 2012b,c). We defined a metric, the vertical temperature homogeneity index (VTHI), as follows (Zhang et al., 2012c):

$$VTHI = \frac{1}{M} \sum_{i=1}^M |Temp_{depth_i} - \frac{1}{M} \sum_{i=1}^M Temp_{depth_i}| \quad (1)$$

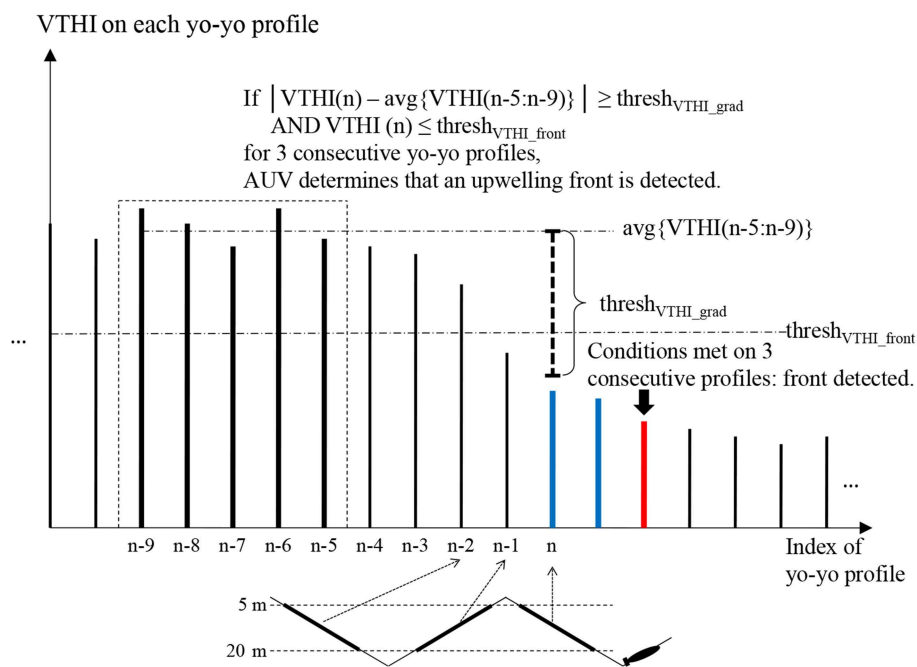
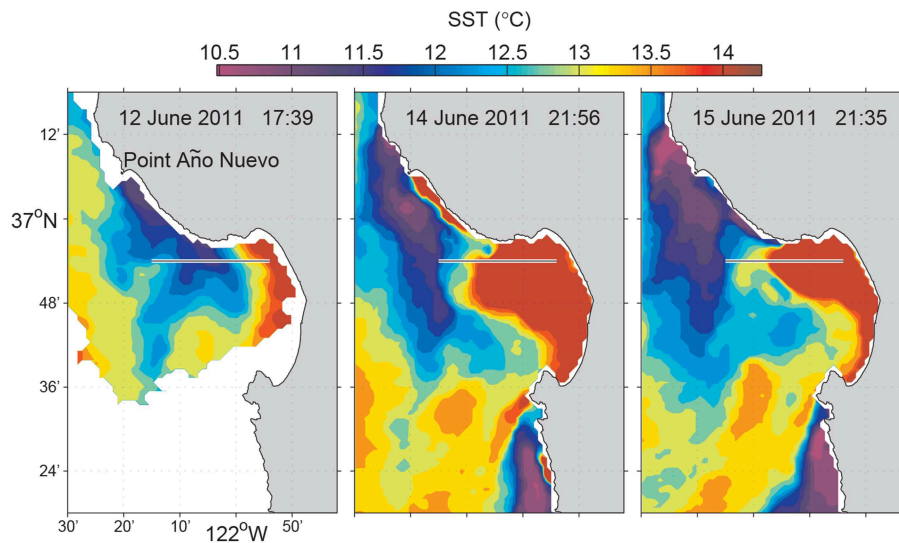
where i is the depth index, and M is the total number of depths included in calculating VTHI. $Temp_{depth_i}$ is the measured temperature at the i th depth. $\frac{1}{M} \sum_{i=1}^M Temp_{depth_i}$ is the average

temperature of those depths. $|Temp_{depth_i} - \frac{1}{M} \sum_{i=1}^M Temp_{depth_i}|$ measures the difference (absolute value) between the temperature at each individual depth and the depth-averaged temperature. The averaged difference over all participating depths, VTHI, is a measure of the vertical homogeneity of temperature in the water column, which is significantly smaller in upwelling water than in stratified water.

Figure 4 illustrates the front detection algorithm. Suppose an AUV flies from a stratified water column to an upwelling water column on a yo-yo trajectory. On each yo-yo profile (descent or ascent), the AUV records temperatures at the participating depths to calculate VTHI in real time. The conditions for front detection are: (1) VTHI falls below a threshold $thresh_{VTHI_front}$. (2) The horizontal gradient (absolute value) of VTHI exceeds a threshold $thresh_{VTHI_grad}$. To avoid false detection due to measurement noise or existence of isolated water patches, the algorithm determines front detection only when both conditions are satisfied on three consecutive yo-yo profiles.

The first deployment of this algorithm in an AUV sampling mission was in a frontal study in Monterey Bay on 13 June 2011. The Dorado AUV flew on a 31-km transect on latitude 36.9°N from an upwelling shadow region (stratified water column), through an upwelling front, into an upwelling water column. This latitude provided a relatively high probability of encountering strongly contrasting water types across an upwelling front (Zhang et al., 2012c), based on multi-year satellite SST and chlorophyll fluorescence line height data for the month of June that showed

¹ Research vessel daily operational cost ranges from \$20,000 to \$60,000.



Running the autonomous front detection algorithm, the AUV successfully classified the three distinct water types, accurately located the narrow front, and acquired targeted water samples from the three water types, as shown in **Figure 5**. The algorithm allocated the ten gulpers to the three types of water columns as follows: three in the stratified water, four in the upwelling front, and the remaining three in the upwelling water. More gulpers were allocated for the upwelling front because of high

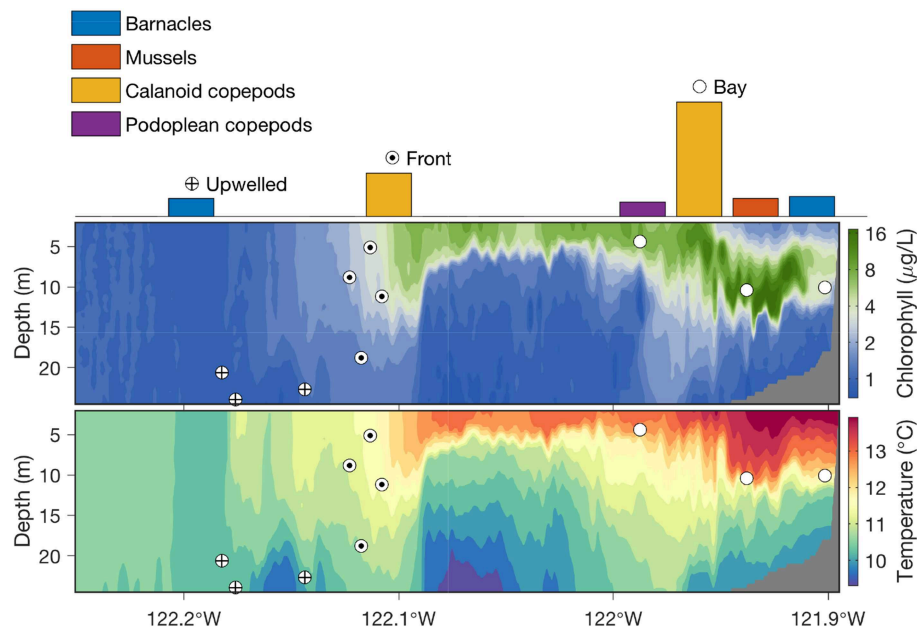


FIGURE 5 | In the 2011 frontal sampling experiment in Monterey Bay, the Dorado AUV flew westward on a 31-km transect along 36.9°N, on a yo-yo trajectory from the surface to 25-m depth (except for a shallow-water portion near the east end of the transect). Chlorophyll fluorescence and temperature measured by the AUV are shown in the upper and lower panels, respectively. Locations of where the AUV's ten gulpers were triggered in the three distinct water columns are marked by the corresponding symbols. Zooplankton abundance in the water samples is shown by color-coded bars.

interest in studying plankton populations inside the front, and also because it was very hard to acquire water samples from the narrow front using traditional methods. Within the stratified water where phytoplankton populations formed dense patches, the AUV directed sampling by applying the peak-capture algorithm (Figure 1) to target the dense patches of planktonic organisms. After the AUV was recovered, the 10 water samples were analyzed using the sandwich hybridization assay (SHA) method (Scholin et al., 1999; Harvey et al., 2012) to measure zooplankton (mussels, barnacles, calanoid copepods, and podoplean copepods) RNA signals. The result (Zhang et al., 2012c) showed that mussel larvae, calanoid copepods, and podoplean copepods were most abundant in the stratified upwelling shadow region, where a subsurface phytoplankton layer was sampled. These organisms were not detected in the upwelling water column on the offshore side of the front. Calanoid copepods were moderately abundant in waters collected from the upwelling front. By integrating horizontal localization of physical features and vertical localization of biological features, targeted sampling capabilities enabled an AUV to autonomously conduct “surgical sampling” of a complex marine ecosystem.

2.3. Tracking a Physical and Biological Front From Upwelling to Relaxation

Using the *VTHI* metric, we developed an AUV algorithm for tracking a stratification front (Zhang et al., 2012b) as it moves due to variations in wind and ocean circulation. Suppose an AUV starts from a strongly stratified water column (where *VTHI* is high), flying toward a weakly stratified water column (where

VTHI is low) on a yo-yo trajectory. When *VTHI* falls below a threshold, the vehicle determines that it has passed the front and entered the weakly stratified water column. The AUV continues flight in the weakly stratified water for a certain distance so as to sufficiently survey the frontal zone and this water type, and then reverses course to fly back to the strongly stratified water. On this course, when *VTHI* rises above the threshold, the AUV determines that it has repassed the front and re-entered the strongly stratified water column. The AUV continues flight in this water type for a certain distance, and then reverses course to fly back to the weakly stratified water. To prevent false detection, the algorithm confirms front crossing only when *VTHI* satisfies the threshold on a certain number of consecutive yo-yo profiles. The AUV repeats the above cycle, thus effectively tracking the dynamic front.

In June 2012, a Tethys-class long-range AUV (LRAUV) (Bellingham et al., 2010; Hobson et al., 2012) ran this algorithm to study the evolution of a frontal zone in Monterey Bay through a period of variability in upwelling intensity (Zhang et al., 2015), as shown in Figure 6. The LRAUV flew on a yo-yo trajectory between the surface and 50 m depth on latitude 36.9°N. The vehicle's average horizontal speed was 0.9 m/s, and its average vertical speed was 0.24 m/s.

The LRAUV made 23 frontal crossings in 4 days, as shown in Figure 7. In the active upwelling phase from 8 to 10 June, an upwelling filament extended southeastward from the Point Año Nuevo upwelling center to the mouth of the bay (Figure 6). As shown in the left panel of Figure 7, the LRAUV tracked the front between the strongly stratified upwelling shadow water

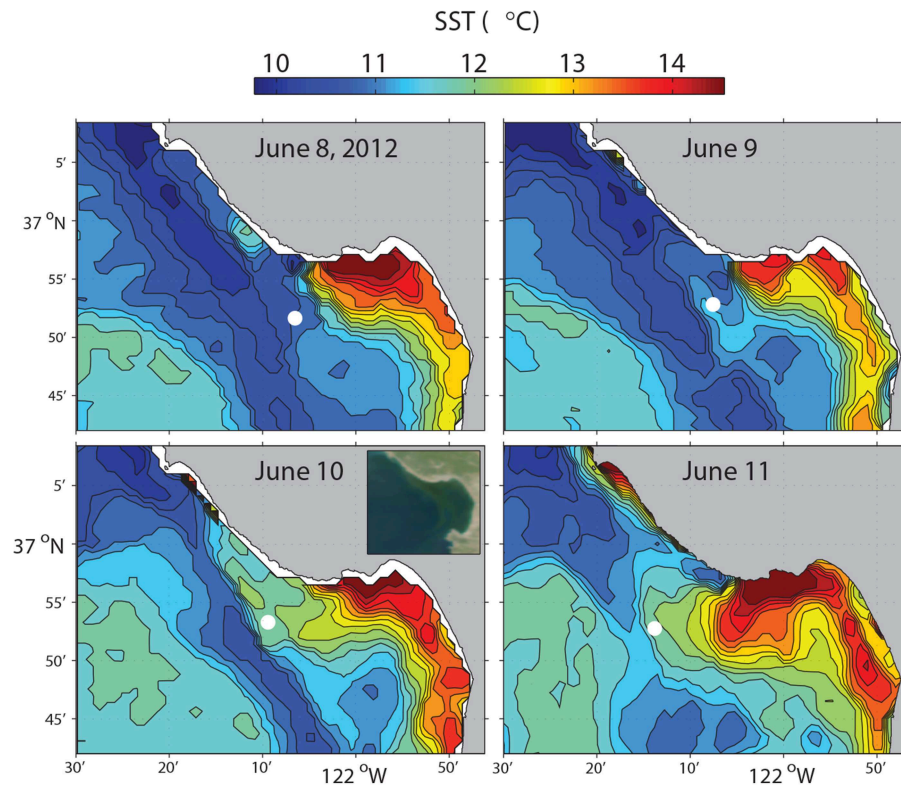


FIGURE 6 | Satellite SST of Monterey Bay on 08-Jun 21:09, 09-Jun 22:30, 10-Jun 22:09, 11-Jun 21:48 (PDT), 2012. The circles mark the LRAUV-tracked front locations which were within 4 h of each SST acquisition time. Satellite ocean color at 10-Jun 12:54 (PDT) is shown in the inset in the lower-left panel. Reused from Zhang et al. (2015) with permission.

(on the inshore side) and the vertically homogenized upwelling filament (on the offshore side). In the relaxation phase from 10 to 12 June, the upwelling filament waned, and the upwelling shadow advanced westward for about 10 km to come in direct contact with the warmer coastal transition zone (CTZ) water [the CTZ refers to the zone between the near-shore upwelling region and the offshore California Current (Huyer et al., 1991)]. The LRAUV tracked the front between the strongly stratified upwelling shadow water (on the inshore side) and the weakly stratified CTZ water (on the offshore side). What enabled the LRAUV to stay with the stratification front through changing conditions was targeting the strong horizontal gradient of *VTHI*. On each instance of front detection, the vehicle adapted path (continuing flight for 4 km and then reversing course) to focus observations on the frontal zone.

The stratification front was also a persistent biological front between the strongly stratified phytoplankton-enriched water inshore of the front, and the weakly stratified phytoplankton-poor water offshore of the front (Figure 7). The biogeochemical nature of the water types to either side of the front changed in response to relaxation of upwelling. The most significant biogeochemical changes from the active upwelling phase to the relaxation phase were increased chlorophyll concentrations on the inshore side of the front (shown in the right panel of Figure 7) and associated increase in oxygen and decrease in nitrate (Zhang

et al., 2015). This was consistent with enhanced productivity in the upwelling shadow during the relaxation response. The LRAUV front tracking provided an unprecedentedly detailed depiction of the frontal zone from active upwelling to relaxation.

2.4. Tracking and Sampling the Microbial Community in the Deep Chlorophyll Maximum Layer in an Open-Ocean Eddy

In the open ocean, photosynthesis is limited by low concentrations of nutrients in shallow water that receives the most sunlight. At the base of the nutrient impoverished surface layer (~100 m depth), nutrient concentrations increase across the strong density gradient of the pycnocline. This creates a vertically limited layer in which photosynthetic microbes can access both nutrients from below and light from above. With its locally enhanced concentration of the photosynthetic pigment chlorophyll, this layer is referred to as the deep chlorophyll maximum (DCM) (Huisman et al., 2006; Cullen, 2015). The DCM is a ubiquitous feature of open-ocean ecosystems.

Eddies alter the vertical distributions of nutrients and DCM microbial populations, thereby influencing the functioning of open-ocean ecosystems and global biogeochemical cycles (McGillicuddy, 2016). In cyclonic eddies (counterclockwise in the northern hemisphere), upward

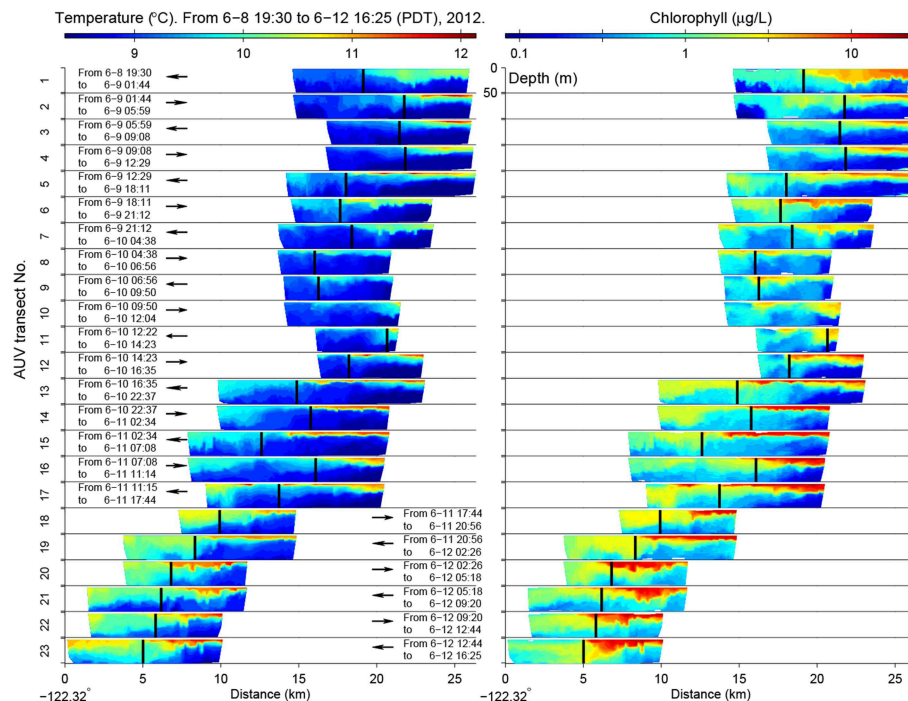
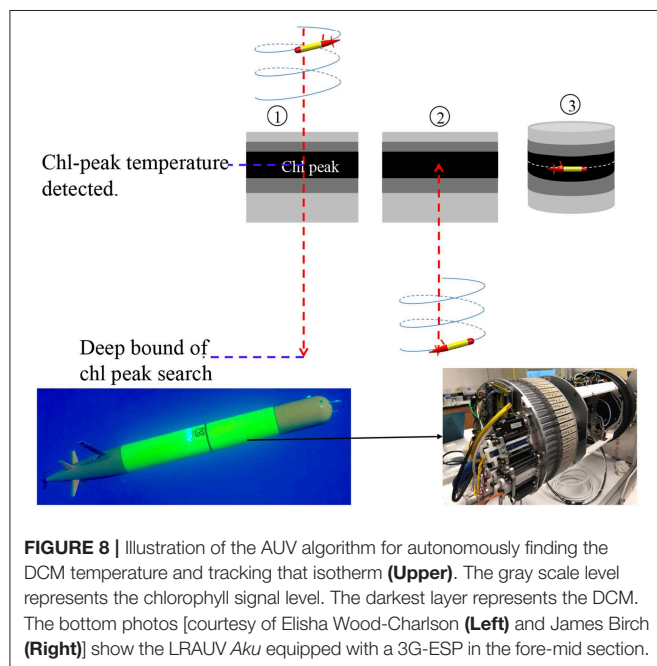


FIGURE 7 | In the 2012 front tracking experiment in Monterey Bay, LRAUV-measured temperature (**Left**) and chlorophyll (**Right**) from the surface to 50 m depth on the 23 front-crossing transects. The vehicle's flight direction is indicated by the arrow (the inshore side is on the right). The LRAUV-tracked front location is marked by the vertical bar. The time range of each transect is also noted. Reused from Zhang et al. (2015) with permission.



transport of nutrients and DCM populations enhances both nutrient and light resources for photosynthesis, resulting in increased productivity and biomass, and changes in

species composition and export of organic matter to the deep sea (Vaillancourt et al., 2003; Brown et al., 2008).

Studies of how eddies influence open-ocean microbial populations have largely relied on ship-based sampling strategies. While this approach permits synoptic descriptions of eddies and microbial populations, it cannot provide effective sampling of DCM microbial populations in their natural frame of reference, which is moving with ocean currents (i.e., Lagrangian).

Horizontal and temporal variations of DCM depth tend to follow those of an isopycnal layer (Letelier et al., 1993; Karl et al., 2002). When density variation is dominated by temperature variation, an isopycnal can be effectively tracked by tracking an isotherm. We developed an algorithm to enable a Tethys-class LRAUV to autonomously track the DCM layer by locking onto the isotherm corresponding to the chlorophyll peak (Zhang et al., 2019a), and to sample the DCM layer using an autonomous robotic sampler designed as a payload in the LRAUV, the 3rd-generation ESP (3G-ESP) (Pargett et al., 2015; Scholin et al., 2017).

The autonomous isotherm finding and tracking algorithm is illustrated in **Figure 8**. It comprises three steps: (1) The AUV descends from the sea surface to a deep bound that is sufficiently deeper than the anticipated DCM depth. On the descent, the AUV finds the peak of the low-pass filtered chlorophyll fluorescence signal, and the corresponding temperature. (2) Once reaching the deep bound, the AUV turns to an ascent. (3) On the ascent, when the AUV reaches the chlorophyll-peak associated temperature, the vehicle stops

Trajectories of *Aku* (red), *Mola* (white), and *Opah* (green) from 28-Mar 13:57 to 1-Apr 14:34 overlaid on 31-Mar 14:00 CMEMS SLA and geostrophic current velocity map

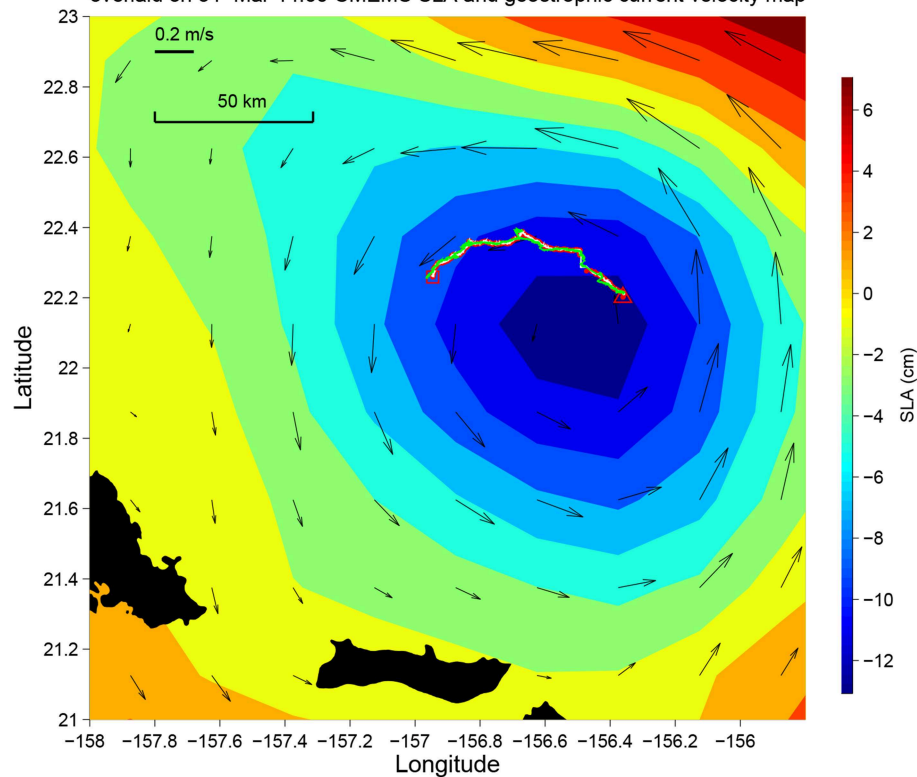


FIGURE 9 | The trajectories of *Aku*, *Opah*, and *Mola* during *Aku*'s 4-day sampling mission in the 2018 Hawaiian Eddy Experiment. Their trajectories are overlaid on the Copernicus Marine Environment Monitoring Service (CMEMS) sea level anomaly (SLA) and geostrophic current velocity map. The triangle and the square mark the start and the end of the mission, respectively. Time is in Hawaii Standard Time (HST).

ascending and thereafter actively adjusts its depth to remain at that temperature.

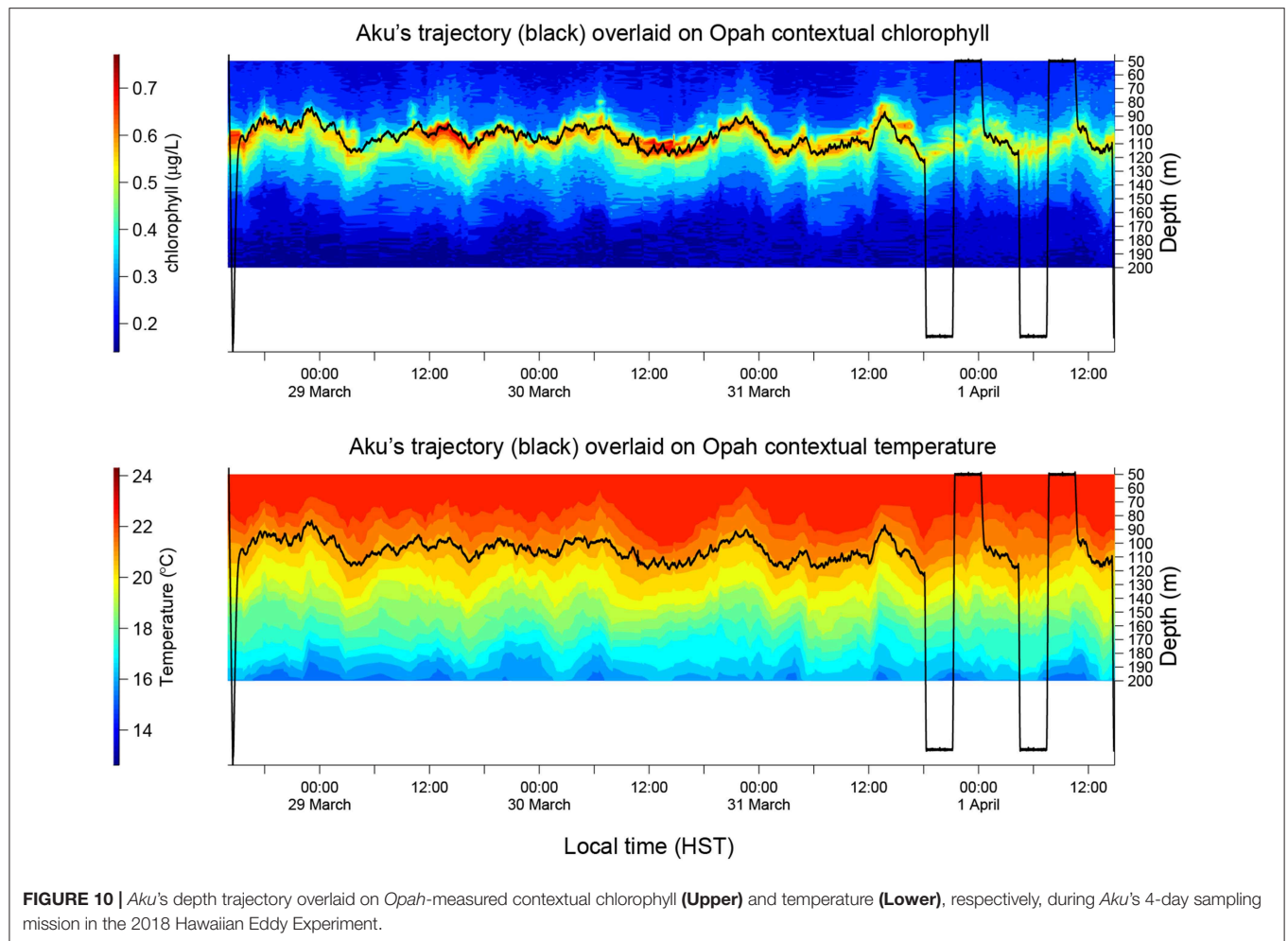
In the March–April 2018 SCOPE (Simons Collaboration on Ocean Processes and Ecology) Hawaiian Eddy Experiment, the LRAUV *Aku* (carrying a 3G-ESP) (bottom photos in **Figure 8**) ran the algorithm to track and sample the DCM microbial community for 4 days in a cyclonic eddy to the northeast of Molokai (Zhang et al., 2019a). The vehicle ran on tight circles (circle radius ~ 10 m) at 1 m/s speed while drifting with the eddy current. The sampling permitted resolution of time-dependent change of the microbial assemblage in response to diel environmental variations.

Aku and a second LRAUV *Opah* as well as a Liquid Robotics Wave Glider *Mola* were each equipped with a Teledyne Benthos directional acoustic transponder (DAT) that integrates an acoustic modem and an ultra-short baseline (USBL) acoustic positioning system. *Opah* acoustically tracked *Aku*, while spiraling up and down between 50 and 200 m depths around *Aku* to measure the contextual water properties. The Wave Glider *Mola* also acoustically followed *Aku* to provide real-time tracking and the functionality of terminating *Aku*'s mission. The three vehicles' tracks are shown in **Figure 9**. In the upper panel of **Figure 10**, *Aku*'s depth trajectory (black line) is overlaid on *Opah*-measured contextual chlorophyll. The overlap of *Aku*'s depth and *Opah*-measured chlorophyll-maximum depth

confirms that *Aku* precisely tracked the DCM layer. In the lower panel, *Aku*'s depth trajectory is overlaid on *Opah*-measured contextual temperature, which shows that *Aku* stayed on the targeted isotherm corresponding to the DCM. The large depth excursions on 1 April marked the transition to a different sampling mode, one designed to acquire a series of samples within, below and above the DCM layer. In 74 h of continuous tracking of the DCM layer, *Aku* drifted in the eddy current at an average drift speed of 0.27 m/s. This speed was consistent with the drift speed (0.27 m/s) of a GPS-tracked drifter (comprising a surface float and a drogue at 120 m depth) deployed near *Aku*, and R/V Falkor (near *Aku*'s route) shipboard ADCP-measured Earth-referenced current velocity (0.25 m/s) at the 103-m depth bin (nearest DCM's mean depth of 105 m). The closeness between *Aku*'s drift speed and that of the drifter as well as the ship ADCP-measured eddy current velocity shows that *Aku* followed the DCM water mass in a quasi-Lagrangian mode (Zhang et al., 2019a).

3. CONCLUSION AND FUTURE WORK

By enabling AUVs to autonomously detect specific oceanic features and in turn adapt their behaviors, we are now able to reliably and effectively characterize targeted processes with greater flexibility than what is possible using manned vessels.



The examples presented in this paper represent several cases that illustrate the utility of this approach, focusing on ecologically significant phenomena commonly observed in coastal and open-ocean settings. Vertical localization of subsurface phytoplankton layers enabled the detection and sampling of the historically most toxic algal populations in Monterey Bay, something that is not possible from routine monitoring at fixed locations. Horizontal localization applied to frontal habitats enabled allocation of discrete water sample collections across two end-member water types and the physical front between them. Where plankton populations formed dense patches within one of the three domains, vertical localization again enabled precise sampling of dense plankton patches. Combined with environmental sensor data, the molecular analyses of autonomously collected samples can provide a detailed, high-resolution view of the relationships between plankton and their pelagic habitat. Targeting the horizontal gradient of vertical stratification enabled an LRAUV to focus observations on a frontal zone from active upwelling to relaxation, which provided an unprecedentedly detailed depiction of the biogeochemical changes on both sides of the front during this transition.

The AUV algorithms can be extended to other mobile platforms under suitable conditions. For example, although a Wave Glider (Hine et al., 2009) can only make near-surface measurement, it can autonomously detect and track an upwelling front by taking advantage of the strong horizontal gradient of near-surface temperature, using an algorithm modified from the AUV algorithm (Zhang et al., 2019b).

In the 2018 SCOPE Hawaiian Eddy Experiment, multi-vehicle collaboration allowed continuous DCM sampling and contextual mapping in a moving eddy field, enabling a new mode of quasi-Lagrangian microbial ecology studies (Hobson et al., 2018). The water sampling LRAUV that stayed in the DCM layer was “near-sighted”—unaware of contextual water properties above and below the DCM layer. The mapping LRAUV provided this context by acoustically tracking the sampling LRAUV and spiraling up and down, yet there was no data exchange between them. In the future we will use inter-vehicle acoustic messaging to enable exchange of key information (e.g., chlorophyll level, vertical homogeneity). By exchanging complementary information of adjacent water columns, the collaborating AUVs can make timely adaptations of survey paths

and behaviors in order to identify and concentrate on the most valuable targets.

AUTHOR CONTRIBUTIONS

YZ, JR, BK, BH, BB, JGB, JMB, CS, and FC proposed and designed AUV targeted sampling methods. YZ, BK, RM, and MG developed AUV software. JH analyzed AUV water samples. All authors contributed to manuscript editing.

FUNDING

This work was supported by the David and Lucile Packard Foundation. The 2015 experiment in Monterey Bay was partially supported by NOAA Ecology and Oceanography of Harmful Algal Blooms (ECOHAB) Grant NA11NOS4780030. The 2018 SCOPE Hawaiian Eddy Experiment was partially supported by the National Science Foundation (OCE-0962032 and OCE-1337601), Simons Foundation Grant #329108, the Gordon and Betty Moore Foundation (Grant #3777, #3794, and #2728), and the Schmidt Ocean Institute for R/V Falkor Cruise FK180310. Publication of this paper was funded by the Schmidt Ocean Institute.

ACKNOWLEDGMENTS

We thank J. Erickson, M. Chaffey, E. Mellinger, B. Raanan, M. J. Stanway, D. Klimov, and T. Hoover for contributions to the LRAUV development. We thank D. Pargett, C. Preston, B.

Roman, K. Yamahara, W. Ussler, S. Jensen, and R. Marin III for contributions to the 3G-ESP development. We thank the MBARI Dorado AUV team lead H. Thomas for supporting tests of the targeted sampling software on the vehicle, team members D. Thompson, D. Conlin, and E. Martin for field operations, and K. Headley for helping setting up the onshore computer that runs simulation tests. For the 2011 and 2012 experiments in Monterey Bay, the satellite Advanced Very High Resolution Radiometer (AVHRR) SST data came from the National Oceanographic and Atmospheric Administration (NOAA) CoastWatch, and the regional ocean color data from the satellite Moderate Resolution Imaging Spectroradiometer (MODIS) sensor were obtained from the NASA LAADS system as Level 1A and processed to Level 3 mapped images using the SeaDAS software. For the 2018 Hawaiian Eddy Experiment, we are thankful for the contributions of MBARI colleagues T. O'Reilly, C. Rueda, K. Gomes, and University of Hawaii colleagues E. DeLong, D. Karl, A. Romano, S. Poulos, S. Wilson, G. Foreman, H. Ramm, A. White, F. Henderikx, R. Tabata, T. Burrell, E. Shimabukuro, T. Clemente, E. Firing, J. Hummon, P. Den Uyl, B. Watkins, E. Wood-Charlson, and L. Fujieki. The Hawaii SLA and geostrophic current velocity data came from the Copernicus Marine Environment Monitoring Service (CMEMS, <http://marine.copernicus.eu/>). We thank M. Salisbury for refining Figure 6 and M. Kelly for providing information about ship operations. We are thankful to D. Au for his support and advice. We are thankful for the help of R/V Zephyr crew in the Monterey Bay experiments and R/V Falkor crew in the Hawaii experiment. We appreciate the very helpful comments from the three reviewers for improving the paper.

REFERENCES

- Barber, R., and Smith, R. L. (1981). "Coastal upwelling ecosystems," in *Analysis of Marine Ecosystems*, ed A. R. Longhurst (London: Academic Press), 31–68.
- Bellingham, J. G., Zhang, Y., Kerwin, J. E., Erikson, J., Hobson, B., Kieft, B., et al. (2010). "Efficient propulsion for the Tethys long-range autonomous underwater vehicle," in *Proceedings of IEEE AUV'2010* (Monterey, CA), 1–6.
- Billings, A., Kaiser, C., Young, C. M., Hiebert, L. S., Cole, E., Wagner, S. J. K., et al. (2017). SyPRID sampler: a large-volume, high-resolution, autonomous, deep-ocean precision plankton sampling system. *Deep Sea Res. II* 137, 297–306. doi: 10.1016/j.dsr2.2016.05.007
- Brown, S. L., Landry, M. R., Selph, K. E., Yang, E. J., Rii, Y. M., and Bidigare, R. R. (2008). Diatoms in the desert: plankton community response to a mesoscale eddy in the subtropical North Pacific. *Deep Sea Res. II* 137, 1321–1333. doi: 10.1016/j.dsr2.2008.02.012
- Camilli, R., Reddy, C. M., Yoerger, D. R., Mooy, B. A. S. V., Jakuba, M. V., Kinsey, J. C., et al. (2010). Tracking hydrocarbon plume transport and biodegradation at Deepwater Horizon. *Science* 330, 201–204. doi: 10.1126/science.1195223
- Cazenave, F., Zhang, Y., McPhee-Shaw, E., Bellingham, J. G., and Stanton, T. (2011). High-resolution surveys of internal tidal waves in Monterey Bay, California, using an autonomous underwater vehicle. *Limnol. Oceanogr. Methods* 9, 571–581. doi: 10.4319/lom.2011.9.571
- Cowles, T. J., Desiderio, R. A., and Carr, M.-E. (1998). Small-scale planktonic structure: persistence and trophic consequences. *Oceanography* 11, 4–9. doi: 10.5670/oceanog.1998.08
- Cruz, N., and Matos, A. C. (2010a). "Adaptive sampling of thermoclines with autonomous underwater vehicles," in *Proceeding of MTS/IEEE Oceans'10* (Seattle, WA), 1–6.
- Cruz, N., and Matos, A. C. (2010b). "Reactive AUV motion for thermocline tracking," in *Proceeding of IEEE Oceans'10* (Sydney), 1–6.
- Cullen, J. J. (2015). Subsurface chlorophyll maximum layers: enduring enigma or mystery solved? *Annu. Rev. Mar. Sci.* 7, 207–239. doi: 10.1146/annurev-marine-010213-135111
- Farrell, J. A., Pang, S., and Li, W. (2005). Chemical plume tracing via an autonomous underwater vehicle. *IEEE J. Ocean. Eng.* 30, 428–442. doi: 10.1109/JOE.2004.838066
- German, C. R., Yoerger, D. R., Jakuba, M., Shank, T. M., Langmuir, C. H., and Nakamura, K.-I. (2008). Hydrothermal exploration with the Autonomous Benthic Explorer. *Deep Sea Res. I* 55, 203–219. doi: 10.1016/j.dsr.2007.11.004
- Govindarajan, A. F., Pineda, J., Purcell, M., and Breier, J. A. (2015). Species- and stage-specific barnacle larval distributions obtained from AUV sampling and genetic analysis in Buzzards Bay, Massachusetts, USA. *J. Exp. Mar. Biol. Ecol.* 472, 158–165. doi: 10.1016/j.jembe.2015.07.012
- Graham, W. M., Field, J. G., and Potts, D. C. (1992). Persistent "upwelling shadows" and their influence on zooplankton distributions. *Mar. Biol.* 114, 561–570. doi: 10.1007/BF00357253
- Graham, W. M., and Largier, J. L. (1997). Upwelling shadows as nearshore retention sites: the example of northern Monterey Bay. *Contin. Shelf Res.* 17, 509–532. doi: 10.1016/S0278-4343(96)00045-3
- Harvey, J. B. J., Ryan, J. P., Marin, R. III., Preston, C. M., Alvarado, N., Scholin, C. A., et al. (2012). Robotic sampling, *in situ* monitoring and molecular detection of marine zooplankton. *J. Exp. Mar. Biol. Ecol.* 413, 60–70. doi: 10.1016/j.jembe.2011.11.022
- Hine, R., Willcox, S., Hine, G., and Richardson, T. (2009). "The wave glider: a wave-powered autonomous marine vehicle," in *Proceedings of MTS/IEEE Oceans'09* (Biloxi, MS), 1–6.
- Hobson, B., Bellingham, J. G., Kieft, B., McEwen, R., Godin, M., and Zhang, Y. (2012). "Tethys-class long range AUVs - extending the endurance of propeller-driven cruising AUVs from days to weeks," in *Proceedings of IEEE AUV'2012* (Southampton, UK), 1–8.

- Hobson, B., Kieft, B., Raanan, B., Zhang, Y., Birch, J., Ryan, J. P., et al. (2018). "An autonomous vehicle based open ocean Lagrangian observatory," in *Proceedings of IEEE AUV'2018* (Porto), 1–5.
- Huisman, J., Pham Thi, N., Karl, D. M., and Sommeijer, B. (2006). Reduced mixing generates oscillations and chaos in the oceanic deep chlorophyll maximum. *Nature* 439:322–325. doi: 10.1038/nature04245
- Huyer, A., Kosro, P. M., Fleischbein, J., Ramp, S. R., Stanton, T., Washburn, L., et al. (1991). Currents and water masses of the coastal transition zone off northern California, June to August 1988. *J. Geophys. Res.* 96, 14809–14831. doi: 10.1029/91JC00641
- Karl, D. M., Bidigare, R. R., and Letelier, R. M. (2002). "Chapter 2: Sustained and aperiodic variability in organic matter production and phototrophic microbial community structure in the North Pacific Subtropical Gyre," in *Phytoplankton Productivity: Carbon Assimilation in Marine and Freshwater Ecosystems*, eds P. J. le B. Williams, D. N. Thomas, and C. S. Reynolds (Osney Mead, UK: Blackwell Science Ltd), 222–264.
- Kukulya, A. L., Bellingham, J. G., Stokey, R. P., Whelan, S. P., Reddy, C. M., Conmy, R. N., et al. (2018). Autonomous chemical plume detection and mapping demonstration results with a COTS AUV and sensor package. *Proceedings of MTS/IEEE Oceans'18* (Charleston, SC), 1–6.
- Lasker, R. (1975). Field criteria for survival of anchovy larvae: the relation between inshore chlorophyll maximum layers and successful first feeding. *Fish. Bull.* 73, 453–462.
- Letelier, R. M., Bidigare, R. R., Hebel, D. V., Ondrusek, M., Winn, C. D., and Karl, D. M. (1993). Temporal variability of phytoplankton community structure based on pigment analysis. *Limnol. Oceanogr.* 38, 1420–1437. doi: 10.4319/lo.1993.38.7.1420
- McGillicuddy, D. J. (2016). Mechanisms of physical-biological-biogeochemical interaction at the oceanic mesoscale. *Annu. Rev. Mar. Sci.* 8, 125–159. doi: 10.1146/annurev-marine-010814-015606
- McManus, M. A., Kudela, R. M., Silver, M. W., Steward, G. F., Donaghay, P. L., and Sullivan, J. M. (2008). Cryptic blooms: are thin layers the missing connection? *Estuar. Coasts* 31, 396–401. doi: 10.1007/s12237-007-9025-4
- Paduan, J. B., Zierenberg, R. A., Clague, D. A., Spelz, R. M., Caress, D. W., Troni, G., et al. (2018). Discovery of hydrothermal vent fields on Alarcón Rise and in Southern Pescadero Basin, Gulf of California. *Geochem. Geophys. Geosyst.* 19, 4788–4819. doi: 10.1029/2018GC007771
- Pargett, D. M., Birch, J. M., Preston, C. M., Ryan, J. P., Zhang, Y., and Scholin, C. A. (2015). "Development of a mobile ecogenomic sensor," in *Proceedings of MTS/IEEE Oceans'15* (Washington, DC), 1–6.
- Petillo, S., Balasuriya, A., and Schmidt, H. (2010). "Autonomous adaptive environmental assessment and feature tracking via autonomous underwater vehicles" in *Proceedings of IEEE Oceans'10* (Sydney), 1–9.
- Petillo, S., and Schmidt, H. (2014). Exploiting adaptive and collaborative AUV autonomy for detection and characterization of internal waves. *IEEE J. Ocean. Eng.* 39, 150–164. doi: 10.1109/OJE.2013.2243251
- Ryan, J. P., Fischer, A. M., Kudela, R. M., McManus, M. A., Myers, J. S., Paduan, J. D., et al. (2010b). Recurrent frontal slicks of a coastal ocean upwelling shadow. *J. Geophys. Res.* 115:C12070. doi: 10.1029/2010JC006398
- Ryan, J. P., Harvey, J. B. J., Zhang, Y., and Woodson, C. B. (2014). Distributions of invertebrate larvae and phytoplankton in a coastal upwelling system retention zone and peripheral front. *J. Exp. Mar. Biol. Ecol.* 459, 51–60. doi: 10.1016/j.jembe.2014.05.017
- Ryan, J. P., Johnson, S. B., Sherman, A., Rajan, K., Py, F., Thomas, H., et al. (2010a). Mobile autonomous process sampling within coastal ocean observing systems. *Limnol. Oceanogr. Methods* 8, 394–402. doi: 10.4319/lom.2010.8.394
- Ryan, J. P., Kudela, R. M., Birch, J. M., Blum, M., Bowers, H. A., Chavez, F. P., et al. (2017). Causality of an extreme harmful algal bloom in Monterey Bay, California, during the 2014–2016 northeast Pacific warm anomaly. *Geophys. Res. Lett.* 44, 1–9. doi: 10.1002/2017GL072637
- Ryan, J. P., McManus, M. A., Paduan, J. D., and Chavez, F. P. (2008). Phytoplankton thin layers caused by shear in frontal zones of a coastal upwelling system. *Mar. Ecol. Prog. Ser.* 354, 21–34. doi: 10.3354/meps07222
- Ryan, J. P., McManus, M. A., and Sullivan, J. M. (2010c). Interacting physical, chemical and biological forcing of phytoplankton thin-layer variability in Monterey Bay, California. *Contin. Shelf Res.* 30, 7–16. doi: 10.1016/j.csr.2009.10.017
- Scholin, C., Birch, J., Jensen, S., Marin, R. III., Massion, E., Pargett, D., et al. (2017). The quest to develop ecogenomic sensors: a 25-year history of the Environmental Sample Processor (ESP) as a case study. *Oceanography* 30, 100–113. doi: 10.5670/oceanog.2017.427
- Scholin, C., Marin, R. III., Miller, P., Doucette, G., Powell, C., Howard, J., et al. (1999). Application of DNA probes and a receptor binding assay for detection of *Pseudo-nitzschia* (Bacillariophyceae) species and domoic acid activity in cultured and natural samples. *J. Phycol.* 35, 1356–1367.
- Scholin, C. A. (2013). "Ecogenomic sensors," in *Encyclopedia of Biodiversity*, 2nd Edn, Vol. 2, ed S. A. Levin (Waltham, MA: Academic Press), 690–700.
- Smith, R. L. (1981). "A comparison of the structure and variability of the flow field in three coastal upwelling regions: Oregon, Northwest Africa, and Peru," in *Coastal Upwelling*, ed F. A. Richards (Washington, DC: American Geophysical Union), 107–118.
- Sullivan, J. M., McManus, M. A., Cheriton, O. M., Benoit-Bird, K. J., Goodman, L., Wang, Z., et al. (2010). Layered organization in the coastal ocean: an introduction to planktonic thin layers and the LOCO project. *Contin. Shelf Res.* 30, 1–6. doi: 10.1016/j.csr.2009.09.001
- Vaillancourt, R. D., Marra, J., Seki, M. P., Parsons, M. L., and Bidigare, R. R. (2003). Impact of a cyclonic eddy on phytoplankton community structure and photosynthetic competency in the subtropical North Pacific Ocean. *Deep Sea Res. I* 50, 829–847. doi: 10.1016/S0967-0637(03)00059-1
- Woodson, C. B., Washburn, L., Barth, J. A., Hoover, D. J., Kirincich, A. R., McManus, M. A., et al. (2009). Northern Monterey Bay upwelling shadow front: observations of a coastally and surface-trapped buoyant plume. *J. Geophys. Res.* 114:C12013. doi: 10.1029/2009JC005623
- Wulff, T., Bauerfeind, E., and von Appen, W.-J. (2016). Physical and ecological processes at a moving ice edge in the Fram Strait as observed with an AUV. *Deep Sea Res. I* 115, 253–264. doi: 10.1016/j.dsr.2016.07.001
- Zhang, Y., Bellingham, J. G., Godin, M. A., and Ryan, J. P. (2012a). Using an autonomous underwater vehicle to track the thermocline based on peak-gradient detection. *IEEE J. Ocean. Eng.* 37, 544–553. doi: 10.1109/OJE.2012.2192340
- Zhang, Y., Bellingham, J. G., Ryan, J. P., and Godin, M. A. (2015). Evolution of a physical and biological front from upwelling to relaxation. *Contin. Shelf Res.* 108, 55–64. doi: 10.1016/j.csr.2015.08.005
- Zhang, Y., Godin, M. A., Bellingham, J. G., and Ryan, J. P. (2012b). Using an autonomous underwater vehicle to track a coastal upwelling front. *IEEE J. Ocean. Eng.* 37, 338–347. doi: 10.1109/OJE.2012.2197272
- Zhang, Y., Kieft, B., Hobson, B., Ryan, J., Barone, B., Preston, C., et al. (2019a). Autonomous tracking and sampling of the deep chlorophyll maximum layer in an open-ocean eddy by a long range autonomous underwater vehicle. *IEEE J. Ocean. Eng.* doi: 10.1109/OJE.2019.2920217
- Zhang, Y., McEwen, R. S., Ryan, J. P., and Bellingham, J. G. (2010). Design and tests of an adaptive triggering method for capturing peak samples in a thin phytoplankton layer by an autonomous underwater vehicle. *IEEE J. Ocean. Eng.* 35, 785–796. doi: 10.1109/OJE.2010.2081031
- Zhang, Y., McEwen, R. S., Ryan, J. P., Bellingham, J. G., Thomas, H., Thompson, C. H., et al. (2011). A peak-capture algorithm used on an autonomous underwater vehicle in the 2010 Gulf of Mexico oil spill response scientific survey. *J. Field Robot.* 28, 484–496. doi: 10.1002/rob.20399
- Zhang, Y., Rueda, C., Kieft, B., Ryan, J. P., Wahl, C., O'Reilly, T. C., et al. (2019b). Autonomous tracking of an oceanic thermal front by a wave glider. *J. Field Robot.* 36, 940–954. doi: 10.1002/rob.21862
- Zhang, Y., Ryan, J. P., Bellingham, J. G., Harvey, J. B. J., and McEwen, R. S. (2012c). Autonomous detection and sampling of water types and fronts in a coastal upwelling system by an autonomous underwater vehicle. *Limnol. Oceanogr. Methods* 10, 934–951. doi: 10.4319/lom.2012.10.934

Conflict of Interest Statement: The authors declare that the research was conducted in the absence of any commercial or financial relationships that could be construed as a potential conflict of interest.

Copyright © 2019 Zhang, Ryan, Kieft, Hobson, McEwen, Godin, Harvey, Barone, Bellingham, Birch, Scholin and Chavez. This is an open-access article distributed under the terms of the Creative Commons Attribution License (CC BY). The use, distribution or reproduction in other forums is permitted, provided the original author(s) and the copyright owner(s) are credited and that the original publication in this journal is cited, in accordance with accepted academic practice. No use, distribution or reproduction is permitted which does not comply with these terms.



Mapping Fish Chorus Distributions in Southern California Using an Autonomous Wave Glider

Camille M. L. S. Pagniello^{1*}, Megan A. Cimino^{1,2} and Eric Terrill¹

¹ Scripps Institution of Oceanography, University of California, San Diego, La Jolla, CA, United States, ² Institute of Marine Sciences, University of California, Santa Cruz, Santa Cruz, CA, United States

OPEN ACCESS

Edited by:

Leonard Pace,
Schmidt Ocean Institute,
United States

Reviewed by:

Robert McCauley,
Curtin University, Australia
Miles James Parsons,
Australian Institute of Marine Science
(AIMS), Australia

*Correspondence:

Camille M. L. S. Pagniello
cpagniello@ucsd.edu

Specialty section:

This article was submitted to
Ocean Observation,
a section of the journal
Frontiers in Marine Science

Received: 15 November 2018

Accepted: 12 August 2019

Published: 29 August 2019

Citation:

Pagniello CMLS, Cimino MA and
Terrill E (2019) Mapping Fish Chorus
Distributions in Southern California
Using an Autonomous Wave Glider.
Front. Mar. Sci. 6:526.
doi: 10.3389/fmars.2019.00526

Passive acoustics is a tool to monitor behavior, distributions, and biomass of marine invertebrates, fish, and mammals. Typically, fixed passive acoustic monitoring platforms are deployed, using *a priori* knowledge of the location of the target vocal species. Here, we demonstrate the ability to conduct coastal surveys of fish choruses, spatially mapping their distributions with an autonomous surface vehicle. For this study, we used an autonomous Liquid Robotics Wave Glider SV3 equipped with a Remora-ST underwater acoustic recorder and hydrophone. The exploratory 15-day deployment transited through three marine reserves, resulting in approx. 200 h of passive acoustic recordings, and revealed five distinct fish choruses from La Jolla to Capistrano Beach, CA (approx. 80 km separation), each with unique acoustic signatures. Choruses occurred in the evening hours, typically in the 40 to 1000 Hz band. There was a lack of both temporal and frequency partitioning amongst the choruses, but some choruses exhibited distinct spatial niches by latitude and water temperature. These results suggest that the mobility of the Wave Glider allows for persistent surveys and studies that otherwise may be too challenging or costly for stationary or ship-based sensors; a critical consideration for documenting biological activity over large spatiotemporal scales, or sampling of nearshore marine reserves.

Keywords: fish chorus, passive acoustics, Wave Glider, fisheries, autonomous platform, fish sounds

INTRODUCTION

Sound production plays an important role in the life history of many marine animals including invertebrates, fish and mammals (Tyack, 1998). Fish, in particular, are known to vocalize while defending their territory, feeding and spawning (Winn, 1964). Fish in some spawning aggregations are known to vocalize during certain time periods over a few hours (Cato, 1978). This “chorus” results in a significant increase in ambient sound pressure levels due to the large number of fishes producing sound at the same time. As such, fish choruses can be used to determine the timing of spawning seasons, species distributions and essential habitat (Gannon, 2008; Luczkovich et al., 2008).

Passive acoustics can be used to record sound production. It enables monitoring of soniferous animal presence and behavior over large temporal (i.e., on the order of years) and spatial (i.e., on the order of 10s km) scales because of the ocean’s transparency to sound (Jensen et al., 2011). While passive acoustic monitoring can generate long temporal records at a single location, the spatial

coverage is small compared to those of interest to ecosystem managers that are required to monitor vast areas and entire coastlines. Given that passive acoustic recorders are traditionally deployed on stationary platforms (Mellinger et al., 2007; Sousa-Lima et al., 2013), there is a need for more instrument platforms that are mobile and capable of expanding the region that is monitored.

Recent studies show the increased deployment of passive acoustic recorders on autonomous mobile vehicles (e.g., Baumgartner and Fratantoni, 2008; Klinck et al., 2009; Wall et al., 2012). Slocum buoyancy gliders, for example, have been used to map the sound production of various fish species including red grouper (*Epinephelus morio*), toadfish (*Opsanus* spp.) and cusk eel (*Lepophidium* sp./*Ophidion* sp.) in the Gulf of Mexico (Wall et al., 2012, 2013, 2014) as well as various species of whales in the Gulf of Maine (Baumgartner et al., 2013). Similar to other autonomous vehicles, the Wave Glider (Hine et al., 2009) is a mobile platform that can be equipped with environmental sensors for measuring temperature, salinity, fluorescence, as well as acoustic doppler current profilers (ADCP), acoustic transponders and GPS motion sensors (e.g., Kraus and Bingham, 2011; Mullison et al., 2011; Bingham et al., 2012). It is unique in that it can harness ocean wave energy for forward platform propulsion, allowing for extended mission durations without the requirement for diving to depth, as is needed for buoyancy gliders. When equipped with passive acoustic recorders, Wave Gliders have been primarily used for the monitoring of marine mammals in deep water. Although the Wave Glider generates mostly low-frequency noise, the source level of low-frequency humpback whale vocalizations is high enough to enable the use of a Wave Glider to study the whale's acoustic behavior (Wiggins et al., 2010; Bingham et al., 2012). Soniferous fish, however, typically produce low-frequency sounds at source levels similar to or lower than marine mammals (Erisman and Rowell, 2017), making it a more challenging signal-to-noise environment for a Wave Glider to operate in.

The aim of this study was to determine if autonomous Wave Gliders can be used to record fish sounds and choruses in California nearshore environments, which are noisier and shallower than open ocean environments. A passive acoustic recorder was attached to a Wave Glider during an exploratory 15-day mission along the southern California coast. Recordings of different chorusing fish species collected during this study show that a Wave Glider equipped with passive acoustic monitoring capabilities enables scientists and managers to collect fisheries-independent data about the distribution of fish over large areas.

MATERIALS AND METHODS

Wave Glider and Sensors

The Wave Glider SV3 (Liquid Robotics, a Boeing company, Sunnyvale, CA, United States) is an autonomous surface platform with a tether that connects a surface float to a subsurface glider with articulating wings (hereafter referred to as the “sub”) (Figure 1). The wings convert vertical wave motion into lift, resulting in forward propulsion. The surface float contains

Iridium satellite communications and control computers as well as batteries charged by solar panels. The location and condition of the Wave Glider was recorded and telemetered every 5 min. The Wave Glider also has an Automatic Identification System (AIS) receiver, which was monitored closely in real-time for boat traffic to avoid collisions.

A Remora-ST underwater acoustic recorder (Loggerhead Instruments, Inc., Sarasota, FL, United States) was attached to custom made steel plates on the topside of the sub at 4 m depth (Figure 1). The recorder sampled at 48 kHz for 3 min every 5 min. The hydrophone had a typical sensitivity of -201 dB V/ μ Pa and had a pre-amplifier of 33 dB gain. The acoustic recorder had a 16-bit analog-to-digital converter with a -1 to 1 V response. The passive acoustic recorder and hydrophone were factory calibrated and thus, no additional calibrations were conducted.

Study Area

The Wave Glider was deployed along the southern California coast from July 20 to August 3, 2017 (Figure 2A). The deployment started and ended in La Jolla, CA, where the vehicle ran inshore-offshore surveys near the kelp forests in the Matlahuayl State Marine Reserve (SMR), a habitat that supports a diverse assemblage of fishes. From July 26 to 30, 2017, the Wave Glider transited from La Jolla to Capistrano Beach, CA and back, passing through the San Diego-Scripps Coastal State Marine Conservation Area (SMCA) and the Swami's SMCA. The vehicle was constrained to waters greater than 10 m depth and approx. 2 km offshore to avoid entanglement in kelp forests, collisions with nearshore rocks and running aground in shallow waters. The Wave Glider track extended further offshore as it approached Oceanside Harbor, a high boat traffic area, and a restricted area within the Camp Pendleton Military exercise area. Overall, the Wave Glider traveled 296 km in a straight path along the coast at an average speed of 0.25 m/s. Locations along the track were not equally sampled during the day and night (Figure 3).

Acoustic Data Processing

Long-term spectral averages (LTSAs) of the passive acoustic recordings were computed using *Triton*, a Matlab-based (The Mathworks, Inc., Boston, MA, United States) acoustic data display and analysis software program (Wiggins, 2003). The program calculates fast Fourier transforms (FFTs), averages successive FFTs into a single spectral average and then, displays them as spectrograms (Wiggins and Hildebrand, 2007). FFTs were calculated using a Hanning window, 0% overlap and 1-Hz frequency bins. Successive FFTs were averaged over 5 s. LTSAs allowed for a visual scan of 199 h of recordings and to discern the start and end times of a chorus.

Choruses were divided into 10 s sub-samples. Spectrograms of each sub-sample were generated by dividing the time series into equal-length segments of 8192 samples having 90% overlap, applying a Kaiser-Bessel window of $\alpha = 2.5$ to each segment, taking the FFT of each segment, and averaging the squared magnitude of the FFT of overlapped, windowed segments. The overall sensitivity (-77.7 dB re 1μ Pa/counts) of the acoustic recorder was applied to the spectrograms to yield

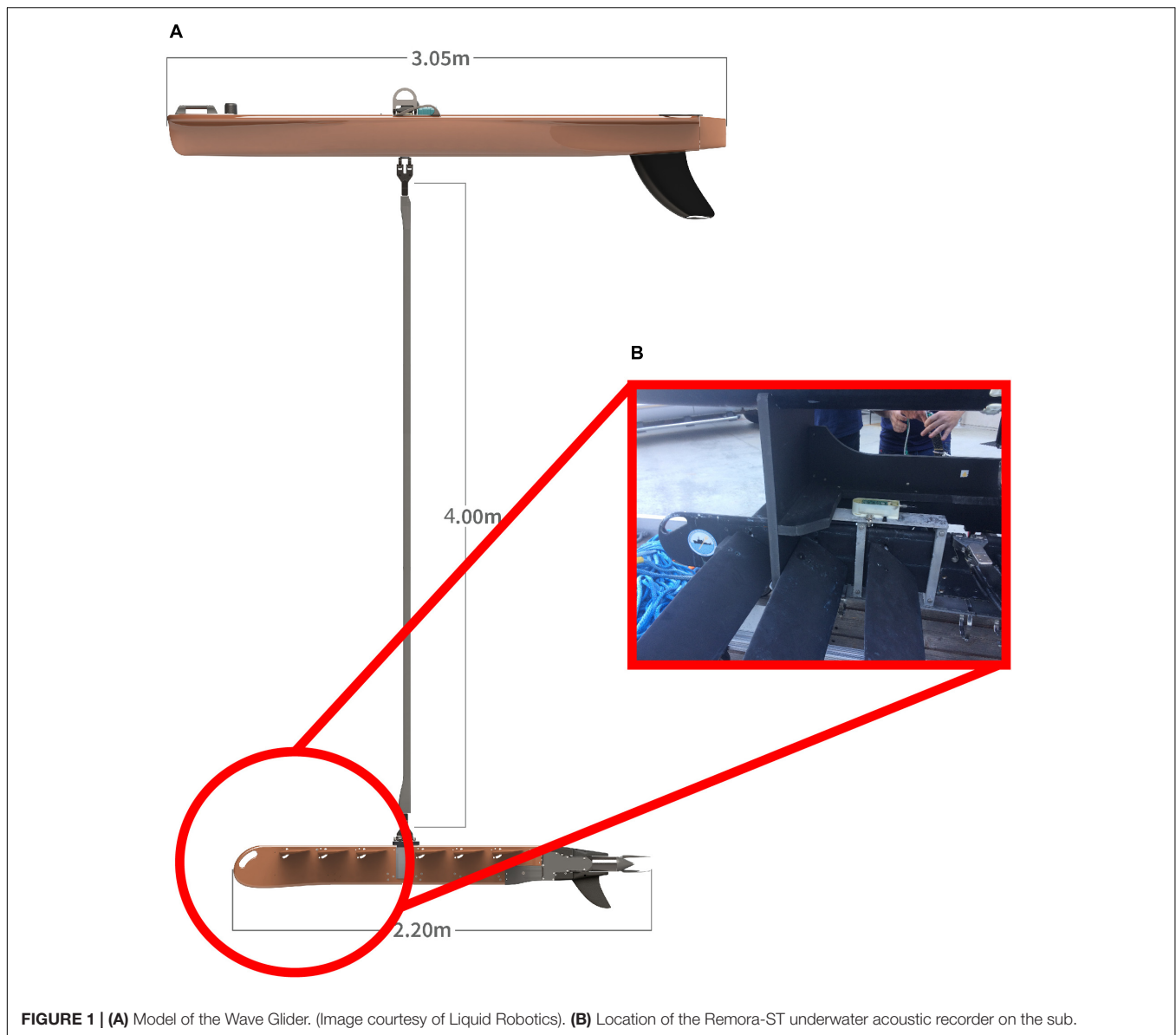


FIGURE 1 | (A) Model of the Wave Glider. (Image courtesy of Liquid Robotics). **(B)** Location of the Remora-ST underwater acoustic recorder on the sub.

calibrated values of spectral density ($\text{dB re } 1 \mu\text{Pa}^2/\text{Hz}$). Frequency bandwidth (Hz) of each chorus was measured directly from spectrograms while peak frequency (Hz) was estimated from pressure spectral density curves. Received level ($\text{dB re } 1 \mu\text{Pa}$ peak-to-peak and rms) of each sub-sample was estimated to determine when the chorus reached its peak after sunset. When individual calls could be identified within a fish chorus, call duration (seconds) and frequency bandwidth (Hz) were measured directly from spectrograms. Peak frequency (Hz) of individual calls were estimated from pressure spectral density curves. Received level ($\text{dB re } 1 \mu\text{Pa}$ peak-to-peak and rms) of the individual calls was also calculated.

Choruses were classified as originating from fish based on the similarity of their acoustic characteristics to other reported fish calls and choruses (e.g., Parsons et al., 2016, 2017; McWilliam et al., 2018). A fish chorus was classified as a distinct type based

on its frequency content, timing and location along the southern California coast as well as the duration and number of pulses of individual calls when possible.

Environmental Data

Environmental data was obtained to identify features that might be indicative of fish habitats. Bathymetric data for California that cover the continental shelf at 10 m contour resolution to a depth of 600 m were acquired from the California Department of Fish and Wildlife (CDFW)¹. The union of kelp canopy data from 1989, 1999, 2002–2006, and 2008 collected during aerial surveys by the CDFW was used to show the persistent extent of kelp in California (i.e., a count of years of overlap per kelp bed)¹. The images were processed and distributed

¹<https://www.wildlife.ca.gov/Conservation/Marine/GIS/Downloads>

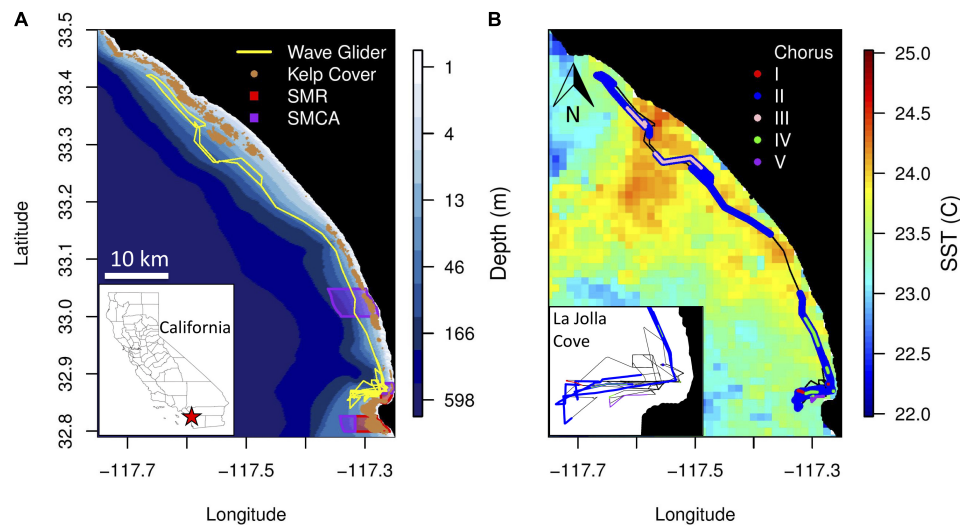


FIGURE 2 | (A) Bathymetry along the Wave Glider track (yellow line) from La Jolla Cove, San Diego, to Capistrano Beach, CA. Historical kelp cover is shown in brown. California State Marine Reserves (SMR) and State Marine Conservation Areas (SMCA) within the study area are shown in red and purple, respectively. **(B)** Average sea surface temperature (°C) during the Wave Glider deployment. The locations where the five fish choruses were recorded are shown in red (Type I), blue (Type II), light pink (Type III), green (Type IV) and purple (Type V). Each chorus is mapped separately in **Supplementary Figure S1**. (Inset) Zoomed in view of the location of the fish choruses recorded near La Jolla Cove.

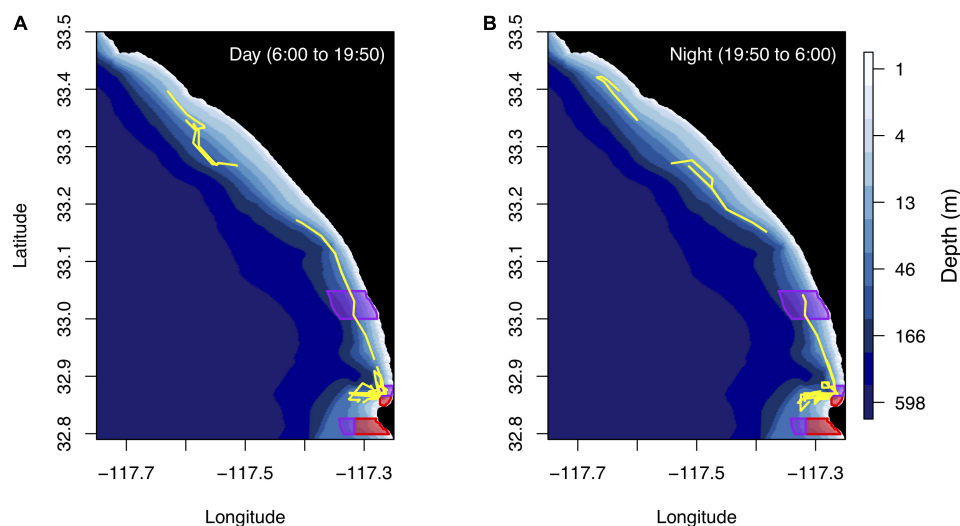


FIGURE 3 | (A) The Wave Glider track during the day from sunrise to sunset. **(B)** The Wave Glider track during the night from sunset to sunrise. Note, some areas were not sampled during both the day and night. Bathymetry along the Wave Glider track (yellow line) from La Jolla Cove, San Diego, to Capistrano Beach, CA and California SMR and SMCA within the study area are shown in red and purple, respectively. Average sunset and sunrise times are also shown on the maps. Times are reported in Pacific Standard Time.

by the CDFW Marine Region GIS Lab with a resolution of 2 m. Daily sea surface temperature (SST) measurements were made by an advanced very high-resolution radiometer aboard NOAA's Polar Operational Environmental Satellites (POES). The measurements have a 0.0125-degree resolution². SST measurements were patchy due to cloud cover during the Wave Glider deployment; therefore, all measurements during the

deployment were averaged to obtain a snapshot of surface water temperature along the coast.

RESULTS

Passive acoustic recordings from the 15-day deployment of the Wave Glider contained a diverse array of anthropogenic and biological sounds including surface crafts, dolphins, sea lions,

²<https://coastwatch.pfeg.noaa.gov/erddap/griddap/erdATssta1day.html>

snapping shrimp, and fish. Low-frequency noise originating from the Wave Glider (i.e., flow noise, the sub wings changing position, and tether strumming) was also recorded. Below 1500 Hz, the most notable sounds recorded are assumed to originate from fish based on the frequency, duration, received levels, and timing of the sound. We identified five distinct fish calls, but the species producing all but one of these choruses are unknown. The acoustic characteristics and spatiotemporal distribution of five different fish choruses (I–V) are described below. All times are reported in Pacific Standard Time.

Acoustic Characteristics and Spatiotemporal Distribution of Fish Choruses

Chorus I was the shortest chorus recorded, starting around 18:58 and ranging from 0.8 to 3.5 h (Figures 4B, 5A and Table 1). It comprised of short-duration (0.25 ± 0.05 s, mean ± SD), mid-frequency (approx. 420–880 Hz) croaks (Figures 5B,C and Table 2). Individual calls were only observed during chorusing. Received levels reached a maximum of 107 ± 2 dB re 1 µPa rms approx. 12 min after sunset. Sunset throughout the deployment was around 19:50. The chorus was only recorded offshore of the La Jolla Cove kelp beds at approx. 32.85°N (Figures 2B, 4A).

Chorus II was the longest chorus recorded, ranging from 6 to 13.5 h and started around 18:53 (Table 1 and Figure 4B). Received levels were a maximum of 119 ± 7 dB re 1 µPa rms in two distinct frequency bands (i.e., approx. 300–600 Hz and 650–1000 Hz) during chorusing (Figure 5D). Chorus II was recorded most often (10 of the 14 nights) and was the only chorus recorded throughout the entire deployment from La Jolla to Capistrano Beach, CA (approx. 32.85 to 33.4°N), including both SMCAs (Figures 2B, 4A). Individual calls were short-duration pulses of 0.19 ± 0.02 s (Figures 5E,F). Very few individual calls were recorded (Table 2). The presence of Chorus II does not appear to be related to the kelp distribution or SST.

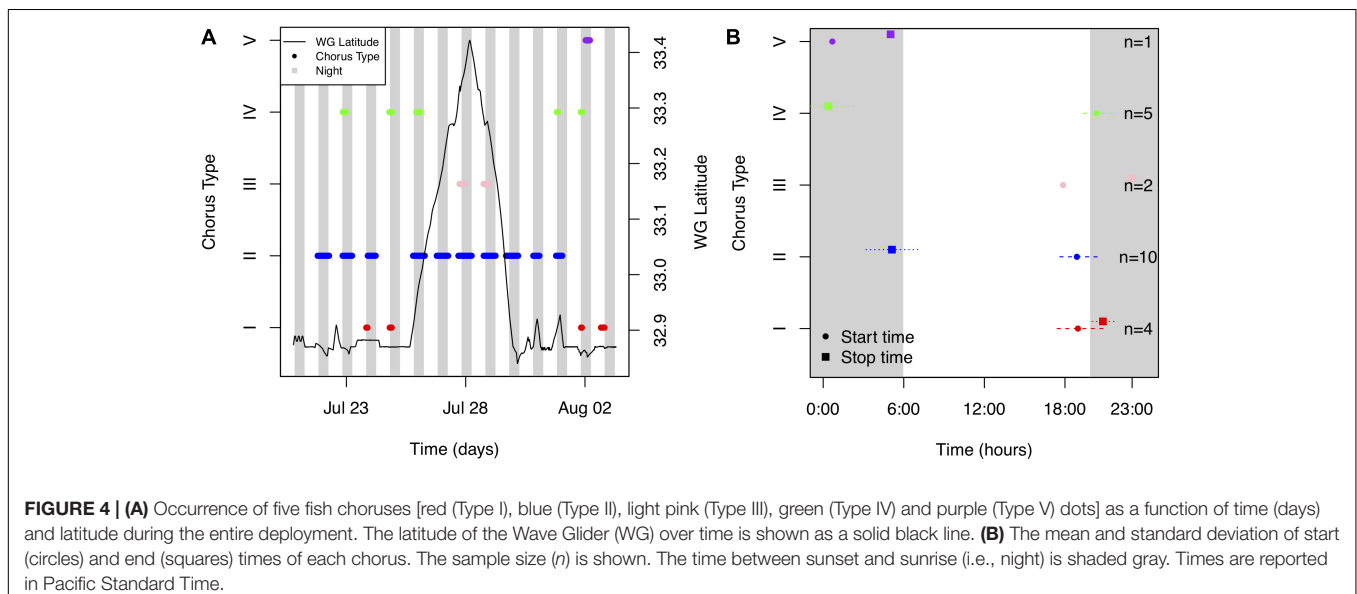
Individual calls of Chorus III comprised of a pulse train, followed by zero to three short grunts (Figures 5H,I). When Chorus III occurred, its energy overlapped with energy from Chorus II in the 300 to 500 Hz frequency band. As such, calls recorded when Chorus II was not present displayed energy from approx. 60 to 540 Hz (Table 2). The chorus was only recorded twice when the Wave Glider transited near an area with elevated SST (Figures 2B, 4A). This area was offshore of the historical kelp beds located 5 km south of San Onofre, CA (approx. 33.3°N). On both July 27 and 28, 2017, the chorus started slightly before 18:00 and lasted between 5 to 6 h (Figures 4B, 5G). Received levels of the chorus peaked at 125 ± 8 dB re 1 µPa rms approx. 40 min before sunset (Table 1).

Chorus IV was recorded offshore of the La Jolla kelp beds up to Solana Beach, CA (approx. 32.85 to 32.99°N, Figures 2B, 4A). Individual calls comprised of a grunt train of two to four grunts, with each grunt decreasing in duration (Figures 5K,L). More individual calls of Chorus IV were recorded compared to any other chorus (Table 2). This chorus started at around 20:20 and its received levels peaked at 119 ± 11 dB re 1 µPa rms on average 1.5 h after sunset (Figures 4B, 5J and Table 1).

Chorus V was only recorded once on August 2, 2017 starting at ~ 00:40 and lasted for 4 h (Figures 4B, 5M and Table 1). It occurred approx. 2 km offshore of La Jolla Cove (approx. 32.85°N). The chorus comprised of one long, continuous tonal with multiple harmonics. No individual calls were recorded.

DISCUSSION

Knowledge of the location of fish choruses and their associated spawning aggregations is vital to the implementation of fisheries protection measures. Five distinct fish choruses were recorded by our Wave Glider equipped with a passive acoustic recorder transiting from La Jolla to Capistrano Beach, CA, confirming that the Wave Glider is a potential tool for future fisheries



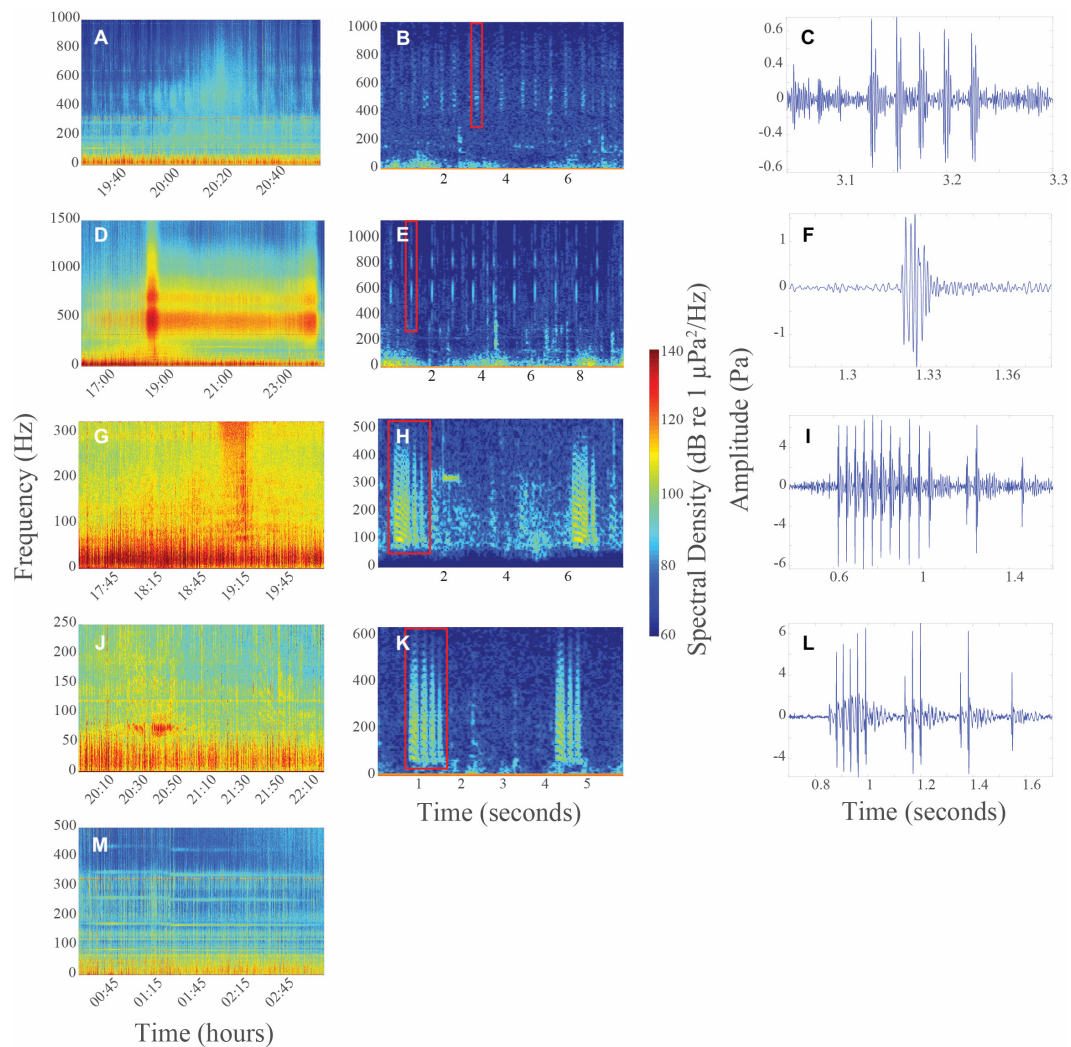


FIGURE 5 | (A) Long-term spectral average (LTSA) of Chorus I on 07/24/2017. **(B)** Spectrogram and **(C)** time series of individual call of Chorus I on 07/24/2017 at 21:10:25 (band pass filter = 395–1015 Hz). **(D)** LTSA of Chorus II on 07/27/2017. **(E)** Spectrogram and **(F)** time series of individual call of Chorus II on 07/26/2017 at 17:57:32 (band pass filter = 335–1115 Hz). **(G)** LTSA of Chorus III on 07/27/2017. **(H)** Spectrogram and **(I)** time series of individual call of Chorus III on 07/28/2017 at 19:15:04 (band pass filter = 40–535 Hz). **(J)** LTSA of Chorus IV on 07/22/2017. **(K)** Spectrogram and **(L)** time series of individual call of Chorus IV on 08/01/2017 at 21:25:42 (band pass filter = 25–635 Hz). **(M)** LTSA of Chorus V on 08/02/2017. All spectrograms used a Hanning window, $f_s = 48$ kHz, NFFT = 8192 and overlap = 90%. Time series are of the individual calls highlighted with a red box on each spectrogram. Color in all LTSAs and spectrograms represents spectral density (dB re $1 \mu\text{Pa}^2/\text{Hz}$), with red indicating highest received levels. Times are reported in Pacific Standard Time.

passive acoustic work in this region. The acoustic characteristics as well as the spatial and temporal occurrence of Chorus I are similar to the fish chorus reported by Butler et al., 2017 and Pagniello et al., 2017; however, individual calls recorded in our study did not provide clear confirmation that these are the same fish choruses. Chorus II is the same chorus first reported by Reshef et al., 2018 near Del Mar, CA. We are, however, the first to identify individual calls of this chorus. We are also the first to document Chorus III; although it is not the first fish chorus recorded near San Onofre, CA (D'Spain et al., 2013). Chorus IV is the same chorus that was recorded by Butler et al., 2017 further south offshore of Bird Rock, San Diego, CA. Given the large number of fish species that are

reported to spawn during the summer months in this area (Love, 2011), it is impossible to identify the species of fish producing choruses I–IV with the currently available information. However, while the species for choruses I–IV are unknown, Chorus V is the hum of a plain midshipmen (*Porichthys notatus*) (Ibara et al., 1983).

While the Wave Glider survey occurred over a short timeframe and more data are needed to determine the full spatial extent and temporal boundaries of the choruses, initial observations suggested the choruses did not exhibit a distinct frequency or temporal niche, but spatial patterns by latitude and SST were observed. All choruses had high received levels primarily in 40 to 1000 Hz band and started near sunset. In

TABLE 1 | Frequency and temporal characteristics (mean \pm standard deviation) of five distinct fish choruses.

Chorus type	Start time	Duration (hours)	Frequency band(s) (Hz)	Peak frequency (Hz)	Maximum received level (dB re 1 μ Pa rms)	Peak time post sunset (hours)	Number of occurrences (n)
I	18:58 \pm 01:51	0.8–3.5	328 \pm 21 to 773 \pm 246	410 \pm 55	107 \pm 2	0.2 \pm 1.7	4
II	18:53 \pm 01:30	6–13.5	307 \pm 31 to 596 \pm 24; 651 \pm 29 to 1002 \pm 197	450 \pm 44	119 \pm 7	–3.8 \pm 8.9	10
III	17:52 \pm 00:00	4.7–5.7	55 \pm 21 to 316 \pm 13	128 \pm 83	125 \pm 8	–0.7 \pm 1.0	2
IV	20:20 \pm 01:11	1.1–4.2	42 \pm 7 to 299 \pm 30	66 \pm 10	119 \pm 11	1.5 \pm 1.4	5
V	00:42	4.3	79, 167, 251, 339, 423	79	109	7.5	1

Start times are reported in Pacific Standard Time.

TABLE 2 | Frequency and temporal characteristics (mean \pm standard deviation) of the individual calls of four distinct fish choruses.

Chorus type	Duration (seconds)	Frequency band(s) (Hz)	Peak frequency (Hz)	Received level (dB re 1 μ Pa peak-to-peak)	Received level (dB re 1 μ Pa rms)	Number of occurrences (n)
I	0.25 \pm 0.05	419 \pm 84 to 880 \pm 96	548 \pm 99	120 \pm 2	99 \pm 2	119
II	0.19 \pm 0.02	435 \pm 60 to 632 \pm 66; 694 \pm 55 to 853 \pm 63	528 \pm 65	127 \pm 5	108 \pm 6	29
III	0.78 \pm 0.14	50 \pm 12 to 297 \pm 72	96 \pm 38	135 \pm 7	117 \pm 6	286
IV	0.74 \pm 0.13	45 \pm 6 to 308 \pm 104	80 \pm 22	132 \pm 4	114 \pm 3	434

the southern region of the deployment, Choruses I, IV and V were only recorded offshore of La Jolla Cove. In comparison, Chorus III was only recorded further north near an area with elevated SST off San Onofre, CA. All choruses, except for Chorus II, were only recorded near historical kelp beds, suggesting kelp could be an important habitat. Chorus II displayed no spatial habitat preferences and was recorded throughout the entire deployment. Yet, Chorus II did not have the highest maximum received levels, suggesting the Wave Glider did not pass as close to Chorus II's location as to the location of other choruses, and thus, possibly explaining why few individual calls were recorded. In addition, we do acknowledge that in this study, all locations along the Wave Glider track were not surveyed at night (i.e., when most fish choruses tend to occur). Survey designs with equal day and night sampling at the same location would provide more insight into the temporal patterns in chorusing observed. Overall, however, our results demonstrate that the Wave Glider can be used for large-scale, exploratory missions to identify regions where soniferous fish are likely spawning.

Due to the constant motion of the Wave Glider and temporal variation in fish sound production, there are two important considerations when planning a survey. First, it is important to consider a chorus' received levels may not be constant throughout the chorusing period due to individual variation in sound production. Additionally, because the Wave Glider is constantly moving, it is impossible to decipher whether the maximum recorded received level was associated with the closest point of approach to the chorus or the most intense time of chorusing. A distinction between these two scenarios could be

made by having the Wave Glider loiter in one location for an extended period of time during a chorus. Second, the exact start and end times (i.e., on the order of minutes) of the choruses were difficult to determine because the chorus signal fades in and out near the beginning and end of chorus. This signal fading is possibly due to the sub, where the hydrophone was attached, changing position in the water column as the Wave Glider moves, and thus, shadowing signal arrivals to the hydrophone. Therefore, these potential fish spawning locations could subsequently be targeted with stationary recorders to determine the long-term temporal patterns associated with spawning activity.

Our results suggest that Wave Gliders are an effective passive acoustic asset as either a stand-alone platform or to complement stationary passive acoustic recording platforms. If used as a stand-alone platform, Wave Gliders equipped with passive acoustic monitoring capabilities allow for the acoustic exploration of an extensive area. If a location of interest is identified, a Wave Glider could also be programmed to "station-keep," and thus, acoustically monitor temporal patterns at a single location. As a precaution, Wave Gliders are not typically operated in shallow waters (<10 m) or in hazardous areas such as kelp beds, where fish choruses are most often reported to occur (e.g., Butler et al., 2017; Pagniello et al., 2017). Thus, strategic mission planning will ultimately be required to ensure that areas as close to the chorus as possible are surveyed during the expected chorusing time frame (i.e., at night). If a Wave Glider was paired with a stationary passive acoustic recording platform, long-term temporal patterns of occurrence as well as spatial extent of a fish

chorus could be defined. Both Wave Gliders and passive acoustic recorders with single hydrophones can be deployed for durations of up to 1 year. Such a dual platform approach to determine the location of chorusing may even eliminate the need of a multi-hydrophone passive acoustic array, which has significantly reduced recording durations compared to single hydrophone passive acoustic recorders. Additionally, this type of combined approach would address the two considerations detailed above (space and time). As such, an approach that uses both stationary and mobile platforms equipped with passive acoustic recorders and hydrophones in concert would be ideal.

Future studies that intend to use the Wave Glider as a platform for passive acoustic monitoring should consider integrating the passive acoustic recorder into glider's real-time system to allow for real-time feedback upon the detection of signals of interest. Furthermore, a wide range of acoustic arrays could be implemented to determine the direction of arriving signals of interest in real-time. Additionally, a depth logger and accelerometer could be attached to the sub to know the exact position of the hydrophone in the water column to determine if the fading chorus signal observed is due to the sub changing position in the water column, the propagation environment or is a natural phenomenon.

Even without these suggested platform improvements, we have shown that large-scale Wave Glider surveys in coastal environments can be used to identify the general location of fish spawning aggregations and to understand their relationships to the ocean's bio-physical properties. If paired with net sampling, diver surveys or cameras to identify the species producing these spawning sounds, the patterns we have documented could be used to create appropriate protected areas or fishing closure regions, if necessary. The Wave Glider's ability to be equipped with a wide variety of oceanographic sampling instruments enables the monitoring of all soniferous species as well as abiotic influences including anthropogenic activity, thus providing a full ecosystem view.

REFERENCES

- Baumgartner, M. F., and Fratantoni, D. M. (2008). Diel periodicity in both sei whale vocalization rates and the vertical migration of their copepod prey observed from ocean gliders. *Limnol. Oceanogr.* 53, 2197–2209. doi: 10.4319/lo.2008.53.5_part_2.2197
- Baumgartner, M. F., Fratantoni, D. M., Hurst, T. P., Brown, M. W., Cole, T. V. N., Van Parijs, S. M., et al. (2013). Real-time reporting of baleen whale passive acoustic detections from ocean gliders. *J. Acoust. Soc. Am.* 134, 1814–1823. doi: 10.1121/1.4816406
- Bingham, B., Kraus, N., Howe, B., Freitag, L., Ball, K., Koski, P., et al. (2012). Passive and active acoustics using an autonomous wave glider. *J. F. Robot.* 29, 911–923. doi: 10.1002/rob.21424
- Butler, J., Parnell, E., and Širović, A. (2017). Who's making all that racket? Seasonal variability in kelp forest soundscapes. *J. Acoust. Soc. Am.* 141:3864. doi: 10.1121/1.4988635
- Cato, D. H. (1978). Marine biological choruses observed in tropical waters near Australia. *J. Acoust. Soc. Am.* 64, 736–743. doi: 10.1121/1.382038
- D'Spain, G. L., Batchelor, H., Helble, T. A., and McCarty, P. (2013). New observations and modeling of an unusual spatiotemporal pattern of fish

AUTHOR CONTRIBUTIONS

MC and ET designed the study. MC led mission programming and deployment of the Wave Glider and analyzed the Wave Glider data, environmental data and created the maps. CP processed and visualized the passive acoustic data. CP wrote the initial manuscript with contributions from MC, and all authors read and helped and revise the final version.

FUNDING

CP was supported in part by a Natural Sciences and Engineering Research Council (NSERC) of Canada Postgraduate Scholarship – Doctoral Program and the Fleet Admiral Chester W. Nimitz Fund.

ACKNOWLEDGMENTS

We are grateful to staff at the Coastal Observing Research and Development Center at Scripps Institution of Oceanography, especially Nixon Carruthers, Daniel Bedenko, Michael Jilka, and Robert Hess for help in Wave Glider programming, setup and deployment. We also wish to acknowledge the U.S. Office of Naval Research DURIP program for supporting the research instrumentation used in this program and their long term commitment to development of unmanned systems, as well as the support of the Friedkin Foundation for research support.

SUPPLEMENTARY MATERIAL

The Supplementary Material for this article can be found online at: <https://www.frontiersin.org/articles/10.3389/fmars.2019.00526/full#supplementary-material>

- chorusing off the southern California coast. *Proc. Meetings Acoust.* 19, 1–7. doi: 10.1121/1.4800997
- Erismann, B. E., and Rowell, T. J. (2017). A sound worth saving: acoustic characteristics of a massive fish spawning aggregation. *Biol. Lett.* 13:20170656. doi: 10.1098/rsbl.2017.0656
- Gannon, D. P. (2008). Passive acoustic techniques in fisheries science: a review and prospectus. *Trans. Am. Fish. Soc.* 137, 638–656. doi: 10.1577/T04-142.1
- Hine, R., Willcox, S., Hine, G., and Richardson, T. (2009). "The wave glider: a wave-powered autonomous marine vehicle," in *Proceedings of the MTS/IEEE OCEANS Conference*, (Biloxi, MS), 1–6.
- Ibara, R. M., Penny, L. T., Ebeling, A. W., van Dykhuizen, G., and Cailliet, G. (1983). "The mating call of the plainfin midshipman fish, *Porichthys notatus*," in *Predators and Prey in Fishes*, eds D. L. G. Noakes, D. G. Lindquist, G. S. Helfman, and J. A. Ward (The Hague: Dr W. Junk Publishers), 205–212. doi: 10.1007/978-94-009-7296-4_22
- Jensen, F. B., Kuperman, W. A., Porter, M. B., and Schmidt, H. (2011). *Computational Ocean Acoustics*, 2nd Edn. New York, NY: Springer New York.
- Klinck, H., Stelzer, R., Jafarmadar, K., and Mellinger, D. K. (2009). "AAS Endurance: an autonomous acoustic sailboat for marine mammal research," in *Proceedings of International Robotic Sailing Conference*, (Matosinhos), 43–48.

- Kraus, N., and Bingham, B. (2011). "Estimation of wave glider dynamics for precise positioning," in *Proceedings of the MTS/IEEE OCEANS Conference*, (Kona), 1–9.
- Love, M. (2011). *Certainly More Than You Want to Know About the Fishes of the Pacific Coast: A Postmodern Experience*. Santa Barbara, CA: Really Big Press.
- Luczkovich, J. J., Mann, D. A., and Rountree, R. A. (2008). Passive acoustics as a tool in fisheries science. *Trans. Am. Fish. Soc.* 137, 533–541. doi: 10.1577/T06-258.1
- McWilliam, J. N., McCauley, R. D., Erbe, C., and Parsons, M. J. G. (2018). Soundscape diversity in the Great Barrier Reef: Lizard Island, a case study. *Bioacoustics* 27, 295–311. doi: 10.1080/09524622.2017.1344930
- Mellinger, D., Stafford, K., Moore, S., Dziak, R., and Matsumoto, H. (2007). An overview of fixed passive acoustic observation methods for cetaceans. *Oceanography* 20, 36–45. doi: 10.5670/oceanog.2007.03
- Mullison, J., Symonds, D., and Trenaman, N. (2011). "ADCP data collected from a liquid robotics wave glider," in *Proceedings of the 2011 IEEE/OES 10th Current, Waves and Turbulence Measurements (CWTM)*, (Monterey, CA), 266–272.
- Pagniello, C. M., Butler, J., D'Spain, G. L., Jaffe, J., Parnell, E., and Širović, A. (2017). Soundscape fishing: spatial variability in a low-frequency fish chorus in the southern California kelp forest. *J. Acoust. Soc. Am.* 142:2503. doi: 10.1121/1.5014140
- Parsons, M. J. G., Salgado Kent, C. P., Recalde-Salas, A., and McCauley, R. D. (2017). Fish choruses off port Hedland. *Western Aust. Bioacoust.* 26, 135–152. doi: 10.1080/09524622.2016.1227940
- Parsons, M. J. G., Salgado-Kent, C. P., Marley, S. A., Gavrilov, A. N., and McCauley, R. D. (2016). Characterizing diversity and variation in fish choruses in Darwin Harbour. *ICES J. Mar. Sci.* 73, 2058–2074. doi: 10.1093/icesjms/fsw037
- Reshef, E. S., Demer, D. A., Wiggins, S., and Baumann-Pickering, S. (2018). *Chorusing Fish Behavioral Changes Potentially Linked to Climate Variability*. in 2018 Ocean Sciences Meeting F14A-0718. Available at: <https://agu.confex.com/agu/os18/meetingapp.cgi/Paper/324358> (accessed February 12, 2018).
- Sousa-Lima, R. S., Norris, T. F., Oswald, J. N., and Fernandes, D. P. (2013). A review and inventory of fixed autonomous recorders for passive acoustic monitoring of marine mammals. *Aquat. Mamm.* 39, 23–53. doi: 10.1578/AM.39.1.2013.23
- Tyack, P. L. (1998). "Acoustic communication under the sea," in *Animal Acoustic Communication: Sound Analysis and Research Methods*, eds S. L. Hopp, M. J. Owren, and C. S. Evans (Berlin: Springer), 163–220. doi: 10.1007/978-3-642-76220-8_6
- Wall, C. C., Lembke, C., Hu, C., and Mann, D. A. (2014). Fish sound production in the presence of harmful algal blooms in the Eastern Gulf of Mexico. *PLoS One* 9:e114893. doi: 10.1371/journal.pone.0114893
- Wall, C. C., Lembke, C., and Mann, D. A. (2012). Shelf-scale mapping of sound production by fishes in the eastern Gulf of Mexico, using autonomous glider technology. *Mar. Ecol. Prog. Ser.* 449, 55–64. doi: 10.3354/meps09549
- Wall, C. C., Simard, P., Lembke, C., and Mann, D. A. (2013). Large-scale passive acoustic monitoring of fish sound production on the West Florida Shelf. *Mar. Ecol. Prog. Ser.* 484, 173–188. doi: 10.3354/meps10268
- Wiggins, S. (2003). Autonomous acoustic recording packages (ARPs) for long-term monitoring of whale sounds. *Mar. Technol. Soc. J.* 37, 13–22. doi: 10.4031/002533203787537375
- Wiggins, S., Manley, J., Brager, E., and Woolhiser, B. (2010). "Monitoring marine mammal acoustics using Wave Glider," in *Proceedings of the MTS/IEEE OCEANS Conference*, (Washington, DC), 1–4.
- Wiggins, S. M., and Hildebrand, J. A. (2007). "High-frequency acoustic recording package (HARP) for broad-band, long-term marine mammal monitoring," in *Proceedings of the 2007 Symposium on Underwater Technology and Workshop on Scientific Use of Submarine Cables and Related Technologies*, (Tokyo: IEEE), 551–557.
- Winn, H. E. (1964). "The biological significance of fish sounds," in *Marine Bio-Acoustics*, ed. W. N. Tavolga (Oxford, UK: Pergamon Press), 213–231.

Conflict of Interest Statement: The authors declare that the research was conducted in the absence of any commercial or financial relationships that could be construed as a potential conflict of interest.

Copyright © 2019 Pagniello, Cimino and Terrill. This is an open-access article distributed under the terms of the Creative Commons Attribution License (CC BY). The use, distribution or reproduction in other forums is permitted, provided the original author(s) and the copyright owner(s) are credited and that the original publication in this journal is cited, in accordance with accepted academic practice. No use, distribution or reproduction is permitted which does not comply with these terms.



Next-Generation Optical Sensing Technologies for Exploring Ocean Worlds—NASA FluidCam, MiDAR, and NeMO-Net

Ved Chirayath* and Alan Li

NASA Ames Laboratory for Advanced Sensing, Mountain View, CA, United States

OPEN ACCESS

Edited by:

Leonard Pace,
Schmidt Ocean Institute,
United States

Reviewed by:

Christoph Waldmann,
University of Bremen, Germany
Steven G. Ackleson,
United States Naval Research
Laboratory, United States

*Correspondence:

Ved Chirayath
ved.c@nasa.gov

Specialty section:

This article was submitted to
Ocean Observation,
a section of the journal
Frontiers in Marine Science

Received: 23 December 2018

Accepted: 12 August 2019

Published: 05 September 2019

Citation:

Chirayath V and Li A (2019)
Next-Generation Optical Sensing
Technologies for Exploring Ocean
Worlds—NASA FluidCam, MiDAR,
and NeMO-Net.
Front. Mar. Sci. 6:521.
doi: 10.3389/fmars.2019.00521

We highlight three emerging NASA optical technologies that enhance our ability to remotely sense, analyze, and explore ocean worlds—FluidCam and fluid lensing, MiDAR, and NeMO-Net. Fluid lensing is the first remote sensing technology capable of imaging through ocean waves without distortions in 3D at sub-cm resolutions. Fluid lensing and the purpose-built FluidCam CubeSat instruments have been used to provide refraction-corrected 3D multispectral imagery of shallow marine systems from unmanned aerial vehicles (UAVs). Results from repeat 2013 and 2016 airborne fluid lensing campaigns over coral reefs in American Samoa present a promising new tool for monitoring fine-scale ecological dynamics in shallow aquatic systems tens of square kilometers in area. MiDAR is a recently-patented active multispectral remote sensing and optical communications instrument which evolved from FluidCam. MiDAR is being tested on UAVs and autonomous underwater vehicles (AUVs) to remotely sense living and non-living structures in light-limited and analog planetary science environments. MiDAR illuminates targets with high-intensity narrowband structured optical radiation to measure an object's spectral reflectance while simultaneously transmitting data. MiDAR is capable of remotely sensing reflectance at fine spatial and temporal scales, with a signal-to-noise ratio 10^{-10^3} times higher than passive airborne and spaceborne remote sensing systems, enabling high-framerate multispectral sensing across the ultraviolet, visible, and near-infrared spectrum. Preliminary results from a 2018 mission to Guam show encouraging applications of MiDAR to imaging coral from airborne and underwater platforms whilst transmitting data across the air-water interface. Finally, we share NeMO-Net, the **N**eural **M**ulti-Modal **O**bservation & Training **N**etwork for Global Coral Reef Assessment. NeMO-Net is a machine learning technology under development that exploits high-resolution data from FluidCam and MiDAR for augmentation of low-resolution airborne and satellite remote sensing. NeMO-Net is intended to harmonize the growing diversity of 2D and 3D remote sensing with *in situ* data into a single open-source platform for assessing shallow marine ecosystems globally.

using active learning for citizen-science based training. Preliminary results from four-class coral classification have an accuracy of 94.4%. Together, these maturing technologies present promising scalable, practical, and cost-efficient innovations that address current observational and technological challenges in optical sensing of marine systems.

Keywords: remote sensing, coral reefs, UAVs, fluid lensing, MiDAR, machine learning, NeMO-Net

INTRODUCTION

Our planet's habitability depends on the health and stability of its largest ecosystem, the global ocean. Persistent multispectral optical remote sensing has been instrumental in monitoring and managing Earth's terrestrial ecosystems for land use and land cover change. Through a sustained satellite land imaging program, first implemented over 40 years ago, remote sensing at various spatial resolutions has provided a global view of our changing planet, enabling scientists to assess ecosystem dynamics, biodiversity, natural hazards, and many other applications. Yet, a comparable sustained marine imaging system, capable of detecting changes in marine ecosystems, remains stubbornly out of reach, albeit increasingly relevant in a changing global biosphere predominantly governed by marine systems. Indeed, as of 2018, 100% of the martian and lunar surfaces have been mapped at a spatial resolution of 100 m or finer in visible wavelengths, compared to an estimated 5% of Earth's seafloor.

Observational, technological, operational, and economic issues are the main factors inhibiting global sustained imaging of the marine environment on par with that of terrestrial ecosystems. Observational challenges arise in remote sensing of aquatic systems due to strong optical attenuation in the water column as well as reflection and refraction from ocean waves at the air-water interface. Remote sensing beyond the photic zone, namely deeper than the first 100 m of the water column in clear waters, cannot be addressed in the near future from airborne, and spaceborne platforms. Instead, underwater vehicles are needed to act as the aircraft and satellites of the ocean realm, creating multispectral optical maps as well as topographic maps with acoustic or optical methods. Technological limitations exist for photon-limited passive remote sensing instruments as well as *in situ* autonomous underwater vehicles (AUVs), which cannot cover the same areas with nearly the same precision as aircraft and spacecraft. Scalable information systems are not well-established to exploit the myriad of data sources available from *in situ* and remote sensing observations. The standardization and normalization of terrestrial remote sensing practices, georeferencing, and dataset processing algorithms are not directly applicable to marine datasets. Significant difficulties remain in harmonizing multi-modal datasets acquired from acoustic and optical instruments above and below the surface to perform ecosystem assessment. Finally, the significant cost associated with marine data collection exacerbates each of these challenges, often limiting new technologies from being able to scale to global areas due to economic constraints.

In this report we highlight three emerging NASA technologies, primarily supported by NASA's Earth Science Technology Office (ESTO), that attempt to address some of the aforementioned observational, technological, operational, and economic challenges in the context of a vital marine ecosystem—coral reefs. While these developments by no means provide a whole solution to the challenges of understanding our global ocean, they present promising scalable, practical, and cost-efficient ongoing innovations in this field.

Needs and Challenges in Remote Sensing of Aquatic Systems

Aquatic ecosystems, particularly coral reefs, remain quantitatively poorly characterized by low-resolution remote sensing as a result of refractive distortion from ocean waves and optical attenuation. Earth's coastal environments and shallow reef ecosystems comprise an extensive and global life-support system playing a crucial role in regulating our planet's climate and biodiversity as well as protecting our coastal cities and infrastructure from storm events. These highly sensitive ecosystems respond rapidly to changes in land management and climate as indicated by precipitous changes in their morphology, composition, and species makeup. As a result, global observation of coastal environments and determination of the health and extent of coral reefs is a vital earth science measurement, referred to in a decadal survey by the National Research Council (NRC) as a "bellwether of climate change as reef health can often presage changing trends in circulation, ocean acidity and biodiversity (Board, 2007)."

At present marine ecosystems are experiencing one of most significant changes in their history on Earth, triggered by unprecedented anthropogenic pressures, warming seas, ocean acidification, sea level rise, habitat destruction, agricultural runoff, and overharvesting, among other contributing stressors (Bellwood et al., 2004). Compounding our understanding of the impacts of these rapidly-changing pressures is a severe lack of sustained global baseline habitat mapping data and knowledge of reef makeup over regional areas and short timescales with effective spatial resolutions unaffected by sea state conditions, which can introduce refractive errors at the air-water interface (Edinger et al., 2000; Chirayath and Earle, 2016; Storlazzi et al., 2016). Such data are vital to accurately assess and quantify reef ecosystem health for adequate management of these aquatic resources (Bellwood et al., 2004).

Coral reef and shallow marine ecosystem remote sensing can be broken down into measurement and determination of habitat, geomorphology, water properties, bathymetry and

currents, and waves (Goodman et al., 2013). Currently, remote sensing is used to examine coral reef ecosystems primarily at meter and km-scale scales through airborne campaigns (e.g., CORAL (PRISM), AVIRIS, DCS) and spaceborne assets (e.g., LandSat, HICO, IKONOS) (Maeder et al., 2002; Andréfouët et al., 2003; Purkis and Pasterkamp, 2004; Corson et al., 2008). Recently, however, it has been shown that low resolution satellite and airborne remote sensing techniques poorly characterize fundamental coral reef health indicators, such as percent living cover and morphology type, at the cm and meter scale (Chirayath and Instrella, accepted). While commercial satellite and airborne remote sensing instruments can achieve effective spatial resolutions (ESR) of 0.3 m over terrestrial targets, ocean waves, and even a flat fluid surface, distort the true location, size, and shape of benthic features. ESR finer than 10 m is within the regime of refractive distortions from ocean waves and requires a remote sensing methodology capable of correcting for these effects. The classification accuracy of coral reefs, for example, is significantly impacted by the ESR of remote sensing instruments. Indeed, current global assessments of coral reef cover and morphology classification based on 10 m-scale satellite data alone can suffer from errors >36% (Figure 1), capable of change detection only on yearly temporal scales and decameter spatial scales, significantly hindering our understanding of patterns, and processes in marine biodiversity.

Even with improved ground sample distance (GSD), state-of-the-art commercial imaging satellites cannot image submerged targets at the same effective spatial resolution (ESR) as terrestrial targets, or consistently georectify benthic surfaces, due to the combined effects of refractive, reflective, and caustic fluid distortions introduced by surface waves (Figure 2) (Chirayath, 2016; Chirayath and Earle, 2016). To address this challenge, we share the NASA FluidCam and fluid lensing technology development, which aims to create a high ESR remote sensing instrument robust to sea state conditions using inexpensive components in a small CubeSat-sized package.

Getting Deeper and Beyond the Photic Zone

Next-generation remote sensing instruments require advances in both passive and active sensing technologies to compare to some of the most sensitive sensors that already exist in the ocean (Tyack, 2000; Madsen et al., 2005). Traditional remote sensing and multispectral imaging of environments from air and space primarily use passive broad-spectrum illumination provided by the Sun coupled with sensitive push broom-style line array photodetectors fitted with narrowband filters to produce multispectral images (Irons et al., 2012). Hyperspectral remote sensing extends this concept further by using photodetectors and scanning spectrometers to resolve hundreds or even thousands of spectral bands (Eismann, 2012). However, in both techniques, atmospheric conditions and the Sun's radiation distribution put limits on which frequencies of light and what SNR are attainable for multispectral imaging on Earth and other planets within our solar system. In aquatic systems, further bounds are introduced as only UV and visible bands of light penetrate

the first 100 meters of the clearest waters, the photic zone. As such, current passive multispectral/hyperspectral imagers are limited by ambient conditions along the optical path, ambient illumination spectrum, optical aperture, photodetector SNR, and, consequently, relatively long integration times.

The physical limitations of solar electromagnetic radiation propagation in oceans is one of the chief factors inhibiting the development of a sustained marine imaging program beyond the photic zone. However, significant progress has been made in the past decade with underwater remotely operated or autonomous underwater vehicles (ROVs and AUVs) (Roberts et al., 2010), unmanned surface vehicles (USVs) (Mordy et al., 2017), and profiling floats (Roemmich and Gilson, 2009) to characterize the seafloor, ocean surface, and ocean column over large geographic areas. Recently, three-dimensional photogrammetry, active acoustical methods, and *in situ* water column measurements have been used with remarkable effectiveness on such platforms to narrow the gap in observational capacity between terrestrial and aquatic systems, revealing mesophotic, and deep sea habitats with unexpected biodiversity and ecological complexity (Pizarro et al., 2004; Bodenmann et al., 2013).

However, the primary means by which global terrestrial ecosystem management has been achieved, through multispectral/hyperspectral remote sensing, is still limited by marine optical instrumentation. Further, relaying data from underwater instruments to and through the surface at bandwidths common to airborne and spaceborne platforms has remained a significant obstacle to sustained deep sea mapping (McGillivray et al., 2018). To address these challenges and extend the depth attainable by airborne remote sensing platforms, we highlight developments behind NASA MiDAR, the Multispectral, Imaging, Detection, and Active Reflectance instrument. MiDAR offers a promising new method for active multispectral *in situ* and remote sensing of marine systems in previously underutilized spectral bands spanning UV-NIR. As an active optical instrument, MiDAR has the potential to remotely sense deeper than the photic zone defined by the Sun's downwelling irradiance. In addition, MiDAR presents a methodology for simultaneous imaging and optical communications within a fluid and through the air-water interface. Finally, MiDAR makes use of inexpensive narrowband laser and light emitting diodes for the MiDAR transmitter and utilizes the computational imaging capability of the FluidCam instruments for MiDAR receivers.

Making Use of All the Data

With the development of any new instrumentation or measurement capability arise questions of scalability, data management, and interoperability with legacy data and products. How science-driven technology developments scale and address questions pertinent to global marine ecosystems is an ongoing challenge, exacerbated by the ever-increasing volume and complexity of datasets from next-generation instruments. Multispectral 3D data gathered from AUVs, for example, offer high-resolution views of deep-sea systems, but ultimately their scientific value remains limited in scope and application owing to their standalone nature. One sensor may offer a view of a system in certain spectral bands, resolution, and location,

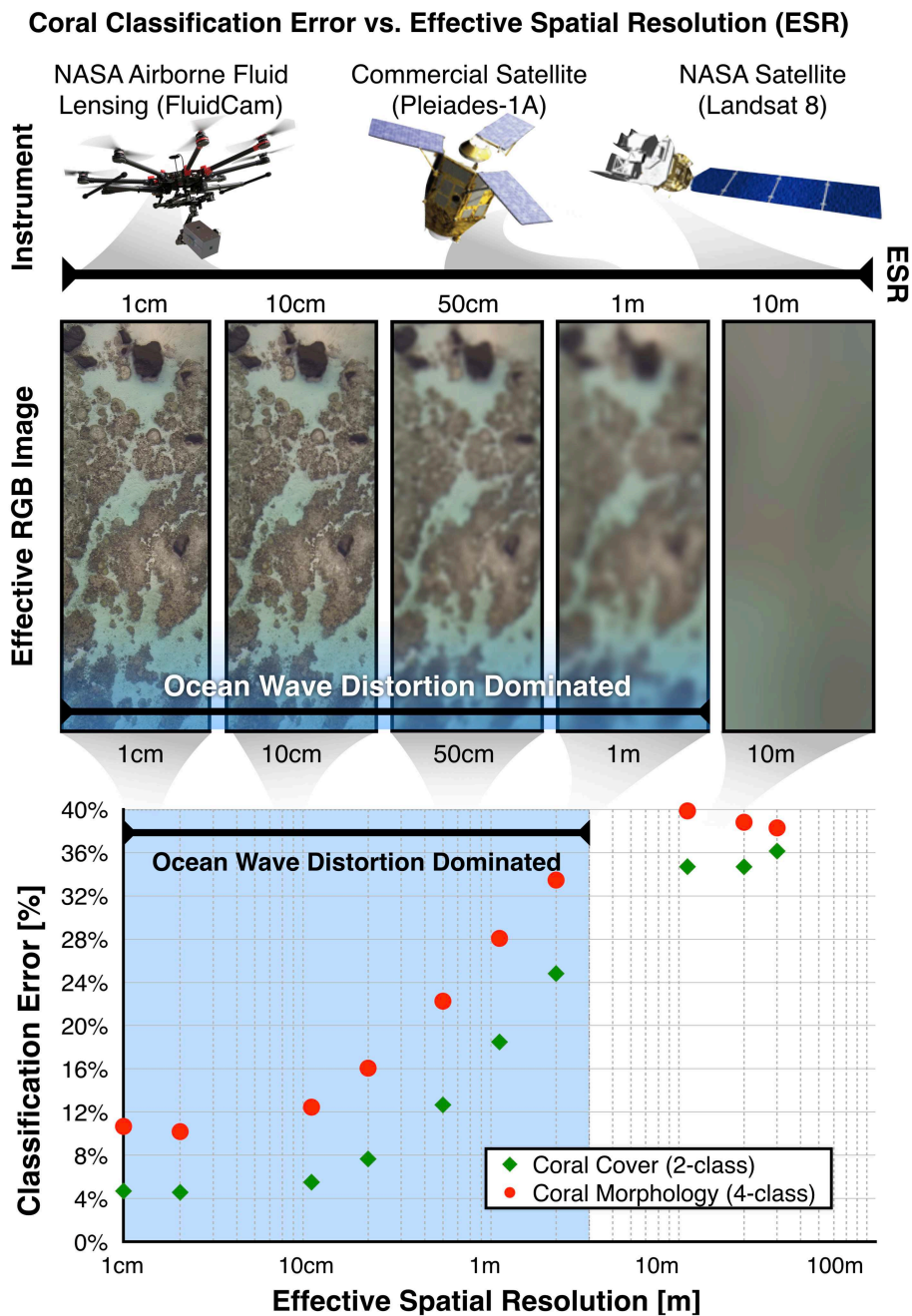


FIGURE 1 | Coral reef classification error as a function of effective spatial resolution (ESR). Using modern machine learning based habitat mapping, coral cover can be determined with <5% error at the cm spatial scale with fluid lensing and FluidCam, under a typical range of sea states, 18% error at the 1 m scale from commercial platforms with a perfectly flat sea state, and 34% error at the 10 m scale, typical of sustained land imaging satellites. Adapted with permission from Chirayath and Instrella (accepted).

while another sensor may gather only topographic data of the same system. Oceanography, in particular, is frequented with such cases of well-understood local systems, captured by independent dedicated field missions, but poorly understood global systems over large time scales. Ultimately, this symptom of marine system sensing is characterized by high spatial and

temporal heterogeneity in datasets and low interoperability among multimodal sensing systems.

Fortunately, instrument technology development has occurred alongside advances in information systems technology, capable of handling the growing volume of data and computational overhead. Machine learning for Earth

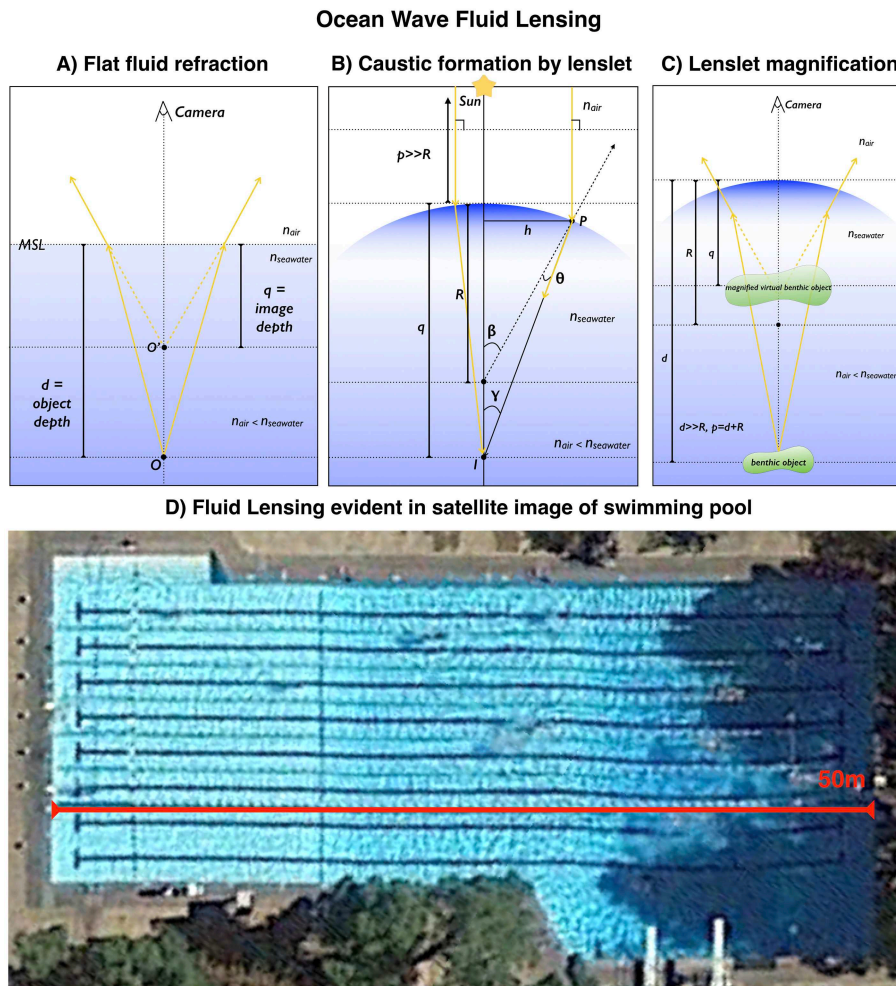


FIGURE 2 | Fluid lensing from ocean waves and its effect on the effective spatial resolution and true location of benthic targets. **(A)** A calm aquatic surface, when remotely sensed from above, distorts the apparent depth, and spatial position of a benthic target. **(B)** A curved aquatic surface, or fluid lenslet formed by surface waves, focuses sunlight, forming bright bands of light, or caustics, on the seafloor. **(C)** A fluid lenslet introduces a net magnification or demagnification effect as a function of curvature. **(D)** These fluid lensing effects combine to reduce the ESR, SNR, and position of benthic targets. An image captured by state-of-the-art commercial satellite systems, such as this 0.3 m GSD Worldview-3 image of an Olympic swimming pool, is noticeably affected by small wave disturbances. Note the distortion of linear lane lines from left to right as a function of surface waves and depth, as well as non-uniform reflectance over pool floor due to caustics. Adapted with permission from Chirayath (2016).

Science applications, in particular, has gained traction, and credibility in recent years as an increasing fleet of commercial and research satellites has driven developments in scaling remote sensing assessment capabilities through semiautonomous and autonomous processing pipelines (Nemani et al., 2011). However, the issue of amalgamating multi-resolution, multispectral, multi-temporal, and multi-sensor input for multimodal remote sensing is still pertinent and challenging in both terrestrial and marine ecosystem science. Currently, there is a need for extrapolating data collected upon local scales toward data collected upon regional/global and fine temporal scales, as issues pertaining to data quality, environmental conditions, and scene and instrumentation-specific calibration often cannot be easily reconciled.

Statistical and predictive learning methods using Earth Science datasets have a long history in many remote sensing applications (Lary et al., 2016). Typically, in a massively multivariate system or one composed of thousands of variables, also known as feature vectors, machine learning excels at discovering patterns, and recognizing similarities within data. In these cases, a training set, or training data, is designated for the algorithm to learn the underlying behavior of the system, which is then applied to a query or test set. The evaluation of error using such methods requires a reference set, also referred to as the truth set, or ground truth, in which the algorithm's predictions can be evaluated objectively through a number of error metrics. Machine learning excels in classification problems and in areas where a deterministic model is too expensive or non-existent,

and hence an empirical model can be constructed from existing data to predict future outcomes. Existing projects cover a wide range of topics, such as characterization of airborne particulates (Lary et al., 2007, 2009), prediction of epi-macro-benthic diversity (Collin et al., 2011), and automated annotators for coral species classification (Beijbom et al., 2015).

An emerging field within machine learning, convolutional neural networks (CNNs), have recently been applied to processing optical remote sensing data for semantic segmentation of ecosystems (Serpico and Roli, 1995; Zhong et al., 2017). To this end, we share developments behind NASA NeMO-Net, the Neural Multi-Modal Observation & Training Network for Global Coral Reef Assessment. NeMO-Net is an open-source machine learning technology under development that exploits high-resolution data from FluidCam and MiDAR for augmentation of low-resolution airborne and satellite remote sensing. NeMO-Net is intended to harmonize the growing diversity of 2D and 3D remote sensing and *in situ* data into a single open-source platform for assessing shallow marine ecosystems globally using active learning for citizen-science based training (Cartier, 2018).

EMERGING NASA TECHNOLOGIES AND METHODS

This section presents preliminary results from two optical remote sensing instruments in maturation, FluidCam and MiDAR, as well as an open-source supercomputer-based deep learning algorithm in development, NeMO-Net, intended to ingest next-generation 3D multispectral datasets produced by instruments such as FluidCam and MiDAR for enhancing existing low resolution airborne and satellite remote sensing data for global marine ecosystem assessment. Each technology was motivated by the observational, technological, operational, and economic issues discussed previously. Full technical descriptions of each technology are beyond the scope of this Technology Report and readers are encouraged to reference citations as provided for relevant background.

Fluid Lensing and the FluidCam Instrument

This portion outlines highlights in the study of the fluid lensing phenomenon encountered in ocean remote sensing, the development of the fluid lensing algorithm, and NASA FluidCam, a passive optical multispectral instrument developed for airborne and spaceborne remote sensing of aquatic systems.

The Ocean Wave Fluid Lensing Phenomenon

The optical interaction of light with fluids and aquatic surfaces is a complex phenomenon. As visible light interacts with aquatic surface waves, such as ocean waves, time-dependent non-linear optical aberrations appear, forming caustic, or concentrated, bands of light on the seafloor, as well as refractive lensing, which magnifies and demagnifies underwater objects as viewed from above the surface. Additionally, light is attenuated through absorption and scattering, among other effects. These combined optical effects are referred to as the ocean wave fluid lensing phenomenon (Chirayath, 2016). The regime of ocean waves

for which such fluid lensing occurs is predominantly wind-driven and commonplace in marine systems. Indeed, ocean wave fluid lensing can introduce significant distortions in imagery acquired through the air-water interface. Aquatic ecosystems are consequently poorly characterized by low effective spatial resolution (ESR) remote sensing owing to such fluid lensing and attenuation (Goodman et al., 2013; Chirayath and Earle, 2016).

The ocean wave fluid lensing phenomenon has been studied in the context of ocean optics to a limited extent. A theoretical model for ocean wave irradiance fluctuations from lensing events was noted first by Airy (1838) and predicted by Schenck (1957). The closest direct analysis of the ocean wave fluid lensing phenomenon by You et al. (2010) modeled the wave-induced irradiance fluctuations from ocean waves and compared the data to field observations. However, this study was chiefly concerned with intensity variations of the light field and not image formation and ray-tracing, which are needed to describe the lensing phenomenon responsible for the observed optical magnification and demagnification associated with traveling surface waves over benthic features. Interestingly, Schenck analytically predicted the irradiance concentration, observable as caustics, for shallow ocean waves, but did not numerically model the system to validate these predictions. Ultimately, this motivated further investigation by the author into the ocean wave fluid lensing phenomenon, which verified such predictions by Schenck and directly addressed Airy's early predictions by direct optical coupling of light and ocean waves in a controlled environment through a Fluid Lensing Test Pool (Figure 3A).

Figure 2 illustrates the basic geometric optics responsible for fluid lensing and the surprising effects they can have on imagery from state-of-the-art commercial marine remote sensing systems. Considering the simplest case of rays propagating from a benthic object through the air-seawater boundary, as depicted in Figure 2A, refraction causes the apparent depth of a benthic object to appear shallower than its true depth, as observed from above the surface. Here, an object *O*, located at depth *d*, with respect to mean sea level (MSL), appears as *O'* at apparent depth *q*. Using Snell's law, it can be shown that the actual depth and the apparent depth are related by the refractive depth distortion equation: $q = -\frac{n_{\text{air}}}{n_{\text{seawater}}}d$. With $n_{\text{air}} = 1$ and $n_{\text{seawater}} = 1.33$, this yields $q = -0.752d$. So, for a flat fluid sea surface and nadir camera viewpoint, the apparent depth is typically three-fourths the actual depth on Earth. This effect appears to magnify an object by an inversely proportional amount. Next, consider the presence of an ocean wave that assumes the form of a small optical lens, or lenslet, of curvature R_{lens} . For an object *O* at height *p* from the lenslet surface, the combined effect of refraction and the curvature of the two-fluid interface will cause light rays emerging from the object to converge at the focal distance *q* and form image *I*, as depicted in Figure 2B. Using the small angle approximation for incident light rays, Snell's law becomes $n_{\text{air}}\theta_1 = n_{\text{seawater}}\theta_2$. Using exterior angle relations, it can be shown that $\theta_1 = \alpha + \beta$ and $\theta_2 = \beta - \gamma$. Combining these expressions yields $n_{\text{air}}\alpha + n_{\text{seawater}}\gamma = \beta(n_{\text{seawater}} - n_{\text{air}})$. It can be shown that $\tan(\alpha) \approx \alpha \approx d/p$, $\tan(\beta) \approx \beta \approx d/R$, and $\tan(\gamma) \approx \gamma \approx d/q$. Substituting these linearized expressions

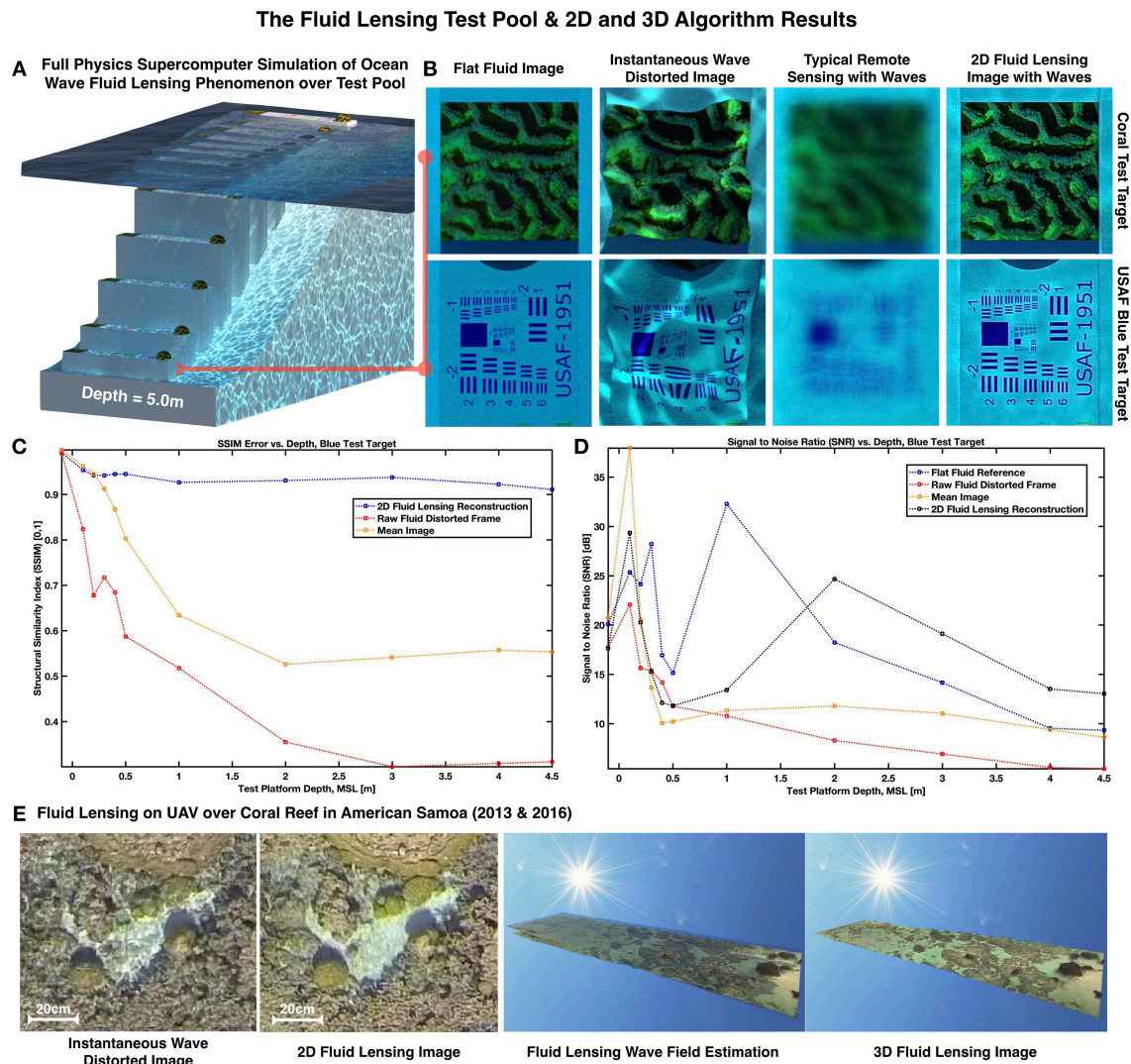


FIGURE 3 | The Fluid Lensing Test Pool, 2D, and 3D Fluid Lensing Algorithm results. **(A)** A side render of the Fluid Lensing Test Pool showing formation of caustics on floor and optical attenuation (water volume removed for clarity). **(B)** 2D Fluid Lensing Algorithm Results as compared to a flat fluid state, instantaneous image, and image with integration time. **(C,D)** Structural Similarity Index (SSIM) and signal-to-noise ratio (SNR) for fluid lensing results as a function of depth. **(E)** 2D and 3D Fluid Lensing Algorithm results from 2013 and 2016 airborne campaigns in American Samoa. Adapted with permission from Chirayath (2016).

into $n_{air}\alpha + n_{seawater}\gamma = \beta(n_{seawater} - n_{air})$ yields the refractive lenslet image equation: $\frac{n_{air}}{p} + \frac{n_{seawater}}{q} = \frac{n_{seawater} - n_{air}}{R}$. In the case of the flat fluid surface, $R \rightarrow \infty$, and the refractive lenslet image equation yields the refractive depth distortion equation shown earlier: $q = -\frac{n_{air}}{n_{seawater}}d$. Finally, in the case of the Sun illuminating a refractive lenslet surface, the refractive lenslet image equation explains the formation of caustic and the phenomenon of caustic focusing from the light gathering area of the lenslet. **Figure 2C** illustrates the formation of an image, I , at focal point q . Given the angular size of the Sun as viewed from Earth and orbital distance, incident light waves are approximated as planar. With $p \gg R$, the refractive lenslet image equation reduced to the following caustic refractive lenslet focusing relation: $\frac{n_{seawater}}{q} = \frac{n_{seawater} - n_{air}}{R}$.

The Fluid Lensing Test Pool

To better understand the effects of ocean wave fluid lensing and create a validation testbed, a full-physics optofluidic simulation was performed on the NASA Ames Pleiades Supercomputer, the fluid lensing test pool (**Figure 3A**). The 3D full-physics simulation is the first of its kind and includes full water column and atmospheric column absorption, dispersion, scattering, refraction, and multiple reflections, comprising more than 50 million CPU hours for 33 s of animation (Chirayath, 2016). The fluid lensing test pool consists of a series of test targets at various depths submerged in a water volume, with optical properties and surface waves characteristic of the primary target ecosystem, shallow marine reefs in clear tropical waters.

The time-dependent air-water surface is modeled using Tessendorf's Fourier domain method (Tessendorf, 2001) based on a Phillips spectrum of ocean waves from measured spectral features characteristic of a fringing coral reef system. A surface mesh generated from a parameterized Phillips spectrum defines the ocean surface height field $h(\mathbf{x}, t)$, represented as the sum of periodic functions such that:

$$h(\mathbf{x}, t) = \sum_{\mathbf{k}} \tilde{h}(\mathbf{k}, t) e^{i\mathbf{k}\mathbf{x}}$$

where k is the wave number, \mathbf{k} is the wave vector, T is the wave period, λ is the wavelength, h is the height of the water, \mathbf{x} is the spatial position of the simulation point, t is time, g is the gravitational constant, P_k is the Phillips spectrum, ξ is an independent draw from a Gaussian random number generator with $\mu = 0$ and $\sigma = 1$, L is the largest permissible wave arising from a given wind speed, ω is the angular frequency, and w is the wind direction.

The set of complex Fourier amplitudes and initial phase values at $t = 0$, is defined by the following expression:

$$\tilde{h}_0(\mathbf{k}) = \frac{1}{\sqrt{2}} (\xi_r + i\xi_i) \sqrt{P_h(\mathbf{k})}$$

where initial parameters are taken from a Gaussian random number generator, ξ_i , and $P_h(\mathbf{k})$ is the Phillips spectrum (Phillips, 1958) from wind-driven waves in shallow reef environments. The Phillips spectrum characterizes the spectral and statistical properties of the equilibrium range of wind-generated gravity waves and is generated by the following expression, put forth by Phillips (Phillips, 1985).

$$P_h(\mathbf{k}) = \frac{A |\hat{\mathbf{k}} \cdot \mathbf{w}|^2 e^{-\frac{1}{(kL)^2}}}{k^4}$$

The second component of modeling the ocean wave fluid lensing phenomenon is simulating the optofluidic interactions of light with the ocean wave synthesis. Ray-tracing and light transport is used to model optofluidic interactions and is performed using LuxRender v.1.6, a physically-based, open-source, and unbiased render engine. For the purposes of simulating the complex optofluidic interactions specific to the ocean wave fluid lensing phenomenon, this work configures LuxRender to use an efficient CPU-based unbiased bidirectional path tracing render engine with Metropolis Light Transport (MLT) for efficient sampling and caustic convergence.

The ocean wave synthesis is coupled to water's empirically-determined optical properties. The absorptive and refractive properties of seawater are based on experimental data from Pope and Fry (1997) and Daimon and Masumura (2007). From Pope and Fry (1997), it is shown that clear seawater and pure water have similar optical properties relevant to this study; however, the inherent optical properties of real-world marine environments may differ significantly due to suspended sediment, carbon-dissolved organic matter (CDOM), phytoplankton, molecular scattering, and salinity, among other things. The fluid lensing

test pool does not model the ocean wave fluid lensing as a function of all of these parameters, but focuses on the dispersive, absorptive, reflective, and refractive properties of water discussed earlier that effectively dominate the fluid lensing phenomenon. However, the framework developed here can easily be extended to model additional complexity in the water column which will be presented in subsequent work.

Based on this modeling work, a number of crucial relationships between surface waves and caustic focusing was discovered and a novel high-resolution aquatic remote sensing technique for imaging through ocean waves, called the general fluid lensing algorithm, was developed (Figure 3) (Chirayath, 2016; Chirayath and Earle, 2016).

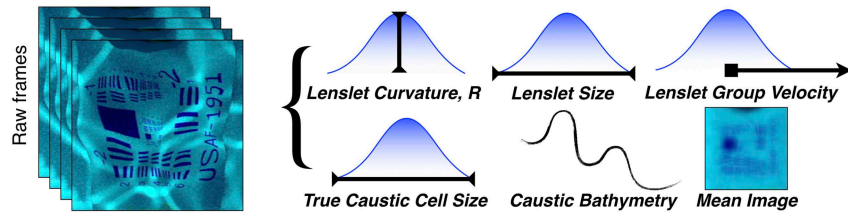
The Fluid Lensing Algorithm

The fluid lensing algorithm itself enables robust imaging of underwater objects through refractive distortions from surface waves by exploiting surface waves as magnifying optical lensing elements, or fluid lensing lenslets, to enhance the effective spatial resolution and signal-to-noise properties of remotely sensed images. Primarily a computer vision technique, which utilizes high-frame-rate multispectral video, the fluid lensing algorithm consists of a fluid distortion characterization methodology, caustic bathymetry concepts, fluid lensing lenslet homography technique based on Scale Invariant Feature Transforms (SIFT) and SIFT Flow (Liu et al., 2011), and a 3D remote sensing fluid lensing algorithm as approaches for characterizing the aquatic surface wave field, modeling bathymetry using caustic phenomena, and robust high-resolution aquatic remote sensing (Chirayath, 2016). The formation of caustics by refractive lenslets is an important concept in the fluid lensing algorithm. Given a lenslet of constant curvature, R , the focal point of caustic rays is constant across spatially distributed lenslets. This behavior is exploited for independently determining bathymetry across the test pool in the caustic bathymetry fluid lensing algorithm. It should be noted that the algorithm specifically exploits positive optical lensing events for improving an imaging sensor's minimum spatial sampling as well as exploiting caustics for increased SNR in deep aquatic systems. An overview of the 2D fluid lensing algorithm is presented in Figure 4. The algorithm is presently provisionally-patented by NASA (Chirayath, 2018b).

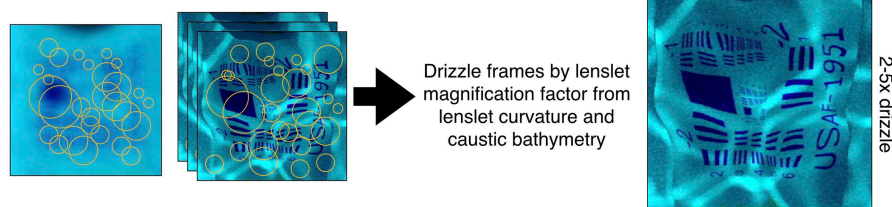
To validate the general fluid lensing algorithm, the fluid lensing test pool was used to quantitatively evaluate the algorithm's ability to robustly image underwater objects in a controlled environment (Figure 3B) (Chirayath, 2016). Results from the test pool, processed with the 2D fluid lensing algorithm show removal of ocean-wave related refractive distortion of a coral test target and USAF test target, as viewed from a nadir observing remote sensing camera. The "flat fluid image" shows the targets under flat fluid conditions. The "instantaneous wave distorted image" shows targets under typical ocean wave distortions characteristic of shallow marine system sea states. The "typical remote sensing with waves image" shows the 1s integration image, characteristic of present remote sensing sensor dwell times. Finally, the "2D fluid lensing image" with 90 frames (1 s of data) successfully recovers test targets and demonstrates

2D Fluid Lensing Algorithm Overview

Process High-frame-rate Multispectral Imagery with Fluid Distortion Characterization & Caustic Bathymetry Fluid Lensing Algorithms



Compute SIFT Features for Mean Image and all Image Frames, Drizzle Frames by Lenslet Curvature Magnification Factor



Perform Fluid Lensing Lenslet Homography using SIFT Flow - Precondition and bound flow vector and displacement from lenslet group velocity, lenslet magnification factor, and lenslet curvature as determined from fluid distortion characterization and caustic bathymetry algorithms. Use mean image as reference and integrate images selectively using higher SNR caustic bands.

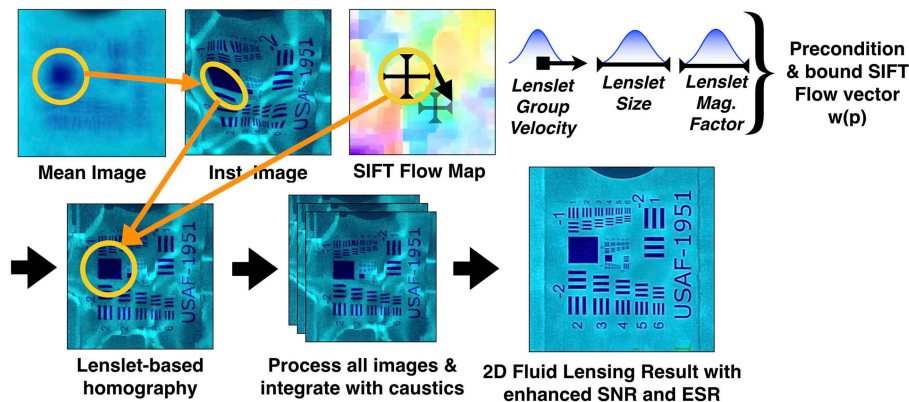


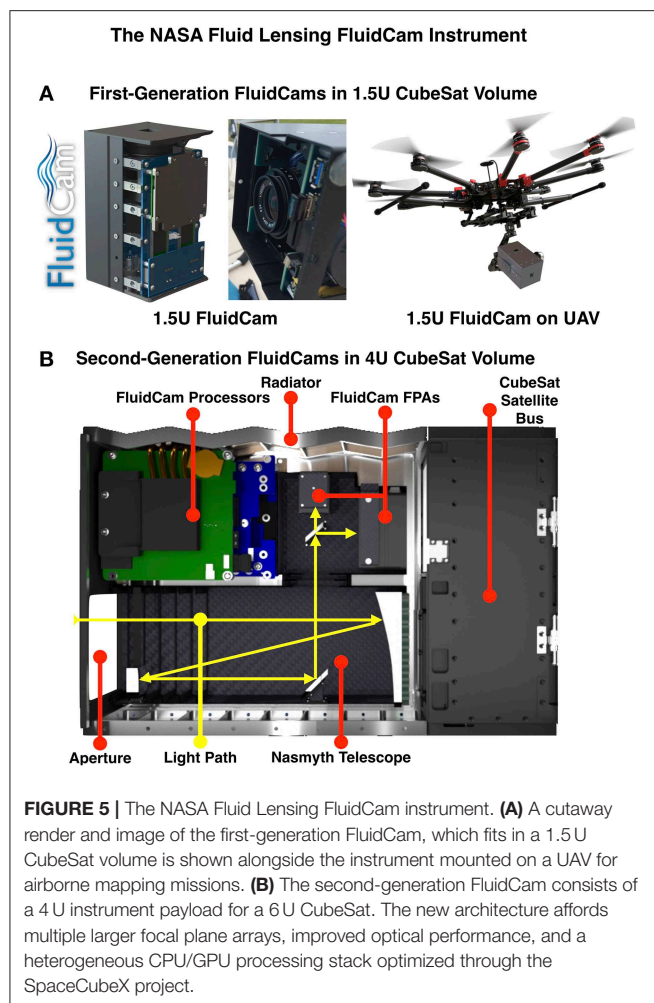
FIGURE 4 | An overview of the 2D Fluid Lensing Algorithm. Adapted with permission from Chirayath (2016).

effective resolution enhancement and enhanced SNR from tracking and exploiting fluid lenslets and caustics, respectively.

Results from the fluid lensing test pool were also used to quantitatively validate the fluid lensing algorithm through image quality assessment of reconstructed two-dimensional objects using the Structural Similarity Index (SSIM) (Figure 3C) (Wang et al., 2004) and Signal-to-Noise Ratio (SNR) (Figure 3D). Results from the validation demonstrate multispectral imaging of test targets in depths up to 4.5 m with an effective spatial resolution (ESR) of at least 0.25 cm vs. a raw fluid-distorted frame with an ESR <25 cm, for the case of an airborne platform at 50 m altitude. Note that this result was achieved with an instrument ground sample distance (GSD) of 1 cm, demonstrating a 4-fold increase in ESR from exploitation of positive lensing events. Enhanced SNR gains of over 10 dB are also measured in comparison to a perfectly flat fluid surface scenario with <1 s

of simulated remotely-sensed image data, demonstrating fluid lensing's ability to exploit caustic brightening to enhance SNR of underwater targets.

Finally, the algorithm was tested in multiple real-world environments for validation, as discussed in the next section. The ocean wave fluid lensing phenomenon is observed from 2013 and 2016 airborne campaigns in American Samoa. Figure 3E shows an instantaneous (0.03 s integration time) airborne image and 2D fluid lensing image of coral (1 s total integration time). Note the branching coral is completely unresolvable in the instantaneous image, while caustics introduce significant noise, especially over the sandy pavement region. The fluid lensing image resolves the coral and sandy benthic floor accurately. These refraction corrected results are used alongside a fluid lensing caustic bathymetry algorithm and structure from motion algorithms to create a 3D fluid lensing image and the



wavefield can be inversely estimated to render the distortions again (Figure 3E).

FluidCam Instrument and Airborne Field Campaigns

The fluid lensing algorithm eventually necessitated the development of dedicated high-frame-rate multispectral full-frame focal plane arrays (FPAs) and powerful heterogeneous computing architectures, which motivated the development of dedicated instruments, NASA FluidCam 1&2 (Chirayath and Instrella, 2016), shown in Figure 5, and follow-on hardware and software optimizations through SpaceCubeX (Schmidt et al., 2017), for scaling to CubeSat form factors and power constraints.

FluidCam 1 & 2, custom-designed integrated optical systems, imagers and heterogeneous computing platforms were developed for airborne science and packaged into a 1.5U ($10 \times 10 \times 15$ cm) CubeSat form factor (Figure 5A) with space capable components and design. Since 2014, both FluidCam 1 (380–720 nm color) and FluidCam 2 (300–1,100 nm panchromatic) have been actively used for airborne science missions over a diverse range of shallow aquatic ecosystems and contributed data for research in the broader international biological and physical oceanographic community (Suosaari et al., 2016; Purkis,

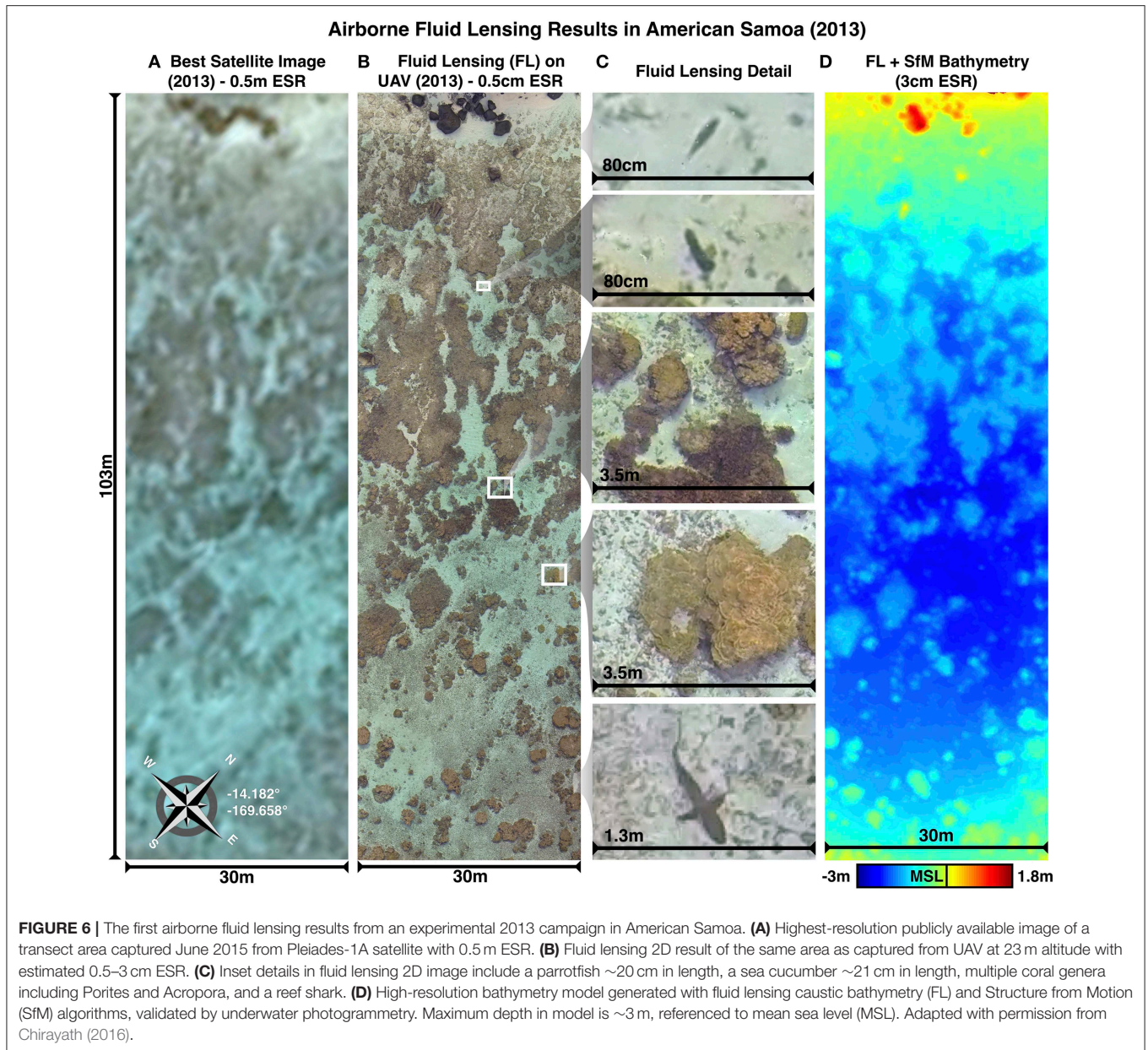
2018; Rogers et al., 2018; Chirayath and Instrella, accepted; Chirayath and Li, in review). The 3D Fluid Lensing Algorithm was validated on FluidCam from aircraft at multiple altitudes in real-world aquatic systems at depths up to 10 m (Figures 3E, 6). Field campaigns were conducted over coral reefs in American Samoa (2013, 2016) (Chirayath and Earle, 2016; Rogers et al., 2018), stromatolite reefs in Western Australia (2014) (Suosaari et al., 2016), and freshwater riverine systems in Colorado in 2018, with 10 more field campaigns planned 2019–2020 for the NeMO-Net project. Fluid lensing datasets revealed these reefs in high resolution, providing the first validated cm-scale 3D image of a reef acquired from above the ocean surface, without wave distortion, in the span of a few flight hours over areas as large as 15 km^2 per mission. The data represent the highest-resolution remotely-sensed 3D multispectral image of a marine environment to date. Figure 7 shows an inset comparing a transect of coral in American Samoa in 2013 and 2016, showing the potential for change detection at fine spatial and temporal scales using this methodology.

While FluidCam 1&2 were designed as instruments for future in-space validation with components selected that met vibrational, thermal and atmospheric requirements, a second-generation system was designed into a 4U form-factor with improved computational capability, redundant data storage, a custom optical telescope, fully radiative cooling and carbon fiber chassis, and updated high-bandwidth multispectral focal plane arrays. Figure 5B shows the 4U FluidCam payload. The optical telescope has been redesigned from the first generation and consists of a proprietary square-aperture Nasmyth focus Ritchey-Chretien reflecting telescope based on a design proposed by Jin et al. (2013).

Airborne field campaign results, along with validation results from the Fluid Lensing Test Pool, suggest the 3D Fluid Lensing Algorithm presents a promising advance in aquatic remote sensing technology for large-scale 3D surveys of shallow aquatic habitats, offering robust imaging capable of sustained shallow marine imaging. However, while the highlights presented here demonstrate applicability of the Fluid Lensing Algorithm to the tested environments, further investigation is needed to fully understand the algorithm's operational regimes and reconstruction accuracy as a function of the inherent optical properties of the water column, turbidity, surface wave fields, ambient irradiance conditions, and benthic topography, among other considerations. Current and future work is already underway to study the impact of these variables on the fluid lensing algorithm and its application to aquatic remote sensing as a whole. This research is ongoing with algorithm performance improvements, FluidCam imaging and processing hardware maturation, and automated fluid lensing dataset analysis tools such as NeMO-Net.

MiDAR—The Multispectral Imaging, Detection, and Active Reflectance Instrument

While FluidCam and fluid lensing offer a new technique for improved passive remote sensing of aquatic systems,



they are passive sensing methods, reliant on the Sun's downwelling irradiance, and thus limited to the photic zone of the ocean. This inspired the development of an active multispectral sensing technology that could extend the penetration depth of remote sensing systems. Here, we share preliminary results and developments behind the recently-patented NASA Multispectral Imaging, Detection, and Active Reflectance Instrument (MiDAR) and its applications to aquatic optical sensing and communications (Chirayath, 2018a).

Active remote sensing technologies such as radio detection and ranging (RADAR) and light detection and ranging (LiDAR) are largely independent of ambient illumination conditions, provided sufficient transmitter irradiance over background, and advantageously contend with attenuation

along the optical path by exploiting phase information using heterodyne receivers. Thus, hardware requirements for receiver sensitivity, aperture and SNR can effectively be relaxed given increased transmitter power (up to MW of power in the case of RADAR). Recent advances in LiDAR have also enabled multiple wavelengths of laser diodes to be used simultaneously in green and two infrared bands to achieve a "color" LiDAR point cloud (Briese et al., 2012, 2013). However, multispectral LiDAR methods are not yet applicable to imaging across the visible optical regime as there exist significant limitations in narrowband laser-diode emitter chemistry and efficiency.

Recent advances in active multispectral imaging have explored the concept of multiplexed illumination via light-emitting diode

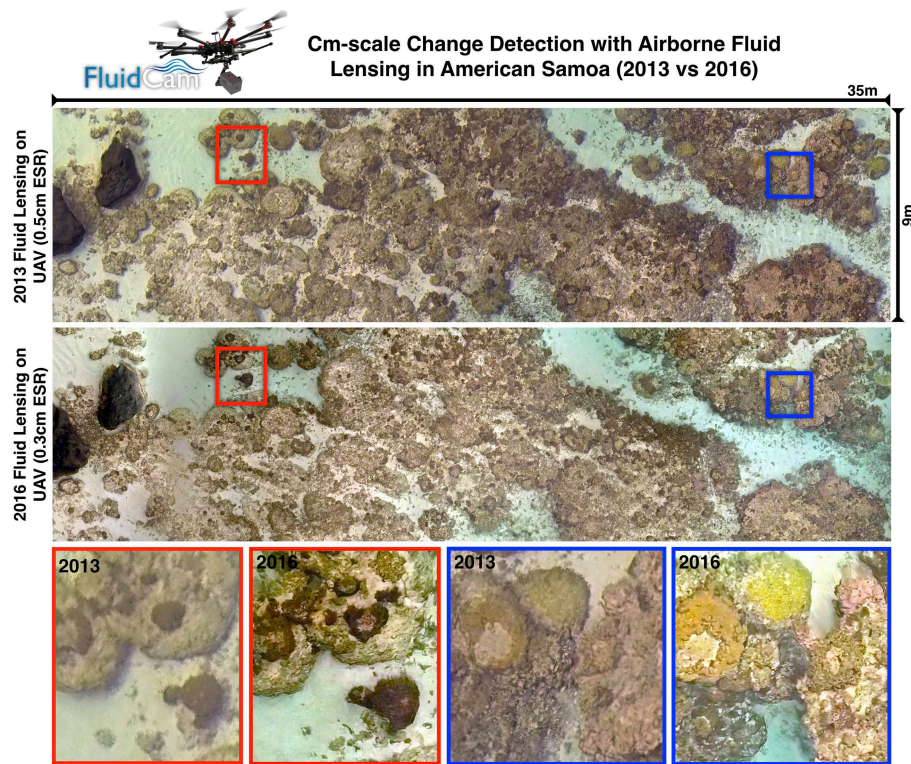


FIGURE 7 | Cm-scale change detection from airborne fluid lensing in American Samoa. Here, 2013 airborne fluid lensing data from a patch of reef are compared with a repeat survey in 2016 showing cm-scale changes in the reef. Color coded regions compare similar areas in each image and show a change in ratio of coral types as well as coral cover. The increased ESR and improved SNR of the 2016 data reflect software and hardware advances in the development of the FluidCam instrument.

(LED) arrays to dynamically illuminate a scene, reconstructing the spectral reflectance of each pixel through model-based spectral reconstruction through a charge-coupled device (CCD) detector (Nischan et al., 2003). Most prototypes at this stage have been relatively low power (~ 10 W), stationary, and unable to achieve the levels of irradiance required for remote sensing applications at larger distances, and hence have been predominantly been purposed for the task of object detection, relighting and close-up monitoring (Park et al., 2007; Parmar et al., 2012; Shrestha and Hardeberg, 2013). However, results have shown significant promise in the system's ability to reveal key features in the spectral domain, reconstruct spectra with surprising accuracy (Goel et al., 2015), and operate in conditions where an active illumination source can be directly controlled as required. In the field of multispectral video, passive systems employing dispersive optical elements through scene-scanning or bandpass filtering (Yamaguchi et al., 2006), while providing high spectral resolution, are unsuitable for achieving high framerates due to limited ambient illumination.

Motivated by the challenges discussed above, MiDAR was developed in pursuit of a next-generation sensing technology capable of expanding the use of multispectral/hyperspectral optical sensing to the seafloor. For aquatic optical sensing, the goal of MiDAR is to reach a state of parity

with terrestrial remote sensing. Namely, to develop an instrument capable of reaching beyond the photic zone with active sensing and integration on AUVs for seafloor mapping.

MiDAR Overview

MiDAR is an active multispectral/hyperspectral system capable of imaging targets with high-intensity narrowband structured optical radiation to measure an object's spectral reflectance, image through fluid interfaces, such as ocean waves, with fluid lensing, and simultaneously transmit high-bandwidth data. MiDAR consists of an active optical transmitter (MiDAR transmitter) and passive receiver (MiDAR receiver) in either a monostatic or bistatic configuration (**Figures 8A,C**). The MiDAR transmitter emits coded narrowband structured illumination to generate high-frame-rate multispectral video, perform real-time spectral calibration per color band, and provide a high-bandwidth simplex optical data-link under a range of ambient irradiance conditions, including darkness. A schema of a bistatic MiDAR, typically used for aquatic remote sensing, is shown in **Figure 8C** as a payload aboard a UAV. The MiDAR receiver, a high-framerate panchromatic focal plane array coupled to a heterogeneous computing stack, passively decodes embedded high-bandwidth simplex communications while reconstructing

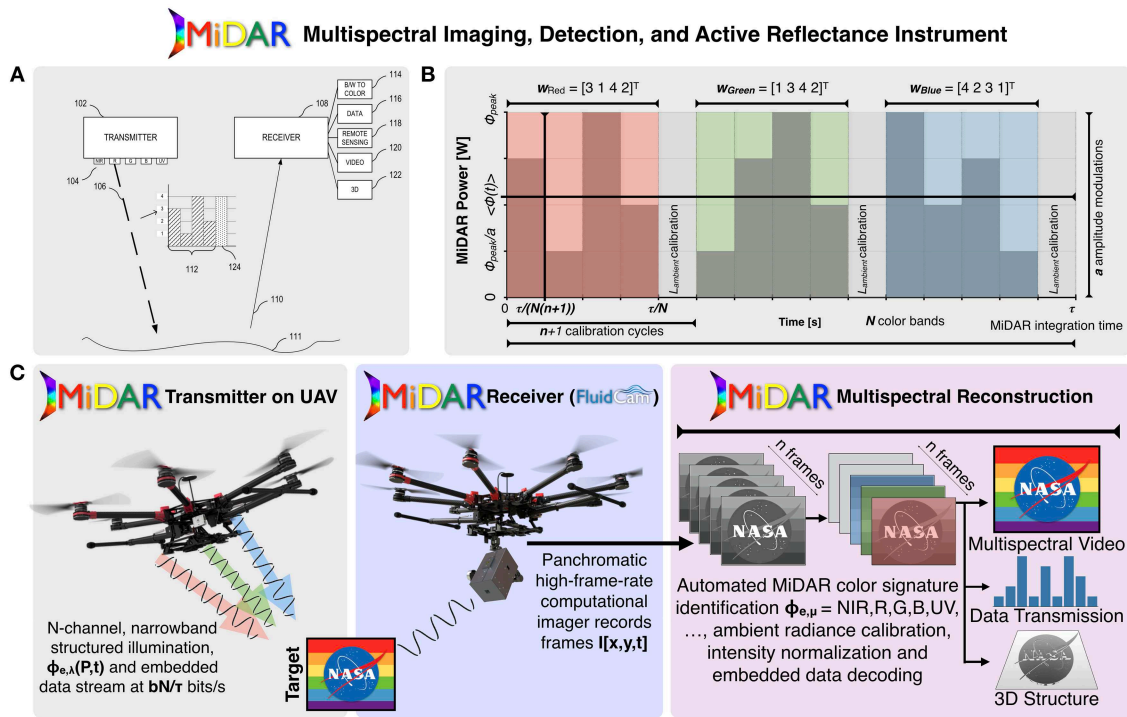


FIGURE 8 | MiDAR, the NASA Multispectral, Imaging, Detection, and Active Reflectance Instrument. **(A)** MiDAR is an active multispectral/hyperspectral instrument that uses multiple narrowband optical emitters to illuminate a target with structured light (MiDAR Transmitter). The reflected light is captured by a telescope and high-frame-rate panchromatic focal plane array (MiDAR Receiver) with a high-performance onboard heterogeneous computing stack, which creates hyperspectral images at video framerates, and decodes embedded optical communications in real-time (Chirayath, 2018a). **(B)** The structured illumination pattern generated by the MiDAR transmitter allows for simultaneous optical communication and calibrated measurement of a target's reflectance at multiple wavelengths, independent of ambient illumination conditions. **(C)** MiDAR can be operated in a bistatic or monostatic configuration. For remote sensing applications, MiDAR has been tested on UAVs.

calibrated multispectral images. A central goal of MiDAR is to decouple the transmitter from the receiver to enable passive multispectral synthesis, robustness to ambient illumination, optical communications, and the ability to select particular multispectral color bands on the fly as a function of changing mission requirements. The MiDAR transmitter and receiver utilize cost-effective components and relax sensitivity requirements on the receiving aperture to achieve multispectral video at a SNR that can be directly modulated from the MiDAR transmitter.

MiDAR multispectral image synthesis is premised upon the following physical approximations:

1. Light is reflected instantaneously from target surfaces. Phosphorescent materials thus are characterized by only by their reflectance.
2. Incoming light from the MiDAR transmitter is reflected from the target surface at the same wavelength. Fluorescent emission can be characterized using a special MiDAR receiver.
3. There are limited participating media. Primary reflectance occurs at a surface element rather than scattering within a material.
4. The bidirectional reflectance distribution function (BRDF) is a function only of three variables, $f(\theta_i, \theta_r, \phi_i - \phi_r)$, where

$\theta_i, \theta_r, \phi_i, \phi_r$ are the respective incident and reflected zenith and azimuthal angles and reflectance is rotationally invariant about the target surface normal.

5. Helmholtz reciprocity applies such that BRDF satisfies $f(\theta_i, \phi_i; \theta_r, \phi_r) = f(\theta_r, \phi_r; \theta_i, \phi_i)$.
6. MiDAR transmitter power, $\phi_{e,peak}$, at range R , results in signal irradiance that is much greater than ambient irradiance, $I_{ambient}$. ($I_{MiDAR} \gg I_{ambient}$).
7. Target reflectance and scene do not change on timescales faster than the MiDAR receiver frequency, f_{Rx} (90 Hz–36,000 Hz for NASA FluidCams).
8. MiDAR receiver frequency f_{Rx} is at least two times greater than MiDAR transmitter driving frequency f_{Tx} . ($f_{Rx} > 2f_{Tx}$).

The MiDAR Transmitter

The MiDAR transmitter achieves narrowband optical illumination of a target at range R with an array of efficient high-intensity laser or light emitting diodes (LEDs) grouped into N multispectral color bands, μ . MiDAR transmitter spectral bands, and their associated emitter diode chemistries, are shown in **Figure 9B**. The laser and LED array, or MiDAR transmitter, is driven by a periodic variable-amplitude input signal to emit modulated structured light. $\phi_{e,\lambda}(P,t)G(\lambda)$ is

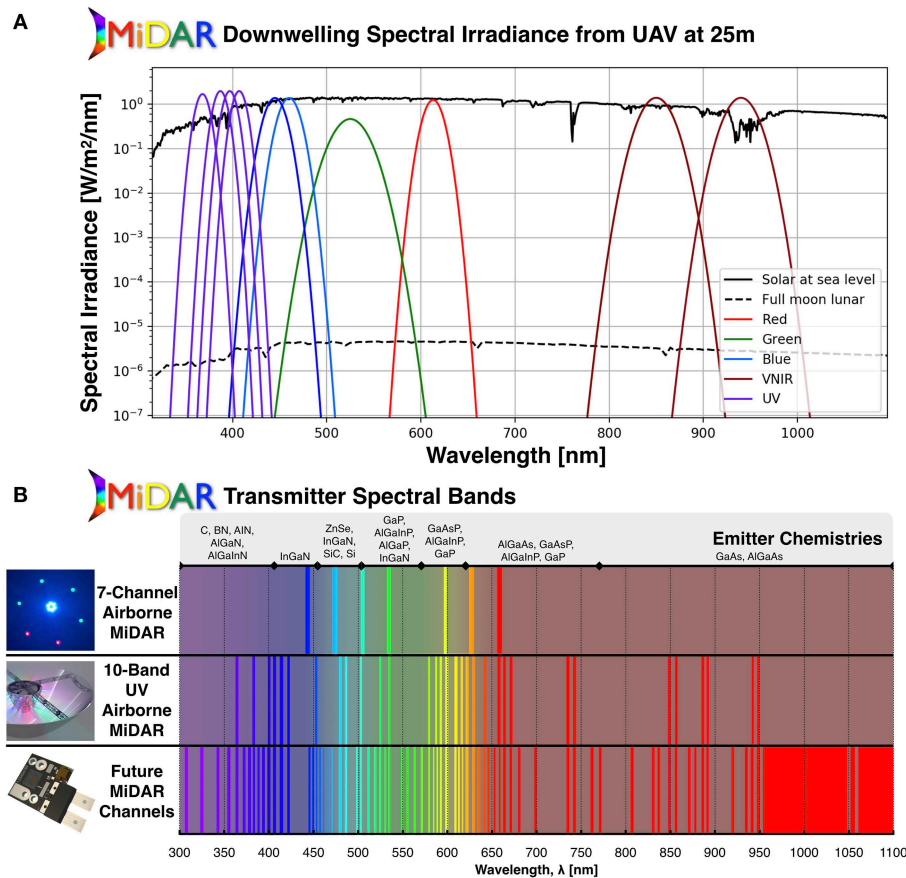


FIGURE 9 | MiDAR power and spectral coverage. **(A)** MiDAR can operate with zero ambient illumination, but also in the presence of ambient light. A 10-band kw-class airborne MiDAR system is under development that matches or exceeds the solar downwelling irradiance from a UAV at 25 m altitude. Typically, MiDAR is used exclusively at twilight and night for maximum SNR, in which case the SNR typically exceeds that of passive instruments by orders of magnitude. **(B)** Multiple MiDAR transmitters have been developed or are presently under development that span the UV-NIR optical spectrum. Emitter chemistries have been identified for each spectral channel that allow for high luminous efficiency.

the time-varying, emitted spectral radiant power distribution of the MiDAR transmitter [$\text{Wnm}^{-1}\text{s}^{-1}$], where $G(\lambda)$ is the gain of the MiDAR transmitter at wavelength λ . Each MiDAR color band, μ , spanning spectral range λ , is assigned a unique amplitude-modulated signature, MiDAR signature \mathbf{w}_μ , defined by modulating the peak power in a color band, $\phi_{e,\text{peak}}$, according to coefficients in column vector \mathbf{w}_μ , consisting of n irradiance calibration cycles per color band, a amplitude modulation levels and one ambient irradiance calibration cycle (Figure 8B). For all color bands, these column vectors form a nxN MiDAR coefficient

$$\text{matrix } W = \begin{bmatrix} w_{\text{Red}_1} & w_{\text{Green}_1} & \cdots & w_{N_1} \\ \vdots & \vdots & & \vdots \\ w_{\text{Red}_n} & w_{\text{Green}_n} & \cdots & w_{N_n} \end{bmatrix}.$$

Reflecting optics are used to distribute the radiation pattern $\Upsilon(x, y)$ uniformly across the scene while N total multispectral color bands $\mu = \text{NIR}, R, G, B, UV, \dots$ (Figure 9B) are cycled through in total MiDAR integration time $\tau = \frac{N(n+1)}{f_{\text{Tx}}}$ seconds (Figure 8B). Modulating power based on coefficients in

the weight matrix W allows for passive detection, independent color band recognition and irradiance normalization by a panchromatic MiDAR receiver. This scheme, subject to the constraints Equation 1, below, allows the MiDAR transmitter to alter the color band order and irradiance in real-time, relying on the MiDAR receiver to passively decode the embedded information and autonomously calibrate to changing illumination intensity. Further, MiDAR signatures allow the transmitter and receiver to operate in a monostatic or bistatic regime with no communication link beyond the embedded optical signal. For additional bandwidth, color bands may have b redundant MiDAR signatures, allowing for b bits of data to be encoded at a bitrate of $\frac{bN}{\tau}$ bit/s.

The MiDAR signature for each color band, $\phi_{e,\mu}$, must remain unique to μ across $\phi(t)$ (Equation 1, ii). For uniform SNR across the color bands, the average integrated power $\langle \phi(t) \rangle$ must be constant over τ/N (Equation 1, i). Finally, to maximize the multispectral video frame-rate, SNR and data transmission bandwidth, the optimization problem in Equation 1 must be solved to minimize τ .

$$\begin{aligned} & \min \tau \ \& \ \max b, \text{ SNR for given } N, n, a \\ \text{subject to } & \begin{cases} \langle \phi_{e, \lambda}(P, t) G(\lambda) \rangle = \int_{\tau} \phi_{e, \lambda}(P, t) G(\lambda) dt = \text{const.} \forall \mu \text{ (i)} \\ \exists b \in \mathbb{Z} \text{ instances where } \phi_{\mu, \text{peak}} \cdot \mathbf{w}_{\mu} \star \phi(t) = 1 \text{ (ii)} \\ n = ka \ \forall k \in \mathbb{Z} \text{ (iii)} \\ \text{SNR}_{\lambda} \approx \text{const. (iv)} \end{cases} \end{aligned}$$

MiDAR transmitter signal optimization problem and constraints for minimum multispectral integration time, maximum bandwidth and uniform SNR.

MiDAR receiver image reconstruction, discussed in the following section, composes the final multispectral image from a weighted average of decoded frames. In the limit of an ideal system, the SNR of a monostatic MiDAR system at a particular wavelength, λ , is proportional to the expression in Equation 2.

$$\text{SNR}_{\lambda} \propto \frac{\phi_{\text{peak}}(\lambda) G(\lambda) \sqrt{\frac{A_r \tau \lambda}{hc(n+1)}} \left(\frac{n}{NR^4} \sqrt{\frac{n}{a}} \sum_{i=1}^a \frac{i}{a} \right)}{\sqrt{\phi_{\text{peak}}(\lambda) G(\lambda) \left(\frac{n}{NR^4} \sqrt{\frac{n}{a}} \sum_{i=1}^a \frac{i}{a} \right) + L_{\text{ambient}}(\lambda) \Omega_{\text{FOV}}}}$$

Idealized MiDAR SNR proportionality for a color band at wavelength λ where $\phi_{\text{peak}}(\lambda)$ is the peak power input to the MiDAR transmitter at wavelength λ and $G(\lambda)$ is the gain of the MiDAR transmitter at wavelength λ . A_r is the MiDAR receiver area, Ω_{FOV} is the field of view, $L_{\text{ambient}}(\lambda)$ is the ambient radiance at wavelength λ and R is the range.

MiDAR Receiver

A passive, high-frame-rate panchromatic FPA coupled to a computational engine functions as the MiDAR receiver. The MiDAR receiver samples reflected structured light from the illuminated object at the MiDAR receiver frequency, f_{Rx} . Onboard algorithms digitally process the high-frame-rate image data to decode embedded simplex communication, perform in-phase intensity and color-band calibration and reconstruct a N -band calibrated multispectral scene at a framerate of τ^{-1} Hz. The MiDAR prototype highlighted here uses the NASA FluidCam instruments as MiDAR receivers.

MiDAR Receiver Multispectral Video Reconstruction Algorithm

The MiDAR receiver digitizes sequential panchromatic images $I[x, y, t]$ at $\{N_x, N_y\}$ pixels and framerate f_{Rx} Hz. N ambient radiance calibration cycles are used to calibrate intensity and the normalized image sequence is then difference transformed:

$$\begin{aligned} u_i &= 1 \text{ if } I_j > I_k \\ &\text{else } u_i = 0 \\ &\forall j, k \text{ where } k > j, i \leq j * k \end{aligned}$$

This method permits varying gains per channel and is robust to noise as a function of the subject being imaged. Note that the length of I here is the same length as w , and mirrors the relative signature pattern of w . The final transformed u is then cross-correlated with the MiDAR coefficient matrix to detect and assign color bands. The MiDAR multispectral reconstruction algorithm composes a calibrated $[N_x \times N_y] \times N \times t$ dimensional

multispectral video scene consisting of N color bands, μ . The multispectral video matrix, $M[x, y, \mu, t]$, is constructed from a weighted average of color-band classified panchromatic images $I[x, y, t]$ over total integration time τ .

MiDAR Optical Communications Decoding Algorithm

Additional simplex communications may be simultaneously embedded in the MiDAR transmitter's spectral radiant power distribution, $\phi_{e, \lambda}(P, t)$. By creating b redundant MiDAR color signatures $\phi_{e, \mu}$, simplex data can be transmitted at a minimum rate of $\frac{bN}{\tau}$ bit/s with no loss to MiDAR multispectral image SNR. For a panchromatic FluidCam-based MiDAR receiver, for example, with $f_{Rx} = 1550\text{Hz}$, $N = 32$ color bands, $a = n = 5$ amplitude modulation and calibration cycles and $b = 10$ redundant MiDAR signatures, this algorithm can achieve a data-rate of 2.58 kbps while performing imaging operations. Using a passive color sensor as the MiDAR receiver, such as the multispectral FluidCam with K color channels, this bandwidth can be increased by simultaneous transmission of multiple MiDAR color bands. In the case that a MiDAR receiver has $K = N$ matching color bands, the data rate increases to $\frac{bN^2}{\tau}$ bit/s, or 82.67 kbps.

MiDAR can be used for long-range optical communications using this methodology with the MiDAR receiver pointed directly at the MiDAR transmitter for increased gain. The SNR for b bits of data transmitted at wavelength λ is then proportional to:

$$\text{SNR}_b \propto \frac{\phi_{\text{peak}}(\lambda) G(\lambda) \sqrt{\frac{A_r \tau \lambda}{hc(n+1)}} \left(\frac{n}{NR^2} \sqrt{\frac{n}{a}} \sum_{i=1}^a \frac{i}{a} \right)}{\sqrt{\phi_{\text{peak}}(\lambda) G(\lambda) \left(\frac{n}{NR^2} \sqrt{\frac{n}{a}} \sum_{i=1}^a \frac{i}{a} \right) + L_{\text{ambient}}(\lambda) \Omega_{\text{FOV}}}}$$

Full descriptions of the MiDAR Receiver Multispectral Video Reconstruction Algorithm and Optical Communications Decoding Algorithm are provided in the MiDAR patent (Chirayath, 2018a).

MiDAR Instrument Development and Preliminary 7-Channel Airborne MiDAR Results

MiDAR transmitter and receiver hardware are currently under active development. Five, seven, and thirty-two band MiDAR transmitter prototypes have thus far been developed with total peak luminous power ratings up to 200 watts and spectral ranges from far UV to NIR, suitable for *in-situ* and short-range active multispectral sensing (Figure 9B). A number of light-emitting diode chemistries have been tested and identified that span much of the UV-NIR electromagnetic spectrum for future implementations (Figure 9). Currently, a 10-band airborne kW-class MiDAR transmitter is in development featuring four UV-band channels. This transmitter is designed to fly on a UAV for active multispectral imaging at an altitude of 25 m. At this altitude, the transmitter is expected to match downwelling solar irradiance at noon, but will operate primarily during twilight and evening for increased SNR (Figure 9A). Compared to daytime passive remote sensing observations with full downwelling solar irradiance, nighttime MiDAR observations with a full lunar phase downwelling irradiance will have

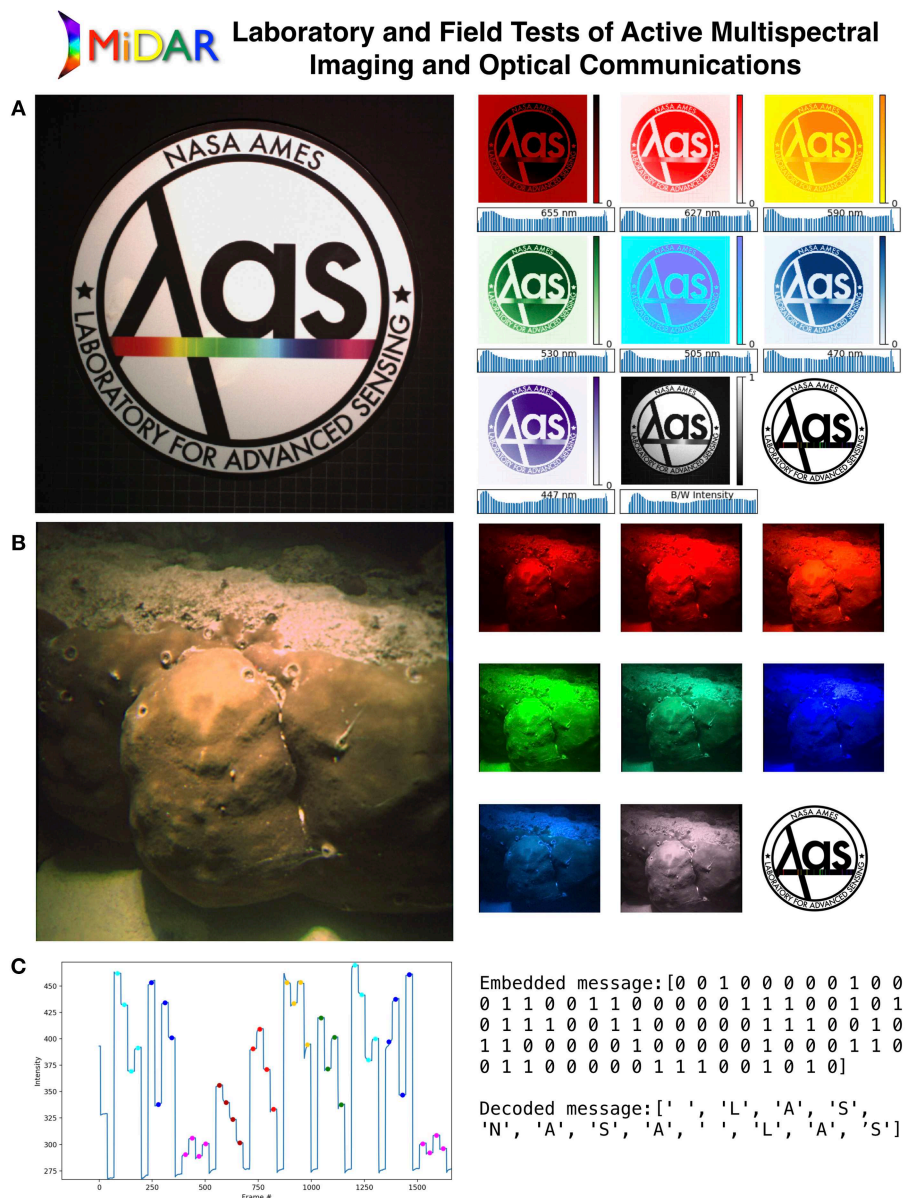


FIGURE 10 | MiDAR Laboratory and Field Tests of Active Multispectral Imaging and Optical Communications. **(A)** 7-Channel monostatic MiDAR imaging test on optical bench with multispectral test target. Here, half of the test target was illuminated with a broadband source to test MiDAR's ability to determine active reflectance independent of ambient conditions. RGB image shown on left. Reflectance maps shown for each spectral band from 655 to 447 nm on right. **(B)** The first 7-channel airborne MiDAR test over coral with an underwater MiDAR receiver from a 2018 field campaign in Guam. Here, MiDAR is operating in a bistatic configuration with a MiDAR transmitter above the surface, and a diver-mounted MiDAR receiver underwater. MiDAR resolves a Porites coral in the same seven multispectral bands as the optical bench test, and simultaneously performs simplex optical communication through the air-water interface. **(C)** Embedded MiDAR data transmission in coral image decodes a simple hidden message.

a SNR 10^{-10^3} times higher in the case of a UAV at 25 m altitude.

Figure 10A shows results from a basic laboratory test of a 7-channel airborne MiDAR in **Figure 9B**. Here, a monostatic MiDAR system is tested using the 7-channel transmitter mounted on an optical bench, collocated with FluidCam as a receiver. The monostatic system was targeted at a multispectral test target 2 m

away under constant diffuse, broad-spectrum ambient lighting conditions of $\sim 1 \text{ W/m}^2$. MiDAR parameters for this experiment were: $N = 7$, $f_{Tx} = 100\text{Hz}$, $n = a = 4$, $\{N_x, N_y\} = \{1024, 1024\}$, $f_{Rx} = 365\text{Hz}$, $\tau = 0.25\text{s}$.

Figure 10B presents results from a 2018 bistatic MiDAR field test in Guam with the 7-channel airborne transmitter above the air-water interface at 1 m illuminating a Porites coral at a

depth of 1 m. The MiDAR receiver is located under the water at a range of 1 m from the coral head. Here, similar MiDAR parameters were used as for the laboratory test. In addition, a simplex transmission was encoded during imaging through the air-water interface. The decoded signal and message are shown in **Figure 10C**.

The MiDAR transmitter spectral radiant power distribution, $\phi_{e,\lambda}(P, t)$ was produced using a 7-channel array of narrowband LEDs (**Figure 9B**), centered at 447, 470, 505, 530, 590, 627, and 655 nm wavelengths with full-width-half-maximum (FWHM) values of $\Delta\lambda = 10, 25, 35, 15, 35, 35$, and 37 nm, respectively. The LED array was driven by microsecond, pulse-width-modulated (PWM) signals generated by an Arduino Uno microprocessor with high-current switching performed by MOSFETs. LED power per color was chosen to compensate for transmitter gain losses, $G(\lambda)$ and receiver losses such for an average emitted power $\langle \phi_{e,\lambda}(P, t) G(\lambda) \rangle = 10 \text{ Watts}$.

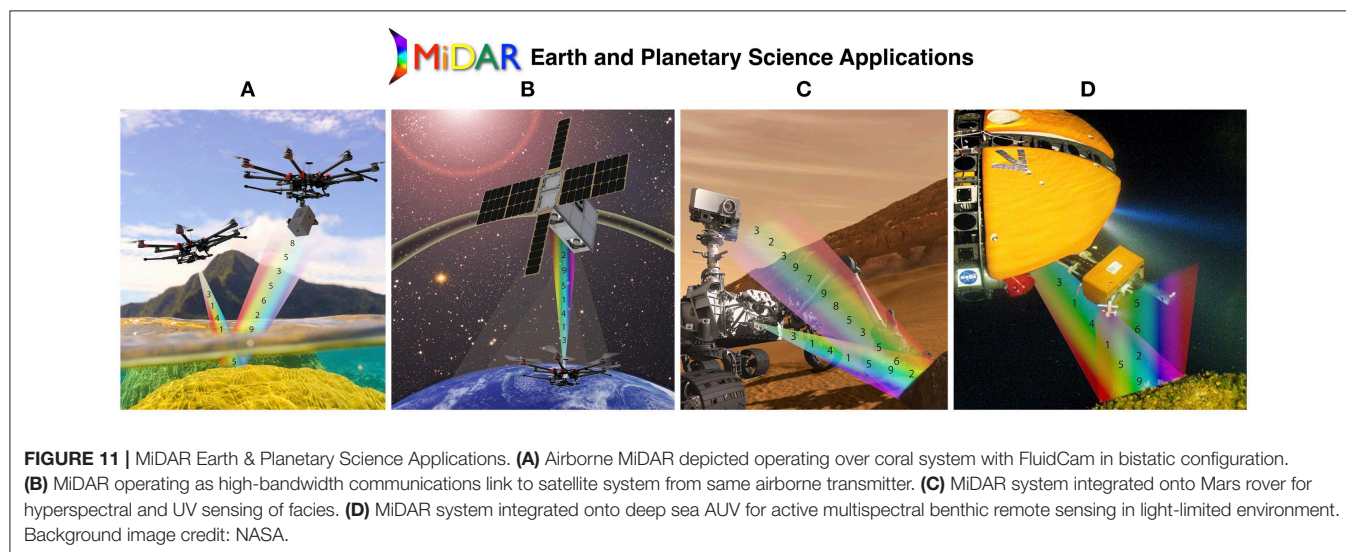
Potential Applications of MiDAR to the Earth and Space Sciences

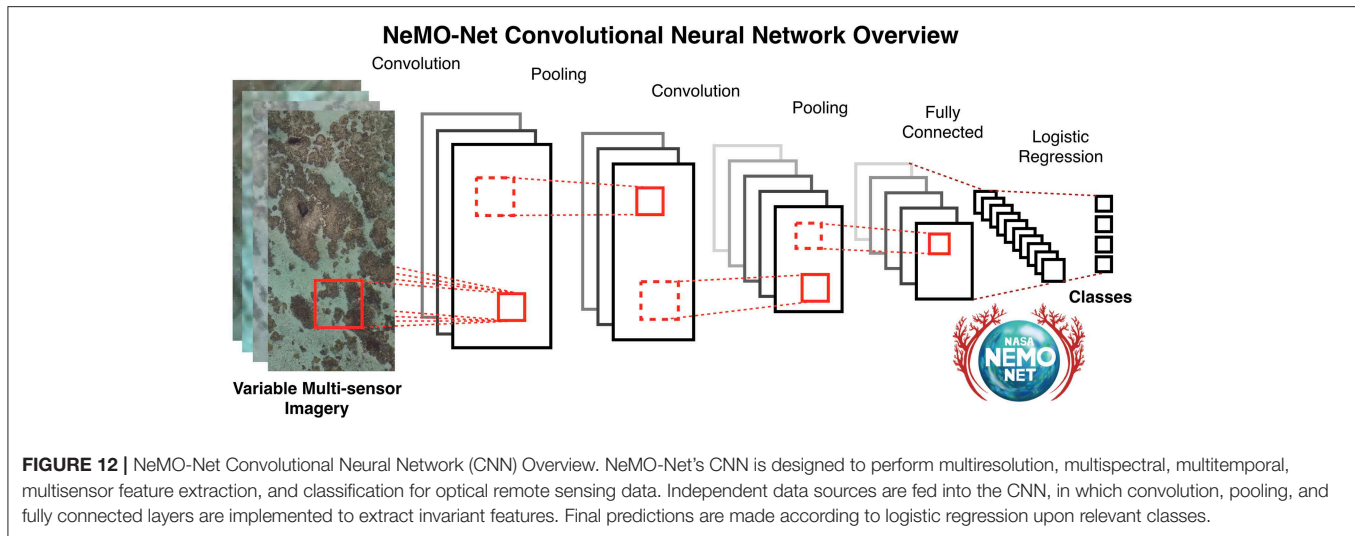
Preliminary MiDAR results at low transmission power ($\sim 10 \text{ W}$) offer promising developments in active optical sensing that are applicable to aquatic systems. As higher-power kW-class MiDAR transmitters are matured, there are a number of potential applications of this technology to Earth and Space Sciences including high-resolution nocturnal and diurnal multispectral imaging from air, space and underwater environments as well as optical communication, bidirectional reflectance distribution function characterization, mineral identification, UV-band imaging, 3D reconstruction using structure from motion, and active fluid lensing for imaging deeper in the water column (**Figure 11**). Multipurpose sensors such as MiDAR, which fuse active sensing and communications capabilities, may be particularly well-suited for mass-limited robotic exploration of Earth and other bodies in the solar system.

NeMO-Net—Neural Multi-Modal Observation and Training Network for Global Coral Reef Assessment

Driven by the need for multimodal optical sensing processing tools for aquatic systems, as well as a toolkit to analyze and exploit the large (TB and PB scale) datasets collected from FluidCam and MiDAR, the NeMO-Net project was initiated in late 2017 (Chirayath et al., 2018a,b). NeMO-Net is highlighted here as an example of a scalable data fusion and processing information systems development that aims to make use of optical datasets from a variety of instruments to answer questions of global scale for aquatic ecosystems. Specifically, NeMO-Net is an open-source deep convolutional neural network (CNN) and interactive active learning training software designed to accurately assess the present and past dynamics of coral reef ecosystems through determination of percent living cover and morphology as well as mapping of spatial distribution (Cartier, 2018). NeMO-Net exploits active learning and data fusion of mm-scale remotely sensed 3D images of coral reefs from FluidCam and MiDAR as well as lower-resolution airborne remote sensing data from commercial satellites providers such as Digital Globe and Planet, as well as NASA's Earth Observing System data from Landsat, to determine coral reef ecosystem makeup globally at the finest spatial and temporal scales afforded by available data.

Previously, it was shown that mm-scale 3D FluidCam imagery of coral reefs could be used to improve classification accuracies of imagery taken from lower-resolution sensors through a communal mapping process based upon principal component analysis (PCA) and support vector machines (SVM) (Chirayath and Li, in review). This work further showed that supervised learning of FluidCam data can be used to identify spectral identification data from higher-dimensional hyperspectral datasets for coral reef segmentation. Consequently, the scope of this work was expanded with the development of NeMO-Net, utilizing supervised and semi-supervised CNNs to recognize and fuse definitive spatial-spectral features across coral reef datasets.





NeMO-Net CNN Architecture

On a high level, CNNs are modeled upon the human image recognition process, where sections of the field of view are independently synthesized and collated over multiple layers (i.e., neurons) to form abstract and high level feature maps which are generally robust and invariant (Lecun et al., 1998). This can be extended to the remote sensing case, where a combination of spatial-spectral properties may be more reflective of segmentation criteria than a single-faceted approach. However, CNNs have only very recently been examined as an alternative to conventional methods for image classification and thematic mapping, and as such is currently an area of active research with many unexplored possibilities (Gomez-Chova et al., 2015).

The structure of NeMO-Net's CNN is shown in **Figure 12**. The input to the CNN is an image or a set of images (different spectral bands and spatial resolutions in our case). The convolution step is used to extract a set of filters through back-propagation, by applying 3×3 convolutions, for example, that are smaller in size than the original image. During the next step, pooling is used to reduce the spatial scale of the filtered images, often down-sampling by a factor of two per dimension. This process can be repeated several times, depending on the image size and feature complexity. Finally, the results from pooling are fed into a fully connected layer where probabilistic votes are combined to predict the class based upon previously trained ground-truth samples. A distinct advantage of the CNN scheme over the standard multi-layer perceptron (MLP) NN schemes is their ability to ingest 2D (e.g., images) or 3D (e.g., spectral images), or higher-dimensional datasets, as direct inputs, whereas the inputs for MLP-NN depend heavily on pre-processing and dimensionality reduction in order for the network to achieve good prediction, and sometimes even to reach convergence. Another advantage of the pooling process inherent with CNN is its low sensitivity to the exact position or skewness of the feature (up to a certain extent), allowing for the augmentation of noisy images. At present, CNNs have already shown promise in remote sensing areas such as land use, hyperspectral, and satellite image classification (Castelluccio

et al., 2015; Chen et al., 2016; Zhong et al., 2017) with greatly increased classification accuracies. Challenges remain, however, especially since tuning large CNNs often require an abundance of training data and significant computational power. To this end, NeMO-Net incorporates a citizen-science based active learning and training application as well as utilizing the NASA Ames Pleiades Supercomputer and NASA Earth Exchange (**Figure 13**).

As primarily an information systems development project, NeMO-Net's overall technical goals are to: (1) develop a malleable CNN architecture specific to aquatic optical sensing datasets for scalable heterogenous computing architectures such as the NASA Ames Pleiades Supercomputer, (2) create a cloud and cloud shadow detection CNN algorithm for masking (Segal-Rozenhaimer et al., accepted), (3) implement domain transfer learning for spectral and spatial resolution transfer learning (super resolution) across multiple sensors, and (4) create a 3D active learning CNN training application in game interface for data training from multiple sensors. NeMO-Net's science objectives include: (1) Developing an accurate algorithm for identification of coral organisms from optical remote sensing at different scales. (2) Globally assessing the present and past dynamics of coral reef systems through a large-scale active learning neural network. (3) Quantifying coral reef percent cover and spatial distribution at finest possible spatial scale. (4) Characterizing benthic habitats into 24 global geomorphological and biological hierarchical classes, resolving coral families with fluid lensing at the finest scales and geomorphologic class at the coarsest scale.

Often the most challenging and limiting aspects of CNNs, such as NeMO-Net, are CNN learning and label training; that is associating pixels in remote sensing imagery with mapping labels such as coral or seagrass. On this topic, the three prevalent issues are:

1) The labeled data is not representative of the entire population distribution. In coral reefs, for example, labels often only correspond to reefs within their immediate geographical vicinity, which are known to vary compositionally and

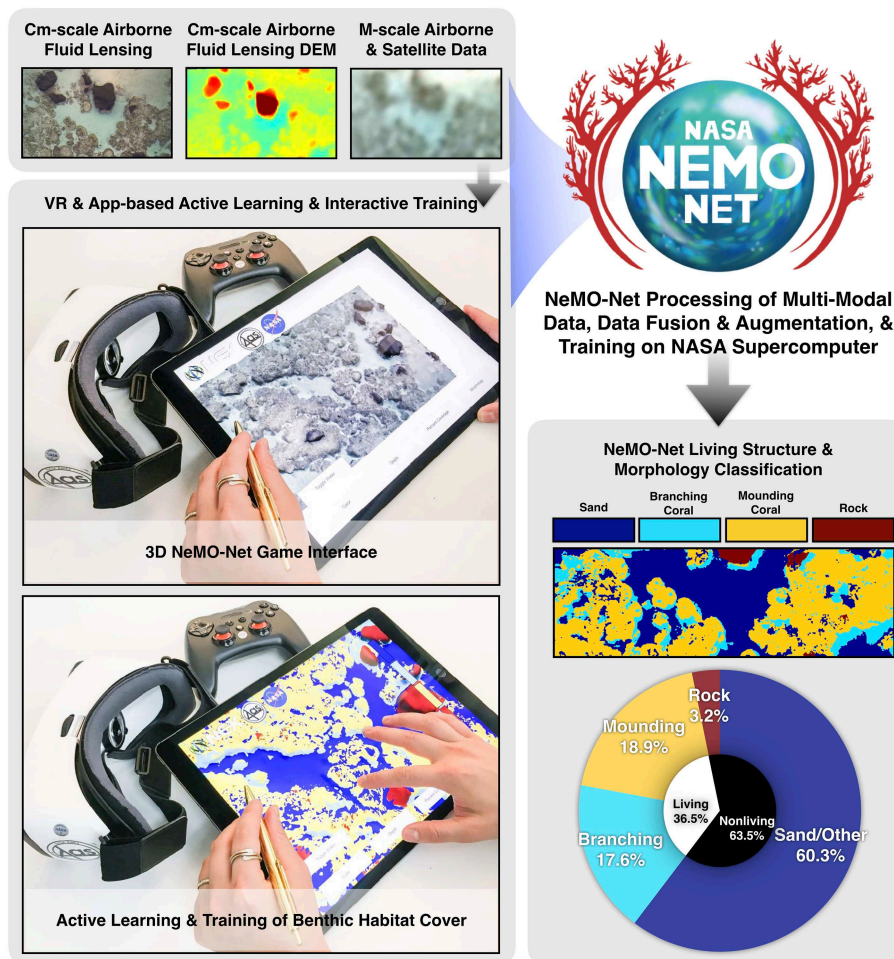


FIGURE 13 | NeMO-Net is aimed at harmonizing the growing diversity of remote sensing and *in situ* imagery into a single open-source platform for assessing shallow marine ecosystems at scale across the globe. An active learning game, playable on tablet and virtual reality platforms, allows users to view 3D FluidCam data of coral reefs and provide training data on coral classes including living cover, morphology type, and family identification. These data, along with their spatial coordinates, are fed into NeMO-Net, which produces a classification map and reef constituent breakdown as well as error analysis based upon training data. This technology is presently under development and will be expanded to third-party georeferenced 3D datasets as well.

structurally worldwide. This can lead to significant generalization error when learned CNN models are tested on particular samples and evaluated upon data points from other areas.

2) The number of available labels is very small (~1% of the data), where the most common criticism associated with CNNs is their dependence upon a vast amount of labeled training data.

3) Spectral mixing and 3D structure confusion occurs in areas of high benthic heterogeneity, conflating multiple ecological classes into small areas.

To address the first and third issues, NeMO-Net utilizes a technique called transfer learning. To address the data skewness issue, for example, NeMO-Net can utilize areas where extensive training label data exist concurrent with instrument data (Chirayath and Earle, 2016; Chirayath and Instrella, 2016). Feature representation learned by the CNN on this dataset is then used to augment the feature representation of other regions. Deep features extracted from CNNs trained on large annotated

datasets of images have been used as generic features very effectively for a wide range of vision tasks, even in cases of high heterogeneity (Donahue et al., 2014). To address the second issue, NeMO-Net utilizes virtual augmentation of data. Here, existing labeled data are subjected to a series of transformations such as spatial rotation, decimation, radiation-specific and mixture-based techniques to reinforce robustness of the algorithm. This allows the simulation of radiometric attenuation, spectral mixing, and noise effects inherent to any spectral based sensing platform.

Additional components of NeMO-Net include the use of semi-supervised learning. Semi-supervised classification combines the hidden structural information in unlabeled examples with the explicit classification information of labeled examples to improve classification performance. The objective here is such that given a small sample of labeled data and a large sample of unlabeled data, the algorithm will attempt to classify the unlabeled data through a set of possible assumptions, such as

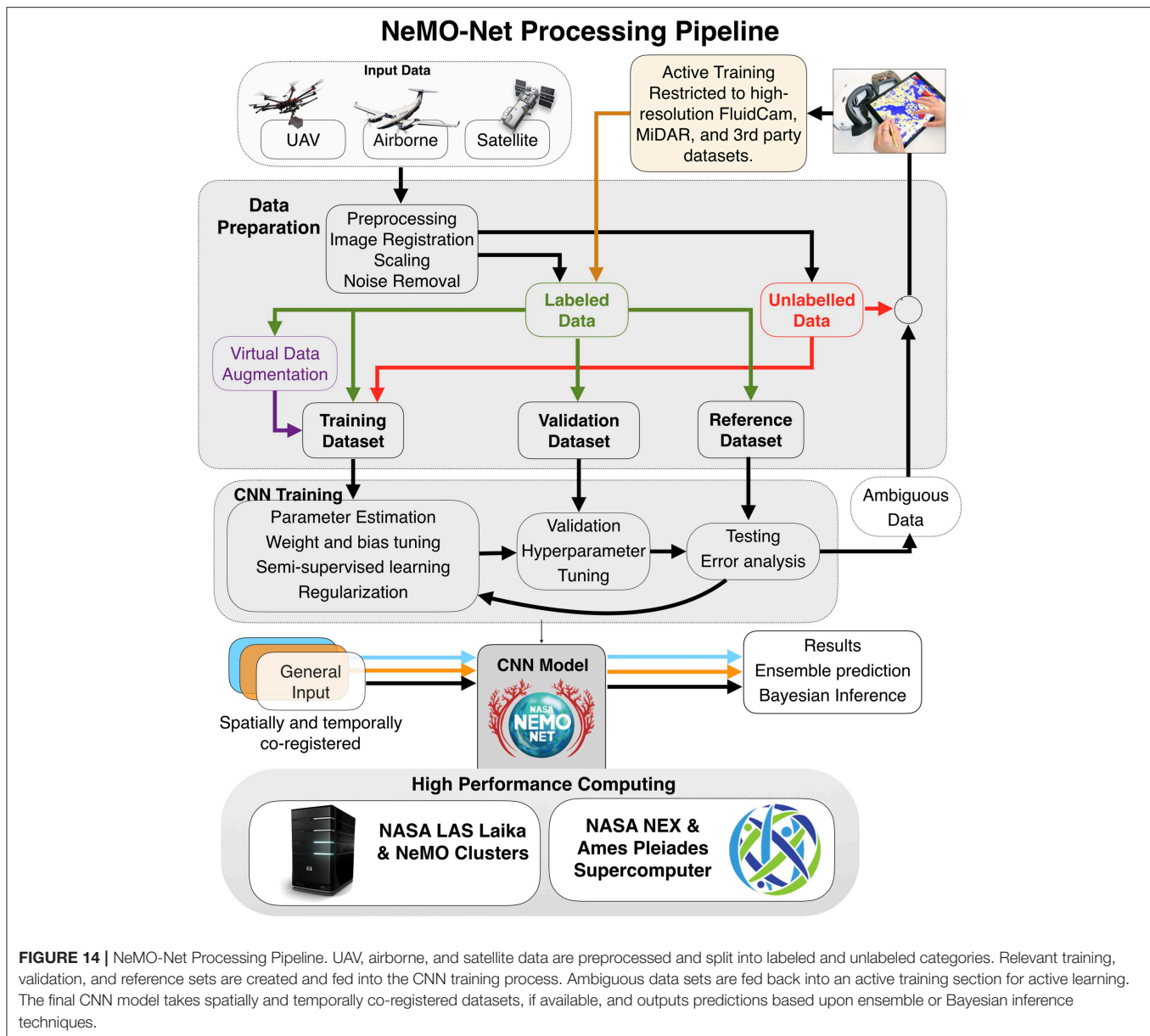


FIGURE 14 | NeMO-Net Processing Pipeline. UAV, airborne, and satellite data are preprocessed and split into labeled and unlabeled categories. Relevant training, validation, and reference sets are created and fed into the CNN training process. Ambiguous data sets are fed back into an active training section for active learning. The final CNN model takes spatially and temporally co-registered datasets, if available, and outputs predictions based upon ensemble or Bayesian inference techniques.

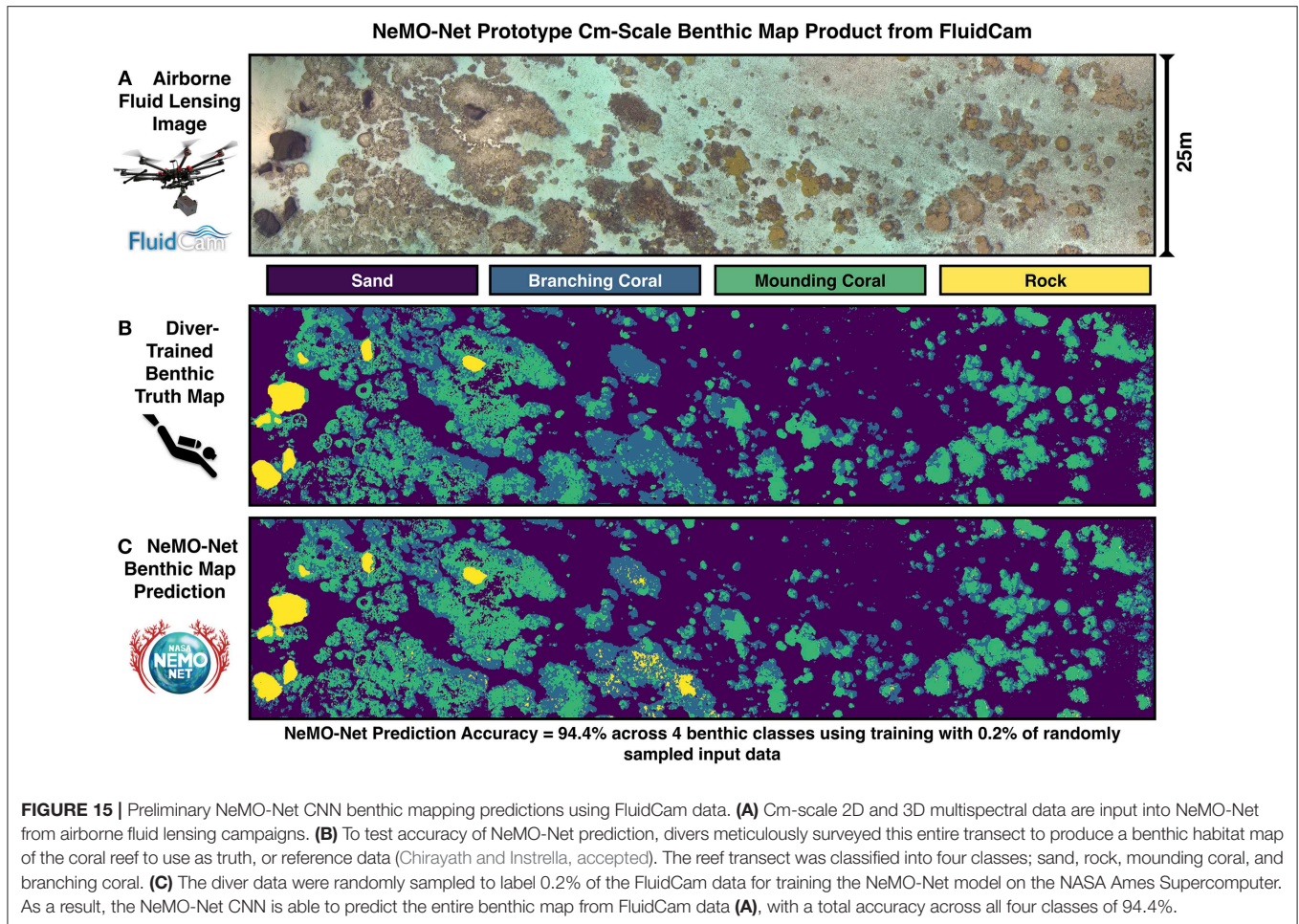
smoothness/continuity, clustering, or manifold representation. Supervised learning in the context of CNNs can be accomplished through pseudo-labels by maximizing the class probabilities of the unlabeled data pool (Lee, 2013). Other approaches include use of standard supervised learning methods such as non-linear embedding (MDS, Isomap) in combination with an optimization routine at each layer of the deep network for structure learning on the unlabeled pool (Weston et al., 2012).

Finally, NeMO-Net augments labeled data through active learning. Active learning is an area of machine learning research that uses an “expert in the loop” to learn iteratively from large data sets that have very few annotations or labels available. In the case of NeMO-Net, the users classifying objects are humans in the loop and the active learning strategy algorithm decides which sample from the unlabeled pool should be given to the expert for

labeling such that the new information obtained is most useful in improving the classifier performance. Common strategies include most likely positive (Sharma et al., 2016) and uncertainty sampling (Lewis and Catlett, 1994). The interactive NeMO-Net tablet application is used for active learning (Figure 13).

The overall algorithmic architecture for NeMO-Net is shown in Figure 14 and consists of:

- 1) Preprocessing of multiplatform data: this includes image registration, scaling and noise removal from affected datasets, allowing easy ingestion into the CNN regardless of sensor platform.
- 2) NeMO-Net training is performed by providing a multitude of classification images from various sources, covering a wide spatial, spectral, and temporal range. The goal is such that



the CNN is able to extract high level spatial-spectral features that are inherent across all relevant datasets. As mentioned previously, to alleviate the issue of labeled data shortage, techniques such as virtual data augmentation, semi-supervised learning, and active learning methods are used.

- 3) To address the issue of data overfitting, regularization, dropout, and activation function selection are used (Krizhevsky et al., 2012).
- 4) Parameter tuning is performed via a validation set and error analysis performed through cross-analysis against a reference set, designed to gauge the robustness, predictive capability and error characteristics of the system.
- 5) Final classifications are calculated via logistic regression into relevant classes. In cases where multiple temporal and spatially co-registered datasets are available, fusion of multiple CNN outputs by ensemble or Bayesian inference techniques is implemented.

NeMO-Net Preliminary Results

Presently, NeMO-Net's CNN is implemented through an open-source Python package that can be integrated with QGIS, an open source geographical information system. With this pairing,

the CNN learning module has access to other useful services such as geolocation, layered data, and other classification tools for comparison. The Python package is also designed to build upon and integrate with existing libraries for machine learning and modern geospatial workflow, such as TensorFlow, Scikit-learn, Rasterio, and Geopandas. To increase computational speed, NeMO-Net takes advantage of heterogeneous CPU and GPU processing on the NASA High-End Computing Capability (HECC) Pleiades supercomputing cluster, located at NASA Ames. The active learning application has been developed on the game development platform Unity Pro and 3D modeling software Maya LT for iOS, with a server for data storage and transfer.

Figure 15 shows an example of NeMO-Net's prototype cm-scale benthic map product from FluidCam, based on field data from American Samoa shown earlier. The reef transect was classified into four classes; sand, rock, mounding coral, and branching coral. Using 0.2% of randomly-sampled label data for training the NeMO-Net CNN is able to predict the entire benthic map from FluidCam data with a total accuracy across all four classes of 94.4%. This result is compared to the 92% accuracy (8% error) achieved at the cm spatial scale in **Figure 1** using an

independent methodology based on MAP estimation (Chirayath and Instrella, accepted).

DISCUSSION AND FUTURE WORK

The three emerging NASA technologies shared here begin to address some of the ongoing observational, technological, and economic challenges encountered in marine sensing, particularly as they apply to coral reef ecosystems.

FluidCam has been utilized extensively on UAVs for scientific surveys of shallow marine environments in small areas, $\sim 15 \text{ km}^2$ at a time. The fluid lensing algorithm has provided a robust way to survey shallow marine ecosystems under various sea states at high-resolution in 3D. In addition, FluidCam and fluid lensing have been tested for applicability to marine mammal conservation, imaging cetaceans at high-resolution in the open seas (Johnston, 2018). Nevertheless, to cover larger swaths of geographically isolated regions at regular intervals and meet earth science measurement requirements, high-altitude airborne or space-based validation of fluid lensing is eventually required. FluidCam will be used in a number of upcoming airborne field missions over coral reefs in Puerto Rico, Guam, and Palau in 2019 for use in NeMO-Net. In these regions, FluidCam data will improve the accuracy of low-resolution airborne and satellite imagery for benthic habitat mapping. However, this is a stopgap measure intended to improve the state-of-art for the foreseeable future. Ultimately, just as in the case with terrestrial ecosystems, only global high-resolution aquatic remote sensing will fully resolve fine-scale dynamics in marine systems. Finally, passive fluid lensing is limited to imaging in the photic zone, like all other passive remote sensing methods, and cannot image in highly turbid environments or areas with continuous wave breaking.

MiDAR is an early TRL (technology readiness level) instrument, but has shown promising results using a novel active multispectral imaging and optical communications capability (Chirayath, 2018a; McGillivray et al., 2018). MiDAR was also designed with future fluid lensing compatibility in mind, helping to extend the depth range of the passive FluidCam instrument from aircraft and be used in underwater applications for entirely light-limited environments. Previously, 5, 7, and 32-band laboratory MiDAR prototypes were developed through NASA CIF and Innovation Awards with total luminous power ratings up to 200 watts and spectral ranges from far UV to NIR, suitable for *in-situ* and short-range active multispectral sensing. Presently, development of the first 10-band kW-class UV VNIR MiDAR transmitter and SpaceCubeX-based (Schmidt et al., 2017) MiDAR receiver is underway for airborne and future spaceborne payload integration. MiDAR will be matured to NASA TRL 4 with a new transmitter and receiver design and flight demonstrated on UAVs. In addition, MiDAR is being tested with divers and AUVs in underwater environments with upcoming tests over mesophotic coral reefs in Puerto Rico and Guam in 2019.

NeMO-Net concludes in early 2020 and will provide a global benthic habitat map for shallow marine systems based on harmonized high-resolution airborne (primarily FluidCam and

MiDAR) and satellite data processed using a CNN. The NeMO-Net citizen-science app (Chirayath et al., 2018a) is anticipated to generate a vast amount of 3D training data pertinent to ongoing habitat mapping of shallow marine systems. The project will result in open-source software packages and be available to the broader community through the NASA Earth Exchange (NEX) repository, which currently houses many existing algorithms and data products related to machine learning and Earth Science for investigators. All final code developed as well as final deliverables will be made available under the GNU General Public License (GPL) for ongoing public use and development. As the first citizen-science based 3D training and classification software, NeMO-Net has many potential future applications to mapping of terrestrial, deep sea, and planetary 3D photogrammetry datasets, among other applications.

While these technologies present promising technological advances, work is needed to mature these systems into sustained marine observing systems. As science requirements change, these technologies must either be improved upon or replaced by better methodologies. Over the coming years, these tools will continue their maturation through ongoing hardware and software development, cost reduction, experimental field campaigns in increasingly diverse and challenging ecosystems, deployments on different sensing platforms, open-source code sharing, citizen-science inputs, and input and adoption from the broader oceanographic community.

AUTHOR CONTRIBUTIONS

VC wrote the manuscript, prepared the figures, and performed all fluid lensing analyses. VC and AL performed analysis for MiDAR and NeMO-Net results.

FUNDING

Funding for this work has been provided through peer-reviewed proposals to NASA's Research Opportunities in Earth and Space Science (ROSES). FluidCam was supported by NASA Earth Science Technology Office (ESTO) grant ATI-QRS-14-0010. MiDAR was funded in part by NASA 2015, 2016, and 2017 Center Innovation Fund (CIF) grants, and NASA ESTO Advanced Information Systems Technology (AIST) grant AIST-QRS-16-0004 and AIST-16-0031. NeMO-Net was supported through ESTO AIST-16-0046. The fluid lensing algorithm, test pool simulations, and airborne field campaigns were developed as part of Chirayath's doctoral research at Stanford University's Department of Aeronautics & Astronautics, supported by the NASA Pathways Program, Point Foundation, NSF grant OCE-1536502, and Professor Juan Alonso.

ACKNOWLEDGMENTS

We would like to acknowledge the significant support and guidance provided by NASA ESTO and program managers Michael Little, Woody Turner, and Paula Bontempi. We

thank members of NASA LAS–Jarrett van den Bergh and Jonas Jonsson, as well as members of the NeMO-Net team—Sylvia Earle, Charlotte Vick, Juan Torres-Perez, Kamalika

Das, and Michal Segal-Rozenhaimer. Finally, we appreciate the invaluable feedback and review of this manuscript by Phil McGillivray.

REFERENCES

- Airy, G. B. (1838). On the intensity of light in the neighbourhood of a caustic. *Trans. Cambridge Philos. Soc.* 6:379.
- Andréfouët, S., Kramer, P., Torres-Pulliza, D., Joyce, K. E., Hochberg, E. J., Garza-Pérez, R., et al. (2003). Multi-site evaluation of IKONOS data for classification of tropical coral reef environments. *Remote Sens. Environ.* 88, 128–143. doi: 10.1016/j.rse.2003.04.005
- Beijbom, O., Edmunds, P. J., Roelfsema, C., Smith, J., Kline, D. I., Neal, B. P., et al. (2015). Towards automated annotation of benthic survey images: variability of human experts and operational modes of automation. *PLoS ONE* 10:e0130312. doi: 10.1371/journal.pone.0130312
- Bellwood, D. R., Hughes, T. P., Folke, C., and Nystrom, M. (2004). Confronting the coral reef crisis. *Nature* 429, 827–833. doi: 10.1038/nature02691
- Board, S. S. (2007). *Earth Science and Applications from Space: National Imperatives for the Next Decade and Beyond*. National Academies Press. Available online at: <https://books.google.com/books?hl=en&lr=&id=5rXB3qv8RoC&pgis=1> (accessed February 8, 2016).
- Bodenmann, A., Thornton, B., and Ura, T. (2013). “Development of long range color imaging for wide area 3D reconstructions of the seafloor,” in *Underwater Technology Symposium (UT)* (Tokyo: IEEE International).
- Briese, C., Pfennigbauer, M., Lehner, H., Ullrich, A., Wagner, W., and Pfeifer, N. (2012). Radiometric calibration of multi-wavelength airborne laser scanning data. *ISPRS Ann. Photogramm. Remote Sens. Spat. Inf. Sci.* 1, 335–340. doi: 10.5194/isprsannals-1-7-335-2012
- Briese, C., Pfennigbauer, M., Ullrich, A., and Doneus, M. (2013). Multi-wavelength airborne laser scanning for archaeological prospection. *Int. Arch. Photogramm. Remote Sens. Spat. Inf. Sci.* 40, 119–124. doi: 10.5194/isprsarchives-XL-5-W2-119-2013
- Cartier, K. M. S. (2018). Coral reef video game will help create global database. *EOS* 99. doi: 10.1029/2018EO112373
- Castelluccio, M., Poggi, G., Sansone, C., and Verdoliva, L. (2015). Land use classification in remote sensing images by convolutional neural networks. *Comput. Vis. Pattern Recognit.* 15:19.
- Chen, Y., Jiang, H., Li, C., Jia, X., and Ghamisi, P. (2016). Deep feature extraction and classification of hyperspectral images based on convolutional neural networks. *IEEE Trans. Geosci. Remote Sens.* 54, 6232–6251. doi: 10.1109/TGRS.2016.2584107
- Chirayath, V. (2016). *Fluid lensing & applications to remote sensing of aquatic environments* (PhD Thesis). Stanford, CA: Stanford University. Available online at: purl.stanford.edu/kw062mg5196
- Chirayath, V. (2018a). *System and Method for Active Multispectral Imaging and Optical Communications*. United States Patent and Trade Office, 15/480,318.
- Chirayath, V. (2018b). *System and Method for Imaging Underwater Environments Using Fluid Lensing*. United States Patent and Trade Office, 62/634,803.
- Chirayath, V., and Earle, S. (2016). Drones that see through waves—preliminary results from airborne fluid lensing for centimetre-scale aquatic conservation. *Aquat. Conserv. Mar. Freshw. Ecosyst.* 26, 237–250. doi: 10.1002/aqc.2654
- Chirayath, V., and Instrella, R. (2016). *Fluid Lensing: Seeing Through Waves*. Available online at: <http://www.nasa.gov/ames/las/fluid-lensing-seeing-through-waves> (accessed February 7, 2016).
- Chirayath, V., and Instrella, R. (accepted). Fluid lensing and machine learning for centimeter-resolution airborne assessment of coral reefs in American Samoa. *Remote Sens. Environ.*
- Chirayath, V., Li, A., Das, K., Segal-Rozenhaimer, M., Torres-Perez, J., and van den Bergh, J. (2018a). *NASA NeMO-Net Homepage*. Available online at: <http://nemonet.info> (accessed August 20, 2018).
- Chirayath, V., Li, A., Das, K., van den Bergh, J., Segal-Rozenhaimer, M., and Torres-Perez, J. (2018b). “NEMO-NET & fluid lensing: the neural multi-modal observation & training network for global coral reef assessment using fluid lensing augmentation of NASA EOS data,” in *Ocean Sciences Meeting* (Portland, OR).
- Collin, A., Archambault, P., and Long, B. (2011). Predicting species diversity of benthic communities within turbid nearshore using full-waveform bathymetric LiDAR and machine learners. *PLoS ONE* 6:e21265. doi: 10.1371/journal.pone.0021265
- Corson, M. R., Korwan, D. R., Lucke, R. L., Snyder, W. A., and Davis, C. O. (2008). “The hyperspectral imager for the coastal ocean (HICO) on the international space station,” in *Geoscience and Remote Sensing Symposium, IGARSS 2008* (Boston, MA: IEEE International).
- Daimon, M., and Masumura, A. (2007). Measurement of the refractive index of distilled water from the near-infrared region to the ultraviolet region. *Appl. Opt.* 46, 3811–3820. doi: 10.1364/AO.46.003811
- Donahue, J., Jia, Y., Vinyals, O., Hoffman, J., Zhang, N., Tzeng, E., et al. (2014). “DeCAF: a deep convolutional activation feature for generic visual recognition,” in *International Conference on Machine Learning* (Beijing).
- Edinger, E. N., Limmon, G. V., Jompa, J., Widjatmoko, W., Heikoop, J. M., and Risk, M. J. (2000). Normal coral growth rates on dying reefs: are coral growth rates good indicators of reef health? *Mar. Pollut. Bull.* 40, 404–425. doi: 10.1016/S0025-326X(99)00237-4
- Eismann, M. T. (2012). *Hyperspectral Remote Sensing*. Bellingham, WA: SPIE Press.
- Goel, M., Patel, S. N., Whitmire, E., Mariakakis, A., Saponas, T. S., Joshi, N., et al. (2015). “HyperCam,” in *Proceedings of the 2015 ACM International Joint Conference on Pervasive and Ubiquitous Computing—UbiComp ’15* (New York, NY: ACM Press), 145–156.
- Gomez-Chova, L., Tuia, D., Moser, G., and Camps-Valls, G. (2015). Multimodal classification of remote sensing images: a review and future directions. *Proc. IEEE* 103, 1560–1584. doi: 10.1109/JPROC.2015.2449668
- Goodman, J. A., Purkis, S. J., and Phinn, S. R. (2013). *Coral Reef Remote Sensing: A Guide for Mapping, Monitoring and Management*. Heidelberg: Springer Science & Business Media.
- Irons, J. R., Dwyer, J. L., and Barsi, J. A. (2012). The next landsat satellite: the landsat data continuity mission. *Remote Sens. Environ.* 122, 11–21. doi: 10.1016/j.rse.2011.08.026
- Jin, H., Lim, J., Kim, Y., and Kim, S. (2013). Optical design of a reflecting telescope for cubesat. *J. Optic. Soc. Korea* 17, 533–537. doi: 10.3807/JOSK.2013.17.6.533
- Johnston, D. W. (2018). Unoccupied aircraft systems in marine science and conservation. *Ann. Rev. Mar. Sci.* 11, 439–463. doi: 10.1146/annurev-marine-010318-095323
- Krizhevsky, A., Sutskever, I., and Hinton, G. E. (2012). ImageNet classification with deep convolutional neural networks. *Adv. Neural Inf. Process. Syst.* 25, 1097–1105. doi: 10.1145/3065386
- Lary, D. J., Alavi, A. H., Gandomi, A. H., and Walker, A. L. (2016). Machine learning in geosciences and remote sensing. *Geosci. Front.* 7, 3–10. doi: 10.1016/j.gsf.2015.07.003
- Lary, D. J., Remer, L. A., Macneill, D., Roscoe, B., and Paradise, S. (2009). Machine learning and bias correction of MODIS aerosol optical depth. *IEEE Geosci. Remote Sens. Lett.* 6, 694–698. doi: 10.1109/LGRS.2009.2023605
- Lary, D. J., Waugh, D. W., Douglass, A. R., Stolarski, R. S., Newman, P. A., and Mussa, H. (2007). Variations in stratospheric inorganic chlorine between 1991 and 2006. *Geophys. Res. Lett.* 34, 28–32. doi: 10.1029/2007GL030053
- Lecun, Y., Bottou, L., Bengio, Y., and Ha, P. (1998). Gradient-based learning applied to document recognition. *Proc. IEEE* 86, 2278–2324. doi: 10.1109/5.726791
- Lee, D. (2013). “Pseudo-label: the simple and efficient semi-supervised learning method for deep neural networks,” in *ICML 2013 Workshop: Challenges in Representation Learning* (Atlanta).

- Lewis, D. D., and Catlett, J. (1994). "Heterogeneous uncertainty sampling for supervised learning," in *Proceedings of the 11th International Conference on Machine Learning* (New Brunswick, NJ).
- Liu, C., Yuen, J., and Torralba, A. (2011). Sift flow: dense correspondence across scenes and its applications. *IEEE Trans. Pattern Anal. Mach. Intell.* 33, 978–994. doi: 10.1109/TPAMI.2010.147
- Madsen, P. T., Johnson, M., de Soto, N. A., Zimmer, W. M. X., and Tyack, P. (2005). Biosonar performance of foraging beaked whales (*Mesoplodon densirostris*). *J. Exp. Biol.* 208, 181–194. doi: 10.1242/jeb.01327
- Maeder, J., Narumalani, S., Rundquist, D. C., Perk, R. L., Schalles, J., Hutchins, K., et al. (2002). Classifying and mapping general coral-reef structure using Ikonos data. *Photogramm. Eng. Remote Sens.* 68, 1297–1306.
- McGillivray, P. A., Chirayath, V., and Baghdady, J. (2018). "Use of multi-spectral high repetition rate LED systems for high bandwidth underwater optical communications, and communications to surface and aerial systems," in *2018 Fourth Underwater Communications and Networking Conference (UComms)* (Lerici).
- Mordy, C. W., Cokelet, E. D., De Robertis, A., Jenkins, R., Kuhn, C. E., Lawrence-Slavas, N., et al. (2017). Advances in ecosystem research: saildrone surveys of oceanography, fish, and marine mammals in the bering sea. *Oceanography* 30, 113–115. doi: 10.5670/oceanog.2017.230
- Nemani, R., Votava, P., Michaelis, A., Melton, F., and Milesi, C. (2011). Collaborative supercomputing for global change science. *Eos. Trans. Am. Geophys. Union* 92, 109–110. doi: 10.1029/2011EO130001
- Nischan, M. L., Joseph, R. M., Libby, J. C., and Kerekes, J. P. (2003). Active spectral imaging. *Lincoln Lab. J.* 14, 131–144.
- Park, J. Il., Lee, M. H., Grossberg, M. D., and Nayar, S. K. (2007). "Multispectral imaging using multiplexed illumination," in *2007 IEEE 11th International Conference on Computer Vision* (Rio De Janeiro).
- Parmar, M., Linsel, S., and Farrell, J. (2012). An LED-based lighting system for acquiring multispectral scenes. *Library*. 2012:82990. doi: 10.1117/12.912513
- Phillips, O. M. (1958). The equilibrium range in the spectrum of wind-generated waves. *J. Fluid Mech.* 4, 426–434. doi: 10.1017/S0022112058000550
- Phillips, O. M. (1985). Spectral and statistical properties of the equilibrium range in wind-generated gravity waves. *J. Fluid Mech.* 156, 505–531. doi: 10.1017/S0022112085002221
- Pizarro, O., Eustice, R., and Singh, H. (2004). "Large area 3D reconstructions from underwater surveys," in *MTS/IEEE Oceans Conference and Exhibition* (Kobe).
- Pope, R. M., and Fry, E. S. (1997). Absorption spectrum (380–700/nm) of pure water. {II.} Integrating cavity measurements. *Appl. Opt.* 36, 8710–8723. doi: 10.1364/AO.36.008710
- Purkis, S. J. (2018). Remote sensing tropical coral reefs: the view from above. *Ann. Rev. Mar. Sci.* 10, 149–168. doi: 10.1146/annurev-marine-121916-063249
- Purkis, S. J., and Pasterkamp, R. (2004). Integrating *in situ* reef-top reflectance spectra with Landsat TM imagery to aid shallow-tropical benthic habitat mapping. *Coral Reefs* 23, 5–20. doi: 10.1007/s00338-003-0351-0
- Roberts, H. H., Shedd, W., and Hunt J Jr. (2010). Dive site geology: DSV ALVIN (2006) and ROV JASON II (2007) dives to the middle-lower continental slope, northern Gulf of Mexico. *Deep Sea Res. Part II Top. Stud. Oceanogr.* 57, 1837–1858. doi: 10.1016/j.dsr2.2010.09.001
- Roemmich, D., and Gilson, J. (2009). The 2004–2008 mean and annual cycle of temperature, salinity, and steric height in the global ocean from the argo program. *Prog. Oceanogr.* 82, 81–100. doi: 10.1016/j.pocean.2009.03.004
- Rogers, J. S., Maticka, S. A., Chirayath, V., Woodson, C. B., Alonso, J. J., Monismith, S. G. (2018). Connecting flow over complex terrain to hydrodynamic roughness on a coral reef. *J. Phys. Oceanogr.* 48, 1567–1587. doi: 10.1175/JPO-D-18-0013.1
- Schenck, H. Jr. (1957). On the focusing of sunlight by ocean waves. *JOSA* 47, 653–657. doi: 10.1364/JOSA.47.000653
- Schmidt, A. G., Weisz, G., French, M., Flatley, T., and Villalpando, C. Y. (2017). "SpaceCubeX: a framework for evaluating hybrid multi-core CPU/FPGA/DSP architectures," in *Aerospace IEEE IEEE Conference* (Big Sky, MT), 1–10.
- Segal-Rozenhaimer, M., Li, A., Das, K., and Chirayath, V. (accepted). Cloud detection algorithm for multi-modal satellite imagery using Convolutional Neural-Networks (CNN). *Remote Sens. Environ.*
- Serpico, S. B., and Roli, F. (1995). Classification of multisensor remote-sensing images by structured neural networks. *IEEE Trans. Geosci. Remote Sens.* 33, 562–578. doi: 10.1109/36.387573
- Sharma, M., Das, K., Bilgic, M., Matthews, B., Nielsen, D., and Oza, N. (2016). "Active learning with rationales for identifying operationally significant anomalies in aviation," in *Joint European Conference on Machine learning and Knowledge Discovery in Databases* (Cham: Springer International Publishing), 209–225.
- Shrestha, R., and Hardeberg, J. Y. (2013). "Multispectral imaging using LED illumination and an RGB camera," *21st Color and Imaging Conference Final Program and Proceedings* (Albuquerque, NM).
- Storlazzi, C. D., Dartnell, P., Hatcher, G. A., and Gibbs, A. E. (2016). End of the chain? Rugosity and fine-scale bathymetry from existing underwater digital imagery using structure-from-motion (SfM) technology. *Coral Reefs* 35, 889–894. doi: 10.1007/s00338-016-1462-8
- Suosaari, E. P., Reid, R. P., Playford, P. E., Foster, J. S., Stolz, J. F., Casaburi, G., et al. (2016). New multi-scale perspectives on the stromatolites of Shark Bay, Western Australia. *Sci. Rep.* 6:20557. doi: 10.1038/srep20557
- Tessendorf, J. (2001). Simulating ocean water. *Simul. Nat. Realis. Interact. Tech. Siggraph*. 1:5.
- Tyack, P. L. (2000). "Functional aspects of cetacean communication," in *Cetacean Societies: Field Studies of Dolphins and Whales*, eds J. Mann, R. C. Connor, P. L. Tyack, and H. Whitehead (Chicago, IL: The University of Chicago Press), 270–307.
- Wang, Z., Bovik, A. C., Sheikh, H. R., and Simoncelli, E. P. (2004). Image quality assessment: from error visibility to structural similarity. *Image Process. IEEE Trans.* 13, 600–612. doi: 10.1109/TIP.2003.819861
- Weston, J., Ratle, F., Mobahi, H., and Collobert, R. (2012). "Deep learning via semi-supervised embedding," in *Neural Networks: Tricks of the Trade*, eds G. Montavon, G. B. Orr, and K.-R. Muller (Berlin: Springer Berlin Heidelberg), 639–655.
- Yamaguchi, M., Haneishi, H., Fukuda, H., Kishimoto, J., Kanazawa, H., Tsuchida, M., et al. (2006). "High-fidelity video and still-image communication based on spectral information: natural vision system and its applications," in *SPIE 6062, Spectral Imaging: Eighth International Symposium on Multispectral Color Science* (San Jose, CA).
- You, Y., Stramski, D., Darecki, M., and Kattawar, G. W. (2010). Modeling of wave-induced irradiance fluctuations at near-surface depths in the ocean: a comparison with measurements. *Appl. Opt.* 49, 1041–1053. doi: 10.1364/AO.49.001041
- Zhong, Y., Fei, F., Liu, Y., Zhao, B., Jiao, H., and Zhang, L. (2017). SatCNN: Satellite image dataset classification using agile convolutional neural networks. *Remote Sens. Lett.* 8, 136–145. doi: 10.1080/2150704X.2016.1235299

Conflict of Interest Statement: The authors declare that the research was conducted in the absence of any commercial or financial relationships that could be construed as a potential conflict of interest.

Copyright © 2019 Chirayath and Li. This is an open-access article distributed under the terms of the Creative Commons Attribution License (CC BY). The use, distribution or reproduction in other forums is permitted, provided the original author(s) and the copyright owner(s) are credited and that the original publication in this journal is cited, in accordance with accepted academic practice. No use, distribution or reproduction is permitted which does not comply with these terms.



Development of Surface Drifting Buoys for Fiducial Reference Measurements of Sea-Surface Temperature

Marc Le Menn^{1*}, Paul Poli², Arnaud David³, Jérôme Sagot³, Marc Lucas⁴, Anne O'Carroll⁵, Mathieu Belbeoch⁶ and Kai Herklotz⁷

¹ Metrology and Chemical Oceanography Department, French Hydrographic and Oceanographic Service (Shom), Brest, France, ² Météo France, Centre de Météorologie Marine, Brest, France, ³ nke Instrumentation, Hennebont, France, ⁴ Collecte Localisation Satellites (CLS), Ramonville-Saint-Agne, France, ⁵ European Organization for the Exploitation of Meteorological Satellites (EUMETSAT), Darmstadt, Germany, ⁶ JCOMM in situ Observations Programme Support Centre (JCOMMops), Plouzané, France, ⁷ Bundesamt für Seeschifffahrt und Hydrographie (BSH), Hamburg, Germany

OPEN ACCESS

Edited by:

Leonard Pace,
Schmidt Ocean Institute,
United States

Reviewed by:

Shinya Kouketsu,
Japan Agency for Marine-Earth
Science and Technology, Japan
R. Venkatesan,
National Institute of
Ocean Technology, India

*Correspondence:

Marc Le Menn
Marc.lemenn@shom.fr

Specialty section:

This article was submitted to
Ocean Observation,
a section of the journal
Frontiers in Marine Science

Received: 08 January 2019

Accepted: 30 August 2019

Published: 13 September 2019

Citation:

Le Menn M, Poli P, David A, Sagot J, Lucas M, O'Carroll A, Belbeoch M and Herklotz K (2019) Development of Surface Drifting Buoys for Fiducial Reference Measurements of Sea-Surface Temperature. *Front. Mar. Sci.* 6:578. doi: 10.3389/fmars.2019.00578

This paper presents the conception and the metrological characterization of a new surface drifting buoy, designed to comply with the requirements of satellite sea-surface temperature (SST) measurement validation and to link, per comparison, these measurements to the SI. The reliability of this comparison is ensured by a High Resolution Sea-Surface Temperature (HRSST) sensor associated with a pressure sensor in a module called MoSens. This module can be calibrated in a laboratory to ensure traceability to the SI with an expanded uncertainty inferior to 0.01°C. This paper estimates the response time of the HRSST sensor based on theoretical considerations and compares the results with measurements carried out in a calibration bath. Once integrated in a number of buoys, the resulting network will contribute to create a fiducial reference measurement (FRM) network. The pressure sensor can be used as an indicator of the sea-state, which is important to consider in order to understand the comparison with satellite data. Two buoy prototypes have been tested at sea during several weeks and compared *in situ* to reference thermometers, demonstrating their reliability and the trueness of temperature measurements.

Keywords: drifting buoys, surface temperature, reference, satellite, measurement uncertainty, SST

INTRODUCTION

Sea-Surface Temperatures (SST) play a key role in the understanding of the ocean-atmosphere interactions, in the characterization of the mesoscale variability of the upper ocean, and also as inputs of numerical weather prediction systems. They have traditionally been measured *in situ*, and since the 1970s, they are also monitored with a global coverage by satellite-borne radiometers (e.g., Prabhakara et al., 1974; Milman and Wilheit, 1985). These instruments measure the radiance emitted by the sea surface. These radiance measurements are sensitive to ocean skin temperature, but are also sensitive to the atmospheric physical state and constituents, and to the sea state. In order to determine more precisely these sources of inaccuracy, methods have been developed to trace radiance measurement uncertainties (Woolliams et al., 2016, 2018; Banks et al., 2017; Merchant et al., 2019). However, to ensure the validity of retrieved SST, comparisons with independent *in situ* measurements are

necessary (O'Carroll et al., 2008). Only after validation, the resulting SST retrievals can be used to generate global datasets with spatio-temporal consistency (e.g., Titchner and Rayner, 2014).

In situ SST measurements go back at least 200 years (Kennedy, 2014). They have been collected for several purposes and with varying instruments. The first measurements were made from seawater collected by buckets, and after by seawater circulating through the steam condenser of the engine room inlets on ships. Since the 1970s, oceanographic vessels of opportunity are equipped with hull thermometers. In quiet sea states, they measure temperature at 5 or 6 m under the surface and, for the last 10 years, many have been equipped with high-resolution and stable Sea-Bird Electronics (SBE)-38 sensors (e.g., Gaillard et al., 2015). Argo profiling float temperatures are also used for comparisons. Since January 2005, they offer comprehensive ocean coverage (Hausfather et al., 2017). Argo products provide temperatures at different depths: 2.5, 5, 10, 20, 30 m, or deeper levels with an initial accuracy close to 2 mK. Sensors are generally stopped several meters below the surface to avoid the fouling of the conductivity cell by surface contaminants. A few floats are equipped with SBE STS (Surface Temperature Salinity) sensors which sample the final meters up to the surface, with a degraded accuracy in salinity, but most of Argo temperatures exploited as SST are measured at 5 m under the surface (Roemmich and Gilson, 2009). While only the initial accuracy has been guaranteed so far, first efforts have been made to recover Argo floats, in order to document potential changes in trueness (BIPM, 2012) over time (e.g., Oka, 2005).

Generally, measurements made in the upper 10 m of the ocean are considered as SST measurements. However, satellite infrared radiometers measure radiations emitted from the upper few tens of microns (skin temperatures) or millimeters (subskin temperatures) for microwave radiometers (Donlon et al., 2004). Therefore, surface drifting buoys observations are preferred for comparisons with satellites data, as their sensors are at a nominal depth of between 10 and 20 cm (Merchant et al., 2012). According to the Data Buoy Cooperation Panel (DBCP) about 1,500 drifting buoys cover nowadays the seas of the globe and according to (Kennedy, 2014), they provide about 90% of *in situ* SST data.

Designed in the 1980s to study ocean currents in the context of the Surface Velocity Program (SVP; World Climate Research Programme, 1988) and for meteorological purposes, these buoys had to be inexpensive, easy to deploy and reliable during at least 18 months. The design specifications of SVP drifters were standardized in 1991. In 1993, it became possible to equip a SVP drifter with a barometer port to measure sea-level air pressure. The result was called a SVP-B drifter. SVP drifters were also equipped with SST sensors. This sensor should have an accuracy of 0.1 K with a stability better than 0.1 K/year (World Climate Research Programme, 1988). There were other documented requirements, though less stringent, with 0.5 K requested in the range from -5 to 30°C (EGOS, 2002). Of note in the SVP-B design manual (Sybrandy et al., 2009), is the requirement that a thermal isolation be included to ensure that

the solar heating of the top of the surface float does not impact the SST measurement. The sensor should be accurate to better than 0.1 K when the inside of the float is 1 K warmer than the sea surface.

In his publication, Kennedy (2014, Table 2, p. 8) cites 10 references dealing with estimates of measurement errors or uncertainties of drifting buoys (with no clear distinction between error and uncertainty). They range from 0.12 to 0.67 K. He discusses also the possibility to separate observation errors or uncertainties into random and systematic components, particularly for drifters, from two earlier publications (Kennedy et al., 2011a,b) and from a publication by Kent and Berry (2008). They find similar results with estimated random components of (respectively) 0.56 and 0.6 K and systematic components of (respectively) 0.37 and 0.3 K. These values are close, for example, to the expected accuracy of the Advanced Along-Track Scanning Radiometer (AATSR) launched in March 2002. It is designed to produce SST retrievals to better than 0.3 K accuracy, with a long-term stability of better than 0.1 K per decade (Lewellyn-Jones et al., 2001). Therefore, the corresponding drifting buoys SST measurements collected so far cannot be considered as references from a metrological point of view. Neither can they be considered as references for the more recent EUMETSAT-operated Copernicus Sentinel-3A, the first in a new generation of satellites designed to collect and monitor long-term climate and ocean data with metrological specifications equivalent to AATSR (Donlon et al., 2012).

Separating systematic and random components is not an easy task for SST measurements, because the data from several authors (see Kennedy, 2014 or Castro et al., 2012) suggest a dependency on the time period considered. If random components come from the variability in time and space of the thermal and dynamical states of the sea, in the case of SVP drifters, the biggest part of systematic components can come from the buoy and sensor conception and from the unknown temporal drift of their SST sensors.

This short review underlines the need to develop a new concept of surface drifting float which would be characterized in metrology laboratory. Its design has to comply with the requirements of satellite SST measurement validation and must allow the link through comparisons of its measurements to the *Système International d'unités* (SI). This need was described in a EUMETSAT tender, the goal of which was to build a Fiducial Reference Measurements (FRM) network of 100 high-resolution SST drifting buoys for the Copernicus Sentinel satellites validation. The development of this network echoes also, for the ocean surface, the need raised by Immler et al. (2010) for upper-air measurements, to constitute an independent infrastructure based on a different measurement principle and for which uncertainties are defined. Beyond the needs underlined by the review, this development answers the necessity of assuring long-term stability of references (World Meteorological Organization, 2016), the uncertainties of which are fully characterized by a metrological approach, for climate change studies.



FIGURE 1 | Photo of SST sensor (left) and of MoSens device with HRSST sensor (right).

CONCEPTION OF THE REFERENCE BUOYS

A drifting buoy with a novel sensor package has been developed, called SVP with Barometer and Reference Sensor for Temperature (SVP-BRST, see Poli et al., 2018). It is a spherical drifter of 40 cm diameter made of high pressure molded polypropylene (see Figure 2). A 12.5 m-long line (including an elastic section) is attached below the buoy and linked to a stainless bracket. A holey sock drogue centered at 15 m depth is suspended to the line. It is 0.8 m in diameter and 6 m in length. The drogue loss is detected by a strain gauge, instead of a submergence sensor (Lumpkin and Pazos, 2006).

A GPS receiver is included in the buoy to provide position estimates, and various GPS quality parameters. The strain gauge reading and the GPS Time To First Fix (TTFF) are transmitted as indicators of drogue loss. The transmission is made hourly, via a 30-bytes iridium Short-Burst Data (SBD) message, in a new dedicated format (Blouch et al., 2018).

The buoy is based on the SVP-B design (Sybrandy et al., 2009). It is equipped with a Vaisala PTB 110 BAROCAP sensor featuring an accuracy of ± 0.6 hPa (according to Vaisala documentation) for temperature variations from 0 to 40°C (± 0.3 hPa for the temperature range from 15 to 25°C). It is delivered with a NIST traceable calibration certificate. The measurement of SST is made by two sensors: a regular SST sensor with an initial trueness superior to 0.1°C and a new High-Resolution SST sensor called HRSST. As recommended by best-practices, both are protected from solar and buoy radiations by a cap. The regular sensor for SST (called analog sensor thereafter) is made with two cupronickel bolts of diameters 1.4 and 1.9 cm, protecting a 6 mm tube in which is inserted a thermistor (see Figure 1). This configuration is used on nke Instrumentation SC-40, and is similar to that of other SVP buoys.

The HRSST sensor is composed of a thermistor inserted in a small stainless steel needle of 0.9 cm length L and 0.12 cm in diameter D . The resolution is 1 mK and its trueness is expected to be better than 0.01 K.

The HRSST sensor is associated with a hydrostatic pressure sensor in a removable cylindrical housing containing the electronic board of the two sensors. The cylindrical housing is necessary to calibrate these instruments in thermo-regulated baths, but it is removed when these modules are integrated in the buoys. This assembly is called MoSens by nke Instrumentation. The MoSens module hydrostatic pressure sensor presents a theoretical trueness of 0.05% on a range of 0–30 dbar and a

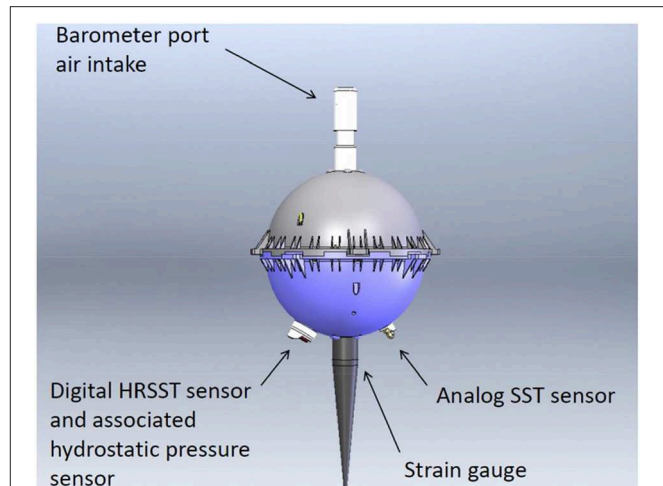


FIGURE 2 | Schema of the buoy with its sensors (the line, the stainless bracket and the holey sock drogue are not represented). Doc. © nke Instrumentation.

resolution of 0.05 dbar. Data are transmitted to the buoy motherboard by a serial link Modbus.

THEORETICAL CONSIDERATIONS ON THE TEMPERATURE MEASUREMENTS

de Podesta et al. (2018) demonstrated that “the radiative error for an air temperature sensor, in flowing air depends upon the sensor diameter and air speed, with smaller sensors and higher air speeds yielding values closer to true air temperature.” HRSST and SST analog sensors are protected from direct solar radiations by a cap but one part of the sunlight enters also the ocean. Seawater is close to a blackbody in the infrared part of the spectrum and the blue-green radiations can be reflected at depths as great as 50 m (Le Traon, 2018). In the ocean, light radiations are reflected by particles or phytoplankton, and absorption and scattering decrease strongly their intensity, and hence their effects on exchanged heat flux. This exchange is therefore secondary compared to the impact of convection or conduction. However, one part is backscattered to the surface and can be detected by satellites to measure ocean color. This part can also be detected by sensitive sensors and it is interesting to evaluate the error induced by radiations on the measurement of the true temperature of seawater.

It is therefore interesting to see if de Podesta’s affirmation is also true in seawater. He establishes the balance equation between the heat flux exchanged in steady state and the fluxes due to irradiation and self-heating as follows:

$$hA(T_s - T_{sw}) = [I^2R + \epsilon_s LDE] + 4\sigma\epsilon_s AT_w^3(T_w - T_s) \quad (1)$$

where h is the heat transfer coefficient, $A = \pi LD$ is the surface of exchange of the sensor considered as a cylinder of length L and diameter D , T_s is the temperature of the sensor’s surface, T_{sw}

is the true temperature of seawater, I^2R is the power of the self-heating due to the current I passing through the sensor resistance R , ϵ_S is the emissivity or absorptivity of the sensor's surface, E is the irradiance, σ is the Stefan-Boltzmann constant, and T_w is the temperature of the walls (surrounding the sensor) assumed to be emitting as a blackbody. The heat transfer coefficient h is the key quantity to understand the intensity of the thermal transfer between the surface of the sensor and the fluid. It takes into account the conjugate effects of conduction, convection, and radiation in the surrounding medium.

We can consider the self-heating as negligible, because the thermistor is fed by a micro-current leading to the maximum error of a few hundred of micro-degrees. If we consider that the radiative environment is almost at the same temperature as the surface of the sensor, $T_w \approx T_S$, then the second part of the right-hand-side of Equation (1) can be neglected. The temperature measurement error can then be described by:

$$(T_S - T_{sw}) = \frac{\epsilon_S E}{\pi h} \quad (2)$$

For a fluid flowing perpendicularly past a cylinder, h can be approximated by the equation:

$$h = \frac{kNu}{D} \quad (3)$$

where k is the thermal conductivity of the fluid and Nu the Nusselt number for a cylinder in a transverse flow. In the case of water, the following empirical expression is often used to calculate Nu in conditions of laminar flow (Schlichting, 1979):

$$Nu = 0.66 Pr^{1/3} Re^{1/2} \quad (4)$$

Pr is the Prandtl number. It describes a fluid with a dynamic viscosity μ and a specific heat capacity C_p :

$$Pr = \frac{\mu C_p}{k} \quad (5)$$

Re is the Reynolds number. It describes the flow of a fluid which would have a speed V and a density ρ :

$$Re = \frac{\rho VD}{\mu} \quad (6)$$

The Equation (6) is valid when $RePr > 0.2$. In the case of a surface seawater with a practical salinity of 35, a temperature of 15°C, even with a very low speed $V = 0.001 \text{ m s}^{-1}$, $RePr = 8.33$ (with $D = 1.2 \text{ mm}$). Combining Equations (2–6) gives:

$$(T_S - T_{sw}) = \frac{\epsilon_S E}{0.66\pi \mu^{-1/6} \rho^{1/2} k^{2/3}} \left(\frac{D}{V} \right)^{1/2} \quad (7)$$

The relation (7) shows that the error due to the irradiance is proportional to the square root of the diameter of the cylindrical sensor (all other parameters assumed equal). Applied to the HRSST sensor with $D = 0.12 \text{ cm}$ and to the SST analog sensor

TABLE 1 | Comparison of ratios D/V and response times for the HRSST sensor and the SST analog sensor in a seawater at 15°C and $S = 35$.

	HRSST sensor		SST Analog sensor	
Sensor diameter (cm)	0.15	0.15	1.4	1.4
Water velocity (m/s)	0.001	1.0	0.001	1.0
Thermal conductivity (W/m°C)	0.59	0.59	0.59	0.59
Reynolds	1.02	1017	11.44	11437
Prandtl	8.19	8.19	8.19	8.19
Nusselt	1.34	42.4	4.50	128.1
$(D/V)^{0.5}$	1.095	0.035	3.674	0.116
Heat transfer coefficient (W/cm²°C)	6.59	208.3	1.96	55.9
Mass of the sensor (g)	0.35	0.35	46.45	46.45
Response time (ms)	77.5	2.5	571	20.1

With a water velocity of 1 m/s, the HRSST is in laminar flux conditions whereas the SST analog sensor is in less favorable, turbulent conditions.

with an average diameter $D = 1.4 \text{ cm}$, the radiative error is divided by 3.4, to the advantage of the HRSST sensor, when the same environmental conditions are considered.

The size difference between the SST analog sensor and the HRSST sensor also has an effect on the response time τ . If we neglect the exchange by radiation, most of the heat exchanged between the sensor and the medium is the result of convection, described by the coefficient h . The quantity of heat propagating in the sensor of mass m and specific heat capacity C_{ps} , results in a temperature variation dT during the time dt . The balance equation can be written:

$$hA (T_S - T_{sw}) = mC_{ps} \frac{dT}{dt} \quad (8)$$

Its resolution leads to the equation:

$$T - T_0 = (T_{sw} - T_0) \cdot \left(1 - e^{-\frac{t}{\tau}} \right) \quad (9)$$

where T_0 is the initial temperature of the sensor and τ is the ratio:

$$\tau = \frac{mC_{ps}}{hA} \quad (10)$$

In Equation (9), the time for which $t = \tau$ represents the constant $1 - e^{-1} = 0.632$ which defines the response time τ . The **Table 1** shows that for a very low seawater velocity and the same environmental conditions, the response time τ is about 7 times larger for the SST analog sensor than for the HRSST sensor. **Table 1** also shows the results of $(D/V)^{0.5}$ ratios for two flow speeds. **Figure 3** shows the response times of both sensors, as a function of velocity.

CALIBRATION AND LABORATORY TESTS OF THE HRSST SENSORS

One of difficulties in constituting a 100-buoy reference network is to calibrate all the buoys with an uncertainty close to a few milli-degrees. The solution found was to first calibrate the MoSens

devices, then to integrate them in the buoys, and finally to verify the lack of added systematic errors due to the integration. Two prototypes were assembled as proofs of concept.

Calibration and Traceability of Temperature Measurements

The MoSens devices are calibrated by comparison in a calibration bath whose thermal stability shows a standard deviations between 0.1 and 0.3 mK during temperature plateaus. The MoSens sensors are completely immersed and placed close to the sensitive part of an SBE 35 reference thermometer. This thermometer is verified and calibrated periodically in triple point of water (ptH₂O) and fusion point of Gallium (pfGa) cells, to ensure the linkage to the International Temperature Scale of 1990 (ITS-90) of the measured temperatures. The ptH₂O and pfGa cells are calibrated by the French National Institute of Metrology (LNE-CNAM), to 0.1 and 0.26 mK, respectively.

Eight temperature plateaus are created between 1 and 35°C to allow the comparison between the devices and to calculate the

coefficients G, H, I, J of the Bennett relation (11), for each MoSens sensor, with a least-squares technique:

$$t(C) = \frac{1}{\left[G + H \ln(x) + I \ln(x)^2 + J \ln(x)^3 \right]} - 273.15 \quad (11)$$

where x is the raw value delivered every second by the sensor.

Once the coefficients are obtained and programmed in the MoSens, the calibration verifications are made. For the two prototypes, the residuals of the least squares calculation are between 0 and 1.1 mK, but the verification made in the bath showed that maximum deviations of 2.4 mK could be obtained (see **Figure 4**), even if most of them are under 2 mK. These deviations can be explained by the thermal inertia and the self-heating of the MoSens modules (see section Measurement of the Response Time of the MoSens Module) equipped with their cylindrical housing. Nonetheless, they remain below the desired threshold values.

Uncertainty of the HRSST Sensors Calibration

The calibration uncertainty budget includes:

- The standard uncertainty on the reference temperatures, u_{tref} assessed to be 0.9 mK from 0 to 35°C. This includes the calibration of the reference thermometer to the fixed reference points of the ITS-90, its drift over the 12 last months, and its reading uncertainties.

TABLE 2 | Calibration uncertainty budget of the two MoSens prototypes.

Uncertainty budget of MoSens calibration	n° 4656 (mK)	n° 4658 (mK)
Reference temperature (u_{tref})	0.9	0.9
Bath stability (u_{Bath})	0.3	0.3
MoSens reproducibility (S)	1.7	0.9
MoSens repeatability (S_{rep})	0.3	0.3
Expanded uncertainty (U_C)	4.0	2.8

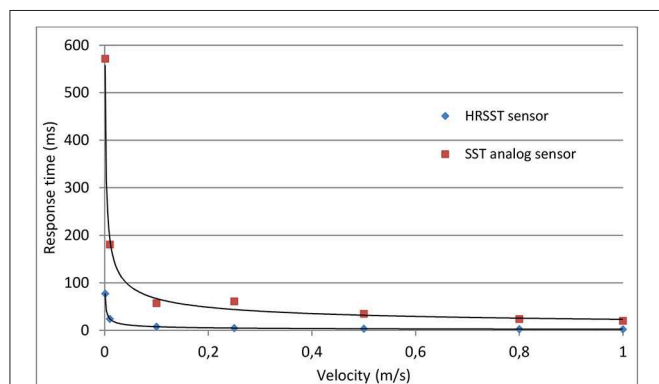


FIGURE 3 | Variation of the sensor response time as a function of the seawater velocity according to relation (8). From at least 0.25 m/s, the SST analog sensor is in turbulent exchange conditions, whereas the HRSST sensor is in laminar conditions even at 1 m/s.

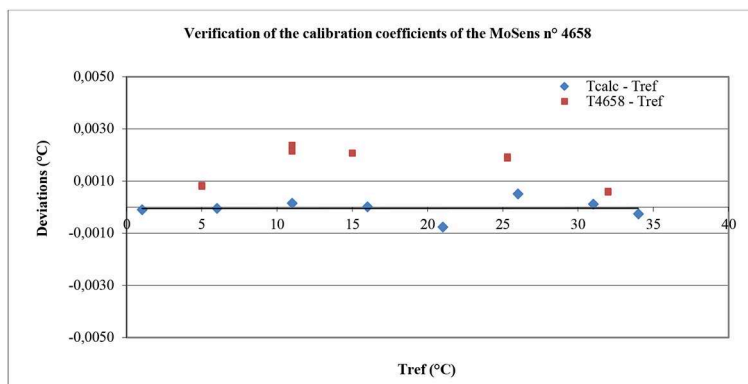


FIGURE 4 | Example of calibration verification made on the MoSens sensor n° 4658. Blue squares represent the residuals and the red squares represent the measured values after the calibration.

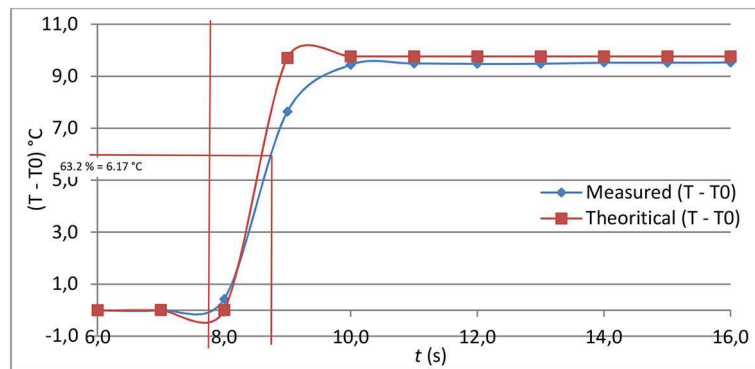


FIGURE 5 | Determination of the response time of MoSens module n° 4656.

- The uncertainty of the bath stability and homogeneity. According to the standard deviations of the measurement series and to homogeneity measurements made on the bath, the standard uncertainty on the bath stability and homogeneity u_{bath} can be assessed to be 0.3 mK.
- The reproducibility S and repeatability S_{rep} of MoSens sensors measurements. The reproducibility is evaluated according to the standard ISO 5725-2 (1994), by calculating the variance of the deviations obtained during the verifications of calibrations. For the prototypes of MoSens n° 4656 and n° 4658, this gives, respectively, $S = 1.7$ mK and $S = 0.9$ mK. The repeatability S_{rep} can be assessed by calculating the average of the standard deviations of the temperatures measured by MoSens sensors. For the two sensors $S_{rep} = 0.3$ mK. This repeatability is strongly correlated to the bath stability.

According to this budget, the model used to calculate the combined uncertainty on the deviations D is:

$$D = T + \delta_{rep} + \delta_{reprod} - T_{ref} + \delta_{bath} \quad (12)$$

In this equation, T is the average of the series of temperature values given by the sensor under calibration, T_{ref} is the average reference temperature, δ_{rep} is the short term variation of the sensor temperature, δ_{reprod} is the long term variation of the sensor temperature and δ_{bath} is the difference in temperature due to the stability and the homogeneity of the bath which introduce small errors between T_{ref} and T at the time of measurements. Applying the GUM method (BIPM, 2008) to relation (12) and assuming a correlation coefficient of 1 between δ_{rep} and δ_{bath} yields:

$$u_D^2 = u_{T_{ref}}^2 + S_{rep}^2 + S^2 + u_{bath}^2 + 2u_{bath}S_{rep} \quad (13)$$

The expanded uncertainty (U_C) on the deviations obtained during the calibration can be calculated by the relation:

$$U_C = 2\sqrt{u_{T_{ref}}^2 + (S_{rep} + u_{bath})^2 + S^2} \quad (14)$$

Table 2 shows the uncertainty budget and the results of relation (14) for the two buoys. For the n° 4656, $U_C = 4.0$ mK, and for the n° 4658, $U_C = 2.8$ mK.

Measurement of the Response Time of the MoSens Module

As the MoSens sampling rate is only 1 s, it has been necessary to fix the initial deviation $T_{sw} - T_0$ of Equation (9), close to 10°C, to allow the assessment of τ . The τ value has been calculated (see **Figure 5**) and it gives 0.200 s°C⁻¹ for the n° 4656 instrument and 0.206 s°C⁻¹ for the n° 4658 instrument in nearly static exchange conditions. The time to obtain 99.99% of the final response can be calculated with the relation $t_{99.99} = \tau \ln(1 - 0.9999)/1000$, and it gives about 1.85 s. The graphical determination of the time to obtain 63.2% of the final response is made with an uncertainty close to 75 ms. It gives a maximum uncertainty value on τ of 17 ms°C⁻¹.

The measured values of τ are about 2.5 times the theoretical value given in **Table 1** in low flow speed conditions and for the HRSST sensor alone. This can be explained by taking into account the heat exchange of MoSens module, in its PVC housing, with the water by convection and radiation, and with the sensor by conduction. This hypothesis is reinforced by drawing the theoretical response curve of HRSST sensor from the relation (9), in which τ would be equal to 0.2 s (**Figure 5**). It appears that the slope of the temperature increase is more important than the measured slope. The response of MoSens module cannot be represented by the simple relation (9) and it doesn't represent exactly the response of HRSST sensor.

The PVC housing and the self-heating of the electronic board of MoSens modules have another effect. It takes longer to reach the final temperature to within ± 2 mK. The time to obtain $T - T_0 = 2$ mK is close to 35 min when $T_{sw} - T_0$ is close to 10°C. This time is not representative of the response time at sea because the MoSens devices are integrated in the buoys without their PVC cylindrical housing and it is always at a temperature that is relatively stable or slowly changing. In other words, the operation carried out here to estimate the sensor response time is sub-optimal, and would need repeating with the sensor integrated in the buoy, but this would pose other practical issues.

Verification of the Calibration of HRSST and SST Sensors of Two Buoys

Once calibrated, the two MoSens sensors have been integrated in buoys and these buoys have been placed in the calibration bath. A platinum $100\ \Omega$ thermometer has been fixed on one of them and protected from the air temperature variations with a piece of foam (see **Figure 6**), in order to measure the external temperature of the buoy and to try to detect its influence on the HRSST and SST measurements. In the calibration mode, the buoys acquire data not every second but every 5 s after having taken off the magnet. Even if the bath temperature is very stable, this reduced sampling rate increases slightly the measurement uncertainty.

Two verification series have been performed on the two buoys. The first series was from 1 to 34°C , the buoys being in contact with the air in the laboratory. For the second series, from 34 to 1°C , the buoys were covered with a survival blanket. The goal of this second series was to measure the effect, on HRSST and SST

analog measurements, of buoy temperatures closer to the water temperature. The blanket has been laid to shield the buoy from radiation within the room and thus to partially insulate the buoy from the room temperature, to enclose the radiations of the bath and to limit the air exchanges.

The results of the first series show that, for the two buoys, the amplitude of the deviations is the same as the amplitudes measured during the verification of MoSens sensors alone (see **Figure 7**). It means that the integration of MoSens in the buoy does not add systematic errors to the HRSST measurements. Furthermore, this implies that MoSens sensors can be calibrated alone, before integration in the buoys, which is an essential point to develop a fiducial reference network.

The results of the second series are given in **Figure 7** and in **Table 3**, for the buoy n° Y17-07. The table shows that in spite of buoy temperatures different between the two series (ambient vs. covered) by as much as 3.2°C , the deviations are similar in amplitude to the first series ($-0.4\ \text{mK}$ at 34°C). It shows also that these deviations are more dependent on the cooling or the warming of the water than of the air temperature, because the maximal deviation is obtained at 16°C and at this temperature, the difference in external buoy temperatures is only 0.7°C . **Figure 7** shows that:

- At 35°C the points are superimposed because it is the last point of the first series and the first point of the second series.
- From 27 to 12°C the deviations show the buoy temperatures are higher than the reference temperatures, probably because of the thermal inertia of the ensemble MoSens-Buoy, as the temperatures of the bath is gradually reduced.
- At 1 and 6°C , the deviation is inverted because the temperature has been generated in increasing order.

The two measurement series realized on the two buoys can be used to assess in details the reproducibility of temperature measurements. By using the deviation (amb.—cover.) (see **Table 3** for n° Y17-07), the relation (14) gives another estimation of the expanded measurement uncertainty of two buoys. **Table 4** shows the results. The main source of uncertainty comes from the reproducibility of measurements impacted by the thermal



FIGURE 6 | Buoys in the calibration bath, close to the reference thermometer. A $\text{pt}100\ \Omega$ thermometer is fixed on one of them and protected with a piece of foam.

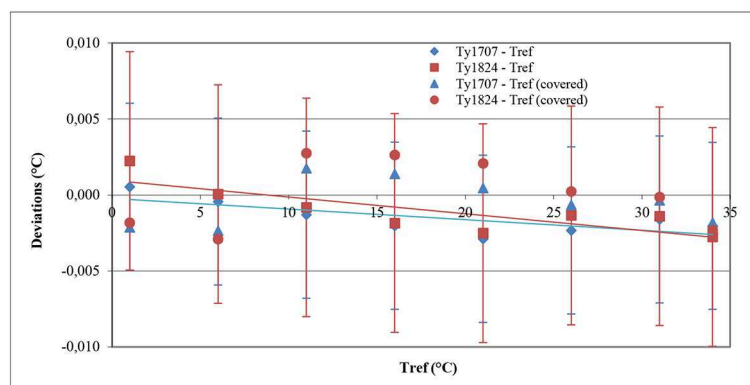


FIGURE 7 | Deviations obtained during the verification of HRSST sensors of two buoys during the two series, with the expanded uncertainty of the verification.

TABLE 3 | Differences between buoys and HRSST ambient and covered temperatures for the buoy n° Y17-07.

Tbuoy (°C) (ambient)	HRSST (°C) (ambient)	Tbuoy (°C) (covered)	HRSST (°C) (covered)	Deviation (amb. -cover.)
19.3	1.0018	14.7	0.9993	0,0025
18.7	6.0008	14.9	5.9988	0,0020
20.1	11.0002	18.1	11.0030	−0.0029
20.2	15.9990	19.5	16.0025	−0.0036
20.5	20.9979	21.2	21.0013	−0.0034
23.0	25.9966	23.1	26.0000	−0.0034
23.2	30.9969	26.9	30.9986	−0.0017
24.0	33.9961	27.2	33.9965	−0.0004

TABLE 4 | Uncertainty budget of buoys HRSST measurements.

Uncertainty budget of HRSST measurements	N° Y17-07 (mK)	N° Y18-24 (mK)
Reference temperature (U_{tref})	0.9	0.9
Bath stability (U_{Bath})	0.3	0.3
Buoy HRSST reproducibility (S)	2.5	3.4
Buoy HRSST repeatability (S_{rep})	0.5	0.5
Expanded uncertainty (U_C)	5.5	7.2

inertia of buoys. Expanded uncertainties are expressed with a coverage factor of 2 including 95.5% of measurements in the case of Gaussian distributions. They are inferior to 0.01°C.

During the two series of HRSST calibration, the temperatures of the SST analog sensors have also been recorded. They have been calibrated by the manufacturer in the range 5–35°C. **Figure 8** shows the results of the verification. The deviations are inferior to $\pm 0.1^\circ\text{C}$, even for the point at 2°C , which is outside the calibration range. If we exclude this point, it is possible to improve the trueness and the uncertainty of SST measurements by calculating the coefficients of a straight line. By considering this linear correction, it is possible to assess the measurement uncertainties of these two SST analog sensors by using the same procedure as for the HRSST sensors. However, it is necessary to take into account a residual linearity error. The results are given in **Table 5**. The expanded uncertainty of SST analog sensors is found to be twice as large as the expanded uncertainty of HRSST sensors. One must keep in mind in addition that the SST analog sensor is much slower to respond than the HRSST sensor, and that it is also more sensitive to radiation effects. All these effects contribute to additional larger systematic errors or measurement uncertainties.

UTILITY AND LABORATORY TEST OF THE HYDROSTATIC PRESSURE SENSOR

In order to try to reduce the uncertainty in the HRSST measurement depth, the MoSens have been equipped with a hydrostatic pressure sensor located near the HRSST sensor. The immersion depth d of the water pressure sensor is given by the

buoy geometry, $d = R \cos(\alpha)$ where R is the radius of the spherical buoy and α is the angle of placement of the sensor in the spherical buoy (measured from the vertical), but this distance from the waterline can vary with the seawater density ρ_w and the traction made by the drogue, but also with the variations of α during rough sea conditions.

During calm sea conditions, the air pressure sensor measuring p_a is at the level of the waterline. Therefore, d can be obtained from the measurement of the pressure p :

$$d = \frac{(p - p_a)}{\rho_w g} \quad (15)$$

where g is the acceleration of gravity at the buoy location (this value depends on latitude in first approximation, for a body that remains on the ocean surface). In this relation, ρ_w needs an assessment of the salinity to be determined with a sufficient accuracy.

When the buoy is in rough sea conditions, or oscillating (rotating) around its center of gravity, it is submitted also to a vertical acceleration a_g added to g . If a_g values are close to g the measurements of water pressure cannot be used directly to retrieve depth without *ad hoc* processing and filtering, but the time-series of pressure at high-frequency can provide an indication of the sea state. This information can be of use to determine whether the water is well-stratified or well-mixed, assuming that the air pressure is stationary (this hypothesis does not hold if the buoy is oscillating up and down in waves with heights of several meters). For comparison with satellite measurements, a well-mixed top layer may suggest that emission from the surface is at the measured water temperature, whereas a stratified top layer may suggest that the radiated temperature may need to be corrected (based on wind and radiation conditions).

Results shown by Poli et al. (2016) corroborate these assertions. When two temperatures measured by previous HRSST buoys are compared, the differences can be reduced to within the digital sensor trueness by considering only well-mixed conditions, selected when the waves in the ERA-Interim (Dee et al., 2011) reanalysis are above 3 m in significant wave height. Another application of trying to infer the sea-state is to better parameterize the emissivity to be used for simulating the radiances seen by the satellite, especially for microwave instruments, with rough seas or swell suggesting white caps and foam (Nicolòs et al., 2007).

During the temperature verifications of the two buoys, the MoSens pressure sensors data have been recorded to observe their drift with respect to temperature. A reference atmospheric pressure P_{atm} has been measured with a recently calibrated WIKA CPC 8000 pressure calibrator. It was therefore possible to calculate a reference pressure $P_{ref} = d + (P_{atm} - 1013.25)/100$, to observe the pressure drifts of sensors as a function of the temperature.

The immersion depth d was estimated to be 0.13 m in the bath (without the weight of the drogue, which remained outside the calibration bath). The results show that the external temperature of the buoy has no significant effect on the measured pressures, but that the temperature of the water leads to maximum

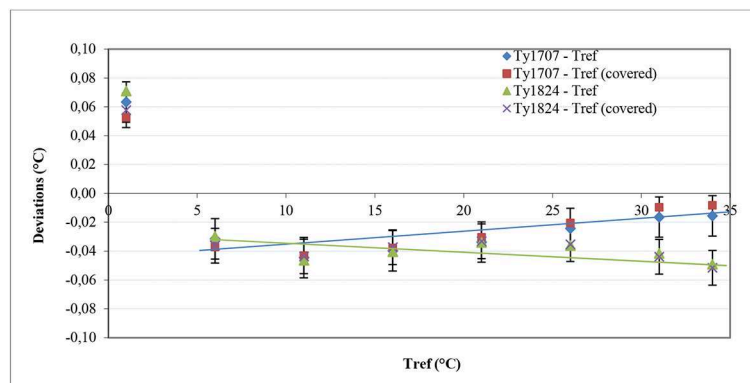


FIGURE 8 | Deviations obtained during the verification of SST sensors of two buoys during the two series, with the expanded uncertainty of the verification.

TABLE 5 | Uncertainty budget of buoys SST measurements in the range 6–35°C.

Uncertainty budget of SST measurements (analog sensor)	N° Y17-07 (mK)	N° Y18-24 (mK)
Reference temperature (u_{Tref})	0.9	0.9
Bath stability (u_{Bath})	0.3	0.3
Buoy SST reproducibility (S)	4.6	3.4
Buoy SST repeatability (S_{rep})	1.9	2.1
Buoy SST linearity error (u_l)	4.7	4.1
Expanded uncertainty (U_C)	14	12

systematic errors of ± 0.15 dbar between 0 and 35°C. They also show that this effect is linear and that this technology of sensor reacts with a good reproducibility to temperature variations. This behavior can hence be corrected for each buoy: a straight line correction curve yields residual errors inferior to ± 0.004 dbar (or 4 mm of water). Since the slopes and offsets for the two sensors are very similar, it is possible to consider correcting the two instruments with average coefficients. The residual errors obtained with the average coefficients slope = -0.0077 dbar/°C and offset = 1.499 dbar are inferior to ± 0.02 dbar, which is close to the accuracy claimed by the manufacturer, and in relation with the technology of the sensors. The same coefficients may be applied to future buoys.

TRIALS AT SEA AND COMPARISON WITH A CTD PROFILER

While the initial concept of buoy development using a pre-calibrated sensor was demonstrated to work in the laboratory, two further elements are needed to build a FRM drifter network. The first element is to demonstrate that the trueness estimate still holds, once the buoys are deployed in the target environment (at sea). The second element is to demonstrate that the trueness estimate remains valid for the lifetime of the buoy (i.e., no significant temporal drift). While it is too early to study the second element, this section explores the first one.

The two prototype buoys were deployed at sea during an oceanographic cruise in Mediterranean Sea. After unpacking on the ship deck to test the transmission and the good transmission of the Iridium SBD messages, a comparison with a CTD profiler (SBE 911⁺) was set up. The CTD profiler was fixed under a Multi-Bottle Sampling Array (MBSA), with a reference thermometer SBE 35 calibrated in the fixed point cells of the ITS-90. The drifters were held in place near the ship by means of a line. When the MBSA was completely immersed, the CTD and the SBE 35 temperature measurements were recorded at about 1 m under the surface. After the surface measurements were collected, the MBSA was lowered to 15 m depth in order to estimate the temperature profile of the first layers. This profile showed that in the four first meters, the temperature of the water was homogeneous and close to 16.4°C, allowing fair comparison with the HRSST buoy. Between 4 and 5.5 m (the depth where Argo floats surface temperature measurements are sometimes used as reference) there was a strong temperature gradient of $-1.25^\circ\text{C m}^{-1}$. Until 15 m depth, the temperature was still very stable but shifted by about 2°C as compared to the surface.

During the subsurface waiting time, 5 measurement series of 29, 57, 113, 53, and 149 values were made with the SBE 35 sampling at 1 Hz, giving an average temperature of 16.3968°C with a standard deviation of 0.0057°C. The CTD temperature at 1.08 m depth is very close to this value: 16.398°C. **Table 6** gives the results of the comparison with the values transmitted by the buoys. The first two lines show the results for the SST analog sensors and the following for the HRSST sensors. In the second column of this array, SST temperatures from the analog sensors have been corrected with the slopes and offsets coefficients of the straight lines of **Figure 8**, in order to fairly compare with what may be expected, at best, from low-cost SST sensors with ideal calibration.

The results of this comparison show that without any correction, HRSST values are in the standard dispersion range of the SBE 35 and the deviations compared to CTD and SBE 35 are inferior to 0.01°C. Without corrections, SST deviations from analog sensors are close to -0.05°C and with the corrections

TABLE 6 | Results of the comparison made at sea, between buoys transmitted values, CTD and SBE 35 measurements.

	Value transmitted	Sst corrected	Ttrans- Tctd	Ttrans- Tsbe35	SSTcor- Tsbe35
SST58002	16.35	16.382	−0.048	−0.047	−0.014
SST 58019	16.35	16.389	−0.048	−0.047	−0.008
HRSST 58002	16.391		−0.007	−0.006	
HRSST 58019	16.398		0.000	0.001	

The first (last) two lines show the results for the SST analog (HRSST sensors, respectively).

calculated in the metrology laboratory, they are within the calculated expanded uncertainties of buoys SST sensors, and also within the estimated standard deviations from the percentiles transmitted by the buoys.

This comparison at sea shows firstly that the temperature values transmitted by the buoys are not erroneous. Secondly, regarding the HRSST sensors, the deviations obtained in comparison to two independent instruments, are small and probably representative of the dispersion of the medium temperatures. They are inferior to the deviations obtained with the SST analog sensors, even after linear correction of SST transmitted values, probably because of their better response time, resolution and calibration uncertainties.

After this comparison, buoys were released in an eddy feature. The details of this deployment are given by Poli et al. (2018). After initial deployment on 26th April 2018, the buoys were initially separated by <1 km and they remained within 10 km of each other until 23rd May. After that, they quickly diverged until the first one ran ashore. At the time of initial writing of this paper, the second buoy was still drifting with its drogue, five and a half month after its deployment.

According to Poli et al. (2018), this comparison showed that “once freely drifting, the buoys observe that the SST spread within 5 min is usually smaller than 0.1 K, especially when the sea-state is well-mixed and the buoys are within an eddy core. The availability of percentiles from the 5-min distribution of SST sampled at 1 Hz (by a sensor with a fast response time) should help users improve their data processing chain to move toward an ensemble approach.” The results of this other paper suggest also that “it is important to consider the sea-state mixing and the ocean surface circulation to understand the representativeness of the *in-situ* SST data, as they both affect observed SST variations (within the day and within 5 min). Consequently, they may both be worth taking into account in the process of satellite SST cal/val.”

CONCLUSION

The goal of this study relates to the conception and the metrological characterization of new surface drifting buoys, design to comply with the requirements of SST satellites measurements validation and to link through comparison these measurements to the SI. This linkage can be achieved by the

calibration of each buoy and the assessment of the instrumental measurement uncertainty, taking into account all the elements of the temperature calibration chain.

Calibrating individually 100 drifting buoys in a calibration bath is time-consuming and unrealistic. This study shows that it is possible to calibrate the sensors and their conditioning electronic circuits beforehand, without adding significant errors or uncertainties to *in situ* measurements even once the sensors have been integrated in buoys, and to keep the instrumental uncertainty under the tolerance of 0.01°C. This was possible through the design of the MoSens modules which include high resolution temperature sensors and hydrostatic pressure sensors. The concept of high resolution includes the possibility to make temperature measurements with a repeatability close to a milli-degree, a fast thermal response time measured in laboratory and a fast sample rate (1 Hz).

The measurements made on the two buoys have also enabled the improvement of the calibration of the SST analog sensors. If, initially, their measurement errors are already included in the $\pm 0.1^\circ\text{C}$ tolerance, it is possible, by using slope and offset correction coefficients, to obtain instrumental expanded measurements uncertainties inferior to 15 mK. With these corrections, *in situ* comparisons have shown that it is possible to reduce the deviation of 0.047 to -0.014°C for one sensor and -0.008°C for the other. However, this correction procedure requires each buoy to be placed in the calibration bath. This is not feasible for an industrial process to ensure repeated accuracy. Also, one must bear in mind that the large size of the SST analog sensors makes them much slower to respond to seawater variations than smaller HRSST sensors, as shown in this paper.

The temperature-dependence of the MoSens pressure sensor has also been studied. It can lead to errors of ± 0.15 dbar in the temperature range 0–35°C. These errors can be compensated with average slope and offset coefficients to improve the determination of HRSST measurements depth during calm sea conditions. In rough sea conditions, this sensor provides an indication of the sea-state, which is essential to understand the deviations between satellites and buoys temperature measurements. The relationship between information contained in the high-frequency data and the sea state should be explored in future work.

The specifications of two prototypes measured in laboratory, have been confirmed during the initial deployment at sea by a comparison to a reference thermometer SBE 35 and a CTD profiler, demonstrating also the good transmission of data and the very good trueness of HRSST measurements in a homogeneous medium.

Future prospects include deploying at least 100 SVP-BRST units, with the aim of closing the metrological loop with buoys that would be recovered from sea, to be verified in a calibration bath. An experiment will also be carried out with a SVP-BRST buoy kept over a long duration at a fixed position at sea, next to a reference moored buoy. This will allow to determine whether

or not the SVP-BRST buoys remain within the initial tolerance of 0.01°C.

AUTHOR CONTRIBUTIONS

MLE: responsible for the metrology part. PP: concept of measurements, deployment of buoys, and data processing. AD and JS: buoy developer. MLu: responsible of the project and data processing. AO'C: initiator of the project and the

requirements. MB: metadata transmission and processing. KH: trials at sea.

FUNDING

This work was a part of the TRUSTED project led by Collecte Localisation Satellite (CLS) following a call to tender by EUMETSAT. TRUSTED is a Copernicus project, funded by the European Commission.

REFERENCES

- Banks, A. C., Mittaz, J., Bialek, A., Woolliams, E., Nightingale, J., Fox, N., et al. (2017). "Metrology in satellite oceanography," in *Conference: Second National Physical Laboratory (UK) – National Institute of Metrology (China) Joint Symposium* (Teddington: NPL).
- BIPM (2008). *Evaluation of Measurement Data – Guide to the Expression of Uncertainty in Measurement*. JCGM 100:2008.
- BIPM (2012). *International Vocabulary of Metrology – Basic and General concepts and Associated Terms (VIM)*, 3rd Edn. JCGM 200.
- Blouch, P., Billon, C., Poli, P. (2018). *Recommended Iridium SBD Dataformats for Buoys (Version 1.7)*. Zenodo.
- Castro, S. L., Gary A. W., William J. E. (2012). Evaluation of the relative performance of sea surface temperature measurements from different types of drifting and moored buoys using satellite-derived reference products. *JGR Oceans* 117:C2. doi: 10.1029/2011JC007472
- de Podesta, M., Bell, S., and Underwood, R. (2018). Air temperature sensors: dependence of radiative errors on sensor diameter in precision metrology and meteorology. *Metrologia* 55, 229–244. doi: 10.1088/1681-7575/aaa52
- Dee, D. P., Uppala, S. M., Simmons, A. J., Berrisford, P., Poli, P., Kobayashi, S., et al. (2011). The ERA-Interim reanalysis: configuration and performance of the data assimilation system. *Q. J. R. Meteorol. Soc.* 137, 553–597. doi: 10.1002/qj.828
- Donlon, C., Berruti, B., Buongiorno, A., Ferreira, M.-H., Femenias, P., Frerick, J., et al. Sciarrà, R. (2012). The Global Monitoring for Environment and Security (GMES) Sentinel-3 mission. *Remote Sens. Env.* 120, 37–57. doi: 10.1016/j.rse.2011.07.024
- Donlon, C. J., Nykjaer, L., and Gentemann, C. (2004). Using sea surface temperature measurements from microwave and infrared satellite measurements. *Int. J. Remote Sens.* 25, 1331–1336. doi: 10.1080/01431160310001592256
- EGOS (2002). *Minimum Specifications and Guidelines for the Operation of EGOS Drifting Buoys*. Technical Document.
- Gaillard, F., Diverres, D., Jacquin, S., Gouriou, Y., Grelet, J., Le Menn, M., et al. (2015). Sea Surface Temperature and Salinity from French research Vessels, 2001–2013. *Nat. Sci. Data* 2:150054. doi: 10.1038/sdata.2015.54
- Hausfather, Z., Cowtan, K., Clarke, D. C., Jacobs, P., Richardson, M., Rohde, R. (2017). Assessing recent warming using instrumentally homogeneous sea surface temperature records. *Sci. Adv.* 3:e1601207. doi: 10.1126/sciadv.1601207
- Immler, J. F., Dykema, J., Gardiner, T., Whiteman, D. N., Thorne, P. W., and Vomel, H. (2010). Reference quality upper-air measurements: guidance for developing GRUAN data products. *Atmos. Meas. Tech.* 3, 1217–1231. doi: 10.5194/amt-3-1217-2010
- ISO 5725-2 (1994). *Accuracy (Trueness and Precision) of Measurement Methods and Results - Part 2: Basic Method for the Determination of Repeatability and Reproducibility of a Standard Measurement Method*. Available online at: <https://www.iso.org/>
- Kennedy, J. J. (2014). A review of uncertainty in *in situ* measurements and data sets of sea surface temperature. *Rev. Geophys.* 52, 1–32. doi: 10.1002/2013RG000434
- Kennedy, J. J., Rayner, N. A., Smith, R. O., Saunby, M., and Parker, D. E. (2011a). Reassessing biases and other uncertainties in sea-surface temperature observations since 1850 Part 1: measurement and sampling errors. *J. Geophys. Res.* 116:D14103. doi: 10.1029/2010JD015218
- Kennedy, J. J., Smith, R., and Rayner, N. (2011b). Using AATSR data to assess the quality of *in situ* sea surface temperature observations for climate studies. *Remote Sens. Environ.* 116, 79–92. doi: 10.1016/j.rse.2010.11.021
- Kent, E., and Berry, D. (2008). *Assessment of the Marine Observing System (ASMOS): Final Report*. Technical Report. National Oceanography Centre, Southampton.
- Le Traon, P. Y. (2018). "Satellites and operational oceanography," in *New Frontiers in Operational Oceanography*, eds E. Chassinet, A. Pascual, J. Tintoré, and J. Verron (GODAE Ocean View), 161–190. doi: 10.17125/gov2018.ch07
- Lewellyn-Jones, D., Edwards, M. C., Mutlow, C. T., Birks, A. R., Barton, I. J., and Tait, H. (2001). AATSR: global-change and surface-temperature measurements from ENVISAT. *ESA Bull.* 105, 10–21.
- Lumpkin, R., Pazos, M. (2006). "Chapter 2: Measuring surface currents with Surface Velocity Program drifters: the instrument, its data, and some recent results," in *Lagrangian Analysis and Prediction of Coastal and Ocean Dynamics (LAPCOD)*, eds A. Griffa, A. D. Kirwan, A. J. Mariano, T. Ozgokmen, and T. Rossby (Cambridge: Cambridge University Press), 39–67. doi: 10.1017/CBO9780511535901.003
- Merchant, C. J., Embury, O., Rayner, N. A., David I. B., Corlett, G. K., Lean, K., et al. (2012). A 20 year independent record of sea surface temperature for climate from Along-Track Scanning Radiometers. *J. Geophys. Res.* 117:C12013. doi: 10.1029/2012JC008400
- Merchant, C. J., Holl, G., Mittaz, J., and Woolliams, E., R. (2019). Radiance uncertainty characterisation to facilitate climate data record creation. *Remote Sens.* 11:474. doi: 10.3390/rs11050474
- Milman, A. S., and Wilheit, T. T. (1985). Sea surface temperatures from the scanning multichannel microwave radiometer on Nimbus 7. *J. Geophys. Res.* 90, 11631–11641. doi: 10.1029/JC090iC06p11631
- Niclòs, R., Caselles, V., Valor, E., and Coll, C. (2007). Foam effect on the sea surface emissivity in the 8–14 mm region. *J. Geophys. Res.* 112:C12020. doi: 10.1029/2007JC004521
- O'Carroll, A., Eyre, J. E., Saunders, R. W. (2008). Three-way error analysis between AATSR, AMSR-E, and *in situ* sea surface temperature observations. *J. Atmos. Ocean. Technol.* 25, 1197–1207. doi: 10.1175/2007JTECHO542.1
- Oka, E. (2005). Long-term sensor drift found in recovered argo profiling floats. *J. Ocean.* 61, 775–781. doi: 10.1007/s10872-005-0083-6
- Poli, P., Emzivat, G., Blouch, P., Férézou, R., and Cariou, A. (2016). "Météo-France/E-SURFMAR HRSST (re)calibration," in *GHRST Workshop on Traceability of Drifter SST Measurements* (La Jolla, CA: Scripps Institution for Oceanography).
- Poli, P., Lucas, M., O'Carroll, A., Le Menn, M., David, A., Corlett, G. K., et al. (2018). The Copernicus Surface Velocity Platform drifter with Barometer and Reference Sensor for Temperature (SVP-BRST): genesis, design, and initial results. *Ocean Sci.* 15, 199–214. doi: 10.5194/os-2018-109
- Prabhakara, C., Dalu, G., and Kunde, V. G. (1974). Estimation of sea surface temperature from remote sensing in the 11- to 13-μm window region. *J. Geophys. Res.* 79, 5039–5044. doi: 10.1029/JC079i033p05039
- Roemmich, D., Gilson, J. (2009). The 2004–2008 mean and annual cycle of temperature, salinity and steric height in the global ocean from the Argo program. *Prog. Oceanogr.* 82, 81–100. doi: 10.1016/j.pocean.2009.03.004
- Schlichting, H. (1979). *Boundary-Layer Theory*. New York, NY: McGraw-Hill, 817.

- Sybrandy, A. L., Niiler, P. P., Martin, C., Scuba, W., Charpentier, E., Meldrum, D. T. (2009). *Global Drifter Programme Barometer Drifter Design Reference*. DBCP Technical Report, Published by the Data Buoy Cooperation Panel (DBCP), Geneva, Switzerland.
- Titchner, H. A., Rayner, N. A. (2014). The Met Office Hadley centre sea ice and sea surface temperature data set, version 2: 1. sea ice concentrations. *J. Geophys. Res. Atmos.* 119, 2864–2889. doi: 10.1002/2013JD020316
- Woolliams, E. R., Mittaz, J., Merchant, C. J., Dilo, A., Fox, N. P. (2016). “Uncertainty and correlation in level 1 and level 2 products: a metrologist’s view,” in *Living Planet Symposium, Proceedings of the Conference*, ed L. Ouwehand (Prague), 80.
- Woolliams, E. R., Mittaz, J., Merchant, C. J., Hunt, S. E., and Harris, P. M. (2018). Applying metrological techniques to satellite fundamental climate data records. *J. Phys. Conf.* 972:012003. doi: 10.1088/1742-6596/972/1/012003
- World Climate Research Programme (1988). *Global Surface Velocity Programme (SVP): Workshop Report of WOCE/SVP Planning Committee and TOGA Pan-Pacific Surface Current Study*. Miami, FL: World Climate Research Programme.
- World Meteorological Organization (2016). “The global observing system for climate: implementation needs,” in *Global Climate Observing System (GCOS)*, eds A. Belward and M. Dowell, 341.
- Conflict of Interest Statement:** AD and JS were employed by company nke Instrumentation.
- The remaining authors declare that the research was conducted in the absence of any commercial or financial relationships that could be construed as a potential conflict of interest.
- Copyright © 2019 Le Menn, Poli, David, Sagot, Lucas, O’Carroll, Belbeoch and Herklotz. This is an open-access article distributed under the terms of the Creative Commons Attribution License (CC BY). The use, distribution or reproduction in other forums is permitted, provided the original author(s) and the copyright owner(s) are credited and that the original publication in this journal is cited, in accordance with accepted academic practice. No use, distribution or reproduction is permitted which does not comply with these terms.



Wave Measurements From Radar Tide Gauges

Laura A. Fiorentino^{1*}, Robert Heitsenrether¹ and Warren Krug^{1,2}

¹ Ocean Systems Test and Evaluation Program, Center for Operational Oceanographic Products and Services, National Oceanographic and Atmospheric Administration, Chesapeake, VA, United States, ² Lynker Technologies, Leesburg, VA, United States

OPEN ACCESS

Edited by:

Leonard Pace,
Schmidt Ocean Institute,
United States

Reviewed by:

Joseph Park,
United States Department of the
Interior, United States
Philip Thompson,
University of Hawaii, United States

*Correspondence:

Laura A. Fiorentino
laura.fiorentino@noaa.gov

Specialty section:

This article was submitted to
Ocean Observation,
a section of the journal
Frontiers in Marine Science

Received: 15 November 2018

Accepted: 05 September 2019

Published: 01 October 2019

Citation:

Fiorentino LA, Heitsenrether R and
Krug W (2019) Wave Measurements
From Radar Tide Gauges.
Front. Mar. Sci. 6:586.
doi: 10.3389/fmars.2019.00586

Currently the NOAA Center for Operational Oceanographic Products and Services (CO-OPS) is transitioning the primary water level sensor at most NWLON stations, from an acoustic ranging system, to microwave radars. With no stilling well and higher resolution of the open sea surface, microwave radars have the potential to provide real-time wave measurements at NWLON sites. Radar sensors at tide stations may offer a low cost, convenient way to increase nearshore wave observational coverage throughout the U.S. to support navigational safety and ocean research applications. Here we present the results of a field study, comparing wave height measurements from four radar water level sensors, with two different signal types (pulse and continuous wave swept frequency modulation-CWFM). A nearby bottom acoustic wave and current sensor is used as a reference. An overview of field setup and sensors will be presented, along with an analysis of performance capabilities of each radar sensor. The study includes results from two successive field tests. In the first, we examine the performance from a pulse microwave radar (WaterLOG H-3611) and two CWFM (Miros SM-94 and Miros SM-140). While both types of radars tracked significant wave height well over the test period, the pulse radar had less success resolving high frequency wind wave energy and showed a high level of noise toward the low frequency end of the spectrum. The pulse WaterLOG radar limitations were most apparent during times of high winds and locally developing seas. The CWFM radars demonstrated greater capability to resolve those higher frequency energies, while avoiding low frequency noise. The initial field test results motivated a second field test, focused on the comparison of wave height measurements from two pulse radar water level sensors, the WaterLOG H3611 and the Endress and Hauser Micropilot FMR240. Significant wave height measurements from both radar water level sensors compared well to reference AWAC measurements over the test period, but once again the WaterLOG radar did not adequately resolve wind wave energy in high frequency bands and showed a high level of noise toward the low frequency end of the spectrum. The E+H radar demonstrated greater capability to resolve those higher frequency energies while avoiding the low frequency aliasing issue observed in the WaterLOG.

Keywords: microwave radar, waves, water level, pulse radar, significant wave height

1. INTRODUCTION

The National Oceanic and Atmospheric Administration (NOAA) National Ocean Service (NOS) Center for Operational Oceanographic Products and Services (CO-OPS) maintains and develops the National Water Level Observation Network (NWLON), which consists of over 200 long-term stations that provide real-time water level observations across coasts in the U.S.. The primary water level measurement system at most stations is an acoustic ranging water level sensor. In 2012 CO-OPS began to transition NWLON station sensors from acoustic to microwave radar water level sensors, which provide many benefits, including lower costs, less maintenance and support, and improved measurements (Park et al., 2014).

Adding real-time wave measurements to the CO-OPS observatory network has been discussed for several years in accordance with the NOAA IOOS National Operational Wave Observation Plan (NOAA and USACE, 2009), as there is a critical need to increase spatial coverage of nearshore wave observations across the U.S. Currently, NOAA CO-OPS does not maintain any of its own operational wave measurement systems. Wave information disseminated via NOAA Physical Oceanographic Real-Time Systems (PORTS) comes from the Scripps Institute of Oceanography (SIO) Coastal Data Information Program (CDIP) Datawell buoys, located nearby PORTS systems. Consistent wave height measurements at multiple NWLON stations along the coast of the U.S. would be useful to port and shipping managers, ocean modelers, and others in the transportation, city management, and scientific communities. Additionally, employing the same single sensor to simultaneously measure both surface gravity waves and longer average water levels, offers an efficient system design and significant savings in costs.

The acoustic sensors used at NWLON stations in the past were not well-suited for direct wave measurements due to resonance and dampening from the protective well (Park et al., 2014). Furthermore, a pressure drop created from currents across the well opening can decrease the water level (Park et al., 2014). The use of radar water level sensors presents the potential opportunity to measure waves directly, as they are non-contact sensors that require no well infrastructure and measure the open sea surface directly (Pérez et al., 2014). All radar sensors reviewed in this study are specified to have beams with a 10° spreading angle, resulting in a measurement footprint at the sea surface ranging from 1.1 to 1.5 m, based on the conditions at the study site (MIROS, NDA,N; Xylem-YSI, ND). Additionally, all sensors are specified to be capable of 1 Hz sampling. Based on these, radar sensors should have the spatial and temporal resolution necessary to simultaneously measure waves and the average sea level.

While previous studies have utilized high frequency water level observations from NWLON stations to derive statistics to serve as a proxy for wave conditions (Sweet, 2016), few studies have presented wave height measured directly from radar water level sensors. Although vendors of commercial off the shelf available radar water level sensors advertise and offer this capability, and scientists in the international sea level monitoring community have been using radars to simultaneously measure waves and water levels, there is little available information

provided in the literature on research into their accuracy and performance. Ewans et al. (2014) show that a SAAB WaveRadar, CWFM radar compares well to radar signal modeling. They also present results from a field experiment in which they compare the radar to a Datawell wave buoy 3 km away. Only significant wave height comparisons are presented, and the authors acknowledge the need for more detailed studies. Pérez Gómez (2014) presents details of Spain's updated sea level monitoring and forecast system REDMAR, whose stations are equipped with Miros CWFM microwave radars. They provide simultaneous sea level results and wave parameters. This work does not provide information on any performance evaluations on the wave measuring capabilities of the radar. Furthermore, both of these references use CWFM microwave radars to measure wave parameters and there are no known sources that provide information on the use of pulse radars for wave measurements.

From 2008 to 2012, CO-OPS conducted a series of extensive laboratory and field tests to assess the long-term water level monitoring capability of several different make/model radar sensors, to evaluate the suitability for use throughout the NWLON. Results identified a pulse type radar as best suited for CO-OPS water level monitoring applications (Heitsenrether and Davis, 2011). Since 2012, all radar sensors installed at NWLON sites have been of the pulse type. CO-OPS' test results for monitoring long term water levels (at 6 min sampling and averaging rate) found no significant difference in measurement accuracy between pulse and CWFM radar, however pulse radar is typically significantly less expensive and has a much lower power draw than the CWFM.

We present the results of two field studies comparing wave height measurements from four radar water level sensors. The first study consisted of three radar water level sensors (one pulse and two continuous wave swept frequency modulation-CWFM). A nearby bottom acoustic wave and current meter was used as a reference. An overview of field setup and sensors will be presented, along with an analysis of the performance capabilities of each sensor. All three radars tracked significant wave height well over the test period, though initial results indicate that the WaterLOG pulse radar is less successful in resolving high frequency wind wave energy. The CWFM radars demonstrate greater capability in resolving those higher frequency energies as well as eliminating low frequency aliasing.

Results from the first initial test suggest that some component of the WaterLOG's internal processing reduces the sensor's potential measurement resolution. This particular sensor is equipped with an SDI-12 interface and an associated layer of additional, proprietary software. Although this SDI-12 interface offers many benefits for real-time water level measurement system applications, the additional layer of software and processing results in uncertainty in lower level data cycles and affects temporal resolution. The purpose of the second field test is to better understand the effects of the WaterLOG's SDI-12 interface and to explore potential improvements to pulse radar wave measurements when the SDI-12 is not present. In this test, we field tested the same type of instrument without the added layer of processing, the Endress+Hauser Micropilot M FMR240. The FMR240 outputs currents from 4 to 20 mA with a linear

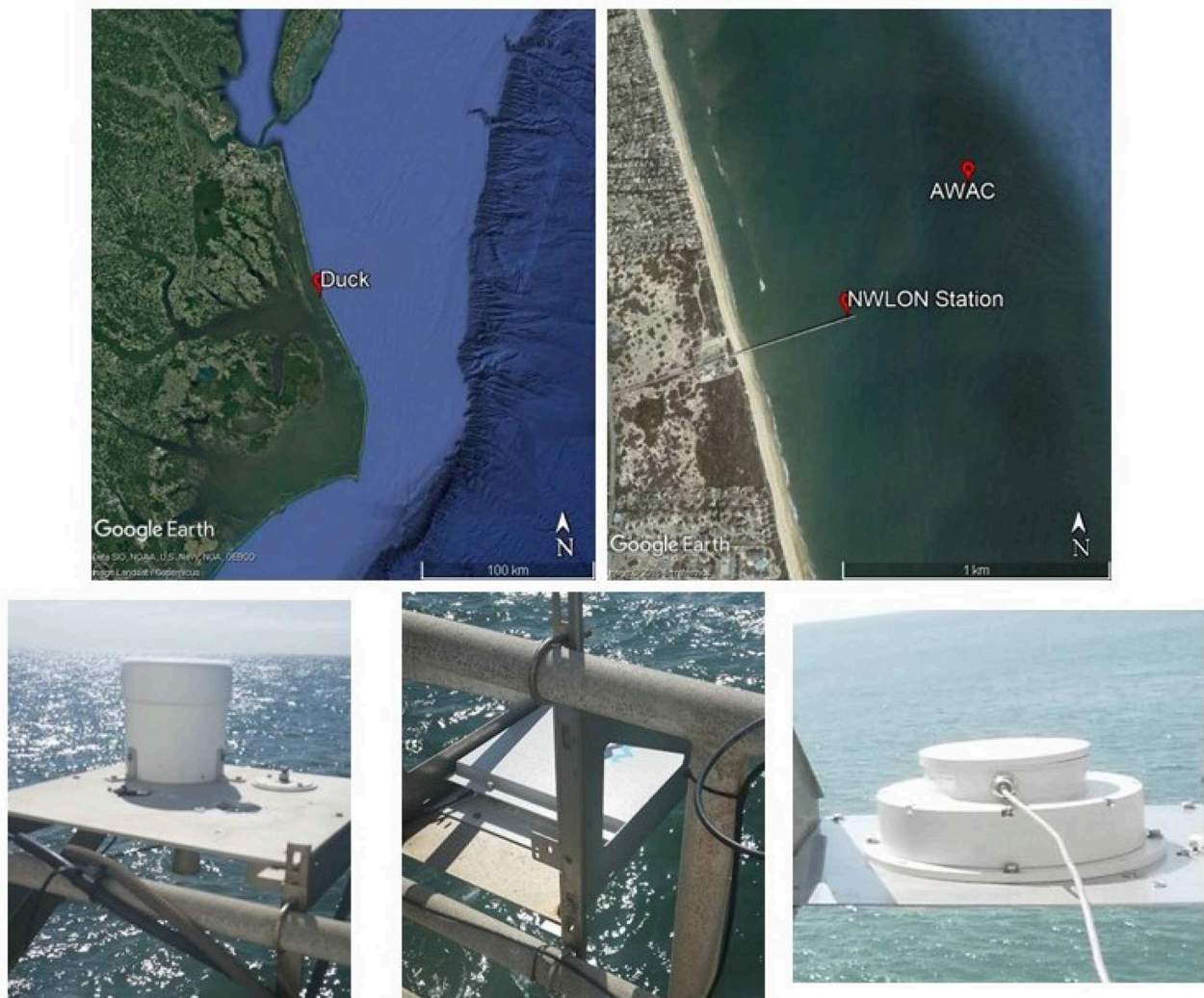


FIGURE 1 | (Top) Map of the location of both field tests, Duck, NC.; **(Bottom left)** WaterLOG radar; **(Bottom middle)** Miros SM-094; **(Bottom right)** Miros SM-140.

relationship to measured ranges. A simple, linear function is used to convert current output to range in meters in an external data logger.

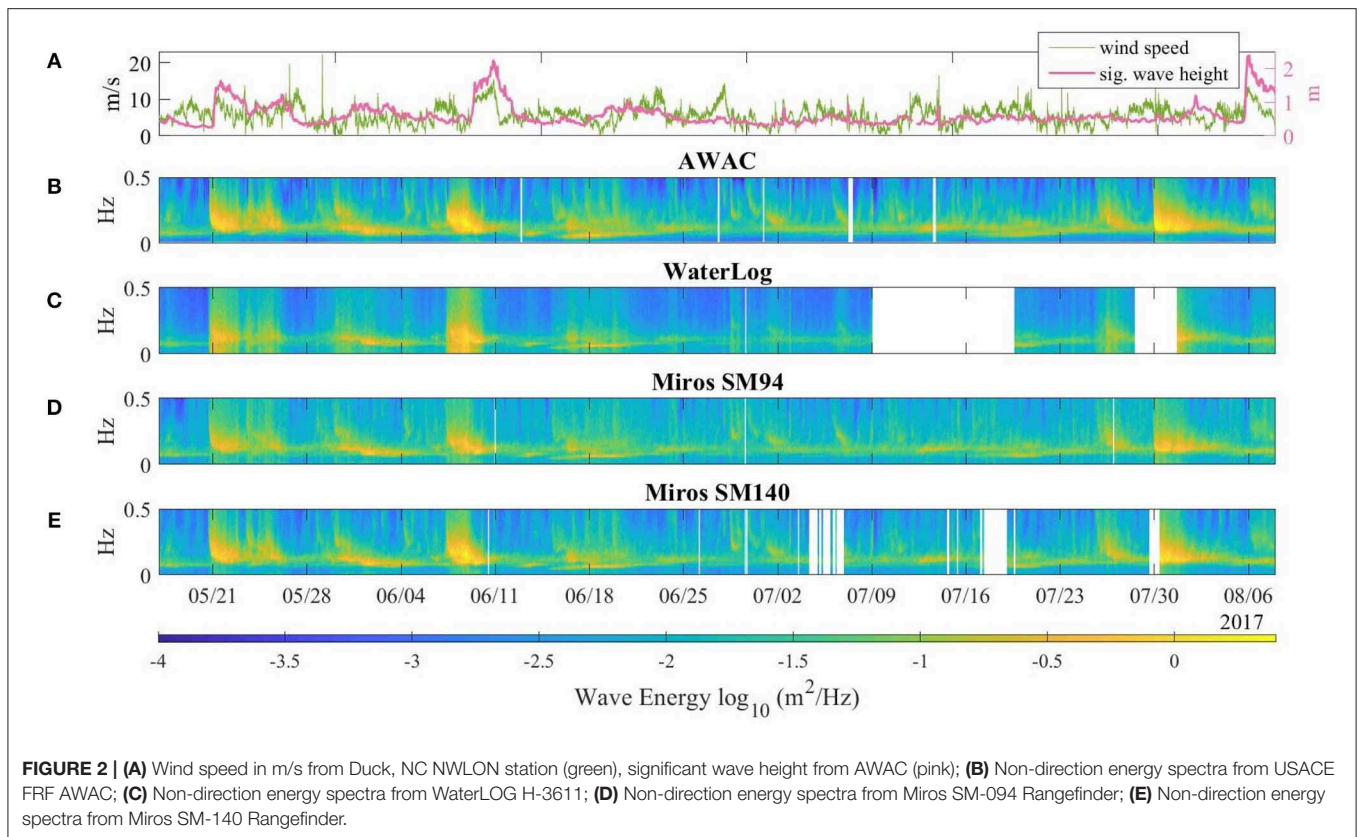
We present the results of our second ongoing study on the use of microwave radar water level sensors for wave measurements, with a focus on the comparison of wave height measurements from two pulse radar water level sensors, the WaterLOG H3611 and the Endress+Hauser Micropilot M FMR240. The nearby bottom acoustic wave and current sensor is again used as a reference. An overview of the second field setup and sensors will be presented, along with an analysis of performance capabilities of each radar sensor.

2. METHODS

2.1. Field Site and Setup

For both of the reported field tests, the test radar sensors were installed alongside an existing NWLON station on the US Army

Corps of Engineers (USACE) Field Research Facility pier in Duck, NC (**Figure 1**). Duck, NC is representative of the type of open ocean NWLON site where the addition nearshore wave observations would be valued by a variety of end users. The site experiences a broad range of wave conditions, relative to east U.S. coastal sites, and the research facility maintains a continuous source of reference wave measurements. For both field tests, radar sensors were installed toward the very end of the pier, approximately 0.5 km offshore, on the south facing side. Sensors were mounted side by side, and securely attached to the pier railing at a location between pylings and with a clear view of the sea surface below. They were located approximately 8.5 m above the water surface, resulting in an approximate beam width of 1.5 m at the water surface. The average water depth at that location of the pier was 6–7 m. Radar range to sea surface measurements were collected at a sampling rate of 1 Hz and recorded using a Sutron Xpert data logger. Based on the 1 Hz sample rate and the radars' 1.5 m beam width at the sea surface (based on the 10°



beam spreading angle), each sensor should have the temporal and spatial resolution to resolve surface gravity waves in the area. For example, using the shallow water dispersion relation, a surface gravity wave with a wavelength twice the radar's beam width, 3 m, will have a period of 1.39 s. As the majority of waves in the area of interest have a period of 2 s, the sensors specifications are sufficient to measure them.

The USACE operates an array of bottom mounted Nortek acoustic wave and current profilers (AWAC) along a series of different isobaths through the surf zone at the facility, and one was used as a reference. Unfortunately, AWACs at the 5 and 6 m isobaths were not operational throughout the radar sensor test period presented here. The closest available reference AWAC is located approximately 0.8 km from the radar sensors on the pier, is at an average depth of 11.41 m, and operates with an acoustic center frequency of 1 MHz. Given the depth differences between the locations of the selected reference AWAC and the test radar water level sensors, we acknowledge that some difference in wave observations between the two may be a result of changing conditions associated with shoaling of the waves over the cross-shore depth gradient. Regardless, we feel that for hourly spectra and bulk parameters, conditions at the 11.4 m isobath in general will be reasonably close to conditions near the end of the pier where the test radar sensors reside, and that in comparison to this, AWAC will provide a useful, first indication of radar sensor wave measurement performance. A comparison of significant wave height and average spectra over a sample time period, for

which both the 5 and 11 m AWACs were operational, resulted in an average significant wave height difference of 2 cm and supports this assumption. Our hope is that results from this study will motivate continuing work that will support a more ideal test setup, with reference wave sensors better collocated with test radar sensors. The NWLON station at Duck is also equipped with a meteorological station that includes a pair of RM Young propeller anemometers that measure winds at a 6 min period.

2.2. Instrumentation—Field Test I

Three sensors were evaluated during this study, the WaterLOG H-3611 pulse radar and the Miros SM-094 and SM-140 Rangefinder CWFM radars. The WaterLOG H-3611 employs a 26 GHz pulse signal to measure range to surface from the time of flight between a transmitted and received signal. It has a beam spreading angle of 10°, a pulse period of 280 ns, and a pulse width of 0.8 ns. This is the particular model radar sensor that is currently being installed at NWLON stations. The Miros SM-094 Rangefinder and its latest model replacement, the SM-140, are continuous wave frequency modulated (CWFM) microwave radars that use a triangular frequency modulation to measure the range to surface. A beat frequency is generated by mixing the transmitted and echo signals and used to compute the distance from the sensor to the target. Both the SM-094 and SM-140 have a frequency of 9.4–9.8 GHz and a beam-spreading angle of 10°. Miros Rangefinders are currently used on NOAA PORTS Air-Gap bridge clearance systems, in part for their long-range

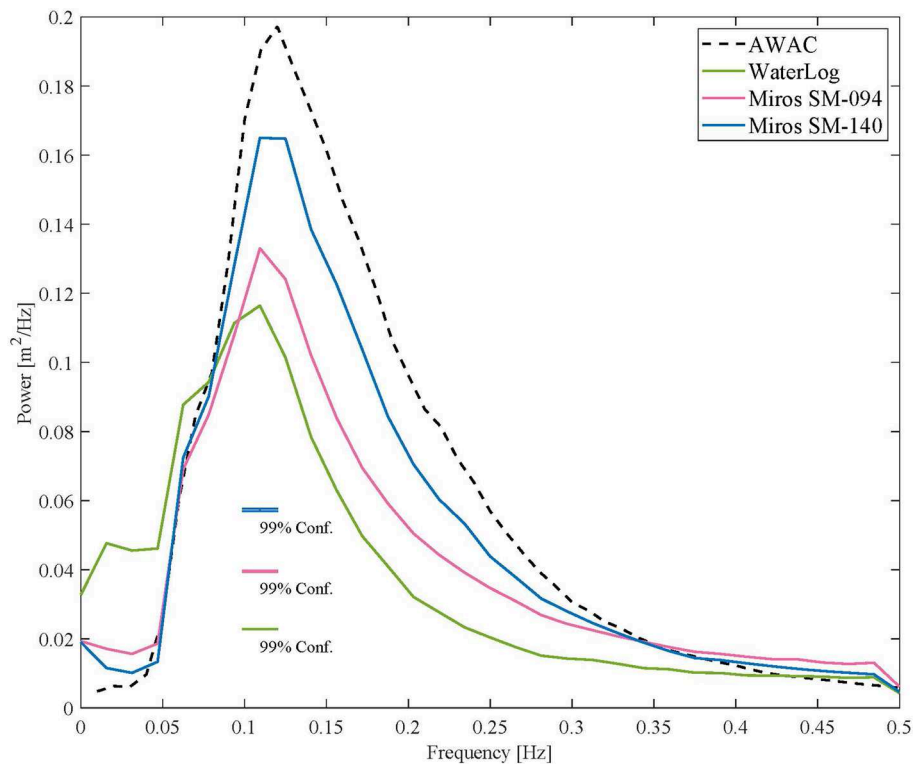


FIGURE 3 | Average power spectral density for each sensor: AWAC (black), WaterLOG (green), Miros SM-094 (pink), Miros SM-140 (blue) [17 May 2017–9 August 2017].

measurement capability (Bushnell et al., 2005). Although the focus of this study is to evaluate the wave measurement capability of the pulse type radars that are being implemented throughout NWLON, spare Miros Rangefinder units were readily available and easily integrated into the field test platform. Inclusion provides additional reference observations and a chance to compare results to those from previous CWFM studies.

2.3. Instrumentation—Field Test II

For the second field test, the WaterLOG H-3611 remained installed and the Endress+Hauser MicropilotM FMR240 (E+H) was added, installed directly alongside the existing WaterLOG (Figure 8). Both sensors employ the identical time-of-flight principle to measure range and share the following signal characteristics: 26 GHz frequency, 280 ns pulse period, 0.8 ns pulse width, and a 10° beam spreading angle. The H-3611 is a water level sensor with SDI-12 serial output and a specialized interface for NOAA water level applications. The E+H Micropilot is the 4–20 mA base sensor of the WaterLOG, without the SDI-12 interface and proprietary processing software. Measurements used for this study include 121 days when data from both radar sensors as well as the reference AWAC were available between 16 April 2018 and 12 July 2018.

2.4. Wave Parameter Calculations

Measurements used for this study, from both field tests, include only times when all radar sensors as well as the reference

AWAC were available. Large gaps in data, particularly in the E+H during the second test were due to intermittent data logger and power issues and are not representative of radar sensor performance (Figures 2, 9).

Hourly power spectral densities (PSD) were computed for each sensor using the first 2,048 1 Hz samples at the top of each hour. Each hourly ensemble of 2,048 samples was wild point edited by removing raw range to surface points outside of 4–20 m in order to exclude random spikes. The samples were then detrended, and the power spectral density was computed using the Welch FFT approximation (pwelch function in Mathworks MATLAB) with an NFFT length of 64, a Hamming window and a 50% window overlap. Significant wave height is estimated as $4\sqrt{m_0}$, where m_0 is the area under the power spectral density curve [the variance of surface elevation (zero moment)] in the frequency band from 0.0156 to 0.5 Hz.

AWAC spectra and bulk wave parameters are calculated with USACE developed algorithms that combine 4 Hz sea surface height measurements from the sensor's Acoustic Surface Tracking beam (AST) and near surface orbital velocities (UV) computed from its three oblique current profiling beams (AST-UV). Sea surface height from the AWAC's pressure sensor is used if AST measurements do not pass an automated quality check. USACE processed AWAC spectra covers 50 0.01 Hz spaced frequency bands, ranging from 0.01 to 0.5 Hz.

Detailed radar versus AWAC wave measurement comparisons presented in the following section include separate comparisons

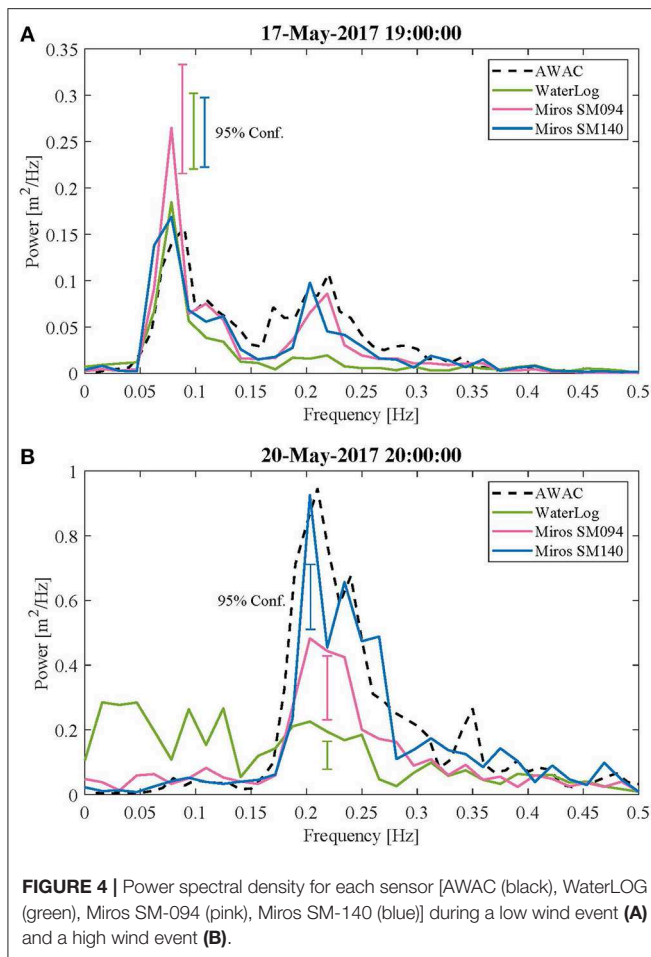


FIGURE 4 | Power spectral density for each sensor [AWAC (black), WaterLOG (green), Miros SM-094 (pink), Miros SM-140 (blue)] during a low wind event (A) and a high wind event (B).

of the swell and wind wave components of spectral estimates. To separate wind waves and swell, we used the 1D wave spectral method proposed by Hwang et al. (2012), which is a modification of the steepness method of Wang and Hwang (2001). This partitioning technique uses the wave frequency spectrum to determine a separation frequency that distinguishes wind waves from sea swell. We use the power spectral density of the AWAC to compute a time series of separation frequencies (f_s). These f_s are used when separating swell and wind waves for the AWAC and three radars.

Hwang defines the separation frequency as

$$f_{s1} = 24.2084f_{m1}^3 - 9.2021f_{m1}^2 + 1.8906f_{m1} - 0.04286 \quad (1)$$

where f_{m1} is the peak frequency of the spectrum integration function

$$I_1(f) = \frac{m_1(f)}{m_{-1}(f)} \quad (2)$$

and m , the n th moment for the wave spectrum, is defined as:

$$m_n(f) = \int_f^{f_u} f'^n S(f') df' \quad (3)$$

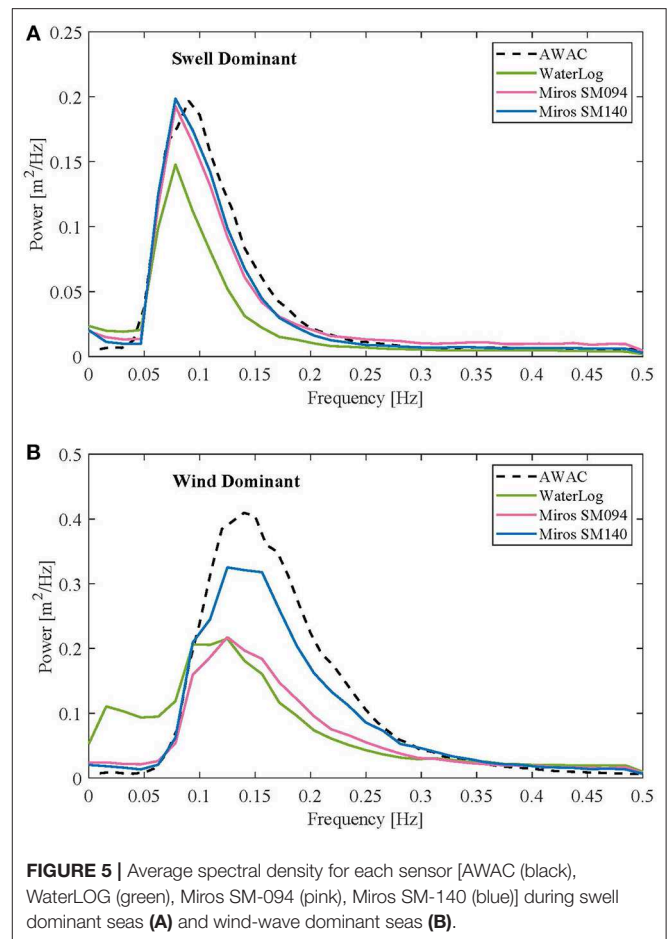


FIGURE 5 | Average spectral density for each sensor [AWAC (black), WaterLOG (green), Miros SM-094 (pink), Miros SM-140 (blue)] during swell dominant seas (A) and wind-wave dominant seas (B).

3. RESULTS, FIELD TEST ONE

Results from field test one include 68 days when data from both radar sensors as well as the reference AWAC were all available between 17 May 2017 and 8 August 2017.

During the test period, the site experienced a range of wave conditions, with varying combinations of wind-sea and swell. The reference AWAC measurements indicate that significant wave heights ranged from 0.2 to 2.4 m, and the NWLON meteorological station on site indicated several high windstorm events, where wind speeds exceeded 10 m/s for more than 20 h (Figure 2A). A qualitative look at the wave energy spectra for each sensor (Figures 2B–D) shows comparable results throughout the time series over a range of conditions.

The average power spectral densities for all sensors throughout the experiment are shown in Figure 3. All four sensors have an energy peak centered near 0.12 Hz. The peak of the Miros SM-140 is about 16% lower than that of the AWAC. The Miros SM-094 and WaterLOG are 33 and 41% lower than the AWAC, respectively, indicating resolution issues. Also, in the WaterLOG average spectrum, we see energy near 0.016 Hz, which is likely low frequency noise that may result from poor resolution and aliasing of higher frequency wave energy.

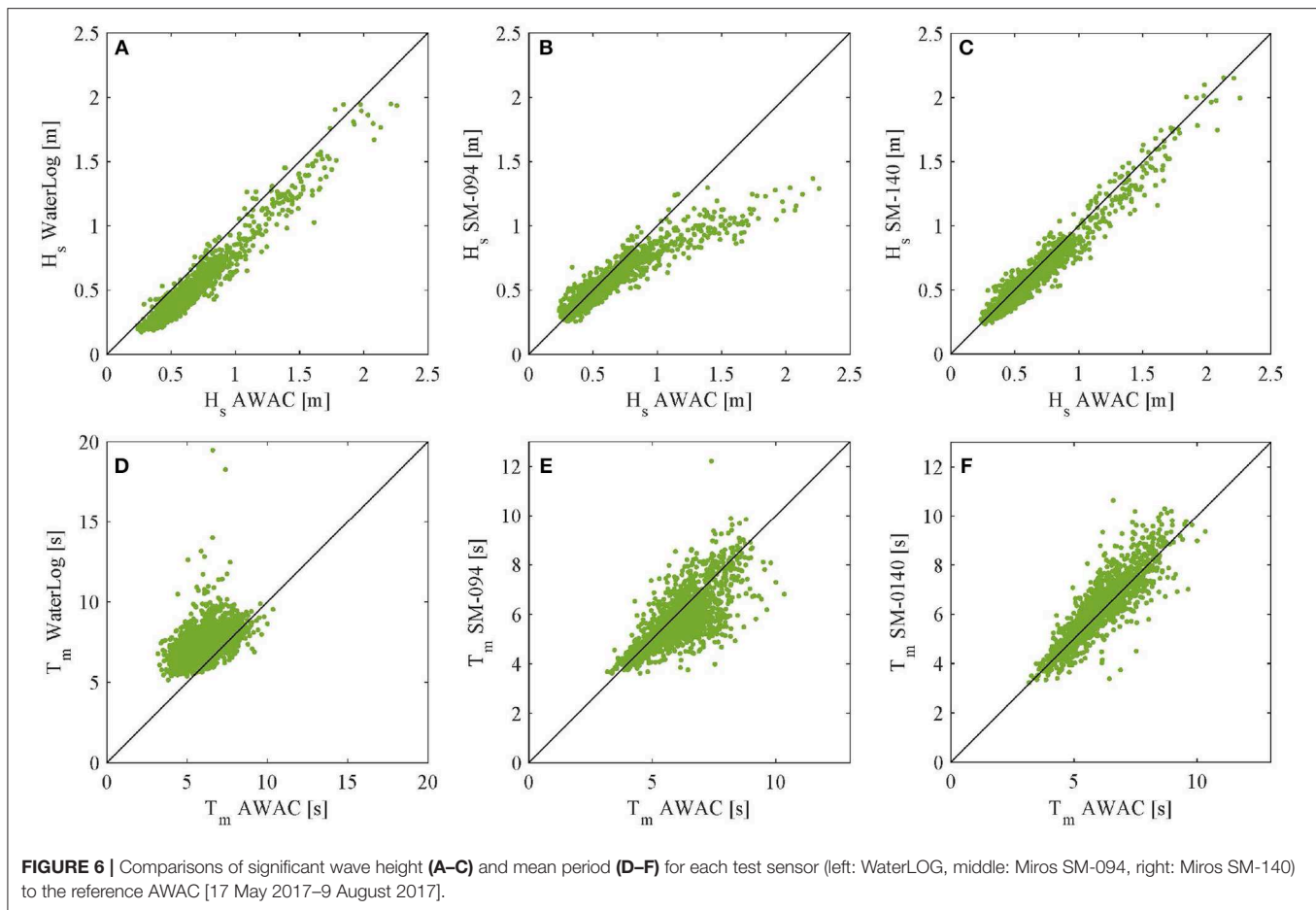


Figure 4 provides two examples of individual, hourly spectra from each sensor, one during a swell dominated sea with low wind speeds (**Figure 4A**) and another during a high wind event with a local wind wave dominated sea (**Figure 4B**). Again, results that reveal wave energy resolution issues, particularly with the WaterLOG radar. During the low wind event with swell dominated seas (average 4.9 m/s), the AWAC and both Miros sensors show two distinct peaks, near 0.08 and 0.22 Hz. Conversely, the WaterLOG sensor only resolves the 0.08 Hz peak and not the 0.22 Hz peak (**Figure 4A**). **Figure 4B** shows an example of a higher wind event (average 9.5 m/s). The Miros SM-140 is in good agreement with the AWAC, which measured an energy peak around 0.2 Hz. The Miros SM-094 has a slightly reduced spectral level at this peak. Again, the PSD of the WaterLOG does not show a true peak near 0.2 Hz and lower frequency peak appears near 0.016 Hz. Again, this is most likely noise that may result from aliasing of higher frequency energy.

While the CWFM sensors provide consistent results for all frequencies, the pulse radar results vary across different frequency bands, during different sea states. It is useful to partition results to examine spectral energy comparisons for different wave environments. To do this we find time periods within our data that are dominated by either wind or swell. Swell (or wind) dominated seas were defined as those in which the

energy on either side of the separation frequency f_s [1] comprised more than 85% of the total energy. The average spectral densities for swell dominated seas, which are comprised of 173 hourly samples, are shown in **Figure 5A**. Here the CWFM sensors are in good agreement with the AWAC, while the WaterLOG only underestimates the energy peak by about 25%. We see an even greater disparity in the average spectra of the wind-wave dominated seas, about 52% (**Figure 5B**). This suggests that the pulse radar, operating at one Hz, is not capable of resolving high frequency wave energy but is more capable of measuring swell.

Next we compare the bulk wave parameters (**Figure 6**, **Table 1**, top). The WaterLOG consistently underestimates the significant wave height. The Miros SM-094 shows good agreement for waves under 1 m, but then underestimates larger waves. The best results are found from the Miros SM-140. There is good and consistent agreement throughout. Mean period comparisons are similar to those of significant wave height. The WaterLOG overestimates the mean wave period and the Miros SM-094 and Miros SM-140 perform better.

Based on the spectral analysis, one would expect the significant wave height results from the pulse radar to be considerably worse than those shown in **Figure 6A**. So again, we wish to partition data to examine individual results during different wave environments. First we separate significant wave

TABLE 1 | Wave parameters.

Field test one	WaterLOG				Miros SM-094				Miros SM-140			
	RMSE	Abs. Mean Diff.	Mean Diff.	Corr Coef.	RMSE	Abs. Mean Diff.	Mean Diff.	Corr Coef.	RMSE	Abs. Mean Diff.	Mean Diff.	Corr Coef.
H_s (cm) All (Figures 5A,B)	16.40	15.00	14.77	0.97	15.47	9.00	6.35	0.93	8.07	6.22	4.30	0.97
T_m (s) All	1.75	1.38	-1.29	0.45	0.86	0.62	0.30	0.74	0.63	0.44	-0.15	0.88
T_p (s) All	5.38	2.33	-1.71	0.26	2.68	1.51	-0.33	0.67	2.52	1.43	-0.29	0.70
H_s (cm) Swell dominant (Figures 6A,B)	13.01	11.37	11.15	0.91	7.24	5.50	0.78	0.93	6.42	4.94	2.07	0.93
H_s (cm) Wind dominant (Figures 6A,B)	19.56	17.24	16.68	0.97	31.61	20.58	18.25	0.93	11.75	9.10	6.52	0.98
H_s (cm) Swell contribution (Figures 6C,D)	12.21	9.22	3.65	0.78	8.44	5.78	3.64	0.90	7.01	5.09	3.12	0.93
H_s (cm) Wind contribution (Figures 6C,D)	19.08	16.27	16.18	0.97	14.57	8.28	5.20	0.95	7.34	5.43	4.19	0.98

Field test two	WaterLOG				E+H			
	RMSE	Abs. Mean Diff.	Mean Diff.	Corr Coef.	RMSE	Abs. Mean Diff.	Mean Diff.	Corr Coef.
H_s (cm) All (Figures 5A,B)	19.17	17.09	16.72	0.98	13.95	11.11	8.61	0.97
T_m (s) All	0.83	0.67	0.18	0.64	0.82	0.72	0.69	0.92
T_p (s) All	5.72	2.20	-1.82	-0.04	1.88	1.05	-0.47	0.55
H_s (cm) Swell dominant (Figures 6A,B)	15.19	13.23	12.65	0.96	12.20	9.42	8.27	0.96
H_s (cm) Wind dominant (Figures 6A,B)	20.31	17.70	16.47	0.96	16.20	12.96	9.68	0.96
H_s (cm) Swell contribution (Figures 6C,D)	16.23	11.49	-0.00	0.89	11.19	7.47	2.82	0.95
H_s (cm) Wind contribution (Figures 6C,D)	23.81	19.61	19.28	0.96	13.34	11.05	9.84	0.98

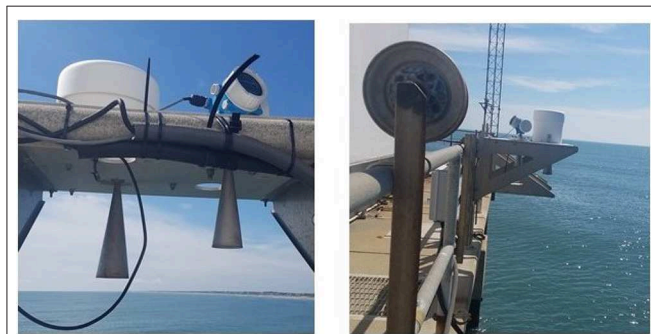
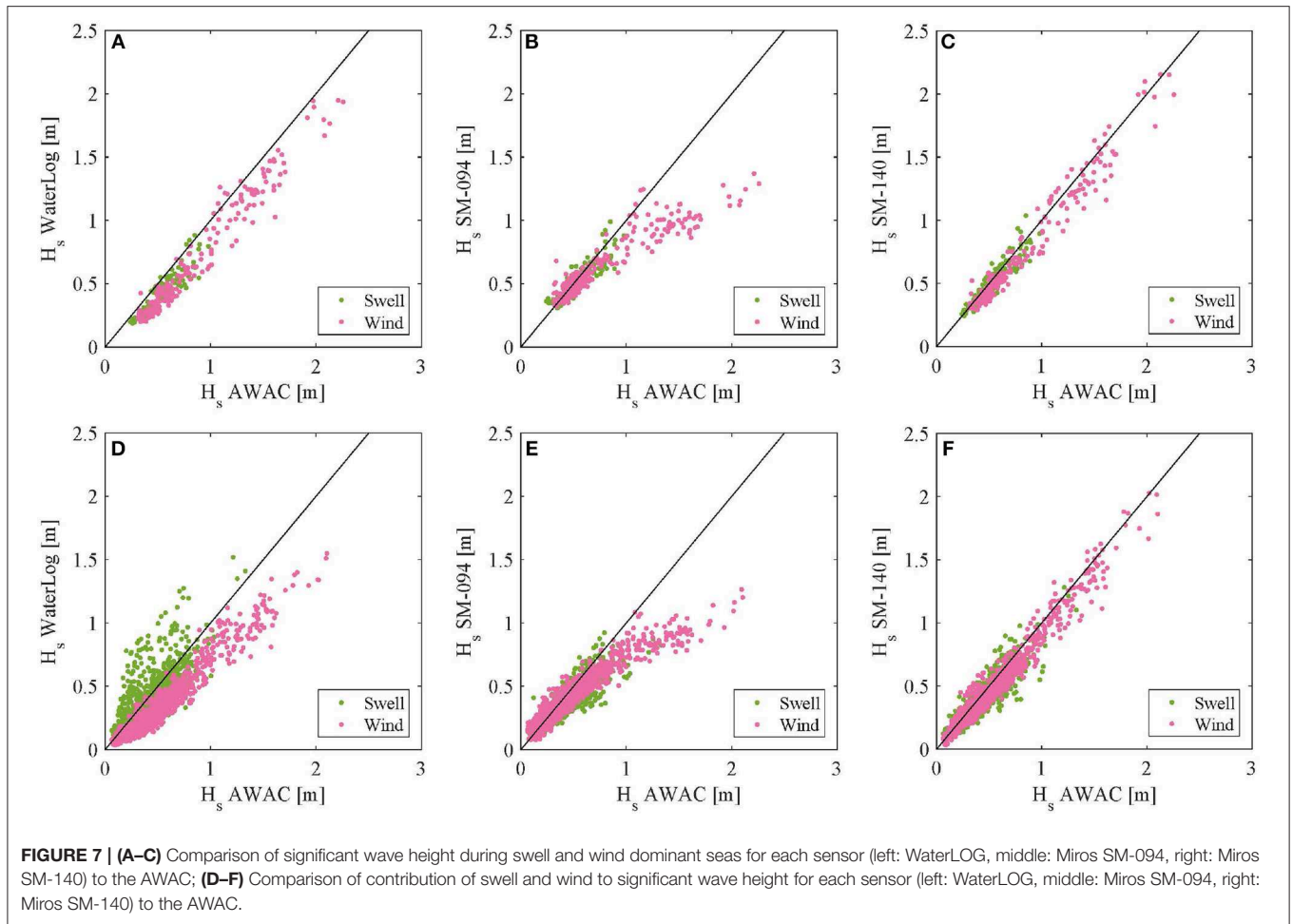
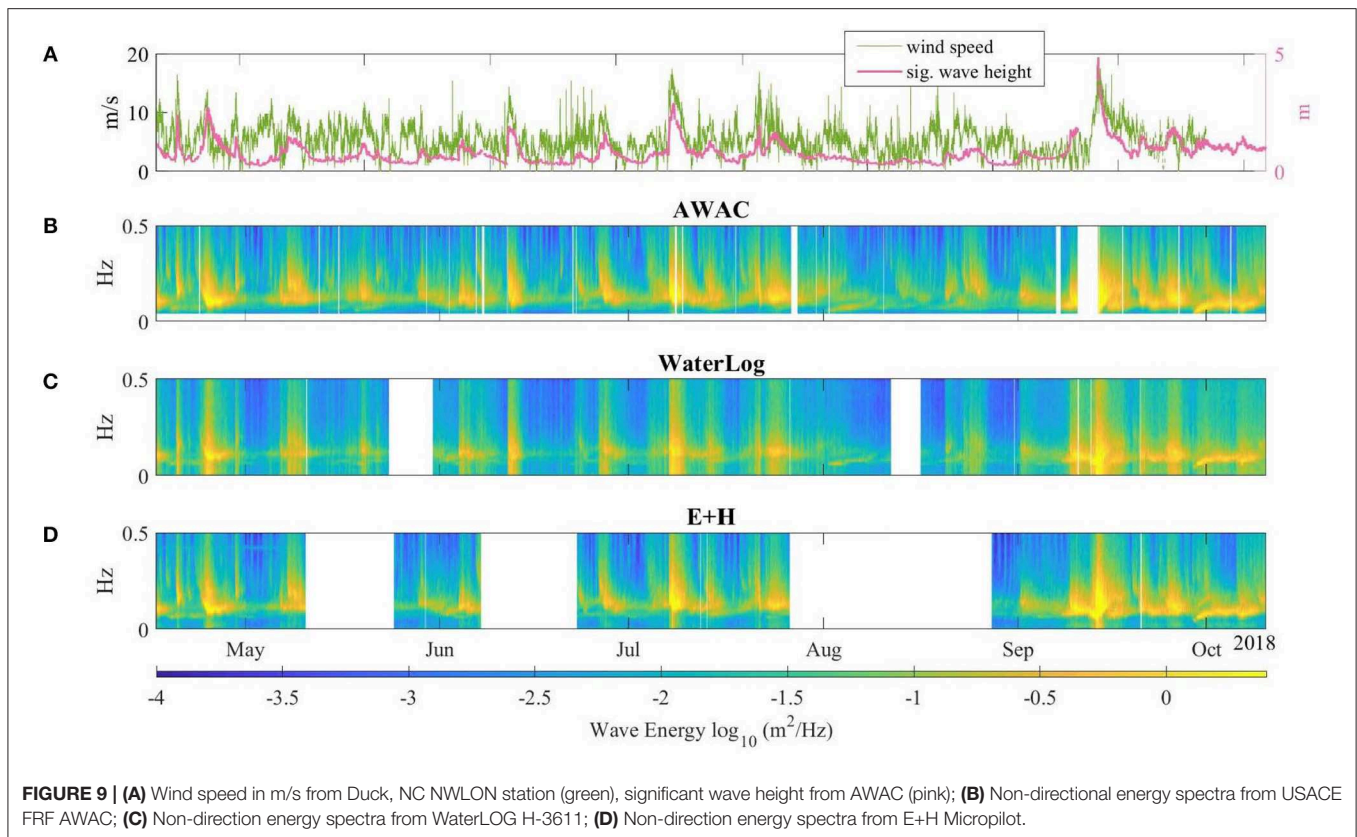


FIGURE 8 | Photographs of radars: WaterLOG (left) E+H (right) in left photo.

height results based on sea state type, during times of swell or wind dominated seas (**Figures 7A–C**). There is no discernible difference in radar versus AWAC H_{m0} comparisons for the two sea types, aside from the what one would expect to see in the Miros SM-094, based on unpartitioned results in **Figure 6B**. The error increases significantly when the reference AWAC's H_{m0} exceeds 1 m.

Next we partition the spectral energy in the frequency domain for each hourly spectrum and then recompute two integral H_{m0} values for each hourly sample, using energy in the swell and the wind frequency bands. The method described above in section 2.3 is used to find the swell and wind separation frequency f_s [1], then we find $H_{s,w} = 4\sqrt{m_0}$, where the m_0 is the area under the energy curve on either side of f_s . Results in **Figures 7D–F** indicate no significant difference between the Miros SM-140 versus the reference AWAC comparisons for H_s and H_w . However, results for the WaterLOG show an average of 3.65 cm underestimation of H_s but can reach up to 57.8 cm over estimation. The WaterLOG underestimated the H_w by an average of 16.18 cm and up to 76.34 cm. This combination of extreme over estimation of swell and underestimation of wind waves explains why H_{m0} comparisons between the WaterLOG and AWAC in **Figure 7A** do not look as bad as one would expect, given the WaterLOG's inability to resolve wind wave energy at frequencies 0.2 Hz and higher. H_{m0} calculated for the WaterLOG as $4\sqrt{m_0}$ includes the integration of bogus low frequency energy. Based on these features of the WaterLOG PSD, resulting H_{m0} values should not be considered an accurate representation of true wave conditions, even if results compare reasonably well with the reference AWAC at times.



4. RESULTS, FIELD TEST TWO

Results from field test one include 55 days when data from both radar sensors as well as the reference AWAC were all available between 16 April 2018 and 26 July 2018.

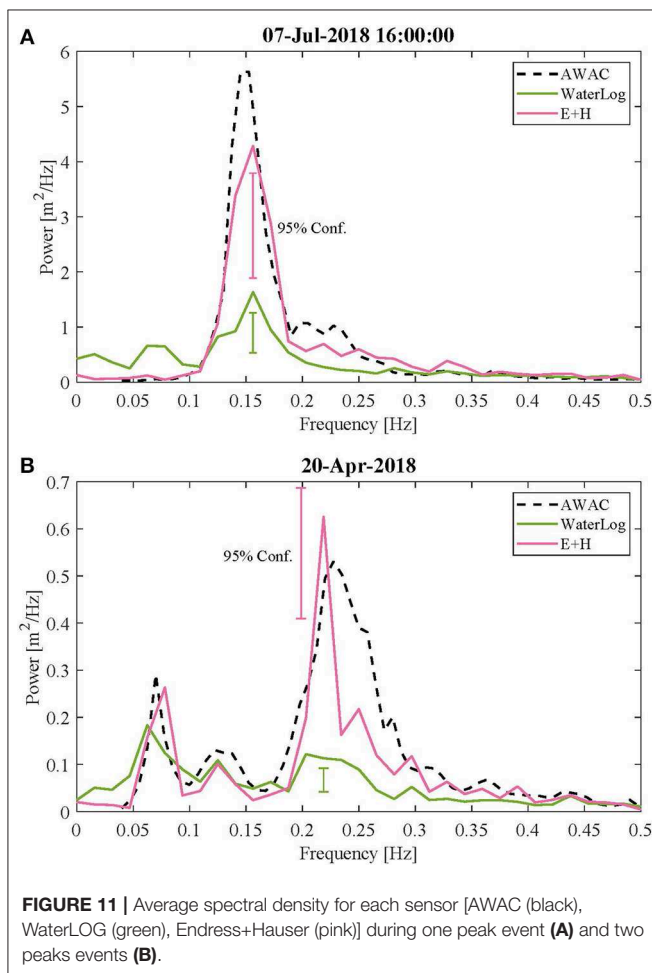
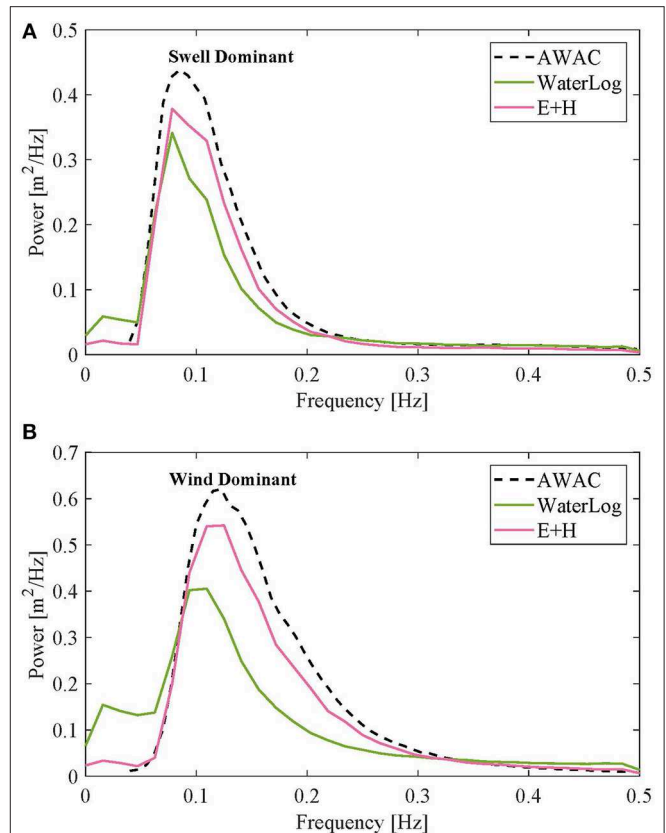
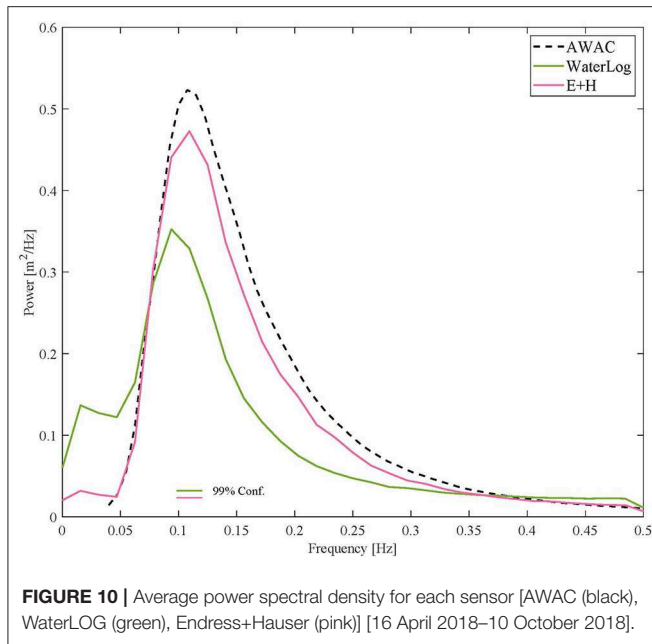
The site again experienced a range of wave conditions, with varying combinations of wind-sea and swell. Wind speeds from the co-located NWLON meteorological station averaged about 5.4 m/s and reached up to 18.5 m/s during several prolonged wind events (**Figure 9A**). The significant wave heights during the test period ranged from 0.2 to 2.9 m. Qualitatively, the wave energy spectral results from the pulse radars and the AWAC compare well throughout the time series (**Figures 9B–D**).

The average power spectral density for each sensor is shown in **Figure 10**. The energy peak for both radars and the reference AWAC are all centered near 0.11 Hz. The WaterLOG results are expected and comparable to those of the first field test. The energy peak of the WaterLOG (at 0.0938) is approximately 33% less than that of the AWAC (at 0.1075), and we see low frequency noise between 0 and 0.08 Hz. Conversely, the average power spectral density of the E+H compares better to the AWAC throughout the frequency range, and no lower frequency noise is present. At most it underestimates wave energy by about 10%. Analysis of individual hourly spectra reaffirms that the E+H sensor, without the WaterLOG SDI-12 interface does not have the same

shortcomings as its counterpart. The E+H does not have noise in low frequencies and its peaks match well to those of the AWAC (**Figure 11A**). For instances in which there are multiple energy peaks, the E+H does not underestimate those in higher frequencies (**Figure 11B**).

In the first field test, the WaterLOG results varied across different frequency bands and over different wind and swell dominated wave conditions. We partitioned results to examine spectral energy comparisons from the different wave environments and found that the WaterLOG underestimated the energy peak to a much greater degree in wind-wave dominated seas. Also, the false low frequency energy only appeared in the wind-wave seas. It performed better in swell dominated conditions. For the second field test, we again perform the wave partition to find swell and wind dominated seas as defined by those in which the energy (based on reference AWAC) on either side of the separation frequency f_s comprised more than 85% of the total energy (**Figure 12**). Again, the WaterLOG performs better in swell dominated environments, where it is more successful in resolving the high-energy peak and has less noise in the lower frequencies. The E+H compares well to the AWAC during both sea states.

Next we examine the wave bulk parameters for each sensor (**Figure 13**, **Table 1**, bottom). In the past field study, the WaterLOG consistently underestimated significant wave height and had higher peak periods than the AWAC. As expected,



results from the second field test show similar performance. The average difference between the significant wave height of the WaterLOG compared to that of the AWAC was 16.72 cm and the average difference of the peak period was -1.82 s. The E+H, on the other hand, is more successful and provides measurements that coincide well with those of the AWAC. Significant wave height measurements are, on average, 8.61 cm less than those of the reference sensor. And the average difference in peak period is -0.47 s. This is an improvement of significant wave height and peak period 49 and 74%, respectively.

In the first field test we discovered that the significant wave height computed as an integral of the spectra from the WaterLOG sensor results were misleading due to the noise in low frequencies and low energy peaks. To determine if the same problem occurs in the E+H, we looked at wave parameters from swell and wind-waves. Using the partitioned wave energy from earlier, we looked at significant wave height during swell dominated seas compared to those from wind dominated seas. The results for both sensors show no noticeable difference during either sea state (Figures 14A,B). The E+H just slightly underestimates the significant wave height (by an average of 8.27 cm in swell dominant seas and 9.68 cm in wind dominant seas), and the

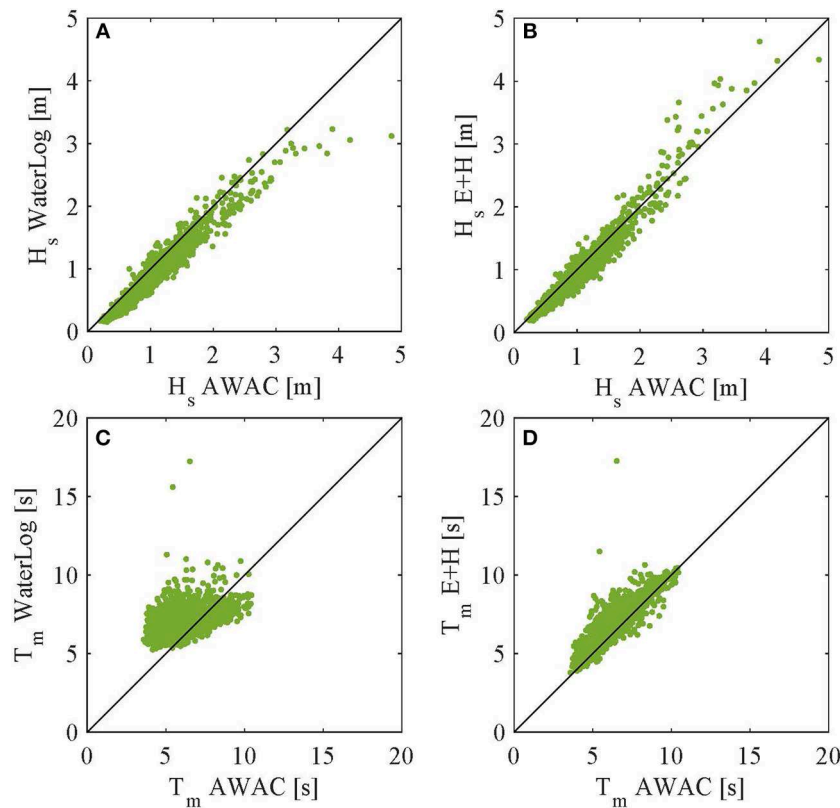


FIGURE 13 | Comparisons of significant wave height (A,B) and mean period (C,D) for each test sensor [AWAC (black), WaterLOG (green), Endress+Hauser (pink)] to the reference AWAC [16 April 2018–10 October 2018].

WaterLOG underestimates it more, in both wind and swell (12.65 and 16.47 cm, respectively).

Next we looked at all data samples but partitioned the contribution of the swell and wind into significant wave heights (H_s and H_w). To do this, the method described above in section 2.3 was used to find the swell and wind separation frequency f_s (1), then the portion of significant wave height resulting from each wave type was calculated as $H_{s,w} = 4\sqrt{m_0}$, where the m_0 is the area under the energy curve on either side of f_s . Now we see a more distinct difference between the two sensors (Figures 14C,D). H_s measurements from the WaterLOG are on average 1.1 cm (12.23 cm average of absolute value) and as much as 40 cm higher than the AWAC. The wind contribution is on average 21.21 cm (21.93 cm absolute value) lower than the reference. The E+H measurements are more consistent between each type of wave influence. The significant wave height contribution from swell is on average 2.88 cm lower than the AWAC (6.97 cm absolute value). The significant wave height contribution from wind is on average 10.17 cm lower than the AWAC (11.34 cm absolute value).

5. CONCLUSIONS

NOAA's recent transition to radar water level sensors across the NWLON network offers a potential opportunity to add

wave measurements to existing NOAA coastal observatories. An increase in real-time wave information across the coastal U.S. would provide critical support to safe navigation and resulting data archives would be valuable for coastal engineering and oceanographic research applications.

The first of two field tests conducted by CO-OPS at the Duck, NC NWLON station indicate that the higher cost, higher power Miros SM-140 CWFM radar sensor outperformed the pulse type radar water level sensor that is currently being transitioned across NWLON, the WaterLOG H3611. Although CO-OPS' primary interest in this study is in the wave measurement performance of pulse type radar sensors, results presented here indicate that the Miros SM-140 hourly power spectral density and significant wave heights compared very well with those of the reference AWAC throughout the majority of the test. These results provide additional support to other organizations currently using the Miros CWFM sensor for wave measurements.

Although the WaterLOG H3611 has served NOAA well for several years, providing 6 min average sea level measurements at many different coastal sites, and its technical specifications indicating adequate spatial and temporal resolution to resolve surface gravity waves of interest, the sensor's hourly power spectral density and bulk wave parameters often compared poorly to those of the reference AWAC. During times when the AWAC and Miros power spectral density indicated a significant level of energy in the higher frequency, local wind-sea band,

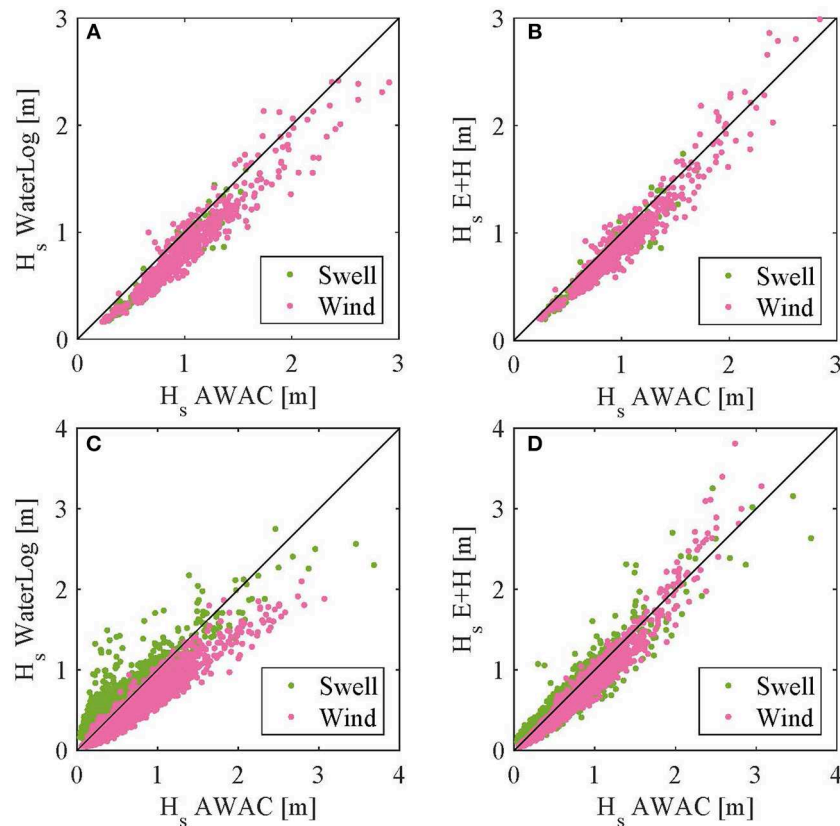


FIGURE 14 | (A,B) Comparison of significant wave height during swell and wind dominant seas for each sensor [AWAC (black), WaterLOG (green), Endress+Hauser (pink)]; **(C,D)** Comparison of contribution of swell and wind to significant wave height for each sensor [AWAC (black), WaterLOG (green), Endress+Hauser (pink)].

the WaterLOG was unable to resolve that energy and showed corresponding low frequency noise, possibly due to aliasing. Furthermore, derived values of significant wave height, based on the area under the power spectral density curve are misleading due to the integration of aliased low frequency noise.

The second field test conducted at the Duck, NWLON station yielded very promising results for a different 26 GHz pulse radar water level sensor with key specifications and a principal of operation identical to those of the WaterLOG, the Endress + Hauser FMR240. The E+H FMR240 is essentially the same radar sensor as the WaterLOG H3611, but without the SDI12 interface and the associated added layer of proprietary processing software. In the second field test, the H3611 produced results consistent with the first test. Again, this sensor did not adequately resolve energy at higher wind-sea frequencies and PSDs showed elevated levels of low frequency noise. The E+H radar sensor however showed significantly improved wave measurement results, and yielded excellent comparisons to the AWAC. On average, the E+H even compared more closely to the AWAC than the Miros SM140 sensor during the first test. The E+H hourly power spectral density indicates that this sensor adequately resolves both swell and wind-sea energy during all conditions, both in swell and wind dominated seas. No low frequency noise was detected in any of the E+H hourly PSD,

indicating this sensor avoided the apparent resolution issues that the WaterLOG experienced during both field tests. Some slightly lower E+H PSD levels compared to the AWAC are likely due to the physical distance between the two sensors, a phenomenon that should be more closely examined in future work. The root mean squared error and average differences of the E+H versus AWAC H_{m0} values (13.95 and 8.61 cm, respectively) are both significantly less than the corresponding values for the WaterLOG vs. AWAC comparison (19.17 and 16.72 cm). The improved E+H sensor results may indicate some additional temporal filtering, or reduction in higher temporal resolution resulting from the WaterLOG sensor's added SDI12 interface.

Based on these initial, promising results, CO-OPS will continue to maintain field testing with the E+H FMR240 radar at the Duck, NC NWLON station to capture a longer data set and wider variety of wave conditions. CO-OPS also plan to establish an additional, E+H FMR240 based field test platform at one of CO-OPS Pacific coast NWLON sites, to gather results in an additional type of coastal wave environment. Continued testing will involve close coordination with partner operating sites to ensure a closer collocation of reference and test sensors, resulting in improved wave measurement comparisons. More extensive field test results will be presented in subsequent work along with an analysis on the impact of distance between the reference and

test sensors. Additionally, CO-OPS plan to share and discuss results with radar sensor vendors to ensure future sensor designs reduce unnecessary filtering beyond 1 Hz, and that sensors are capable of temporally resolving all physical processes of interest.

AUTHOR CONTRIBUTIONS

All authors were involved in the instrumentation setup and installation. Data analysis was conducted

by LF. The manuscript was written by LF, with input from RH.

ACKNOWLEDGMENTS

We thank Kent Hathaway and others at the USACE Field Research Facility in Duck, NC for assistance and use of their AWAC data. We also thank the rest of our team, Winston Hensley, Eric Breuer, and Scott Mowery for their support.

REFERENCES

- Bushnell, M., Bosley, K., and Mero, T. (2005). *Microwave Air Gap-Bridge Clearance Sensor Test, Evaluation, and Implementation Report*. NOAA.
- Ewans, K., Feld, G., and Jonathan, P. (2014). On wave radar measurement. *Ocean Dyn.* 64, 1281–1303. doi: 10.1007/s10236-014-0742-5
- Heitsenrether, R. and Davis, E. (2011). *Test and Evaluation Report: Limited Acceptance of the Design Analysis Waterlog? h-3611i Microwave Radar Water Level Sensor*. NOAA.
- Hwang, P. A., Ocampo-Torres, F. J., and GarcíNava, H. (2012). Wind sea and swell separation of 1D wave spectrum by a spectrum integration method. *J. Atmos. Ocean. Technol.* 29, 116–128. doi: 10.1175/JTECH-D-11-00075.1
- MIROS (NDa). *Specification Sheet, SM-094 Rangefinder*. MIROS.
- MIROS (NDb). *Specification Sheet, SM-140 Rangefinder*. MIROS. Available online at: <https://www.miros-group.com/wp-content/uploads/2019/04/Miros-RangeFinder-Datasheet.pdf>
- NOAA and USACE (2009). *A National Operational Wave Observation Plan*. Report, National Atmospheric and Oceanic Administration and US Army Corps of Engineers.
- Park, J., Heitsenrether, R., and Sweet, W. (2014). Water level and wave height estimates at noaa tide stations from acoustic and microwave sensors. *J. Atmos. Ocean. Technol.* 31, 2294–2308. doi: 10.1175/JTECH-D-14-00021.1
- Pérez Gómez, B. (2014). *Design and Implementation of an Operational Sea Level Monitoring and Forecasting System for the Spanish Coast* (Thesis). Universidad De Cantabria, Santander, Spain.
- Pérez, B., E. Álvarez Fanjul, E., Pérez, S., de Alfonso, M., and Vela, J. (2014). Use of tide gauge data in operational oceanography and sea level hazard warning systems. *J. Oper. Oceanogr.* 6, 1–18. doi: 10.1080/1755876X.2013.11020147
- Sweet, W. (2016). “New ways to measure waves and their effects at noaa tide gauges,” in *American Geophysical Union, Ocean Sciences Meeting 2016, Abstract EC24C-1127* (New Orleans, LA).
- Wang, D. W., and Hwang, P. A. (2001). An operational method for separating wind sea and swell from ocean wave spectra. *J. Atmos. Ocean. Technol.* 18, 2052–2062. doi: 10.1175/1520-0426(2001)018<2052:AOMFSW>2.0.CO;2
- Xylem-YSI (ND). *Specification Sheet, Model H-3611/3612/3613: Family of SDI-12 Radar Water Level Sensors*. Xylem-YSI.

Conflict of Interest: The authors declare that the research was conducted in the absence of any commercial or financial relationships that could be construed as a potential conflict of interest.

Copyright © 2019 Fiorentino, Heitsenrether and Krug. This is an open-access article distributed under the terms of the Creative Commons Attribution License (CC BY). The use, distribution or reproduction in other forums is permitted, provided the original author(s) and the copyright owner(s) are credited and that the original publication in this journal is cited, in accordance with accepted academic practice. No use, distribution or reproduction is permitted which does not comply with these terms.



Coastal Harmful Algae Bloom Monitoring via a Sustainable, Sail-Powered Mobile Platform

Jordon S. Beckler^{1*†}, Ethan Arutunian², Tim Moore³, Bob Currier⁴, Eric Milbrandt⁵ and Scott Duncan²

OPEN ACCESS

Edited by:

Leonard Pace,
Schmidt Ocean Institute,
United States

Reviewed by:

Christopher Sabine,
University of Hawai'i, United States
Steven Lohrenz,
University of Massachusetts
Dartmouth, United States

*Correspondence:

Jordon S. Beckler
jbeckler@fau.edu

† Present address:

Jordon S. Beckler,
Geochemical Sensing Laboratory,
Harbor Branch Oceanographic
Institute, Florida Atlantic University,
Fort Pierce, FL, United States

Specialty section:

This article was submitted to
Ocean Observation,
a section of the journal
Frontiers in Marine Science

Received: 15 November 2018

Accepted: 05 September 2019

Published: 04 October 2019

Citation:

Beckler JS, Arutunian E, Moore T,
Currier B, Milbrandt E and Duncan S
(2019) Coastal Harmful Algae Bloom
Monitoring via a Sustainable,
Sail-Powered Mobile Platform.
Front. Mar. Sci. 6:587.
doi: 10.3389/fmars.2019.00587

¹ Ocean Technology Research Program, Mote Marine Laboratory, Sarasota, FL, United States, ² Navocean, Inc., Seattle, WA, United States, ³ Ocean Process Analysis Laboratory, Durham, NH, United States, ⁴ Gulf of Mexico Coastal Ocean Observing System, Texas A&M University, College Station, TX, United States, ⁵ SCCF Marine Laboratory, Sanibel-Captiva Conservation Foundation, Sanibel, FL, United States

Harmful algae blooms (HABs) in coastal marine environments are increasing in number and duration, pressuring local resource managers to implement mitigation solutions to protect human and ecosystem health. However, insufficient spatial and temporal observations create uninformed management decisions. In order to better detect and map blooms, as well as the environmental conditions responsible for their formation, long-term, unattended observation platforms are desired. In this article, we describe a new cost-efficient, autonomous, mobile platform capable of accepting several sensors that can be used to monitor HABs in near real time. The Navocean autonomous sail-powered surface vehicle is deployable by a single person from shore, capable of waypoint navigation in shallow and deep waters, and powered completely by renewable energy. We present results from three surveys of the Florida Red Tide HAB (*Karenia brevis*) of 2017–2018. The vessel made significant progress toward waypoints regardless of wind conditions while underway measurements revealed patches of elevated chl. *a* likely attributable to the *K. brevis* blooms as based on ancillary measurements. Measurements of colored dissolved organic matter (CDOM) and turbidity provided an environmental context for the blooms. While the autonomous sailboat directly adds to our phytoplankton/HAB monitoring capabilities, the package may also help to ground-truth satellite measurements of HABs if careful validation measurements are performed. Finally, several other pending and future use cases for coastal and inland monitoring are discussed. To our knowledge, this is the first demonstration of a sail-driven vessel used for coastal HAB monitoring.

Keywords: autonomous and remotely operated vehicle, harmful algal bloom, mapping, *Karenia brevis* HABs, CDOM, West Florida Shelf, surface vehicle, satellite remote sensing

INTRODUCTION

In the last few decades, harmful algae blooms (HABs) have increased in number, intensity, and duration due to cultural eutrophication, increasing rainfall, and warming temperatures (Brand and Compton, 2007; O'Neil et al., 2012). Through the generation of toxins or by creating locally hypoxic conditions, HAB effects can range from acute sickness and respiratory irritation potentially affecting local economies (Kirkpatrick et al., 2006; Hoagland et al., 2009; Backer et al., 2010) to massive marine fish and mammal mortality events (Scholin et al., 2000; Gannon et al., 2009), or even to chronic human poisoning and death through ingestion of contaminated shellfish or drinking water (Carmichael, 2001; Fleming et al., 2002; Reich et al., 2015). HAB blooms are most frequently observed and display the most detrimental ecosystem and human health impacts in coastal or inland marine and freshwater bodies (Anderson et al., 2002), for example, in areas with coastal recreation, fishing, mari/aquaculture, and drinking water intake systems. Recent years have experienced extreme HAB events with unparalleled public recognition, for example, the summer of 2014 and 2016 *Microcystis aeruginosa* blue-green cyanoblooms in Lake Erie and the Indian River Lagoon (Florida) (Smith et al., 2015; Stockley et al., 2018) that poisoned drinking water and decreased property values, respectively, the *Pseudo-nitzschia* bloom of 2015 in California waters that led to the closing of the Dungeness crab fishing season (McCabe et al., 2016), and the 2017–2018 *Karenia brevis* bloom in west Florida (ongoing as of the time of writing) that has led to a declaration of a state of emergency. This “Florida Red Tide” bloom is poised to be the worst on record and has brought an unprecedented amount of national attention to this particular HAB (Ducharme, 2018).

To plan for and mitigate the occurrence and effects of HABs, it is ideal to both monitor the algae and/or toxins directly and collect additional ancillary information regarding the chemical and physical ecology of the ecosystems. Traditional routine monitoring is inherently expensive and time consuming, and the spatial and temporal resolution of discrete measurements in many HAB-prone regions is often not sufficient to elucidate bloom causes or properly initiate models. According to a recent HAB scientist community consensus, an observing system consisting of satellite, moored, and mobile data collection platforms will most likely emerge as the most effective holistic approach (Bowers and Smith, 2017). Careful consideration must be given to important trade-offs existing between desired sensor specificity (e.g., pigments, species, or toxins) and platform compatibility (i.e., fixed location versus mobile), which together determine cost, sampling resolution, and reliability. For example, while satellite-based remote sensing is inexpensive, the technique suffers from low temporal (e.g., daily) and spatial resolution (e.g., ~1 km), non-species specificity, and interferences from the seafloor, suspended sediment, and clouds. Fixed-location, unattended monitoring devices (i.e., shoreline or moorings) have drastically advanced the temporal resolution of data collection, especially at the species level (Smith et al., 2015; Stockley et al., 2018), but the installation

of enough locations to provide sufficient spatial resolution is cost-prohibitive (Shapiro et al., 2015). Given the vertical heterogeneity of HABs, three-dimensional monitoring platforms, such ocean-going autonomous underwater vehicle buoyancy gliders, are promising and have been successfully deployed in near-shore and open ocean environments (Robbins et al., 2006). However, the submerged nature of these vehicles creates communications, power, and reliability constraints that currently limit sensor options and few species-level options exist. In turn, two-dimensional Autonomous Surface Vehicles (ASV) such as those powered by sail or waves, e.g., “Wave Gliders” or Saildrone (Daniel et al., 2011; Mordy et al., 2017), while not providing depth data, may alleviate these constraints and are more conducive in accepting complex instrumentation payloads. However, to our knowledge, all existing long-duration autonomous vehicles are not designed to operate effectively in shallow and/or near-shore waters less than a few meters depth, their size, form, or performance prohibit shallow water operation, and their operation is challenging for non-expert resource managers.

For over a decade on the southwest Florida Shelf, fixed-location, species-specific optical devices (i.e., Optical Phytoplankton Discriminators; OPD) have been employed as part of a State of Florida- and NOAA-funded HAB observatory (Sarasota Operations of the Coastal Ocean Observing Lab of Mote Marine Laboratory; SO-COOL). Additionally, AUVs (Slocum gliders) outfitted with either an OPD or a chl. *a* fluorometer are also routinely used to locate and track *K. brevis* HABs (Shapiro et al., 2015). While these efforts have yielded valuable insights into the conditions surrounding HAB bloom formation, these glider operations have presented challenges over the years. Deployments are logistically challenging, requiring an initial transit to deeper waters, and once deployed, have a minimum depth limitation of 10 m (i.e., 20 km from the coast). Finally, cost has prohibited sufficient spatial and temporal coverage, and deployments have been met with unanticipated buoyancy-related operational challenges such as aborts due to nuisance remora “suckerfish” attacking and sinking gliders (there are widespread anecdotal observations by USF, UGA, and Mote scientists).

In 2016, Mote Marine Laboratory began a collaboration with Navocean, Inc., to utilize their autonomous sail-powered surface vehicle for *K. brevis* bloom monitoring. Navocean offers small, 2-m-long vessels that are reliable, and can accept versatile sensors. Navocean boats fill a current niche in both the Autonomous Surface Vehicle (ASV) and the HAB mapping markets, being powered solely from renewable sources, inexpensive, navigable in shallow waters (>1 m), and deployable from shore by a single person. To demonstrate proof of concept for HAB monitoring, a Navocean Nav2 boat was outfitted with a three-channel fluorometer (Turner Designs) configured to measure chl. *a* as a proxy for phytoplankton pigments, as well as CDOM and turbidity to provide ancillary environmental information. The boat was deployed for periods of up to 1 week in the winter of 2017, during the start of what has become one of the worst *K. brevis* blooms on record. This work describes the system design, testing, and *in situ* validation, and then discusses other potential applications

for HAB monitoring and other environmental applications for this unique vehicle.

VESSEL DESIGN AND OPERATION

The *Nav2* ASV (**Figure 1** and **Table 1**) is small, lightweight, easy to launch/land, and non-hazardous in the event of collision. The base cost is <\$75k and daily operating costs are primarily satellite data fees (\$25–\$55 typical). The vessel is 2 m in length, drafts 0.75 m, and weighs between 38 and 45 kg (depending on battery configuration). The boat has a fiberglass shell with a thick foam core providing reserve buoyancy. The fin keel and rudder are designed to shed seaweed and debris and have proven resistant to tangling in fishing lines and lobster and crab gear in previous missions. The 2-m-tall mast has a bright orange sail for high visibility. A “Bermudan” style rig consists of a reinforced carbon mast with high-strength Dacron sails (main sail and a small jib) and chafe-resistant lines. The *Nav2* is outfitted with an Airmar 200WX IPX7 marine grade meteorological sensor for wind speed and direction for navigation/scientific purposes, as well as air temperature and barometric pressure for scientific purposes. The *Nav2* is controlled via an iOS

application (iPad or iPhone) that is in constant communication to the boat using WiFi, Cellular, or Iridium satellite in either manual mode for line of sight control or autonomous mode for waypoint navigation (**Figure 2**), which includes up-wind tacking in variable wind and sea states. For most missions, the operator must only monitor the vessel a few times per day to ensure that mission goals are being met, with very few adjustments necessary under normal circumstances. However, adjustments can be made to meet science goals (e.g., surveying HAB bloom patches) or during launch and recovery, or if the ASV enters an unfavorable zone of currents. An onboard, standard passive AIS receiver relays nearby broadcasting ship locations to the user for collision avoidance purposes, although no active avoidance systems are present. A small electric thruster also provides back-up propulsion for flat calm-wind conditions and for facilitating deployment and recovery, as needed. The standard battery bank consists of up to $5 \times$ LiFePO4 batteries, for a total of 100 A h and 1200 W h. Nominal 35-W solar panels provide solar recharge of the onboard battery bank for long-duration missions (up to several months).

A three-channel fluorometer (Turner Designs Cyclops Integrator/C3) configured for measurement of chlorophyll *a* (Excitation 465 nm/Emission 696 nm), colored dissolved

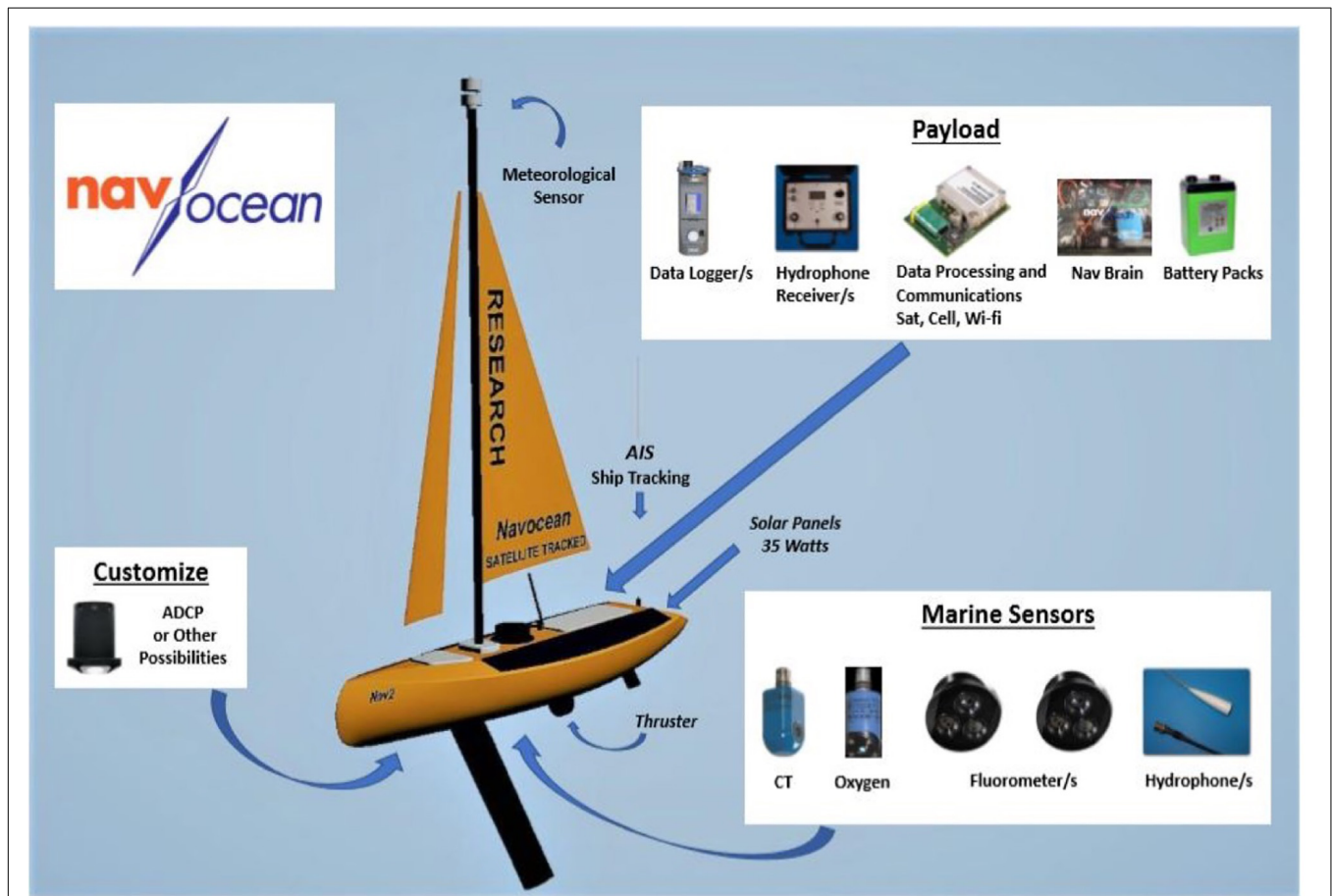


FIGURE 1 | Diagram of the Navocean Nav2 Autonomous Sail Vehicle and components.

organic matter (CDOM; measured via fluorescence proxy at 325/470 nm), and turbidity (backscatter at 850 nm) was installed in the hull, behind the main keel, facing downward. The chl. *a* and turbidity channels underwent single-point linear cross-calibration in the laboratory using ultrapure deionized water and a natural estuarine surface grab sample from Sarasota Bay. The reference measurement was made with a Turner-7F fluorometer operating at the same wavelengths as the sailboat sensor (the surface bottle sample had a turbidity of 0.48 NTU and $0.58 \mu\text{g L}^{-1}$ chl. *a*). The CDOM channel was calibrated using the same surface bottle sample, but first filtered ($0.2 \mu\text{m}$). As the CDOM fluorometric measurement is a relative index of CDOM concentration and not a true absorption measurement, the response from the CDOM channel was operationally calibrated based on relationships to CDOM absorption at 440 nm measured on field samples in the laboratory (the surface bottle sample a_{440} was 0.127 m^{-1}).

ASSESSMENT

Vehicle Performance

For the HAB monitoring trials, the *Nav2* vehicle was deployed from the beach three times between December 18, 2017 and February 7, 2018, for deployments of increasing length of 1, 3, and 7 days (Table 2 and Figure 3), in which case the boat traveled a total of 254 nautical miles (i.e., 470 km;

1 NM = 1.9 km) at an average rate of 1.0 knots (1 knot = 1 NM h^{-1}). Winds were relatively low during this time period, corresponding to an overall average of 6.3 knots as compared to average monthly December and January magnitudes of 10–13 knots¹.

Each mission was operated in a similar manner. The initial waypoints were entered in advance via WiFi using the chart-based app. Iridium satellite communication was used after deployment to monitor the vehicle's progress and send updated waypoints as desired, but all navigation was controlled autonomously. To start each mission, the *Nav2* was deployed from Sanibel Beach by hand rolling the ASV on its cart out to a depth of $>0.75 \text{ m}$, pointing it offshore, and providing a mild push. At the end of each mission, the *Nav2* was directed to sail straight to shore until the keel grounded in shallow water. The *Nav2* was then placed back onto the wheel cart and pulled on-shore. For the 25-h deployment beginning 2040 UTC December 18, 2017 (Figure 3A), the *Nav2* was directed to head straight out and back; sailing first nearly due south to a point 10 NM offshore and then returning north to the beach. On the way back, in response to very calm winds, the thruster was turned on at minimal power to provide a speed of 1 knot, which was enough to reach shore at a convenient time for pick-up. Some drift was caused by local currents, which presents as a bend in the transect line. Despite the boat experiencing a near full tidal cycle in both the southward and northward direction of travel and experiencing winds between 0 and 3 knots for most of the deployment, the *Nav2* steadily progressed. This first short mission served as a data collection test of the fluorometer, which was logging to an SD card on board. For the 77-h deployment beginning 1422 UTC December 20, 2017 (Figure 3B), the *Nav2* was again deployed directly from Sanibel Beach. The intent of this mission was to sail through an area with a known HABs bloom. The *Nav2* was directed to first travel south in a zig-zag pattern to cover increased area compared to the first deployment. In response to updated satellite imagery, the *Nav2* was then directed west 15 NM and then north returning to a convenient pick up location at the NE limits of Sanibel Island. The decision was made to persist with sail power for nearly the entire mission to better assess performance in the very calm wind conditions. Depending on solar gain and battery status, the thruster can be used for up to 48 + continuous hours to complete straight transects in a timely manner. Tidal current drift effected the precision of transect lines when the wind was <3 knots. The vessel was removed from the water mid-deployment by a recreational boater, who mistakenly assumed the vessel was lost, and who then traveled with the *Nav2* in a northwest direction for 5 km. The *Nav2* was tracked during this time and contact was established with the recreational boaters, who were instructed to place the vessel back into the water. At the end of this mission, a more prominent statement was added to the *Nav2*'s sail, indicating boldly its nature as a tracked and monitored research vessel. No such problem has occurred since. Near the end of the mission, the winds were calm and the thruster was used at low power to return in a timely manner for pickup

TABLE 1 | Specifications for the *Nav2* Autonomous Sail Vehicle (Navocean).

Nav2 ASV specifications and capabilities

Mission duration	Up to 6 months
Speed	1–3 Knots
Length	2 m (6.5')
Draft	0.75 m (2.5')
Weight	85 lbs plus payload
Rigging	Main + Jib "storm" sails and chafe resistant lines
Mast	Unstayed reinforced carbon
Winch	Electric with anti-jamming spool
Rudder and Keel	No-tangle design sheds lines and seaweed
Power	12 V, 35 W solar array
Batteries	Up to 120 Ah LiFePO ₄
Standard sensors	GPS, PRH, Meteorological, AIS (passive receiver on ASV for informing the operator of the location of nearby ships via the iPad application)
Optional sensors	Water quality: O ₂ , CT, backscatter, 3/6 channel fluorometer (chl. <i>a</i> , phycocyanin, phycoerythrin, CDOM, turbidity, oil) Acoustic: Pinger Tracking, Cetaceans, Telemetry Custom: ADCP and many others
Navigation	Autonomous to waypoints + manual option
Charts	NOAA RNC included
UI	Chart based iOS App + web portal
Dashboard	Location, speed, course, heading, true and apparent wind, pitch, roll, power, battery and solar voltage, sail and rudder position, thruster RPM, connectivity status, waypoint ETA
Comms	Iridium SBD (Sat), Cell, and WiFi
Real-time	Configurable telemetry and sensor data

¹https://www.windfinder.com/windstatistics/southwest_of_tampa_bay_buoy

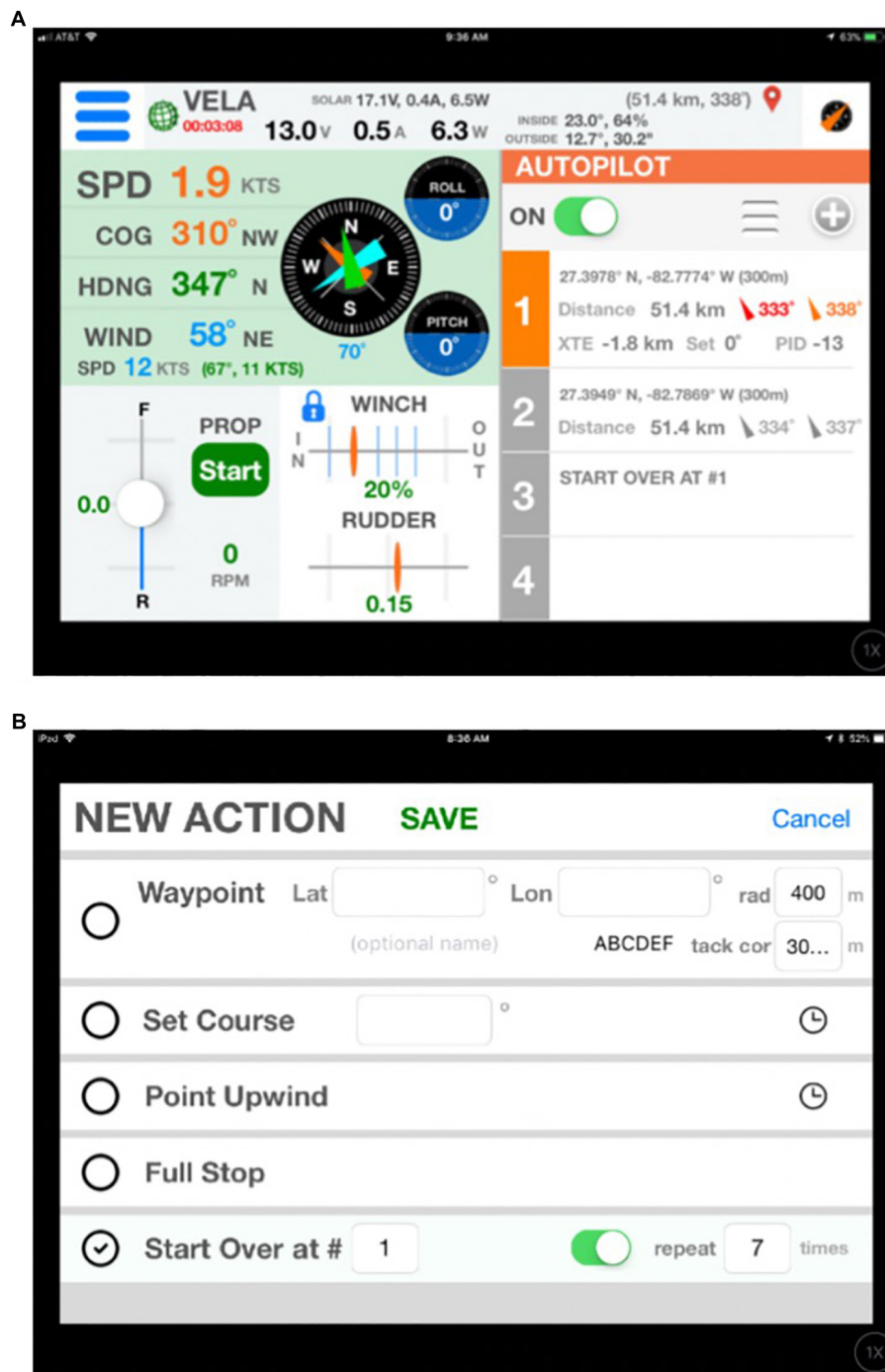


FIGURE 2 | Screenshots of the iOS control software running on an iPad, illustrating operation via Manual Control (A) or via Waypoint navigation (B).

at the beach. For the 148-h deployment beginning 1841 UTC January 31, 2018 (Figure 3C), the vessel was again deployed from Sanibel Beach with the intent of traversing a significant distance of the West Florida Shelf. The vessel traveled west around Sanibel Island and then proceeded northward along the coast between 10 and 30 km offshore. After approaching Tampa Bay, the *Nav2* was given waypoints to perform several longitudinal

transects, until eventually being directed to the south for retrieval at Venice Beach.

To evaluate the sailing capabilities of the *Nav2* vessel, a polar diagram was constructed (Figure 4). The diagram illustrates the obtained vessel speed as a function of realized apparent winds as sensed by the onboard wind sensor (Figure 1). For winds from angles directly behind the vessel to as far as 45° into the

TABLE 2 | Summary of the environmental conditions and the Nav2 ASV performance during harmful algae bloom tracking deployments.

Mission dates	Number of hours	Wind speed average (apparent)	Boat speed average (knots)	Sea state Beaufort (range)	Distance covered (NM)	Percent thruster use (%)
December 18–19, 2017	25	3.2	0.9	0–2	22.5	12
December 21–24, 2017	77	3.6	0.7	0–3	53.9	10
January 31–February 6, 2018	148	8.2	1.2	0–5	177.6	3

The distance covered includes periods of using the thruster at low speeds (~1 knot) in calm winds to return the ASV to shore for a convenient pickup time. Alternatively, the thruster can be used temporarily to complete important transects if the wind dies or for entire short missions of ~1 day.

wind while under waypoint navigation, the vessel autonomously steers directly to the desired destination and the colored lines represent Velocity Made good on Course (VMC). If the Nav2 is traveling toward a desired waypoint that happens to be directly into the wind (with a threshold of 45° port or starboard), the vessel instead autonomously chooses to tack and achieves a net Velocity Made Good (VMG) toward the waypoint. Represented in **Figure 4** are therefore two separate calculations; if winds are < 45° off of the bow, the VMG instead represents the apparent velocity with respect to the destination. Increasing apparent wind velocities results in higher Nav2 velocities for speeds at least as high as 25 knots, under which conditions the vessel is capable of traveling at average speeds > 2 knots. The Nav2 is capable of reaching average speeds > 1 knot if winds are at least 5–10 knots and greater than 60° away from the wind. Under low wind conditions < 5 knots, the vessel realizes VMC/VMG > 0.5 knots for all apparent wind directions > 30°. Overall, the vessel is capable of realizing significant forward progress, regardless of wind direction, in all but the most unfavorable wind conditions (> 40 km day⁻¹).

To evaluate if there were effects of bubbles on the fluorometric data, the three measured parameters were binned according to the wind speed at the time of data collection (**Figure 5**). We are assuming in this case that higher wind speeds would generate more choppy ocean conditions and thus a larger number of bubbles that may provide measurement artifacts both attenuating and amplifying signals, depending on several factors. However, we observe that the fluorometric data do not appear to depend on wind speed. While there is an increase in chl. *a* values at lower apparent wind speeds, this is likely just coincident with the Nav2 experiencing lower winds closer to shore in the first two deployments, in the presence of the confirmed algae bloom (described in the next section).

Harmful Algal Bloom and Environmental Monitoring

To explore the utility of the Nav2 as a platform for HAB detection and mapping, the chl. *a* fluorometer was used as a semi-quantitative proxy for algal presence. The CDOM and turbidity

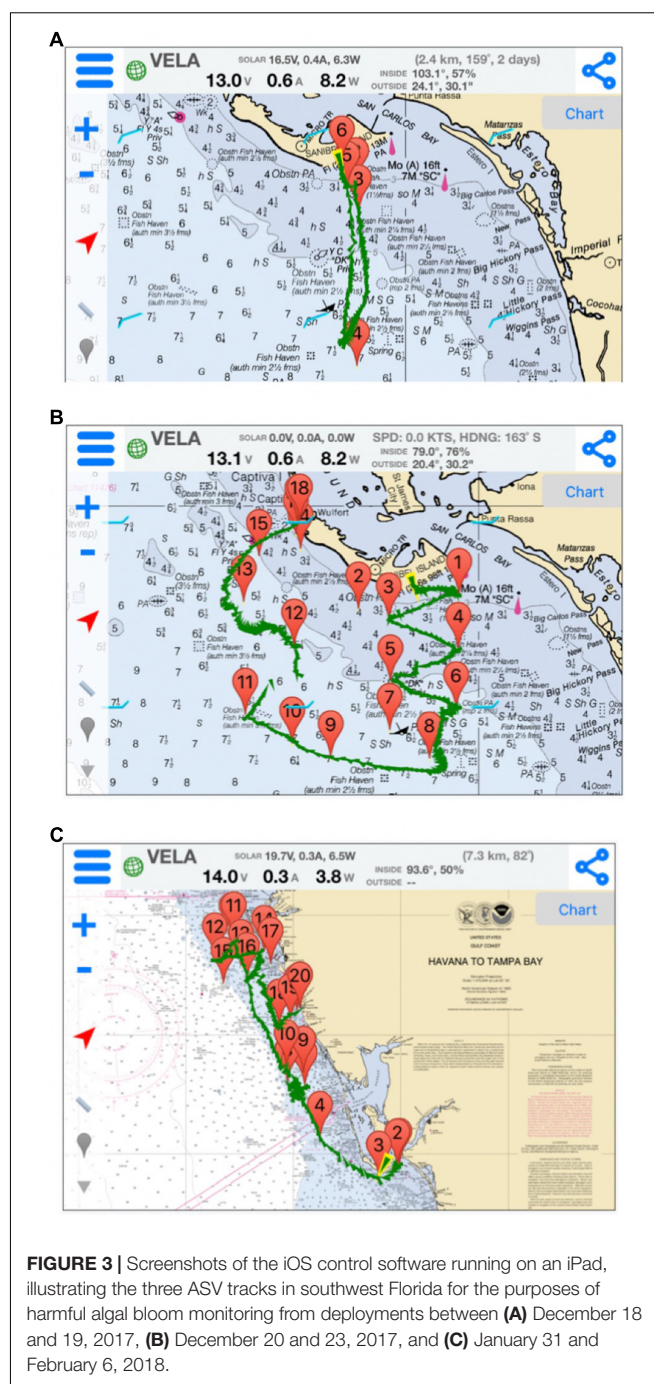
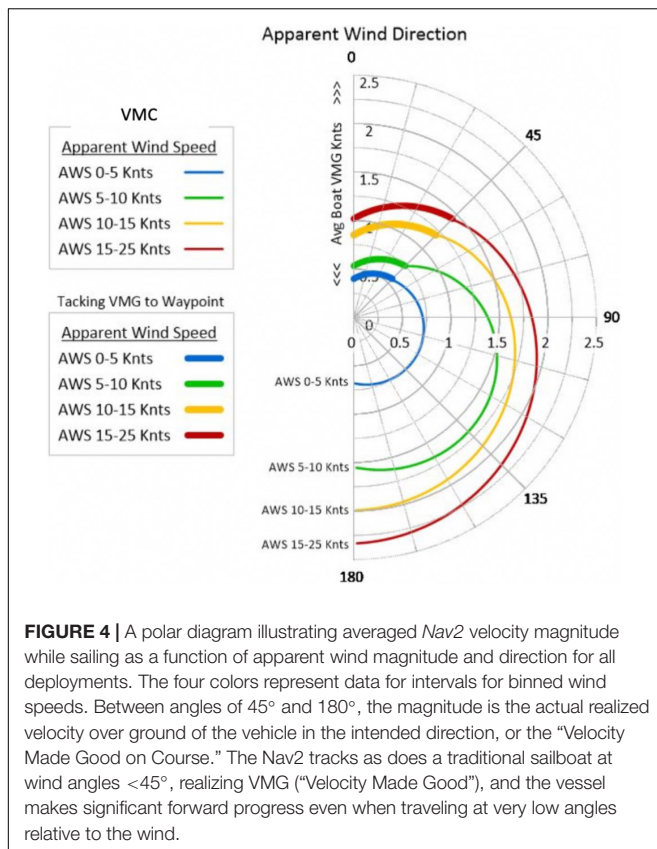


FIGURE 3 | Screenshots of the iOS control software running on an iPad, illustrating the three ASV tracks in southwest Florida for the purposes of harmful algal bloom monitoring from deployments between (A) December 18 and 19, 2017, (B) December 20 and 23, 2017, and (C) January 31 and February 6, 2018.

channels provide additional insights into particulate densities and environmental conditions. These results are placed in the context of ancillary/confirmatory low spatial resolution water sampling and satellite remote sensing measurements. Sentinel-3A level-1 data were acquired from the European Space Agency web portal² and processed to level 2 using NASA's SeaDAS package (version 7.5). Satellite chlorophyll and spectral remote sensing reflectance image data were extracted from Nav2 GPS matchup positions.

²<https://scihub.copernicus.eu/>

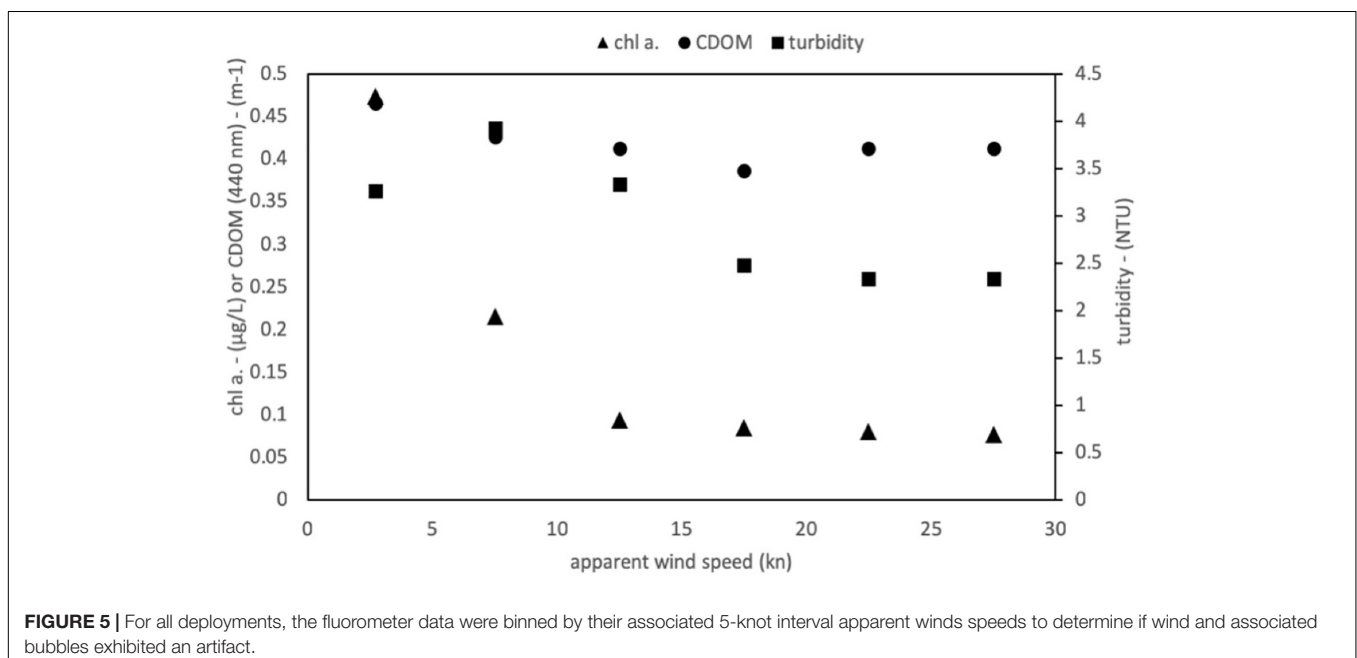


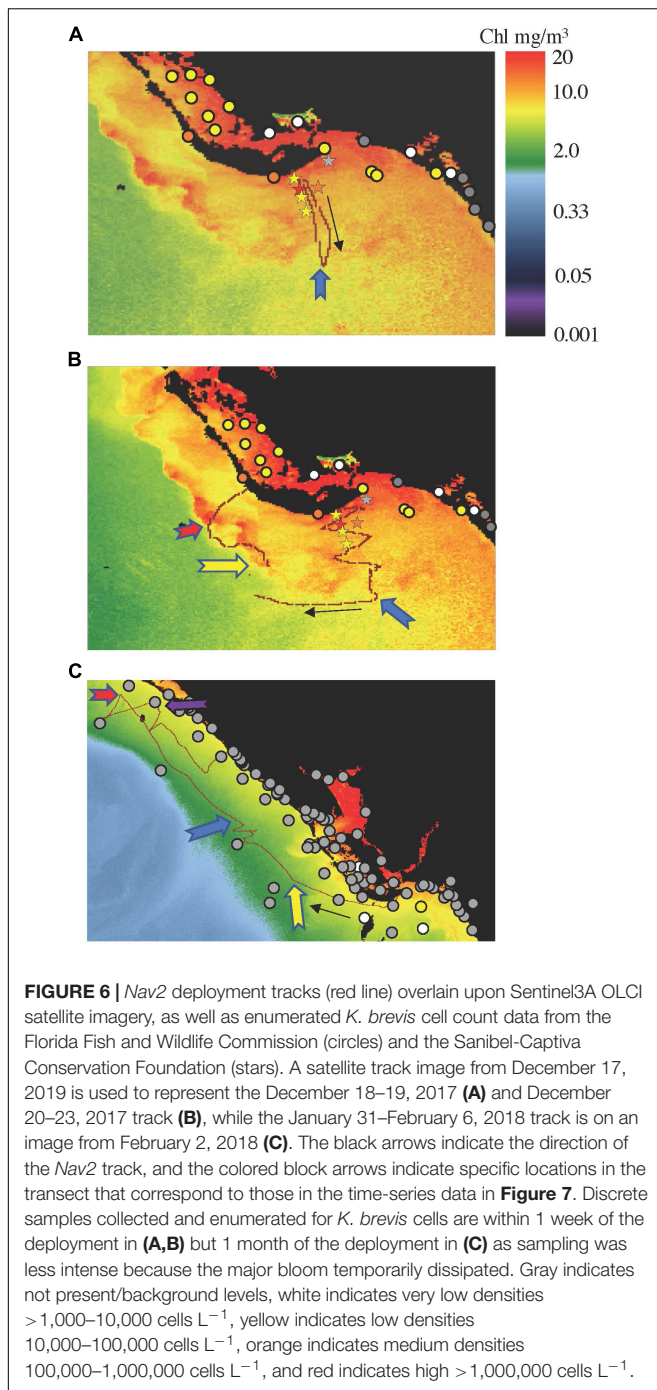
Two individual images from December 17, 2017 and February 1, 2018 were used to generate matchups for the three tracks. In this case, the two *Nav2* segments from December (December 19–24)

were applied to December 17, 2017, and the track data from January 31 to February 6 were applied to the February 1 image.

For the first two, shorter deployments, a large and intense *K. brevis* (Florida Red Tide) bloom was present nearshore (~2 km) toward which the vessel was directed (**Figures 6A,B**). These deployments simulate a potential mission to map spatial HAB bloom patterns in localized areas in response to a bloom, perhaps to guide adaptive sampling, generate semi-quantitative spatial maps and locate hotspots, and determine bloom heterogeneity (i.e., patchiness). The third deployment of 1-week duration on the other hand was intended to demonstrate the potential for the boat to be used for sustained, large-area monitoring, perhaps in a situation where no known blooms are expected, even in off-shore environments (**Figure 6C**). Generally, the spatial trends of the *in situ* fluorometric data were consistent with results from water samples and satellite imagery (**Figure 7**). Elevated chl. *a* south/southwest of Sanibel Island was probably due primarily to *K. brevis*, given that this species was identified locally at $>10^6$ cells L^{-1} (discrete samples in **Figures 6A–C**). However, chl. *a* concentrations derived via remote sensing (see color bars in **Figure 6** and satellite matchups in **Figures 7D–F**) were significantly higher than the *in situ* fluorometer data ($\sim 10\times$). *In situ* measurements also revealed more bloom heterogeneity than did the satellite data.

For the first deployment between December 18 and 19, 2017 (**Figure 6A**), the vessel encountered an elevated chl. *a* patch immediately south of the beach deployment location. Peak *in situ* concentrations in the patch were $\sim 6 \mu g L^{-1}$ but were more typically between 1 and $3 \mu g L^{-1}$. Interestingly, the initial *Nav2* transect (i.e., southward) only recorded chl. *a* concentrations less than $1.5 \mu g L^{-1}$, illustrating the heterogeneity within the patch. In contrast, the remotely sensed background patch was





larger and concentrations were higher, between 5 and 20 $\mu\text{g L}^{-1}$. The second deployment between December 20 and 23, 2017, again revealed a high degree of spatial heterogeneity. For the first portion of the deployment, chl. *a* concentrations rarely exceeded 2 $\mu\text{g L}^{-1}$. After traveling further west, the vessel soon encountered two chl. *a* patches greater than 5 $\mu\text{g L}^{-1}$, consistent with a concentrated bloom on the SW end of Sanibel observable via satellite (Figure 6B), which also illustrated a patchy distribution. For the final deployment beginning 5 weeks

later, between January 31 and February 6, 2018, *in situ* chl. *a* values were an order of magnitude lower than in December 2017. Just south of Sanibel Island, chl. *a* approached as high as 0.4 $\mu\text{g L}^{-1}$, but then remained less than 0.2 $\mu\text{g L}^{-1}$ for most of the remainder of the deployment. The higher values are consistent with the vessel being closer to shore, but also probably also with the residual bloom, as *K. brevis* cell counts were still detectable at very low concentrations to the west of the deployment location. Indeed, routine monitoring grab samples did not indicate the presence of *K. brevis*. While satellite chl. *a* was again much greater than the *in situ* Nav2 data, its relative magnitude also decreased by approximately an order of magnitude, with concentrations $\sim 5 \mu\text{g L}^{-1}$ nearshore and less than 2 $\mu\text{g L}^{-1}$ for the offshore portion of the deployment. Interestingly, several portions of the color track show conspicuously less chl. *a* when unexpected, such as traveling parallel to shore along an isobath. Upon further investigation, this phenomenon was revealed to be the result of diel variations (Figure 8C). Very distinct depressions of the chl. *a* signal were observed between the daylight hours of 1300 and 2300 UTC (8:00 am and 6:00 pm locally). These variations are likely explainable by vertical diel migration (Haphey-Wood, 1976) or by variations in pigment expression, quenching, or measurement artifacts (Babin et al., 1996). These intraday variations were not observed in other deployments where *K. brevis* was likely present (i.e., patchy, elevated chlorophyll in Figures 8A,B), or during the very first day of the 2018 deployment (most elevated chl. *a* values in Figure 7A near the probable *K. brevis*, consistent with the knowledge that this organism does not migrate downward during the day) (Schofield et al., 2006).

Turbidity and CDOM data provide further information regarding the environmental context of these organisms (Figures 7G–L), as well as evidence for the proper functioning of the Nav2/fluorometer package, i.e., that the data are consistent with expectations. The CDOM data are represented as absorption at 440 nm despite being fluorometrically obtained. While this is not traditional, we argue that an estimation of CDOM absorption is arguably more useful than representing data in more traditional units (e.g., quinine-sulfate units), and a linear response would be expected either way. Thus, while the CDOM magnitude may not be completely accurate (although values between 0.05 and 0.3 m^{-1} are consistent with CDOM data measured at the Caloosahatchee River outflow) (Del Castillo et al., 2000), the spatial variance in the observed CDOM should in fact be accurate. For all three deployments, CDOM increased nearshore, consistent with freshwater discharge from inlets, both at deployment and retrieval sites but also during mid-deployment transects (e.g., February 2, 2018; Figure 7I). Other increases appear associated with *K. brevis* patches (based on the chl. *a* signature) or river plumes (e.g., December 19, 2017; Figure 7G).

Along these lines, in the absence of a bloom and in a coastline receiving discharge from a single freshwater source, the CDOM data may serve as a rough proxy for salinity (although the presence of CDOM-generating HABs may affect accuracy). Turbidity, being measured as the amount of light scattered at 90° from a source at a

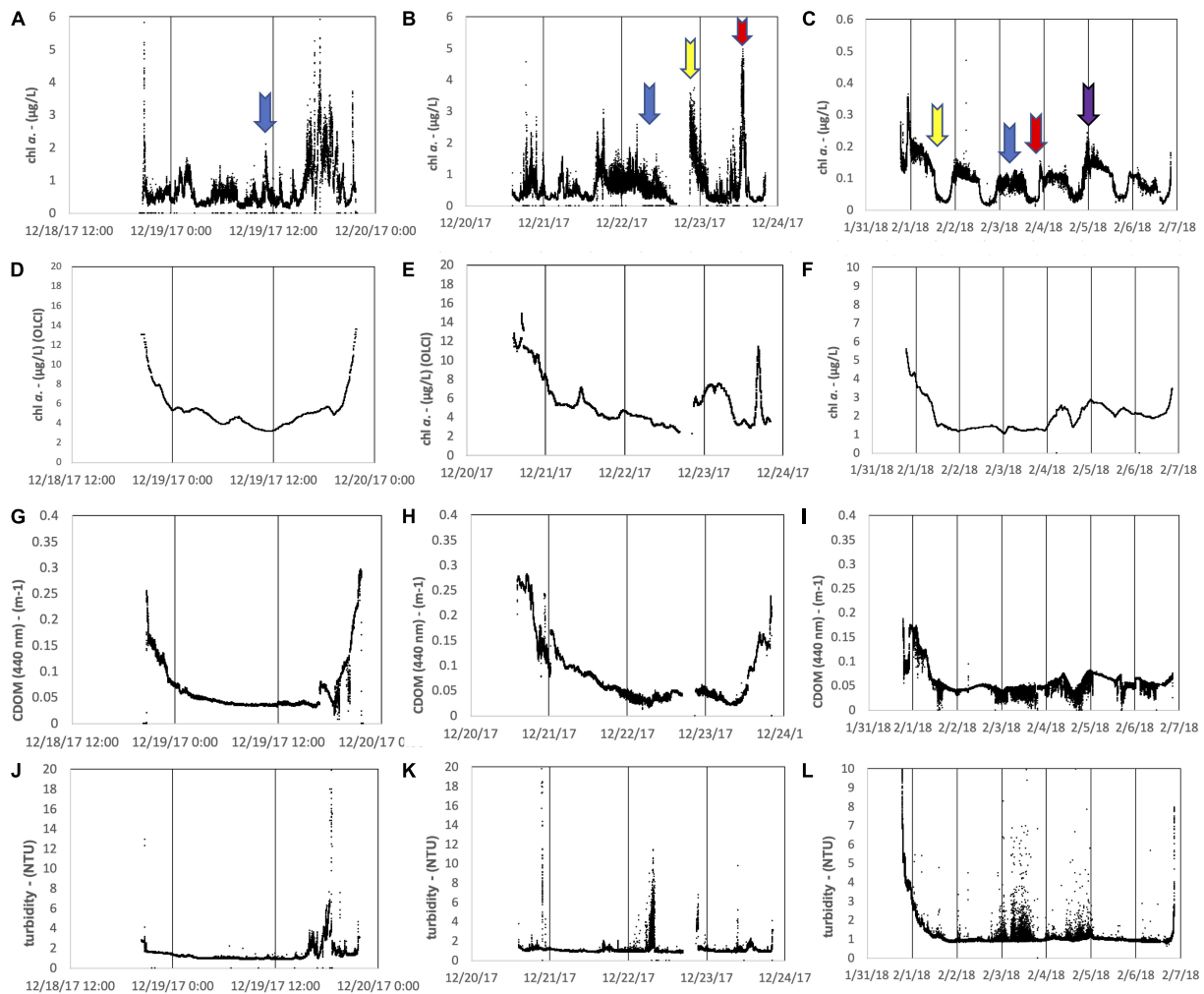


FIGURE 7 | For the December 18–19, 2017, December 20–23, 2017, and January 31–February 6, 2018 deployments, the Nav2 fluorometrically measured chl. *a* time series is represented in (A–C) respectively, Sentinel3A OLCI satellite chl. *a* is measured in (D–F). CDOM measured via fluorometric proxy is represented in (G–I), and turbidity is represented in (J–L). Note that the y-axis magnitudes are different for the January 31–February 6, 2018 deployment.

single wavelength, appears to more reflect a combination of suspended sediment and phytoplankton cells (Figures 7J–L). Turbidity measurements were more transient and less precise at a single location than CDOM (e.g., February 3 and 4, 2018; Figure 7L), consistent with transient suspended sediments and a heterogeneous water column. Winds were indeed in the 12- to 25-knot range on February 3 from around UTC 0600 to 2200, and then periodically elevated on February 4 throughout the day, which may provide an explanation for these observations. Turbidity increases were also observed near *K. brevis* bloom patches (evidenced by elevated chl. *a*; Figure 7J). It is notable that CDOM measurements have a higher precision than the turbidity measurements (e.g., Figures 7I, L). This is expected because the dissolved CDOM will be much more homogeneously mixed than will particulates measured via turbidity.

Interestingly, the Sentinel3 OLCI satellite matchup data (Figures 7D–F) matched much more closely with Nav2 CDOM

measured *in situ* with the fluorometer (Figures 7G–I) than it did with either chl. *a* or turbidity Nav2 measurements. Correlation coefficients between OCLI CDOM and Nav2 CDOM were between 0.65 and 0.39 (Table 3), with the strength of the correlation decreasing with increasing mission duration, probably an analytical artifact because a single satellite image corresponding to a single day was compared to multiple-day Nav2 missions.

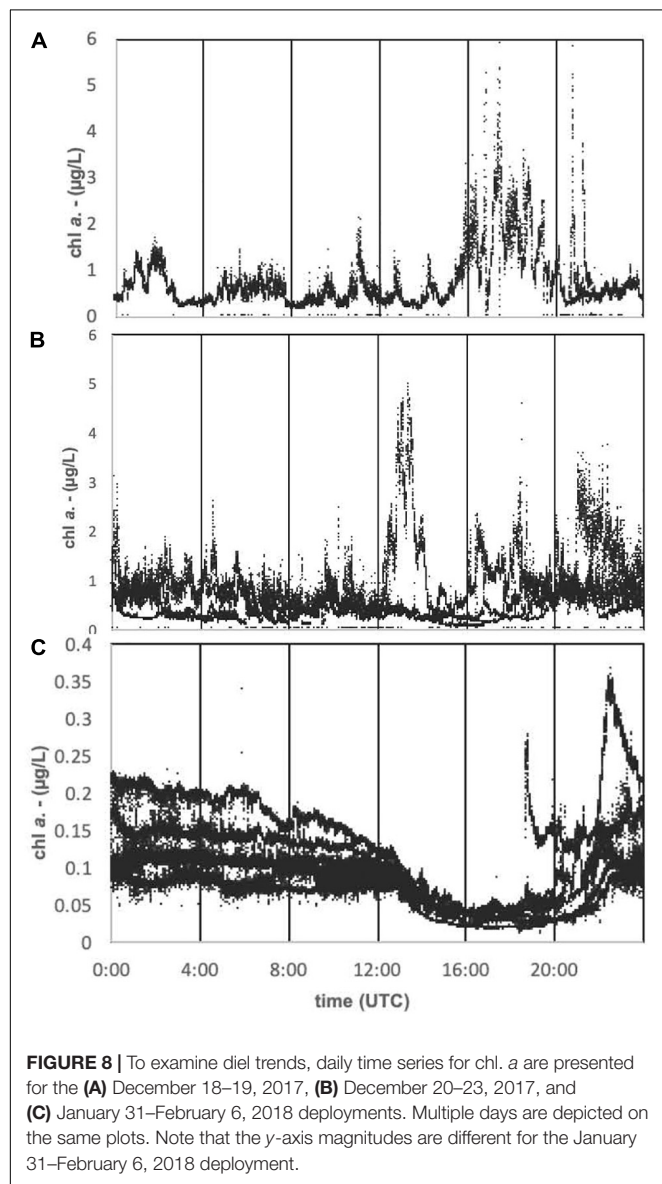
DISCUSSION

Platform Functionality

Though three deployments of increasing duration, the Nav2 autonomous sail vehicle successfully demonstrated the potential for the platform to provide mobile, unattended monitoring of the surface coastal ocean. The Nav2 is a unique platform in that it is small enough to be deployed in coastal and inland waters, and by

TABLE 3 | Sentinel3 satellite (OLCI) chl. *a* data matchup statistics revealed from linear regression analysis when correlated to each of the parameters measured using *in situ* fluorometry by the *Nav2* boat.

Nav2 fluorometer measurement	OLCI chl. <i>a</i> matchup (1-day mission begin December 18, 2017)			OLCI chl. <i>a</i> matchup (3-day mission began December 21, 2018)			OLCI chl. <i>a</i> matchup (7-day mission began January 31, 2018)		
	<i>n</i>	<i>R</i> ²	<i>p</i>	<i>n</i>	<i>R</i> ²		<i>n</i>	<i>R</i> ²	
Chl. <i>a</i>	18,221	0.0008	1.85E−4	52,587	0.015	<0.0001	103,881	0.39	<0.0001
CDOM	18,221	0.65	<0.0001	52,587	0.59	<0.0001	103,881	0.39	<0.0001
Turbidity	18,221	0.057	<0.0001	52,587	0.012	<0.0001	103,881	0.36	<0.0001



functioning identically to a real sailboat, it can obtain high speeds relative to most other autonomous ocean-going platforms and accurately navigate and map areas of interest. The deployments

demonstrated that the vessel is robust enough to reliably operate and survey under non-ideal sea states with winds up to 25 knots (although we have tested the vehicle in winds > 30 knots in coastal waters of New England and Washington State and more recently > 40 knots on the east coast of Florida, unpublished). Under conditions encountered in southwest Florida with winds averaging less than 4 knots, however, the boat still managed to cover 17–22 NM per day, and 29 NM per day with winds averaging eight knots (Table 2). These winds were not necessarily directed from behind the boat; indeed, the vessel can sail into the wind via autonomous tacking, under which significant forward progress is still made at a VMG of 10 NM per day (Figure 4). The vessel is capable of efficiently reaching preselected (or adjusted on the fly) waypoints (Figures 2, 3). On the other hand, during deployment and retrieval, the boat can be operated manually in sailing mode, or with a thruster (Table 2). The thruster is particularly useful in areas of high currents or ship traffic. Using the thruster only, the *Nav2* can be used for short missions (up to 48 h) without the sail. The thruster is manually operated by the user depending on vehicle performance under sail propulsion.

We demonstrated deployments of up to 1 week. The vessel was operating exceptionally at the time of retrieval and could have continued longer. Indeed, *Nav2* deployments since the time of writing this report have lasted for 15 + days. Power efficiency improvements are ongoing with multi-sensor, multi-month mission lengths feasible. Approximately 1–5 W extra power is available for sensors. The power availability and length of mission will vary with solar conditions. In solar conditions typical of Florida, the panels typically provide an average of 200 W h day^{−1}. In low-light conditions typical of northern latitudes in the winter, mission planning needs to be adjusted accordingly.

Deployment or retrieval of the *Nav2* is simple but exciting and can be achieved from a boat ramp or from the beach under calm seas by a single operator. All three deployments described herein were initiated from the beach. For deployment, the operator simply walks the small hand-held trailer into the surf zone into waist-deep water until it is floating, and then slides the trailer out from underneath the vessel. The operator can leave the iOS device on shore during the actual deployment or place it into a waterproof case and hold with a lanyard. For retrieval, the vehicle can be lifted back onto its wheel cart by hand in shallow water and then pulled on shore. The *Nav2* is also capable of being lifted from the water directly from a small boat. An easily overlooked aspect of using the vehicle is the attention that it garners from

beachgoers. This is an opportunity for community outreach, and the southwest Florida HAB monitoring deployments were met with great inquiry and enthusiasm, eventually becoming the subject of several media features. Unfortunately, however, this curiosity also led to mission interruption on December 22, 2017, when a recreational boater pulled the *Nav2* from the water and proceeded toward shore until seeing the contact information and statement on the ASV. Under extremely low winds, if the vessel is not obviously making forward progress, it can appear “lost.” Of course, theft is always an issue, especially of a smaller 2-m-long boat. Future versions of the vehicle are expected to be slightly larger to hold a larger number of sensors; this may also serve the dual purpose of being a theft deterrent. The “curiosity” effect has been better managed since these deployments by adding a large bold statement directly on the sail indicating the *Nav2* is a “RESEARCH VESSEL” “TRACKED AND MONITORED AT ALL TIMES.” Boaters are increasingly aware that drones of all types on land or sea are carefully monitored. No problems with curiosity or theft have occurred since. Other ongoing improvements with the *Nav2* vehicle include an increased vehicle size to more easily accommodate a variety of sensors, the integration and testing of additional sensors, refinements to the autonomous steering algorithm to reduce oversteering and increase average speed, improved consistency of performing desirable straight data collection transects in variable currents, and improved power efficiency to provide greater power for sensors and in low-light conditions.

Applications for Marine HAB Monitoring

The utility of the platform was demonstrated for the specific application of harmful algal bloom monitoring of the Florida Red Tide species *K. brevis*. The recurring *K. brevis* blooms ravaging southwest Florida are challenging to monitor because blooms are most detrimental nearshore but in many cases are transported shoreward from deeper waters (Vargo, 2009). Depth-resolved measurements are ideal and have been routinely obtained with AUV buoyancy gliders as part of the State of Florida monitoring program. These deployments have provided extremely valuable insights into waters > 10 m deep. In shallower systems, however, gliders progress slowly horizontally, especially in physically dynamic environments. Gliders are also more expensive to operate in shallow waters (they require more frequent attention and battery and buoyancy pump servicing), prohibiting continuous operation. Finally, gliders possess a limited selection of sensors and face many sensor design constraints especially when fluidics are involved (as buoyancy is affected), currently limiting the wide use of species-level detection techniques. Regardless, by the time *K. brevis* blooms approach the coast within a few kilometers, they are usually at the surface of a well-mixed water column and the need for depth-resolved measurements is decreased (Robbins et al., 2006). Thus, there will, for the foreseeable future, be a niche that must be filled for sustained coastal surface monitoring for this species.

The work presented herein used a fluorometric chl. *a* sensor, which has since 2015 been the primary sensor employed on Slocum buoyancy gliders for *K. brevis* monitoring by the State of Florida. The success of the platform/sensor combination for

monitoring *K. brevis* and in generating high-quality fluorometric data is demonstrated by good relationships between water sample *K. brevis* cell counts (i.e., highest chl. *a* measured nearshore and to the SW in **Figures 6, 7**), good matchup to satellite remotely sensed chl. *a* in the areas with the most intense blooms (i.e., nearshore in **Figure 6A** and to the west in **Figure 6B**), repeatable diel variations (**Figure 8C**), high resolution of bloom “patchiness” (**Figures 7A–C**), obtainment of reasonable ancillary fluorometric data (**Figures 7G–L**), and a lack of discernible bubble artifacts (**Figure 5**). The reproducible diel *Nav2* chl. *a* variations during the 7-day mission in which the vessel encountered Beaufort sea states as high as 5 suggest that bubbles are not an issue (**Figure 8**). Overall, the excellent time resolution and reproducibility (i.e., **Figure 8C**) of the measurements highlight the appropriateness of the platform for use in surface water quality monitoring when employing a fluorometric sensor.

Interestingly, the chl. *a* data obtained *in situ* were of much lower concentration than those detected by satellite. These variations are expected based on the very different nature of the measurements. Satellite measurements integrate over a depth interval and calculated concentrations are therefore representative of an average concentration of the surface water column. Fluorometric chl. *a* is only considered to be semi-quantitative, so absolute chl. *a* concentrations are probably not as informative as spatial variations. *In situ* chl. *a* measurements reveal much greater spatial variability than the satellite measurements, consistent with our knowledge of *K. brevis* in which cell concentrations can easily vary by an order of magnitude just a few meters from each other. Satellite measurements are also more challenging in turbid and CDOM-rich optically complex waters where we conducted the deployments. Indeed, the far greater correlation between *Nav2* chl. *a* and OLCI CDOM (**Table 3**) is sensible in this context. Indeed, certain regional correction algorithms have been demonstrated to be more accurate for determining the presence of *K. brevis*, and these may be evaluated in the future (Hu et al., 2005). Overall, however, results serve as justification for the investment into compatible HAB species-specific sensors and satellite algorithms.

An unexpected result was the repeatable diel variations observed during the longer mission (**Figure 8C**). Fluorometric measurements of chl. *a* can be subject to solar-induced photoinhibition (e.g., Kiefer, 1973), various packaging effects, and fluorescence quenching, especially at higher concentrations. Numerous accessory pigments can also contribute to the signal (Babin et al., 1996; Schofield et al., 2006). Similar results are routinely observed on the West Florida Shelf during multi-day, routine glider missions in which no *K. brevis* is present based on cell counts (example datasets are available in the GCOOS repository)³. *K. brevis* cells exhibit positive phototaxis migratory behavior during the daylight hours, which may increase the fluorescence signature (Schofield et al., 2006). *K. brevis* blooms also typically dominate the taxa when present and exhibit extreme small-scale spatial variability. We therefore propose that in this

³https://gandalf.gcoos.org/data/gandalf/mote/mote-genie/2016/2016_12_12/plots/

geographic region subject to frequent *K. brevis* blooms, elevated and patchy chl. *a* patterns like those in **Figures 8A,B** that far exceed a background diel signature (i.e., **Figure 8C**) can be used as a potential signature for *K. brevis*. While the presence of the organism would of course need to be verified, the *Nav2* dataset could, in this fashion, be used to guide adaptive sampling. With a fleet of *Nav2* vehicles traveling ~20 NM per day in a repeatable triangular or “lawnmower” raster pattern, several vehicles have the potential to continuously survey a large area, regardless of water depth. The *Nav2* equipped with a fluorometer, while perhaps not as accurate at a species level as satellite remote sensing using the most current and optimal algorithms, can reveal *K. brevis* surface heterogeneity at a high spatial resolution once a bloom has been confirmed.

Other Monitoring Applications

While chl. *a* measurements were the primary focus of this project, the ancillary fluorometric data streams also shed light on some in-water processes and allude to future applications of the *Nav2* vessel. The fluorescence response of organic matter has been extensively used as a proxy since terrestrially based coastal CDOM can, for discrete regions and time intervals, display nearly linear relationships with salinity and FDOM (Coble, 1996; Del Castillo et al., 2000). CDOM is of interest to biogeochemists for its role in dominating ocean color, playing a critical role in photobiology, photochemistry (Helms et al., 2008), and photoproduction of CO₂ (Clark et al., 2004), contributing to aspects of the oceanic sulfur cycle (Gali et al., 2016), and controlling the absorption of light energy and the subsequent impacts on heat flux (Hill, 2008) and other ocean–climate interactions, and in serving as a tracer of freshwater (Fichot and Benner, 2012). The fluorometrically measured CDOM exhibited intensities and spatial concentration distributions that are expected in southwest Florida (Del Castillo et al., 2000). Earlier in the project, we did install a conductivity-temperature-depth CTD package onto the vehicle. However, conductivity measurements were unreasonable, perhaps because the CTD was configured immediately behind the rudder in an area where bubble creation is visibly intense. While we still aim to resolve this issue with a different installation configuration, it is worth considering the use of CDOM as a rough proxy for salinity, with the assumption that there is a single source of freshwater input that has a high CDOM concentration (i.e., the Charlotte Harbor and the Caloosahatchee River). The use of CDOM as a rough proxy for salinity has been well demonstrated by several research groups and is one of the primary means to estimate salinity from remote sensing as long as the regional proxy is well defined and the inputs into the system are known (Bowers and Brett, 2008; Del Castillo and Miller, 2008).

The *Nav2* is inherently a meteorological sensor (e.g., for wind speed and magnitude, atmospheric temperature, and humidity). Previously, the *Nav2* has been successfully configured with fisheries sensors, including a pinger tracking hydrophone system (Sonotronics) and a cetacean and noise monitoring hydrophone (Song Meter). Trials demonstrated successful location of crab tracking pingers on the Washington coast and acoustic detection of various cetacean species. As of the time of writing, we are

currently adding a Wetlabs BB3 Scatterometer and a Solinst CT logger for HABs surveys on Lake Okeechobee and the Indian River Lagoon in Florida. Addition of Oxygen/Temp Optode (Aanderaa AADI) and CT sensors as well as an ADCP (Nortec) are under consideration to provide a complete water quality monitoring suite.

CONCLUSION

The Navocean autonomous sail vehicle (*Nav2*) has been demonstrated to serve as a reliable mobile platform for wide-area surface coastal monitoring. To our knowledge, this is the first demonstration of a sail-driven vessel used for coastal HAB monitoring. The scientific results were shown to be reasonable and demonstrate the potential for mapping unispecies HAB blooms and guiding adaptive sampling, while simultaneously collecting important environmental data. While the *Nav2* does not capture depth variations or collect instantaneous large surface area measurements as do underwater gliders and satellites, respectively, the platform is a useful tool in a larger arsenal for coastal or inland monitoring. The primary benefits of using the *Nav2* vehicle are that it is fast and has reliable, autonomous navigation, has a completely renewable power source with no consumables, can function in shallow or deep water inland or offshore, and is operable by a single person. There are several additional demonstrated payload options as well as some currently in preparation. At least with the planar-style optical sensors, bubbles do not appear to contribute significant artifacts.

Harmful cyanobacterial blooms are also increasing in intensity in global freshwater bodies (Paerl et al., 2018). The *Nav2* vehicle is ideal for monitoring blooms in these frequently shallow lakes, especially by limnologists who may have less training with more traditional oceanographic tools. To this end, we have recently deployed the *Nav2* for freshwater *M. aeruginosa* HAB monitoring in Lake Okeechobee in February 2019. A second three-channel fluorometer was installed to provide phycocyanin and phycoerythrin measurements that help discriminate multiple algal species. The deployment garnered press from at least eight news outlets and the vehicle successfully navigated a series of transects in the lake (available on GCOOS Gandalf, 2019 data archive). Until the summer of 2018, there were few traditional monitoring efforts and no real-time water quality monitoring sensors on Lake Okeechobee, and even now, only one stationary optical sensor is providing ground-truthing data for satellite efforts. We plan in the future to augment this fixed location monitoring with *Nav2* surveys to both add a mobile monitoring element and constrain the spatial variability of the surface optical properties in relation to remote sensing data. Ultimately, we envision the *Nav2* platform becoming a critical tool in multiple monitoring programs.

AUTHOR CONTRIBUTIONS

JB authored the manuscript, provided scientific oversight, and participated in field campaigns. EA was the lead designer of

the autonomous vehicle hardware and software. TM performed the satellite matchup validation. BC developed the live data visualization interface. EM coordinated the field campaigns. SD designed the sailboat and conducted the deployments.

FUNDING

This work was supported in part by a National Academies Gulf Research Program Early-Career Fellowship award #2000007281

REFERENCES

- Anderson, D. M., Glibert, P. M., and Burkholder, J. M. (2002). Harmful algal blooms and eutrophication: nutrient sources, composition, and consequences. *Estuaries* 25, 704–726. doi: 10.1007/bf02804901
- Babin, M., Morel, A., and Gentili, B. (1996). Remote sensing of sea surface sun-induced chlorophyll fluorescence: consequences of natural variations in the optical characteristics of phytoplankton and the quantum yield of chlorophyll a fluorescence. *Int. J. Remote Sens.* 17, 2417–2448. doi: 10.1080/01431169608948781
- Backer, L. C., McNeel, S. V., Barber, T., Kirkpatrick, B., Williams, C., Irvin, M., et al. (2010). Recreational exposure to microcystins during algal blooms in two California lakes. *Toxicon* 55, 909–921. doi: 10.1016/j.toxicon.2009.07.006
- Bowers, D. G., and Brett, H. L. (2008). The relationship between CDOM and salinity in estuaries: an analytical and graphical solution. *J. Mar. Sys.* 73, 1–7. doi: 10.1016/j.jmarsys.2007.07.001
- Bowers, H., and Smith, G. J. (2017). “Sensors for monitoring of harmful algae, cyanobacteria and their toxins,” in *Workshop Proceedings*, ed. A. F. C. Technologies (Moss Landing, CA: Moss Landing Marine Laboratories).
- Brand, L. E., and Compton, A. (2007). Long-term increase in *Karenia brevis* abundance along the Southwest Florida coast. *Harmful Algae* 6, 232–252. doi: 10.1016/j.hal.2006.08.005
- Carmichael, W. W. (2001). Health effects of toxin-producing cyanobacteria: “The CyanoHABs”. *Hum. Ecol. Risk Assess. Int. J.* 7, 1393–1407. doi: 10.1080/20018091095087
- Clark, C. D., Hiscock, W. T., Millero, F. J., Hitchcock, G., Brand, L., Miller, W. L., et al. (2004). CDOM distribution and CO₂ production on the southwest Florida shelf. *Mar. Chem.* 89, 145–167. doi: 10.1016/j.marchem.2004.02.011
- Coble, P. G. (1996). Characterization of marine and terrestrial DOM in seawater using excitation emission matrix spectroscopy. *Mar. Chem.* 51, 325–346. doi: 10.1016/0304-4203(95)00062-3
- Daniel, T., Manley, J., and Trenaman, N. (2011). The wave glider: enabling a new approach to persistent ocean observation and research. *Ocean Dyn.* 61, 1509–1520. doi: 10.1007/s10236-011-0408-5
- Del Castillo, C. E., Gilbes, F., Coble, P. G., and Muller-Karger, F. E. (2000). On the dispersal of riverine colored dissolved organic matter over the West Florida Shelf. *Limnol. Oceanogr.* 45, 1425–1432. doi: 10.4319/lo.2000.45.6.1425
- Del Castillo, C. E., and Miller, R. (2008). On the use of ocean color remote sensing to measure the transport of dissolved organic carbon by the Mississippi River Plume. *Remote Sens. Environ.* 112, 836–844. doi: 10.1016/j.rse.2007.06.015
- Ducharme, J. (2018). Red tide is killing marine life and scaring away tourists in Florida. Here's what to know about it *Time Magazine Online*. doi: 10.1016/j.rse.2007.06.015
- Fichot, C. G., and Benner, R. (2012). The spectral slope coefficient of chromophoric dissolved organic matter (S_{275–295}) as a tracer of terrigenous dissolved organic carbon in river-influenced ocean margins. *Limnol. Oceanogr.* 57, 1453–1466. doi: 10.4319/lo.2012.57.5.1453
- Fleming, L. E., Rivero, C., Burns, J., Williams, C., Bean, J. A., Shea, K. A., et al. (2002). Blue green algal (cyanobacterial) toxins, surface drinking water, and liver cancer in Florida. *Harmful Algae* 1, 157–168. doi: 10.1016/s1568-9883(02)00026-4
- Gali, M., Kieber, D. J., Romera-Castillo, C., Kinsey, J. D., Devred, E., Perez, G. L., et al. (2016). CDOM sources and photobleaching control quantum yields for oceanic DMS photolysis. *Environ. Sci. Technol.* 50, 13361–13370. doi: 10.1021/acs.est.6b04278
- GCOOS Gandalf (2019). *The Gulf AUV Network and Data Archiving Long-term Storage Facility*. https://gandalf.gcoos.org/data/gandalf/mote/mote-genie/2016/2016_12_12/plots/ (accessed June 8, 2019).
- Gannon, D. P., Berens McCabe, E. J., Camilleri, S. A., Gannon, J. G., Brueggen, M. K., Barleycorn, A. A., et al. (2009). Effects of *Karenia brevis* harmful algal blooms on nearshore fish communities in southwest Florida. *Mar. Ecol. Prog. Ser.* 378, 171–186. doi: 10.3354/meps07853
- Happy-Wood, C. M. (1976). Vertical migration patterns in phytoplankton of mixed species composition. *Br. Phycol. J.* 11, 355–369. doi: 10.1080/00071617600650411
- Helms, J. R., Stubbins, A., Ritchie, J. D., Minor, E. C., Kieber, D. J., and Mopper, K. (2008). Absorption spectral slopes and slope ratios as indicators of molecular weight, source, and photobleaching of chromophoric dissolved organic matter. *Limnol. Oceanogr.* 53, 955–969. doi: 10.4319/lo.2008.53.3.0955
- Hill, V. J. (2008). Impacts of chromophoric dissolved organic material on surface ocean heating in the Chukchi Sea. *J. Geophys. Res. Oceans* 113:C07024.
- Hoagland, P., Jin, D., Polansky, L. Y., Kirkpatrick, B., Kirkpatrick, G., Fleming, L. E., et al. (2009). The costs of respiratory illnesses arising from Florida Gulf Coast *Karenia brevis* blooms. *Environ. Health Perspect.* 117, 1239–1243. doi: 10.1289/ehp.0900645
- Hu, C., Muller-Karger, F. E., Taylor, C., Carder, K. L., Kelble, C., Johns, E., et al. (2005). Red tide detection and tracing using MODIS fluorescence data: a regional example in SW Florida coastal waters. *Remote Sens. Environ.* 97, 311–321. doi: 10.1016/j.rse.2005.05.013
- Kiefer, D. A. (1973). Fluorescence properties of natural phytoplankton populations. *Mar. Biol.* 22, 263–269. doi: 10.1007/bf00389180
- Kirkpatrick, B., Fleming, L. E., Backer, L. C., Bean, J. A., Tamer, R., Kirkpatrick, G., et al. (2006). Environmental exposures to Florida red tides: effects on emergency room respiratory diagnoses admissions. *Harmful Algae* 5, 526–533. doi: 10.1016/j.hal.2005.09.004
- McCabe, R. M., Hickey, B. M., Kudela, R. M., Lefebvre, K. A., Adams, N. G., Bill, B. D., et al. (2016). An unprecedented coastwide toxic algal bloom linked to anomalous ocean conditions. *Geophys. Res. Lett.* 43, 10366–10376.
- Mordy, C. W., Cokelet, E. D., De Robertis, A., Jenkins, R., Kuhn, C. E., Lawrence-Slavas, N., et al. (2017). Advances in ecosystem research saildrone surveys of oceanography, fish, and marine mammals in the Bering Sea. *Oceanography* 30, 113–115.
- O’Neil, J. M., Davis, T. W., Burford, M. A., and Gobler, C. J. (2012). The rise of harmful cyanobacteria blooms: the potential roles of eutrophication and climate change. *Harmful Algae* 14, 313–334. doi: 10.1016/j.hal.2011.10.027
- Paerl, H. W., Otten, T. G., and Kudela, R. (2018). Mitigating the expansion of harmful algal blooms across the freshwater-to-marine continuum. *Environ. Sci. Technol.* 52, 5519–5529. doi: 10.1021/acs.est.7b05950
- Reich, A., Lazensky, R., Faris, J., Fleming, L. E., Kirkpatrick, B., Watkins, S., et al. (2015). Assessing the impact of shellfish harvesting area closures on neurotoxic shellfish poisoning (NSP) incidence during red tide (*Karenia brevis*) blooms. *Harmful Algae* 43, 13–19. doi: 10.1016/j.hal.2014.12.003
- Robbins, I. C., Kirkpatrick, G. J., Blackwell, S. M., Hillier, J., Knight, C. A., and Moline, M. A. (2006). Improved monitoring of HABs using autonomous underwater vehicles (AUV). *Harmful Algae* 5, 749–761. doi: 10.1016/j.hal.2006.03.005

ACKNOWLEDGMENTS

We would like to thank L. Kellie Dixon, Jim Hillier, and Karl Henderson at Mote, and last but not least our former high school intern Gabriel Rey for assistance with the field work.

- Schofield, O., Kerfoot, J., Mahoney, K., Moline, M., Oliver, M., Lohrenz, S., et al. (2006). Vertical migration of the toxic dinoflagellate *Karenia brevis* and the impact on ocean optical properties. *J. Geophys. Res. Oceans* 111:C06009.
- Scholin, C. A., Gulland, F., Doucette, G. J., Benson, S., Busman, M., Chavez, F. P., et al. (2000). Mortality of sea lions along the central California coast linked to a toxic diatom bloom. *Nature* 403, 80–84. doi: 10.1038/47481
- Shapiro, J., Dixon, L. K., Schofield, O. M., Kirkpatrick, B., and Kirkpatrick, G. J. (2015). “Chapter 18—New sensors for ocean observing: The optical phytoplankton discriminator,” in *Coastal Ocean Observing Systems*, eds Y. Liu, H. Kerkering, and R. H. Weisberg (Boston: Academic Press), 326–350. doi: 10.1016/b978-0-12-802022-7.00018-3
- Smith, D. R., King, K. W., and Williams, M. R. (2015). What is causing the harmful algal blooms in Lake Erie? *J. Soil Water Conserv.* 70, 27A–29A. doi: 10.2489/jswc.70.2.27a
- Stockley, N. D., Sullivan, J. M., Hanisak, D., and McFarland, M. N. (2018). “Using observation networks to examine the impact of Lake Okeechobee discharges on the St. Lucie Estuary, Florida,” in *Proceedings of SPIE Defense + Security*, (Bellingham, WA: SPIE), 8.
- Vargo, G. A. (2009). A brief summary of the physiology and ecology of *Karenia brevis* Davis (G. Hansen and Moestrup comb. nov.) red tides on the West Florida Shelf and of hypotheses posed for their initiation, growth, maintenance, and termination. *Harmful Algae* 8, 573–584. doi: 10.1016/j.hal.2008.11.002

Conflict of Interest: EA and SD were employed by Navocean, Inc.

The remaining authors declare that the research was conducted in the absence of any commercial or financial relationships that could be construed as a potential conflict of interest.

Copyright © 2019 Beckler, Arutunian, Moore, Currier, Milbrandt and Duncan. This is an open-access article distributed under the terms of the Creative Commons Attribution License (CC BY). The use, distribution or reproduction in other forums is permitted, provided the original author(s) and the copyright owner(s) are credited and that the original publication in this journal is cited, in accordance with accepted academic practice. No use, distribution or reproduction is permitted which does not comply with these terms.



Virtual Reality and Oceanography: Overview, Applications, and Perspective

Noah L. Walcutt¹, Benjamin Knörlein², Tom Sgouros³, Ivona Cetinić^{4,5} and Melissa M. Omand^{1*}

¹ Graduate School of Oceanography, University of Rhode Island, Narragansett, RI, United States, ² Center for Computation and Visualization, Brown University, Providence, RI, United States, ³ Department of Computer Science, Brown University, Providence, RI, United States, ⁴ Ocean Ecology Laboratory, NASA Goddard Space Flight Center, Greenbelt, MD, United States, ⁵ GEAR/Universities Space Research Association, Columbia, MD, United States

OPEN ACCESS

Edited by:

Eric Delory,
Oceanic Platform of the Canary
Islands, Spain

Reviewed by:

Martin Pratt,
Washington University in St. Louis,
United States
Benoît Pirenne,
Ocean Networks Canada, Canada

*Correspondence:

Melissa M. Omand
momand@uri.edu

Specialty section:

This article was submitted to
Ocean Observation,
a section of the journal
Frontiers in Marine Science

Received: 15 November 2018

Accepted: 01 October 2019

Published: 17 October 2019

Citation:

Walcutt NL, Knörlein B, Sgouros T,
Cetinić I and Omand MM (2019)
Virtual Reality and Oceanography:
Overview, Applications, and
Perspective. *Front. Mar. Sci.* 6:644.
doi: 10.3389/fmars.2019.00644

With the ongoing, exponential increase in ocean data from autonomous platforms, satellites, models, and in particular, the growing field of quantitative imaging, there arises a need for scalable and cost-efficient visualization tools to interpret these large volumes of data. With the recent proliferation of consumer grade head-mounted displays, the emerging field of virtual reality (VR) has demonstrated its benefit in numerous disciplines, ranging from medicine to archeology. However, these benefits have not received as much attention in the ocean sciences. Here, we summarize some of the ways that virtual reality has been applied to this field. We highlight a few examples in which we (the authors) demonstrate the utility of VR as a tool for ocean scientists. For oceanic datasets that are well-suited for three-dimensional visualization, virtual reality has the potential to enhance the practice of ocean science.

Keywords: virtual reality, VR, oceanography, data visualization, digital holographic microscopy

1. INTRODUCTION

Virtual Reality (VR) allows a user to immerse herself in a computer generated environment. The feeling of presence (Slater and Wilbur, 1997) is therein generated by simulating sensory feedback of the environment in response to a user's action. This allows a user to coexist and interact with virtual entities in the same three-dimensional space. Various display technologies have evolved to facilitate these experiences. While most systems only simulate visual and auditory feedback, e.g., head-mounted displays (Sutherland, 1968) or room-scaled CAVE environments (Cruz-Neira et al., 1992), the feedback can also stimulate other senses, e.g., proprioceptive, or haptic sensations. In VR, a user perceives only the computer generated content while the real world is absent. In contrast, Augmented Reality (AR) and Mixed Reality (MR) overlay the virtual simulation on top of the real world creating a mixture of real and virtual feedback perceived in collocated space.

Researchers from a range of scientific disciplines have benefited from the application of virtual reality. At the Brown University Center for Computation and Visualization (CCV), over two decades of interdisciplinary visualization collaborations paved the way for state-of-the-art scientific VR applications today. While VR visualization takes varying degrees of effort to achieve, the benefits of visualizing scientific data in VR include faster analysis, greater spatial understanding, and new types of exploration (LaViola et al., 2009). Interest in developing VR applications has intensified recently with the development of cost-effective consumer grade head-mounted

displays (HMD), which have made the benefits of interactive VR-based scientific visualization more widely accessible (Castelvecchi, 2016; Matthews, 2018). With the ongoing, exponential increase in oceanographic datasets resolution, coverage, and diversity, there arises the need for scalable and cost-efficient visualization tools to begin to interpret these large volumes and varieties of data (Huang et al., 2015; Liu et al., 2017).

Here, we describe the outcomes and lessons learned from a collaboration between Brown CCV and oceanographers at the URI Graduate school of Oceanography that we hope will convey the emerging enthusiasm that is the state of VR in ocean science. First, we will review a selection of previous work and provide a guide to getting started with VR visualization. Next, we will provide some more detailed examples from our collaborative work in how we applied these technologies. Finally, we will conclude with a discussion of these applications including some outlook for future developments in this field.

2. PREVIOUS WORK

Virtual reality allows immersive visualizations of underwater scenes to be experienced, both real (observed) and simulated (modeled) data. The application of VR has steadily increased since the 1990s to today, and we anticipate that this trend will continue, or even accelerate, in the future (Figure 1). In this section, we review a selection of these works to illustrate the impact that VR has to date realized in ocean science. From live VR video feeds to simulated VR environments, from user-centric to animal-centric applications, VR applications have demonstrated a growing array of benefits.

Early utilization of VR for ocean exploration focused on remotely operated vehicle (ROV) navigation, and these efforts demonstrated the utility of VR for increasing ROV pilot situational awareness in harsh, low-visibility environments (Hine et al., 1994; Fleischer et al., 1995; Stoker et al., 1995; Lin and Kuo, 1998). Fast forward over 25 years, this concept has seen vast technological refinement with the application of off-the-shelf VR components, including HMDs, such as the Oculus Rift, and improved haptic devices, which add a greater field of view, faster head tracking, and more intuitive feedbacks for the remote control of the ROV manipulator arm (Lynch and Ellery, 2014; Candeloro et al., 2015). In addition, the feedback from these haptic control devices (e.g., vibration) can help avoid collisions with expensive equipment (Lynch and Ellery, 2014; Sivčev et al., 2018). These visualizations and controls have also been aided by stereoscopic cameras, which utilize synchronized cameras to take 3D images and have the advantage of mimicking human binocular vision while also enabling more accurate spatial measurement (Shortis et al., 2007). Underwater exploration via ROV now includes methods for underwater 3D mapping, which use laser scanning (Shigematsu and Moriya, 1997; Massot-Campos et al., 2015) and acoustics (Griffiths et al., 1997; Chapman et al., 1999; Palmese and Trucco, 2008) to explore terrain at even higher

resolution. Photogrammetric approaches to the reconstruction of underwater 3D maps is a recent development, and provides a cost-effective, accurate, and reproducible method to re-creating marine habitats (Kwasnitschka et al., 2013; Marre et al., 2019). In support of this growing data capacity, network architecture also continues to improve, with internet connected ships (Raineault et al., 2018) and ROVs enabling multiple users to coordinate efforts simultaneously with the aid of real time AR applications (Chouiten et al., 2012).

Onshore, VR has been used to render educational underwater scenes for the benefit of students and the general public, offering interactive access to underwater ocean ecosystems and dynamics via CAVEs and HMDs (Frohlich, 2000; Chen et al., 2012; Jung et al., 2013). Submersible AR and VR applications are a more recent development, and various projects have made use of waterproof hardware to create experiences which combine swimming with animation and actual underwater images (Bellarbi et al., 2013; Oppermann et al., 2016; Costa et al., 2017).

Similarly, VR has enabled novel experiments to study marine megafauna. Rather than using VR to project humans into a simulated environment, captive animals are subjected to virtual environments which mimic their natural environment to trigger behavioral response, e.g., to elicit camouflage (Jaffe et al., 2011; Josef, 2018, Figure 2) or predator-avoidance responses (Butail et al., 2012; Trivedi and Bollmann, 2013). These simulations demonstrate how VR has enabled researchers to pursue new and creative avenues for studying marine physiology and ecology.

While not strictly ocean science, data visualization has benefited the natural sciences in general through improved data readability, interpretability, and enabled the communication of dynamic four dimensional flows (Lin and Loftin, 1998; Ohno and Kageyama, 2007; Rautenhaus et al., 2017). Computer-generated visualizations of four dimensional flows, such as geophysical models of ocean currents, yield the most complete picture of oceanic processes when visualized in four dimensions (Nations et al., 1996) and exploration of complex datasets using VR can provide a method for quickly detecting patterns and unseen features (Billen et al., 2008).

3. VR RECIPE

Virtual reality requires three main ingredients: A VR Display, software capable of displaying VR content, and of course, the content itself. In the following, we will give an overview over the different possibilities commonly available and provide guidelines on how to choose the components.

3.1. VR Displays

While VR can generate feedback for all senses we will only give an overview about visual display devices, as auditory devices usually are simple headphones and devices providing feedback for other modalities, e.g., haptic or olfactory, are not widely used and targets of active research. Visual VR devices can be divided into three different categories: Mobile phone based VR, Consumer grade HMDs and CAVE systems, capable of providing feedback for multiple users. Each device

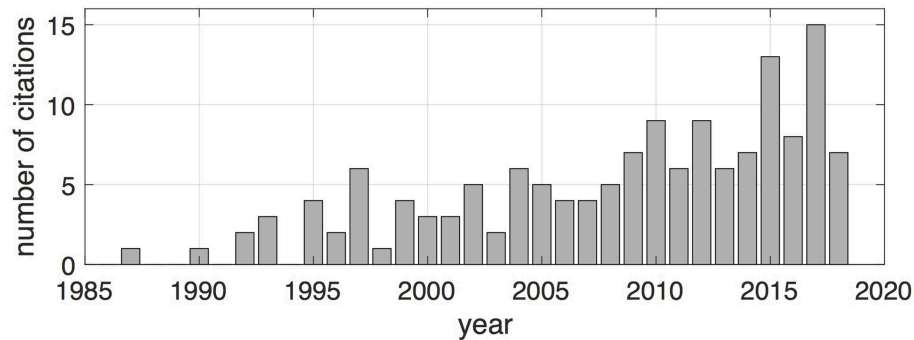


FIGURE 1 | The frequency of ocean science-related publications involving virtual reality has increased since the early 1990s. The search criteria for these works was focused on ocean data visualization-related terms, including both observed and modeled data. Google Scholar key word searches included: VR, virtual reality, immersive, 3D virtual environment, 3D user interfaces, telepresence, marine, underwater, oceanography, oceans, virtual, technology, head-mounted display, HMD, Oculus Rift, HTC Vive, CAVE. This search was concluded after a total of 150 citations was reached.

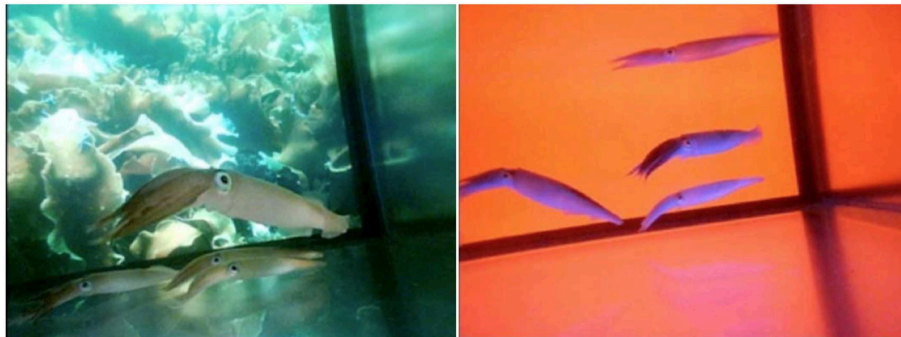


FIGURE 2 | Virtual reality used in a laboratory settings to study light stimulus response in *Loligo opalescens*. Image courtesy of Jules Jaffe, Scripps Institution of Oceanography.

comes with several advantages and disadvantages when regarding immersion, availability, and interaction.

Mobile phone based VR is the most accessible of the technologies currently available. In this case a mobile phone is put into a VR Headset which encompasses two lenses to provide a stereo view. In the simplest case, devices are made out of cardboard¹ with costs on the order of several dollars. Immersion in the VR environment is then achieved by rendering the scene for the point of view of a user determined by the internal sensors of the mobile device. However, while current research continues to investigate the use of the internal camera to determine translational movement of the user², mobile phone VR is currently only able to determine head rotations, which limits the interaction and immersion of a user. In other words, a user can look around in the VR environment, but is not able to move around in the scene by using his real physical motion. A similar limitation exists for interaction with the environment. While some headsets provide a controller, this controller's position is known only by its rotation. This limits the interaction to a laser

pointer metaphor. Despite these limitations, the technology is extremely valuable for outreach due to the low cost.

Head-mounted Displays (HMDs) have seen an increase in attention in recent years due to major developments. While 10 years ago HMDs were extremely expensive and immersion not satisfactory due to the limited field of view, development of mobile phone screens and cheaper sensors made design of consumer grade devices possible. Currently several devices are available at costs on the order of several hundred dollars, e.g., HTC Vive, Oculus Rift, or Windows Mixed Reality. Devices usually consist of a display encompassed with two lenses in plastic goggles similar to mobile phone VR. However, they exhibit two major differences to mobile phone VR. While mobile phone VR only uses rotation of a user's head motion or controllers, HMDs use additional sensors to determine translational motion. This enables a user to move and interact in the virtual space as in the real world. A user can move around an object, grab an object or crouch down to see novel perspectives increasing immersion and providing a higher level of fidelity. However, as the name implies, HMDs are only the display. In order to render the virtual scene, a PC with a high quality GPU is required, raising the cost of such a system by one to two thousand dollars. This limits its application

¹<https://vr.google.com/cardboard/>

²<https://developers.google.com/vr/discover/worldsense>

as only a limited number of users can participate at the same time and applications are only usable by a smaller subset of people when compared to mobile phone VR. Nonetheless, due to the higher fidelity, better immersion and increased interaction they are best suited for VR applications in the scientific context.

CAVE systems have been widely used at universities and research centers in the past, when results with HMDs were not satisfactory for VR. In contrast to HMDs and mobile phone based VR, the displays are in this case not worn, but surround the users. The position and orientation of the user and (usually) her controllers are determined using motion capture systems; shutter glasses are used to provide a stereoscopic view. This permits rendering the scene for each display as if it is a window to the virtual world, making CAVE systems similar to the well-known Star Trek HoloDeck. Similar to HMDs a user can walk around in the simulated space and interact with its entities freely, but due to its design they provide different advantages and disadvantages. In HMD systems a user does not see her real environment, while in CAVE systems a user can still see his real surroundings. This not only leads to better acceptance and less cyber sickness, but allows use by multiple users, facilitating discussions and collaboration with peers. However, it has to be noted that most CAVE systems, with a few exceptions (Blom et al., 2002; Fröhlich et al., 2005), only track the position of one user which results in the rendering being only optimal for her and diminishes the experience for others. As a drawback, CAVE systems usually require more support for maintenance as well as software development due to their complexity, while the consumer market has made usability and software development for HMDs easier.

3.2. VR Software

In order to render content on a VR device, a VR-capable application is required. Similar to the devices, different possibilities exist depending on the devices used, as well as the fidelity and interaction targeted. Efforts to build the VR experience can range from several minutes to several weeks depending on the tools and the desired interaction. While for certain types of data specialized software exists, we would like to give a short overview of three different approaches freely available to visualize content in VR and highlight their advantages and limitations: ParaView, a VR-capable visualization tool for scientific data; Unity3D, a 3D game engine to create VR applications; and custom software development using traditional programming languages.

Paraview³ is a visualization application widely used in scientific data visualization which supports VR display in HMDs⁴ as well as CAVE systems⁵. It supports import and visualization of many different data types and visualization primitives. There is good documentation available including many tutorials, and data can usually be loaded within minutes and presented in VR with the ease of a click. However, interaction in VR with the data is quite limited and it does not support mobile phone VR. However, given the ease and wide range of supported data types

and visualizations, it is a valuable tool to see the data in an immersive environment.

Unity3D became the most common design tool for VR applications due to its good support of VR devices as well as its large user base. It also supports many different data types, and behavior of entities in the application can be defined through game logic. Due to the large user base, many tutorials can be found on YouTube. Additional functionality can be added to the application by downloading packages, called “prefabs,” from the Unity Store for free or a small fee. Functionality of prefabs can range from simple three-dimensional models to packages used to plot data, e.g., Immersive Analytics Toolkit⁶ or packages which simplify interactions in VR like grabbing an object, e.g., Virtual Reality Toolkit⁷. While most of the application design can be done with the Unity3D user interface, it is still recommended to have some experience with scripting or programming. However, due to the examples and tutorials available, even a novice user can develop a simple VR application within a couple of days. As Unity3D is a tool for designing a 3D application, interaction in the virtual environment is customizable and the deployment and distribution of the final application is easy across different VR systems. As a consequence, most applications recently developed for VR (especially in the sciences) are built using Unity3D.

Custom Software Development can be used to build VR applications using a wide range of programming languages, e.g., Python, MATLAB, C++. However, achieving satisfactory results requires more effort when compared to Unity3D and is only advised if restrictions of the data or the VR system do not permit the use of Unity3D. Several libraries can be used to facilitate the development of VR applications, e.g., MinVR⁸, but the process still requires significant knowledge of the programming language and the VR system used.

3.3. VR Content

Finally, as a last ingredient the content displayed should also be considered when designing the VR experience, e.g., if data is two-dimensional, visualization in a three-dimensional space will not provide significant advantage over traditional methods. However, if the data is of three or higher dimensions, the visualization in an immersive manner can provide novel perspectives that lead to scientific insight. Combined with custom tools designed to interact with the environment, novel insights can be gained in an exploratory setting. However, it has to be taken into account that while some data can be easily incorporated in its raw state, other data might require additional preprocessing to extract higher dimensional information or efforts have to be undertaken to combine different datatypes in the same reference frame. A VR display for scientific data is actually an experience for the user, and the specifics of the audience and the goal of the visualization deserve attention, as they should have a significant impact on the design of tools required to interact with the data.

³<https://www.paraview.org/>

⁴<https://blog.kitware.com/taking-paraview-into-virtual-reality/>

⁵<https://www.paraview.org/immersive/>

⁶<https://github.com/MaximeCordeil/IATK>

⁷<https://vrtoolkit.readme.io/>

⁸<https://github.com/MinVR/MinVR>

4. OUR APPROACH

In the following section, we detail our applications in order to share some lessons learned, to convey caution in some cases, and ideally to inspire other ocean scientists to implement their own VR experience. The three VR applications developed to date by our group provide only a glimpse of the possibilities derived from this rapidly growing technology, and also present a range of challenges. For example, part of our goal was rendering the data in the YURT system which required special algorithms and is not supported by Unity3D. Subsequently, our first two applications were developed using custom software development with C++ after a first exploration of the data in ParaView. Nonetheless, the developed applications were also used in a HMD setting during field work. The third application was developed using Unity3D for HMDs. Representative 2D movies are provided (See **Supplementary Information**), but evaluation of VR is optimally experienced on a VR-enabled device. Source code has been uploaded⁹ while the pre-compiled applications for windows can be downloaded¹⁰.

4.1. Data Visualization—Autonomous Platform Tracks and Observations

As the data acquired during autonomous underwater platforms (drifting and powered) is associated with their position, depth and time, these datasets are a natural application for VR. The dynamic ocean environment surrounding these vehicles often result in data records that convolve space and time. Rendering these observations in a 3D (x,y,z) setting allows a user to more easily identify aspects of their record that are likely associated with a spatial feature as opposed to a temporal change.

In our testbed application, we wanted to be able to review data from a free-drifting, wave-powered profiler called a Wirewalker, within its hydrographic context Rainville and Pinkel (2001). We used VR to combine Wirewalker sensor data with its geolocated drift paths as well as with corresponding satellite imagery (see **Supplementary Movie 1**). Given the limited ability of GPS signal to penetrate through water depth, pre-processing steps were necessary to estimate the submerged horizontal coordinates of the Wirewalker. These coordinates were simple, “straight line” approximations between successive surface GPS positions. These positions were linearly interpolated spatially and temporally using MATLAB prior to VR rendering. Visualization of submerged physical and chemical variables were presented using a linearly spaced color scale. However, in future versions of this application we recommend that the color map scales be selected to adhere to best practices for the given variable for improved visual accuracy (Thyng et al., 2016). This spatial and temporal series of vertical profiles of the top 120 m of the water column (Omand et al., 2017) was combined with satellite observations of incident light interacting with particles in the water (also known as ocean color) thus creating a 50 square kilometer ocean color map (NASA Ocean Biology Processing Group, 2015) of the Wirewalker drift track. Successive

Wirewalker profiles were used to create an animation of the drift track, while physical and chemical variables were shown for the whole surrounding region using color scales (**Figure 3**). Using the VR controllers, users could navigate through the virtual seascape via flying through water column profiles, while toggling between different physical and chemical variables recorded by the Wirewalker. For more detailed analysis, the users were also provided tools to analyze data points with a simple pointing gesture. Although C++ was used for our application, this type of data would be readily viewed with Unity3D and is highly recommended for those who plan to use HMDs.

4.2. Data Visualization—Holographic Microscopy

In our second application we targeted the visualization of holographic microscopy data. As the holographic microscope images 3D volumes in a single camera frame, rapidly and without the use of mechanical lenses (Beers et al., 1970; Jericho et al., 2013), its data seemed well-suited to VR applications at a first glance. However, the technology only allows users to refocus the microscopic image at different distances to the instrument within the 3D volume (**Figure 4**) and in order to visualize the whole volume in an immersive environment the particles recorded in the hologram first needed to be detected, segmented and extracted.

We therefore developed a custom hologram processing pipeline which first computes a sharpness score for each pixel across all image planes in the whole volume and stores for each pixel the maximum value (Guildenbecher et al., 2012; Ihan et al., 2014). As neighboring pixels in focus are likely to belong to the same object, pixels are grouped to segments in a second step. For each segment the optimal focus distance is computed based on the same sharpness score of the first step, but for the whole region (see **Figure 4c**). Finally the image is refocused for each segment at the optimal distance and the particle is segmented using the grabcut algorithm (Rother et al., 2004). This resulted in a focused 2D representation (see **Figure 4d**) for each particle as well as its three-dimensional position within the volume. These 2D silhouettes combined with their 3D position in the microscope imaging volume are well-suited for visualization in VR.

For our application we used a digital inline holographic microscope¹¹; which allows a wide range of marine particle size classes (5–1,000 μm) to be imaged *in situ* so as to preserve their delicate, undisturbed forms and morphologies. To showcase the use of VR in combination with the acquired data from the instrument, we developed three different VR scenarios.

4.2.1. Phytoplankton Trophy Room

In the Trophy room, a collection of particles from several holographic images are combined to display in a single volume (see **Supplementary Movie 2**). Visualizing different images in the same space removes information about objects’ spatial relationships to each other, but it allows a user to make comparisons of size and shape between the different data sets.

⁹<https://github.com/BenKnorlein>

¹⁰<https://github.com/VRocean>

¹¹<http://4-deep.com/>

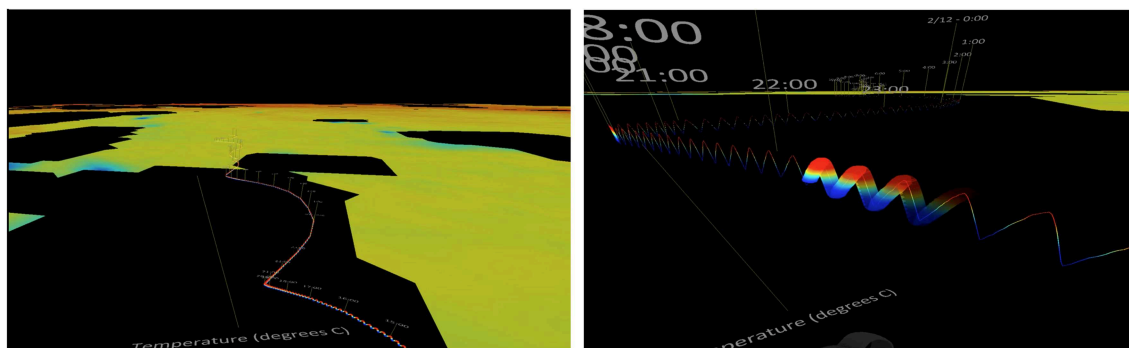


FIGURE 3 | A VR user's view inside the autonomous vehicle data visualization application. **Left:** Satellite ocean color data (NASA Ocean Biology Processing Group, 2015) is combined with Wirewalker drift tracks and *in situ* sensors. This bird's eye view of data shows a three day deployment in the North Pacific. **Right:** Successive, high resolution profiles of the top 120 m of the water column are combined to create animations of the vehicle's 3D position throughout the course of the vehicle deployment. Each real world vertical profile (10–20 min per profile) is replayed in VR at 2 s per profile. Users can toggle between CTD variables, fly through the scene, and change the spatial scaling in the vertical dimension with the Oculus Touch Controllers.

The Trophy Room is also well-suited to communicate the abundance and variety of the phytoplankton world to scientist and novices in an engaging and immersing manner.

4.2.2. Phytoplankton Safari

As the holographic microscope can operate autonomously, we mounted it to the ship's CTD during a five week cruise onboard the R/V Falkor. This permitted us to record vertical holographic microscope image profiles of the North Pacific alongside the standard suite of physical, chemical, and biological variables (see **Supplementary Movie 3**). In the “Safari” successive holograms from a CTD cast were then “stacked” on top of each other, providing a phytoplankton view from a descending CTD rosette down to a maximum depth of 2,000 m. The VR controllers allowed the user to “fly” through the CTD cast. Functionality was added for tagging interesting objects like phytoplankton and marine snow, viewing the “ambient” CTD variables, and measuring spatial distances between interesting hologram features (**Figure 5**).

4.2.3. Phytoplankton Locomotion

As the holographic microscope is also able to capture a 3D volume at a rate of 16 fps, we developed a holographic movie player (see **Supplementary Movie 4**). While the recording of movies in the field is not suitable as plankton move in and out of the volume too fast due to chaotic flow patterns, we recorded a holographic movie of a swimming *Akashiwo sanguinea* in a more quiescent laboratory experiment. In addition to the navigation in the previous examples, a user can also use traditional movie controls like fast-forward, rewind or pause allowing users to follow the motion of the particles not only in the two-dimensional image planes, but to understand their motion in the three-dimensional volume.

4.3. Education—An Interactive Plankton Zoo

Due to the response to the data visualization applications at outreach events from researchers, as well as novices, we decided to develop an educational experience to engage younger

audiences to learn about phytoplankton. This led us to create an interactive plankton zoo (**Figure 6**; see **Supplementary Movie 5**). We found the ease of creating animated, underwater virtual scenes was greatly increased with the use of popular gaming engine Unity 3D¹² by using the Virtual Reality Toolkit¹³. We used this software suite to integrate 3D plankton models (previously prepared for a video used for outreach) into an underwater scene and provided users with a novel way to interact with the diversity of different phytoplankton types. Participants could use the VR controllers to grab 3D models of floating plankton and then read small descriptions of each organism and experience these morphologies up close (adapted from PACE Phytopia)¹⁴.

5. DISCUSSION

We successfully tested these VR applications in a CAVE and HMD and found new perspectives on the potential for the use of VR in our future work. In this section we explore these new insights gained and weigh the merits of the invested effort against the results. In extrapolating to future states of this technology, we consider the types of data well-suited for VR, the potential benefits of this novel data interaction style, the benefits to having access to this immersive data exploration style in the field, the new possibilities for remote collaboration, and finally how this impacts communication/education.

Our experience in rendering different data types in VR, be it from autonomous platforms or holographic microscope, was that varying degrees of effort are required to achieve an effective visualization. Autonomous vehicle, CTD, and bathymetric data sets are readily accessible for viewing in VR with minimal processing. Furthermore, toggling between and layering together a diverse set of chemical and physical variables in these environments, from a range of different sensors, required minimal data manipulation and time stamp synchronization.

¹²<https://unity3d.com/>

¹³<https://vrtoolkit.readme.io/>

¹⁴<https://pace.oceansciences.org/phytopia.htm>

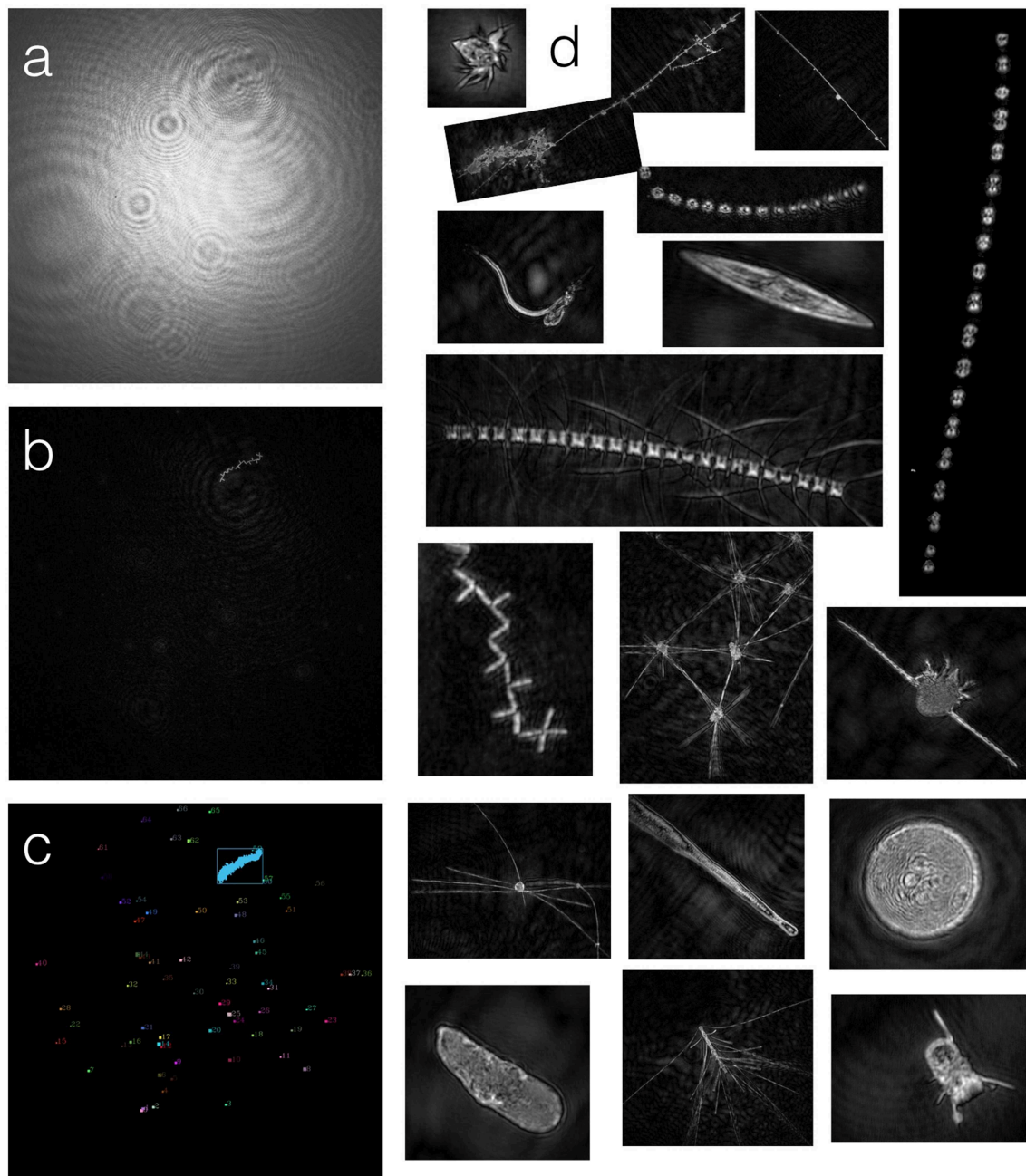


FIGURE 4 | The custom hologram processing pipeline extracts 2D contours from the imaged 3D volume. **(a)** A raw 2D hologram. **(b)** A refocused hologram image at 16,250 μm from the laser source, revealing a *Thalassionema* type chain-forming diatom. **(c)** Regions of interest (colored and sorted) derived from the image processing pipeline **(d)** An assortment of re-focused hologram contours illustrate the variety of marine particle types imaged by the holographic microscope, including diatoms, detritus, and zooplankton.

Datasets, such as these are well-suited for VR. In contrast, holographic image data require much greater effort to prepare for VR visualization because the positions of the in-focus objects is unknown prior to the pre-processing steps. Intensive pre-processing was required to visualize regions of interest, and a custom C++ application was created for the final rendering and interaction tools in VR.

There are many ongoing discussions about data standards in oceanography and wider marine science community, especially with respect to open source software, cloud data storage and cloud computing. With regard to VR and data standards, porting some of the standard data APIs (netCDF, HDF, etc.) to VR-friendly environments would improve the workflow from station- and time-series data to VR rendering. Although this is

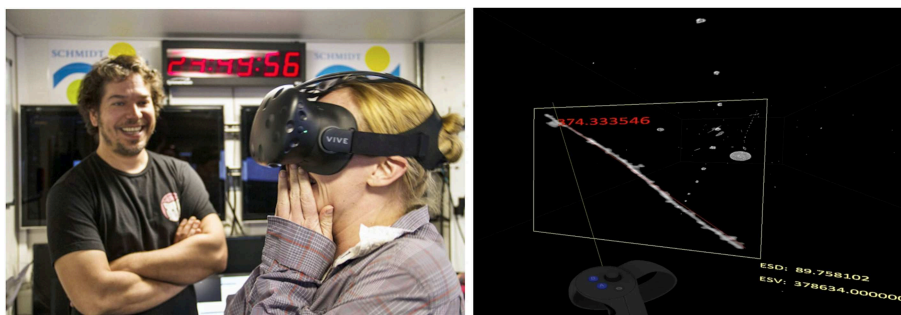


FIGURE 5 | Holographic microscope data was processed and rendered in VR at sea. **(Left)** A virtual reality “Holodeck” was set up inside the CTD control room of the R/V Falkor for viewing holographic microscope data that had been mapped to CTD profiles. Image credit: Schmidt Ocean Institute/Monika Naranjo Gonzalez. Written informed consent was obtained for the publication of this image. **(Right)** A user’s view inside the VR visualization of the holographic microscope data shows how easy it is to tag interesting objects and measure lengths using the Oculus Touch controllers.

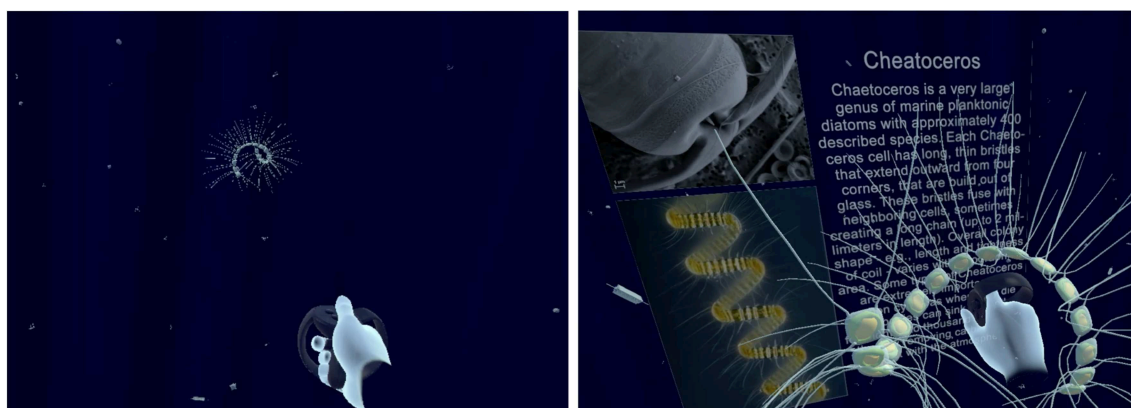


FIGURE 6 | Five different plankton types and morphologies were rendered in the application, providing users with a novel way to collect and learn about these different types. **(Left)** A user’s view inside the Oculus Rift head-mounted display while capturing a floating phytoplankton. **(Right)** A user’s view inside the Oculus Rift head-mounted display while holding a “3D Chaetoceros” in the Plankton Zoo VR application.

not within the scope of this paper, ongoing and future discussions will have to take into consideration the presence and potential impact that VR will have on facilitating more widespread utilization of public data for numerous applications, including furthering our understanding of complex interconnections within the Earth system as a whole.

The interaction style within each of the applications provides a glimpse into how VR-enabled problem solving environments can aid in discovery in ocean science. During demonstrations at the 2017 American Geophysical Union Ocean Sciences Meeting and at the University of Rhode Island, conversations with other marine scientists led to improved spatial interpolation of Wirewalker data. Immersive VR exploration of Wirewalker data provided a more interconnected view of water mass properties throughout space and time, as we were able to fly through the semi-Lagrangian drift tracks and begin to speculate about the presence of persistent water mass features. In the future, we envision additional parameter visualizations may enhance the ability to identify these water mass properties, including layered visualizations of model output and objective mapping algorithms.

While the autonomous platform visualization enabled a more synoptic, macroscale view of the data, the holographic microscope visualization brought us one step closer to the microscale perspective of the plankton. The power to change camera angle with a tilt of the head enables the user to interact with the virtual plankton as if they were actually floating there in the real world, measuring distances and tagging interesting features for rapid, intuitive exploration. This interaction style minimized the bias of spatial distance within a hologram as compared with 2D renderings, as the VR visualization engine accurately re-scaled object sizes according to its distance from the user’s virtual position. This feature is crucial for point-source holographic microscope images, in which particles become magnified the further from the camera they are captured.

In contrast to the holographic microscope visualization, spatial distortions were a necessary feature of the autonomous platform visualization. Vertical lengths were scaled up for improved readability, as the 120 m vertical profiles of the water column were small compared to the tens of kilometers the drifter traveled over several days. This non-uniform axis scaling made it easier to see vertical structure in the water column, while uniform

axis scaling gave a better sense of how depth corresponds to the overall scale of the Wirewalker drift track. The ability to manually change this aspect ratio provided a valuable demonstration of scale that is not readily rendered in 2D print graphics.

The relatively compact, portable nature of HMDs make this technology well-suited to take into the field for fast exploration of data sets. With as little as nine square feet of space, a VR system could be setup in the main lab or mission planning area of a research vessel for on-the-fly decision making tasks. Data quality could be monitored as it is being collected, and this could lead to adjustments in the cruise plan or sensor deployment configurations. Our experience aboard the R/V Falkor provided a glimpse into this future, as the HTC Vive HMD was set up adjacent to the ship's CTD monitoring station. While we reviewed freshly recorded holographic microscope profiles just hours after they were recorded, we began to consider the practicality of VR-enabled water-column sampling in which prominent features could be rendered alongside recent CTD casts. This integrated view of the water column might improve interdisciplinary collaboration, as multiple viewpoints could work to identify complementary features.

VR has the potential to transform collaboration at sea and onshore into co-located but remote experiences. All stakeholders could access the same virtual environment, and this may aid in mission planning, task delegation, and policy making. At the University of Rhode Island's Inner Space Center¹⁵, telepresence has become central to remote ocean exploration. We imagine multiple users having the ability to meet in VR, and this could facilitate more meaningful discussion and analysis with participants viewing minimally curated, minimally biased data. For example, the application ConfocalVR¹⁶ allows multiple users to interact in a virtual space and this has shown to be beneficial for understanding cellular structure (Stefani et al., 2018). VR-enabled collaboration could also be used for policy making, as has been previously done for coastal management and planning when stakeholders used these visualizations to assess the potential outcome of marine conservation and sustainability projects (Newell et al., 2017). While viewing holographic microscope and Wirewalker data in the Brown CCV YURT, multiple users had access to the same 3D visualization simultaneously without the use of a HMD (see **Supplementary Movie 6**) and this led to lively conversation and interaction. For students and researchers, VR could enable deeper multi-institution collaboration as well as richer educational experiences.

We found VR to be an engaging educational tool, particularly for younger audiences who were excited and curious to experience the new technology. During outreach events at the Waikiki Aquarium, Brown University, and the University of Rhode Island we found engagement to be lively and feedback to be positive. Underwater environments are a natural fit for VR, as these experiences are often impossible to get to in any other way. For example, conveying a sense of the concentration and relative size of phytoplankton inside a drop of seawater, what it would be like walking on the seafloor, or zooming from the

1km scale of a vehicle dive up to the 100 km scale of the vehicle path, are experiences that only VR can provide. Science education VR apps have become more popular recently (Merchant et al., 2014), and these experiences enable audiences to get closer to the actual data. They have a more personal experience with it while they control the camera angle and play in an open-ended, less constrained way. With the possibility of reaching even broader audiences through online VR app stores like Steam¹⁷, we see high potential to recruit the next generation of ocean scientists using VR animations and data visualizations.

With reduced technical barriers to developing software packages, virtual reality is being increasingly applied in ocean science as a tool for scientific exploration, discovery, and education. While mainstream adoption of VR is yet to be realized in ocean science, early adopters will be rewarded by the simple joy of developing and sharing these tools. Virtual reality provides a less curated experience than two dimensional data visualization, allowing users to interact with and interpret data in a manner that is less constrained by the author's perspective, influence, or bias. Although still in the early stages of development, our group's experience with applying VR in ocean science was productive in terms of education, outreach, and exploration. We are hopeful that VR will inspire new, unexpected, and serendipitous observations in ocean science and help bridge the gap between marine observation and data analysis. We have made several of the applications discussed herein available for download, and encourage the reader to experience the potential for VR themselves.

AUTHOR CONTRIBUTIONS

BK and TS created the hologram processing pipeline and visualization in the Brown CCV YURT. BK created the head-mounted display VR apps and the VR educational demonstration. NW, BK, and MO recorded the hologram, CTD, and Wirewalker data. IC helped with data collection, and concept of the VR educational demonstration. NW and BK drafted the paper with contributions from MO.

FUNDING

This work was funded by the Rhode Island Science and Technology Advisory Council (Award ID AWD05225), with student support provided through NSF (Award ID AWD05524 and AWD05643) and NASA's PACE mission. For work performed aboard the R/V Falkor, the authors are grateful to Schmidt Ocean Institute for ship time funding, as well as the ships crew for their enthusiasm and support.

SUPPLEMENTARY MATERIAL

The Supplementary Material for this article can be found online at: <https://www.frontiersin.org/articles/10.3389/fmars.2019.00644/full#supplementary-material>

Supplementary Movies 1–6 | Screen capture movies of the VR applications developed by the authors illustrate several uses of VR in marine science.

¹⁵<http://innerspacecenter.org>

¹⁶<http://www.confocalvr.com/>

¹⁷<https://store.steampowered.com/>

REFERENCES

- Beers, J. R., Knox, C., and Strickland, J. D. H. (1970). A permanent record of plankton samples using holography. *Limnol. Oceanogr.* 15, 967–970.
- Bellarbi, A., Domingues, C., Otmame, S., Benbelkacem, S., and Dinis, A. (2013). “Augmented reality for underwater activities with the use of the DOLPHYN,” in *2013 10th IEEE International Conference on Networking, Sensing and Control (ICNSC)* (Evry), 409–412.
- Billen, M. I., Kreylos, O., Hamann, B., Jadamec, M. A., Kellogg, L. H., Staadt, O., et al. (2008). A geoscience perspective on immersive 3d gridded data visualization. *Comput. Geosci.* 34, 1056–1072. doi: 10.1016/j.cageo.2007.11.009
- Blom, K., Lindahl, G., and Cruz-Neira, C. (2002). “Multiple active viewers in projection-based immersive environments,” *Conference: Immersive Projection Technology Workshop* (Ames, IA), 6.
- Butail, S., Chicoli, A., and Paley, D. A. (2012). “Putting the fish in the fish tank: Immersive VR for animal behavior experiments,” in *2012 IEEE International Conference on Robotics and Automation* (St Paul, MN: IEEE), 5018–5023.
- Candeloro, M., Valle, E., Miyazaki, M. R., Skjetne, R., Ludvigsen, M., and Srensen, A. J. (2015). “HMD as a new tool for telepresence in underwater operations and closed-loop control of ROVs,” in *OCEANS 2015–MTS* (Washington, DC: IEEE), 1–8.
- Castelvecchi, D. (2016). Low-cost headsets boost virtual reality lab appeal. *Nat. News* 533:153. doi: 10.1038/533153a
- Chapman, P., Wills, D., Brookes, G., and Stevens, P. (1999). Visualizing underwater environments using multifrequency sonar. *IEEE Comput. Graph. Appl.* 19, 61–65.
- Chen, G., Li, B., Tian, F., Ji, P., and Li, W. (2012). Design and implementation of a 3d ocean virtual reality and visualization engine. *J. Ocean Univ. China* 11, 481–487. doi: 10.1007/s11802-012-2112-6
- Chouiten, M., Domingues, C., Didier, J.-Y., Otmame, S., and Mallem, M. (2012). “Distributed mixed reality for remote underwater telerobotics exploration,” in *Proceedings of the 2012 Virtual Reality International Conference, VRIC '12* (New York, NY: ACM), 1:1–1:6.
- Costa, R., Guo, R., and Quarles, J. (2017). “Towards usable underwater virtual reality systems,” in *Virtual Reality (VR), 2017 IEEE* (San Antonio, TX).
- Cruz-Neira, C., Sandin, D. J., DeFanti, T. A., Kenyon, R. V., and Hart, J. C. (1992). The CAVE: audio visual experience automatic virtual environment. *Commun. ACM* 35, 64–72. doi: 10.1145/129888.129892
- Fleischer, S. D., Rock, S. M., and Lee, M. J. (1995). “Underwater vehicle control from a virtual environment interface,” in *Proceedings of the 1995 Symposium on Interactive 3D Graphics, I3D '95* (New York, NY: ACM), 25.
- Fröhlich, B., Blach, R., Stefani, O., Hochstrate, J., Bues, M., Hoffmann, J., et al. (2005). “Implementing multi-viewer stereo displays,” in *WSCG 2005 Conference Proceedings* (Weimar), 8.
- Frohlich, T. (2000). The virtual oceanarium. *Commun. ACM* 43, 94–94. doi: 10.1145/341852.341868
- Griffiths, H. D., Rafik, T. A., Meng, Z., Cowan, C. F. N., Shafeeu, H., and Anthony, D. K. (1997). Interferometric synthetic aperture sonar for high resolution 3-D mapping of the seabed. *Sonar Navigat. IEEE Proc. Radar* 144, 96–103. doi: 10.1049/ip-rsn:19971076
- Guildenbecher, D. R., Gao, J., Reu, P. L., and Chen, J. (2012). “Digital holography reconstruction algorithms to estimate the morphology and depth of nonspherical absorbing particles,” in *Interferometry XVI: Techniques and Analysis, Vol. 8493* (Albuquerque, NM: International Society for Optics and Photonics), 849303.
- Hine, B. P., Stoker, C., Sims, M., Rasmussen, D., Fong, T. W., Steele, J., et al. (1994). “The application of telepresence and virtual reality to subsea exploration,” in *Conference Paper, The 2nd Workshop on Mobile Robots for Subsea Environments, Proc. ROV'94* (Mountain View, CA), 10.
- Huang, D., Zhao, D., Wei, L., Wang, Z., and Du, Y. (2015). Modeling and analysis in marine big data: advances and challenges. *Math. Probl. Eng.* 2015, 1–13. doi: 10.1155/2015/384742
- Ihan, H. A., Doğar, M., and Özcan, M. (2014). Digital holographic microscopy and focusing methods based on image sharpness. *J. Microsc.* 255, 138–149. doi: 10.1111/jmi.12144
- Jaffe, J. S., Laxton, B., and Zylinski, S. (2011). “The sub sea holodeck: a 14-megapixel immersive virtual environment for studying cephalopod camouflage behavior,” in *OCEANS 2011 IEEE–Spain* (Santander: IEEE), 1–6.
- Jericho, S. K., Jericho, M. H., and Kreuzer, H. J. (2013). “Holographic microscopy of marine organisms,” in *Imaging Marine Life* (Halifax, NS: Wiley-Blackwell), 48–66.
- Josef, N. (2018). Cephalopod experimental projected habitat (CEPH): virtual reality for underwater organisms. *Front. Mar. Sci.* 5:73. doi: 10.3389/fmars.2018.00073
- Jung, S., Choi, Y.-S., Choi, J.-S., Koo, B.-K., and Lee, W. H. (2013). “Immersive virtual aquarium with real-walking navigation,” in *Proceedings of the 12th ACM SIGGRAPH International Conference on Virtual-Reality Continuum and Its Applications in Industry* (Daejeon: ACM), 291–294.
- Kwasnitschka, T., Hansteen, T. H., Devey, C. W., and Kutterolf, S. (2013). Doing fieldwork on the seafloor: photogrammetric techniques to yield 3d visual models from ROV video. *Comput. Geosci.* 52, 218–226. doi: 10.1016/j.cageo.2012.10.008
- LaViola, J. J., Prabhat, Forsberg, A. S., Laidlaw, D. H., and Dam, A. V. (2009). “Virtual reality-based interactive scientific visualization environments,” in *Trends in Interactive Visualization: State-of-the-Art Survey*, Advanced Information and Knowledge Processing, eds R. Liere, T. Adriaansen, and E. Zudilova-Seinstra (London: Springer London), 225–250.
- Lin, C.-R., and Loftin, R. B. (1998). “Application of virtual reality in the interpretation of geoscience data,” in *Proceedings of the ACM Symposium on Virtual Reality Software and Technology, VRST '98* (New York, NY: ACM), 187–194.
- Lin, Q., and Kuo, C. (1998). A virtual environment-based system for the navigation of underwater robots. *Vir. Real.* 3, 267–277.
- Liu, Y., Qiu, M., Liu, C., and Guo, Z. (2017). Big data challenges in ocean observation: a survey. *Pers. Ubiquit. Comput.* 21, 55–65. doi: 10.1007/s00779-016-0980-2
- Lynch, B., and Ellery, A. (2014). Efficient control of an AUV-manipulator system: an application for the exploration of Europa. *IEEE J. Ocean. Eng.* 39, 552–570. doi: 10.1109/OJE.2013.2271390
- Marre, G., Holon, F., Luque, S., Boissery, P., and Deter, J. (2019). Monitoring marine habitats with photogrammetry: a cost-effective, accurate, precise and high-resolution reconstruction method. *Front. Mar. Sci.* 6:276. doi: 10.3389/fmars.2019.00276
- Massot-Campos, M., Oliver-Codina, G., Massot-Campos, M., and Oliver-Codina, G. (2015). Optical sensors and methods for underwater 3d reconstruction. *Sensors* 15, 31525–31557. doi: 10.3390/s151229864
- Matthews, D. (2018). Virtual-reality applications give science a new dimension. *Nature* 557:127. doi: 10.1038/d41586-018-04997-2
- Merchant, Z., Goetz, E. T., Cifuentes, L., Keeney-Kennicutt, W., and Davis, T. J. (2014). Effectiveness of virtual reality-based instruction on students' learning outcomes in K-12 and higher education: a meta-analysis. *Comput. Educ.* 70, 29–40. doi: 10.1016/j.compedu.2013.07.033
- NASA Ocean Biology Processing Group (2015). *SeaWiFS Level 3 Binned Particulate Organic Carbon Data Version 2014*. Greenbelt, MD: NASA Goddard Space Flight Center, Ocean Ecology Laboratory.
- Nations, S., Moorhead, R., Gaither, K., Aukstakalnis, S., Vickery, R., Couvillion, W., et al. (1996). “Interactive visualization of ocean circulation models,” in *Proceedings of Seventh Annual IEEE Visualization '96* (San Francisco, CA: ACM), 429–432.
- Newell, R., Canessa, R., and Sharma, T. (2017). Visualizing our options for coastal places: exploring realistic immersive geovisualizations as tools for inclusive approaches to coastal planning and management. *Front. Mar. Sci.* 4:290. doi: 10.3389/fmars.2017.00290
- Ohno, N., and Kageyama, A. (2007). Scientific visualization of geophysical simulation data by the CAVE VR system with volume rendering. *Phys. Earth Planet. Interiors* 163, 305–311. doi: 10.1016/j.pepi.2007.02.013
- Omand, M. M., Cetinić, I., and Lucas, A. J. (2017). Using bio-optics to reveal phytoplankton physiology from a wirewalker autonomous platform. *Oceanography* 30, 128–131. doi: 10.5670/oceanog.2017.233
- Oppermann, L., Blum, L., and Shekow, M. (2016). “Playing on AREEF: evaluation of an underwater augmented reality game for kids,” in *Proceedings of the 18th International Conference on Human-Computer Interaction with Mobile Devices and Services, MobileHCI '16* (New York, NY: ACM), 330–340.
- Palmese, M., and Trucco, A. (2008). From 3-D sonar images to augmented reality models for objects buried on the seafloor. *IEEE Trans. Instr. Meas.* 57, 820–828. doi: 10.1109/TIM.2007.913703

- Raineault, N. A., Bell, K. L. C., and Girguis, P. (2018). Advancing ocean science and exploration through telepresence. *Deep Sea Res. II Top. Stud. Oceanogr.* 150, 1–3. doi: 10.1016/j.dsr2.2018.05.008
- Rainville, L., and Pinkel, R. (2001). Wirewalker: an autonomous wave-powered vertical profiler. *J. Atmos. Ocean. Technol.* 18, 1048–1051. doi: 10.1175/1520-0426(2001)018<1048:WAAWPV>2.0.CO;2
- Rautenhaus, M., Kirby, R. M., and Mirzargar, M. (2017). Visualization in meteorology—a survey of techniques and tools for data analysis tasks. in *IEEE Trans. Vis. Comput. Graph.* 24, 3268–3296. doi: 10.1109/TVCG.2017.2779501
- Rother, C., Kolmogorov, V., and Blake, A. (2004). “GrabCut”: interactive foreground extraction using iterated graph cuts,” in *ACM SIGGRAPH 2004 Papers, SIGGRAPH '04* (New York, NY: ACM), 309–314.
- Shigematsu, B., and Moriya, N. (1997). Development of a deep-water topological survey system using a laser scanner with a GPS. *J. Jpn. Soc. Photogramm. Rem. Sens.* 36, 24–34. doi: 10.4287/jsprs.36.5_24
- Shortis, M., Harvey, E., and Seager, J. (2007). “A review of the status and trends in underwater videometric measurement,” *Invited Paper, SPIE Conference, Vol. 6491* (Parkville, VIC), 1–26.
- Sivčev, S., Coleman, J., Omerdić, E., Dooly, G., and Toal, D. (2018). Underwater manipulators: a review. *Ocean Eng.* 163, 431–450. doi: 10.1016/j.oceaneng.2018.06.018
- Slater, M., and Wilbur, S. (1997). A framework for immersive virtual environments (FIVE): speculations on the role of presence in virtual environments. *Presence Teleoper. Virt. Environ.* 6, 603–616. doi: 10.1162/pres.1997.6.6.603
- Stefani, C., Lacy-Hulbert, A., and Skillman, T. (2018). ConfocalVR: immersive visualization for confocal microscopy. *J. Mol. Biol.* 430, 4028–4035. doi: 10.1016/j.jmb.2018.06.035
- Stoker, C. R., Burch, D. R., Hine, B. P., and Barry, J. (1995). Antarctic undersea exploration using a robotic submarine with a telepresence user interface. *IEEE Exp.* 10, 14–23. doi: 10.1109/64.483008
- Sutherland, I. E. (1968). “A head-mounted three dimensional display,” in *Proceedings of the December 9–11, 1968, Fall Joint Computer Conference, Part I, AFIPS '68* (Fall, Part I) (New York, NY: ACM), 757–764.
- Thyng, K. M., Greene, C. A., Hetland, R. D., Zimmerle, H. M., and DiMarco, S. F. (2016). True colors of oceanography: guidelines for effective and accurate colormap selection. *Oceanography* 29, 9–13. doi: 10.5670/oceanog.2016.66
- Trivedi, C. A., and Bollmann, J. H. (2013). Visually driven chaining of elementary swim patterns into a goal-directed motor sequence: a virtual reality study of zebrafish prey capture. *Front. Neural Circuits* 7:86. doi: 10.3389/fncir.2013.00086

Conflict of Interest: The authors declare that the research was conducted in the absence of any commercial or financial relationships that could be construed as a potential conflict of interest.

Copyright © 2019 Walcutt, Knörlein, Sgouros, Cetinić and Omand. This is an open-access article distributed under the terms of the Creative Commons Attribution License (CC BY). The use, distribution or reproduction in other forums is permitted, provided the original author(s) and the copyright owner(s) are credited and that the original publication in this journal is cited, in accordance with accepted academic practice. No use, distribution or reproduction is permitted which does not comply with these terms.



The Development and Validation of a Profiling Glider Deep ISFET-Based pH Sensor for High Resolution Observations of Coastal and Ocean Acidification

Grace K. Saba^{1*}, Elizabeth Wright-Fairbanks¹, Baoshan Chen², Wei-Jun Cai², Andrew H. Barnard³, Clayton P. Jones⁴, Charles W. Branham³, Kui Wang² and Travis Miles¹

OPEN ACCESS

Edited by:

Leonard Pace,
Schmidt Ocean Institute,
United States

Reviewed by:

Vassilis Kitidis,
Plymouth Marine Laboratory,
United Kingdom
Philip Andrew McGilivray,
United States Coast Guard Pacific
Area, United States

*Correspondence:

Grace K. Saba
saba@marine.rutgers.edu

Specialty section:

This article was submitted to
Ocean Observation,
a section of the journal
Frontiers in Marine Science

Received: 14 December 2018

Accepted: 10 October 2019

Published: 30 October 2019

Citation:

Saba GK, Wright-Fairbanks E, Chen B, Cai W-J, Barnard AH, Jones CP, Branham CW, Wang K and Miles T (2019) The Development and Validation of a Profiling Glider Deep ISFET-Based pH Sensor for High Resolution Observations of Coastal and Ocean Acidification. *Front. Mar. Sci.* 6:664. doi: 10.3389/fmars.2019.00664

¹ Center for Ocean Observing Leadership, Department of Marine and Coastal Sciences, School of Environmental and Biological Sciences, Rutgers University, New Brunswick, NJ, United States, ² School of Marine Science and Policy, University of Delaware, Newark, DE, United States, ³ Sea-Bird Scientific, Philomath, OR and Bellevue, WA, United States, ⁴ Teledyne Webb Research, North Falmouth, MA, United States

Coastal and ocean acidification can alter ocean biogeochemistry, with ecological consequences that may result in economic and cultural losses. Yet few time series and high resolution spatial and temporal measurements exist to track the existence and movement of water low in pH and/or carbonate saturation. Past acidification monitoring efforts have either low spatial resolution (mooring) or high cost and low temporal and spatial resolution (research cruises). We developed the first integrated glider platform and sensor system for sampling pH throughout the water column of the coastal ocean. A deep ISFET (Ion Sensitive Field Effect Transistor)-based pH sensor system was modified and integrated into a Slocum glider, tank tested in natural seawater to determine sensor conditioning time under different scenarios, and validated *in situ* during deployments in the U.S. Northeast Shelf (NES). Comparative results between glider pH and pH measured spectrophotometrically from discrete seawater samples indicate that the glider pH sensor is capable of accuracy of 0.011 pH units or better for several weeks throughout the water column in the coastal ocean, with a precision of 0.005 pH units or better. Furthermore, simultaneous measurements from multiple sensors on the same glider enabled salinity-based estimates of total alkalinity (A_T) and aragonite saturation state (Ω_{Arag}). During the Spring 2018 Mid-Atlantic deployment, glider pH and derived A_T/Ω_{Arag} data along the cross-shelf transect revealed higher pH and Ω_{Arag} associated with the depth of chlorophyll and oxygen maxima and a warmer, saltier water mass. Lowest pH and Ω_{Arag} occurred in bottom waters of the middle shelf and slope, and nearshore following a period of heavy precipitation. Biofouling was revealed to be the primary limitation of this sensor during a summer deployment, whereby offsets in pH and A_T increased dramatically. Advances in anti-fouling coatings and the ability to

routinely clean and swap out sensors can address this challenge. The data presented here demonstrate the ability for gliders to routinely provide high resolution water column data on regional scales that can be applied to acidification monitoring efforts in other coastal regions.

Keywords: ocean acidification, pH, glider, monitoring, U.S. Northeast Shelf, Mid-Atlantic

INTRODUCTION

Ocean acidification (OA) has presented great research challenges and has significant societal ramifications that range from economic losses due to the decreased survival of commercially important organisms to the ecological consequences associated with altered ecosystems (Cooley et al., 2009; Doney, 2010). Particular areas of the coastal ocean are more susceptible to sustained, large increases in carbon dioxide (CO_2), including those in upwelling zones (Feely et al., 2008, 2010a), bays (Thomsen et al., 2010), and areas with high riverine and/or eutrophication influence (Salisbury et al., 2008; Cai et al., 2011). Yet few observations exist to track upwelling and movement of low pH water.

Past OA monitoring efforts have been limited to surface buoys equipped with sensors that measure pH and/or $p\text{CO}_2$ (the concentration of CO_2 in seawater measured as partial pressure of the gas), flow-through $p\text{CO}_2$ systems utilized by research vessels, and water column sampling during large field campaigns (e.g., U.S. Joint Ocean Global Flux Study, Bermuda Atlantic Time Series, Hawaiian Ocean Times Series) with low spatial resolution (mooring) or with low temporal resolution and high cost (research cruises). Only a fraction of these efforts include the U.S. continental shelves (e.g., Gulf of Mexico Ecosystems and Carbon Cycle Cruises [GOMECC], East Coast Ocean Acidification [ECO] cruises) (Jiang et al., 2008; Wang et al., 2013, 2017; Wanninkhof et al., 2015), commercially important coastal regions where finfish, lobster, and wild stocks of shellfish are present (Hales et al., 2005; Feely et al., 2008; Vandemark et al., 2011; Xue et al., 2016). Furthermore, very few sampling locations (spatial and temporal scale) include more than one of the four measurable carbonate chemistry parameters (pH; dissolved inorganic carbon concentration, or DIC; total alkalinity, or A_T ; and $p\text{CO}_2$). At least two out of the four are necessary in order to fully characterize the marine carbonate system, including determinations of aragonite saturation state (Ω_{Arag}), an approximate measure of whether calcium carbonate (in the form of aragonite) will dissolve or precipitate in calcifying organisms (Lee et al., 2006; Cai et al., 2010; Johnson, 2010; Wang et al., 2013).

The recent development of sensors for *in situ* measurements of seawater pH has resulted in a growing number of autonomous pH monitoring stations in the United States (Seidel et al., 2008; Martz et al., 2010). New pH sensors that can rapidly respond to pH change and also withstand higher pressure (depth) show great value in monitoring coastal systems. A Deep-Sea ISFET (Ion Sensitive Field Effect Transistor) profiling pH sensor was recently developed by Monterey Bay Aquarium Research Institute (MBARI) and Honeywell and has been successful

in collecting high quality data on a depth-profiling mooring (Johnson et al., 2009, 2016; Martz et al., 2010). These recent measurements in the open and coastal ocean have shown that the pH varies greatly in time and space, reflecting complex circulation patterns that are likely due to the influence of low pH deep water through mixing and the intrusion of low pH, fresh and/or estuarine water (Dore et al., 2009; Byrne et al., 2010; Hofmann et al., 2011; Yu et al., 2011). Earlier, an innovative approach of combined *in situ* pumping and shipboard measurements of $p\text{CO}_2$ also demonstrated rapid spatial variations of the CO_2 system in the upwelling margin offshore Oregon, United States (Hales et al., 2005). These fluctuations may lead to large ecological and economic impacts, thus reinforcing the need for reliable high-resolution observations of the full water column.

Significant improvements could be immediately achieved with the implementation of a real-time monitoring network that quantifies the spatial location, duration, and transport of the low pH/ Ω_{Arag} water in coastal regions (Feely et al., 2010b; Martz et al., 2010). The spatial, temporal, and depth resolution achieved from Teledyne Webb Slocum glider data far exceeds that from traditional sampling from ships and moorings (Rudnick et al., 2004; Schofield et al., 2007). These systems can sample in depths as shallow as 4 meters and as deep as 1000 m and have been used in a broad range of challenging environments including near ice shelves in the Antarctic, beneath hurricanes and coastal storms, and on river dominated continental shelves. Recent calls for a national (Baltes et al., 2014) and international observational network for OA identified underwater gliders as a potential pH monitoring instrument that “could resolve shorter space-time scale variability of the upper ocean” (Feely et al., 2010b; Martz et al., 2010). A variety of sensors have successfully been mounted on Slocum gliders. To date, however, no direct measurements of ocean pH have been collected by pH sensors integrated into these gliders.

We present here the recent development of the first integrated glider platform and sensor system for collecting pH data in the water column of the coastal ocean on a regional scale. Specifically, we modified and integrated a deep-depth rated version of the ISFET-based pH sensor system (Johnson et al., 2009, 2016; Martz et al., 2010), into a Slocum G2 glider science bay. In addition to pH, the glider is equipped with sensors that provided profiles of conductivity, temperature, depth, spectral backscatter, chlorophyll fluorescence, and dissolved oxygen (DO) that enabled the mapping of ocean pH against the other variables and the calculation of A_T and Ω_{Arag} . Here, we describe the performance of the new sensor from seawater tank tests and from the first *in situ* deployments within the U.S. Northeast Shelf (NES), one of the nation’s most economically valuable coastal

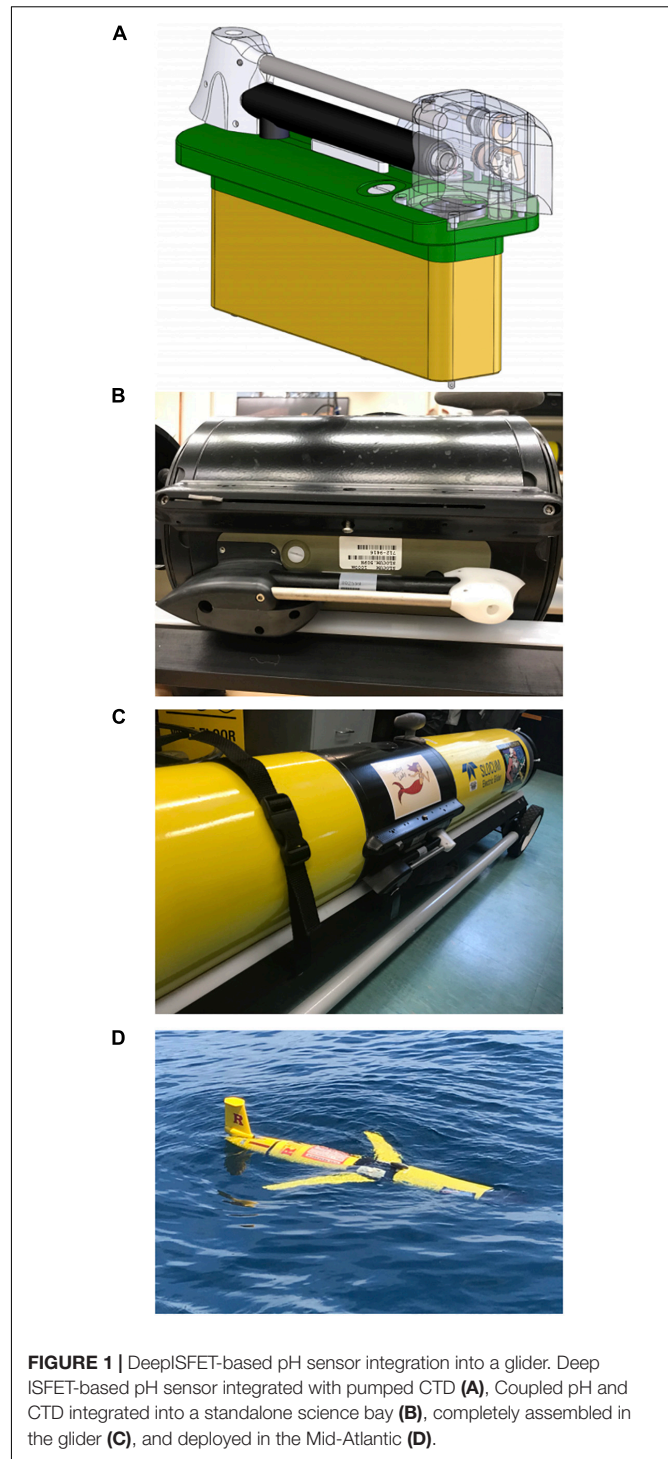
fishing regions. Water column pH measurements in this region are sorely lacking; hence, the glider deployments presented here deliver a much-needed full characterization of water column pH dynamics in this coastal region from the nearshore to the shelf-break and demonstrate the application of glider-based acidification monitoring in other coastal regions.

EXPERIMENTAL SECTION

pH Sensor Integration

The deep ISFET-based pH sensor was modified by Sea-Bird Scientific, and its integration into a Slocum Webb G2 glider (200 m) was a coordinated effort between Rutgers, Sea-Bird Scientific, and Teledyne Webb Research. To optimize the performance of the pH sensor for use on a glider Sea-Bird Scientific significantly modified the original design of Deep-Sea DuraFET, and ISFET-based sensor developed by MBARI (Johnson et al., 2016). Given the light sensitivity of the sensor and desire to be closely coupled with CTD (conductivity, temperature, depth) data acquisition, the deep ISFET-based sensor was reconfigured by Sea-Bird Scientific to fit into the existing rectangular glider CTD port utilizing a shared pumped system to pull seawater in past both the pH and CTD sensor elements (**Figure 1A**). Prior to integration with the glider CTD, the deep ISFET-based pH sensor was calibrated in a custom temperature-controlled pressure vessel filled with 0.01 N HCl over the range of 5–35°C and 0–3000 psi (Johnson et al., 2016). After the temperature and pressure calibration was completed, the pH sensor was integrated with the glider SBE41CP pumped CTD and conditioned in natural seawater for 1 week (Johnson et al., 2016). Based on the laboratory data collected at Sea-Bird Scientific the current specifications for the glider-based Deep-Sea DuraFET pH sensor are ± 0.05 pH units in accuracy and ± 0.001 pH units in precision. The resulting streamlined version utilizes the same mounting form factor as the SBE41CP pumped CTD, the standard model presently installed in Slocum gliders. Teledyne Webb Research facilitated the integration of the new deep ISFET pH/CTD unit into a standard glider science bay hull section (**Figure 1B**). This standalone science bay was also outfitted with a Sea-Bird Scientific ECO puck (BB2FL) configured for simultaneous fluorescence, CDOM, and optical backscatter measurements, and complimented the existing Aanderaa optode integrated into the aft of the glider for measuring DO. Teledyne Webb Research environmentally cycled (pressure and temperature), bench tested, and performed in-water tests on the completed assembly prior to deployment. A proglot was written for the glider science processor to ingest, store, and make available the data at each surface interval.

After the sensor calibrations and pre-deployment tests were completed by Sea-Bird Scientific and Teledyne Webb Research, the science sensor bay was assembled into the glider (**Figure 1C**) and placed in a natural seawater tank at Rutgers University for a minimum of 1 week at room temperature and pressure in order for the pH sensor to condition to seawater off the coast of Atlantic City, New Jersey (Bresnahan et al., 2014; Johnson et al., 2016).



pH Data Analysis

pH_{total} was calculated using the glider-measured reference voltage, pressure, sea water temperature, salinity, and sensor-specific calibration coefficients. Calculations were completed in Matlab (Johnson et al., 2017), and the code is provided in the **Supplementary Material**. The final equation used to calculate pH (below) was derived and modified from previous efforts

(Khoo et al., 1977; Millero, 1983; Dickson et al., 2007; Martz et al., 2010; Johnson et al., 2016):

$$pH_{total} = \frac{V_{ref} - k_0 - k_2 * t - f(p)}{S_{ernst}} + \log(Cl_T) \\ + 2 * \log(\gamma_{HCl})_{T,P} - \log\left(1 + \frac{S_T}{K_{STP}}\right) \\ - \log\left(\frac{1000 - 1.005 * S}{1000}\right)$$

Where:

$$S_{ernst} = \frac{R * T * \ln(10)}{F}$$

$$\log(\gamma_{HCl})_{T,P} = \log(\gamma_{HCl})_T + \left(\frac{V_{HCl}^{*p}}{\ln(10)RT}\right) / 2$$

R is the universal gas constant = 8.314472 J/(mol*K);

t is the temperature in °C;

T is the temperature in K;

S is salinity in psu;

P is the pressure in dbar;

p is the pressure in bar;

F is the Faraday constant = 96485.3415 C/mol;

k₀ is the cell standard potential offset;

k₂ is the cell standard temperature slope;

f(p) is the sensor pressure response function;

V_{ref} is the reference voltage;

V_{HCl} is the partial molar volume of HCl;

Cl_T is total chloride;

(γ_{HCl})_T is the HCl activity coefficient at T;

(γ_{HCl})_{T,P} is the HCl activity coefficient at T and p;

S_T is total sulfide;

K_{STP} is the acid dissociation constant of HSO_{4,T&P}.

Tank Tests to Determine Sensor Conditioning Time

We conducted a series of tests October 17–November 6, 2018 to determine ISFET sensor conditioning time (**Figure 2A**). First, the glider was placed in a tank filled with natural seawater collected from nearshore waters near Atlantic City, NJ, United States. The pH/CTD sensors were immediately turned on with data continuously recording and transmitting in real-time using a Freewave modem linked to Teledyne Webb Slocum Fleet Mission Control software. This test defined the time required of an “off the shelf” pH sensor to condition or equilibrate to local seawater. A second set of tests investigated the response of the pH sensor to various wet/dry exposure time frames, representing scenarios wherein the sensor may be kept dry for periods of a few hours to days, such as during local, overnight, or distant transit from the laboratory facility to the field prior to a deployment (**Figures 2B–E**). Specifically, the second set of tests determined conditioning period after: (1) the glider was turned off for 2 h while the pH sensor remained submerged in the tank, then turned back on (**Figure 2B**); (2) the glider was removed from the tank

and the pH sensor dried for 3 h, then the glider was placed back in the tank and turned on (**Figure 2C**); (3) the glider was removed from the tank and the pH sensor dried for 1 day then the glider was placed back in the tank and turned on (**Figure 2D**); and (4) the glider was removed from the tank and the pH sensor dried for 3 days then the glider was placed back in the tank and turned on (**Figure 2E**). The pH sensor was considered conditioned for each set of tests after the pH measurements stabilized with minimum drift (± 0.0001 pH units hour⁻¹ or ± 0.003 pH units day⁻¹).

During the tank tests, discrete seawater samples were collected from the tank next to the glider at least three times daily and measured immediately on a spectrophotometric pH system set up next to the seawater tank. Accuracy of the glider pH sensor was determined as the pH measurement offset between glider pH and pH measured spectrophotometrically after the pH glider sensor was conditioned.

First Glider Deployments

After the sensor integration, factory calibration, testing, and conditioning was complete, we tested the capability of the glider sensor package in two deployments in coastal waters along the U.S. Northeast Shelf. Slocum gliders operate by increasing and decreasing volume with a buoyancy pump to dive and climb in repeat sawtooth sampling patterns. Wings, a pitch battery, and the shape of the glider body result in forward motion with an aft rudder and internal compass maintaining a pre-programmed heading while underwater. At pre-programmed surface intervals the glider acquires new location information, downloads new mission parameters, and sends back real time data. The glider, RU30, used in this study was a coastal glider with a 200 m rated pump. Coastal gliders profile vertically at 10–15 cm s⁻¹ and travel horizontally at speeds of ~20 km day⁻¹. Science sensors sample at 0.5 Hz resulting in measurements at every 20–30 cm intervals vertically.

We first deployed the glider on May 2, 2018 ~9 km off the coast of Atlantic City, NJ (17 m water depth) (**Figures 1D, 3**, magenta track). This glider was powered by alkaline battery pack which supports a typical deployment for 3–4 weeks. Upon deployment, we conducted a CTD hydrographic profile and several individual casts with a 5 L Niskin bottle to sample discrete seawater samples for validating the sensor (see below) while the glider was conducting dives 50–100 m from the vessel. Once water sampling was completed, the glider was sent toward its next offshore waypoint to begin its cross-shelf transect. The glider completed a full cross-shelf transect in 20 days, and was recovered on May 22, 2018 ~24 km off the coast of Atlantic City, NJ (25 m water depth). A subset of the full glider datasets were sent to shore in near real time via Iridium satellite cell phone located in the glider tail. After each glider sampling segment the glider surfaces, inflates an air bladder in the tail section, and connects to shore via iridium satellite cell phone. These datasets included all science variables necessary to calculate pH. This allowed for initial data quality checks while the glider was deployed, and ensured that if the glider was lost critical science data was still collected. After the glider was recovered, the full datasets were downloaded from the science memory cards stored onboard and are the datasets used throughout this publication. We have made

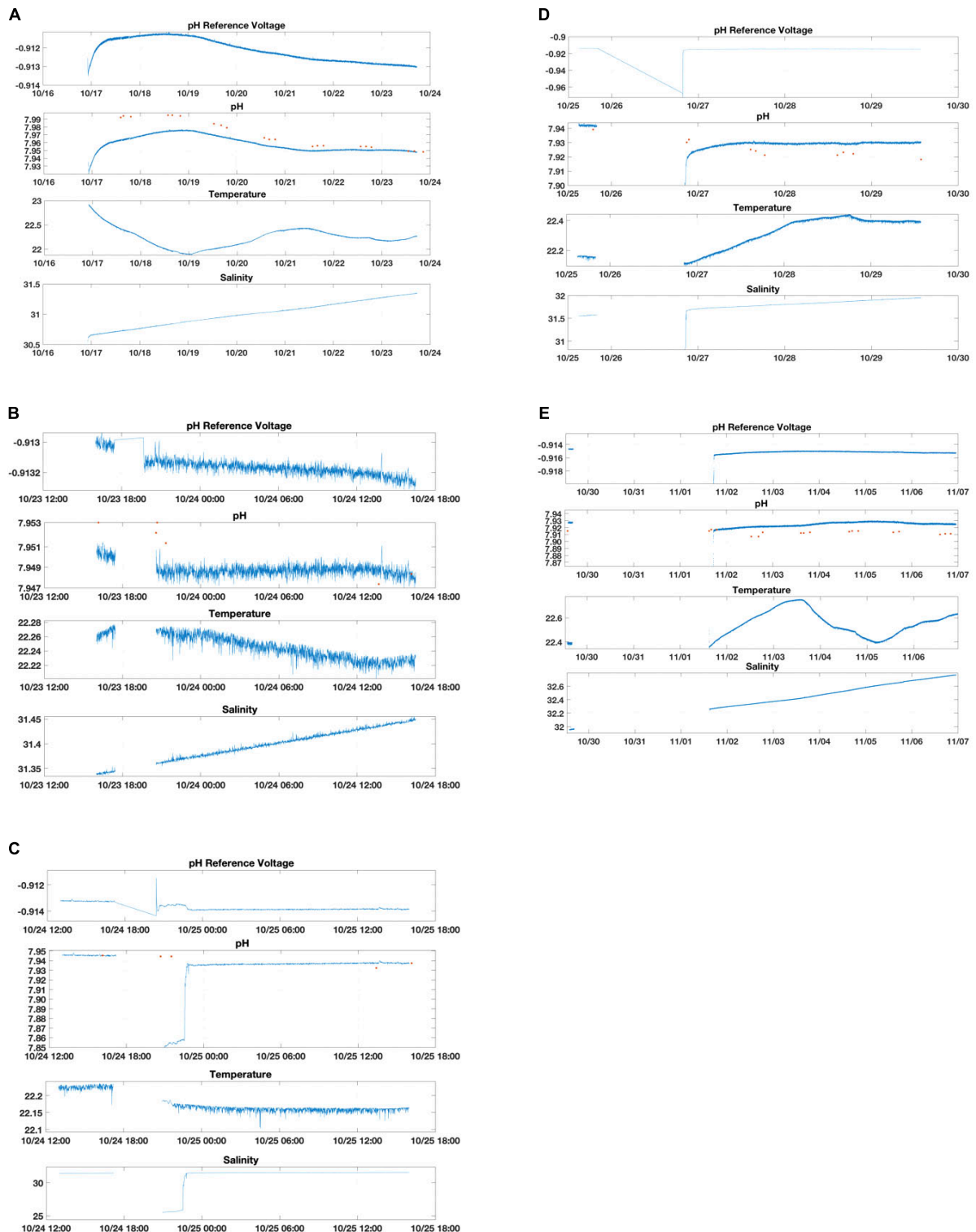
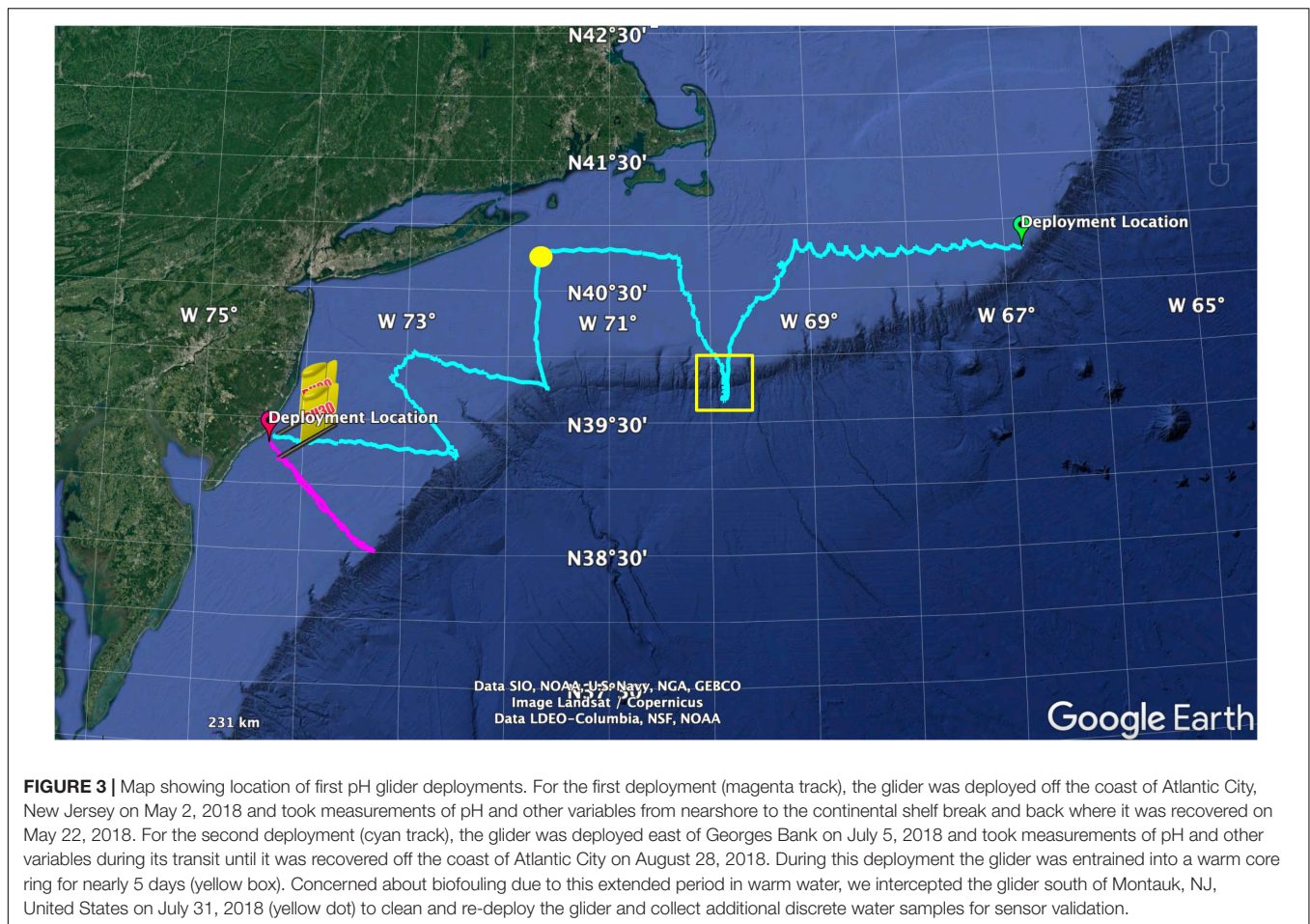


FIGURE 2 | Glider pH and discrete (spectrophotometric) pH tank test conditioning experiments. Data shown includes pH reference voltage measurements, calculated pH, temperature and salinity over time (month/day, for longer conditioning periods; month/day time, for shorter conditioning periods). The glider was placed in a saltwater tank and the pH/CTD sensor was turned on to determine times for initial conditioning from a sensor “off the shelf” (**A**); conditioning after pH/CTD sensor turned off for 3 h while submerged in tank then turned back on (**B**); conditioning after glider removed from tank and sensor dry for 2 h then placed back in the tank and turned on (**C**); conditioning after glider removed from tank and sensor dry for 1 day then placed back in the tank and turned on (**D**); conditioning after glider removed from tank and sensor dry for 3 days then placed back in the tank and turned on (**E**). Data gaps represent the dry/off period.



the glider variable data available and openly accessible on the ERDDAP server. The delayed mode time-series that contains all of the data as present in the source data files is accessible at: <http://slocum-data.marine.rutgers.edu/erddap/tabledap/ru30-20180502T1355-trajectory-raw-delayed.html>. The raw profile dataset that contains the data but broken up by glider profiles (not a time-series) is accessible at: <http://slocum-data.marine.rutgers.edu/erddap/tabledap/ru30-20180502T1355-profile-raw-delayed.html>. The science dataset that contains only scientifically relevant variables is accessible at: <http://slocum-data.marine.rutgers.edu/erddap/tabledap/ru30-20180502T1355-profile-sci-delayed.html>. Glider data processing, including analyses for sensor time lag corrections (below), was conducted using Slocum Power Tools available at: <https://github.com/kerfoot/spt>.

A second glider deployment occurred on the eastern edge of Georges Bank on July 5, 2018 (Figure 3, cyan track). This glider was powered by a lithium battery pack (configuration was 78 DD cells in a three series) which supports a typical deployment for nearly 60 days. At the time of this deployment, discrete seawater samples were collected in surface waters within 5 m from the pH/CTD glider sensor. After which the glider was sent west over Georges Bank. During a 4–5 days period (July 18–22), the glider was entrained in a warm core ring on the shelf break in waters

off southern New England (Figure 3, yellow box). Concerned about biofouling due to this extended period in warm water, we intercepted the glider south of Montauk, NJ on July 31, 2018 (Figure 3, yellow dot) to clean the glider and collect additional discrete water samples for sensor validation. The glider was moderately biofouled and included biofouling inside the sensor intake (Figure 4). The glider and sensor were cleaned as much as possible by flushing with seawater and using brushes and cloth, but we were unable to remove biofouling in the far reaches of the internal sensor surfaces. The glider was re-deployed and continued on its transit where it was recovered off the coast of Atlantic City, NJ, United States on August 28, 2018. Due the evidence of biofouling during this summer deployment, we do not present here the full datasets and only report biofouling impacts on pH measurements and derived A_T .

Sensor Time Lag Corrections

Thermal lag corrections were applied to conductivity measurements prior to calculating pH. In a standard Sea-Bird CTD temperature is measured outside of the conductivity cell while conductivity is measured inside of the cell resulting in a mismatch in the measurements then used to calculate salinity, density, and subsequently pH (Garau et al., 2011). Thermal lag typically results in incorrect salinity and density estimates



FIGURE 4 | Biofouling on the glider deep ISFET-based pH sensor after 26 days during the July–August, 2018 deployment. The glider was intercepted, cleaned, and re-deployed south of Montauk, NJ, United States on July 31, 2018.

when the glider profiles through sharp interfaces. To address the thermal lag, temperature and conductivity data were binned in 0.25 m increments. Sequential temperature and conductivity profile pairs (one upcast and one downcast) were averaged together and the average profile was interpolated back to the original sampling depths. Salinity was calculated based on the corrected temperature and conductivity profiles.

Reference voltage and derived pH measurements exhibited a time lag during deployment, identified as skewed shifts in upcast and downcast measured (reference electrode) and derived pH (**Figures 5A,B**). To correct this lag, we first identified all upcast/downcast pairs (where there is an upcast followed by a downcast during the deployment). To determine the time shift that best matches the location of the clines, in this case typically a halocline, in an upcast and subsequent downcast, each pair was run through iterations of time shifts from 0 to 120 s at 5 s intervals. Optimal time shift was identified as the shift that minimized the difference of reference voltage in the two arms of the inverse V trajectory (upcast and subsequent downcast). We plotted optimal time shift for each upcast/downcast pair over time (**Figure 5C**) and optimal time shifts throughout full deployment as a histogram to determine shift peaks over time (**Figure 5D**). We observed 2 peaks during the May 2018 deployment, so one shift (47 s) was applied to first 1/3 of the deployment and a second shift (30 s) was applied to the last 2/3 (**Figures 5A,B**). July had 3 peaks (46, 81, 104 s) which were applied to those corresponding sections of deployment (data not shown).

Total Alkalinity Estimations and Aragonite Saturation State Calculations

To complement our glider pH measurements and to fully resolve the carbonate system, A_T was estimated from simultaneous glider salinity measurements. A_T exhibits near-conservative behavior with respect to salinity in the Atlantic along the east coast of the

United States (Cai et al., 2010; Wang et al., 2013). To estimate A_T , we used the following linear regression equation, determined from the salinity- A_T relationship at three cross-shelf transects along the U.S. NES (Massachusetts, New Jersey, and Delaware) sampled during the ECOA-1 cruise (summer 2015) (total 170 pairs of A_T and salinity data, $R^2 = 0.99$).

$$A_T = 50.04 * x + 564.08$$

Where x is salinity.

Final carbonate system parameters, including Ω_{Arag} , were calculated in Matlab using CO2SYS (van Heuven et al., 2011), with glider measured temperature, salinity, pressure, and pH and glider-derived salinity-based A_T as inputs. We used total pH scale (mol/kg-SW), K_1 and K_2 constants (Mehrbach et al., 1973) with refits (Dickson and Millero, 1987), and the acid dissociation constant of $KHSO_4$ in seawater (Dickson, 1990).

Quality Assurance and Quality Control (QA/QC)

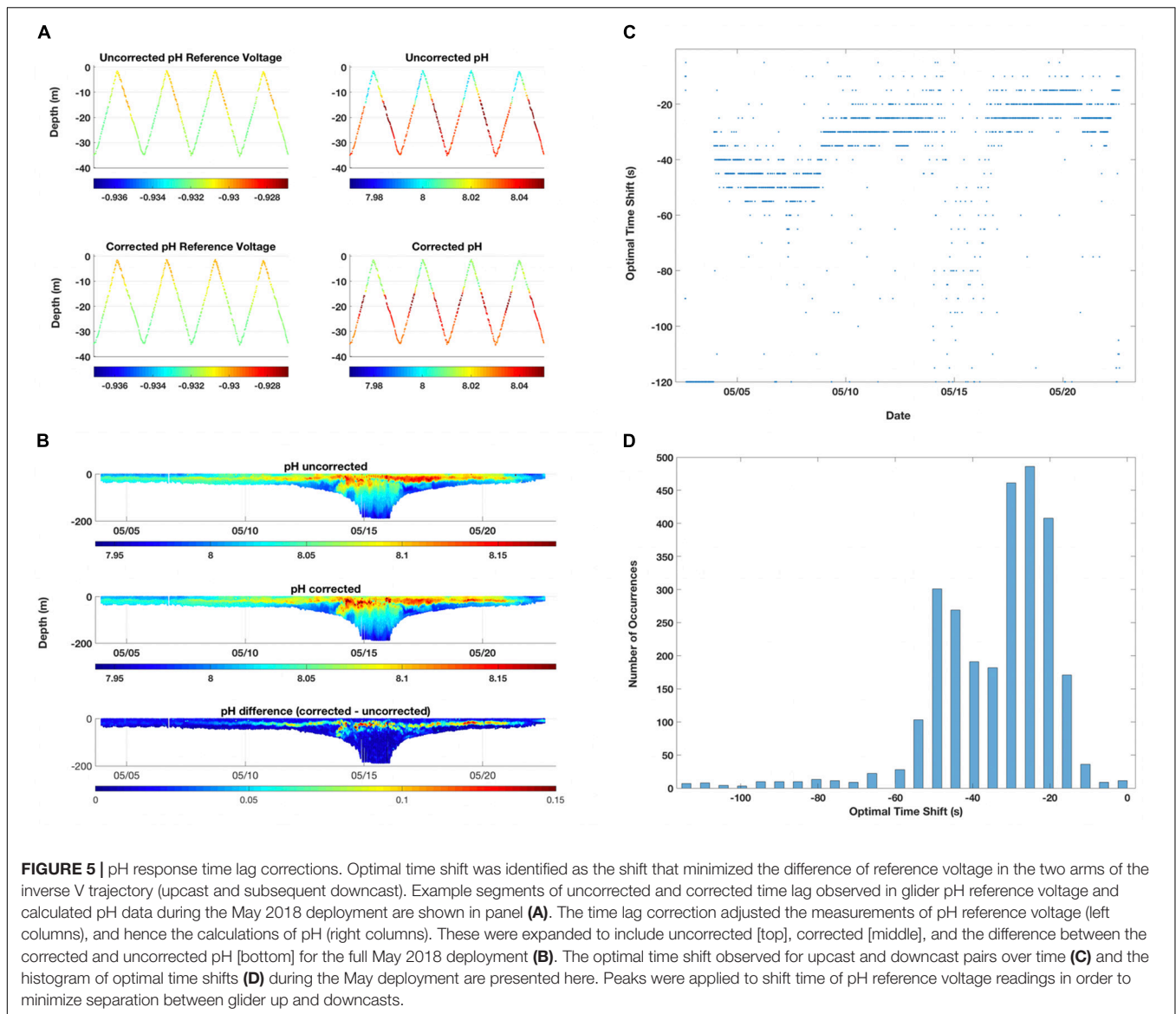
The hydrographic (CTD) and DO data collected during the glider missions follows the QA/QC procedures outlined in an approved EPA Quality Assurance Project Plan (QAPP) that was developed specifically for glider observations of DO along the New Jersey coast (Kohut et al., 2014). The procedures include pre- and post-deployment steps for each sensor to ensure data quality for each deployment. Beyond these common measurements, the science bay of the glider was outfitted with an ECO puck and the profiling deep ISFET-based pH sensor. QA/QC procedures for each sensor are described in detail below.

CTD

The hydrographic data for each mission was sampled with a pumped CTD specifically engineered for this glider. Based on manufacturer specifications, the CTD was factory calibrated by SeaBird Scientific upon completion of the CTD-pH sensor integration. The QAPP requires a two-tier approach to verify the temperature and conductivity data from the glider CTD (Kohut et al., 2014). The first-tier test is a pre- and post-deployment verification between the glider CTD and a factory calibrated Sea-Bird-19 CTD in our ballast tank at Rutgers University in New Brunswick, NJ, United States. The second-tier test is an *in situ* verification at both the deployment and recovery of the glider. For each deployment and recovery, we lowered a manufacturer calibrated SeaBird-19 CTD to compare to the concurrent glider profile. This second-tier test gives an *in situ* comparison within the hydrographic conditions of the mission.

Aanderaa Optode

The DO data was sampled with an optical sensor unit manufactured by Aanderra Instruments called an optode. Like the CTD, we deployed a glider optode that is factory calibrated at least once per year. In addition to these annual calibrations, we also completed pre- and post-deployment verifications. To do this we compared optode observations to concurrent Winkler titrations of a sample at both 0



and 100% saturation. The verification for this deployment met the QAPP requirement that all optode measurements are within 5% saturation of the results of the Winkler titrations for both the 0 and 100% saturation samples (Kohut et al., 2014).

BB2FL ECO Puck

The puck we deployed was standard factory calibration from WET Labs (recommended every 1–2 years for pucks in gliders).

Profiling Deep ISFET-Based pH Sensor

We followed Best Practices for autonomous pH measurements with the DuraFET, including the recommended rigorous calibration and ground truthing procedure (Bresnahan et al., 2014; Martz et al., 2015; Johnson et al., 2016). Using a 5 L Niskin bottle aboard the vessel during deployment and recovery,

replicate water samples were collected near the glider from multiple depths (0.5 m, depth of thermocline, and 2 m from bottom; see Table 1). During this 1–2 h sampling procedure, the glider sampled the water column near the vessel. Water samples were collected for pH, DIC, and A_T analysis from the Niskin bottle into two 250 mL borosilicate glass bottles for a specific depth, with one bottle for DIC and A_T and another bottle for pH. Sampling involved overflow of seawater for at least one to two volumes, after which bottles were gently filled completely to avoid gas exchange with surrounding air. One mL of sample was removed to create a small headspace to allow for seawater expansion. The sample was then poisoned with 50 μ L of saturated mercuric chloride, sealed with a pre-greased glass stopper and rubber band, and stored in a cool, dark location until analysis at Cai's laboratory (University of Delaware). Discrete sample pH was measured spectrophotometrically at 25° Celsius on the total

TABLE 1 | Comparisons between glider pH and derived total alkalinity (A_T) and discrete pH and A_T measured from seawater samples during the spring glider deployment (May 2018).

Date	Depth (m)	Glider pH	Discrete pH	pH Difference (Glider – Discrete)	Glider A_T	Discrete A_T	A_T Difference (Glider – Discrete)
May 2	0.5	7.945	7.977	−0.032	2119.3	2149.7	−30.4
May 2	0.5	7.945	7.975	−0.030	2119.3	2149.8	−30.5
May 2	0.5	7.945	7.976	−0.031	2119.3	2147.6	−28.3
May 2	11	7.947	7.938	0.009	2130.1	2154.3	−24.2
May 2	11	7.947	7.941	0.006	2130.1	2154.1	−24.0
May 2	11	7.947	7.942	0.005	2130.1	2155.0	−24.9
May 2	15	7.973	7.958	0.015	2141.3	2153.8	−12.5
May 2	15	7.973	7.972	0.001	2141.3	2154.1	−12.8
May 2	14	7.972	7.955	0.017	2138.9	2152.7	−13.8
May 22	0.5	8.010	8.026	−0.016	2079.8	2091.7	−11.9
May 22	0.5	8.010	8.024	−0.014	2079.8	2091.0	−11.2
May 22	9	7.988	8.001	−0.013	2094.0	2108.2	−14.2
May 22	9	7.988	8.002	−0.014	2094.0	2106.9	−12.9
May 22	23	7.987	7.998	−0.011	2142.1	2155.0	−12.9
May 22	23	7.987	7.993	−0.006	2142.1	2155.1	−13.0

At glider deployment (May 2) and recovery (May 22), water samples were collected from various depths using a 5 L Niskin bottle, preserved, and returned to the laboratory for determination of pH, A_T , and Dissolved Inorganic Carbon (DIC). During this 1–2 h water sampling procedure, the glider sampled the water column in proximity to the vessel. Values displayed here are replicate discrete pH measurements (corrected for *in situ* temperature and salinity) and glider pH measurements averaged at each sample depth (± 0.5 m) over the sampling period. Additionally, glider A_T ($\mu\text{mol kg}^{-1}$) was calculated using a linear regression determined from the salinity- A_T relationship at three cross-shelf transects along the U.S. Northeast Shelf (Massachusetts, New Jersey, and Delaware) sampled during the ECOA-1 cruise (summer 2015).

pH scale using purified M-Cresol Purple purchased from R. Byrne at the University of South Florida (Clayton and Byrne, 1993; Liu et al., 2011). Cai's lab has built a spec-pH unit similar to the Dickson Lab (Carter et al., 2013). The accuracy of pH data was verified against *Tris* buffers (Millero, 1986; DelValls and Dickson, 1998) purchased from Andrew Dickson at UCSD Scripps Institute of Oceanography and through joining inter-laboratory comparisons. A_T titrations were performed using open cell Gran titration and Apollo Scitech A_T titrator AS-ALK2 following previously described methods (Cai et al., 2010; Huang et al., 2012; Chen et al., 2015). DIC was measured using an Apollo Scitech DIC analyzer AS-C3, which acidifies a small volume of seawater (1.0 mL) and quantifies the released CO_2 with a LI-7000 Non-Dispersive InfraRed analyzer (Huang et al., 2012; Chen et al., 2015). Precision of A_T and DIC are better than $\pm 0.1\%$. Measurements of A_T and DIC were quality controlled using CRMs obtained from Andrew Dickson at UCSD Scripps Institute of Oceanography. The internal consistency was first evaluated among DIC, A_T , and pH using the Excel version of CO2SYS (Pierrot et al., 2006). Then we conducted temperature correction for the measured pH values to the *in situ* conditions using the same Excel version of CO2SYS the guidelines for input (analysis) and output (*in situ*) temperature, a total pH scale (mol/kg-SW), K_1 and K_2 constants (Mehrbach et al., 1973) with refits (Dickson and Millero, 1987), and the acidity constant of KHSO_4 in seawater (Dickson, 1990). These discrete samples were compared to the glider deep ISFET pH measurements. Discrete pH and A_T measurements collected during this work are available below and in the **Supplementary Material**. Final carbonate system parameters on the discrete water samples were calculated using CO2SYS (Pierrot et al., 2006).

RESULTS AND DISCUSSION

Sensor Conditioning Time and Performance

Two processes occur when the Deep-Sea pH sensor is introduced to a new sample of seawater. First, the external electrode equilibrates with the new ionic concentration of the seawater or conditioning. This conditioning can take minutes to days depending on how different the ionic composition of the seawater is from the seawater the pH sensor was calibrated in at Sea-Bird (Pacific seawater collected near Hawaii). Second, the ISFET and counter electrode polarize. This polarization can take minutes to hours to complete. Once the conditioning of the pH sensor is complete, if sensor power is removed or the connection between the ISFET and the counter electrode is broken (e.g., a drying period) the sensor will need to repolarize again. We conducted a series of tests to determine sensor conditioning time initially (**Figure 2A**), and conditioning after variable time periods when the sensor was either turned off and kept wet or removed from tank and kept dry (**Figures 2B–E**). In the initial test, pH determined from the new sensor conditioned and reached within 0.005 pH units from the discrete pH values after 4–5 days of soak time in the natural seawater tank (**Figure 2A** and **Supplementary Material**). This is most likely due to the sensor equilibrating to the new seawater for the first time.

After this initial conditioning time, the pH/CTD sensor was turned off for 2 h while submerged in the tank then turned back on with the pH measurements stabilizing immediately and the offset between glider and discrete pH returning to within 0.003 pH units (**Figure 2B** and **Supplementary Material**). The glider and sensor were then turned off and removed from tank and

kept dry for 3 h then placed back in the tank and turned on. The pH measurements stabilized and the offset returned to within 0.002 pH units within 17 h, and this likely occurred much sooner but discrete samples were not collected during the overnight period to confirm (**Figure 2C** and **Supplementary Material**). This conditioning was likely due to either a bubble trapped on the sensor that was cleared shortly after it was turned back on or the sensor repolarizing after being dried. The glider and sensor were then turned off and removed from tank and kept dry for 24 h then placed back in the tank and turned on. The pH sensor conditioned within 17 h, but the pH offset stabilized (± 0.003 pH units) between 0.006 and 0.008 pH units for the next few days (**Figure 2D** and **Supplementary Material**). This test was repeated, except the dry period lasted 3 days prior to placing the glider/sensor back in the tank. The pH offsets stabilized (± 0.003 pH units) after nearly 3 days, but this final offset between glider and discrete pH measurements was larger ($0.012 - 0.015$ pH units) (**Figure 2E** and **Supplementary Material**).

It is likely that after the 4–5 days of initial sensor stabilization, the sensor continued to condition or drift but at slower, gradual rate until reaching an average pH offset from discrete samples of 0.013 ± 0.001 after 18 days. This pH offset was similar to that seen *in situ* after initial sensor conditioning during the 3-week May 2018 glider deployment in the Mid-Atlantic Bight (absolute value range: 0.001–0.017; mean \pm SD: 0.011 ± 0.005 , $n = 12$). Therefore prior to a glider deployment, we recommend a minimum of 5 days of soak time in natural seawater collected from the field location. Another possibility for the gradual increase in pH offset between the glider and the discrete samples could be biofouling in the tank. The tank was filled with coarsely filtered, unsterilized natural seawater and kept at room temperature (not temperature-controlled). Although it was not visibly apparent, it is possible that a biofilm layer could have developed during the 18-day trial and contributed to or primarily caused the gradual sensor drift.

Nonetheless, an accuracy of 0.013 pH units achieved in the tank test (and 0.011 pH units in the field; see below) exceeded our expectations given the current specifications for this deep ISFET-based pH sensor are ± 0.05 pH units in accuracy and ± 0.001 pH units in precision.

In situ Glider and Discrete Sample pH and A_T Comparisons

On the first deployment (May 2018), absolute pH differences observed between glider pH and pH measured spectrophotometrically from discrete samples were quite variable, ranging from 0.001 to 0.032 pH units (**Table 1**). Discrepancies in the surface water at deployment were largest (mean \pm SD: 0.031 ± 0.001 , $n = 3$) compared to surface water at recovery and subsurface water at both deployment and recovery (absolute value range: 0.001–0.017; mean \pm SD: 0.011 ± 0.005 , $n = 12$). We attribute the large pH discrepancies in the surface at the start of the deployment and water sample collection to the sensor not yet being stabilized or conditioned after being out of the tank for 4–5 h during transit from the lab to the field. Offsets observed in surface water at recovery and subsurface water at both deployment and recovery might represent the

logistical challenges faced when attempting to collect discrete water samples next to the glider, resulting in either salinity inputs, depth, and/or sampling time differences between glider pH measurement and pH in discrete seawater samples.

The Niskin sampling bottle used for seawater collection did not have a CTD attached which posed two challenges. First, to calculate pH using the spectrophotometric method, temperature and salinity data at target depths from the initial CTD cast conducted prior to Niskin water bottle sampling commenced were used as inputs to calculate pH. Therefore, potential salinity (and pH) changes at target depths between the CTD cast and water sampling (0.5 – 1.5 h) could have occurred due to boat drift and/or currents. Second, cable metered markings were relied upon to reach target depths, and currents or slack on the cable could have resulted in sampling at depths above the target causing mismatch between glider pH and spec pH measurements. This is supported also by high variability observed in discrete pH between replicate Niskin casts/bottle samples at certain depths (May 2, 15 m: discrepancy of 0.014 pH units; **Table 1**). Improvements in sampling techniques are now being employed. For example, upon deployment on July 2, surface seawater samples were collected using a Niskin water bottle deployed adjacent to the glider just after its deployment from the vessel (within a 5 m distance from the glider pH sensor), which greatly reduced the discrepancies between glider pH and discrete pH seen in the first deployment (range: 0.001–0.004 pH units; **Table 2**). Further improvements in water sampling technique could be made, specifically for subsurface seawater pH comparison, by using a CTD mounted on a rosette frame with multiple Niskin bottles to ensure sampling occurs at target depth and simultaneous measurements of salinity and temperature with each depth-specific sample collection.

The greatest challenge with *in situ* sensor validation was obtaining subsurface water samples next to the glider. During the time water sampling was being conducted on board (1–2 h), the pH glider conducted repetitive dives to sample the full water column near the vessel. While water sampling was conducted in proximity to the glider (within ~ 100 m), it could have occurred far enough away that different patches were sampled by the two methods creating the offset in pH measurements. Simply, the two different sampling techniques were not measuring pH (glider) or collecting seawater for pH measurements (Niskin/discrete) at the same depths at the same place and at the same time. Future missions should test different sampling techniques (e.g., attaching glider to CTD rosette) to improve subsurface sensor validation that will minimize discrepancies at depth.

During multiple deployment and recovery practices in the U.S. NES, glider salinity-based estimations of A_T were consistently lower than A_T measured in discrete samples (**Tables 1–3**). Overall, the differences in water column showed similar ranges of -11.2 to $-30.5 \mu\text{mol kg}^{-1}$ for the spring deployment and recovery (**Table 1**) and of -7.3 to $-41.8 \mu\text{mol kg}^{-1}$ and -6.0 to $-34.8 \mu\text{mol kg}^{-1}$ for summer deployments and recoveries (**Tables 2, 3**), with averages of -18.5 ± 7.5 , -22.9 ± 11.1 , and $-26.5 \pm 10.9 \mu\text{mol kg}^{-1}$, respectively. The discrepancies between glider salinity-based estimates and discrete A_T likely reflect differences in water properties and/or water masses measured

TABLE 2 | Comparisons between glider pH and derived total alkalinity (A_T) and discrete pH and A_T measured from seawater samples during the summer glider deployment (July/August 2018).

Date	Depth (m)	Glider pH	Discrete pH	pH Difference	Glider A_T (Glider – Discrete)	Discrete A_T	A_T Difference (Glider – Discrete)
July 5	0.5	8.043	8.042	0.001	2270.8	2278.1	–7.3
July 5	0.5	8.043	8.039	0.004	2270.8	2279.3	–8.5
August 28	0.5	7.716	7.934	–0.218	2100.1	2120.2	–20.1
August 28	0.5	7.716	7.965	–0.249	2100.1	2119.6	–19.5
August 28	0.5	7.716	7.936	–0.220	2100.1	2119.8	–19.7
August 28	8.5	7.705	7.858	–0.153	2099.5	2128.5	–29.0
August 28	8.5	7.705	7.885	–0.180	2099.5	2112.2	–12.7
August 28	8.5	7.705	7.850	–0.145	2099.5	2125.0	–25.5
August 28	18	7.766	7.752	0.014	2108.2	2140.4	–32.2
August 28	15	7.766	7.732	0.034	2108.2	2143.5	–35.3
August 28	16	7.766	7.682	0.084	2108.2	2150.0	–41.8

At glider deployment (July 5) and recovery (August 28), water samples were collected from various depths using a 5 L Niskin bottle, preserved, and returned to the laboratory for determination of pH, A_T , and Dissolved Inorganic Carbon (DIC). During this 1–2 h water sampling procedure, the glider sampled the water column in proximity to the vessel. Values displayed here are replicate discrete pH measurements (corrected for in situ temperature and salinity) and glider pH measurements averaged at each sample depth (± 0.5 m) over the sampling period. Additionally, glider A_T ($\mu\text{mol kg}^{-1}$) was calculated using a linear regression determined from the salinity- A_T relationship at three cross-shelf transects along the U.S. Northeast Shelf (Massachusetts, New Jersey, and Delaware) sampled during the ECOA-1 cruise (summer 2015).

TABLE 3 | Biofouling impacts on glider pH measurements.

Depth (m)	Glider pH pre-clean	Glider pH post-clean	Discrete pH	pH Difference pre-clean (Glider – Discrete)	pH Difference post-clean (Glider – Discrete)	Glider A_T pre-clean	Glider A_T post-clean	Discrete A_T	A_T Difference pre-clean (Glider – Discrete)	A_T Difference post-clean (Glider – Discrete)
1	7.966	7.969	8.000	–0.034	–0.031	2171.4	2145.6	2178.3	–6.9	–32.7
8	7.952	7.984	8.033	–0.081	–0.049	2180.6	2177.7	2183.7	–3.1	–6.0
20	8.070	7.957	8.091	–0.021	–0.134	2154.6	2174.3	2199.2	–44.6	–24.9
30	8.016	7.902	7.872	0.144	0.030	2180.8	2179.8	2214.6	–33.8	–34.8
35	7.997	7.929	7.917	0.080	0.012	2187.0	2187.1	2213.5	–26.5	–26.4
55	7.926	7.848	7.893	0.033	–0.045	2193.5	2194.4	2228.6	–35.1	–34.2

During deployment in July 2018, the pH glider experienced moderate biofouling. On July 31, the glider was intercepted off of Long Island, NY, United States. Upon glider retrieval, seawater samples were collected at various depths and preserved for later analysis for comparison of glider and discrete pH and total alkalinity (A_T) measurements. An attempt was made to clean the glider and pH/CTD sensor unit before the glider was re-deployed. The data shown here are comparisons between glider pH and derived total alkalinity (A_T), just before (pre-clean) and after (post-clean) attempted cleaning of biofouling, and discrete pH and A_T measured from seawater samples. Glider pH measurements were averaged at each sample depth (± 0.5 m) over the sampling period. Glider A_T ($\mu\text{mol kg}^{-1}$) was calculated using a linear regression determined from the salinity- A_T relationship at three cross-shelf transects along the U.S. Northeast Shelf (Massachusetts, New Jersey, and Delaware) sampled during the ECOA-1 cruise (summer 2015).

during these glider deployments and the summer 2015 ECOA-1 cruise (where/when the salinity- A_T relationship was derived). These include seasonal differences in low-salinity end-member and nearshore organic alkalinity input, and ultimately, challenges for sampling and validation in this dynamic environment. The offsets between glider-derived and discrete A_T yielded lower glider-estimated Ω_{Arag} , offset from discrete Ω_{Arag} by -0.010 to -0.025 for surface waters during the Spring deployment (see **Supplementary Material**). Further work is needed for better evaluation of the relationship between A_T and salinity at nearshore lower salinity waters and different water masses in order to reduce the uncertainty that is propagated in the calculations of Ω_{Arag} using CO2SYS.

Sensor Time Lags

Two patterns emerged from the pH sensor time lag correction analyses. First, there was a change in time lag throughout

the deployment in May 2018 (47 s during first week, 30 s for last 2 weeks) (**Figures 5C,D**). This may indicate a pH sensor conditioning period, wherein the sensor was acclimating to new seawater conditions. Second, the time shift had the greatest effect in areas of abrupt water type transition, specifically in the thermocline and halocline and offshore where we encountered a warmer, saltier water mass (**Figure 5B**). The glider moved rapidly ($10\text{--}15\text{ cm s}^{-1}$) through these vertically narrow transition zones without acclimating completely, which possibly increased pH sensor response time and caused the increased time lag observed at these depths. This could be due to either a lag in the thermal equilibration of the sensor or salinity response of the reference electrode or relatively slow flushing of the cell by the CTD pump. Further investigations on sensor conditioning, response time, and variability are recommended in order to improve this initial lag correction method. Additionally, modifications in CTD pump flow rate

or glider dive approaches in highly stratified periods in coastal systems, including slower dives or step-wise vertical descents/ascents, should be considered.

Carbonate Chemistry Dynamics in the Mid-Atlantic Bight

The pH and Ω_{Arag} ranges observed during this Spring (May 2018) deployment were 7.906–8.205 and 1.48–2.22 respectively. pH was frequently observed highest in subsurface waters and was associated with the depth of chlorophyll and oxygen maximums (Figure 6). Higher pH values in the chlorophyll maximum throughout the transect ranged between 7.993 and 8.127. During primary production, photosynthesis increases pH due to the uptake of CO_2 . So, while the observed association between pH and chlorophyll was not surprising, the ability to resolve the subsurface pH peak from the high-resolution vertical sampling with the glider provides a valuable perspective from which to not only evaluate concurrent vertical distributions of pelagic organisms, but also to put into context past pH monitoring efforts that mostly sample surface waters (Boehme et al., 1998; Wang et al., 2013, 2017; Wanninkhof et al., 2015; Xu et al., 2017). Higher pH in offshore slope waters was also associated with a warmer, saltier water mass and suggests mixing processes could play a major role in driving pH dynamics on the shelf. During the deployment, the glider measured warmer water in the upper mixed layer on its return transect, depicting the strengthening of seasonal summer stratification in the upper mixed-layer due to incident solar radiation. These warm surface waters on the return transect were associated with increased pH values (Figure 6). Higher Ω_{Arag} values were consistently observed in surface waters throughout the deployment, and highest values were associated with the warm, salty, higher alkaline water mass (Figure 6).

The lowest pH typically occurred in bottom waters of the middle shelf and slope and nearshore following a period of heavy precipitation (Figure 6). Lower pH values in the mid-shelf and slope bottom waters ranged between 7.918 and 8.027. Lower pH in mid-shelf bottom water occurred in the Cold Pool as defined by remnant winter water in the Mid-Atlantic Bight centered between the 40 and 70 m isobaths (Lentz, 2017). The Cold Pool is fed by Labrador Sea slope water and is isolated when vernal warming of the surface water sets up the seasonal thermocline. The annual formation of Cold Pool water means its carbonate chemistry should reflect near real-time increases in atmospheric CO_2 and $p\text{CO}_2$ in its Labrador source water which is weakly buffered and exhibits lower pH and Ω_{Arag} (Wanninkhof et al., 2015). Thus, the dominant drivers of low pH, as well as high DIC and low Ω_{Arag} (Wang et al., 2013), in shelf bottom water were likely a combination of stratification, biological activity (i.e., higher respiration at depth), and the inflow of Labrador Sea slope water into the Cold Pool. Nearshore, lower pH was associated with lower salinity from freshwater input that was most substantial during a high period of precipitation near the end of the deployment, whereby 4.45 inches of rainfall was recorded at Atlantic City Marina, NJ, between May 12–22 (NJ Weather & Climate Network¹; Figure 6). This storm event

resulted in the freshening of the entire water column near shore (30 m; Figure 6). River runoff has low pH from the equilibration with atmospheric CO_2 concentrations, and its zero salinity and low/zero alkalinity greatly reduces buffering capacity to offset changes in $p\text{CO}_2$ and contributes to low Ω_{Arag} (Salisbury et al., 2008; Johnson et al., 2013). Lowest Ω_{Arag} values consistently occurred in bottom waters on the shelf (Figure 6). This was likely driven by lower pH in these bottom waters.

When pH is plotted as a function of temperature and salinity (Figure 7), the pH characteristics of specific water masses become more apparent. For example, the fresher nearshore surface waters and surface water over the mid-shelf are distinctively different in pH (Figure 7). Thus, carbonate chemistry variability in this system over a range of scales will be driven by: (1) episodic storm mixing, upwelling, and precipitation events; (2) Mixing of water masses and the degree of horizontal intrusion of offshore water masses onto the shelf; (3) Seasonal stratification and vertical mixing/overturning processes; and (4) a combination of biological and physical drivers on the shelf and in shelf source waters. Both the horizontal and vertical gradients of pH observed were, at times, particularly sharp, and this new glider pH sensor suite demonstrated the ability to characterize the variability and drivers of this variability in these critical zones.

Current Limitations and Need for Future Research and Development

Comparative results between the glider deep ISFET-based pH sensor and pH measured spectrophotometrically from discrete seawater samples indicate that the glider pH sensor is capable of accuracy of 0.011 pH units or better for several weeks throughout the water column in the coastal ocean, with a precision of 0.005 pH units or better. These values are similar to those reported for the Deep-Sea DuraFET sensor deployed on moorings in Johnson et al. (2016).

However, in addition to the logistical issues related to sampling seawater next to the glider for *in situ* validation described above, the primary limitation we encountered and foresee is glider and sensor biofouling during deployments. Glider batteries have been evolving over time, from alkaline to lithium one-time use to rechargeable lithiums that have greatly improved the endurance capability of gliders and glider sensors. But as the potential deployment time for gliders has increased, the chance of biofouling is increased. Biofouling can impact glider flight behavior (e.g., increased drag and reduced efficiency; Rudnick, 2016) and greatly reduce sensor performance, as was observed in the SeaFET on week to month timescales (Bresnahan et al., 2014).

During our July deployment, we experienced moderate biofouling after about 3 weeks (Figure 4), which degraded the pH measurements over deployment time (Tables 2, 3). This suggests that, at a minimum, the sensor unit was impacted, yielding unreliable pH voltage data and subsequent calculations of pH. This biofouling was likely intensified when the glider was entrained in a warm core ring for a 4–5 days period. After this event, the glider was intercepted south of Montauk, NY, United States. Seawater samples collected near the glider showed

¹<https://www.njweather.org/data/daily/272>

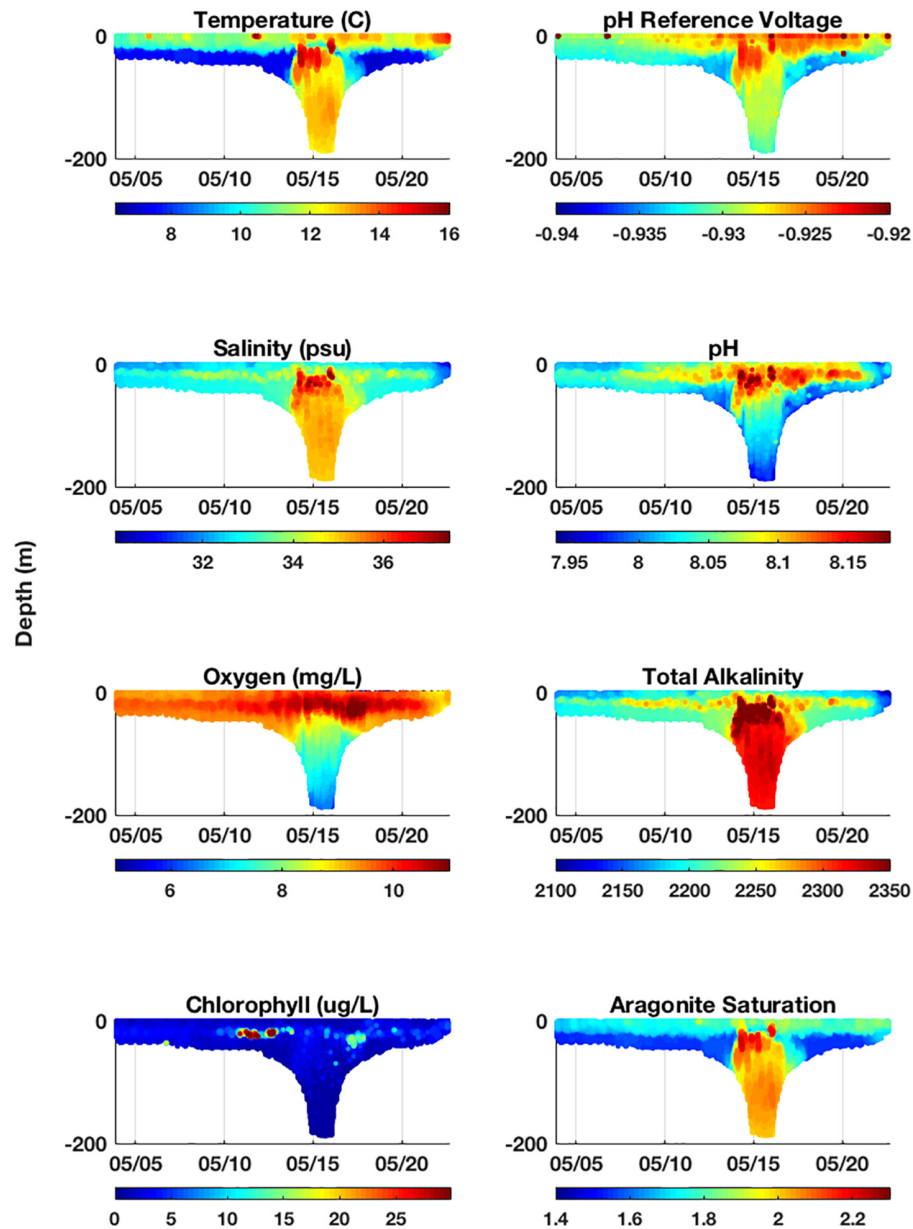


FIGURE 6 | Complete cross-sections of variables measured by the glider and calculated from glider measurements during deployment in May 2018. The glider's on-board scientific instruments measure temperature, conductivity (used to calculate salinity), dissolved oxygen concentration, chlorophyll fluorescence, and pH reference voltage (used to calculate pH). Salinity was used to estimate total alkalinity (TA) throughout deployment (see Methods). TA and pH were used as inputs into CO2SYS to resolve all carbonate system parameters, including aragonite saturation state, shown here.

the pH offsets between the glider and discrete samples were much higher compared to those at deployment (Tables 2, 3). Offsets between glider and discrete pH ranged from -0.144 to 0.081 pH units (Table 3). We made an attempt to clean the glider and sensor by flushing the sensor with seawater and using brushes of various sizes on the outer structures of the glider and sensor unit, but biofouling in the internal structure of the pH sensor unit that we could not access was still evident. Nonetheless the glider was redeployed after this cleaning process. The offsets between glider and discrete pH, ranging from -0.03 to 0.134 pH units,

remained unsatisfactory (Table 3). These offsets worsened rapidly over time, and when the glider was recovered on August 28, offsets in pH measurements ranged from -0.084 to 0.249 pH units (Table 2). The magnitude and the variability of the offsets resulting from heavy biofouling yielded pH data not acceptable for OA research. The biofouling impact seems specific to the pH sensor and not the CTD, specifically the conductivity sensor. Comparisons of salinity between the glider CTD profiles and the hand-lowered SeaBird-19 CTD conducted at each glider deployment and recovery passed the *in situ* verification process.

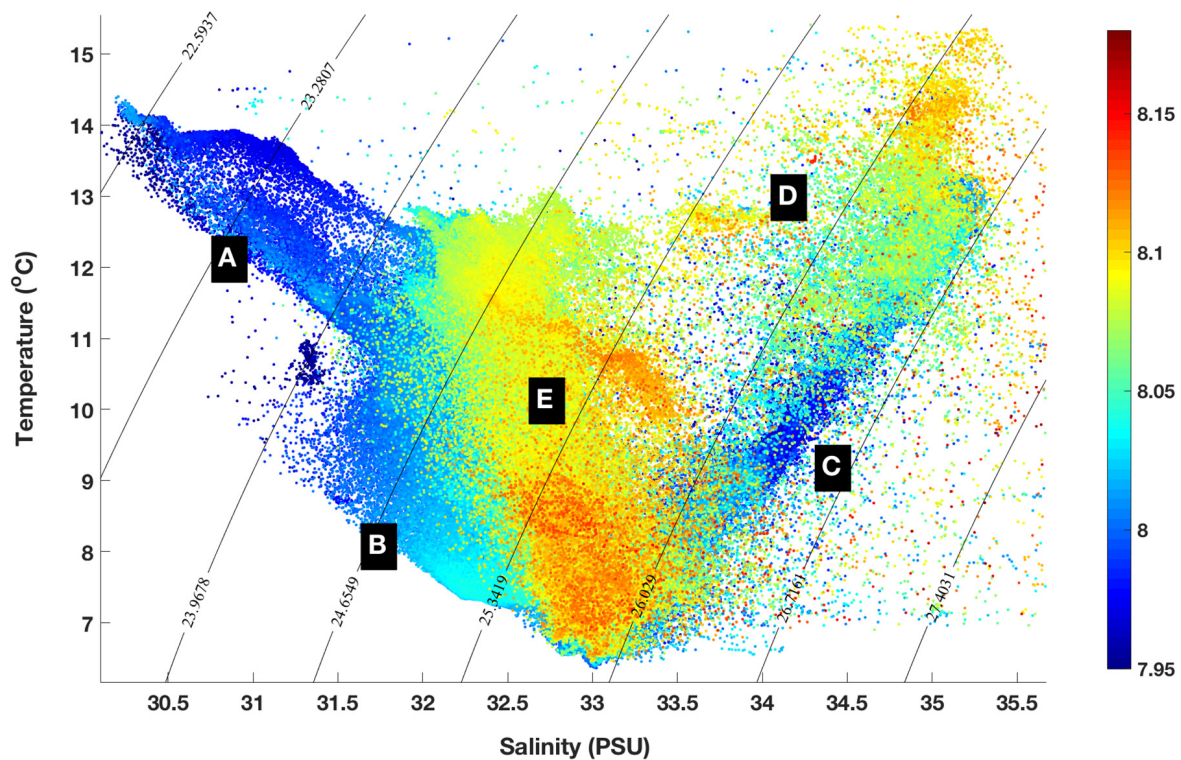


FIGURE 7 | Temperature/Salinity plot of pH. During the May 2018 deployment, lower pH water was found in fresher nearshore surface waters (**A**) and bottom waters of the colder mid-shelf (**B**) and shelf break (**C**). Higher and more variable pH was found in surface water of the shelf break (**D**) and mid-shelf (**E**).

Furthermore, the offsets between glider derived salinity-based calculations of A_T and discrete A_T on July 31 (when the glider was intercepted and re-deployed; 24.8 ± 14.3 , $n = 20$) and August 28 (when the glider was recovered; 26.2 ± 9.2 , $n = 9$) were similar to those from the May deployment (18.5 ± 7.5 , $n = 15$). It is likely that biofouling impacted pH sensor response time, as indicated by the increasing sensor time lag corrections that were applied to the glider data from the start of the deployment on July 5 to recovery on August 28 (46–81–104 s).

Current biofouling prevention measures for this sensor are the enclosure of the coupled pH/CTD sensor to block light, an anti-fouling cartridge in the pH sensor's intake, and the active seawater pumping capability of the CTD that flushes water through the sensor package continuously during deployment. However, advances to improve anti-fouling mechanisms would greatly improve sensor performance, durability, endurance, and applicability. Approaches could include installation of an additional anti-fouling cartridge in the sensor intake and turning the glider CTD pump off at regular intervals during deployment to facilitate diffusion, concentration, and exposure of the anti-fouling agent into the water chamber surrounding the pH sensor. Furthermore, to enable sustained glider-based acidification monitoring in a coastal system, especially in warm and shallow conditions, researchers will require the ability to routinely clean and/or swap out sensors to prevent data degradation over time from biofouling.

Additionally, investigation of the mechanism that impacts pH measurements (i.e., affects on sensor response time or reference voltage readings) needs to be conducted. Finally, the current salinity- A_T relationship in the U.S. NES is only based on summer data. This relationship may be subject to change with time, particularly during other seasons, and under different conditions that impact freshwater influx and/or the presence of distinctive water masses in this dynamic coastal region. We recommend to determine a salinity- A_T relationship in collected water samples before and after the glider survey in order to use the salinity-based A_T together with the glider pH to reduce the uncertainty of estimating Ω_{Arag} .

SIGNIFICANCE

This new glider pH sensor suite has demonstrated its potential to: (1) Provide high resolution measurements of pH in a coastal region; (2) Determine natural variability that will provide a framework to better study organism response and design more realistic experiments; and (3) Identify and monitor high-risk areas that are more prone to periods of reduced pH and/or high pH variability to enable better management of essential habitats in future, more acidic oceans. The first glider deployment reported here provided data in habitats of commercially important fisheries in the U.S. Northeast Shelf, and allowed for the examination of temporal and spatial pH

variability, the identification of areas and periods of lower pH water, better understanding of how mixing events and circulation impact pH across the shelf, and the creation of a baseline to track changes over time during future, scheduled deployments. Furthermore, the integration of simultaneous measurements from multiple sensors on the glider provides the ability to not only distinguish interactions between the physics, chemistry, and biology of the ecosystem, but also to conduct salinity- and temperature-based estimates of A_T in order to derive Ω_{Arag} . As such, if made commercially available, this sensor suite could undoubtedly be integrated in the planned national glider network (Baltes et al., 2014; Schofield et al., 2015; Rudnick, 2016) to provide the foundation of what could become a national coastal OA monitoring network serving a wide range of users including academic and government scientists, monitoring programs including those conducted by OOI, IOOS, NOAA and EPA, water quality managers, and commercial fishing companies. Finally, data resulting from this project and future applications can help build and improve biogeochemical and ecosystem models. A range of data validated and data assimilative modeling systems has matured rapidly over the last decade in the ocean science community. Many of these systems are being configured to assimilate glider data (temperature and salinity) (i.e., ROMs). The technology produced from this project will contribute to efforts to develop coastal forecast models with the capability to predict the variability and trajectory of the low pH water.

AUTHOR CONTRIBUTIONS

GS introduced the research ideas and led the proposal that funded this work. AB and CB developed and finalized the glider deep ISFET-based pH sensor design and provided technical support for the duration of this project. CJ worked with AB and CB on the deep ISFET-based pH sensor integration into the glider to ensure seamless hardware and software compatibility. EW-F and TM led glider data analysis efforts and figure production.

BC, W-JC, and KW analyzed all discrete samples for pH, A_T , and DIC. GS wrote the draft. All authors contributed to the writing of the manuscript.

FUNDING

This project was funded by the National Science Foundation's Ocean Technology and Interdisciplinary Coordination Program (NSF OCE1634520). EW-F received support from the Rutgers University Graduate School Excellence Fellowship.

ACKNOWLEDGMENTS

We thank the Rutgers University Center for Ocean Observing Leadership (RU COOL) glider technicians David Aragon, Nicole Waite, and Chip Haldeman for glider preparation, deployment planning, and piloting glider missions. We also thank Rutgers undergraduate students Brandon Grosso and Laura Wiltsee for glider-based laboratory and field support, and RU COOL faculty Oscar Schofield, Josh Kohut, Scott Glenn, and Michael Crowley for facility support. We acknowledge Dave Murphy, Cristina Orrico, Vlad Simontov, and Dave Walter at Sea-Bird Scientific and Christopher DeCollibus, Clara Hulburt, and staff at Teledyne Webb Research for technical assistance. This original work was presented in October 2018 at the OCEANS'18 MTS/IEEE meeting in Charleston, SC, United States and in May 2019 at the 8th EGO meeting and International Glider Workshop in New Brunswick, NJ, United States.

SUPPLEMENTARY MATERIAL

The Supplementary Material for this article can be found online at: <https://www.frontiersin.org/articles/10.3389/fmars.2019.00664/full#supplementary-material>

REFERENCES

- Baltes, B., Rudnick, D., Crowley, M., Schofield, O., Lee, C., Barth, J., et al. (2014). *Toward A U.S. IOOS Underwater Glider Network Plan: Part of a Comprehensive Subsurface Observing System*. Silver Spring, MD: NOAA.
- Boehme, S. E., Sabine, C. L., and Reimers, C. E. (1998). CO₂ fluxes from a coastal transect: a time series approach. *Mar. Chem.* 63, 49–67. doi: 10.1016/s0304-4203(98)00050-4
- Bresnahan, P., Martz, T. R., Takeshita, Y., Johnson, K. S., and LaShomb, M. (2014). Best practices for autonomous measurement of seawater PH with the honeywell durafet. *Methods Oceanogr.* 9, 44–60. doi: 10.1016/j.mio.2014.08.003
- Byrne, R. H., Mecking, S., Feely, R. A., and Liu, X. (2010). Direct observations of basin-wide acidification of the North Pacific Ocean. *Geophys. Res. Lett.* 37:L02601.
- Cai, W.-J., Hu, X., Huang, W.-J., Jiang, L.-Q., Wang, Y., Peng, T.-H., et al. (2010). Alkalinity distribution in the western North Atlantic Ocean margins. *J. Geophys. Res.* 115:C08014.
- Cai, W.-J., Hu, X., Huang, W.-J., Murrell, M. C., Lehrter, J. C., Lohrenz, S. E., et al. (2011). Acidification of subsurface coastal waters enhanced by eutrophication. *Nat. Geosci.* 4, 766–770. doi: 10.1021/es300626f
- Carter, B. R., Radich, J. A., Doyle, H. L., and Dickson, A. G. (2013). An automated system for spectrophotometric seawater pH measurements. *Limnol. Oceanogr. Methods* 11, 16–27. doi: 10.4319/lom.2013.11.16
- Chen, B., Cai, W.-J., and Chen, L. (2015). The marine carbonate system of the Arctic Ocean: assessment of internal consistency and sampling considerations, summer 2010. *Mar. Chem.* 176, 174–188. doi: 10.1016/j.marchem.2015.09.007
- Clayton, T. D., and Byrne, R. H. (1993). Spectrophotometric seawater pH measurements: total hydrogen ion concentration scale calibration of m-cresol purple and at-sea results. *Deep Sea Res. I* 40, 2115–2129. doi: 10.1016/0967-0637(93)90048-8
- Cooley, S. R., Kite-Powell, H. L., and Doney, S. C. (2009). Ocean acidification's potential to alter global marine ecosystem services. *Oceanography* 22, 172–181. doi: 10.5670/oceanog.2009.106
- DelValls, T. A., and Dickson, A. G. (1998). The pH of buffers based on 2-amino-2-hydroxymethyl-1,3-propanediol ('tris') in synthetic sea water. *Deep Sea Res. Part I* 45, 1541–1554. doi: 10.1016/s0967-0637(98)00019-3
- Dickson, A. G. (1990). Standard potential of the reaction $\text{AgCl(s)} + 0.5\text{H}_2(\text{g}) = \text{Ag(s)} + \text{HCl(aq)}$ and the standard acidity constant of the ion HSO_4^- in synthetic sea water from 273.15 to 318.15 K. *J. Chem. Thermodynam.* 22, 113–127. doi: 10.1016/0021-9614(90)90074-z

- Dickson, A. G., and Millero, F. J. (1987). A comparison of the equilibrium constants for the dissociation of carbonic acid in seawater media. *Deep Sea Res. Part A* 34, 1733–1743. doi: 10.1016/0198-0149(87)90021-5
- Dickson, A. G., Sabine, C. L., and Christian, J. R. (2007). Guide to best practices for ocean CO₂ measurements. *PICES Spec. Publ.* 3:191.
- Doney, S. C. (2010). The growing human footprint on coastal and open-ocean biogeochemistry. *Science* 328, 1512–1516. doi: 10.1126/science.1185198
- Dore, J. E., Lukas, R., Sadler, D. W., Church, M. J., and Karl, D. M. (2009). Physical and biogeochemical modulation of ocean acidification in the central North Pacific. *Proc. Natl. Acad. Sci. U.S.A.* 106, 12235–12240. doi: 10.1073/pnas.0906044106
- Feely, R. A., Alin, S. R., Newton, J., Sabine, C., Warner, M., Devol, A., et al. (2010a). The combined effects of ocean acidification, mixing, and respiration on pH and carbonate saturation in an urbanized estuary. *Estuar. Coast Shelf Sci.* 88, 442–449. doi: 10.1016/j.ecss.2010.05.004
- Feely, R. A., Fabry, V. J., Dickson, A. G., Gattuso, J.-P., Bijma, J., Riebesell, U., et al. (2010b). “An international observational network for ocean acidification,” in *Proceedings of OceanObs’09: Sustained Ocean Observations and Information for Society*, eds J. Hall, D. E. Harrison, and D. Stammer, (Auckland: ESA Publication).
- Feely, R. A., Sabine, C. L., Hernandez-Ayon, J. M., Ianson, D., and Hales, B. (2008). Evidence for upwelling of corrosive ‘acidified’ water onto the continental shelf. *Science* 320, 1490–1492. doi: 10.1126/science.1155676
- Garau, B., Ruiz, S., Zhang, W. G., Pascual, A., Heslop, E., Kerfoot, J., et al. (2011). Thermal lag correction on slocum CTD glider data. *J. Atmos. Ocean. Technol.* 28, 1065–1071. doi: 10.1175/JTECH-D-10-05030.1
- Hales, B., Takahashi, T., and Bandstra, L. (2005). Atmospheric CO₂ uptake by a coastal upwelling system. *Glob. Biogeochem. Cycles* 19:GB1009.
- Hofmann, G. E., Smith, J. E., Johnson, K. S., Send, U., Levin, L. A., Micheli, F., et al. (2011). High-frequency dynamics of ocean pH: a multi-ecosystem comparison. *PLoS One* 6:e28983. doi: 10.1371/journal.pone.0028983
- Huang, W.-J., Wang, Y., and Cai, W.-J. (2012). Assessment of sample storage techniques for total alkalinity and dissolved inorganic carbon in seawater. *Limnol. Oceanogr. Methods* 10, 711–717. doi: 10.4319/lom.2012.10.711
- Jiang, L.-Q., Cai, W.-J., Wang, Y., Wanninkhof, R., and Lüger, H. (2008). Air-sea CO₂ fluxes on the U.S. South Atlantic bight: spatial and seasonal variability. *J. Geophys. Res.* 113:C07019. doi: 10.1029/2007JC004366
- Johnson, K. S. (2010). Simultaneous measurements of nitrate, oxygen, and carbon dioxide on oceanographic moorings: observing the redfield ratio in real time. *Limnol. Oceanogr.* 55, 615–627. doi: 10.4319/lo.2010.55.2.0615
- Johnson, K. S., Berelson, W. M., Boss, E. S., Chase, Z., Claustre, H., Emerson, S. R., et al. (2009). Observing biogeochemical cycles at global scales with profiling floats and gliders: prospects for a global array. *Oceanography* 22, 216–225. doi: 10.5670/oceanog.2009.81
- Johnson, K. S., Jannasch, H. W., Coletti, L. J., Elrod, V. A., Martz, T. R., Takeshita, Y., et al. (2016). Deep-Sea DuraFET: a pressure tolerant pH sensor designed for global sensor networks. *Anal. Chem.* 88, 3249–3256. doi: 10.1021/acs.analchem.5b04653
- Johnson, K. S., Plant, J. N., and Maurer, T. L. (2017). *Processing BGC-Argo pH Data at the DAC Level*. Plouzané: Ifremer.
- Johnson, Z. I., Wheeler, B. J., Blinberry, S. K., Carlson, C. M., Ward, C. S., and Hunt, D. E. (2013). Dramatic variability of the carbonate system at a temperate coastal ocean site (Beaufort, North Carolina, USA) is regulated by physical and biogeochemical processes on multiple timescales. *PLoS One* 8:e85117. doi: 10.1371/journal.pone.0085117
- Khoo, K. H., Ramette, R. W., Culbertson, C. H., and Bates, R. G. (1977). Determination of hydrogen ion concentrations in seawater from 5 to 40 degree C: standard potentials at salinities from 20 to 45‰. *Anal. Chem.* 49, 29–34. doi: 10.1021/ac50009a016
- Kohut, J., Haldeman, C., and Kerfoot, J. (2014). “Monitoring dissolved oxygen in new jersey coastal waters using autonomous gliders,” in *Proceedings of the U.S. Environmental Protection Agency*, Washington, DC.
- Lee, K., Tong, L. T., Millero, F. J., Sabine, C. L., Dickson, A. G., Goyet, C., et al. (2006). Global relationships of total alkalinity with salinity and temperature in surface waters of the world’s oceans. *Geophys. Res. Lett.* 33:L19605.
- Lentz, S. J. (2017). Seasonal warming of the middle atlantic bight cold pool. *J. Geophys. Res. Oceans* 122, 941–954. doi: 10.1002/2016jc012201
- Liu, X., Patsavas, M. C., and Byrne, R. H. (2011). Purification and characterization of meta-cresol purple for spectrophotometric seawater pH measurements. *Environ. Sci. Technol.* 45, 4862–4868. doi: 10.1021/es200665d
- Martz, T., McLaughlin, K., and Weisberg, S. B. (2015). *Best Practices for Autonomous Measurement of Seawater pH With the Honeywell Durafet pH Sensor*. California: California Current Acidification Network (C-CAN).
- Martz, T. R., Connery, J. G., and Johnson, K. S. (2010). Testing the honeywell durafet® for seawater pH applications. *Limnol. Oceanogr. Methods* 8, 172–184. doi: 10.4319/lom.2010.8.172
- Mehrbach, C., Culbertson, C. H., Hawley, J. E., and Pytkowicz, R. M. (1973). Measurement of the apparent dissociation constants of carbonic acid in seawater at atmospheric pressure. *Limnol. Oceanogr.* 18, 897–907. doi: 10.4319/lo.1973.18.6.0897
- Millero, F. J. (1983). Influence of pressure on chemical processes in the sea. *Chem. Oceanogr.* 8, 1–88. doi: 10.1016/b978-0-12-588608-6.50007-9
- Millero, F. J. (1986). The pH of estuarine waters. *Limnol. Oceanogr.* 31, 839–847. doi: 10.4319/lo.1986.31.4.0839
- Pierrot, D. E., Lewis, E., and Wallace, D. W. R. (2006). *MS Excel Program Developed for CO₂ System Calculations Oak Ridge National Laboratory, Carbon Dioxide Information Analysis Center*. Oak Ridge: US Department of Energy.
- Rudnick, D. L. (2016). Ocean research enabled by underwater gliders. *Ann. Rev. Mar. Sci.* 8, 519–541. doi: 10.1146/annurev-marine-122414-033913
- Rudnick, D. T., Davis, R. E., Eriksen, C. C., Fratantoni, D. M., and Perry, M. J. (2004). Underwater gliders for ocean research. *Mar. Technol. Soc. J.* 38, 48–59.
- Salisbury, J., Green, M., Hunt, C., and Campbell, J. (2008). Coastal acidification by rivers: a threat to shellfish? *Eos Transl. Am. Geophys. Union* 89, 513–528.
- Schofield, O., Jones, C., Kohut, J., Kremer, U., Miles, T., Saba, G., et al. (2015). Developing Coordinated Communities of Autonomous Gliders for Sampling Coastal Ecosystems. *Mar. Tech. Soc. J.* 49, 9–16. doi: 10.4031/mts.49.3.16
- Schofield, O., Kohut, J., Aragon, D., Creed, L., Graver, J., Haldeman, C., et al. (2007). Slocum gliders: robust and ready. *J. Field Robot.* 24, 1–14.
- Seidel, M. P., DeGrandpre, M. D., and Dickson, A. G. (2008). A sensor for in situ indicator-based measurements of seawater pH. *Mar. Chem.* 109, 18–28. doi: 10.1016/j.marchem.2007.11.013
- Thomsen, J., Gutowska, M. A., Saphörster, J., Heinemann, A., Trübenbach, K., Fietzke, J., et al. (2010). Calcifying invertebrates succeed in a naturally CO₂-rich coastal habitat but are threatened by high levels of future acidification. *BioScience* 7, 3879–3891. doi: 10.5194/bg-7-3879-2010
- van Heuven, S., Pierrot, D., Rae, J. W. B., Lewis, E., and Wallace, D. W. R. (2011). *MATLAB Program Developed for CO₂ System Calculations. ORNL/CDIAC-105b. Carbon Dioxide Information Analysis Center*. Oak Ridge: U.S. Department of Energy.
- Vandemark, D., Salisbury, J. E., Hunt, C. W., Shellito, S. M., Irish, J. D., McGillis, W. R., et al. (2011). Temporal and spatial dynamics of CO₂ air-sea flux in the Gulf of Maine. *J. Geophys. Res.* 116:C01012.
- Wang, H., Hu, X., Cai, W.-J., and Sterba-Boatwright, B. (2017). Decadal fCO₂ trends in global ocean margins and adjacent boundary current-influenced areas. *J. Geophys. Res.* 44, 8962–8970. doi: 10.1002/2017GL074724
- Wang, Z. A., Wanninkhof, R., Cai, W.-J., Byrne, R. H., Hu, X., Peng, T.-H., et al. (2013). The marine inorganic carbon system along the Gulf of Mexico and Atlantic coasts of the United States: Insights from a transregional coastal carbon study. *Limnol. Oceanogr.* 58, 325–342. doi: 10.4319/lo.2013.58.1.0325
- Wanninkhof, R., Barbero, L., Byrne, R., Cai, W.-J., Huang, W.-J., Zhang, J.-Z., et al. (2015). Ocean acidification along the Gulf Coast and East Coast of the USA. *Cont. Shelf Res.* 98, 54–71. doi: 10.1016/j.csr.2015.02.008

- Xu, Y.-Y., Cai, W.-J., Gao, Y., Wanninkhof, R., Salisbury, J., Chen, B., et al. (2017). Short-term variability of aragonite saturation state in the central Mid-Atlantic Bight. *J. Geophys. Res. Oceans* 122, 4274–4290. doi: 10.1002/2017JC012901
- Xue, L., Cai, W.-J., Hu, X., Sabine, C., Jones, S., Sutton, A. J., et al. (2016). Sea surface carbon dioxide at the georgia time series site (2006–2007): Air–sea flux and controlling processes. *Prog. Oceanogr.* 140, 14–26. doi: 10.1016/j.pocean.2015.09.008
- Yu, P. C., Matson, P. G., Martz, T. R., and Hofmann, G. E. (2011). The ocean acidification seascape and its relationship to the performance of calcifying marine invertebrates: laboratory experiments on the development of urchin larvae framed by environmentally-relevant pCO₂/pH. *J. Exp. Mar. Biol. Ecol.* 400, 288–295. doi: 10.1016/j.jembe.2011.02.016

Conflict of Interest: AB and CB were employed by Sea-Bird Scientific/WET Labs. CJ was employed by Teledyne Webb Research.

The remaining authors declare that the research was conducted in the absence of any commercial or financial relationships that could be construed as a potential conflict of interest.

Copyright © 2019 Saba, Wright-Fairbanks, Chen, Cai, Barnard, Jones, Branham, Wang and Miles. This is an open-access article distributed under the terms of the Creative Commons Attribution License (CC BY). The use, distribution or reproduction in other forums is permitted, provided the original author(s) and the copyright owner(s) are credited and that the original publication in this journal is cited, in accordance with accepted academic practice. No use, distribution or reproduction is permitted which does not comply with these terms.



SHiPCC—A Sea-going High-Performance Compute Cluster for Image Analysis

Timm Schoening*

GEOMAR Helmholtz Centre for Ocean Research Kiel, Kiel, Germany

OPEN ACCESS

Edited by:

Marlon R. Lewis,
Dalhousie University, Canada

Reviewed by:

Sparsh Mittal,
Indian Institute of Technology
Hyderabad, India
Jann Paul Mattern,
University of California, Santa Cruz,
United States

*Correspondence:

Timm Schoening
tschoening@geomar.de

Specialty section:

This article was submitted to
Ocean Observation,
a section of the journal
Frontiers in Marine Science

Received: 13 September 2018

Accepted: 12 November 2019

Published: 27 November 2019

Citation:

Schoening T (2019) SHiPCC—A
Sea-going High-Performance
Compute Cluster for Image Analysis.
Front. Mar. Sci. 6:736.
doi: 10.3389/fmars.2019.00736

Marine image analysis faces a multitude of challenges: data set size easily reaches Terabyte-scale; the underwater visual signal is often impaired to the point where information content becomes negligible; human interpreters are scarce and can only focus on subsets of the available data due to the annotation effort involved etc. Solutions to speed-up the analysis process have been presented in the literature in the form of semi-automation with artificial intelligence methods like machine learning. But the algorithms employed to automate the analysis commonly rely on large-scale compute infrastructure. So far, such an infrastructure has only been available on-shore. Here, a mobile compute cluster is presented to bring big image data analysis capabilities out to sea. The Sea-going High-Performance Compute Cluster (SHiPCC) units are mobile, robustly designed to operate with electrically impure ship-based power supplies and based on off-the-shelf computer hardware. Each unit comprises of up to eight compute nodes with graphics processing units for efficient image analysis and an internal storage to manage the big image data sets. The first SHiPCC unit has been successfully deployed at sea. It allowed us to extract semantic and quantitative information from a Terabyte-sized image data set within 1.5 h (a relative speedup of 97% compared to a single four-core CPU computer). Enabling such compute capability out at sea allows to include image-derived information into the cruise research plan, for example by determining promising sampling locations. The SHiPCC units are envisioned to generally improve the relevance and importance of optical imagery for marine science.

Keywords: sea-going equipment, big data analysis, cluster computer, modular hardware, image analysis

1. INTRODUCTION

Data science is becoming more important in many research domains and marine science is no exception. Artificial intelligence methods and visualization tools help to extract quantitative and semantic information from big data sets (Schoening et al., 2012, 2017). Traditional, desktop-style computer hardware is usually sufficiently powerful to apply such data science methods to data sets of kilobyte to megabyte size. Larger data sets at Gigabyte to multi-Terabyte-scale can be analyzed more efficiently by clusters of computers (Beloglazov et al., 2012). Those clusters can apply a selected algorithm to multiple data items in parallel by distributing the workload onto many compute nodes. Such clusters are usually operated by central computing centers of research institutes. They are commonly stationary, mounted in 19" racks, cooled and may consist of tens of thousands of compute nodes. Their individual units are heavy and rely on a consistent

power grid. Also, the main computing element is most often a Central Processing Unit (CPU) which can become a bottleneck for some algorithmic tasks. Especially in image and video analysis, many compute operations can be further parallelized efficiently with Graphics Processing Units (GPUs) (Mittal and Vetter, 2015). In the marine sciences, CPU and GPU compute clusters are most often used for climate simulations and other modeling tasks (Park and Latif, 2010). Nevertheless, those studies are shore-based and not time-critical. In case the data analysis has to be executed in near-realtime at sea, most existing compute clusters cannot be used. Data transfer to shore is bottlenecked even at the Gigabyte-scale by low internet bandwidth and transmission costs. Some vessels (e.g., RV Falkor) do have a CPU-based compute cluster on board but these cannot be flexibly deployed on other vessels and do not feature the efficiency of GPU clusters for image analysis (<https://schmidtoccean.org/technology/high-performance-computing/>).

Thus, image analysis is currently conducted in the months and years after an expedition. Interesting features hidden in the data can only be further investigated subsequently during an additional expedition to the same area. In case of rapid processes or a high temporal variance of a process, a detected feature may be impossible to be investigated again (e.g., a large food fall like a whale carcass, a hydrothermal vent site, a tidally influenced gas seepage, a group of fauna showing coordinated behavior). Hence, near-realtime analysis is important when information contained in unstructured data sets like imagery shall guide further expedition actions. An example use case is an Autonomous Underwater Vehicle (AUV) imaging a large seafloor area at low resolution. If the obtained data could be analyzed by a compute cluster at sea to determine faunal abundance, hotspots in the abundance could then immediately be targeted by higher-resolution gear like a Remotely Operated Vehicle (ROV). Apart from such benefits when operating in a changing environment, image analysis at sea can similarly speed up traditional marine image based science. It can help with laser point detection (Schoening et al., 2015) to provide scaling information as well as plankton image vignetting toward identification (Robinson et al., 2017).

Here, the “Sea-going High-Performance Compute Cluster” (SHiPCC) is presented, to enable efficient and effective image and video analysis at sea. It is mobile, modular and GPU based, features a grid-independent power connection and provides storage capacity for tens of Terabytes of imagery. One SHiPCC unit has already been deployed at sea to determine methane bubble characteristics. It is expected to provide novel applications for image analysis and to increase the value and impact of image data for marine sciences.

In the following, section two presents the technical details of the system. Section three explains the application of the system to a real world use case at sea and section four discusses the status of the system and gives an outlook to future improvements.

2. MATERIALS AND METHODS

High-performance image analysis can be conducted in a massively parallel manner. Hence the SHiPCC is designed in a single-instruction, multiple-data architecture (according to

Flynn’s taxonomy) with Ethernet-based shared storage. A high number of GPUs per CPU core was targeted. All IT hardware of the clusters is available commercially off-the-shelf from the consumer segment. The units are built to fit into standard aluminum boxes, commonly used for container transports in marine science. Furthermore the units can be connected directly to the main power grid of research vessels by filtering the electric current produced by the engines.

2.1. Hardware

All hardware components of a SHiPCC unit are shown in **Figures 1B–J**. The main elements of one unit are eight compact gaming computers equipped with GPUs that act as the compute nodes. These are ZOTAC Magnus EN1070 computers with an NVIDIA GeForce® GTX 1070 graphics card (mobile version) and an Intel Core i5-6400T processor (Quad-core, 2.2 GHz). In this setup, a single GPU is utilized by four CPU cores. Each node is equipped with a 500 GB SSD for local storage and 32 GB of main memory.

One mini PC (Intel NUC7I3DNKE) serves as a gateway to the compute nodes and manages the required software packages. This PC does not run compute intensive tasks but provides tools like a web server, database and the image annotation software BIIGLE 2.0 (Langenkämper et al., 2017).

Large data storage is enabled by one Synology Rackstation RS815+ network attached storage (NAS) device, equipped with 24 TB of storage space. The NAS, the compute nodes and the gateway NUC are connected via a D-Link DGS-1210-16 Gigabit Ethernet switch.

Each node has an estimated compute performance of 10 GFlop/s per CPU and 6.5 TFlop/s per GPU. Hence, one SHiPCC unit of eight nodes has a combined compute performance of ca. 52 TFlop/s. The combined price of all components amounts to ca. 15,000 EUR for one unit (288 EUR/TFlop/s).

All hardware is mounted in a rigid aluminum frame (see **Figure 2**). The frame has an outer dimension of ca. 72 × 51 × 52 cm³ (W×H×D) with additional bumpers on the bottom and handles at the top that can be removed if necessary. One unit fits inside a Zarges K470 (40566) box and weighs 53 kg in total.

Electrical power has to be supplied by the research vessel. Each compute node is powered by a 180 W power supply. Including the network storage and network switch, the entire system would require four independent 16A power sockets which are rarely available in research labs at sea. Hence, the SHiPCC units can be connected directly to the raw power grid of the ship by a 32A power plug. When operating many units in parallel, a further power distribution box can be used (INDU-Electric 11400748, see **Figure 1A**). This box connects to a 63A outlet and provides six 32A sockets. The SHiPCC units feature a current filter (EPA NF-K-4-42), an internal RCBO, and independent fuses for all loads.

2.2. Software

All compute nodes and the gateway operate on Ubuntu Linux 18.04. They all feature NVIDIA CUDA, the GNU C compiler and Python. Hence, arbitrary, linux-enabled image analysis software can be compiled and executed.

The gateway hosts an apt package repository such that the compute nodes never have to be connected to the Internet. It

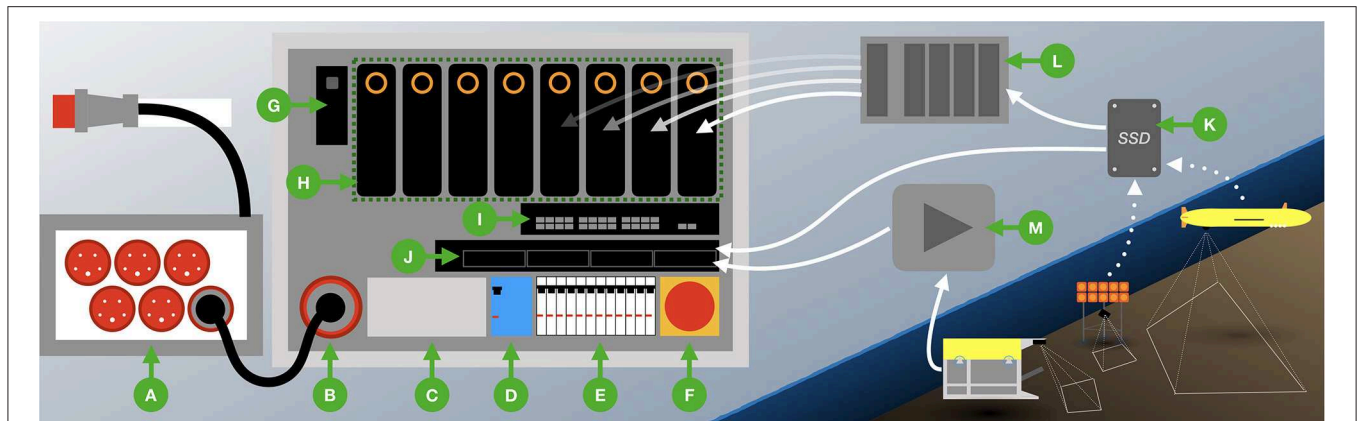


FIGURE 1 | Depiction of a SHiPCC unit setup (B–J) and its power (A) and data (K–M) supply. A power distribution box (A), capable of providing energy to six SHiPCC units, connects to the ship's power grid and converts from 63A to 32A (400V). Each cluster unit has a 32A input (B), a filter to smooth the provided current (C) an FI fuse (D), several independent fuses for the compute components (E) and an emergency off-switch (F). Thus the control computer (G), the eight compute nodes conducting the actual computation with their eight individual GPUs and four CPU cores (H), the network switch (I) and the NAS (J) can be powered securely from the research vessel's main power grid. Data from untethered gear like AUVs or landers is retrieved by data medium (K). This data can either be directly transferred to the NAS or be multiplied by an external data duplication device (L). Multiplied data on several independent media can be connected to the compute nodes via USB to prevent costly data accesses over the internal Gigabit Ethernet network. Tethered gear like ROVs or towed telemetry systems can provide a live data feed, which a stream grabbing device (M) can store on the NAS. Each of the nodes has a Gigabit Ethernet connection to the NAS to read and write data.

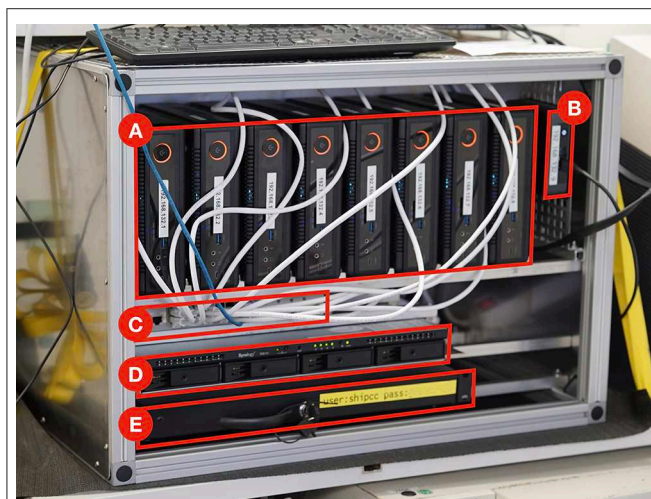


FIGURE 2 | Setup of the one SHiPCC unit as deployed on cruise POS526 comprising eight compute nodes (A), one job scheduling control node (B), a Gigabit Ethernet switch (C), a four bay network attached storage of 24TB (D) and a drawer for further equipment like portable hard disks (E). The dimensions of one unit are 72 × 51 × 52 cm (W × H × D).

also runs an Network Time Protocol (NTP) server to synchronize the clocks of all compute nodes. Furthermore, it provides a web interface to monitor the compute status and job results. At present, no job scheduling software is used as the system is likely to be operated by a single user.

2.3. Data Transfer

Data can be transferred to the compute nodes in three ways, as shown in Figures 1K,L. Most often a mobile storage device will be connected directly to the NAS for copying. From there, each compute node can access the data over the Gigabit network

within the SHiPCC unit. A mobile storage device can also be multiplied by an external device first, creating copies to be connected to the individual nodes directly. This can be beneficial in case the network access would be too slow for the image analysis. For tethered systems that can provide a live stream, a video grabbing device is needed.

2.4. Deployment Usecase

The first SHiPCC unit was successfully deployed on research cruise POS526 with RV Poseidon in July 2018. It provided data storage capacity for five image data sets and three video data sets acquired during the cruise by AUV, towed cameras, stationary cameras attached to landers and a range of cameras operated by the manned submersible JAGO.

One data set of imagery was analyzed live at sea to determine methane bubble fluxes. Bubbles were imaged during several dives by the BubbleBox stereo camera system (Jordt et al., 2015) attached to JAGO. Several bubble streams were investigated, each yielding a separate image sequence. The data set was analyzed by a custom-built C++ program based on the GPU extensions of OpenCV to determine bubble sizes and bubble rising speeds. Individual bubbles were detected in each image by a four step procedure (see Figure 3). First, twenty of the images in a sequence were randomly selected and used to compute a median image for this sequence. This median image represents an empty frame without bubbles being visible (Figure 3B). Second, each image in the sequence was subtracted individually by the median image. This difference image shows high intensity values at pixels where bubbles occur and is close to zero at pixels without bubbles. Third, an intensity threshold was applied to create a binary image showing bubble candidate regions in each image (Figure 3C). Finally, each bubble candidate was segmented by a contour finding algorithm and subjected to a size threshold

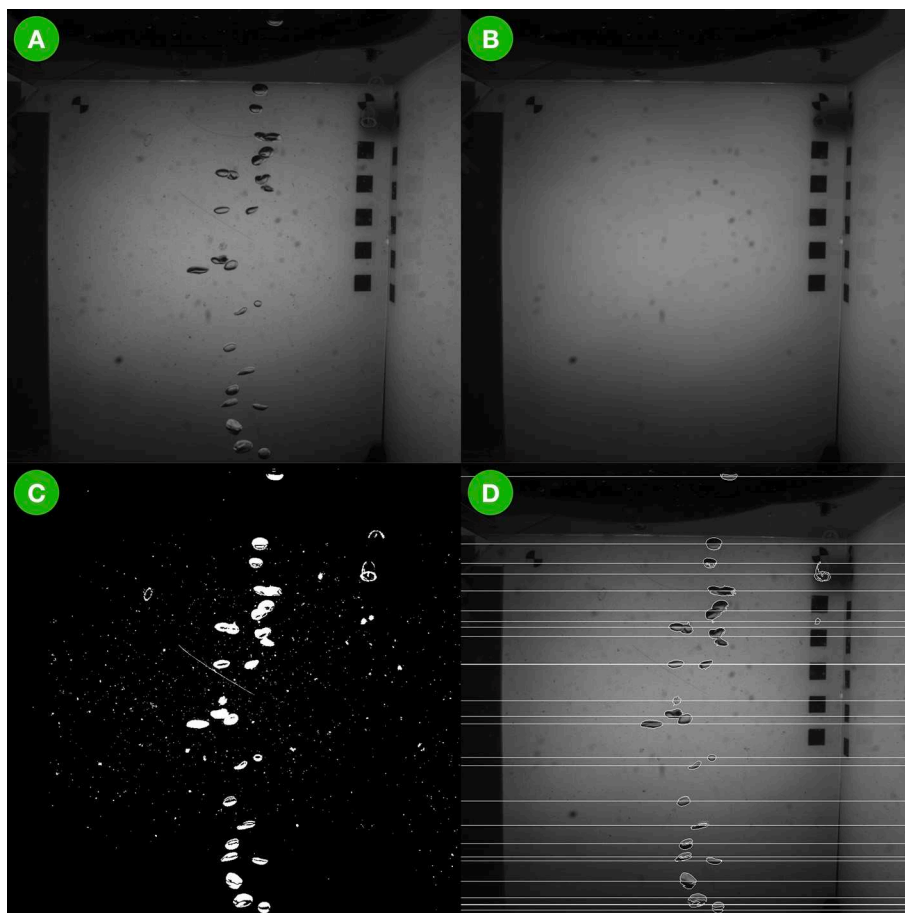


FIGURE 3 | The bubble image processing pipeline executed on the SHiPCC during cruise POS526 as a demonstration of operability. In **(A)** an original image is shown as acquired by the BubbleBox. In **(B)** the median-filtered version is shown where only the background remains and the foreground (i.e., the bubbles) has been removed. **(C)** Shows the binarized subtraction of **(B)** from **(A)**. Vertical bubble locations and outlines are marked in **(D)**.

to remove candidates below and above meaningful size values (3–7,854 mm² corresponding to a bubble radius of 1–50 mm).

Bubble size was estimated by a known conversion factor of 5.7 px/mm for bubbles rising in the center of the BubbleBox. Bubble rising speed was estimated by linking bubble locations from subsequent images. Bubble locations detected in one image I_t were compared to detected locations in the next image I_{t+1} . A bubble detected in I_{t+1} had to be within a 50 pixel search radius above any of the bubbles in I_t to be identified as that specific bubble. The upper bound of 50 pixels distance corresponds to ca. 8.8 mm distance traveled and thus a maximum expected rising speed of ca. 0.9 m/s. The distance an individual bubble traveled was combined with the known acquisition rate of the BubbleBox of 100 Hz to finally provide bubble rising speed estimates.

3. RESULTS

Three units of the compute cluster are now available for deployment at sea (see section 4).

3.1. Rapid Bubble Size Estimation

Two JAGO dives with BubbleBox deployments provided ca. 1 TB of gray scale imagery representing eight individual bubble streams. **Figure 3** shows an example image as acquired by the BubbleBox system during cruise POS526 and the images representing intermediate analysis steps toward the bubble size distribution and bubble volumes shown in **Figure 4**. In total, more than 900,000 images were analyzed by one SHiPCC unit of eight compute nodes within 99 min. On a single, four core, CPU computer the execution would have taken more than 2,900 min (2 days). This includes all computational steps on the CPU as well as GPU and data transfer times in between. 118,928 bubbles were detected, corresponding to a total volume of 144.5 L. The average bubble rising speed was determined as 0.25 m/s (± 0.01 m/s). This value is much smaller than the maximum expected rising speed applied in the bubble tracking heuristic.

The bubble use case was introduced here to show that the SHiPCC system is operable and has the capability of analyzing Terabytes of imagery at sea. Improved algorithms that exploit the capabilities of the BubbleBox stereo system

are under development and will improve the accuracy of the bubble measurements.

4. DISCUSSION

Common hardware for compute clusters is rack-mountable. Modern research vessels feature such racks in server rooms, used for ship operation hardware. In some cases those racks might be available for scientific computing gear. However, a review among the German vessels showed that additional hardware could not be installed on a per-cruise basis. This is partly due to space restrictions but mostly due to concerns regarding the safe operation of the vessels. Mobile 19 inch racks would have been an alternative mechanical design choice. They were neglected in favor of the presented scheme. Mainly, to adhere to the standard *Zarges* box format for marine scientific logistics while also maintaining the highest spatial yield.

We chose the SHiPCC setup—utilizing compact, commercial off-the-shelf desktop computers—to fulfill four goals: (i) create a system with few CPUs per GPU (ii) enable simple transport by using standard marine scientific transport casing (iii) achieve high computational performance per invested money and (iv) enable execution of software on x86 CPUs. We considered other

computation hardware for our mobile image processing cluster (see **Table 1**). The NVIDIA DGX-1 was neglected as it features less GPUs per CPU (8 GPUs for 40 CPUs), is only rack-mountable and costs ca. 470 EUR / TFlop/s. A DGX-1 would also not have been affordable due to the total cost of 80,000 EUR per unit. A 19" rack-mountable off-the-shelf solution (Dell R730, two NVIDIA Tesla K80 GPUs, two Intel E5-2640v4 CPUs) was neglected for the same reasons at costs of ca. 1,113 EUR / TFlop/s. A cluster of NVIDIA Jetson TX2 nodes was neglected as it requires special software and compilers due to its ARM CPUs and is also less cost-effective than the SHiPCC units at ca. 450 EUR/TFlop/s. Nevertheless, a cluster of Jetsons would likely be more energy-efficient than the SHiPCC units.

The full setup of three SHiPCC units, comprised of a total of 20 compute nodes achieves a theoretical performance of 130 TFlop/s. Assuming an image processing effort of 100 operations per pixel the SHiPCC could analyze 6.3 video streams in 4K resolution in real time. This theoretical capability will be limited by other factors like network bandwidth which can be circumvented by distributing the video signal over SDI and equipping each node with video grabbing hardware rather than using an Ethernet file stream.

Cooling of the cluster has been neglected in the design of the units. Each node manages the heat it creates by built-in copper coolers and active fans. The SHiPCC nodes are equipped with further, larger fans to distribute the heat away from the cluster frames. It is assumed that cooling for the SHiPCC nodes will be provided by the research vessel itself. Some vessels provide climatized server rooms where the nodes could be set up. In most cases, though, the compute cluster will be setup in a climatized lab room where the temperature can be adjusted to the required operations. At least for the medium and large German vessels, cooling power in the range of several hundreds of kilowatts is available. The heat created by the SHiPCC nodes can be neglected in those cases. A further choice would be containing a SHiPCC unit inside a climatized, mobile frame, which could be shipped as an additional piece of equipment in case no climatized labs are available.

At the moment, a total of three SHiPCC units have been built. Two are units as presented here, the third is a down-scaled mini-SHiPCC. It features only four compute nodes but has a total weight of less than 23 kg including the transport box. This enables transport of the system by standard air freight, making it useful not only for research cruises. To advance the system toward multi-user operations, a job scheduling software will be required.

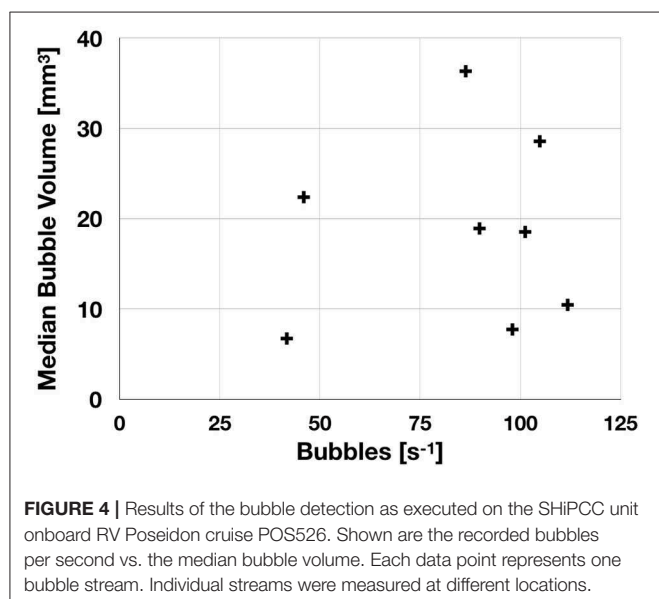


TABLE 1 | Comparison of designs for a mobile compute cluster.

Type of cluster	EUR/unit	EUR/TFlop/s	GPUs/CPU core	EUR/CUDA Unit
NVIDIA DGX-1	80,000	470	8/40 = 0.20	2.79
Dell R730	20,000	1,113	2/8 = 0.25	1.99
NVIDIA Jetson TX2	27,500	450	1/2 = 0.50	3.05
SHiPCC	15,000	288	1/4 = 0.25	0.98

For the Jetson TX2 a cluster of 35 nodes is assumed to achieve comparable TFlop/s per unit as one SHiPCC unit. Bold values are optimal for each category. Overall the SHiPCC design achieves the highest value for money.

Commercial and open source solutions exist for this task but were neglected until now to keep the system simple to setup.

Within the full image analysis pipeline, from acquisition to understanding, there are many bottlenecks that require new tools and workflows (Schoening et al., 2018). Acquisition can only be sped-up by multiplying the number of acquisition devices. Interpretation is envisioned to be accelerated by machine learning methods and the compute power of systems like the SHiPCC units. Nevertheless, data transfer toward the analysis computers remains an impediment. By bringing the hardware out to sea, slow satellite connections are bypassed as well as the physical transport of hard disks to shore. For tethered systems, a live stream could be fed into a SHiPCC unit through video grabbing hardware. For untethered systems, one has to wait until the gear has been recovered and data been downloaded from the device. An immediate analysis of an ROV video stream is targeted for the next deployment of the SHiPCC units.

In summary, a new type of equipment for the marine sciences has been presented here. The *Sea-going High-Performance Compute Cluster* is specifically designed to conduct high-throughput image analysis on research vessels. Other use cases like at-sea oceanographic and biogeochemical modeling can be envisioned as these also operate on large volumes of gridded data that is subject to cell-wise operations that can efficiently be parallellized on GPUs. Using a SHiPCC unit on cruises will increase the impact of big data sets having just been acquired at sea. It provides the hardware basis for intelligent algorithms extracting quantitative and

semantic information from these data sets efficiently and effectively. Such extracted information can streamline knowledge discovery, guide further sensor deployments and enables joint interpretation in the inspiring environment of a research team at sea.

AUTHOR CONTRIBUTIONS

TS designed the equipment and obtained funding for it, developed the test algorithms, deployed the system at sea, and wrote this manuscript.

FUNDING

This project was funded by the Cluster of Excellence 80 The Future Ocean. The Future Ocean was funded within the framework of the Excellence Initiative by the Deutsche Forschungsgemeinschaft (DFG) on behalf of the German federal and state governments.

ACKNOWLEDGMENTS

Special thanks go to the Technologie und Logistikzentrum (TLZ) of GEOMAR for their support in building the SHiPCC units. This is publication number 40 of the Deep Sea Monitoring Group at GEOMAR. We thank the three reviewers for their input to this improved manuscript.

REFERENCES

- Beloglazov, A., Abawajy, J., and Buyya, R. (2012). Energy-aware resource allocation heuristics for efficient management of data centers for cloud computing. *Fut. Generat. Comput. Syst.* 28, 755–768. doi: 10.1016/j.future.2011.04.017
- Jordt, A., Zelenka, C., von Deimling, J. S., Koch, R., and Köser, K. (2015). The bubble box: towards an automated visual sensor for 3d analysis and characterization of marine gas release sites. *Sensors* 15, 30716–30735. doi: 10.3390/s151229825
- Langenkämper, D., Zuerowietz, M., Schoening, T., and Nattkemper, T. W. (2017). Biigle 2.0-browsing and annotating large marine image collections. *Front. Mar. Sci.* 4:83. doi: 10.3389/fmars.2017.00083
- Mittal, S., and Vetter, J. S. (2015). A survey of CPU-GPU heterogeneous computing techniques. *ACM Comput. Surv.* 47:69. doi: 10.1145/2788396
- Park, W., and Latif, M. (2010). Pacific and Atlantic multidecadal variability in the kiel climate model. *Geophys. Res. Lett.* 37, 1–6. doi: 10.1029/2010GL045560
- Robinson, K. L., Luo, J. Y., Sponaugle, S., Guigand, C., and Cowen, R. K. (2017). A tale of two crowds: public engagement in plankton classification. *Front. Mar. Sci.* 4:82. doi: 10.3389/fmars.2017.00082
- Schoening, T., Bergmann, M., Ontrup, J., Taylor, J., Dannheim, J., Gutt, J., et al. (2012). Semi-automated image analysis for the assessment of megafaunal densities at the arctic deep-sea observatory HAUSGARTEN. *PLoS ONE* 7:e38179. doi: 10.1371/journal.pone.0038179
- Schoening, T., Jones, D. O., and Greinert, J. (2017). Compact-morphology-based poly-metallic nodule delineation. *Sci. Rep.* 7:13338. doi: 10.1038/s41598-017-13335-x
- Schoening, T., Köser, K., and Greinert, J. (2018). An acquisition, curation and management workflow for sustainable, terabyte-scale marine image analysis. *Sci. Data* 5:180181. doi: 10.1038/sdata.2018.181
- Schoening, T., Kuhn, T., Bergmann, M., and Nattkemper, T. W. (2015). DELPHI-fast and adaptive computational laser point detection and visual footprint quantification for arbitrary underwater image collections. *Front. Mar. Sci.* 2:20. doi: 10.3389/fmars.2015.00020

Conflict of Interest: The author declares that the research was conducted in the absence of any commercial or financial relationships that could be construed as a potential conflict of interest.

Copyright © 2019 Schoening. This is an open-access article distributed under the terms of the Creative Commons Attribution License (CC BY). The use, distribution or reproduction in other forums is permitted, provided the original author(s) and the copyright owner(s) are credited and that the original publication in this journal is cited, in accordance with accepted academic practice. No use, distribution or reproduction is permitted which does not comply with these terms.



Emerging Technologies and Coral Reef Conservation: Opportunities, Challenges, and Moving Forward

Elizabeth M. P. Madin^{1*}, Emily S. Darling^{2,3} and Marah J. Hardt⁴

¹ Department of Biological Sciences, Macquarie University, Sydney, NSW, Australia, ² Department of Ecology & Evolutionary Biology, University of Toronto, Toronto, ON, Canada, ³ Marine Program, Wildlife Conservation Society, Bronx, NY, United States, ⁴ Future of Fish, Bethesda, MD, United States

OPEN ACCESS

Edited by:

Eric Delory,
Oceanic Platform of the Canary
Islands, Spain

Reviewed by:

Ivor Douglas Williams,
Pacific Islands Fisheries Science
Center (NOAA), United States
Pennober Gwenaëlle,
Université de la Réunion, France

*Correspondence:

Elizabeth M. P. Madin
emadin@hawaii.edu

†Present address:

Elizabeth M. P. Madin,
Hawaii Institute of Marine Biology,
University of Hawaii, Manoa, HI,
United States

Specialty section:

This article was submitted to
Ocean Observation,
a section of the journal
Frontiers in Marine Science

Received: 14 November 2018

Accepted: 08 November 2019

Published: 10 December 2019

Citation:

Madin EMP, Darling ES and
Hardt MJ (2019) Emerging
Technologies and Coral Reef
Conservation: Opportunities,
Challenges, and Moving Forward.
Front. Mar. Sci. 6:727.
doi: 10.3389/fmars.2019.00727

Coral reefs worldwide are declining at an accelerating rate due to multiple types of human impacts. Meanwhile, new technologies with applications in reef science and conservation are emerging at an ever faster rate and are simultaneously becoming cheaper and more accessible. Technology alone cannot save reefs, but it can potentially help scientists and conservation practitioners study, mitigate, and even solve key challenges facing coral reefs. We examine how new and emerging technologies are already being used for coral reef science and conservation. Examples include drones, autonomous underwater vehicles (AUVs), 3D mapping and modeling tools, high resolution and nano satellite imagery, and a suite of monitoring and surveillance tools that are revolutionizing enforcement of sustainable reef fisheries. We argue that emerging technologies can play a pivotal role in tackling many of the critical issues facing coral reef conservation science and practice, but maximizing the impact of these technologies requires addressing several significant barriers. These barriers include lack of awareness of technologies and tools, prohibitive cost, lack of transferability across systems and/or scales, lack of technical expertise, and lack of accessibility. We discuss where analogous challenges have been overcome in another system and identify insights that can provide guidance for wise application of emerging technologies to coral reef science and conservation. Thoughtful consideration of, and adaptation to, these challenges will help us best harness the potential of emerging and future technological innovations to help solve the global coral reef crisis.

Keywords: technology, coral reef, remote sensing, satellites, drones, sensors, citizen science, open source

INTRODUCTION

Today, new technologies are emerging at an ever faster rate and are becoming cheaper and more accessible, due in large part to continued, rapid advances in computing power over the last half-century (as predicted by Moore, 1965). Increasingly, conservation biologists and managers seek to harness these new tools to better inform sustainable management of threatened ecosystems. This is especially true for coral reefs, which are historically difficult to study and govern due to their underwater, often-remote, locations and their extremely rich biodiversity. Yet, perhaps no ecosystem is more in need of support: global declines in coral reefs have accelerated in recent

decades, with approximately one-third of the world's largest coral reef system already lost (Hughes et al., 2018b) – a pattern which is likely reflective of many other reef systems globally. The loss of coral reefs puts at risk the many benefits corals provide to society, such as food security and coastal protection for tens of millions of people at least (Moberg and Folke, 1999), and medicinal resources (Bruckner, 2002) for fighting multiple common and life-threatening illnesses, including cancer, HIV, and heart disease.

The future of coral reefs depends upon swift and effective action at local, national, and international levels. Such action requires better science to inform better management—and better science depends on generating and analyzing more data, faster, and across larger scales than ever before. Technology is a critical part of the solution, but deployment of new technology alone is not enough.

Here, we outline some of the ways technological innovation is helping to generate more data and, importantly, note the barriers that are preventing conservation practitioners, scientists, and managers from maximizing application of this technology and implementing solutions at scale. By examining initiatives that currently utilize technological solutions for coral reefs, we also uncover common strategies for success and opportunities for future progress in this space. Our goal is to provide a framework for the coral reef conservation community to guide more effective engagement with technology in order to accelerate conservation and sustainable management of these threatened ecosystems.

CHALLENGES AND EXISTING SOLUTIONS

Today, coral reef scientists, managers, and conservationists are developing or using a wide range of technologies and associated data analytics to address three pressing problems for coral reef conservation:

1. A dearth of data: over time, space, and at the appropriate resolution to understand threats and evaluate potential mitigation plans;
2. A lack of analytical power: faster and more complex analyses are necessary to handle growing volumes of data generated by new technologies; additional analyses are then needed in order to translate that data to more sophisticated and effective decision-making;
3. Appropriate governance: applying science- and technology-based management in culturally appropriate and effective ways.

To meet these challenges, practitioners are experimenting with a proliferation of both hardware and software innovations, many of which have been topics at key academic and conservation conferences. For example, at the Emerging Technology for Coral Reef Science and Conservation session at the most recent International Coral Reef Symposium (2016), researchers gave talks about applying a diversity of new technologies, such as drones, underwater remotely operated vehicles (ROVs), autonomous underwater vehicles (AUVs), and satellites to

gather data on coral reefs. Each of these technologies generate information about reef ecology and health across a diverse range of depths, conditions, and spatial and temporal scales. For example, drones, ROVs, and AUVs can provide very high spatial resolution imagery of localized areas of reef, while satellites can provide a coarser-scale view of far larger areas of reef. Similarly, 3D maps of reefs are allowing new methods of assessing the functional importance of corals (Fontoura et al., in press; Zawada et al., 2019). Collectively, these tools can help scientists and managers quantify aspects of reef ecosystem health across a wide range of spatial resolutions, depths, and locations. Despite these advantages, each of these tools has limitations, many of which involve trade-offs between spatial and temporal resolution and geographic coverage.

Likewise, advances in sensors and tracking systems are providing more accurate information about the movement of species and dynamic environmental conditions—in some cases, even in real- or near-real-time (Maxwell et al., 2015; Kroodsmas et al., 2018). The application of such technology is wide: citizen-scientist surfers are piloting Smartfins to share data on ocean properties via sensors in their surfboard fins; smaller vessel monitoring systems (VMS) units by Pelagic Data Systems are providing new ways to track fishing vessels and, potentially, fishing gear; and new types of acoustic tags and receivers continue to lend insight into fish behavior, habitat use, and effectiveness of different kinds of fisheries management.

Another intersection between technology and marine science is in automation of image capture and processing, as well as development of platforms and algorithms to better analyze the enormous data sets generated by these new technologies. Some examples include underwater camera company View Into the Blue's self-cleaning, time lapse camera systems to record coral bleaching events over multiple months, developed for the film *Chasing Coral*; Bayesian clustering models for labeling seafloor imagery from the Australian Centre for Field Robotics (Steinberg et al., 2015); application of facial recognition software to identify fishers' catch, such as the FishFace program at The Nature Conservancy; algorithms to detect illegal fishing practices based on vessel tracks, such as those developed by Eyes on the Seas and Global Fishing Watch (Figure 1.2; McCauley et al., 2016); and new software by DeepLabCut that digitally identifies limbs and tracks body movements of animals from within any video.

These developments have helped to advance knowledge of oceans and human impacts to marine ecosystems. However, in the context of globally threatened coral reefs, we argue that the full potential of technology to positively advance conservation has not yet been tapped. To better understand how we can maximize the potential of emerging technologies to benefit coral reef science and conservation, we use qualitative analysis of a suite of existing initiatives that utilize technology to advance science or conservation of coral reefs. First, we looked for common “sticking points,” where practitioners from different projects have encountered similar challenges. Such reoccurring or common problems often point to underlying, systemic barriers that, if resolved, can help open opportunities across a sector. Secondly, we examined aspects of programs and projects that



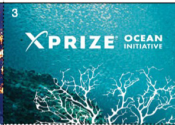
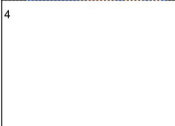
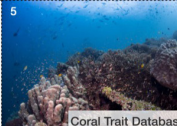




		Strategies		
		Build technology expertise	Democratize data and tools • Open source • Low cost	Develop new models for innovation
Barriers	Data without insight	1 	2 	3 
	Efforts and data are fragmented	4 	5 	6 
	Limited accessibility to technology	7 	8 	9 

FIGURE 1 | Matrix of illustrative coral reef science and conservation technology solutions that match innovative strategies to known barriers. From top left to bottom, (1) *Google Earth Outreach* offers free training and access to their remote sensing platforms to assist with geospatial data analysis; (2) *Global Fishing Watch* allows managers and scientists to freely monitor illegal fishing activity worldwide; (3) the *Wendy Schmidt Ocean Health XPRIZE* incentivizes ocean technology solutions from teams of engineers, scientists and innovators in a global competition; (4) represents open space where technology tools should strive to meet this gap; (5) the *Coral Trait Database* is a growing compilation of freely available coral species data to centralize and standardize previously fragmented scientific information; (6) *MERMAID* is an open source web application developed by coral reef field biologists and web designers to manage underwater transect data; (7) organizations like *Conservation Drones* and *She Flies* provide training in using unmanned aerial vehicles (drones) for ocean monitoring and biodiversity conservation; (8) *Open ROV* seeks to make telerobotic submarines available at low-cost for affordable underwater exploration; similarly, GoPro cameras and the *Liquid Robotics Wave Glider* (not shown) are examples of affordable cameras and ocean robots, respectively, to allow scientists to access ocean health information; (9) *Planet Labs* is a private Earth imaging company that manufactures nano satellites for commercial uses but provides free high resolution imaging data to scientists. All photographs provided by named organizations, with the exceptions of (5) Emily Darling; (6) James Morgan; (7) www.amazon.com.

facilitated progress within a project and looked for similarities in these success factors across multiple initiatives. Identifying patterns in successful approaches to problem solving can point to strategies for scaling success more widely.

Figure 1 provides an overview of the three key barriers, as well as three potential strategies for success, that we identified, and notes examples of specific projects or initiatives that are tackling a given barrier with a specific strategy. While not comprehensive, these examples highlight several key barriers preventing more effective use of technology in coral reef science and conservation and provide insight into how we may begin to scale solutions to overcome these core sticking points in the system.

Barriers to Scaling Technological Innovation for Coral Reef Conservation and Science

1. **Data Without Insight:** Several initiatives had the similar challenge of turning newly generated data into insights that could inform understanding or management of coral reefs. These problems include generation of too much data to process in a timely or accurate manner; the challenge of developing algorithms that work at both small and large scales; and a lack of cross-disciplinary

training of individuals in both science and technology to accelerate and improve interpretation of data. The result is a condition where more and more data are generated, but without capacity to realize the full potential impact of these data on the management or understanding of the ecosystem.

2. **Efforts and Data are Fragmented:** A lack of coordination permeates the system. The majority of existing projects are one-off and isolated from one another, and larger platforms for shared learning remain scarce, especially given the rapid pace of technology development and usage. In addition, scientists and conservation practitioners have different and potentially competing priorities for what they need from technology, which stifles progress—particularly as it prevents a coordinated funding strategy to support technology development and data collection across the field.
3. **Limited Accessibility to Technology:** There are several different, but related, factors that prevent more widespread access to novel tools for coral reef science and conservation. First, although costs have largely come down, innovations remain expensive, especially for developing world practitioners and scientists, preventing many from using existing tools. Second, the rapidly evolving field makes communication about new tools or processes difficult and

means many users remain unaware of potentially valuable and useful resources—this limits progress and can lead to wasted resources as individuals work to design a solution that already exists. Even once a tool is widely known, the technological expertise to apply it is often lacking. Finally, infrastructure limitations continue to hamstring use of tools and platforms where reliable electricity, high-speed internet connections, or other key elements to effective deployment of a technological solution may be missing.

Strategies for Success

1. *Build technology expertise:* Several technology-based conservation efforts have found success by providing focused training, often for free, to field practitioners who can then apply new technologies directly to the problem at hand (**Figures 1.1, 1.7**). Rather than relying on technology specialists, these programs often work to make their technology accessible to core users through online and in-person courses, online tutorials and other materials, and follow up help when necessary.
2. *Democratize data and tools:* Like the push for Open Science, this strategy reflects an ethos of more data/tools, in more hands, makes for greater progress. A core tenet is reduction of redundancy, allowing for scientists and managers to capitalize on data and methods generated by one another. Doing so allows them to direct limited resources toward novel analyses or technology design, rather than re-generating data or re-developing methods that have already been created. This principle for success often manifests as open platforms for data sharing, open-source software and hardware, and other models that seek to reduce costs for technology innovation and access (**Figures 1.2, 1.5, 1.8**).
3. *Develop new models for innovation:* New approaches to adapting or harnessing the tech development pipeline, spanning the conception to implementation phases, is key to effectively designing and applying technologies to meet marine science and conservation needs. Currently, several initiatives are experimenting effectively in this space, including as a means to: (a) drive marine science or conservation-focused tech development (**Figure 1.3**); (b) generate methods to collectively handle existing, disparate scientific data from across the world (**Figure 1.6**); and (c) re-purpose tech developed for other uses to further conservation science (**Figure 1.9**). Each is an example of how novel business models or design platforms can accelerate effective application of new technologies for advancing coral reef science and conservation. Importantly, collaboration within this process between tech developers and the scientific and management communities is key (e.g., **Box 1**).

In many cases, a single project may tackle multiple barriers with one or more strategies. **Figure 2** describes one ongoing project's journey integrating emerging technologies into reef conservation science by highlighting the barriers encountered and the strategies used to overcome these barriers to achieve its goals.

BOX 1 | Learning from other systems.

What can be learned by coral reef scientists and conservation practitioners from other systems? The Global Forest Watch (GFW) project (Popkin, 2016) provides a recent and ongoing example of how many of these common challenges can be overcome by using the strategies identified in **Figure 1**. The GFW partnership, originally conceived by the World Resources Institute and partners and made possible by the open source Google Earth Engine platform (**Figure 1.1**), is “an interactive online forest monitoring and alert system designed to empower people everywhere with the information they need to better manage and conserve forest landscapes” (www.globalforestwatch.org). GFW focuses on the global challenge of deforestation, which—similar to many of the world's coral reefs—occurs largely in remote, hard-to-access locations around the globe.

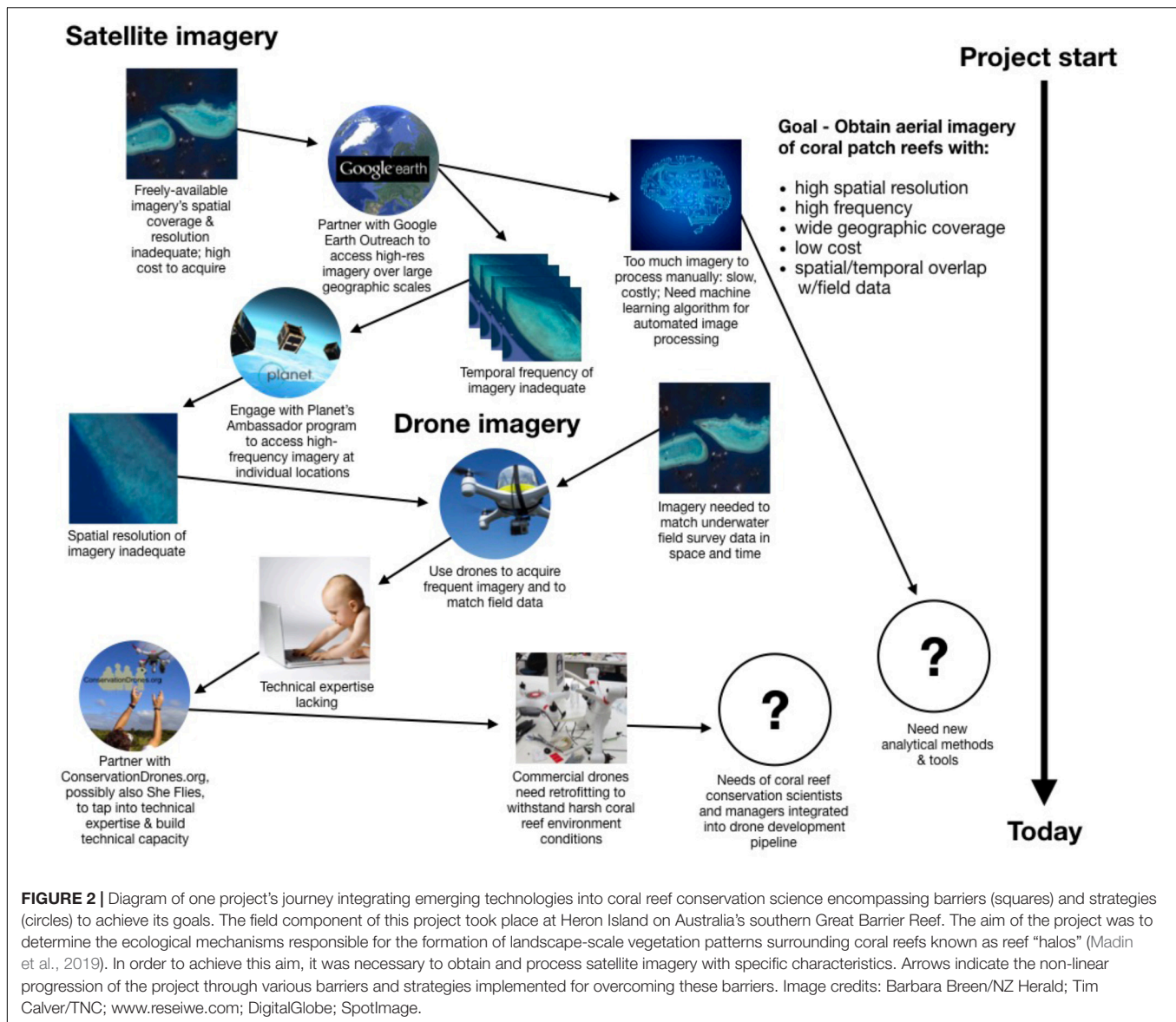
Through its online platform, GFW uses cloud based computing to make satellite data of forest cover freely accessible in near-real-time (overcoming lack of accessibility to the tools behind the data) within a single platform (overcoming fragmented data). In the process, it provides instantaneous two way feedback with users, such as sending alerts to changes in users' local forests and conversely receiving uploaded alerts to the system where users observe changes on the ground (overcoming lack of insights generated from data). Aspects of this system tap into key strategies for overcoming these barriers: GFW is built on new analytical tools and software to generate these data and is (1) designed to allow users to rapidly gain the technical expertise needed to use the system, (2) democratizes global forest imagery and the data it produces (i.e., is open source and free for all users), and (3) is constantly improved by data input from users via local or regional observations. In addition, secondary analytical tools to generate further insight have been built on the base platform, such as GFW Commodities, a tool to address deforestation in commodity supply chains, and GFW Fires, which helps monitor emerging fires, identify potential causes, and analyze impacts of fires on forests and people.

Global Forest Watch offers guidance for coral reef science and conservation in that it provides a real-world example of how the technology community, scientists, conservation practitioners, and local citizens can collectively overcome barriers to applying emerging technology to an insidious conservation challenge. GFW also exemplifies focusing cooperative funding from diverse sources—including governmental, non-governmental, scientific, private philanthropic, and private sector organizations—on a common environmental challenge. Envisioning how the coral reef conservation community might adopt similar approaches could provide a valuable “guiding light” toward embracing emerging technologies and gaining new insights from them.

In addition to existing initiatives focused on coral reefs, other sectors working to integrate technological innovation with science and conservation can provide critical insights. See **Box 1** for a specific example from the forestry realm. Similarly, cross-system, global scale examples of observation and monitoring initiatives that rely on emerging technologies include iNaturalist (Van Horn et al., 2018) and GEO BON (Scholes et al., 2012), which rely upon citizen and professional scientists, respectively. These and other related efforts, while diverse in nature, share the common aim of improving monitoring of the natural world through technology.

CONCLUSION: MOVING FORWARD AND SCALING UP

Effectively engaging with technology can accelerate the conservation and sustainable management of coral reefs. Drones (Chirayath and Earle, 2016; Kiszka et al., 2016), microsatellites (Asner et al., 2017), cloud databases (McCauley et al., 2016),



UAV mapping (Williams et al., 2010; Burns et al., 2015), and other remote sensing approaches (Thompson et al., 2017) are just a few examples of the kinds of new tools that can help track ongoing changes in coral reef ecosystems or improve enforcement and management of coral reef areas. The question is: how might we strategically develop and deploy these and other technologies so they can be applied at larger scales and inform greater understanding, monitoring, and management? The barriers and strategies identified here provide insights into how to answer this challenge.

A critical first step is standardization and coordination of data workflows and reporting in order to curate global datasets of coral reef information (sensu historical, ongoing Global Coral Reef Monitoring Network and NOAA Coral Reef Watch Program). These datasets then need to be housed within platforms that allow for free or low cost, equitable, and easy

access to diverse users across disciplines and geographies. One example for how to effectively do this exists within the Coral Trait Database (Figure 1.5; Madin et al., 2016), which collates existing information to help identify gaps in knowledge and provide more efficient and effective analyses based on existing information. For example, the Coral Trait Database allows any user with an internet connection to access its global quality-controlled database of peer-reviewed data on coral trait data at a species level (e.g., demographic parameters, geographic ranges, etc.). Access to the database eliminates the need for 1) access to potentially costly peer reviewed literature and b) extremely time-consuming extraction of data from that literature, in the process dramatically speeding up the pace at which insights can be generated from this vast body of knowledge.

Strategies to achieve up-scaling of data collection also include leveraging citizen science projects, such as OpenROV

(Figure 1.8)¹, where the lay public can engage in data collection in a robust and systematic manner— but success relies on creating the repositories where this information can be organized and accessed. Cloud based data storage and open source tools can help create accessible data infrastructure, but they require trainings and a community of coding scientists. The Coral Reef Science and Cyberinfrastructure Network² is one model for how to build this capacity. Such efforts reflect a need for continued work to identify and build platforms that can funnel ever-growing information streams into useable, digestible formats. As technology continues to provide an increasing influx of data—from remote sensing, machine learning, and unmanned robotics systems, to name just a few—new platforms will be needed to collate, analyze, and distribute findings in an equitable and timely manner.

Adopting new technologies is risky, and requires time, effort, and training. Nations with greater capacity have more resources to trial and buy-in to new technologies, but amplifying support for developing world practitioners will optimize solution-building in the regions where coral reefs primarily exist. Strategic partnerships between nations with capacity and those with fewer resources can help offset the risk and costs of new technologies, while at the same time creating opportunity for mutually sharing lessons learned. Organizations such as Conservation Drones (Figure 1.7), a worldwide initiative to make and promote the use of low-cost drones, particularly in developing nations, is helping to build capacity and democratize technology use (Koh and Wich, 2012). Design challenge platforms, such as the Ocean Health XPrize (Figure 1.3), could be designed to specifically solicit ideas from more geographically diverse countries. Such injection of resources at early pilot stages would go a long way toward helping resource-strapped regions overcome initial barriers to entry into technological use and development.

New models for collaboration can lead to engagement among multiple stakeholders, such as technology companies, programmers, developers, and conservation scientists. An example of this is the nano satellite company Planet's (Figure 1.9) staff scientist whose job is to liaise with the scientific and other communities to increase the company's environmental and humanitarian engagement and impact. Planet's model has resulted in numerous nascent projects with environmental and societal benefit potential, at least one of which has already resulted in assessments of difficult-to-access coral reef regions undergoing rapid human-induced change (Asner et al., 2017).

Ultimately, innovative funding models are needed to plant the seeds for scalable technologies and collaborations. The Moore

Foundation's Data-Driven Discovery Initiative, the Paul G. Allen Foundation's investments in technology for conservation, and Google Earth Outreach (Figure 1.1) provide a few examples of existing direct or in-kind funding opportunities that support adoption of technology by conservation and scientific organizations. However, other types of funding support are needed. Accelerators such as Ocean X Labs and Ocean Solutions Incubator, traditionally focused on supporting early stage technology entrepreneurs to tackle general ocean challenges, could be harnessed or adapted to focus on coral reef-specific issues. Likewise, with so many livelihoods and food security dependent on coral health, more creative use of economic development funds is warranted.

With shrinking recovery windows between global bleaching events (Hughes et al., 2018a) and the increasing human footprint of consumption, carbon, and globalization, coral reefs face a grim future. Emerging technologies can help take the pulse of remote, underwater ecosystems to identify and protect the last remaining reefs as well as identify promising outliers, which are withstanding the onslaught and may hold clues for understanding resiliency (Guest et al., 2018). While technologies can collect more and more data, these workflows must be developed collaboratively with stakeholders and with an explicit vision to strengthen scientific and technological capacities in the world's coral reef regions. With robust data, meaningful collaborations between scientists, stakeholders and technology developers, and targeted funding to support the scaling up of coordinating technologies, coral reef science and conservation may just be able to keep up in a changing world.

AUTHOR CONTRIBUTIONS

EM led the study. All authors contributed to design of the study and writing of the manuscript.

FUNDING

EM was supported by an Australian Research Council DECRA Fellowship (DE120102614).

ACKNOWLEDGMENTS

The authors would like to thank Macquarie University's Genes to Geoscience Research Centre for supporting the workshop that led to the development of the manuscript. In particular, we would like to thank Mark Westoby, Mike Gillings, Mariella Herberstein, and Wade Tozer.

¹ <https://www.sofarocan.com>

² <https://www.earthcube.org/group/crescynt-coral-reef-science-cyberinfrastructure-network>

REFERENCES

- Asner, G. P., Martin, R. E., and Mascaro, J. (2017). Coral reef atoll assessment in the South China Sea using Planet Dove satellites. *Remote Sens. Ecol. Conserv.* 3, 57–65. doi: 10.1002/rse2.42
- Bruckner, A. W. (2002). Life-saving products from coral reefs. *Issues Sci. Technol.* 18:35.

- Burns, J., Delparte, D., Gates, R., and Takabayashi, M. (2015). Integrating structure-from-motion photogrammetry with geospatial software as a novel technique for quantifying 3D ecological characteristics of coral reefs. *PeerJ* 3:e1077. doi: 10.7717/peerj.1077
- Chirayath, V., and Earle, S. A. (2016). Drones that see through waves – preliminary results from airborne fluid lensing for centimetre-scale aquatic

- conservation. *Aquat. Conserv. Mar. Freshw. Ecosyst.* 26, 237–250. doi: 10.1002/aqc.2654
- Fontoura, L., Zawada, K., D'agata, S., Baird, A., Álvarez-Noriega, M., Woods, R., et al. (in press). Climate-driven shift in coral morphological structure predicts decline of juvenile reef fishes. *Glob. Chang. Biol.* doi: 10.1111/gcb.14911
- Guest, J. R., Edmunds, P. J., Gates, R. D., Kuffner, I. B., Andersson, A. J., Barnes, B. B., et al. (2018). A framework for identifying and characterising coral reef “oases” against a backdrop of degradation. *J. Appl. Ecol.* 55, 2865–2875. doi: 10.1111/1365-2664.13179
- Hughes, T. P., Anderson, K. D., Connolly, S. R., Heron, S. F., Kerry, J. T., Lough, J. M., et al. (2018a). Spatial and temporal patterns of mass bleaching of corals in the Anthropocene. *Science* 359, 80–83. doi: 10.1126/science.aan8048
- Hughes, T. P., Kerry, J. T., Baird, A. H., Connolly, S. R., Dietzel, A., Eakin, C. M., et al. (2018b). Global warming transforms coral reef assemblages. *Nature* 556, 492–496. doi: 10.1038/s41586-018-0041-2
- Kiszka, J. J., Mourier, J., Gastrich, K., and Heithaus, M. R. (2016). Using unmanned aerial vehicles (UAVs) to investigate shark and ray densities in a shallow coral lagoon. *Mar. Ecol. Prog. Ser.* 560, 237–242. doi: 10.3354/meps11945
- Koh, L. P., and Wich, S. A. (2012). Dawn of drone ecology: low-cost autonomous aerial vehicles for conservation. *Trop. Conserv. Sci.* 5, 121–132. doi: 10.1177/194008291200500202
- Kroodsma, D. A., Mayorga, J., Hochberg, T., Miller, N. A., Boerder, K., Ferretti, F., et al. (2018). Tracking the global footprint of fisheries. *Science* 908, 904–908. doi: 10.1126/science.aao5646
- Madin, E. M. P., Precoda, K., Harborne, A. R., Atwood, T. B., Roelfsema, C., and Luiz, O. J. (2019). Multi-trophic species interactions shape seascape-scale coral reef vegetation patterns. *Front. Ecol. Evol.* 7:102. doi: 10.3389/fevo.2019.00102
- Madin, J. S., Hoogenboom, M. O., Connolly, S. R., Darling, E. S., Falster, D. S., Huang, D., et al. (2016). A trait-based approach to advance coral reef science. *Trends Ecol. Evol.* 31, 419–428. doi: 10.1016/j.tree.2016.02.012
- Maxwell, S. M., Hazen, E. L., Lewison, R. L., Dunn, D. C., Bailey, H., Bograd, S. J., et al. (2015). Dynamic ocean management: defining and conceptualizing real-time management of the ocean. *Mar. Policy* 58, 42–50. doi: 10.1016/j.marpol.2015.03.014
- McCauley, D. J., Woods, P., Sullivan, B., Bergman, B., Jablonicky, C., Roan, A., et al. (2016). Ending hide and seek at sea. *Science* 351, 1148–1150. doi: 10.1126/science.aad5686
- Moberg, F., and Folke, C. (1999). Ecological goods and services of coral reef ecosystems. *Ecol. Econ.* 29, 215–233. doi: 10.1016/s0921-8009(99)00009-9
- Moore, G. E. (1965). Cramming more components onto integrated circuits. *Electronics* 38, 1–4.
- Popkin, G. (2016). Satellite alerts track deforestation in real time. *Nature* 530, 392–393. doi: 10.1038/530392a
- Scholes, R. J., Walters, M., Turak, E., Saarenmaa, H., Heip, C. H. R., Tuama, E. O., et al. (2012). Building a global observing system for biodiversity. *Curr. Opin. Environ. Sustainab.* 4, 139–146.
- Steinberg, D. M., Pizarro, O., and Williams, S. B. (2015). Hierarchical Bayesian models for unsupervised scene understanding. *Comput. Vis. Image Understand.* 131, 128–144. doi: 10.1109/TPAMI.2009.22
- Thompson, D. R., Hochberg, E. J., Asner, G. P., Green, R. O., Knapp, D. E., Gao, B. C., et al. (2017). Airborne mapping of benthic reflectance spectra with Bayesian linear mixtures. *Remote Sens. Environ.* 200, 18–30. doi: 10.1016/j.rse.2017.07.030
- Van Horn, G., Mac Aodha, O., Song, Y., Cui, Y., Sun, C., Shepard, A., et al. (2018). “The iNaturalist species classification and detection dataset,” in *Proceedings of the IEEE Conference on Computer Vision and Pattern Recognition*, (Salt Lake City, UT: IEEE), 8769–8778.
- Williams, S. B., Pizarro, O., Webster, J. M., Beaman, R. J., Mahon, I., Johnson-Roberson, M., et al. (2010). Autonomous underwater vehicle-assisted surveying of drowned reefs on the shelf edge of the Great Barrier Reef, Australia. *J. Field Robot.* 27, 675–697. doi: 10.1002/rob.20356
- Zawada, K. J. A., Madin, J. S., Baird, A. H., Bridge, T. C. L., and Dornelas, M. (2019). Morphological traits can track coral reef responses to the Anthropocene. *Funct. Ecol.* 33, 962–975.

Conflict of Interest: The authors declare that the research was conducted in the absence of any commercial or financial relationships that could be construed as a potential conflict of interest.

The reviewer IW declared a past co-authorship with one of the authors, MH, to the handling Editor.

Copyright © 2019 Madin, Darling and Hardt. This is an open-access article distributed under the terms of the Creative Commons Attribution License (CC BY). The use, distribution or reproduction in other forums is permitted, provided the original author(s) and the copyright owner(s) are credited and that the original publication in this journal is cited, in accordance with accepted academic practice. No use, distribution or reproduction is permitted which does not comply with these terms.



Fish Spawning Aggregations Dynamics as Inferred From a Novel, Persistent Presence Robotic Approach

Laurent M. Chérubin^{1*}, Fraser Dalglish^{1,2}, Ali Khaleel Ibrahim³, Michelle Schärer-Umpierre⁴, Richard S. Nemeth⁵, Anthony Matthews⁶ and Richard Appeldoorn⁷

¹ Harbor Branch Oceanographic Institute, Florida Atlantic University, Boca Raton, FL, United States, ² Harris Corporation, Melbourne, FL, United States, ³ Department Computer & Electrical Engineering and Computer Science, Florida Atlantic University, Boca Raton, FL, United States, ⁴ HJR Reefscaping, Boquerón, PR, United States, ⁵ Center for Marine and Environmental Studies, University of the Virgin Islands, St. Thomas, US Virgin Islands, ⁶ EPS Corporation, Panama City Beach, FL, United States, ⁷ Caribbean Coral Reef Institute, University of Puerto Rico, Mayaguez, PR, United States

OPEN ACCESS

Edited by:

Leonard Pace,
Schmidt Ocean Institute,
United States

Reviewed by:

William David Heyman,
LGL (United States), United States
Christoph Waldmann,
University of Bremen, Germany

*Correspondence:

Laurent M. Chérubin
lcherubin@fau.edu

Specialty section:

This article was submitted to
Ocean Observation,
a section of the journal
Frontiers in Marine Science

Received: 14 December 2018

Accepted: 03 December 2019

Published: 10 January 2020

Citation:

Chérubin LM, Dalglish F,
Ibrahim AK, Schärer-Umpierre MT,
Nemeth RS, Matthews A and
Appeldoorn R (2020) Fish Spawning
Aggregations Dynamics as Inferred
From a Novel, Persistent Presence
Robotic Approach.
Front. Mar. Sci. 6:779.
doi: 10.3389/fmars.2019.00779

Fish spawning aggregations (FSAs) consist of the temporary gathering of a large number of fishes at a specific location to spawn. Monitoring of FSA is typically conducted by divers, but surveys are often restricted to a limited area and dependent upon sea conditions, thus our knowledge of FSA dynamics is extremely limited. Fisheries independent research strives for new technology that can help remotely and unobtrusively quantify fish biomass and abundance. Since some fish species, such as groupers, produce sounds during reproductive behaviors, Eulerian passive acoustic monitoring provides information when divers cannot access the FSA site. Fish sounds provide an innovative approach to assess fish presence and potentially their numbers during reproductive events. However, this technology is limited by the sound propagation range, hence the distance between the fish emitting sounds and the hydrophone location. As such, this Eulerian monitoring approach implicitly creates a knowledge gap about what happens beyond the range of the recorders. Furthermore, the large datasets make the detection process by human ears and eyes very tedious and inconsistent. This paper reports on two innovative approaches to overcome these limitations. To facilitate fish call detections, we have developed an algorithm based on machine learning and voice recognition methods to identify and classify the sounds known to be produced by certain species during FSA. This algorithm currently operates on a SV3 Liquid Robotics wave glider, an autonomous surface vehicle which has been fitted to accommodate a passive acoustic listening device and can cover large areas under a wide range of sea conditions. Fish sounds detections, classification results, and locations along with environmental data are transmitted in real-time enabling verification of the sites with high detections by divers or other *in situ* methods. Recent surveys in the

US Virgin Islands with the SV3 Wave Glider are revealing for the first time the spatial and temporal distribution of fish calls surrounding known FSA sites. These findings are critical to understanding the dynamics of fish populations because calling fish were detected several kilometers away from the known FSAs. These courtship associated sounds from surrounding areas suggest that other FSAs may exist in the region.

Keywords: spawning aggregation, grouper, wave glider, machine learning, fish sounds

INTRODUCTION

Fisheries sustainability and ecosystem health not only rely on habitat quality and biodiversity but also on reproductive success (Mumby et al., 2006). In coral reef ecosystems, some large predatory species such as groupers, aggregate to spawn in large numbers at specific locations and times (Domeier and Colin, 1997). These fish spawning aggregation (FSA) sites are shared by multiple species that may overlap in time (Heyman and Kjerfve, 2008) and as such, constitute breeding hotspots requiring some form of protection (Erisman et al., 2017). Because FSAs are temporally predictable and are characterized by strong site fidelity, once located, they become vulnerable to overfishing if not properly managed (Sadovy, 1997; Sala et al., 2001). Numerous historical FSAs in the Caribbean and the Bahamas have been reported (Smith, 1972; Eklund et al., 2000), but only a few are documented to date while many remain unprotected (Sadovy De Mitcheson et al., 2008).

During the winter and spring months (December to May) in the northern hemisphere soniferous grouper species such as the red hind (*Epinephelus guttatus*), Nassau (*Epinephelus striatus*), yellowfin (*Mycteroperca venenosus*), and black grouper (*Mycteroperca bonaci*) (Nemeth, 2005, 2012a; Schärer et al., 2014; Rowell et al., 2015) aggregate to spawn at existing FSAs in the Intra-Americas Seas (i.e., the Caribbean Sea, Gulf of Mexico, and the Bahamas region). Spawning time is usually associated with the lunar and diurnal cycles, but also with water temperatures and local current conditions (Nemeth, 2009). FSAs are challenging to observe and monitor because they are mostly found at remote locations near the shelf break (Claro and Lindeman, 2003; Kobara and Heyman, 2010; Kobara et al., 2013), in water depths between 30 and 80 m while spawning activities occur mostly at dusk. While many of these sites are known to fishers and represent areas of intensive harvest, not all FSA locations have been documented. As such, there may be a significant number of unreported FSAs, which, if located, could provide a better estimate of the status of certain populations of grouper species such as Nassau, Warsaw (*Hyporhamphus nigritus*), black, red hind, goliath (*Epinephelus itajara*) and their critical habitats used for spawning.

Data on the FSA dynamics of these species is critical to the study and management of these stocks in several countries whose local populations might be connected through larval dispersal (Cowen et al., 2006). Such countries include the Bahamas, Belize, Cuba, Mexico, Eastern Caribbean island nations and the United States (U.S.) whether in the Gulf of Mexico or in the northeastern Caribbean Sea. Determination of the timing, duration and intensity of spawning will be of direct utility for the

design and evaluation of management actions, stock assessment, and effective conservation measures.

Passive acoustic monitoring (PAM) is a fisheries-independent approach that can provide *in situ* observations of soniferous fishes, such as groupers (Mann et al., 2010; Rowell et al., 2011, 2015; Schärer et al., 2012a,b, 2014; Wall et al., 2014, 2017). Additionally, PAM can be relatively non-intrusive and provides data on timing and duration of grouper activity and distribution. In particular, PAM can be used to monitor courtship associated sounds (CASs) at FSA sites to assess grouper reproductive behaviors. As grouper populations begin to recover from overfishing, new or previously extirpated aggregations may reform, also making this technology particularly relevant for surveying and evaluating the recovery of groupers and critical for understanding their biology and ecology. To date, fisheries monitoring efforts using PAMs have primarily used an Eulerian approach; recordings are made from fixed stations at known FSAs (Rowell et al., 2012). However, these FSAs are spatially dynamic and can shift outside the range of fixed stations in a relatively short period. As such, more mobile approaches with PAMs are required to best encapsulate FSA dynamics. For example, the use of autonomous platforms such as buoyancy-driven gliders or wave-gliders that are equipped with PAM systems can be programmed more accurately to encompass FSA spatial extents as well as scout regions of the shelf edge in the exploration of unknown FSAs. Wall et al. (2014) used a Slocum glider, a buoyancy driven autonomous underwater glider (AUG), to conduct a large-scale spatial mapping across the West Florida shelf of red grouper (*E. morio*) sound production. A similar survey was conducted with the same technology along the southeast U.S. (Wall et al., 2017). This survey was conducted during winter when fishery-independent survey data were lacking from traditional ship-based approaches (due to prolonged periods of inclement weather) and covered the winter-spawning dynamics of multiple managed species.

The Slocum glider surveys were conducted with low power acoustic recorders (DSG – Loggerhead Instruments¹), which are self-contained acquisition-only devices that are not integrated to their host, and do not allow for onboard processing and analysis. Therefore, AUG surveys are not capable of characterizing FSAs in real-time, nor can they provide information such as the species composition of FSA aggregates, precise location and timing, population size and the fish behavior or distance from the glider. But automated data collection means that surveys can take place at times and in places where it would be too expensive or dangerous to send human observers (Marques et al., 2013). These

¹www.loggerheadinstruments.com

early attempts to survey fish sound production from spawning aggregations as a new technique for stock assessment led us to conceive a real-time detection and classification PAM system that can be integrated on any glider. Our glider of choice was the SV3 wave glider (WG) because of its continuous real-time transmission and positioning capabilities, which are crucial to the localization of FSAs that are typically transient events.

The main objective of this paper is to present a new persistent robotic approach to conduct PAM surveys and its application to the study of grouper FSA dynamics. The robotic platform was deployed in the U.S. Caribbean near known FSAs and was used to explore the shelf edge up to 20 km away surrounding these known sites. Its findings reveal the presence of CAS of the same aggregating species both scattered and aggregated at other locations along the shelf break. In Section “The Persistent Robotic Approach” we describe the autonomous platform and the PAM system. In Section “Fish Sound and Detectability” we present the acoustic characteristics of CAS and a red hind CAS detection threshold analysis. The fish sounds detection and classification algorithms are described in Section “Grouper Calls Detections Algorithms.” Results and interpretation of the wave glider survey in the U.S. Virgin Islands are presented in Section “Red Hind Spawning Aggregation Dynamics.” Results from the Wave Glider survey are presented in Section “Wave Glider Survey During the Red Hind Peak Calling Week.” A discussion follows in Section “Discussion” and conclusions are drawn in Section “Conclusion.”

THE PERSISTENT ROBOTIC APPROACH

Marine Autonomous Systems

Underwater autonomous systems, including subsea gliders and AUVs, are revolutionizing our ability to map and monitor the marine environment (Yoerger et al., 1998, 2007; Rudnick et al., 2004; German et al., 2008; Caress et al., 2008). Such autonomous systems, although deployed from a research vessel, are not tethered to the vessel and operate without direct human control while collecting data (Yoerger et al., 1998, 2007; Griffiths, 2003). Therefore, they enable data acquisition in parts of the ocean such as beneath ice sheets in polar regions previously inaccessible to vessel-based sampling methods (Bellingham et al., 2000; Brierley et al., 2002; Nicholls et al., 2006; Wadhams et al., 2006; Dowdeswell et al., 2008; Jenkins et al., 2010; Graham et al., 2013), and are improving spatial and temporal resolution of undersea measurements (Niewiadomska et al., 2008; Caldeira et al., 2014). They also provide transformative opportunities to fisheries scientists and oceanographers to study marine population and ecosystem dynamics (Fernandes et al., 2003; Ohman et al., 2013).

Autonomous underwater gliders, such as the Spray glider (Rudnick et al., 2004), the Slocum gliders (Teledyne Webb Research) and the Seaglider (Eriksen et al., 2001) are all capable of sampling continuously throughout the water column as deep as 6,000-m depth for the latter by adjusting their buoyancy and attitude to glide on wings (Rudnick et al., 2004). Slocum and Spray gliders can also be configured to operate in shallow shelf environments (<200 m). Their deployments can last over 1 month and their range can expand over 100 km, with periodic

surfacing for data offload and GPS positioning. In recent years AUGs have been used in ocean soundscape mapping (Matsumoto et al., 2011; Bingham et al., 2012; Wall et al., 2012; Baumgartner et al., 2013) and more recently in fisheries independent surveys (Wall et al., 2014, 2017) on the shelf of the continental U.S. AUGs surveys are less contingent upon large amount of funding being available for ship and personnel time and therefore have the potential to provide long time series at a relatively lower cost. Data collected through passive acoustic surveys are used to assess the presence of soniferous fish with the ultimate goal of assessing biomass and supporting stock assessment activities, while studying the ecological importance of many important commercial species in the U.S.

Autonomous surface vehicles (ASVs) such as Wave-Gliders (WG) have the advantage of continuous GPS positioning, data access and extraction over AUGs. Therefore, WG equipped with PAM systems can be programed more accurately to encompass FSA spatial extents as well as scout regions of the shelf edge in the exploration of unknown FSAs. The SV3 WG is a self-propelled, unmanned persistent mobile data-gathering platform that harvests both solar and wave energy for propulsion and power (**Figure 1**). It can be used as station keeping or mobile data collection platform for up to 12 months powered by the sun only. It provides a real-time communication gateway and has the modularity and capacity to accommodate new prototype sensors and software interfaces that can eventually be integrated and operated with other systems (Manley et al., 2009; Willcox et al., 2009). The WG consists of a surface float tethered with an umbilical cable to a submersible glider (**Figure 1**). The surface float houses the command and control unit, which is used for communications, navigation, and powering of the WG systems, and a user-specified modular payload unit. The submersible glider has a series of paired wings that generate gliding lift, a rudder to provide steering and a thruster for emergency maneuvers and adverse current. The WG harnesses wave energy for propulsion. The heave of the wave forces the submersible forward ahead of the float, which is then pulled forward over the submersible, and so on. A lithium ion battery pack in the WG hold, charged by solar panels on the deck of the surface float, supplies power to systems inside the WG's command and control unit and modular payload unit. During mission, control system and sensor data are sent through a Web-based interface, called WGMS from the WG to the pilot and commands back from the pilot to the WG. It also provides a precise and intelligent navigation web interface. Cellular network or Iridium satellite provides two-way transmission and real-time navigational, operational, and sensor control as well as real- or near-real-time data reporting (Greene et al., 2014). Our submersible glider is connected to a custom-built two-body designed to carry a variety of off-the-shelf acoustic systems. The neutrally buoyant tow-body trails directly behind the submersible glider to which it is connected with a sinusoidal-shaped tow cable, 4 to 10-m below the ocean surface. Slack-tensioning elements, which cause the sinusoidal shape, significantly reduce pitch, roll, and yaw of the tow body in comparison to a conventional tow cable (**Figure 1**). Greene et al. (2014) thus used, instead of manned vessels,

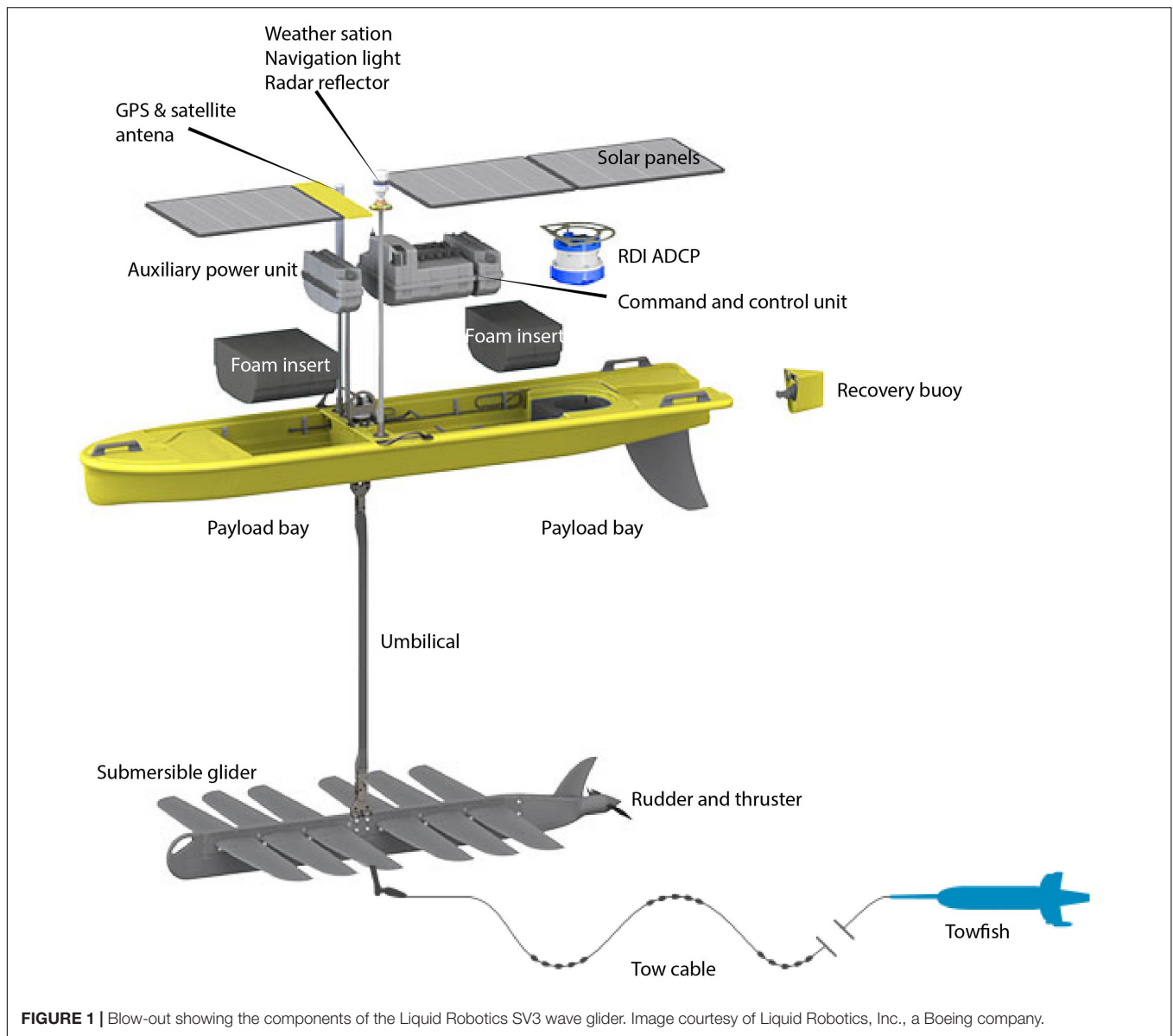


FIGURE 1 | Blow-out showing the components of the Liquid Robotics SV3 wave glider. Image courtesy of Liquid Robotics, Inc., a Boeing company.

WGs equipped with multifrequency, split-beam acoustic sonar to conduct fisheries surveys and we used in this study a similar strategy to conduct fishery independent surveys of FSAs in the United States Caribbean islands.

SV3 Wave Glider Instrumentation

SV3-WG Instruments and Payload

The WG operating system collects navigational and environmental data that are directly available to the operator in real-time. As such, a water velocity sensor informs the operator of the surface current speed and direction. The wind speed and direction are also recorded by the wave glider. In addition, our SV3-WG is equipped with a 600 kHz Workhorse ADCP, which measures current profiles down to 50-m in real-time. The data is readily available through WGMS.

Passive Acoustic Monitoring System

The PAM system consists of two distinct sub systems: one located on the tow-body below the sea surface and the other, located in the surface float section of the SV3-WG. In particular, the sub-surface section of the system hosts two ultra-low frequency hydrophones (HTI-96-Min Hydrophones) and an embedded data processing module optimized in design for such application. The hydrophone frequency response is 2 Hz to 30 kHz with a sensitivity of -201 dB re: $1 \text{ V}/\mu\text{Pa}$ without pre-amp. The system is connected to the host vehicle through the tow-body electrical tow cable. The hydrophone housing is a tubular, oil-filled sealed enclosure that can accommodate up to three hydrophones (**Figure 2**), rated for 100 m depth. The forward side of the tube ends with a fairing that mitigates unnecessary, disruptive noise caused by flow around the tow cable, eddies induced by edges on the tow-body, or any other features that

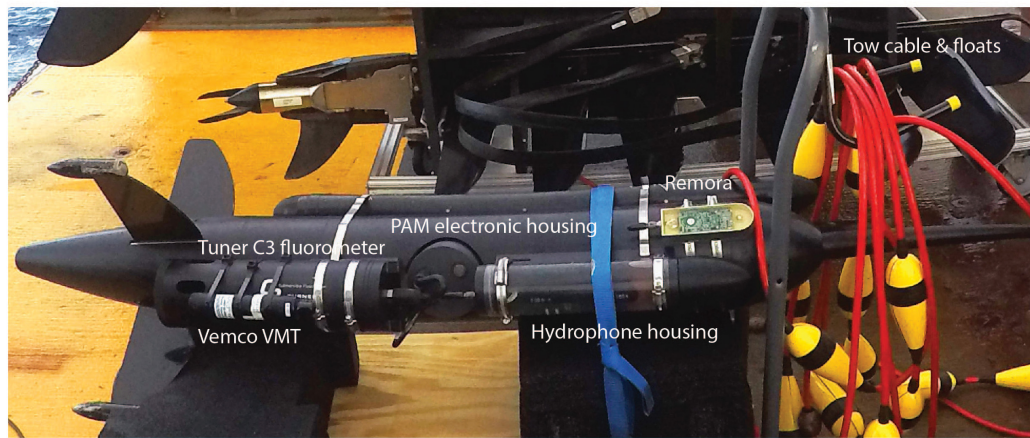


FIGURE 2 | Components and payload of the wave glider's tow-body.

would cause low frequency acoustic vibrations due to turbulent flow. The tube is made of clear polyvinyl chloride (PVC) material, making the housing acoustically transparent. It is oil-filled to couple the hydrophones to the vibrations at wall of the tube. The hydrophone housing is rigidly fixed to the tow-body using internal bolts and a machined plastic spacer. Located inside of the hydrophone housing, is a data acquisition card that contains a high-speed digital-analog converter (ADC), band-pass filter and embedded processor used to continuously collect and buffer data, which is then streamed for signal detection and classification.

The PAM electronic housing, which is located inside the tow-body holds the main processing computer that runs the detection and classification algorithm. The electronic package consists of an off-the-shelf Texas Instrument Beaglebone Black single board computer (SBC). The SBC connects to a stack of breakout daughter boards. The PAM's BeagleBone Black computer runs on Debian, an open-source variation of the Linux operating system maintained by the Debian Project. The software architecture employs the publisher-subscriber model in order to push data to multiple applications at the same time. Seven “port” modules publish data acquired from various sources (sensors, devices, algorithms). Consumer modules subscribe to receive only the data they need and at the rate at which it becomes available. The open-source Lightweight Communication and Marshalling (LCM) middleware library uses the User Datagram Protocol (UDP) to provide the needed publish-subscribe mechanisms.

Seven port modules interact with the payload or other data sources. Five of these ports are respectively connected to (1) a SIMRAD NSS7 Evo2 echosounder with structurescan sonar and with frequency modulation (CHIRP) sonarhub. Sonar screen movies are recorded for sound detection validation. The sonarhub is mounted on the aft of the WG. (2) An onboard AST4000 pressure sensor. (3) A Turner C3 Fluorometer, which measures CDOM, Chlorophyll-a, and backscattering fluorescence (**Figure 2**). (4) Hydrophones. (5) A fish sounds detection and classification algorithm. The PAM records 10 s audio files every 30 s. This cycle allows enough time for data buffering and processing by the machine learning algorithm

while optimizing data storage. The duty cycle can be modified to meet the mission requirements. Each audio file is analyzed by the detection algorithm and if there is a detection, a 3 s snippet that contains the sound detected is produced by the software. However, only one hydrophone channel is currently used for the detection analysis and the data is written in ASCII. The data is stored locally on the PAM on a microSD card and then copied to the vehicle payload computer for real-time access and transmission via GSM network or satellite (RUDICS). Finally, a self-powered, self-logging EXO¹ YSI multiparameter sonde is attached to the tow-body and collects, pressure, pH, temperature, salinity, and dissolved oxygen (DO). Other sensors such as external Remora hydrophone from Loggerhead Instruments, or VEMCO VMT receiver/transmitter for underwater acoustic telemetry have also been used on the tow-body (**Figure 2**).

FISH SOUND AND DETECTABILITY

Grouper Courtship Associated Sounds

For many species of fish, including Epinephelidae, sound plays a critical role in reproduction and therefore the survival and success of the species (Mann and Lobel, 1995; Bass and McKibben, 2003; Luczkovich et al., 2008; Walters et al., 2009; Mann et al., 2010; Montie et al., 2016, 2017). Effective communication requires both species and mate recognition for reproduction (Myrberg and Lugli, 2006; Amorim et al., 2015). In known sound-producing groupers, acoustic signals are used by different taxa for recognition, attracting mates, defending territories, agonism and as an alarm system against predators (Mann et al., 2010; Schärer et al., 2012a,b, 2013, 2014; Rowell et al., 2018). The different call types of a species may consist of multiple different sounds or sections produced in series to create a species-specific acoustic call structure (Zayas, 2019). Grouper species that co-occur at FSA sites in the U.S. Caribbean (Nemeth et al., 2006; Heyman and Kjerfve, 2008) and have documented CAS are described in **Table 1**. CAS are consistent with reproductive behaviors and can provide an estimation of relative reproductive behavior

TABLE 1 | Grouper sound characteristics from the published literature.

Species	Frequency range (Hz)	Peak frequency (Hz)	Bandwidth (Hz)	Duration (s)
Red hind	130–500	166 ± 36	46.4 ± 20.6	1.8 ± 1.0
Nassau grouper	51–206	99 ± 34	22.4 ± 12.2	1.6 ± 0.3
Yellowfin grouper pulse train	101–132	121 ± 7.5	33.0 ± 6.1	3.0 ± 1.0
Yellowfin grouper tonal call	89–142	121 ± 12.6	43.2 ± 4.0	3.1 ± 1.0
Black grouper	67–96	83.5 ± 8.6	6.1 ± 2.7	4.3 ± 1.3

activity and relative abundance through the spawning period (Rowell et al., 2012). Therefore, PAMs can be used to locate spawning aggregations (Luczkovich et al., 1999, 2008; Walters et al., 2009; Rowell et al., 2011) and determine temporal patterns in reproductive behavior and habitat use by different species during FSAs (Locascio and Mann, 2008; Mann et al., 2009, 2010; Nelson et al., 2011; Schärer et al., 2012a,b).

The species-specific sounds produced by grouper during reproductive behaviors are somewhat stereotyped and can be audibly and visually (in spectrograms) distinguished from each other due to unique duration, peak frequency, call structure and tonal characteristics (Table 1). The call structure and tonal characteristics make spectrogram distinguishable as shown in Figure 3 from sounds recorded by the WG. The Nassau grouper (*E. striatus*) CAS consist of a combination of pulse and tonal sounds with a mean peak frequency of 99 Hz and average duration of 1.6 s (Schärer et al., 2012a) (Figure 3A). The yellowfin grouper (*M. venenosus*) CAS consist of two parts (one pulse train and one tonal) that are usually combined with mean peak frequency of 121 Hz and approximately 3 s duration (Figure 3B – tonal call) (Schärer et al., 2012b). The red hind (*E. guttatus*) produce at least two main types of CAS with mean peak frequency between 166 Hz (Mann et al., 2010) and for each type of CAS 173 and 201 Hz (Zayas, 2019). Red hind CAS usually consists of a single or variable number of pulses, with a second tonal portion mean duration between 1 and 2.4 s (Figures 3C,D). Black grouper (*M. bonaci*) produces a CAS consisting of two parts, one a low frequency pulse train usually combined with a modular tonal call, of mean peak frequency 83.5 Hz and a duration between 2.4 and 7.9 s (Schärer et al., 2014). The black grouper CAS was not identified in the recordings during the WG survey. Because red hind is the dominant spawning species during the time of survey, red hind CAS rate patterns during the main spawning week will be used to interpret the PAM detections and evaluate the usefulness of WG CAS surveys for monitoring reproductive activity at FSAs.

The call structures previously described and shown in Figure 3 may not reflect the full variation of acoustic repertoire for each species as has been recently discovered in the data presented in this paper as well as in the most recent literature. For example, an agonistic call type produced by Nassau grouper was identified from a spawning aggregation in Puerto-Rico by Bingham et al. (2012). For red hind the acoustic repertoire has recently been characterized by Zayas (2019) from animals held in

captive conditions, increasing to five types of sounds with their associated behaviors.

PAM Detection Threshold and Grouper Sound Detectability

The average source level (SL) of the grouper species targeted in this study is between 100 and 150 dB re 1 μ Pa, with a mean that varies between 90 and 150 Hz and a bandwidth between 20 and 45 Hz (Mann et al., 2009; Schärer et al., 2012a,b, 2014) (Table 1). The PAM system was designed to detect sound specifically in a frequency band that encompasses all the grouper species in Table 1, and with detection threshold above the ambient noise in that frequency range. Following Brunoldi et al. (2016), we used the passive sonar equation, Eq. (1), with the intent to set a lower limit to the signal-to-noise ratio at the hydrophones in order to permit detection of grouper CAS with various ambient noise levels.

$$SNR(r) = SL - (TL(r) + NL + BW) \quad (1)$$

where the signal-to-noise ratio (SNR) at the receiver for a fixed range (r) is given by the difference between the source level (SL) and the sum of the transmission loss (TL) of the grouper sound and of ocean-noise (NL) within the spectral bandwidth (BW) of the source signal. For the direct detection scheme used for the work described in this paper, the SNR should exceed the detection threshold (DT), for a valid signal to be extracted from ambient noise, Eq. (2).

$$SNR(r) \geq DT \quad (2)$$

The sound emitted by the grouper species identified in this study has been chosen as the source signal for target detection by the acoustic system. The PAM sampling frequency is $f_s = 10$ kHz thus oversampling in the time domain to further improve SNR by signal integration. To calculate of the detection threshold (DT), we first set the detection P(D) and false alarm P(FA) probabilities of the passive sonar to be P(D) = 0.9 and P(FA) = 0.05. Then we estimated the detection index (d) from the Receiving Operating characteristic Curves (ROC) provided by Urlick (1983) from which we obtained $d = 9$. The detection index d represents the difference between the mean values of the sum of the signal and noise, and the noise-only probability density functions (PDF). The greater the d -value, the greater the likelihood of detecting an event, here a grouper call is.

Let S be the signal power in the receiver bandwidth measured at the hydrophones. Let N be the noise power in the receiver bandwidth also measured at the hydrophones. The detection threshold is given by:

$$DT = 10 \log_{10} \left(\frac{S}{N} \right) \quad (3)$$

The detection index d is proportional to the signal-to-noise ratio $\left(\frac{S}{N}\right)^2$ and as shown in Brierley et al. (2002) it can be written as

$$d = m \left(\frac{S}{N} \right)^2 \quad (4)$$

where m , is the number of samples within the integration period of the signal considered, which by definition is the ratio

between the sampling frequency ($f_s = 10 \text{ kHz}$) and the maximum frequency of the source signal to be detected ($f_{max} = 350 \text{ Hz}$). From Eq. (4) we have

$$\left(\frac{S}{N}\right)^2 = \frac{d}{m} = \frac{9}{28.6} \sim 0.31 \quad (5)$$

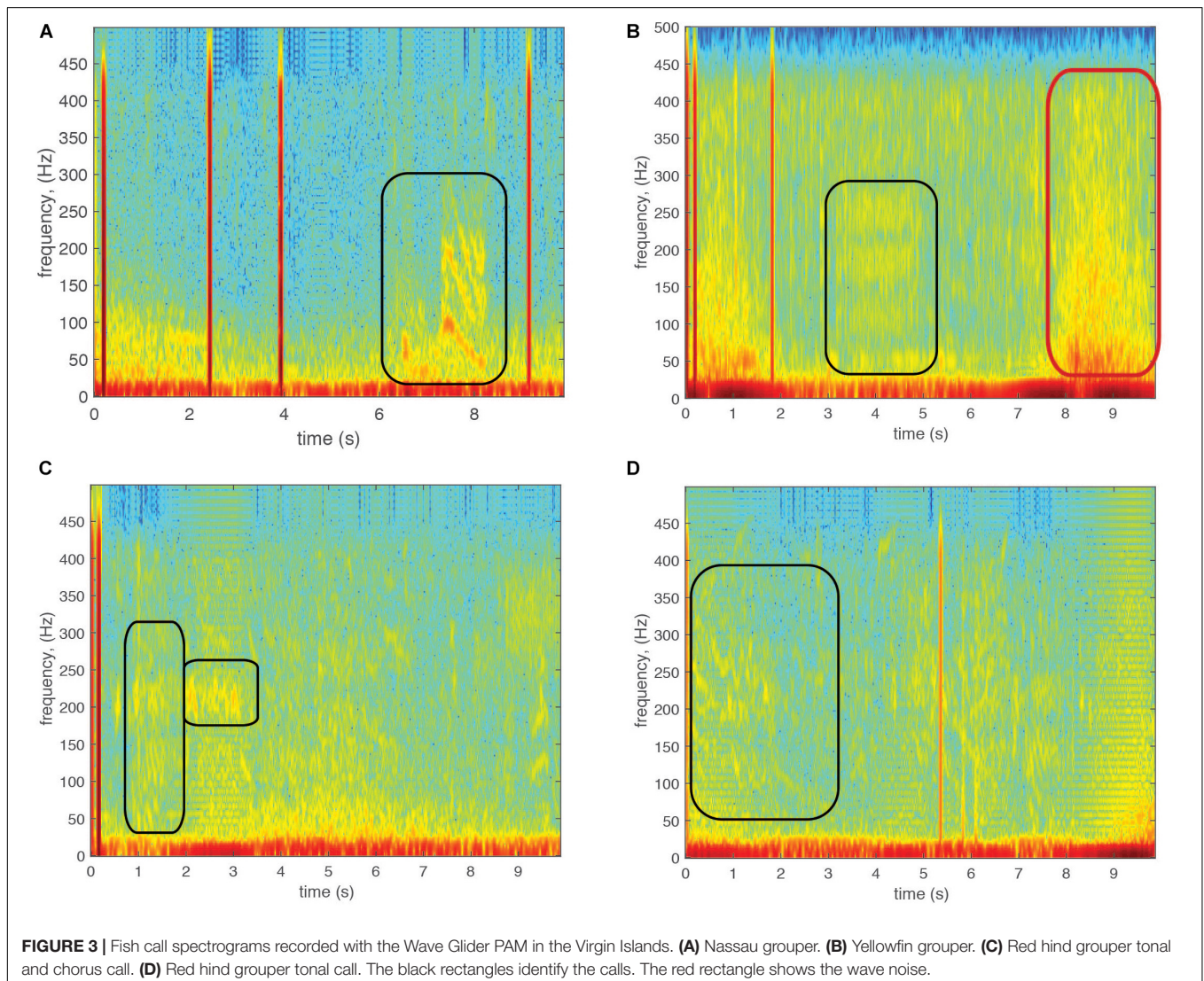
Therefore, the detection threshold is

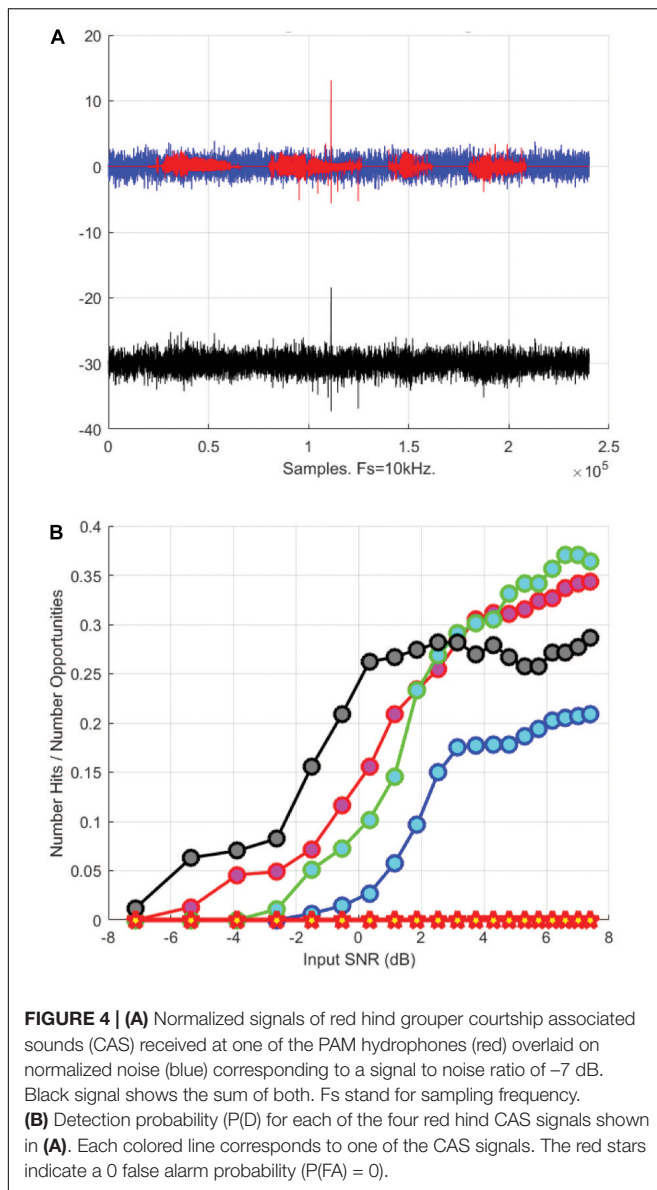
$$DT = 10 \log_{10} \left(\frac{S}{N}\right) = 5 \log_{10} \left(\frac{d}{m}\right) = -2.54 \text{ dB}. \quad (6)$$

The DT found with the above analysis was then verified with red hind grouper CAS recorded by the PAM system. We use a random selection of CAS utterances that were denoised before being superimposed on a simulated noise with the same frequency band as the CAS signal in order to generate a controllable SNR (Figure 4A). We varied the SNR of the input signal and used a matched filter kernel derived from a high SNR recorded CAS to build a detector based on local temporal

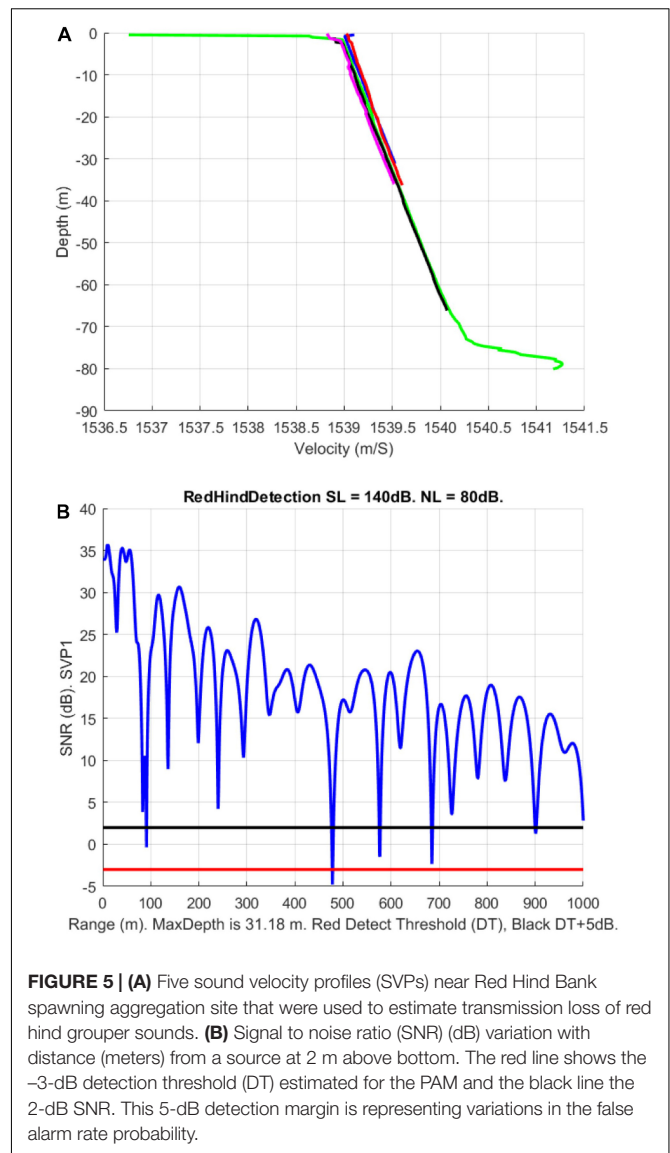
carrier frequency and local temporal modulation frequency. The detector results were analyzed and are shown in Figure 4B for four CAS detections. Using a threshold where the false alarm $P(\text{FA})$ is 0.05, the data indicates detection thresholds between -6 and 2 dB , which encompasses the value previously estimated. Therefore, the DT of the PAM was set to -3 dB for grouper CAS.

In order to estimate grouper sound detectability on the southern shelf of the U.S. Virgin Islands, we simulated the red-hind call sound propagation using the Personal Computer Shallow Water Acoustic Tool-Set (PC-SWAT) (Sammelmann, 2002), which is a user-friendly sonar model that simulates low frequency propagation and scattering in shallow water environment. The model was implemented with several sound velocity profiles characteristic of the region of interest in the winter months that ranged from 30 to about 80 m of water (Figure 5A) in the vicinity of the red hind known spawning aggregation site at Red Hind Bank (Figure 6). The virtual hydrophone was set to be at 10-m depth and the sources





(groupers) 2-m above the bottom. The bottom was assumed to be flat and made of sand. Simulations were made for source levels ranging from 150 and 110 dB re $1 \mu\text{Pa}$. Using ocean noise budget from Miller et al. (2008), noise levels of 90, 85, and 80 dB re $1 \mu\text{Pa}$ were added and the TL for each SL with either NL was simulated. A detection threshold at both -3 and $+2$ dB was used to estimate the maximum range of the grouper sounds as shown in **Figure 5B**. The results are presented in **Tables 2, 3**, which show the ranges at which the prescribed DT is met as a function of NL and SL. For depths at which the groupers FSA are located, namely between 35 and 60 m, the detection range peaked mostly at 100 (1000) m for a 140 (150) dB SL with $DT = -3$ dB. The detections ranges were less than 100-m for SLs less than 130 dB (not shown). The detection ranges were relatively variable between SVPs although they exhibit relatively small variations



between them, which suggests that detection range can vary throughout the day due to small changes in density due to surface wind cooling, diurnal cycle, depth of thermocline or tide induced upwelling and downwelling (Cherubin et al., 2011; Jossart et al., 2017).

GROUPE CALLS DETECTIONS ALGORITHMS

The PAM computer on the tow-body operates in real-time the fish acoustic detection algorithm research (FADAR) program. It is an automated identification tool for fish sounds based on acoustic feature extraction used by a machine-learning algorithm for classification (Ibrahim et al., 2018b). FADAR was designed to detect four grouper species (**Table 1**). Grouper sounds were first labeled by humans and used for training and testing of various

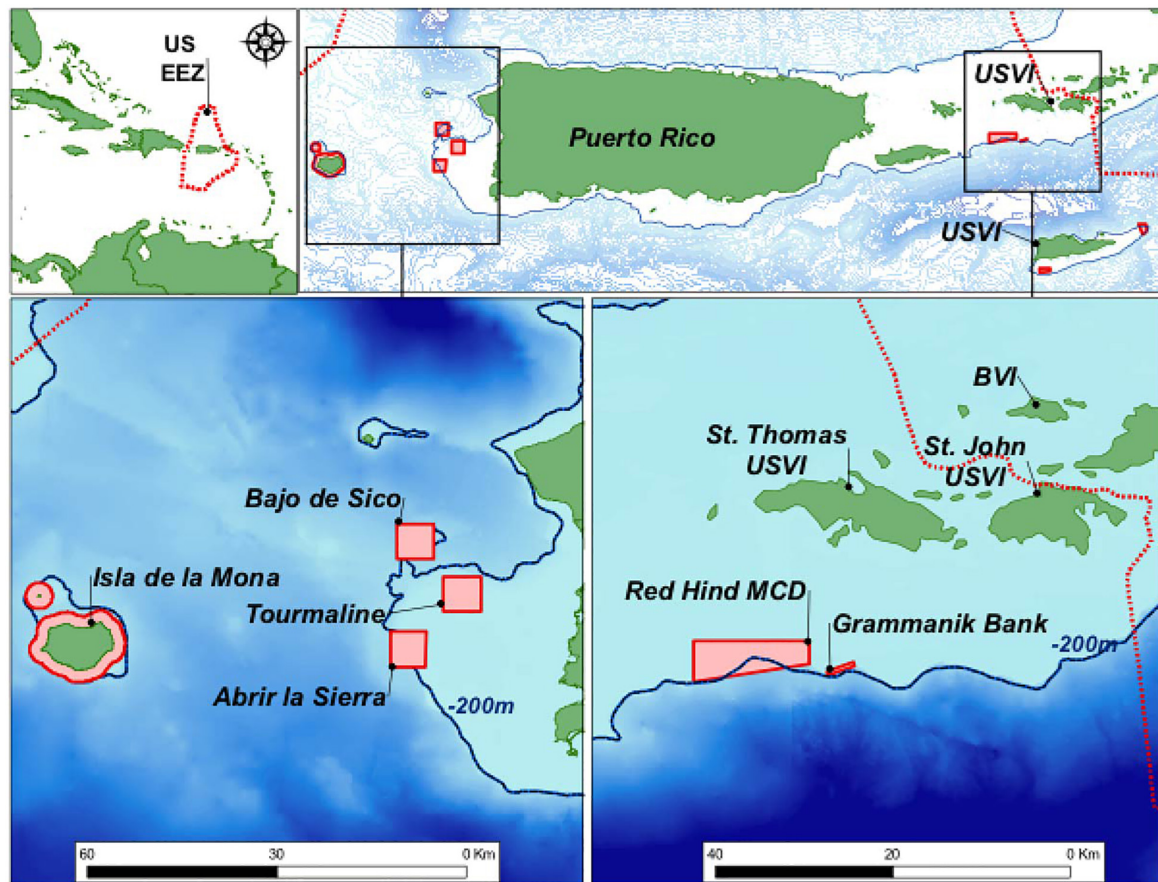


FIGURE 6 | Fish spawning aggregation (FSA) sites on the western shelf of Puerto-Rico, including Abrir La Sierra (ALS) and on the southern shelf of St. Thomas in the U.S. Virgin Islands, namely the Red Hind Marine Conservation District (MCD) where the Red Hind Bank (RHB) is located and the Grammanik Bank (GB).

feature extraction and classification methods. Grouper sound data collected from bottom moored hydrophones at known FSAs were used for training. They provided the advantage of higher SNR for fish sounds than on the SV3-WG, which improves acoustic feature extraction and algorithm positive detection rate for data collected in similar conditions. However, the algorithm showed poor performance for the SV3-WG data, which have lower SNR. Therefore, the algorithm was specifically trained with low SNR fish calls from the WG, which improved its accuracy in the field. In the feature extraction phase, a mel frequency cepstral coefficients (MFCC) feature extraction method was used. The MFCCs are short-term spectral based features, which provide a powerful representation of sound structures. They can also be improved to include the dynamic characteristics of the sound as shown in Ibrahim et al. (2018b). The overall percentage of identification reached 82.7% accuracy although the accuracy varied per species. *E. guttatus* and *M. venenosa* presented the highest accuracy, slightly higher than *E. striatus* detection accuracy. *M. bonaci* accuracy rate was the lowest of all. The algorithm was initially developed in MATLAB and was then converted into a C executable, which is embedded on the PAM computer of the tow-body package.

Although FADAR is an automated algorithm, it relies heavily on a carefully designed preprocessing and feature extraction method and it is likely to underperform in low SNR environments. In a recent study, we showed that deep learning-based detectors and classifiers such as autoencoders, convolutional neural networks (CNNs), and recurrent neural networks (RNNs), can be used as both feature extractors and classifiers (Zhang et al., 2017). While CNNs are suited for identifying spatial patterns from images, RNNs are capable of extracting discriminative patterns from time signals. However, the vanishing gradients feature prevents a standard RNN from memorizing long-term dependency of an input time sequence. Long short-term memory (LSTM) networks instead, cope with this problem by using parameters that selectively memorize or forget certain attributes of an input sequence (Hochreiter and Huber, 1997; Gers et al., 2003; Graves, 2012; Sak et al., 2014). In Ibrahim et al. (2018a), we revealed the effectiveness of using CNNs and LSTM networks for classifying fish calls and we evaluated the performance of such methods against the MFCC approach. Ibrahim et al. (2018a) showed that a data-driven feature extractor can substantially outperform a hand-crafted one, like the one used in Ibrahim et al. (2018b). The LTSM

networks achieved 93.5% accuracy, a significant improvement over the former FADAR algorithm. This latest version of FADAR will now be installed on the SV3-WG for future missions with the addition of random ensemble of stacked encoders that enable the distinction between call types within individual species as shown by Ibrahim et al. (2019).

RED HIND SPAWNING AGGREGATION DYNAMICS

Declining regional abundances of Nassau and red hind grouper due to overfishing of their spawning aggregations prompted permanent and seasonal fisheries closures in the US Virgin Islands (USVI; Olsen and LaPlace, 1979; Beets and Friedlander, 1992, 1999; Nemeth, 2005). As these species produce sounds associated with reproductive behaviors (Mann et al., 2010; Schärer et al., 2012b), PAM was used to determine the species present, the temporal patterns of reproductive activity, site usage, and fish movements at grouper FSAs within the two marine protected areas (MPAs) in the USVI: Red Hind Bank Marine Conservation District (RHB) and the Grammanik Bank (GB) (**Figure 6**). The spawning aggregation site within the RHB is located 12 km south of St. Thomas, along the shelf edge and is made of well-developed linear reef 35–45 m deep of high topographic complexity (Nemeth et al., 2007). The GB is a reef system that lays at the same depth range as RHB and is also located on the southern shelf edge of St. Thomas, about 3 km east of RHB and known for its multi-species FSA for several commercially important groupers and snapper species (Kadison et al., 2006; Nemeth et al., 2006). Yellowfin and Nassau groupers aggregate to spawn in larger numbers at GB, with peak spawning around the full moon (FM) between February and May (Nemeth et al., 2006, 2020; Rowell et al., 2015).

In the eastern Caribbean, red hind form annual spawning aggregations around the FM from December through March (Sadovy et al., 1994; Nemeth, 2005; Schärer et al., unpublished). During the weeks ahead of the spawning season, red hind migrate to spawning areas and remain aggregated up to 7 days before the FM (Nemeth, 2012a). Since the year 2000, the

TABLE 3 | Same as **Table 2** for 150 dB source level (SL).

SL 150 dB	NL 80 dB	NL 85 dB	NL 90 dB
SVP 1	1000 m	480–1000 m	90–480 m
SVP 2	1000 m	1000 m	100–1000 m
SVP 3	210–1000 m	210 m	210 m
SVP 4	1000 m	340 m	180 m
SVP 5	1000 m	1000 m	100–1000 m

RHB FSA site has been monitored by drift-fishing, setting fish traps, diving around the aggregation and recording GPS coordinates (Nemeth, 2005; Nemeth et al., 2007). The area used by red hind within the RHB during this time was calculated to be 0.24 km² in both 2000 and 2001 and 0.35 km² in 2003 and the spawning population size was estimated to be 80,000 fish (Nemeth, 2005). Changes in population density among years were assessed using visual SCUBA surveys and catch per unit effort, i.e., per trap haul (Nemeth, 2005). Most visual surveys were conducted around the FM period and encompassed their spawning peaks, which could occur up to 4 days before the FM (Beets and Friedlander, 1999; Nemeth et al., 2007). Visual surveys were used to measure both the average and peak spawning densities and revealed that the aggregation usually peaks in January and that spawning can occur from 0 to 4 days before the FM (Shapiro et al., 1993; Beets and Friedlander, 1999; Nemeth, 2005; Nemeth et al., 2007). During this study, visual surveys at RHB continued annually during January and February spawning periods (Nemeth et al. unpublished).

Red hind males produce low frequency mixed tonal-pulse sounds associated with courtship and territorial behaviors at spawning aggregations (Mann and Locascio, 2008; Mann et al., 2010; Zayas, 2019). Two main types of CAS are common during the spawning aggregation and daily sound production levels recorded at fixed stations within the FSA show trends similar to the density increase leading to spawning and sharp decrease associated to post-spawning departure described by Nemeth et al. (2007). Maximum sound production was observed around sunset (Mann et al., 2010) prior to when red hind spawn (Colin et al., 1987). Using acoustic recording data and visual surveys, Rowell et al. (2012) showed a significant correlation between red hind CAS production and fish density at a spawning site in Puerto Rico. This passive acoustic approach has been used at multiple red hind and other grouper FSA sites and allows for the continuous monitoring of the red hind spawning aggregations at both RHB and GB.

However, to date a consistent relation between spawning and sound production for the groupers listed in **Table 1** has not been established, although a correlation between reproductive behaviors that precede spawning and grouper sounds during the aggregation has (Mann et al., 2010; Schärer et al., 2012a,b, 2013, 2014; Bingham et al., 2012; Zayas, 2019). Nemeth et al. (2007) estimated that peak spawning of red hind typically occurred within 2 days of the FM at RHB, along with the highest density. At another FSA on the western Puerto-Rican shelf (**Figure 6**) Rowell et al. (2012) showed that peak density of red hind occurred

TABLE 2 | Maximum detection ranges in meters of grouper calls simulated by the Personal Computer Shallow Water Acoustic Tool-set for a source level of 140 dB for five sound velocity profiles (SVP) measured on the southern shelf of St. Thomas, US Virgin Islands.

SVPs/noise levels	NL 80 dB	NL 85 dB	NL 90 dB
SVP 1 (31.2 m)	90–480 m	90 m	90 m
SVP 2 (36.3 m)	100–1000 m	100 m	100 m
SVP 3 (80 m)	200 m	75–210 m	75–210 m
SVP 4 (66 m)	180 m	60–175 m	60 m
SVP 5 (36 m)	100 m	100 m	100 m

Detection thresholds were set at +2 dB and −3 dB respectively. The first number indicates the maximum detection range associate with +2 dB and the second one with −3 dB. When only one number is indicated, the detection range is the same for both thresholds.

8 days after the full moon (DAFM), sound levels and vocalizations peaked 7 DAFM and dropped to almost zero immediately after that, suggesting that peak spawning occurred and fish departed soon after. Fixed digital spectrogram recorders (DSG – Ocean, Loggerhead Instruments) were deployed at RHB and GB, at the yellowfin grouper main aggregation area during the 2016–2017 spawning season. They were duty cycled and recorded 20-s files every 5 min. Therefore, 4 min of ocean sounds were recorded every hour. The number of calls over 4 min was then converted to number of calls over an hour with the assumption that the call rate would remain the same over an hour. The daily CAS rate was calculated as the sum of the number of hourly calls over 24 h and is shown in **Figure 7**.

The red hind daily CAS production at RHB exhibited two peaks of similar magnitude but different duration. The first was an extended peak observed from December 30th to January 20th, which spans from 14 days before the January FM to 8 DAFM. This peak was followed by a period of lesser CAS production attesting to the presence of fish that remained at the aggregation site, and supports visual surveys at this site by Nemeth et al. (2007). The second peak, in February lasted for about 1 day on the night of February 14th, 3 DAFM. Red hind CASs were recorded at both sites and followed similar daily patterns on 08–14 February, 2017 as shown in Section “Wave Glider Survey During the Red Hind Peak Calling Week,” suggesting that another red hind FSA exists at GB yellowfin grouper main aggregation area. The CAS rate however at GB site was lower than at RHB.

WAVE GLIDER SURVEY DURING THE RED HIND PEAK CALLING WEEK

As part of a study on the effect of management on red hind stock enhancement in the U.S. Caribbean Islands, and based on the knowledge of the timing of red hind FSA at RHB,

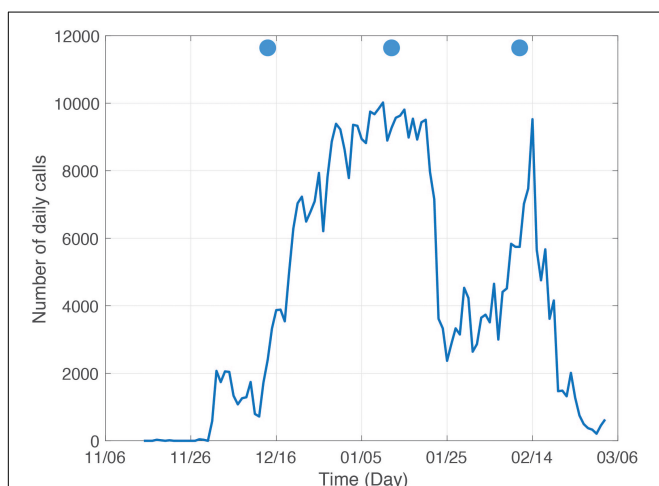


FIGURE 7 | Daily calls at Red Hind Bank fish spawning aggregation from November 2016 to March 2017. The blue disks indicate the day of full moon.

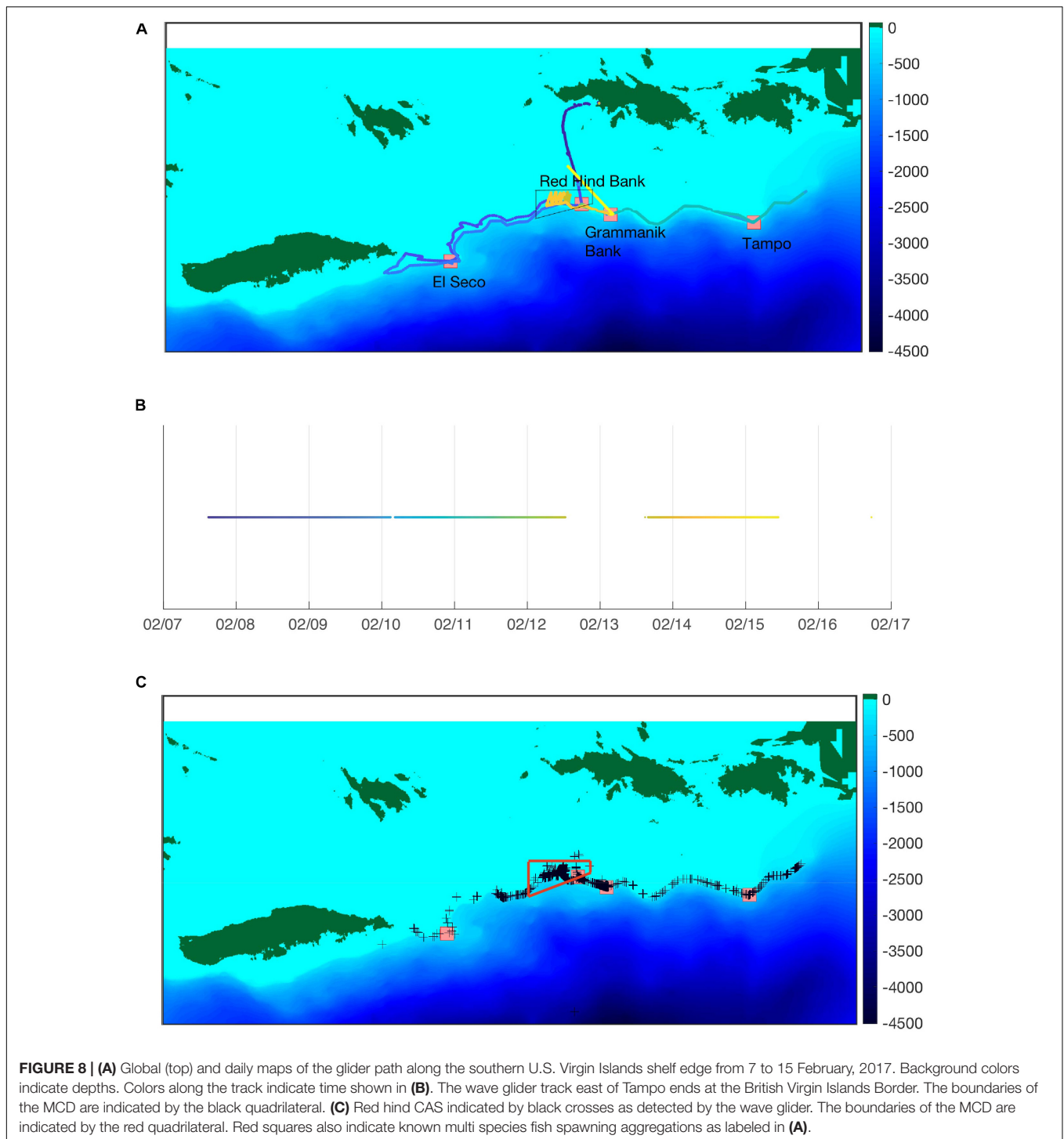
four wave glider surveys were initially scheduled over two spawning seasons. Two in January and February 2016 and 2017 respectively. Our first goal was to show the usefulness of the wave glider platform at mapping reproductive activity by detecting CAS rate patterns beyond the known FSAs. Our second goal was to identify other potential FSA sites. And our third goal was to demonstrate that our system could provide repeated CAS rate distribution patterns that could be used to assess the interannual variability of reproductive activity based on environmental conditions, such as current and water temperature. In 2016, because of delay in the readiness of the PAM system, only one survey occurred in March–April 2016. Noise associated with the tow-body cable and persistent high sea states (four to five on the Beaufort scale) contributed to poor acoustic data quality with few fishes (mostly yellow fin groupers) heard. The next survey scheduled during the week of the FM in January 2017 was canceled because of equipment failure and the second survey ultimately occurred during the week of the FM in February 2017. The survey took place between 07 and 15 February, 2017 along the southern shelf of the Island of St. Thomas, in the U.S. Virgin Islands as shown in **Figure 8**. Although environmental data were collected, the ADCP was not functional and no current data were collected, except for surface currents. The analysis of environmental data did not reveal any significant correlation between the call rate patterns and temperature, or salinity, or Chl-a, or turbidity. Temperature and salinity were relatively uniform during the survey, confirming a well-mixed environment observed during winter months (Corredor and Morell, 2001).

Mapping Reproductive Activity Based on CAS

The analysis of the PAM system detections confirmed the efficacy of our system at detecting CAS not only at known FSAs such as RHB and GB but also at many other locations beyond those two sites. As shown in **Figure 8C**, CAS were recorded all along the shelf edge. This information provides an indication of the spatial extent of the fish distribution as revealed by the wave glider survey. It confirms that red hinds are located in more areas than the points monitoring has been focused on. In addition, the real-time detection enables researchers or managers to potentially verify the fish presence and assess the potential of an FSA by sending a team of divers when possible. It could also inform of the presence of vessels in the vicinity of the CAS locations, which could help authorities and managers deal with illegal fishing activities.

An Opportunity for Repeated Surveys at Multiple Locations

Although the results presented here are limited to one survey of the southern shelf edge between Vieques and the British Virgin Islands border over 7 days, red hind CAS rates were measured at least twice at the same locations at a different time as shown for example on **Figure 9** when the wave glider surveyed the shelf edge west of RHB. The glider surveyed the same area over two consecutive days and at different times allowing the



identification of CAS rate changes over the same locations. **Figure 9** also shows that over two consecutive days, CAS were not always heard at the same locations. Changes in CAS rates at the same location or changes in CAS locations taken alone are impossible to interpret unless the call type could be identified as it can be related to territorial or courtship behaviors during encounters between fish as shown by Zayas (2019). However,

the presence of CAS alone would inform of the location of potential spawning habitat, which is a useful information in itself. Ultimately, repeating this survey over multiple years and comparing the locations of CAS detected as well as the CAS rates at the same time along with environmental data would provide valuable information on changes in reproductive behavior and spawning habitat. Such information would not be possible to

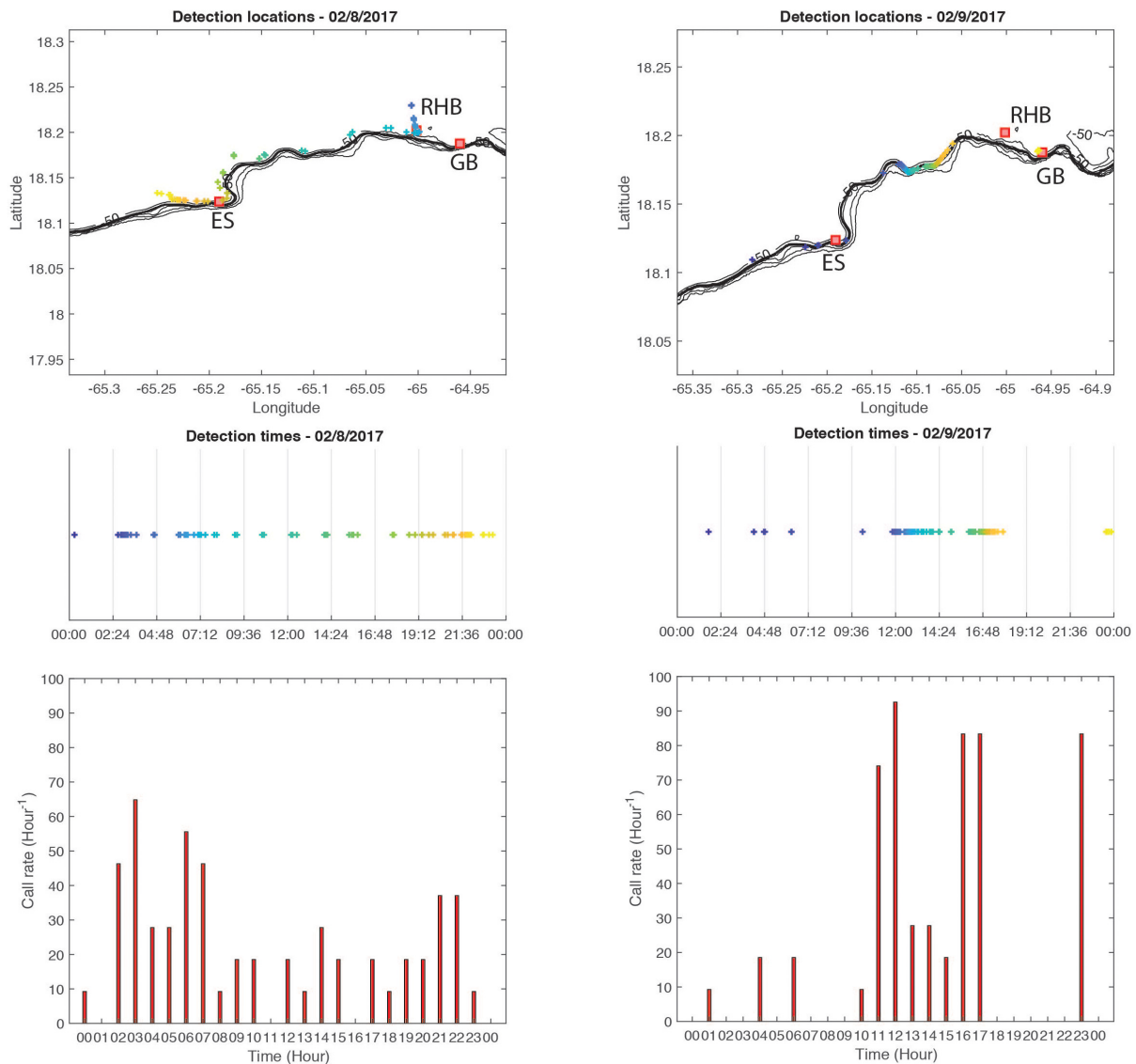


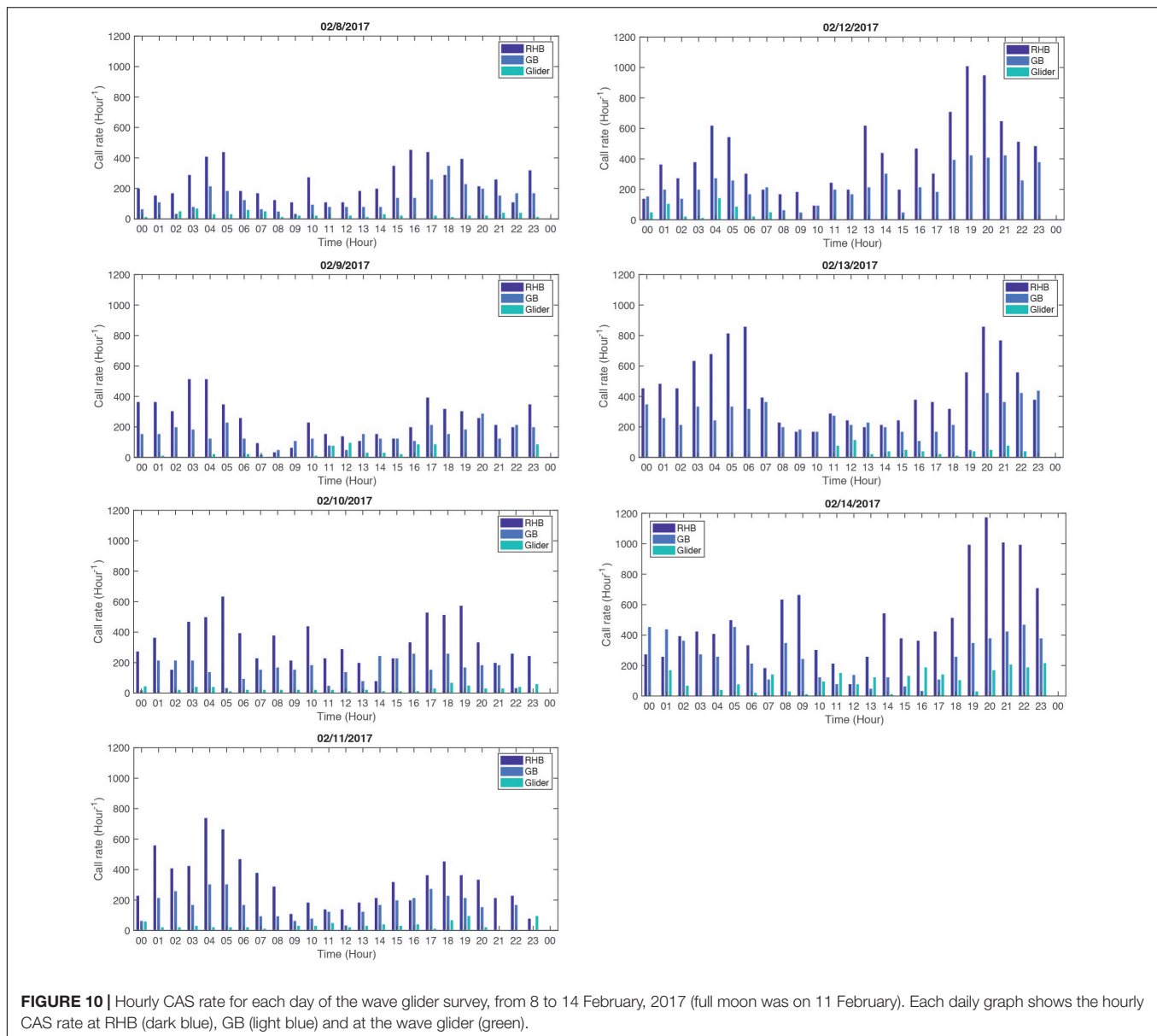
FIGURE 9 | Example of variations in red hind CAS location distribution over two consecutive surveys of the same area. Left column show detection location (**top**), local time of detection (**middle**), and hourly call rate (**bottom**) for 08 February, 2017 and right column shows the same variables for 09 February, 2017. The detection locations are colored by time shown in the middle graph.

acquire without the use of an autonomous platform and would be cost efficient in comparison to manned vessel or diver surveys.

Identifying Potential Spawning Aggregations Sites

As mentioned in Section “Red Hind Spawning Aggregation Dynamics,” DSGs were deployed at both RHB red hind FSA and GB Yellowfin FSA, and recorded red hind CAS during the week of the wave glider survey. In order to interpret the wave glider CAS rate patterns, we propose to use the CAS rate patterns observed at both RHB and GB FSAs as reference patterns associated with red hind reproductive behavior. We assume in this approach, that CAS reproductive behavior that will lead

to spawning follows the temporal patterns on an hourly basis observed at both RHB and GB FSAs during the peak calling week. Therefore, we assume that any locations surveyed by the wave glider that exhibited an equal or higher CAS rate than at RHB or GB FSAs could be indicative of a potential FSA habitat. In order to conduct the analysis, we interpolated the glider recording cycle to an hourly cycle and we accounted for the motion of the glider. Because the glider command system provides real-time speed over ground data, we estimated the averaged ground speed of the glider to be 0.5 ms^{-1} . At such speed the glider was traveling over 100 m in about 6.48 min. As shown in Section “PAM Detection Threshold and Grouper Sound Detectability,” the average distance over which grouper sound SL is less than the DT is about 100 m, meaning that



in a 100-m segment centered around the glider, the PAM could record CAS from both preceding and succeeding adjacent segments. Therefore, the CAS rate in each individual 100 m was calculated as an average over three consecutive segments and the daily rate for each segment was extrapolated from the PAM recording cycle.

The results from this analysis are shown in **Figure 10** where the resampled hourly CAS rate are shown simultaneously for RHB, GB and the WG. The daily CAS rate pattern at RHB and GB exhibits on most days a bi-modal structure with equally high CAS rates between the period 03:00–06:00 and the period 15:00–19:00 from 07 to 10 February, 2017. On 11 February, 2017, the morning CAS rate was even higher than the afternoon one. That tendency shifted to an evening CAS rate higher than in the morning as peak calling was approached on the night of 14 February, 2017. In addition, the mean hourly CAS rate doubles at both sites with

the days approaching 14 February as shown in **Table 4**. The daily variation cycles were the most in phase on 11 and 12 February and the least on 10 February. The standard deviation ratio in **Table 4** shows that the difference in CAS rate between RHB and GB increased most significantly from 8 to 9 February but remained relatively constant after that.

The CAS rates collected by the wave glider are not in phase with RHB or GB, however on some days and at certain times the wave glider CAS were higher, equal, or slightly less than at RHB and GB. For example, on 9 February, 2017, at 12:00, local time, the CAS rate was higher at the wave glider location than at GB and higher than at RHB on 11 February, 2017 at 23:00. Based on these criteria, we identified several locations that could be spawning habitat for red hind as shown in **Figure 11**. The majority of these location are within the MCD area; however, it appears that

TABLE 4 | Pattern statistics of the courtship associated sounds at RHB and GB.

Days	Mean RHB	Mean GB	R	σ^*
Day 8	234	123	0.66	1.6
Day 9	236	136	0.62	2.0
Day 10	319	139	0.15	2.0
Day 11	303	145	0.80	2.1
Day 12	398	214	0.88	2.0
Day 13	425	246	0.59	2.1
Day 14	478	242	0.56	2.0

The statistical parameters include the arithmetic mean of the daily CAS rate, the linear correlation coefficient R between daily CAS rates at RHB and GB and the normalized standard deviation σ^* , which is the ratio between the CAS rate standard deviation at RHB and at GB respectively. R is indicative of the agreement between CAS rate patterns and σ^* of the agreement in amplitude.

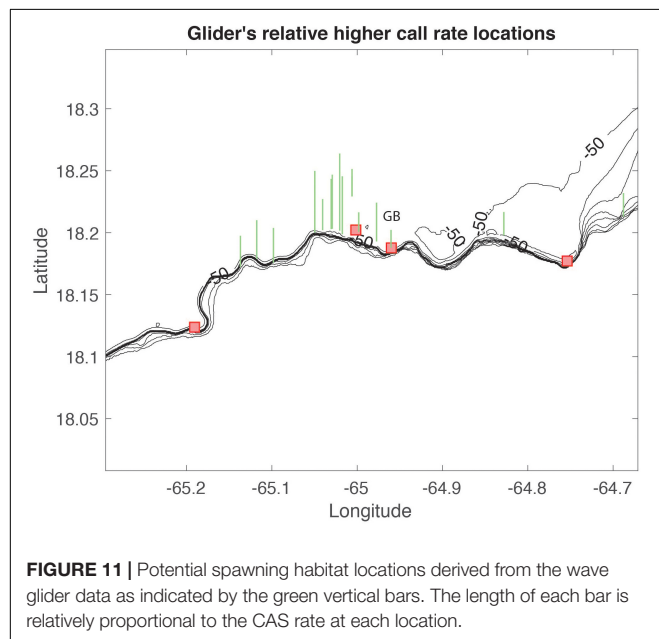


FIGURE 11 | Potential spawning habitat locations derived from the wave glider data as indicated by the green vertical bars. The length of each bar is relatively proportional to the CAS rate at each location.

some specific spawning habitat could be located just west of the MCD, near RHB main spawning site, between RHB and GB, near GB Yellowfin grouper FSA site, west of Tampo and near the BVI border.

Follow-up surveys were conducted on January 18, 2019 (3 days before full moon) by a team of technical divers using closed circuit rebreathers and underwater scooters at three potential red hind spawning aggregation sites identified by the wave glider. Two of these sites had 20 to 40 red hind on well-developed mesophotic coral reef at 40 to 50 m depth where males exhibited signs of territorial defense and coloration patterns similar to those that occur on spawning grounds (Nemeth, 2012b). These two nearby site were located on the northern boundary of the Grammanik Bank seasonal closed area and about 150–300 m northeast and 600–1100 m northwest of the GB yellowfin grouper main aggregation area (Nemeth et al., 2006, in press), which is the site identified on **Figure 11** by the wave glider near GB and revealed by our analysis.

DISCUSSION

Findings from the wave glider survey provide for the first time an extensive spatial and temporal view of the distribution of grouper spawning habitat along the extent of the southern shelf of the U.S. Virgin Islands during the main calling week in February 2017. These findings suggest that the reproductively active red hind groupers are widely distributed warranting directed diver observations at specific sites and a fine-scale analysis of the CAS types produced by grouper. Indeed, evidence is emerging that within a species, CAS types can be associated with particular behaviors (Bingham et al., 2012; Zayas, 2019). Therefore, such analysis would provide a better understanding of the reproductive strategies of grouper, migrations for spawning and the reproductive behavior dynamics prior to and after spawning. However, our observations are limited to 1 week but could be easily repeated over multiple spawning seasons with the wave glider platform. Yearly surveys could provide insightful information on the spatiotemporal dynamics of groupers reproductive behaviors in correlations with oceanographic interannual variability but also long-term changes and fishing pressure. In addition, with the recent development in fish call types detections and classification, future surveys could provide a refined call type spatial and temporal distribution, hence a habitat related call type. Such information would be conducive to understanding the role of specific habitat in reproductive behaviors.

Nonetheless, despite the lack of repeated surveys over multiple spawning events, a few realizations can be made. Grouper calling rates appeared to follow the same patterns across a wider extent of habitat compared with the known FSA sites monitored with fixed hydrophones. The corollary is that CAS rates collectively increased as the date of full moon got closer and up to 3 days after. The wave glider survey also revealed the existence of multiple potential spawning aggregation sites for red hind and their relative distribution throughout habitats on the southern shelf. It confirmed that the red hind tends to occupy habitats on the shelf rather than the shelf break (Colin et al., 1987; Beets and Friedlander, 1992; Nemeth, 2005), unlike larger grouper species (Kobara and Heyman, 2010; Nemeth et al., 2020). It also revealed the existence of habitats that support a relatively wide distribution of potential red hind aggregations west of RHB, within the MCD, near the GB yellowfin grouper spawning aggregation site, and also further east near the BVI border.

Because a red hind FSA at RHB had been visually confirmed (Nemeth, 2005; Nemeth et al., 2007), and because CAS rate patterns at GB showed similar daily patterns and similar increase in CAS rates, we used changes in the CAS rates throughout the spawning week at RHB and GB recorded with fixed hydrophone as controls to assess the changes in CAS rates collected during the WG survey. To calculate the hourly call rate from the wave glider data, we assumed that CAS could be heard no further than 100-m. As shown by the TL analysis, the detections range can be up to 1000-m due to changes in environmental conditions, meaning that fish sounds heard at any location could be located much further than 100 m away. But this is the case for both the wave glider hydrophones and the fixed hydrophones. Therefore,

the daily call rate estimate, whether in a 100-m segment or at fixed hydrophones are both equally biased by calls outside the surrounding 100-m radius area, and therefore consistent with each other.

In addition to the U.S. Caribbean wave glider surveys, we have conducted surveys in the Florida Keys National Marine Sanctuary and on the East Florida shelf at two occasions. Each mission's problems helped us streamlined the PAM system on the wave glider, by reducing instrument and system noise, by improving PAM payload efficiency and management and by improving some other aspects of our custom payload such as the echosounder screen movie streaming and recording, and lastly the ADCP data acquisition. We now consider that we have a robust system than can collect fish sound in a wide range of oceanographic conditions. However, our ocean sound detection probability can be affected by ocean state, when wave crashing noise becomes too loud. Such noise is shown on **Figure 3B**. In other instances, the fish sounds that we seek to detect, which are in the lowest frequencies, could be masked by ship noise in the same frequency band.

CONCLUSION

We presented in this study a new PAM autonomous surface platform for the study of FSAs of soniferous species. This platform can carry a payload that includes environmental sensors, a current profiler, and a PAM system that can record and classify (in real-time) at least four species-specific grouper CAS based on the automated detection algorithm by Ibrahim et al. (2018b). Although, we focused this study on red-hind grouper, other species' CAS from Nassau and yellowfin grouper were also identified. Environmental data and ocean sounds were collected from the sensors on the tow-body located 8 to 15 m below the surface and about 10 m behind the wave glider in depths ranging from 30 to 80 m and in various sea states.

In this study we demonstrated the usefulness of such platform for monitoring grouper reproductive behaviors and identifying their reproductive habitat. It enables scientists and resource managers to conduct low cost repeated surveys at any frequency in order to capture the variability of the reproductive dynamics that they intend to study. It also provides an oceanographic context to the CAS temporal patterns and spatial distribution, which can be used to assess long term anthropogenic effects including climate change and warming ocean temperatures. This platform can also be used for an initial assessment of the presence of FSAs, anywhere and constitute in itself an efficient

tool for analyzing acoustic data. One of the products of the PAM system is an analyzed acoustic dataset, which would take months to process by a human. In addition, boat traffic, currently classified as noise could be added as a product of the detection algorithm. More sophisticated algorithms will support a larger number of soniferous species including both fish, crustaceans and marine mammals that can be accurately identified, which would increase the range of passive acoustic fisheries application and ecosystem studies of the wave glider platform. However, in regards to FSA, parallel monitoring from fixed hydrophones and diver observations is paramount to the interpretation of any moving platform data.

DATA AVAILABILITY STATEMENT

The datasets generated for this study are available on request to the corresponding author.

AUTHOR CONTRIBUTIONS

LC, RN, MS-U, and RA designed the study. FD and LC designed the PAM system on the wave glider. RN participated technical diver surveys. LC, AI, MS-U, and AM conducted data analysis. LC wrote the manuscript with contributions from all co-authors.

FUNDING

The authors acknowledge the Harbor Branch Oceanographic Institute Foundation and the National Science Foundation's Virgin Islands Established Program to Stimulate Competitive Research (VI-EPSCoR, #1355437) for supporting part of this research. LC, AI, RN, and MS-U were also supported in part by NOAA Saltonstall-Kennedy grant NA15NMF4270329.

ACKNOWLEDGMENTS

The authors are grateful for the help provided on shore and in the field by University of the Virgin Islands and for letting us use the campus facilities. The authors are particularly thankful to the staff and students of the Center for Marine and Environmental Studies at University of the Virgin Islands and commercial fishers R. Silva and E. Font for assistance in transporting the WG equipment to St. Thomas. This is contribution # 203 to the University of the Virgin Islands' Center for Marine and Environmental Studies.

REFERENCES

- Amorim, M. C. P., Conti, C., Modesto, T., Gonçalves, A., and Fonseca, P. J. (2015). Agonistic sounds signal male quality in the Lusitanian toadfish. *Physiol Behav.* 149, 192–198. doi: 10.1016/j.physbeh.2015.06.002
- Bass, A. H., and Mckibben, J. R. (2003). Neural mechanisms and behaviors for acoustic communication in teleost fish. *Prog. Neurobiol.* 69, 1–26. doi: 10.1016/s0301-0082(03)00004-2
- Baumgartner, M. F., Fratanoni, D. M., Hurst, T. P., Brown, M. W., Cole, T. V., Van Parijs, S. M., et al. (2013). Real-time reporting of baleen whale passive acoustic detections from ocean gliders. *J. Acoust. Soc. Am.* 134, 1814–1823. doi: 10.1121/1.4816406
- Beets, J., and Friedlander, A. (1992). Stock analysis and management strategies for red hind, *Epinephelus guttatus*, in the U.S. Virgin Islands. *Proc. Gulf Caribb. Fish. Inst.* 42, 66–79.
- Beets, J., and Friedlander, A. (1999). Evaluation of a conservation strategy: a spawning aggregation closure for red hind, *Epinephelus guttatus*, in the US Virgin Islands. *Environ. Biol. Fish.* 55, 91–98.
- Bellingham, J. G., Streitlien, K., Overland, J., Rajah, S., Stein, P., Stannard, J., et al. (2000). An Arctic Basin observational capability

- using AUVs. *Oceanography* 13, 64–70. doi: 10.5670/oceanog.2000.36
- Bingham, B., Kraus, N., Howe, B., Freitag, L., Ball, K., Koski, P., et al. (2012). Passive and active acoustics using an autonomous wave glider. *J. Field Robot.* 29, 911–923. doi: 10.1002/rob.21424
- Brierley, A. S., Fernandes, P. G., Brandon, M. A., Armstrong, F., Millard, N. W., McPhail, S. D., et al. (2002). Antarctic krill under sea ice: elevated abundance in a narrow band just south of ice edge. *Science* 295, 1890–1892.
- Brunoldi, M., Bozzini, G., Casale, A., Corvisiero, P., Grosso, D., Magnoli, N., et al. (2016). A permanent automated real-time passive acoustic monitoring system for bottlenose dolphin conservation in the Mediterranean Sea. *PLoS One* 11:e0145362. doi: 10.1371/journal.pone.0145362
- Caldeira, R. M. A., Stegner, A., Couvelard, X., Araújo, I. B., Testor, P., and Lorenzo, A. (2014). Evolution of an oceanic anticyclone in the lee of Madeira Island: in situ and remote sensing survey. *J. Geophys. Res. Oceans* 119. doi: 10.1002/2013JC009493
- Caress, D. W., Thomas, H., Kirkwood, W. J., McEwen, R., Henthorn, R., Clague, D. A., et al. (2008). “High-resolution multibeam, sidescan and subbottom surveys using the MBARI AUV D. Allan B,” in *Marine Habitat Mapping Technology for Alaska, Alaska Sea Grant College Program*. eds H. G. Greene, and J. R. Reynolds (Fairbanks: University of Alaska), 47–69.
- Cherubin, L. M., Nemeth, R. S., and Idrisi, N. (2011). Flow and transport characteristics at an *Epinephelus guttatus* (red hind grouper) spawning aggregation site in St. Thomas (US Virgin Islands). *Ecol. Model.* 222, 3132–3148. doi: 10.1016/j.ecolmodel.2011.05.031
- Claro, R., and Lindeman, K. C. (2003). Spawning aggregation sites of snapper and grouper species (Lutjanidae and Serranidae) on the insular shelf of Cuba. *Gulf Caribb. Res.* 14, 91–106.
- Colin, P. L., Shapiro, D. Y., and Weiler, D. (1987). Aspects of the reproduction of two groupers, *Epinephelus guttatus* and *E. striatus*, in the West Indies. *Bull. Mar. Sci.* 40, 220–230.
- Corredor, J. E., and Morell, J. M. (2001). Seasonal variation of physical and biogeochemical features in eastern Caribbean surface water. *J. Geophys. Res.* 106, 4517–4525. doi: 10.1029/2000jc000291
- Cowen, R. K., Paris, C. B., and Srinivasan, A. (2006). Scaling connectivity in marine populations. *Science* 311, 522–527. doi: 10.1126/science.1122039
- Domeier, M. L., and Colin, P. L. (1997). Tropical reef fish spawning aggregations: defined and reviewed. *Bull. Mar. Sci.* 60, 698–726.
- Dowdeswell, J. A., Evans, J., Mugford, R., Griffiths, G., McPhail, S., and Millard, N. (2008). Autonomous underwater vehicles (AUVs) and investigations of the ice-ocean interface in Antarctic and Arctic waters. *J. Glaciol.* 54, 661–672. doi: 10.3189/002214308786570773
- Eklund, A. M., McClennal, D. B., and Harper, D. E. (2000). Black grouper aggregations in relation to protected areas within the Florida Keys National Marine Sanctuary. *Bull. Mar. Sci.* 66, 721–728.
- Eriksen, C. C., Osse, T. J., Light, R. D., Wen, T., Lehman, T. W., Sabinet, P. L., et al. (2001). Seaglider: a long-range autonomous underwater vehicle for oceanographic research. *IEEE J. Ocean. Eng.* 26, 424–436. doi: 10.1109/48.972073
- Erisman, B., Heyman, W., Kobara, S., Ezer, T., Pittman, S., Aburto-Oropeza, O., et al. (2017). Fish spawning aggregations: where well-placed management actions can yield big benefits for fisheries and conservation. *Fish Fish.* 18, 128–144. doi: 10.1111/faf.12132
- Fernandes, P. G., Stevenson, P., Brierley, A. S., Armstrong, F., and Simmonds, E. J. (2003). Autonomous underwater vehicles: future platforms for fisheries acoustics. *ICES J. Mar. Sci.* 60, 684–691. doi: 10.1016/s1054-3139(03)00038-9
- German, C. R., Yoerger, D. R., Jakuba, M., Shank, T. M., Langmuir, C. H., and Nakamura, K. (2008). Hydrothermal exploration with the autonomous benthic explorer. *Deep Sea Res. I* 55, 203–219. doi: 10.1016/j.dsr.2007.11.004
- Gers, F. A., Schraudolph, N. N., and Schmidhuber, J. (2003). Learning precise timing with LSTM recurrent networks. *J. Mach. Learn. Res.* 3, 115–143.
- Graham, A. G. C., Dutrieux, P., Vaughan, D. G., Nitsche, F. O., Gyllencreutz, R., Greenwood, S. L., et al. (2013). Seabed corrugations beneath an Antarctic ice shelf revealed by autonomous underwater vehicle survey: origin and implications for the history of pine island glacier. *J. Geophys. Res.* 118, 1356–1366. doi: 10.1002/jgrf.20087
- Graves, A. (2012). *Supervised Sequence Labelling with Recurrent Neural Networks*. Berlin: Springer, 385.
- Greene, C. H., Meyer-Gutbrod, E. L., McGarry, L. P., Hufnagle, L. C. Jr., Chu, D., McClatchie, S., et al. (2014). A wave glider approach to fisheries acoustics: transforming how we monitor the nation's commercial fisheries in the 21st century. *Oceanography* 27, 168–174.
- Griffiths, G. (2003). *Technologies and Applications of Autonomous Underwater Vehicles*. London: Taylor and Francis, 360.
- Heyman, W. D., and Kjerfve, B. (2008). Characterization of transient multi-species reef fish spawning aggregations at Gladden Spit, Belize. *Bull. Mar. Sci.* 83, 531–551.
- Hochreiter, S., and Huber, J. S. (1997). Long short-term memory. *Neural Comput.* 9, 1735–1780.
- Ibrahim, A. K., Zhuang, H., Chérubin, L. M., Schärer Umpierre, M. T., Ali, A. M., Nemeth, R. S., et al. (2019). Classification of red hind grouper call types using random ensemble of stacked autoencoders. *J. Acoust. Soc. Am.* 146, 2155–2162. doi: 10.1121/1.5126861
- Ibrahim, A. K., Chérubin, L. M., Zhuang, H., Schärer Umpierre, M. T., and Erdol, N. (2018a). Automatic classification of grouper species by their sounds using deep neural networks. *J. Acoust. Soc. Am.* 144:EL196. doi: 10.1121/1.5054911
- Ibrahim, A. K., Zhuang, H., Chérubin, L. M., Schärer Umpierre, M. T., Dalgleish, F., Erdol, N., et al. (2018b). An approach for automatic classification of grouper vocalizations with passive acoustic monitoring. *J. Acous. Soc. Am.* 143, 666–676. doi: 10.1121/1.5022281
- Jenkins, A., Dutrieux, P., Jacobs, S. S., McPhail, S. D., Perrett, J. R., Webb, A. T., et al. (2010). Observations beneath Pine Island Glacier in West Antarctica and implications for its retreat. *Nat. Geosci.* 3, 468–472. doi: 10.1038/ngeo0890
- Jossart, J., Nemeth, R. S., Primack, A., and Stolz, R. (2017). Extreme passive acoustic telemetry detection variability on a mesophotic coral reef, United States Virgin Islands. *Mar. Biol.* 164:180. doi: 10.1007/s00227-017-3213-y
- Kadison, E., Nemeth, R. S., Herzlieb, S., and Blondeau, J. (2006). Temporal and spatial dynamics of *Lutjanus cyanopterus* and *L. jocu* (Pisces: Lutjanidae) spawning aggregations on a multi-species spawning site in the USVI. *Rev. Biol. Trop.* 54(Suppl. 3), 69–78.
- Kobara, S., and Heyman, W. D. (2010). Sea bottom geomorphology of multi-species spawning aggregation sites in Belize. *Mar. Ecol. Prog. Ser.* 405, 231–242.
- Kobara, S., Heyman, W. D., Pittman, S. J., and Nemeth, R. S. (2013). Biogeography of transient reef fish spawning aggregations in the Caribbean: a synthesis for future research and Management. *Ocean. Mar. Biol. Ann. Rev.* 51, 281–326.
- Locascio, J. V., and Mann, D. A. (2008). Diel patterns of fish sound production in Charlotte Harbor, FL. *Trans. Am. Fish Soc.* 137, 606–615. doi: 10.1577/t06-069.1
- Luczakovich, J. J., Mann, D. A., and Rountree, R. A. (2008). Passive acoustics as a tool in fisheries science. *Trans. Am. Fish Soc.* 137, 533–541. doi: 10.1577/t06-258.1
- Luczakovich, J. J., Sprague, M. W., Johnson, S. E., and Pullinger, R. C. (1999). Delimiting spawning areas of weakfish *Cynoscion regalis* (Family Sciaenidae) in Pamlico Sound, North Carolina using passive acoustic surveys. *Bioacoustics* 10, 143–160. doi: 10.1080/09524622.1999.9753427
- Manley, J., Willcox, S., and Westwood, R. (2009). The Wave Glider: an energy harvesting unmanned surface vehicle. *Mar. Technol. Rep.* 27–31.
- Mann, D. A., and Locascio, J. V. (2008). Acoustic communication in fishes. *Bioacoustics* 17, 43–45. doi: 10.1080/09524622.2008.9753758
- Mann, D. A., Locascio, J. V., Coleman, F. C., and Koenig, C. C. (2009). Goliath grouper *Epinephelus itajara* sound production and movement patterns on aggregation sites. *Endang. Spec. Res.* 7, 229–236. doi: 10.3354/esr010109
- Mann, D. A., Locascio, J. V., Scharer, M. T., Nemeth, M. I., and Appeldoorn, R. S. (2010). Sound production by red hind (*Epinephelus guttatus*) in spatially segregated spawning aggregations. *Aquat. Biol.* 10, 149–154. doi: 10.3354/ab00272
- Mann, D. A., and Lobel, P. S. (1995). Passive acoustic detection of sounds produced by the damselfish, *Dascyllus albisella* (Pomacentridae). *Bioacoustics* 6, 199–213. doi: 10.1080/09524622.1995.9753290
- Marques, T. A., Thomas, L., Martin, S. W., Mellinger, D. K., Ward, J. A., Moretti, D. J., et al. (2013). Estimating animal population density using passive acoustics. *Biol. Rev.* 88, 287–309. doi: 10.1111/brv.12001

- Matsumoto, H., Haxel, J. H., Dziak, R. P., Bohnenstiehl, D. R., and Embley, R. W. (2011). Mapping the sound field of an erupting submarine volcano using an acoustic glider. *J. Acoust. Soc. Am.* 129, EL94–EL99. doi: 10.1121/1.3547720
- Miller, J. H., Nystuen, J. A., and Bradley, D. L. (2008). Ocean noise budgets. *Bioacoustics* 17, 133–136. doi: 10.1021/acs.accounts.5b00282
- Montie, E. W., Kehrer, C., Yost, J., Brenkert, K., O'Donnell, T., and Denson, M. R. (2016). Long-term monitoring of captive red drum *Sciaenops ocellatus* reveals that calling incidence and structure correlate with egg deposition. *J. Fish. Biol.* 88, 1776–1795. doi: 10.1111/jfb.12938
- Montie, E. W., Hoover, M., Kehrer, C., Yost, J., Brenkert, K., O'Donnell, T., et al. (2017). Acoustic monitoring indicates a correlation between calling and spawning in captive spotted seatrout (*Cynoscion nebulosus*). *PeerJ* 5:e2944. doi: 10.7717/peerj.2944
- Mumby, P. J., Dahlgren, C. P., Harborne, A. R., Kappe, C. V., Micheli, F., Brumbaugh, D. R., et al. (2006). Fishing, trophic cascades, and the process of grazing on coral reefs. *Science* 311, 98–101. doi: 10.1126/science.1121129
- Myrberg, A. A. Jr., and Lugli, M. (2006). “Reproductive behavior and acoustical interactions,” in *Communication in Fishes*, Vol. I, eds F. Ladich, S. P. Colin, P. Moller, and B. G. Kapoor (Enfield: Science Publishers), 149–1176.
- Nelson, M. D., Koenig, C. C., Coleman, F. C., and Mann, D. A. (2011). Sound production of red grouper *Epinephelus morio* on the West Florida Shelf. *Aquat. Biol.* 12, 97–108. doi: 10.1111/jfb.12500
- Nemeth, R. S. (2005). Population characteristics of a recovering US Virgin Islands red hind spawning aggregation following protection. *Mar. Ecol. Prog. Ser.* 286, 81–97. doi: 10.3354/meps286081
- Nemeth, R. S. (2009). “Chapter 4: Dynamics of reef fish and decapod crustacean spawning aggregations: underlying mechanisms, habitat linkages and trophic interactions,” in *Ecological Connectivity Among Tropical Coastal Ecosystems*, ed. I. Nagelkerken (Berlin: Springer), 73–134. doi: 10.1007/978-90-481-2406-0_4
- Nemeth, R. S. (2012a). “Ecosystem aspects of spawning aggregations. Chapter 2,” in *Reef Fish Spawning Aggregations: Biology, Research and Management*, eds Y. Sadovy de Mitcheson, and P. Colin (Berlin: Springer), 21–56.
- Nemeth, R. S. (2012b). “Species Case studies: red hind – *Epinephelus guttatus*. Chapter 12.3,” in *Reef Fish Spawning Aggregations: Biology, Research and Management*, eds Y. Sadovy, and P. Colin (Berlin: Springer), 412–417.
- Nemeth, R. S., Blondeau, J., Herzlieb, S., and Kadison, E. (2007). Spatial and temporal patterns of movement and migration at spawning aggregations of red hind, *Epinephelus guttatus*, in the U.S. Virgin Islands. *Environ. Biol. Fish.* 78, 365–381. doi: 10.1007/s10641-006-9161-x
- Nemeth, R. S., Kadison, E., Blondeau, J., and Brown Peterson, N. J. (2020). Reproductive biology and behavior associated with a spawning aggregation of the yellowfin grouper *Mycteroperca venenosa* in the US Virgin Islands. *Bull. Mar. Sci.* 96. doi: 10.5543/bms.2019.0028
- Nemeth, R. S., Kadison, E., Herzlieb, S., Blondeau, J., and Whiteman, E. (2006). “Status of a yellowfin grouper (*Mycteroperca venenosa*) spawning aggregation in the US Virgin Islands with notes on other species,” in *Proceedings of the 57th Gulf Caribbean Fish Institute*, Vol. 57, (St. Petersburg, FL), 543–558.
- Nicholls, K. W., Abrahamsen, E. P., Buck, J. J. H., Dodd, P. A., Goldblatt, C., Griffiths, G., et al. (2006). Measurements beneath an Antarctic ice shelf using an autonomous underwater vehicle. *Geophys. Res. Lett.* 33:L08612.
- Niewiadomska, K., Claustre, H., Prieur, L., and d'Ortenzio, F. (2008). Submesoscale physical- biogeochemical coupling across the Ligurian current (northwestern Mediterranean) using a bio-optical glider. *Limnol. Oceanogr.* 53, 2210–2225. doi: 10.4319/lo.2008.53.5_part_2.2210
- Ohman, M. D., Rudnick, D. L., Chekalyuk, A., Davis, R. E., Feely, R. A., Kahru, M., et al. (2013). Autonomous ocean measurements in the California current ecosystem. *Oceanography* 26, 18–25. doi: 10.1371/journal.pone.0101268
- Olsen, D. A., and LaPlace, J. A. (1979). A study of a Virgin Islands grouper fishery based on a breeding aggregation. *Gulf Caribb. Fish. Inst. Proc.* 31, 130–144.
- Rowell, T., Nemeth, R., Schärer, M., and Appeldoorn, R. (2015). Fish sound production and acoustic telemetry reveal behaviors and spatial patterns associated with spawning aggregations of two Caribbean groupers. *Mar. Ecol. Prog. Ser.* 518, 239–254. doi: 10.3354/meps11060
- Rowell, T. J., Appeldoorn, R. S., Rivera, J. A., Mann, D. A., Kellison, T., Nemeth, M., et al. (2011). Use of passive acoustics to map grouper spawning aggregations, with emphasis on red hind, *Epinephelus guttatus*, off western Puerto Rico. *Proc. Gulf. Caribb. Fish. Inst.* 63, 139–142.
- Rowell, T. J., Schärer, M. T., and Appeldoorn, R. S. (2018). Description of a new sound produced by nassau grouper at spawning aggregation sites. *Gulf Caribb. Res.* 29, GCFI22–GCFI26. doi: 10.18785/gcr.2901.12
- Rowell, T. J., Schärer, M. T., Appeldoorn, R. S., Nemeth, M. I., Mann, D. A., and Rivera, J. A. (2012). Sound production as an indicator of red hind density at a spawning aggregation. *Mar. Ecol. Prog. Ser.* 462, 241–250. doi: 10.3354/meps09839
- Rudnick, D. L., Davis, R. E., Eriksen, C. C., Fratantoni, D. M., and Perry, M. J. (2004). Underwater gliders for ocean research. *Mar. Technol. Soc. J.* 38, 73–84.
- Sadovy, Y. (1997). The case of the disappearing grouper: *Epinephelus striatus* (Pisces: Serranidae). *J. Fish Biol.* 46, 961–976.
- Sadovy, Y., Rosario, A., and Roman, A. (1994). Reproduction in an aggregating grouper, the red hind, *Epinephelus guttatus*. *Environ. Biol. Fish.* 41, 269–286. doi: 10.1111/jfb.12555
- Sadovy De Mitcheson, Y., Cornish, A., Domeier, M., Colin, P., Russel, M., and Lindeman, K. C. (2008). A global baseline for spawning aggregations of reef fishes. *Conserv. Biol.* 22, 1233–1244. doi: 10.1111/j.1523-1739.2008.01020.x
- Sak, H., Senior, A., and Beaufays, F. (2014). “Long short-term memory recurrent neural network architectures for large scale acoustic modeling,” in *Proceedings of the 15th Annual Conference of the International Speech Communication*, Singapore, 1–5.
- Sala, E., Ballesteros, E., and Starr, R. M. (2001). Rapid decline of nassau grouper spawning aggregations in Belize: fishery management and conservation needs. *Fisheries* 26, 23–30. doi: 10.1577/1548-8446(2001)026<0023:rdongs>2.0.co;2
- Sammelmann, G. S. (2002). *Personal Computer Shallow Water Acoustic Tool-Set (PC SWAT) 7.0: Low Frequency Propagation and Scattering. Technical Report*. Panama: FL: Naval Surface Warfare Center.
- Schärer, M. T., Nemeth, M. I., Mann, D. A., Locascio, J. V., Appeldoorn, R. S., and Rowell, T. J. (2012a). Sound production and reproductive behavior of yellowfin grouper (*Mycteroperca venenosa*) (Serranidae), at a spawning aggregation. *Copeia* 1, 136–145.
- Schärer, M. T., Rowell, T. J., Nemeth, M. I., and Appeldoorn, R. S. (2012b). Sound production associated with reproductive behavior of Nassau grouper *Epinephelus striatus* at spawning aggregations. *Endanger. Spec. Res.* 19, 29–38.
- Schärer, M. T., Nemeth, M. I., Rowell, T. J., and Appeldoorn, R. S. (2014). Sounds associated with the re-productive behavior of the black grouper (*Mycteroperca bonaci*). *Mar. Biol.* 161, 141–147. doi: 10.1007/s00227-013-2324-3
- Schärer, M. T., Rowell, T. J., Nemeth, M. I., and Appeldoorn, R. S. (2013). Sound production associated with reproductive behavior of Nassau grouper *Epinephelus striatus* at spawning aggregations. *Endanger. Species Res.* 19, 29–38. doi: 10.3354/esr00457
- Shapiro, D. Y., Sadovy, Y., and McGehee, M. A. (1993). Size, composition, and spatial structure of the annual spawning aggregation of the red hind. *Epinephelus guttatus* (Pisces: Serranidae). *Copeia* 1993, 399–406. doi: 10.2307/1447138
- Smith, C. L. (1972). A spawning aggregation of Nassau grouper, *Epinephelus striatus* (Bleeker). *Trans. Am. Fish. Soc.* 101, 225–261. doi: 10.1111/j.1523-1739.2008.01020.x
- Urick, R. (1983). *Principles of Underwater Sound*, Vol. 1. New York, NY: McGraw-Hill.
- Wadhams, P., Wilkinson, J. P., and McPhail, S. D. (2006). A new view of the underside of Arctic sea ice. *Geophys. Res. Lett.* 33:L04501.
- Wall, C. C., Lembke, C., and Mann, D. A. (2012). Shelf-scale mapping of sound production by fishes in the eastern Gulf of Mexico using autonomous glider technology. *Mar. Ecol. Prog. Ser.* 449, 55–64. doi: 10.3354/meps09549
- Wall, C. C., Mann, D. A., Lembke, C., Taylor, C., He, R., and Kellison, T. (2017). Mapping the soundscape off the Southeastern USA by using passive acoustic glider technology. *Mar. Coast. Fish.* 9, 23–37. doi: 10.1080/19425120.2016.1255685
- Wall, C. C., Simard, P., Lindemuth, M., Lembke, C., Naar, D. F., Hu, C., et al. (2014). Temporal and spatial mapping of Red Grouper *Epinephelus morio* sound production. *J. Fish Biol.* 85, 1469–1487. doi: 10.1111/jfb.12500

- Walters, S., Lowerre-Barbieri, S., Bickford, J., and Mann, D. (2009). Using a passive acoustic survey to identify spotted seatrout spawning sites and associated habitat in Tampa Bay, Florida. *Trans. Am. Fish Soc.* 138, 88–98. doi: 10.1577/t07-106.1
- Willcox, S., Manley, J., and Wiggins, S. (2009). The Wave Glider, an energy harvesting autonomous surface vessel. *Sea Technol.* 2009, 29–31.
- Yoerger, D. R., Bradley, A. M., Jakuba, M., German, C. R., Shank, T., and Tivey, M. (2007). Autonomous and remotely operated vehicle technology for hydrothermal vent discovery, exploration, and sampling. *Oceanography* 20, 152–161. doi: 10.5670/oceanog.2007.89
- Yoerger, D. R., Bradley, A. M., Walden, B. B., Singh, H., and Bachmayer, R. (1998). Surveying a subsea lava flow using the Autonomous Benthic Explorer (ABE). *Int. J. Syst. Sci.* 10, 1031–1044. doi: 10.1080/00207729808929596
- Zayas, C. (2019). *Red hind Epinephelus guttatus Vocal Repertoire Characterization, Temporal Patterns and Call Detection With Micro Accelerometers*. MS Thesis. University of Puerto Rico: Mayagüez, PR, 68.
- Zhang, C., Yu, C., and Hansen, J. H. L. (2017). An Investigation of deep-learning frameworks for speaker verification anti-spoofing. *IEEE J. Select. Topics Sign. Proc.* 11, 684–694.
- Conflict of Interest:** MS-U was employed by company HJR Reefscaping. AM was employed by company EPS Corporation.
- The remaining authors declare that the research was conducted in the absence of any commercial or financial relationships that could be construed as a potential conflict of interest.
- Copyright © 2020 Chérubin, Dalglish, Ibrahim, Schärer-Umpierre, Nemeth, Matthews and Appeldoorn. This is an open-access article distributed under the terms of the Creative Commons Attribution License (CC BY). The use, distribution or reproduction in other forums is permitted, provided the original author(s) and the copyright owner(s) are credited and that the original publication in this journal is cited, in accordance with accepted academic practice. No use, distribution or reproduction is permitted which does not comply with these terms.



Using Ship-Deployed High-Endurance Unmanned Aerial Vehicles for the Study of Ocean Surface and Atmospheric Boundary Layer Processes

Christopher J. Zappa^{1*}, Scott M. Brown¹, Nathan J. M. Laxague¹, Tejendra Dhakal¹, Ryan A. Harris¹, Aaron M. Farber² and Ajit Subramaniam¹

¹ Lamont-Doherty Earth Observatory, Columbia University, Palisades, NY, United States, ² L3 Latitude, Tucson, AZ, United States

OPEN ACCESS

Edited by:

Leonard Pace,
Schmidt Ocean Institute,
United States

Reviewed by:

Zhongping Lee,
University of Massachusetts Boston,
United States
João Tasso Sousa,
University of Porto, Portugal

*Correspondence:

Christopher J. Zappa
zappa@ldeo.columbia.edu

Specialty section:

This article was submitted to
Ocean Observation,
a section of the journal
Frontiers in Marine Science

Received: 15 December 2018

Accepted: 03 December 2019

Published: 21 January 2020

Citation:

Zappa CJ, Brown SM,
Laxague NJM, Dhakal T, Harris RA,
Farber AM and Subramaniam A
(2020) Using Ship-Deployed
High-Endurance Unmanned Aerial
Vehicles for the Study of Ocean
Surface and Atmospheric Boundary
Layer Processes.
Front. Mar. Sci. 6:777.
doi: 10.3389/fmars.2019.00777

Unmanned aerial vehicles (UAVs) are proving to be an important modern sensing platform that supplement the sensing capabilities from platforms such as satellites, aircraft, research vessels, moorings, and gliders. UAVs, like satellites and aircraft can provide a synoptic view of a relatively large area. However, the coarse resolution provided by satellites and the operational limitations of manned aircraft has motivated the development of unmanned systems. UAVs offer unparalleled flexibility of tasking; for example, low altitude flight and slow airspeed allow for the characterization of a wide variety of geophysical phenomena at the ocean surface and in the marine atmospheric boundary layer. Here, we present the development of cutting-edge payload instrumentation for UAVs that provides a new capability for ship-deployed operations to capture a unique, high resolution spatial and temporal variability of the changing air-sea interaction processes than was previously possible. The modular design of the base payload means that new instruments can be incorporated into new research proposals that may include new instruments for expanded use of the payloads as a long-term research facility. Additionally, we implement a novel capability for vertical take-off and landing (VTOL) from research vessels. This VTOL capability is safer and requires less logistical support than previous ship-deployed systems. The payloads developed include thermal infrared, visible broadband and hyperspectral, and near-infrared hyperspectral high-resolution imaging. Additional capabilities include quantification of the longwave and shortwave hemispheric radiation budget (up- and down-welling) as well as direct air-sea turbulent fluxes. Finally, a UAV-deployed dropsonde-microbuoy was developed in order to profile the temperature, pressure and humidity of the atmosphere and the temperature and salinity of the near-surface ocean. These technological advancements provide the next generation of instrumentation capability for UAVs. When deployed from research vessels, UAVs will provide a transformational science prism unequaled using 1-D data snapshots from ships or moorings alone.

Keywords: unmanned aerial vehicle (UAV), unmanned aircraft system (UAS), infrared (IR) imaging, air-sea interaction, turbulent fluxes of momentum heat and water vapor, longwave and shortwave irradiance, vertical take-off and landing (VTOL)

INTRODUCTION

The unmanned aerial vehicle (UAV) is proving to be an important modern sensing platform (Elston et al., 2014). It supplements the sensing capabilities from traditional platforms such as satellites, aircraft, research vessels, moorings, and gliders. In the single previous decade, there have been significant reductions in volume, weight, and power requirements from commercial, high-accuracy and high-sensitivity ocean and atmospheric sensors used on traditional platforms. Additionally, the resources required to operate and maintain UAVs represent significantly lower impact than those of traditional platforms. These reductions in high-accuracy sensor operating requirements and of the resources required to maintain and operate UAVs (relative to larger platforms) are tipping the scale toward ubiquitous UAV operations (Johnston, 2019).

Some clear advantages of the UAV platform are lower manufacturing and maintenance costs; fewer personnel and less environmental impact; lower fuel and power requirements while preserving operational longevity. UAVs, like satellites and aircraft, can provide a synoptic view of a relatively large area, but can additionally provide several orders of magnitude increase in spatio-temporal resolution. While they are like some aircraft that are able to fly under cloud decks to observe the ocean surface in regions that are perennially cloud covered such as the Arctic (Cassano et al., 2010; Williams et al., 2016) or the Inter Tropical Convergence Zone (Chen et al., 2015), they can additionally fly much slower to provide unprecedented ground resolutions as fine as 1 cm. Further, UAVs can be tightly coordinated with other, non-UAV field ops in ways that an aircraft mission staged from a far-off airfield cannot. UAVs can be flown in conditions that may be deemed too dangerous for manned flight, such as over areas with unsafe terrain like melting sea ice. More extreme uses include low altitude flights of UAVs launched from manned aircraft into hurricanes (Cione et al., 2016, 2019), and flight near and through dangerous thunderstorms and tornadoes (Elston et al., 2011). Additionally, the simultaneous deployment of dual or more UAVs have the potential to provide unprecedented spatio-temporal mapping with multiple types of sensors (atmospheric, imaging, radiation, etc.). Some challenges of the UAV platform are the size, weight, and power limitations for instrument hardware, along with flight endurance, and the ability to obtain flight permissions for UAV operations in areas of scientific interest. However, there are some observations afforded only to the UAV platform that are not possible from any other platform.

Satellites are often brought to bear in order to study spatially varying physical characteristics of the Earth's oceans. However, they are limited by their spatial resolution of order 0.01 km to 1 km and by interference due to clouds. Some parts of the world are almost never "seen" by satellites during certain times of the year due to pervasive cloud cover. Many land and ocean processes occur at scales smaller than 1 km and therefore are not resolved by satellites. Specifically, coastal regions, lakes, rivers, coral reefs are examples of locations are not well observed by the coarse resolution satellite data. In addition,

effects of anthropogenic impact of coastal urban areas are also not amenable to observation by coarse satellite data.

Given that UAVs are able to be deployed from research vessels, there is a fantastic opportunity to expand the physical descriptions of ocean surface processes that would come from 1-dimensional data snapshots from ships or moorings alone. Applications for UAVs in air-sea interaction span from the polar regions to study polynya (Cassano et al., 2010; Knuth and Cassano, 2014) and the marginal ice zones, to the tropics to study ocean waves, turbulent air-sea fluxes and mixed-layer dynamics (Reineman et al., 2013, 2016). Furthermore, unmanned aircraft have been used to make measurements of the vertical profiles of atmospheric aerosols in polar regions (Bates et al., 2013). UAVs are also useful platforms for rapid assessment of phytoplankton blooms in oceans, bays and estuaries using hyperspectral measurements (Shang et al., 2017), as well as imaging spectroscopy of quantitative biochemical and biophysical characteristics of terrestrial environments (Lucieer et al., 2014). Exploration of upper ocean physical processes is necessary to advance our understanding of the fluxes into and across the ocean mixed layer. These dynamics in the upper ocean boundary layer (OBL) are critical to the coupling between the atmosphere, the wave surface and the deeper ocean, linking the atmosphere to the deep ocean and determining the vertical profiles of essentially all physical, chemical, biological, optical and acoustic variables in the upper ocean.

Regional variability of ocean surface thermal properties is known to be important to air-sea fluxes; by using UAV-equipped imaging systems, one is able to observe small-scale structures (on the scale of kilometers or smaller) within the IR imagery that may drive or enhance exchange under low wind speed conditions (Zappa and Jessup, 2004, 2005; Farrar et al., 2007). The diurnal surface heat budget, air-sea fluxes, upper-ocean heating/cooling, and mixed-layer processes have been studied through traditional ship-based means as coupled boundary layer systems in low winds (Zappa and Jessup, 2005; Edson et al., 2007; Farrar et al., 2007) and in the context of the Madden-Julian Oscillation (Moum et al., 2014; Chen et al., 2015). Furthermore, UAV-based observations offer the ability to study phenomena which are small enough in scale (hundreds of meters and smaller) to be "sub-pixel" of satellite ocean color and SST products. These types of measurements will transform our understanding of biogenic slicks and their impact on surface ocean physics, chemistry, and biology.

For the work that follows, our specific charge was to improve overall UAV air-sea and atmosphere-ice-ocean observational capabilities, particularly by increasing the spatio-temporal resolution of physical and biogeochemical measurements. The final design specifications clearly demonstrate the unprecedented spatial (10 cm sampling at 1000 m altitude) and temporal (10–100 Hz sampling) resolution attained for these UAV payloads. Here, we describe the development and application of sensor payloads for flight on ship-deployed UAVs. First, we will present the observational campaigns. Next, we will describe the UAVs and the technical details of the instrument payloads (see **Table 1**). The nominal payloads are: (a) VIS-TIR/Hi-TIR: Thermal Infrared and Visible Imaging with LiDAR,

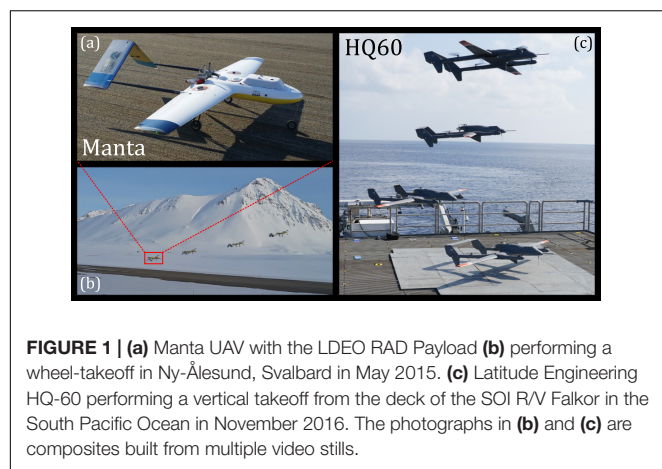
TABLE 1 | Description of each instrument payload, including sensor components, measurement outputs and performance specifications.

Payload	Sensor	Raw measurement and specification	What it provides
BASE	Novatel SPAN OEM719 + STIM300 IMU	GPS Timing, Position, Angular Rotations and Rates at 100 Hz, MEMS IMU angle accuracy of 0.01°. 100 Hz post-processed horizontal position accuracy of ± 1 cm RMS and vertical position accuracy of ± 2 cm RMS.	Mapping capabilities, orthorectification of all imagery and MET data streams
BASE	Heitronics CT09 IR Pyrometer (Up- and Down-Looking)	8–14 μm longwave radiation; 3° FOV surface and sky brightness temperatures (lab calibrated to 0.1°C accuracy) at 10 Hz	Surface and sky temp, SST, and IST mapping
HI-TIR	Sofradir-EC MITIE	7.7–9.3 μm longwave IR imagery (640 by 512) up to 100 Hz, Stirling-cooled with NETD of 0.02°C.	Skin SST and IST mapping
VIS-TIR	Sofradir-EC Atom1024 LWIR Microbolometer	8–14 μm longwave IR high-resolution imagery (1024 by 768) up to 30 Hz, with NETD of 0.05°C.	Variability of brightness temperature, SST, and IST mapping.
VIS-TIR	Imperx Bobcat 6MP Visible Camera	Monochrome; 400–800 nm visible high resolution swath up to 15 Hz (2756 \times 2208 pixels)	Surface visible imagery mapping
VIS-TIR	IO Industries 4 MP model Flare 4M180-CL Visible Camera	Color; 400–800 nm visible high resolution swath up to 30 Hz (2048 \times 2048 pixels)	Surface visible imagery mapping
VIS-TIR	ULS LiDAR	Distance ranging up to 500 m (± 0.02 m), with sampling up to 200 Hz and a FOV of 3 milliradians	Surface topography and ocean waves
RAD	Imperx Bobcat 5MP Visible Camera	400–800 nm visible high resolution swath up to 15 Hz	Surface visible imagery mapping
RAD	Hukseflux SR03 Pyranometer (Up- and Down-Looking)	285–3000 nm shortwave hemispheric solar irradiance in W m^{-2} at 1-s response time	Net solar irradiance and albedo
RAD	Hukseflux IR02 Pyrgeometer (Up- and Down-Looking)	4.5–40 μm hemispheric longwave irradiance in W m^{-2} at fast 1 s response time	Net longwave/IR irradiance
HYP-VNIR	Headwall Micro-HyperSpec VNIR A-Series Imaging Spectrometer	Surface-emitted radiance (400–1000 nm) with horizontal 32° field-of-view (12 mm), 10.5 mm slit length, 1.86 nm spectral resolution (601 bands), 1004 spatial pixels	Surface visible imagery, bio, and biochemical mapping
HYP-VNIR	OceanOptics USB2000 Irradiance Spectrometer (Up-Looking)	Sky-emitted irradiance (350–1000 nm)	Sky irradiance spectrogram
HYP-VNIR	OceanOptics OceanFX Radiance Spectrometer (Up-Looking)	Sky-emitted radiance (350–1000 nm)	Sky radiance spectrogram for surface-reflected sky radiance correction
HYP-VNIR	OceanOptics OceanFX Radiance Spectrometer (Down-Looking)	Total Surface Radiance (350–1000 nm)	Surface radiance spectrogram
HYP-NIR	Headwall Micro-HyperSpec NIR T-Series Imaging Spectrometer	Total Surface Radiance (900–1700 nm)	Surface near-IR imagery, bio, and biochemical mapping
DD μ D	Drone Deployed micro-Drifter Launcher	Air temperature, air pressure, water temperature and salinity, up to 1 week of in-water logging	During drop: fast response atmospheric profile Post-drop buoy: GPS position, temp/salinity profile at 0.1 m, 0.4 m, 1.0 m depths
MET	Novatel OEM719 + KVH1700 IMU	GPS Timing, Position, Angular Rotations and Rates, fiber-optic gyro IMU angle accuracy of 0.001°. 100 Hz post-processed horizontal position accuracy of ± 1 cm RMS and vertical position accuracy of ± 2 cm RMS.	Mapping capabilities, orthorectification of all imagery and MET data streams
MET	Aeroprobe 5-port Gust Probe and Logger	3D Air Velocity at 100 Hz	Turbulent momentum flux
MET	Krypton KH20 Fast Response Hygrometer	Absolute humidity at 100 Hz	Turbulent latent heat flux
MET	Opsens OTG-F Temperature Probe	Air temperature at 50 Hz	Turbulent sensible heat flux
MET	ULS LiDAR	Distance ranging up to 500 m (± 0.02 m), with sampling up to 200 Hz and a FOV of 3 milliradians	Surface topography and ocean waves

(b) HYP-VNIR/HYP-NIR: Visible Near-Infrared and Near-Infrared Hyperspectral Imaging Systems, (c) RAD: Longwave and Shortwave Irradiance, (d) DD μ D: Drone-Deployed micro-Drifter, and (e) MET: Meteorological Measurements with LiDAR. Finally, we present some examples of data from each payload and discuss the results.

OBSERVATIONAL CAMPAIGNS

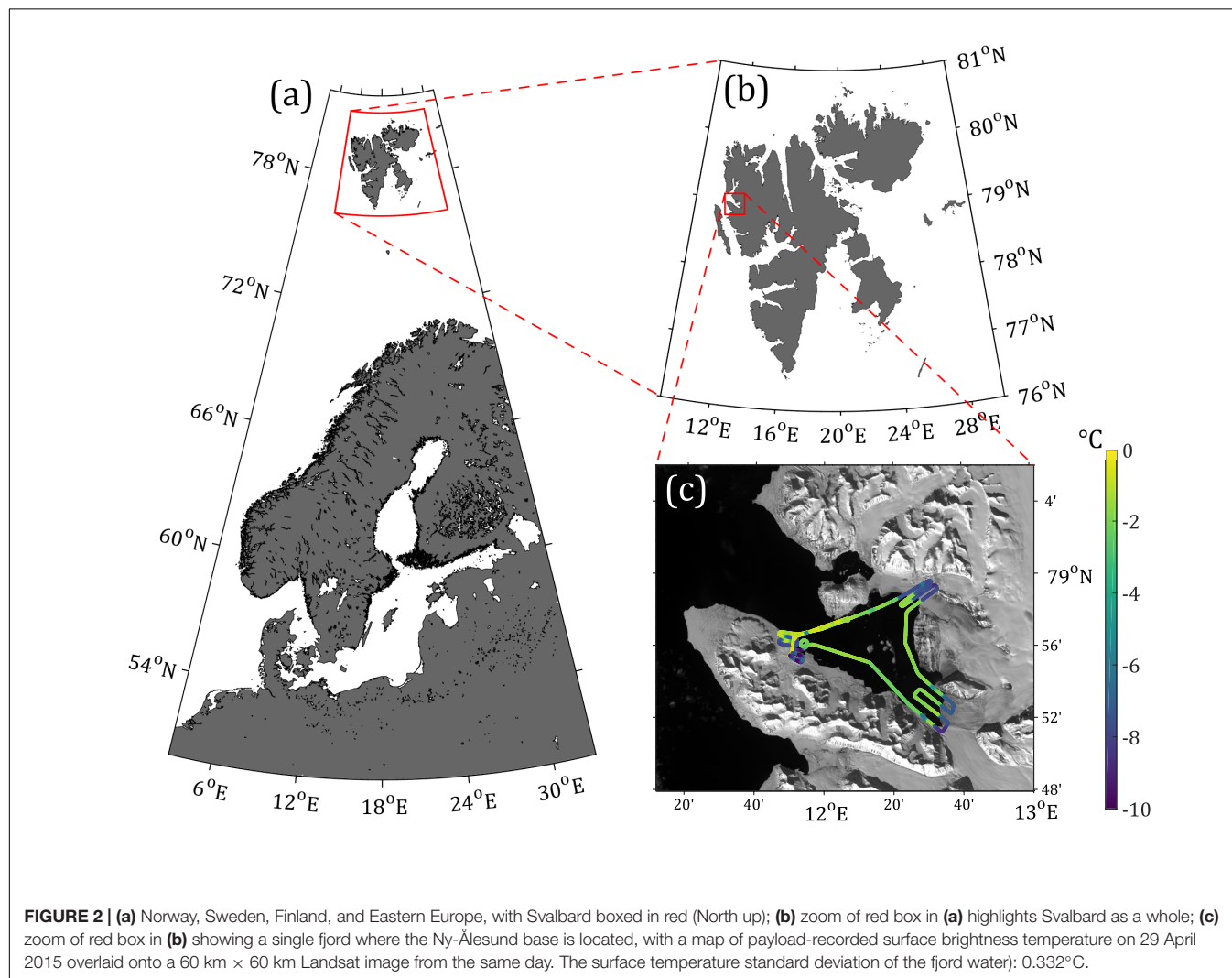
In 2013, we launched an ambitious program to develop scientific instrument payloads for moderate-size UAVs. The payloads were first integrated into the Sensintel Manta UAV (**Figures 1a,b**) and operated in April 2015 at the Ny-Ålesund Research Village

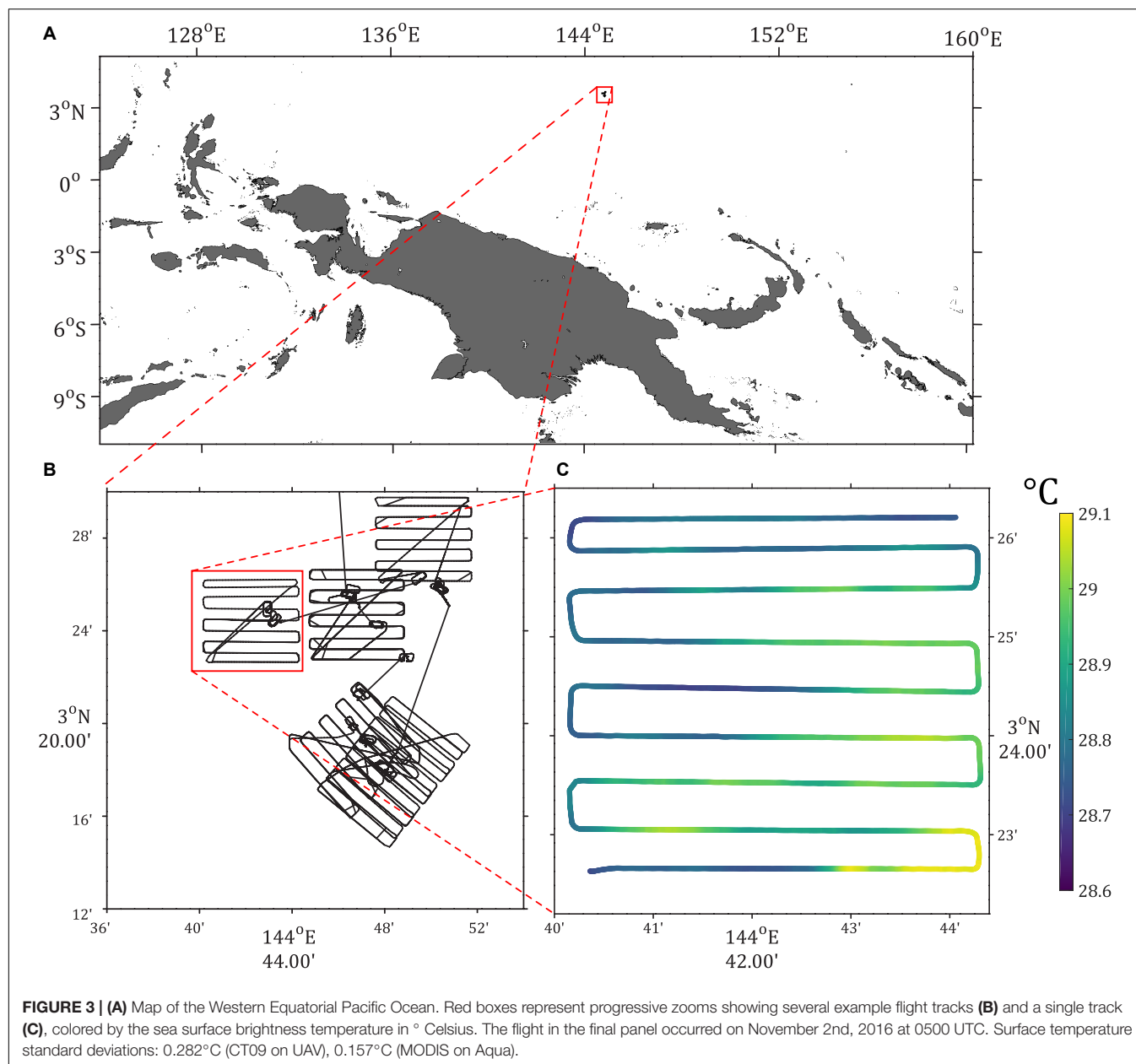


(79° N) on the island of Spitsbergen in the Svalbard archipelago, Norway (**Figure 2**). The chosen UAV platform was the Manta, produced by BAE Systems and owned and operated by the

NOAA Pacific Marine Environmental Laboratory. The Manta can support up to 4.5 kg of payload mass, a volume of 28 cm × 18 cm × 23 cm (D × W × H), and 40 W of steady power. We successfully acquired eight flights of atmosphere-ice-ocean data during the Ny-Ålesund deployment, which represented the third UAV deployment since 2013 with science payloads designed and built at Lamont-Doherty Earth Observatory (LDEO). In all, we implemented seven different science payloads (described below), each designed for different sensing applications.

We determined that fixed-wing flight with vertical take-off and landing capability (VTOL) would be essential for ship deployments that allow for high endurance. In 2016, we integrated all our payloads on the Latitude model HQ-60 fixed wing UAV with VTOL capability. Observations were made in the Western Pacific 400 nautical miles south of Guam during cruise FK161010 (11 October to 10 November 2016; R/V Falkor). **Figure 3** shows a map of the focus region north of Papua New Guinea and several UAV flight missions, including one flight track coded with surface brightness temperature. These operations demonstrated the utility of the ship-deployed UAVs





using the HQ-60 from the *R/V Falkor* (Rahlff et al., 2018; Wurl et al., 2018). We demonstrated the impact of scientific UAV usage extends into the realm of upper-ocean biological processes. The sea surface microlayer (SML; the upper 40–100 μm of the ocean surface) is a region of dynamic biological, chemical and physical activity, is a challenging environment to observe (Kurata et al., 2016; Engel et al., 2017; Ribas-Ribas et al., 2017). Through high resolution thermal and hyperspectral imaging of the sea surface, one is able to investigate the idea that biogenic slicks, of Phytoplankton and other sea surface microlayer constituents will affect the transfer of heat into the water column and thereby significantly alter the surface heat budget and the response of the mixed layer (Wurl et al., 2018).

TECHNICAL DETAILS

Unmanned Aerial Vehicle Characteristics

The term Unmanned Aircraft System (UAS) is used to describe the entire suite of technology used for UAV flight. This includes the ground control station, antennas, communication devices, operator, and the UAV itself. Because the developments relevant to the present work are focused around the aircraft and its payloads, the term UAV will be used exclusively throughout the rest of the paper.

For any ocean experiment aboard a research vessel, UAV takeoff and landing are critical to the success of the flight missions. Many land-based UAVs take off using a catapult

system; nearly all do when deployed from research vessels. Their recovery is typically made using a net or some wing capture mechanism, like the SkyHook for the Boeing *in situ* Scan Eagle [e.g., (Reineman et al., 2016)]. Both the catapult and recovery mechanisms, while viable, are cumbersome to deploy during ship operations requiring considerable personnel and deck space. These violent, high-load recoveries have proven more difficult as payloads have become more sophisticated.

We have determined that, in order to alleviate these difficulties, the vertical takeoff and landing (VTOL) capability is ideal for ship-based UAV deployments. There are a number of possible aircraft options. We have focused in on the HQ-60B (see **Figure 1c**), a new concept for long endurance VTOL that integrates the Piccolo autopilot from Cloud Cap Technology. Hybrid Quadrotor (HQ) technology offers an innovative and logistically simple solution to the problem of VTOL: it combines the VTOL capabilities of a quadrotor and the efficiency, speed, and range of a normal fixed-wing aircraft. Some of the advantages afforded by HQ technology include:

- Reduced operational footprint – no runway requirement, no approach obstacle issues, no launch/recovery infrastructure required.
- Portability – by eliminating launch and recovery equipment, there are significantly fewer items to transport and ship.
- Lower initial system cost – no launch and recovery infrastructure or expensive aircraft sensors required for VTOL capability.
- Reduced ongoing operational costs – fewer complex and cumbersome system elements to maintain, fewer people required to operate the system.

The HQ-60B cruises at an airspeed of 23 m s^{-1} , with an endurance of 15 h at a nominal 4.5 kg payload. The HQ-60B can reach altitudes of 4,200 m above mean sea level, has a wingspan of 381 cm and a mass of 43 kg. The flexible payload capacity using swappable instrument mounting brackets combined with HQ-60B's large amount of available onboard power (250 W at 24 VDC) allows deployment of extensive sensor suites. Compared with helicopters, HQ technology is less complex, more cost effective, more reliable, and has better endurance. Compared with pure multi-rotors, HQ technology has higher top speed, greater endurance, improved wind tolerance, and can cover more ground. Compared with fixed wing aircraft, HQ technology may be deployed from more locations, a greater variety of terrain, and from more types of platforms, all for less cost. Recently, we have upgraded to the HQ-90B with increased payload of 6.8 kg and swappable nose cones and fuselage mounting, all with similar endurance to the HQ-60B. It has a wingspan of 470 cm a mass of 52 kg. L3 Latitude's HQ line of aircraft represents a giant leap in UAV capability, enabling long-endurance missions with VTOL and optimized to perform in remote locations such as Alaska's Arctic coastal communities.

These systems have been well tested by LDEO with over 50 total flights and over 150 total flight hours. We have demonstrated the utility of the HQ systems as ship-deployed

platforms on the R/V Falkor in October–November 2016 between Australia and Guam (Rahlff et al., 2018; Wurl et al., 2018) and have recently deployed them in the field in Kotzebue Alaska in April–May 2018 and 2019.

Instrument Payloads for UAVs

In order to facilitate multiple types of scientific observations from a single platform, a modular payload style was developed (**Figures 4, 5; Table 1**). The imaging sensors chosen for this project have increased spatio-temporal resolutions and sensitivities for visible, thermal infrared, and imaging spectrometer sensors relative to the bulk of previous UAV work. These advancements are principally due to hardware miniaturization of newly developed R&D sensors with specifications that maintain or build upon the more widely available technology. Solar and longwave hemispheric radiometers and the corresponding acquisition hardware have also been downsized while maintaining comparable response times and overall measuring capabilities with their larger analogs. A new kind of launchable drone-deployed drifter was engineered in-house which combines the abilities of a temperature-salinity buoy and an atmospheric profiling dropsonde. The module has been termed the Drone- Deployed Micro Drifter (DD μ D). The DD μ D is designed to telemeter temperature, pressure, and relative humidity data while it falls through the atmosphere and, with its integrated GPS antenna, to map water temperature and water conductivity data while it drifts in open water. A meteorological payload which incorporates a suite of instruments enables the calculation of eddy-covariance flux. The required measurements for this calculation are fast-response temperature, relative humidity, and 3-D wind velocities sampled simultaneously. Traditional eddy-covariance flux systems have a large volume and weight, and so miniaturization represented the biggest obstacle for these instruments to be viable for a UAV platform. With a desire to build payloads with both efficiency and redundancy, the imaging equipment, the drifter launcher, and the broadband radiation packages were designed to occupy the same volume and utilize the same acquisition hardware. This modular design allowed for the various science instruments to be swapped, while leaving the acquisition, GPS-IMU, and power systems relatively permanently mounted. This feature reduced wear maintenance inherent with changing instruments, and enhanced flexibility for weather-dependent science flight planning, which can change on the order of hours before deployment.

Base Payload

Overview

All science payloads utilize a common system referred to as the “Base” payload (see **Figure 4** and **Table 1**). The Base payload provides power distribution, computing, a GPS receiver, an Inertial Measurement Unit, and the acquisition and storage hardware for the science instruments, allowing it to remain mounted while the science instruments were interchanged. Custom device drivers were developed to acquire each of the varying sensors with a common hardware. The resulting modular, “hot-swap” feature between the sensors and the Base

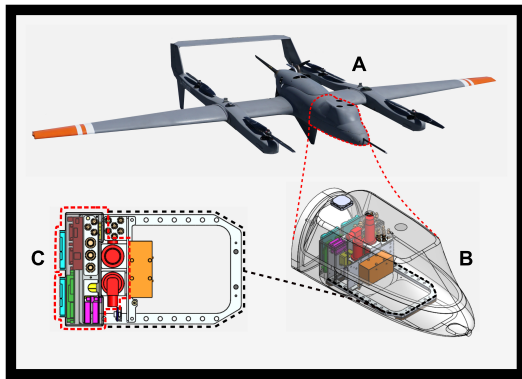


FIGURE 4 | (A) Image of the Latitude Engineering HQ-60 UAV with propellers for both flying and for vertical take-off and landing (VTOL). **(B)** Profile view of the HQ-60 modular nose cone and lid, with the skin transparent to reveal the Base payload acquisition system mounted inside. **(C)** Top view of the Base payload within the red-dash line and its square bracket within the black-dash line indicating available mounting holes for the modular ATOM, VNIR, RAD, and DD μ D payloads (the Base payload consists of the power supply, imagery DVR, GPS, IMU, and up-and-down looking IR pyrometers).

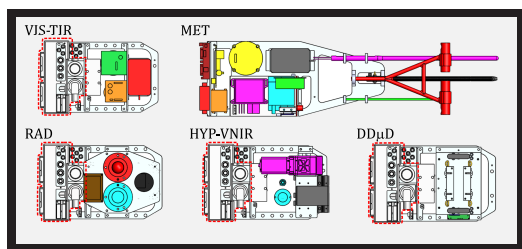


FIGURE 5 | Mechanical drawings of ATOM, RAD, VNIR, and DD μ D payload sensors. The Base payload acquisition system (also shown in **Figure 4**) are indicated by the red dashed line. The MET payload is completely different from the other payloads, which primarily has a completely different acquisition system, with nose-exiting probes and stingers to measure fast-response 3D wind, temperature, and humidity, and an industry-leading GPS and fiber-optic gyro IMU to correct for in-flight UAV motion to the highest possible accuracies.

payload allowed quick determination and modification of science flight planning, which can be dependent on rapidly changing weather conditions. The Base payload also includes permanent upward- and downward-looking pyrometers to measure surface temperature on all flights, a radio transmitter for telemetering data from any drifting DD μ Ds within range, and an internal relative humidity/temperature probe for monitoring the payload environment. We note that, except for its power distribution system, the Meteorological (MET) payload utilizes different base hardware due to the nature and synchronization requirements of its sensors. Additionally, we have outfitted the Base payload with custom telemetry software to transmit sensor status messages to the UAV ground control station.

Power Supply and Conditioning

Sensor and acquisition hardware require both 12-volt and 5-volt rails to supply the required 45 watts of steady power while

recording. Vicor 5V output and 12V output DC-DC switching power converters were connected in parallel to the UAV supply battery. The Vicor supplies were chosen for their robust industrial operation, low noise and ripple, fault, surge, and regulation features, and low weight and size.

The electromagnetic interference (EMI) shielding of power distribution was a top priority. An active EMI filter was installed between the UAV batteries and the Vicor input terminals to address input line voltage ripple. A grounded aluminum enclosure housed the EMI filter and the two Vicor supplies, and through-capacitors were used as the terminals to further isolate the power components inside the aluminum enclosure. The output wiring exiting the housing terminals was twisted/shielded pair terminated into six positive-lock connectors for each of the 5-volt and 12-volt rails. The six terminators on each rail allowed for quick connect/disconnect of hardware.

GPS and IMU for Aircraft Motion

The inertial navigation system in the Base payload consists of a Novatel SPAN GNSS with an OEM719 receiver and a STIM300 MEMS IMU. The GPS updates at 5 Hz, while the IMU updates at 125 Hz. The receiver provides NMEA and PPS signals to synchronize acquisition hardware to <20 μ s RMS. The receiver also has access to multiple GPS frequencies to accommodate all latitudes between the equator and both poles, including L1/L2, GLONASS, SBAS, and QZSS. The fixed GPS reference/master station is a Leica GX1220 Triple Frequency receiver recording at 10 Hz with a Leica AX1202GG choke ring antenna. Using the Novatel Waypoint Inertial Explorer software, a tightly coupled, post-processed TSPI solution of the raw GPS + IMU data is generated to achieve horizontal position accuracy of ± 1 cm RMS and vertical position accuracy of ± 2 cm RMS. The post-processed IMU roll/pitch accuracy is 0.006° RMS and 0.019° RMS in heading. We used the long record from the GPS base station as our ground control point validation for the Waypoint solution to be within the calculated accuracy.

Imagery acquired from aboard the UAV during flight was orthorectified according to the algorithm described in Zhou (2009). In summary, the UAV's instantaneous position and attitude derived from the combined GPS/IMU solution provided the three-dimensional rotation geometry for each camera image. Rectification and geolocation were validated by comparison of rectified imagery, showing overlap within a single pixel over successive UAV sea-ice edge passes.

Embedded Computer

A Versallogic Raven (VL-EPU-3312) embedded computer was used as the host for non-imagery sensor data logging, for bi-directional, in-flight communications between the UAV and the ground station operators, and for in-flight payload sensor status. The Raven is small ($3.74'' \times 3.74'' \times 1.08''$), light (0.2 kg), powerful, and offers several features that are well suited for simultaneous acquisition and control of multiple digital sensors. It can operate in ambient temperatures of -40 to $+80^\circ\text{C}$, is rated MIL-STD-202G for vibration and shock, and accepts a wide input voltage of 8–30 VDC. All Base payload and non-imagery sensor payloads are configured and logged locally by the Raven,

running 32-bit Windows7 with many background services and security features disabled. The imagery sensors are logged on the IO Industries Core CameraLink Base Framegrabber.

Frame Grabber for Digital Video Recording

The IO Industries, Inc., Core™ DVR and the Windows-based IO Industries, Inc., Streams7™ software are used for device acquisition of all measurements except the hemispheric radiometers in the RAD payload. With NMEA and PPS inputs, the Core and Streams7 software synchronize multiple devices to within 1 millisecond of GPS time, even when devices are sampling at different rates. Streams7 device drivers can be written to enable acquisition of USB devices. Not only do the synchronization and timing specifications of the IO Industries system make it favorable for a UAV application, it also presents a solution for centralized acquisition of multiple devices with low development time and cost.

Infrared Radiometers

The Base payload also had amenable space for the two narrow field-of-view (FOV; 3°) pyrometers chosen to provide skin temperature measurements. The Heitronics CT09 models were selected for their small size and relative performance, able to sample brightness temperature at 10 Hz. Both up- and down-looking sensors are required to correct for the reflected atmospheric signal. The CT09 spectral response is 8–14 μm; they are accurate within 0.1°C of target temperature.

Science Payloads

VIS-TIR/HI-TIR: Thermal Infrared and Visible Imagery With LiDAR

High-resolution thermal infrared (IR) imagery measured from the HQ-60B are used to remotely sense the characteristics of ocean skin temperature, or SST_{skin}, at the air-sea interface. With the instruments in this payload one is able to characterize the properties of the surface associated with time varying atmospheric conditions and the ocean surface processes that are relevant to atmosphere-ocean interaction. One is also enabled to provide surface information at higher spatial resolution and with better temporal sampling than is available from ship data, moorings, gliders, etc.

This payload is used in two configurations. The first incorporates a small sensitive Stirling-cycle cooled IR camera to map the temperature structure of the ocean's surface. The Sofradir-EC model MiTIE Stirling-cooled Mercury-Cadmium-Telluride (MCT) focal plane array of 640 × 480 elements is sensitive to 7.7–9.3 μm radiation and has an FOV of 21.7° × 16.4°. The MCT focal plane array performance will allow for the determination of temperature variability of less than 0.02°C NETD and with spatial resolution 1.5 m at 1000 m altitude at a frame rate of 100 Hz. The second configuration includes a Sofradir model ATOM microbolometer with resolution of 1024 × 728 elements (FOV 38.4° × 28.8°) that are sensitive to 8–14 μm sensitive to temperature variability of less than 0.05°C NETD with spatial resolution of less than 1 m at 1000 m altitude at a frame rate of 30 Hz. Both NETDs were confirmed prior to

and during all field operations using the SBIR model EX-04-B-L-25-FS/ES blackbodies with accuracy to ±0.001°C. The additional space afforded by this smaller sensor allows for the inclusion of a downward-looking high-resolution broadband visible (400–800 nm) imager, either IO Industries' 4 MP Flare 4M180-CL color (2048 × 2048 pixels at a frame rate of 30 Hz) or Imperx Bobcat 6MP monochrome (2756 × 2208 pixels at a frame rate of 15 Hz). These provide imagery at 1000 m altitude with spatial resolutions of 0.3 and 0.1 m, respectively. This combination of cameras allows us to capture surface feature variability over a multitude of scales of order 0.1–1000 m. A LiDAR model ULS-1000 measures the surface elevation/displacement at 200 Hz accurate to ±2.0 cm with a maximum range of 500 m and with a FOV of 3 milliradians. **Figure 6** shows the thermal infrared and visible imagery of sea ice drifting on the ocean surface within the fjord near Ny-Ålesund. The temperature of the sea ice is colder than the surrounding ocean surface with significant variability between −4.4 and −1.5°C. Note that the colder pieces of sea ice in the infrared are related to the brighter sea ice in the visible. The ocean surface surrounding the sea ice varies in brightness temperature significantly less, roughly −1.0 to −2.0°C. Furthermore, the structure of the ocean surface temperature suggests that the variability is due to near surface turbulence generated by the sea ice itself, simultaneously mixing up the cooler sea ice melt water.

HYP-VNIR/HYP-NIR: Hyperspectral Imaging Systems

In the HYP-VNIR/HYP-NIR payloads, the Visible/Near-Infrared (VNIR/NIR) signature of the sea surface is sensed via Headwall Photonics model Micro-Hyperspec® VNIR airborne hyperspectral aberration-corrected imaging spectrometers to measure VNIR (400–1000 nm) and model Micro-Hyperspec® for NIR (900–1700 nm) spectral radiance of the upper-ocean to determine ocean color. The A-Series model VNIR silicon CCD sensor has a spectral resolution of 1.86 nm with 323 spectral bands and 1004 spatial pixels (spatial resolutions of 0.6 m at 1000 m altitude) and a sampling rate of 30 Hz (integration time of 10–40 ms, depending on light conditions). The T-Series model NIR InGaAs array has a spectral resolution of 9.97 nm with 82 spectral bands and 640 spatial pixels (spatial resolutions of 1.5 m at 1000 m altitude) and a sampling rate of 60 Hz (integration time nominally 5.3 ms). Both the NVIR and NIR sensors have been laboratory calibrated to within NIST standards by Headwall Photonics. Additionally, an Ocean Optics USB2000+ measures down-welling hemispheric irradiance signal (FOV is 180°) in the 210–1050 nm range (signal-to-noise, SNR is 250:1) and two Ocean Optics model FX Spectrometer to measure the up- and down-welling radiance in the 350–1000 nm range (SNR = 290:1) with a FOV of 3° (1°–14° possible).

RAD: Longwave and Shortwave Irradiance

We utilize up- and down-looking Hukseflux model IR-02 pyrgeometers to measure the net longwave radiation (4.5–40 μm) and up- and down-looking Hukseflux model SR-03 pyranometers to measure the net shortwave (solar) radiation (285–3000 nm). The pyrgeometers feature 150° fields of view and a response time of less than 1 s (custom reduced from 18 s) with a calibration

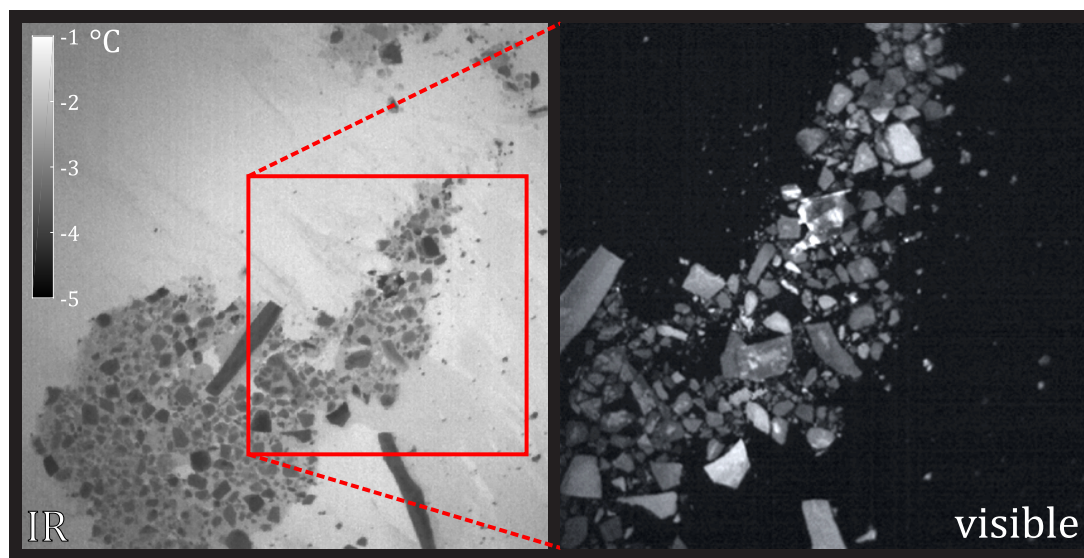


FIGURE 6 | Imagery of fjord water with loose sea ice obtained from Manta equipped with the ATOM payload. The thermal image in the **left panel** was obtained from the Atom microbolometer and the visible image in the **right panel** was obtained from the Flare camera.

uncertainty of 3.69 W m^{-2} and a sensitivity of 0.06 W m^{-2} . The pyrgeometer sensor directly measures net irradiance. Through the inclusion of a 10 k thermistor and the Stefan-Boltzmann law, the sensor's own irradiance is estimated and the irradiance incoming to the sensor is isolated. The pyranometers feature 180° fields of view and a response time of less than 1 s with a calibration uncertainty of 1.31 W m^{-2} and a sensitivity of 0.07 W m^{-2} . The pyranometer has a platinum resistance thermometer (PT-100) to provide temperature compensated calibration. Rooftop comparisons were performed against industry standard Kipp and Zonen model CGR4 pyrgeometer and model CMP22 pyranometer. These are paired with an onboard high-resolution broadband visible (400–800 nm) imager. The downward-looking Imperx model 2520 Bobcat digital monochrome visible camera has a sensing array of 2500×2000 elements, providing imagery with a spatial resolution of 0.3 m at 1000 m altitude in order to characterize the ocean wave state.

DD μ D: Drone-Deployed Micro-Drifter

The DD μ D consists of a small suite of sensors enclosed in a durable polyurethane body. Up to four DD μ D packages are loaded in the launcher for in-flight ejection. Once ejected from the UAV during flight, the DD μ D behaves as a profiler as it descends through the atmosphere, measuring air temperature (accurate to 0.1°C with a sensitivity of 0.0045°C and a response time of 1.2 s), pressure (accurate to 1.5 mbar with a sensitivity of 0.065 mbar and a response time of 8.2 ms), and relative humidity (accurate to 1.8% with a precision of 0.2%, a sensitivity of 0.03% and a response time of less than 4 s). The humidity sensor has an additional temperature sensor accurate to 0.2°C with a precision of 0.1°C , a sensitivity of 0.015°C and a response time of less than 5 s. The data is telemetered to the Raven PC on the UAV throughout the descent. Once it falls and lands on the sea surface,

the DD μ D behaves as a surface-drifting ocean buoy, deploying a string of sensors that measure temperature and conductivity of the upper 2–3 m of the ocean at fifteen min intervals for up to 2 weeks. The ocean sensors on the DD μ D collect and store data that is then transmitted back to the UAV as it flies overhead up to 16 km away, even if on subsequent flights. The temperature measurement is accurate to 0.1°C with a sensitivity of 0.0045°C and a response time of 0.3 s, while the conductivity measurement is sensitive to $9e^{-4} \text{ mS cm}^{-1}$ with a response time of 1 s. In order to ensure validity of these observations, the DD μ D's temperature and salinity sensors were calibrated against a Seabird SBE-37.

The DD μ D has a number of innovative features that allows it to make measurements with high accuracy while keeping the total power consumption low. It implements a custom designed precision current source required for measuring air and water temperatures with platinum resistance temperature

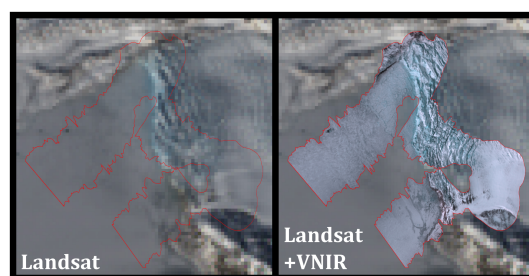


FIGURE 7 | Satellite (Landsat) imagery of the Conwaybreen glacier in Svalbard, acquired on April 27th, 2015. A pushbroom image created from the VNIR imager's RGB channels is overlaid on the right panel and is outlined in red on both. The satellite image has been slightly darkened to emphasize the VNIR image.

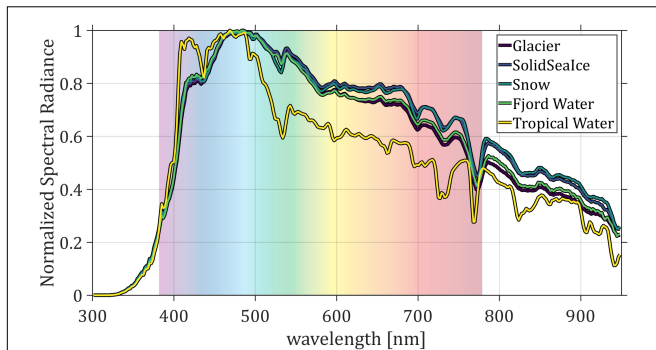


FIGURE 8 | Surface-leaving spectral radiance, normalized by peak radiance, including the effects of reflected sky radiance and anomalous sun glint. The ‘Tropical Water’ trace represents a measurement made in the equatorial Pacific Ocean while the others represent measurements made from a flight over Svalbard, Ny-Ålesund. The faded rainbow in the background indicates the color of visible light for each wavelength.

detectors (RTD). The salinity sensor subsystem implements a novel alternating current activation source to limit electrode erosion that maintains the sensor accuracy throughout the deployment period. The microprocessor switches on one sensor at a time to make a measurement, keeping others powered off while not in use. This not only reduces the overall power consumption but also improves the measurement accuracy by limiting self-heating and eliminating interference between the

sensors. As an atmospheric profiler, the DD μ D samples all the sensors at 10 Hz. After landing, it samples all the sensors at 1 Hz. Between data collection cycles, the microprocessor powers off all components and enters a sleep state itself, reducing the current consumption to less than 1 mA. While in the sleep state, an ultra-low power real-time clock (RTC) keeps time and wakes the microcontroller into low-power data collection mode every 15 min. The microcontroller then wakes up the GPS to get a position fix. As soon as the GPS gets a valid fix, all other sensors are turned on and ten sets of measurements are taken at 1 Hz. The UAV will continuously transmit a “wake up pulse” during flight, so the UAV finds the buoy simply by coming within the 16 km radio range. When the UAV flies in range of the DD μ D and a ping is received, the DD μ D reliably transmits the data it has collected on its flash storage to the aircraft using RDP protocol. If the flash storage is not acknowledged as received by the UAV, the buoy continues collecting data until the next successful connection and successful data transmission occurs. If no valid fix is acquired by GPS within 3 min of waking up, the microcontroller switches the GPS off and initiates the data collection. All the sensors are then turned off and the microcontroller goes into sleep state waiting for a wake up call from RTC for next data collection period. The DD μ Ds are supported by an intelligent and interactive software onboard the UAV that allows the receiver onboard to simultaneously communicate with multiple DD μ Ds in the area and download data from the DD μ Ds automatically or under direction of a user from the UAV base. In order to reduce the environmental impact, the DD μ D uses all RoHS compliant

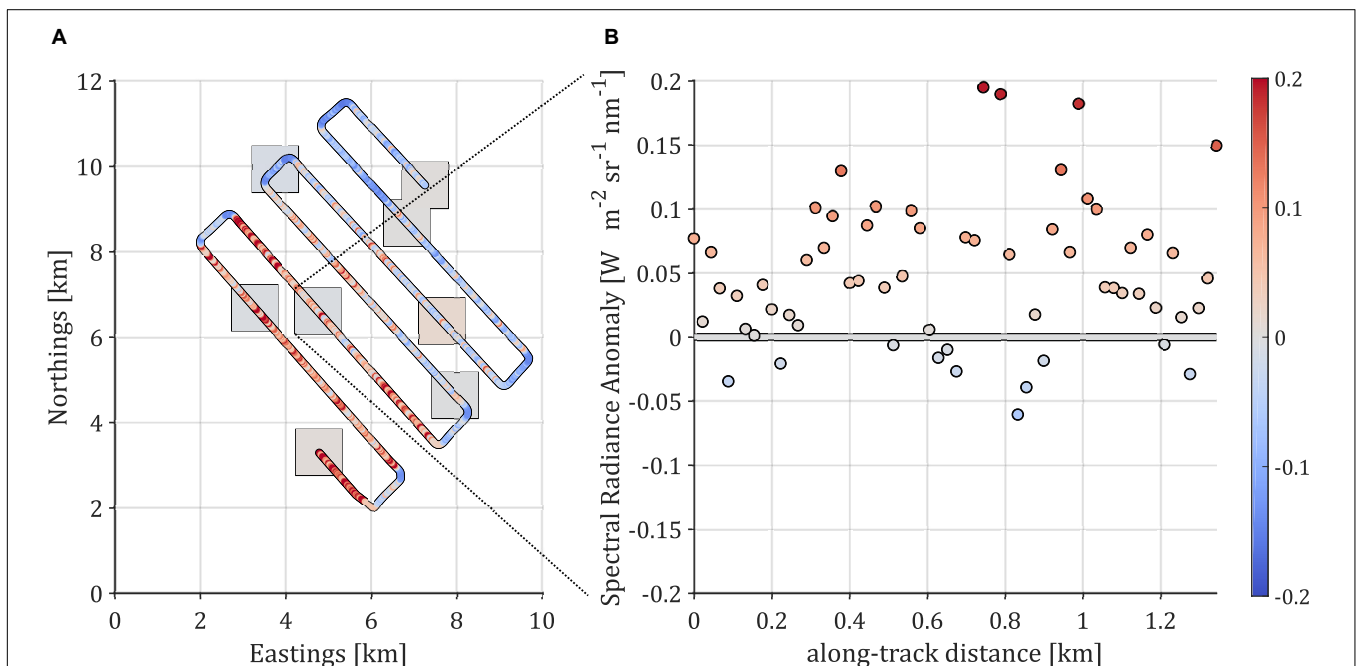


FIGURE 9 | Spectral radiance anomaly in $\text{W m}^{-2} \text{sr}^{-1} \text{nm}^{-1}$ at 488 nm wavelength, VNIR and MODIS, represented relative to the mean value of the latter over the entire UAV Flight001 area of operation. **(A)** UAV track overlaid on sample MODIS acquisition points (gray squares). Marker sizes are approximately equal to the size of each data point: 1 km by 1 km for MODIS and 175 m in the cross-track for the VNIR imager. **(B)** Snippet from track (as indicated by dotted lines), highlighting variability of spectral radiance within a single MODIS pixel (standard deviation: $0.0651 \text{ W m}^{-2} \text{sr}^{-1} \text{nm}^{-1}$). Colorbar represents the spectral radiance anomaly shown as the vertical axis in **(B)**.

components, lead-free solder, NiMH batteries and streamers made out of an eco-friendly water-soluble material.

MET: Meteorological Measurements With LiDAR

The final suite of instruments – the suite incorporated into the MET payload – enables the direct calculation of turbulent flux via eddy-covariance. The required measurements for this calculation are fast-response temperature, specific humidity,

and 3-D wind velocities sampled simultaneously. Traditional eddy-covariance flux systems are large in volume and weight, so miniaturization represented the biggest obstacle for these instruments to be viable for a UAV platform. The wind velocities are measured from a self-logging 5-port gust probe [e.g., Hacker and Crawford (1999)] designed and built by Aeroprobe Corporation based on our design requirements. Because this was a custom-build, Aeroprobe performed a noise characterization to

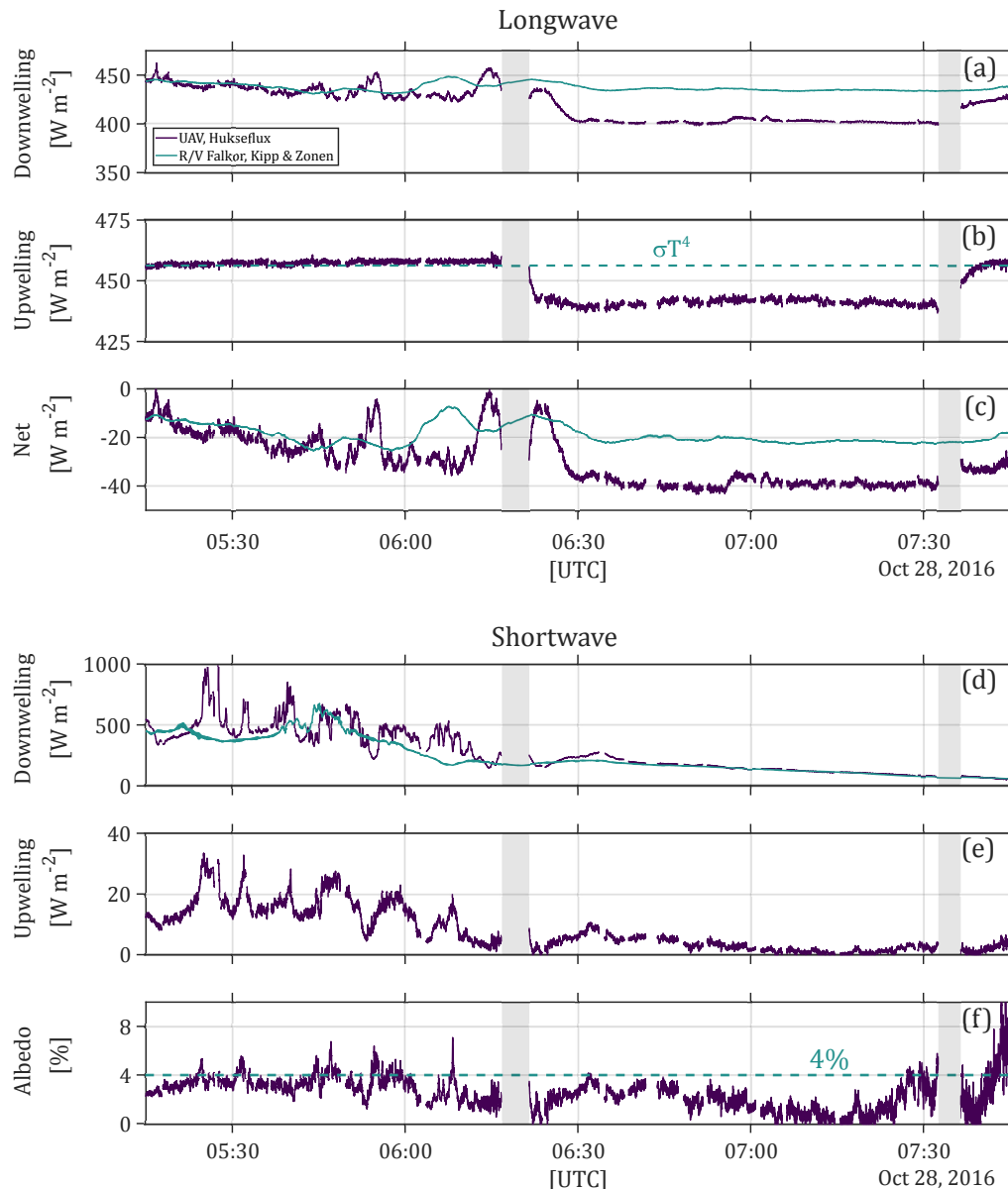


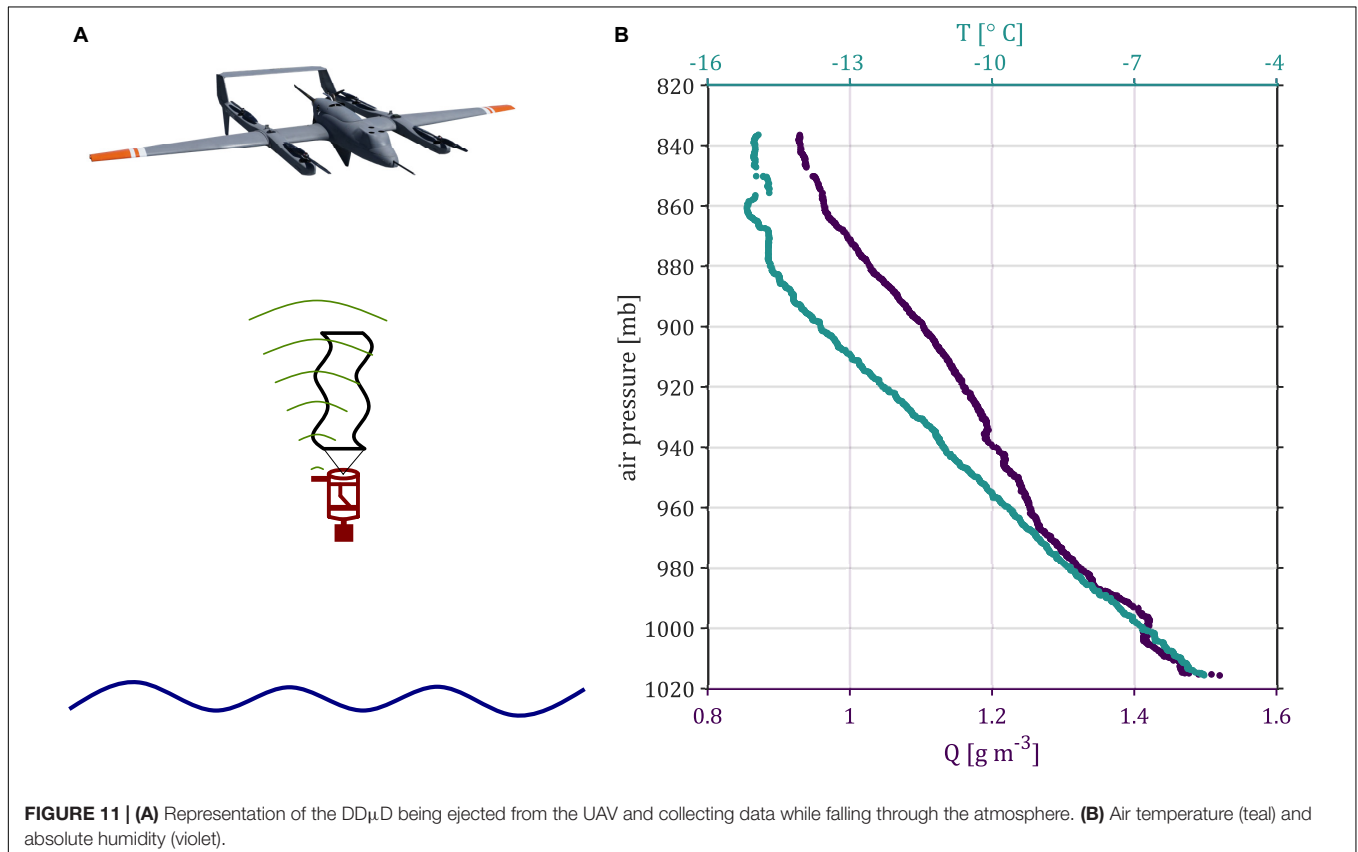
FIGURE 10 | Radiant flux sensed via the pyrgometers (longwave, **a–c**) and pyranometers (shortwave, **d–f**) from UAV Flight 001. The pyrgometers are sensitive to electromagnetic radiation in the wavelength range of 4.5–40 μm , while the pyranometers are sensitive to electromagnetic radiation in the wavelength range of 285–3000 nm. The violet and teal traces always represent measurements made via UAV and ship, respectively. The gray shaded regions indicate the times of ascent and descent of the UAV. The dashed line in **(b)** represents theoretical radiation computed using the sea surface temperature and an assumed emissivity of 0.96. The dashed line at 4% in **(f)** represents the classical value of Payne (1972) which is typical for clear skies and high solar angle.

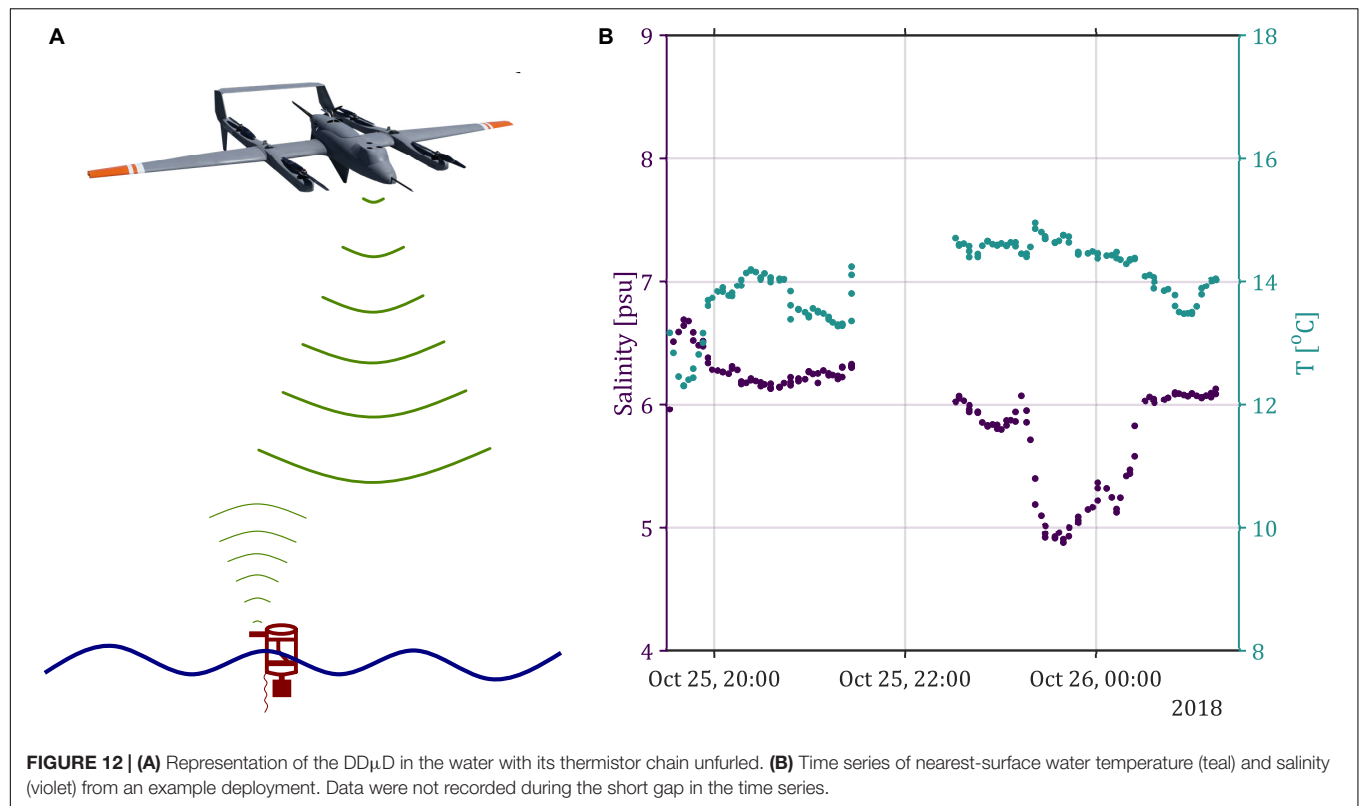
determine total system accuracy. Aeroprobe provided additional assessment and validation in their wind flume to ensure the instrument performed according to our specifications. The high sensitivity pressure transducers give a system accuracy of 0.03 m s^{-1} at up to 100 Hz. Fast response temperature is measured by the Opsens Fiber Optic GaAs tip measuring probe and is captured digitally by the Opsens signal conditioner at 50 Hz. It is accurate to $\pm 0.15^\circ\text{C}$ or better, with a resolution of $\pm 0.01^\circ\text{C}$ and operates with a 5.0 ms response time. Fast response specific humidity is measured by the modified Krypton KH-20 Hygrometer (accurate to $\pm 0.17 \text{ g m}^{-3}$, sensitive between 1.7 and 19.5 g m^{-3}) at 100 Hz. The OPSSENS temperature sensor and Krypton KH-20 hygrometer showed frequency response through the wind velocity spectra inertial subrange, allowing for estimation of sensible and latent heat fluxes. The LiDAR model ULS-1000 measures the surface elevation/displacement at 200 Hz accurate to $\pm 2.0 \text{ cm}$ with a maximum range of 500 m and with a FOV of 3 milliradians. The Geodetics iNAV was outfitted with the KVH-1700 Fiber-Optic Gyroscope IMU (accurate to 0.001° in pitch/roll) to increase inertial velocity measurements by an order of magnitude over the STIM300 MEMS IMU used in the Base Payload. The same Novatel OEM-719 GPS receiver was used to maintain high-precision positioning.

Both the Opsens and LiDAR provide digital RS-232 data. The various MET-flux sensors providing temperature (Opsens), humidity (KH20 Hygrometer), and 3-component turbulent wind velocity (Aeroprobe) must be sampled at the exact same

moment in time to provide a true flux measurement. Because of that requirement and the fast sampling rates (50 Hz for the Opsens and 200 Hz for the LiDAR), the OS latencies on the Raven PC do not allow for required synchronization of Opsens temperature data. To avoid OS latencies and achieve the required timing accuracy, a Sparkfun Electronics Logomatic V2 serial data logger was chosen to log both Opsens and LiDAR. LDEO developed custom firmware to implement logging of Opsens and LiDAR serial data synchronized to PPS timing (i.e., accurate to better than $10 \mu\text{s}$). To address the different latencies of data queries between LiDAR and Opsens, the firmware was programmed to adjust the start time of the logging based on the sensor-specific latency (difference between when the logger queries data and when it receives it). This allows the measurement to be time stamped and synchronized to the PPS trigger.

The Omega OM-USB-1608FS analog-to-digital converter (ADC) in triggered mode is used for acquiring the KH20 analog hygrometer data. This digital logging created challenges to timing synchronization, since the logger depends on the system time and is subject to OS latencies. To address this, custom software was implemented to trigger the ADC using the PPS and to update the OSNetwork Time Protocol (NTP) software running on the Raven PC using the incoming GPS and PPS signals. The NTP software timing accuracy is as accurate as the sampling clock of the ADC, which is of order $10 \mu\text{s}$, as opposed to milliseconds for the computer.



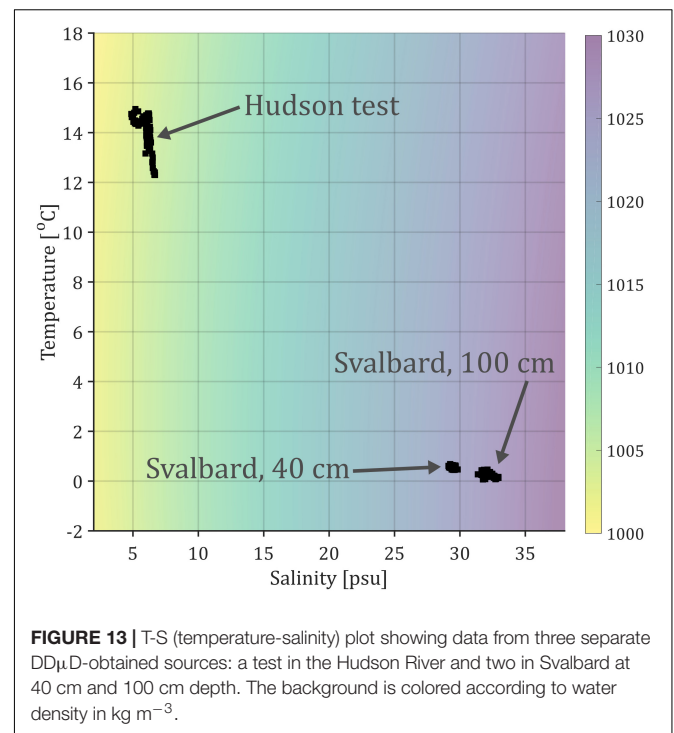


RESULTS AND DISCUSSION

Here, we provide a number of scientific applications for the combined UAV-sensor payload system. In **Figure 7**, identical Landsat images of the Conwayreen glacier are shown side by side, one featuring the overlay of a georectified swath created from the red, green, and blue channels of the VNIR pushbroom imager. As described in the Technical Details, recording of the aircraft's instantaneous position and attitude in three dimensions allows for the geolocation of each pixel. Each Landsat pixel is 30 m by 30 m, while the each VNIR pixel is approximately 50 cm wide in the cross-look direction. This combination of data and processing yields more than simple RGB imagery of the surface; full spectral radiance is obtained at each point along the UAV flight track. **Figure 8** shows the normalized spectral radiance (including the effects of reflected sky radiance and sun glint) observed to be emitted from a variety of surfaces across the two field campaigns: glacial ice, solid sea ice, snow, fjord water, and tropical water. A faded rainbow is set behind the spectra to show the color for each wavelength band. Note the spectral peak in the blue and the small emitted spectral radiance in the red.

In addition to comparing mean spectral radiances between different surfaces, one may investigate the small-scale spatial variability of radiance at given wavelength bands. A comparison of spectral radiance obtained from MODIS on Aqua and the VNIR imager on the HQ60 is shown in **Figure 9**. Values are given relative to the mean MODIS spectral radiance (as anomalies) and represented along the track of the UAV. The size of the large

square markers on **Figure 9** represents the approximate area on the ocean surface over which each data point was produced. In this way, measurements made using the VNIR imager reveal the



variability at scales smaller than the MODIS Level 2 pixel size of 1 km by 1 km.

The RAD payload offers a complementary mode of describing the radiative properties of the ocean surface and sky. UAV observations have a distinct advantage over ship-based observations because they are capable of making observations of upwelling irradiance measurements which are unobstructed by any superstructure such as the ship or tower. Observations made from the UAV and ship-based hemispheric pyrgometers and pyranometers are shown in **Figure 10**. The upper portion (a–c) describes measurements of broadband infrared irradiance while the lower portion (d–f) describes measurements of solar irradiance. Portions during which the UAV was in the process

of making a turn were excluded from the record shown here. The gray shaded regions indicate UAV ascent and descent, respectively, between 240–66 m altitude above local mean sea level. The downwelling longwave from the UAV and from the Falkor are in close agreement at lower altitude. However, at higher altitude the downwelling irradiance from the UAV sensor is 40 W m^{-2} less due to the colder atmosphere at higher altitude. In addition to its measurement from the downward-looking pyrgometer aboard the UAV, the irradiance from the ocean was estimated from sea surface temperature using the Stefan-Boltzmann law and an assumed spectrally integrated emissivity of 0.96. During the UAV's lower level of flight, this computed value agrees well with direct observations of upwelling. At the

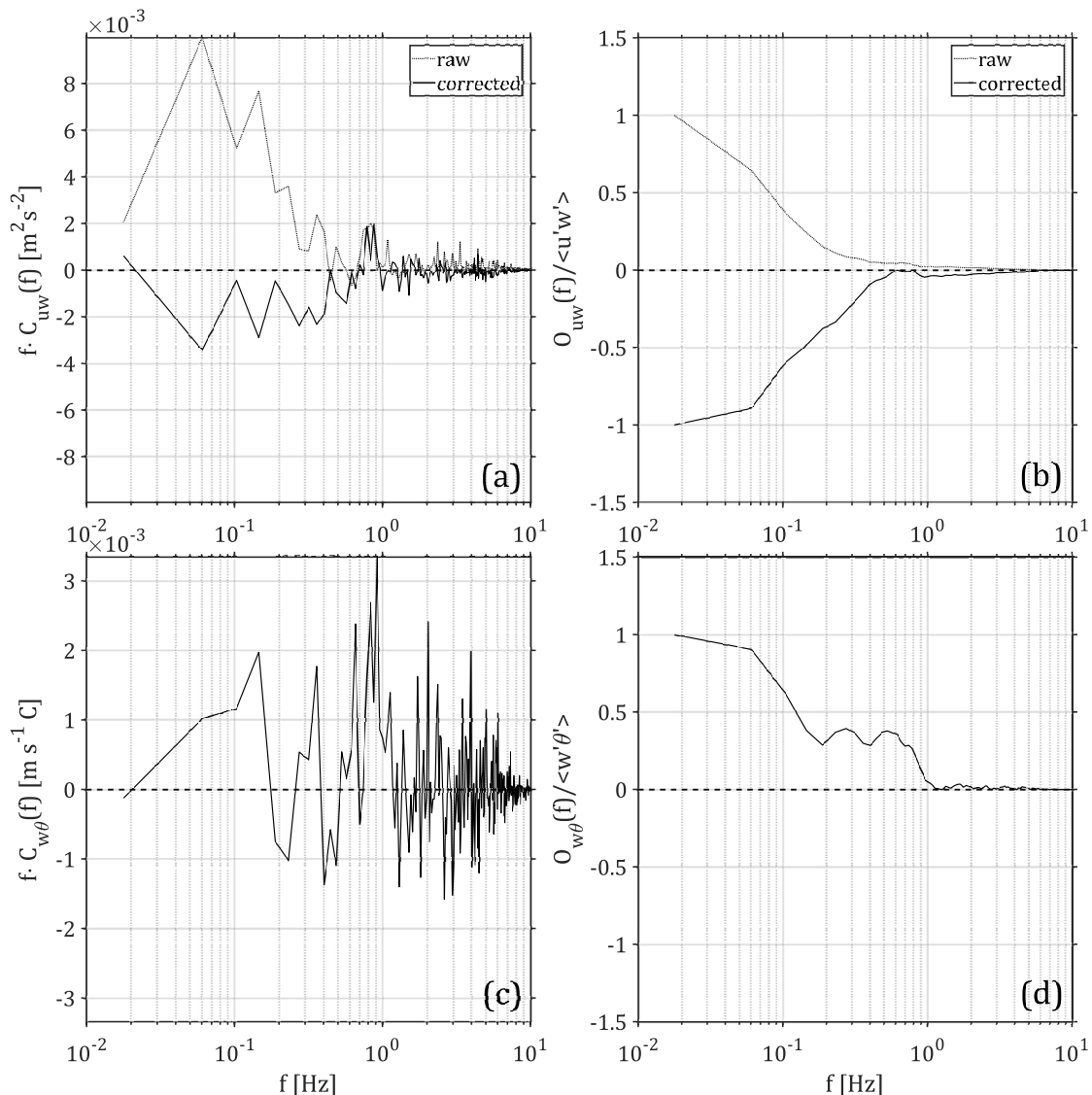


FIGURE 14 | Cospectra (a,c) and ogives (b,d). Computed using the vertical velocity time series and the alongstream velocity (a,b) or the air temperature (c,d). Ogives represent the cumulative flux density, with the lower limit of integration moving from right (high frequency) to left (low frequency). Integrating the cospectra yields wind stress $\tau = 0.0053 \text{ N m}^{-2}$ and sensible heat flux $H_s = -2.6 \text{ W m}^{-2}$. In both cases, positive is downward (into the ice/ocean), a negation of the values of the cospectra.

higher level of flight, the computed value is approximately 15 W m^{-2} higher than observed; this is to be expected for the cooler atmosphere at higher altitude. Downwelling solar irradiance observed from the UAV-based and shipboard sensors agree well toward the beginning and end of the flight, when the aircraft was nearly collocated with the ship. During the flight, short-period variability is observed by the UAV-based sensor, likely the result of spatial inhomogeneity in cloud conditions. Measurements of broadband albedo of the ocean surface computed from the downwelling and upwelling solar irradiance show variability throughout the flight about the classical values of Payne (1972), very nearly 4%, a value which is typical for clear skies and high solar angle.

Representations of the DD μ D in action are shown in **Figures 11, 12**. For the first stage of deployment (**Figure 11**), the DD μ D is ejected and falls from the UAV (a), providing an atmospheric sounding as it passes through the air (b). The example shown in **Figure 11B** demonstrates the ability of the DD μ D to make measurements of fundamental quantities in the atmospheric boundary layer, here air temperature, pressure, and absolute humidity. These measurements can be used to quantify the sensible and latent heat fluxes (Edson et al., 2004; Knuth and Cassano, 2014). In the second stage of deployment (**Figure 12**), the DD μ D hits the ocean surface, deploys its thermistor chain, and records physical properties of the water. In this case (b), it is shown that the DD μ D records a time series of water temperature and salinity. This is done at multiple depths (100 and 40 cm), allowing for reconstruction of the temperature-salinity profile of the water body. The wide space of conditions in which the DD μ D was tested are shown in **Figure 13**, ranging from warmer and fresher (the Hudson river) to colder and saltier (the fjord in Svalbard).

The high-frequency data streams provided by the MET payload require a particular type of processing in order to yield meaningful products, rendering fluxes of momentum and heat from basic measurements of the physical characteristics of fluids through eddy covariance (Edson et al., 1998; Sun et al., 2001; Reineman et al., 2013; Elston et al., 2014). When describing atmospheric boundary layer turbulent fluxes, it is useful to make use of Fourier analysis in order to determine the scales of fluid velocity fluctuations relevant to physical transfer processes. As an example, the cospectra shown in **Figure 14** were computed using turbulent vertical wind velocities in addition to along-stream wind velocity (a) and air temperature (c). Notice that the application of motion correction changes the direction of the flux in (a); the earth-referenced fluid velocity here indicates the downward exchange of forward momentum. The ogives shown in (b,d) represent the cumulative flux density of the cospectra as integrated from the high frequencies to the low frequencies (French et al., 2007). They are normalized by the total integrated covariances and show the dominant frequency scales of flux.

Measurements from UAVs will fill a fundamental gap in our understanding of ocean surface and marine atmospheric boundary layer physical processes. For example, point measurements have provided evidence that air-sea fluxes are

affected by sea surface temperature fronts (Friehe et al., 1991), while satellite observations have revealed that such fronts impact the wind field over the ocean (Chelton et al., 2004). However, further study is needed of processes which exist over areas large enough to require synoptic observations yet vary on scales small enough to be obscured by satellite-based measurements. These include submesoscale (0.1–10 km) variations in sea surface temperature and sea surface microlayer biochemical properties near frontal regions. Although substantial subsurface turbulent kinetic energy dissipation has been observed near these fronts (D'Asaro et al., 2011), the connection between these types of properties and air-sea heat, momentum, and gas fluxes is not fully understood. Proper description of the nature of these processes will improve our understanding of the ocean surface heat budget and mixed layer dynamics. Furthermore, submesoscale ocean surface motions are known to strongly impact buoyant material transport (D'Asaro et al., 2018).

CONCLUSION

We have described systems that combine the best of modern developments in UAV operation with advanced sensor technologies. High-endurance (15 h) UAV flight missions allow for extensive coverage of large-scale geophysical phenomena. The VTOL capability afforded by the HQ series of UAVs allows for ship-based deployment that is safer and requires less logistical support than previous modes of launch and recovery. The sensor suites used in the payloads described here represent the cutting edge of ocean surface and marine atmospheric boundary layer observational technology. Together, these enable the study of multiscale physical and biogeochemical processes which are at the heart of topics with broad environmental and human impact. For example, submesoscale currents and the effects of oceanic fronts on transport and surface biochemical properties elude many traditional observational techniques. These processes exist near the operational boundaries of modern sensing capabilities – too large in scale to be adequately sampled by ship or mooring, too finely varying to be properly characterized via satellite. The UAV sensing systems described here offer a strong mode for filling this observational need. Ultimately, improvements to measurements like the ones described here will lead to advances in the forecasting of weather and climate systems.

DATA AVAILABILITY STATEMENT

The datasets generated during the current study are available in a public repository at Columbia Academic Commons (doi: 10.7916/d8-mh4p-zp21).

AUTHOR CONTRIBUTIONS

CZ was responsible for the overall development project, including concept and design, guided the data analysis, and led

the writing. SB, TD, and RH developed the payloads. SB, NL, and TD contributed to the manuscript discussion and writing. SB and NL completed the data processing and analysis, as well as figure preparation. AF provided technical expertise regarding the UAV systems. AS provided the satellite data products and ocean color expertise.

FUNDING

This work was supported by the Gordon & Betty Moore Foundation (Grant #3596: “Payloads for Investigations of Spatial and Temporal Variability of Ocean and Ice Conditions In and Near the Marginal Ice Zone”, Grant #5448: “Bridging the Scientific and Indigenous Communities to Study Sea Ice

Change in Arctic Alaska”, and Grant #4886), the Schmidt Ocean Institute (Award Number: SOI CU16-2285), and NASA (Grant NNX16AJ08G).

ACKNOWLEDGMENTS

We thank R. Storvold of Norut for the invitation to participate in CICC13 in Ny-Ålesund, Svalbard, Norway in 2015; T. Bates, S. Stalin, and N. Delich of NOAA-PMEL for operating the Mantas in Ny-Ålesund; the cruise chief scientist O. Wurl of the University of Oldenburg, the captain and crew members of the *R/V Falkor* (cruise FK161010); and J. Armer, S. Bowers, and J. McDaniel of the Latitude Engineering flight crew for piloting the HQ-60s aboard the *R/V Falkor*. This is LDEO contribution number 8367.

REFERENCES

- Bates, T. S., Quinn, P. K., Johnson, J. E., Corless, A., Brechtel, F. J., Stalin, S. E., et al. (2013). Measurements of atmospheric aerosol vertical distributions above Svalbard, Norway, using unmanned aerial systems (UAS). *Atmos. Meas. Tech.* 6, 2115–2120. doi: 10.5194/amt-6-2115-2013
- Cassano, J. J., Maslanik, J. A., Zappa, C. J., Gordon, A. L., Cullather, R. I., and Knuth, S. L. (2010). Observations of antarctic polynya with unmanned aircraft systems. *EOS Trans. Am. Geophys. Union* 91, 245–246. doi: 10.1029/2010EO280001
- Chelton, D. B., Schlax, M. G., Freilich, M. H., and Milliff, R. F. (2004). Satellite measurements reveal persistent small-scale features in ocean winds. *Science* 303, 978–983. doi: 10.1126/science.1091901
- Chen, S. S., Kerns, B. W., Guy, N., Jorgensen, D. P., Delanoë, J., Viltard, N., et al. (2015). Aircraft observations of dry air, ITCZ, convective cloud systems and cold pools in MJO during DYNAMO. *Bull. Am. Meteorol. Soc.* 91, 245–246. doi: 10.1175/BAMS-D-13-00196.1
- Cione, J. J., Bryan, G. H., Dobosy, R., Zhang, J. A., de Boer, G., Aksoy, A., et al. (2019). Eye of the storm: observing hurricanes with a small unmanned aircraft system. *Bull. Am. Meteorol. Soc.* doi: 10.1175/BAMS-D-19-0169.1
- Cione, J. J., Kalina, E. A., Uhlhorn, E. W., Farber, A. M., and Damiano, B. (2016). Coyote unmanned aircraft system observations in Hurricane Edouard (2014). *Earth Space Sci.* 3, 370–380. doi: 10.1002/2016EA000187
- D’Asaro, E., Lee, C., Rainville, L., Thomas, L., and Harcourt, R. (2011). Enhanced turbulence and energy dissipation at ocean fronts. *Science* 332:1201515. doi: 10.1126/science.1201515
- D’Asaro, E. A., Shcherbina, A. Y., Klymak, J. M., Molemaker, J., Novelli, G., Guigand, C. M., et al. (2018). Ocean convergence and the dispersion of flotsam. *Proc. Natl. Acad. Sci. U.S.A.* 115:1162. doi: 10.1073/pnas.1718453115
- Edson, J. B., Crawford, T., Crescenti, J., Farrar, J. T., Frew, N., Gerbi, G., et al. (2007). The coupled boundary layers and air-sea transfer experiment in low winds (CBLAST-LOW). *Bull. Am. Meteorol. Soc.* 88, 341–356.
- Edson, J. B., Hinton, A. A., Prada, K. E., Hare, J. E., and Fairall, C. W. (1998). Direct covariance flux estimates from mobile platforms at sea. *J. Atmos. Ocean. Technol.* 15, 547–562. doi: 10.1175/1520-0426(1998)015<0547:dcfebm>2.0.co;2
- Edson, J. B., Zappa, C. J., Ware, J., McGillis, W. R., and Hare, J. E. (2004). Scalar flux profile relationships over the open ocean. *J. Geophys. Res.* 109:C08S09. doi: 10.1029/2003JC001960
- Elston, J., Argrow, B., Stachura, M., Weibel, D., Lawrence, D., and Pope, D. (2014). Overview of small fixed-wing unmanned aircraft for meteorological sampling. *J. Atmos. Ocean. Technol.* 32, 97–115. doi: 10.1175/JTECH-D-13-00236.1
- Elston, J. S., Roadman, J., Stachura, M., Argrow, B., Houston, A., and Frew, E. (2011). The tempest unmanned aircraft system for in situ observations of tornadic supercells: design and VORTEX2 flight results. *J. Field Robot.* 28, 461–483. doi: 10.1002/rob.20394
- Engel, A., Bange, H. W., Cunliffe, M., Burrows, S. M., Friedrichs, G., Galgani, L., et al. (2017). The ocean’s vital skin: toward an integrated understanding of the sea surface microlayer. *Front. Mar. Sci.* 4:165. doi: 10.3389/fmars.2017.00165
- Farrar, J. T., Zappa, C. J., Weller, R. A., and Jessup, A. T. (2007). Sea surface temperature signatures of oceanic internal waves in low winds. *J. Geophys. Res. Oceans* 112:C06014. doi: 10.1029/2006JC003947
- French, J. R., Drennan, W. M., Zhang, J. A., and Black, P. G. (2007). Turbulent fluxes in the hurricane boundary layer. Part I: momentum flux. *J. Atmos. Sci.* 64, 1089–1102. doi: 10.1175/JAS3887.1
- Friehe, C. A., Shaw, W. J., Rogers, D. P., Davidson, K. L., Large, W. G., Stage, S. A., et al. (1991). Air-sea fluxes and surface layer turbulence around a sea surface temperature front. *J. Geophys. Res.* 96, 8593–8609. doi: 10.1029/90JC02062
- Hacker, J. M., and Crawford, T. L. (1999). The BAT-probe: the ultimate tool to measure turbulence from any kind of aircraft (or sailplane). *J. Techn. Soar.* 23, 43–46.
- Johnston, D. W. (2019). Unoccupied aircraft systems in marine science and conservation. *Ann. Rev. Mar. Sci.* 11, 439–463. doi: 10.1146/annurev-marine-010318-095323
- Knuth, S. L., and Cassano, J. J. (2014). Estimating sensible and latent heat fluxes using the integral method from in situ aircraft measurements. *J. Atmos. Ocean. Technol.* 31, 1964–1981. doi: 10.1175/JTECH-D-14-00008.1
- Kurata, N., Vella, K., Hamilton, B., Shivji, M., Soloviev, A., Matt, S., et al. (2016). Surfactant-associated bacteria in the near-surface layer of the ocean. *Sci. Rep.* 6:19123. doi: 10.1038/srep19123
- Lucieer, A., Malenovsky, Z., Veness, T., and Wallace, L. (2014). HyperUAS—Imaging spectroscopy from a multirotor unmanned aircraft system. *J. Field Robot.* 31, 571–590. doi: 10.1002/rob.21508
- Moum, J. N., Szoek, S. P. D., Smyth, W. D., Edson, J. B., DeWitt, H. L., Moulin, A. J., et al. (2014). Air-sea interactions from the westerly wind bursts during the November 2011 MJO in the Indian Ocean. *Bull. Amer. Meteor. Soc.* 95, 1185–1199. doi: 10.1175/BAMS-D-1112-00225.00221
- Payne, R. E. (1972). Albedo of the sea surface. *J. Atmos. Sci.* 29, 959–970. doi: 10.1175/1520-0469(1972)029<0959:aotss>2.0.co;2
- Rahlf, J., Ribas-Ribas, M., Brown, S. M., Mustafa, N. I. H., Renz, J., Peck, M. A., et al. (2018). Blue pigmentation of neustonic copepods benefits exploitation of a prey-rich niche at the air-sea boundary. *Sci. Rep.* 8:11510. doi: 10.1038/s41598-018-29869-7
- Reineman, B. D., Lenain, L., and Melville, W. K. (2016). The use of ship-launched fixed-wing UAVs for measuring the marine atmospheric boundary layer and ocean surface processes. *J. Atmos. Ocean. Technol.* 33, 2029–2052. doi: 10.1175/JTECH-D-15-0019.1
- Reineman, B. D., Lenain, L., Statom, N. M., and Melville, W. K. (2013). Development and testing of instrumentation for UAV-based flux measurements within terrestrial and marine atmospheric boundary layers. *J. Atmos. Ocean. Technol.* 30, 1295–1319. doi: 10.1175/jtech-d-12-00176.1
- Ribas-Ribas, M., Mustafa, N. I. H., Rahlf, J., Stolle, C., and Wurl, O. (2017). Sea Surface scanner (S3): a catamaran for high-resolution measurements of biogeochemical properties of the sea surface microlayer. *J. Atmos. Ocean. Technol.* 34, 1433–1448. doi: 10.1175/jtech-d-17-0017.1

- Shang, S., Lee, Z., Lin, G., Hu, C., Shi, L., Zhang, Y., et al. (2017). Sensing an intense phytoplankton bloom in the western Taiwan Strait from radiometric measurements on a UAV. *Remote Sens. Environ.* 198, 85–94. doi: 10.1016/j.rse.2017.05.036
- Sun, J., Vandemark, D., Mahrt, L., Vickers, D., Crawford, T. L., and Vogel, C. (2001). Momentum transfer over the coastal zone. *J. Geophys. Res. Atmos.* 106, 437–412.
- Williams, G. D., Fraser, A. D., Lucieer, A., Turner, D., Cougnon, E., Kimball, P., et al. (2016). Drones in a cold climate. *EOS Trans. Am. Geophys. Union* 97, 245–246. doi: 10.1029/2016EO043673
- Wurl, O., Bird, K., Cunliffe, M., Landing, W. M., Miller, U., Mustaffa, N. I. H., et al. (2018). Warming and inhibition of Salinization at the Ocean's surface by cyanobacteria. *Geophys. Res. Lett.* 45, 4230–4237. doi: 10.1029/2018GL077946
- Zappa, C. J., and Jessup, A. T. (2004). "Variability of ocean skin temperature from airborne infrared imagery during CBLAST-Low," in *Proceedings of the 16th Symposium on Boundary Layers and Turbulence*, Portland, MA.
- Zappa, C. J., and Jessup, A. T. (2005). High resolution airborne infrared measurements of ocean skin temperature. *Geosci. Remote Sens. Lett.* 2, 146–150. doi: 10.1109/LGRS.2004.841629
- Zhou, G. (2009). Near real-time orthorectification and mosaic of small UAV Video flow for time-critical event response. *IEEE Trans. Geosci. Remote Sens.* 47, 739–747. doi: 10.1109/TGRS.2008.2006505

Conflict of Interest: AF is employed by L3 Latitude, the company hired by Lamont-Doherty Earth Observatory of Columbia University to operate the UAVs, and he contributed general technical expertise about UAV systems.

The remaining authors declare that the research was conducted in the absence of any commercial or financial relationships that could be construed as a potential conflict of interest.

Copyright © 2020 Zappa, Brown, Laxague, Dhakal, Harris, Farber and Subramaniam. This is an open-access article distributed under the terms of the Creative Commons Attribution License (CC BY). The use, distribution or reproduction in other forums is permitted, provided the original author(s) and the copyright owner(s) are credited and that the original publication in this journal is cited, in accordance with accepted academic practice. No use, distribution or reproduction is permitted which does not comply with these terms.



Remote Sensing of Natural Waters Using a Multichannel, Lidar-Compatible Raman Spectrometer and Blue Excitation

Andréa de Lima Ribeiro* and Helen Pask

Department of Physics and Astronomy, MQ Photonics Research Centre, Macquarie University, Sydney, NSW, Australia

OPEN ACCESS

Edited by:

Leonard Pace,
Schmidt Ocean Institute,
United States

Reviewed by:

Atsushi Matsuoka,
Laval University, Canada
Cédric Jamet,
UMR8187 Laboratoire d'océanologie
et de géosciences (LOG), France

*Correspondence:

Andréa de Lima Ribeiro
andrea.delimaribeiro@mq.edu.au

Specialty section:

This article was submitted to
Ocean Observation,
a section of the journal
Frontiers in Marine Science

Received: 03 June 2019

Accepted: 22 January 2020

Published: 14 February 2020

Citation:

de Lima Ribeiro A and Pask H (2020)
Remote Sensing of Natural Waters
Using a Multichannel,
Lidar-Compatible Raman
Spectrometer and Blue Excitation.
Front. Mar. Sci. 7:43.
doi: 10.3389/fmars.2020.00043

The design and operation of a custom-built LIDAR-compatible, four-channel Raman spectrometer integrated to a 473 nm pulsed laser is presented. The multichannel design allowed for simultaneous collection of Raman photons at spectral regions identified as highly sensitive to changes in water temperature. Four independent temperature markers were calculated for ultrapure (Milli-Q) and natural water samples [two-color(||), two-color(\perp), depolarisation(A), and depolarisation(B)]. Temperature accuracies of up to $\pm 0.5^\circ\text{C}$ were achieved for both water types when predicted by two-color(||) markers. Multiple linear regression models were constructed considering all simultaneously acquired temperature markers, resulting in improved accuracies of up to $\pm 0.2^\circ\text{C}$. The potential benefits of blue laser excitation in relation to avoiding overlap between the Raman signal and fluorescence by chlorophyll-a are discussed, along with the higher Raman returns anticipated compared to the more-conventional green laser excitation.

Keywords: raman spectroscopy, remote sensing, water temperature, LIDAR, blue excitation

INTRODUCTION

Temperatures on our planet have increased at concerning rates following the industrial developments from the 19th and 20th centuries due to changes in Earth's radiative balance (IPCC, 2014), an equilibrium relationship between how much of the heat received by our planet can be either re-emitted back to space or absorbed by the planet's heat sinks, such as the oceans. The oceans act as massive thermal reservoirs due to the high specific heat capacity of water, demanding large amounts of heat in order to change its temperature. Increased greenhouse gases emissions from industrial and agricultural activities have reduced the amount of radiation re-emitted by the Earth, generating a radiation unbalance which needs to be compensated by increased heat absorption by the heat sinks. Recent discussions regarding climate changes brought public awareness to the consequences of this thermal unbalance, leading to increased temperatures, thermal expansion of water and sea level rise at coastal areas directly impacting human activities. In a world undergoing accelerated climate changes, measuring water temperatures is essential for risk assessment and continuously monitoring oceanic and coastal zones.

Water temperature information can be assessed by traditional and remote sensing methods. Traditional *in situ* methods such as thermometers, CTDs and buoys have been broadly used in oceanographic investigations, collecting highly accurate depth-resolved temperature data; however, they are restricted to providing non-continuous information from sampling stations, present high costs associated with data acquisition and processing and are not compatible with time and space

scales of many processes occurring at oceanic and coastal zones (Dickey, 2002). As an alternative when traditional methods are not compatible with the scales being studied, researchers rely on remote sensing tools to collect information from the environment.

Remote sensing techniques retrieve information from a target without direct interaction with the object under investigation. In oceanography, it involves the study of the oceans, the atmosphere and their interactions by analyzing electromagnetic radiation emitted by these media. Satellite sensors and LIDAR methods (Light Detection and Ranging) are the most conventional remote sensing techniques for studying the oceans (Rees, 2001; Solan et al., 2003).

Satellite sensors, such as AVHRRs (Advanced Very High Resolution Radiometers) collect infrared signal passively emitted by the first micrometers of water column, exhibiting accuracies for temperature measurements up to $\pm 0.1^\circ\text{C}$ and typical spatial resolution of 4 km. However, the accuracy and periodicity of AVHRR measurements are compromised by the presence of clouds and require several atmospheric corrections, as the infrared signal is absorbed by water vapor, carbon dioxide and methane present in the atmosphere (Breschi et al., 1992; Soloviev and Lukas, 2014). Recently, (Brewin et al., 2017) compared sea surface temperature acquired by AVHRR sensors with *in situ* reference measurements performed by buoys and surfers along the UK coast, finding discrepancies from ± 0.4 to $\pm 0.6^\circ\text{C}$ for measurements on offshore sites and from ± 1.0 to $\pm 2.0^\circ\text{C}$ for coastal stations. This indicates that, additionally to not providing depth-resolved information, infrared satellite temperature predictions may vary substantially from real values at coastal zones.

The evolution of operational oceanography and the increasing need for new tools to validate satellite data and fast vertical profiling of aquatic environments led to the development of a new class of remote sensing techniques, known as LIDAR. Active LIDAR systems comprise (1) a pulsed light source in the visible or near-infrared range; and (2) fast detectors allowing for time-resolved signal collection. As the excitation light is transmitted in water, it interacts with water molecules and other active optical constituents, with a fraction of the incident photons being scattered back to the surface (backscattered signal). The interpretation of the backscattered, time-resolved, signal enables assessment of water bulk characteristics and systematic bathymetric mapping in coastal areas (Gordon, 1982; Churnside, 2008).

In 1979 a scientific seminar was organized to discuss the use of LIDAR methods for monitoring the oceans, and consideration was given to the use of several spectroscopic techniques for measuring water temperature, such as Raman spectroscopy (Gordon, 1980). Raman spectroscopy is a technique based on the inelastic scattering of an incident photon, usually from a laser source, such that scattered photons exhibit lower (Stokes) or higher (anti-Stokes) frequencies, corresponding to the natural frequencies of vibrational modes in the scattering media. Liquid water is a substance governed by hydrogen-bonding processes, exhibiting a tetrahedral structure with several intra and intermolecular Raman-active modes (Carey

and Korenowski, 1998). The water Raman spectrum exhibits temperature-dependent behavior, firstly identified by the authors of Walrafen et al. (1986), which can be clearly seen at the spectral region known as OH stretching band. For pure water, the OH stretching band is located between 2,900 and 3,900 cm^{-1} and includes a temperature-insensitive point known as the isosbestic point. The polarization properties of Raman-scattered photons are also temperature-dependent (Whiteman et al., 1999).

As a consequence of the temperature-dependent behavior found for unpolarized and polarized components of the water Raman spectra, there exist Raman temperature markers: ratios calculated from signals at distinct spectral positions whose values vary linearly with water temperature (hereafter referred to as “markers”). These markers can be calculated from Raman signals having the same polarization state and are known as “two-color” ratios, or from the number of photons having perpendicular/parallel polarization, referred to as “depolarisation” ratios. These ratios form the basis for numerous studies undertaken from the 1970s until the present time, aimed at using Raman spectroscopy to remotely determine water temperature (Chang and Young, 1972; Leonard et al., 1979; Leonard and Caputo, 1983; Artlett and Pask, 2015). When used in combination with LIDAR methods, there exists great potential to obtain depth-resolved measurements of subsurface water temperature. Such a capability would address currently un-met needs of modern oceanography and is, in principle, compatible with airborne, surface or underwater platforms. The over-arching goals of our research project, of which this paper is a part, is to develop a straightforward instrumentation that could be used to determine subsurface water temperature with accuracy $\leq \pm 0.5^\circ\text{C}$, depth resolution $\leq 0.5\text{ m}$ in near-real time.

In (Artlett and Pask, 2015) accuracies of $\pm 0.1^\circ\text{C}$ were reported for water temperature measurements performed in the laboratory using a commercial dispersive Raman spectrometer (Enwave-EZRaman I), incorporating a 532 nm, continuous wave, excitation laser. That work utilized unpolarized Raman spectra, two-color markers, and Reverse-Osmosis laboratory water. When trying to conduct the same analysis for temperature predictions in natural waters, we found substantially lower accuracies, which we attributed to the overlapping of the Raman peak for 532 nm excitation and fluorescence signals (de Lima Ribeiro et al., 2019a). The commercial dispersive Raman spectrometer (RS) used in Artlett and Pask (2015) and de Lima Ribeiro et al. (2019a) did not fulfill LIDAR-compatibility requirements and, in order to transition from commercial equipment toward LIDAR-compatible technologies, we designed and assembled a LIDAR-compatible multichannel RS integrated to a 532 nm pulsed excitation laser (de Lima Ribeiro et al., 2019b). The equipment allowed for simultaneous Raman signal collection in four spectral channels, and two-color and depolarisation markers were estimated for ultrapure (Milli-Q) and natural water sample, achieving best accuracies of $\pm 0.3^\circ\text{C}$ in both cases. The simultaneous Raman signal collection enabled the Linear Combination (LC) methods to be used; these enabled temperatures to be predicted based on all four temperature markers.

The complexities of working with Raman spectroscopy in natural waters include laser-induced fluorescence arising from optically-active constituents and overlapping of these signals with the water Raman peak (James et al., 1999; Lin, 1999, 2001). These issues are particularly concerning when using 532 nm (green) excitation as the water Raman peak overlaps with fluorescence from Chlorophyll-a (Chl-a), compromising the accuracy of temperature predictions. The authors of James et al. (1999) and Lin (1999, 2001) recommended using shorter wavelengths for excitation, such as blue light around 480 nm in order to avoid overlapping with the broad Chl-a fluorescence band, which is centered around 680 nm. For comparative purposes, the water Raman peak (OH stretching band) lies between 550 and 575 nm when excited by blue light at 473 nm, and between 635 and 660 nm when excited by green light at 532 nm. **Figure 1** shows our measured Raman spectra for milli-Q water at various temperatures, when using (a) blue and (b) green laser excitation. Note the differences in shape are due to different spectral resolutions for the two measurements (the spectra in **Figure 1A** are not fully resolved). Nevertheless, the temperature dependent behavior is clear in both cases.

Blue excitation light has not been widely used for Raman remote sensing of water temperature, and most oceanographic LIDAR methods for bathymetric measurements employ green excitation at 532 nm. Nevertheless, the use of blue lasers would be beneficial for LIDAR implementations in natural waters for the following reasons: (1) avoiding direct overlapping between the Raman peak and fluorescence from Chl-a at 680 nm (James et al., 1999; Lin, 2001); (2) Blue light has high transmission in most coastal and oceanic waters, achieving higher depths than green light (Jerlov, 1968); (3) the Raman cross-section of liquid water is inversely proportional to the wavelength of Stokes-shifted photons (Faris and Copeland, 1997); (4) wavelengths for Raman shifted photons generated by blue excitation are in the green range, undergoing lower transmission losses for returned Raman photons around 560 nm (for blue excitation) than 650 nm (for green excitation). Despite being effective in avoiding overlap with the Chl-a fluorescence peak, Raman signals scattered from blue excitation are more susceptible to overlap with DOM fluorescence. Accordingly, it is necessary to evaluate which excitation wavelength will be less likely to overlap with fluorescence from natural water constituents and provide better accuracy for Raman temperature predictions.

In this work we present a multichannel, LIDAR-compatible Raman spectrometer (RS) integrated to a 473 nm (blue) pulsed laser which is used to determine the temperature of small volumes (cuvettes) of ultrapure and natural samples. We have evaluated the effectiveness of the two-color and depolarisation temperature markers, each of which is calculated from spectral channels acquired simultaneously by the RS, in terms of sensitivity to temperature change, % error in the markers and the accuracy with which temperature can be predicted. Finally, we explore the relative merits of using blue vs. green laser excitation, with a view to understanding which source might ultimately be best for use in field measurements. This is firstly in terms of comparing the measured accuracies with those reported in de Lima Ribeiro et al. (2019b) using green excitation. Second, we use

simple LIDAR equations to estimate the relative Raman returns for the cases of blue and green excitation.

METHODS AND ANALYSIS

Spectrometer Design

The experimental setup for our multichannel LIDAR-compatible Raman spectrometer using a 473 nm laser is shown in **Figure 2** (hereafter this will be referred as “blue multichannel RS”). Milli-Q (ultrapure) and natural water samples collected at a location inside Sydney Harbor were placed inside a temperature-controlled cuvette holder (QNW QPod2e, accuracy of $\pm 0.2^\circ\text{C}$) and their temperature was varied from 18 to 40°C , stepping every 2°C . For natural water samples, Raman signals were acquired within a few hours of collection. Blue light produced by a linearly-polarized 473 nm pulsed laser (Nd:YAG, 5 μJ per pulse, 1.5 ns at FWHM, 5 kHz repetition rate) was collimated by lenses and coupled into the samples via a Dichroic Mirror (DM, Semrock Di02-R488, $R \sim 94\%$ from 471 to 491 nm, $T \sim 93\%$ between 499.8 and 900 nm). Raman-scattered photons passed through a Long Pass filter (LP, Semrock BLP01-473R, $T \sim 93\%$ between 486 and 900 nm) in order to eliminate Rayleigh scattering, and were split into 2 beams by means of a 50/50 Beam Splitter Cube (BSC). Each beam then passed through a Band Pass filter: BP_{low}^{561} acquiring photons at the low shift end (Semrock FF01-561/4, central wavelength at 561 nm and band pass of 8 nm at the FWHM) and BP_{high}^{568} acquiring Raman photons at the high shift end (Semrock LL01-568, central wavelength of 568 nm and band pass of 4 nm at the FWHM). The choice of BP filters was constrained by commercial availability, and the pass band for each of these filters is indicated in **Figure 3**. In units of wavenumbers, the spectral widths at the FWHM were 254 cm^{-1} for the low shift channel and 136 cm^{-1} for the high shift channel.

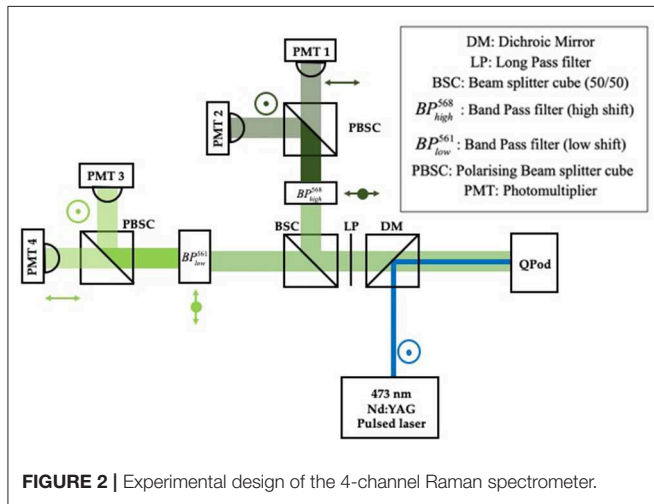
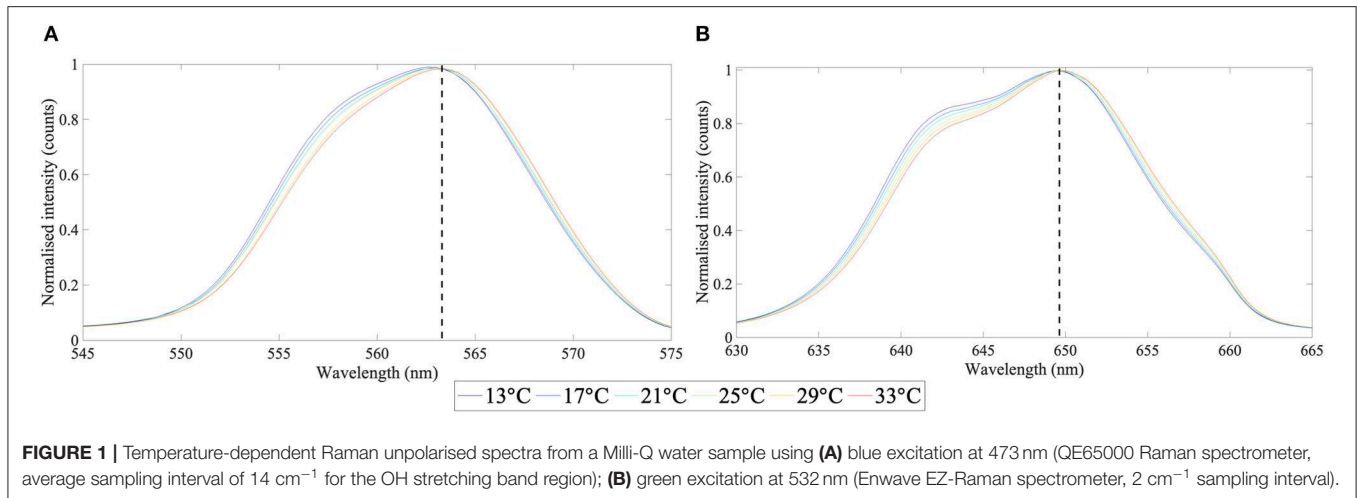
After passing through the BP filters, each beam was divided into two polarized components by a Polarizing Beam Splitter Cube (PBSC), which were finally focused by lenses ($f = 25\text{ mm}$) onto fast-response photomultipliers (PMT, Hamamatsu H10721-20). The PMT gains were set around 700 V, well-below the setting for maximum gain (900 V). Signals from each channel were registered by a four-channel oscilloscope (Tektronix DPO4104B), with averaging over 512 pulses.

In order to estimate signal-to-noise ratios (SNR), acquisitions were performed with and without excitation light, with averaging over 512 pulses. SNRs were calculated for each spectral channel according to Equation 1:

$$SNR = \frac{\int \text{Signal}_{(FWHM)}}{\int \text{Noise}_{(FWHM)}} \quad (1)$$

where $\int \text{Signal}_{(FWHM)}$ represents the integrated Raman signal pulse around the full width of half maximum (FWHM); and $\int \text{Noise}_{(FWHM)}$ refers to the integrated noise signals over the same time period.

Table 1 shows a list of information regarding each spectral channel of collection, including polarization state, band pass filter used, typical SNRs and the nomenclature which will be adopted in this paper.



Temperature Markers Calculations

Each average of 512 pulses acquired by the oscilloscope was integrated in Matlab (Mathworks, R2017b) using the trapezoid method over an approximate range of 2.0 ns around the FWHM, corresponding to 10 data points (Figure 4). Raman signals corresponding to those spectral channels were used to calculate four types of temperature markers, according to Equations 2–5.

$$Two - color(\parallel) = \frac{I_{\parallel}^{high}}{I_{\parallel}^{low}} \quad (2)$$

$$Two - color(\perp) = \frac{I_{\perp}^{high}}{I_{\perp}^{low}} \quad (3)$$

$$Depolarisation(A) = \frac{I_{\perp}^{high}}{I_{\parallel}^{low}} \quad (4)$$

$$Depolarisation(B) = \frac{I_{\perp}^{low}}{I_{\parallel}^{high}} \quad (5)$$

where I_{pol}^{xxx} indicates the intensity of Raman signal at a certain channel (high/low) on a given polarization state.

For each water sample, three independent acquisitions were performed for each temperature, hence three sets of two-color and depolarisation markers could be calculated for each temperature. Aiming to increase robustness, the markers calculated from the independent acquisitions were averaged, giving origin to a new (fourth) dataset for each temperature marker hereafter referred as the “average markers dataset.” In order to determine the uncertainties in the temperature markers, percentage errors (%) were estimated by adding the percentage uncertainties associated with SNRs calculated for each channel used in the marker calculation.

Marker Sensitivity to Temperature

Sensitivities, i.e., the % change in a marker per $^{\circ}\text{C}$, were estimated for markers calculated for each water sample. As outlined in Artlett and Pask (2015) the use of mean-scaled temperature markers is most useful for sensitivity calculations. Those are determined by scaling each marker by the mean value of all markers within a set of temperature measurements (Equation 6). The linear model generated from the relationship between mean-scaled markers and reference temperatures provided the information necessary to estimate sensitivities for each water sample.

$$\text{Mean - scaled markers sensitivity} = \frac{d(\text{marker})}{dT} \frac{1}{\text{mean}(\text{marker})} \quad (6)$$

Predicting Temperature Using a Single Marker

In keeping with previous studies (Artlett and Pask, 2015, 2017; de Lima Ribeiro et al., 2019b), the relationships between temperature markers and reference temperatures are found to be linear, allowing for the use of linear regression models with coefficients gradient and intercept. These coefficients were then rearranged in order to calculate a new set of

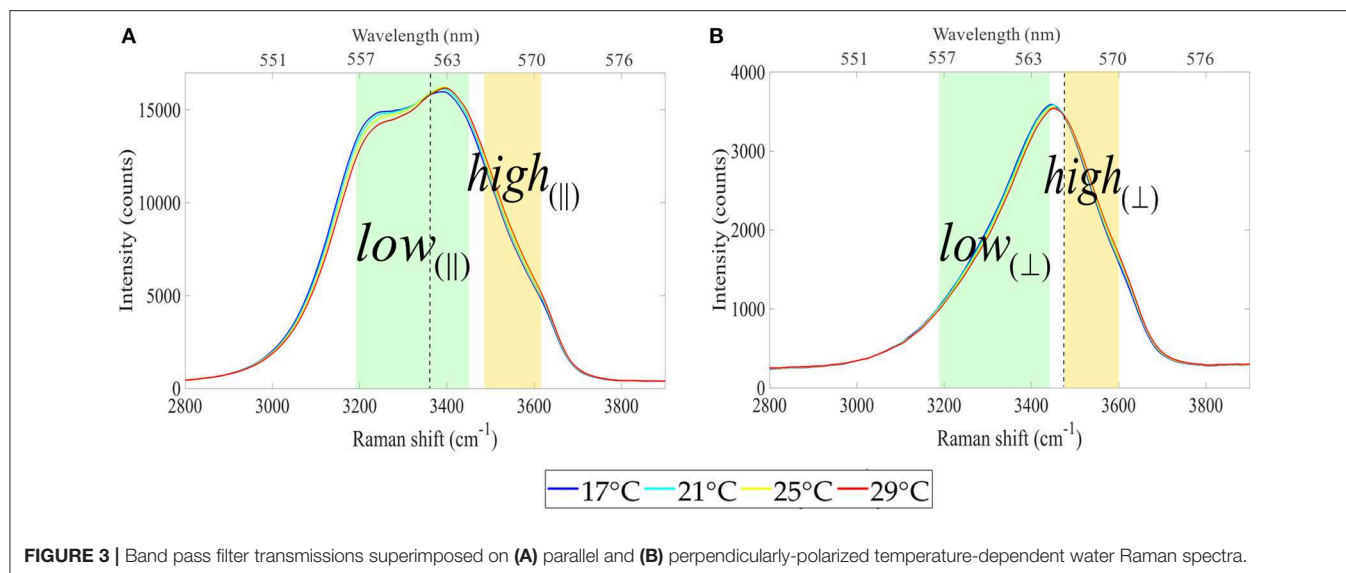


TABLE 1 | Nomenclature adopted for each spectral channel and typical SNRs.

Channel number	Polarization state	Band Pass filter	Nomenclature	Typical SNR
1	Parallel	BP_{high}^{568}	I_{high}^{\parallel}	6,221
2	Perpendicular	BP_{high}^{568}	I_{high}^{\perp}	1,749
3	Perpendicular	BP_{low}^{561}	I_{low}^{\perp}	3,255
4	Parallel	BP_{low}^{561}	I_{low}^{\parallel}	4,533

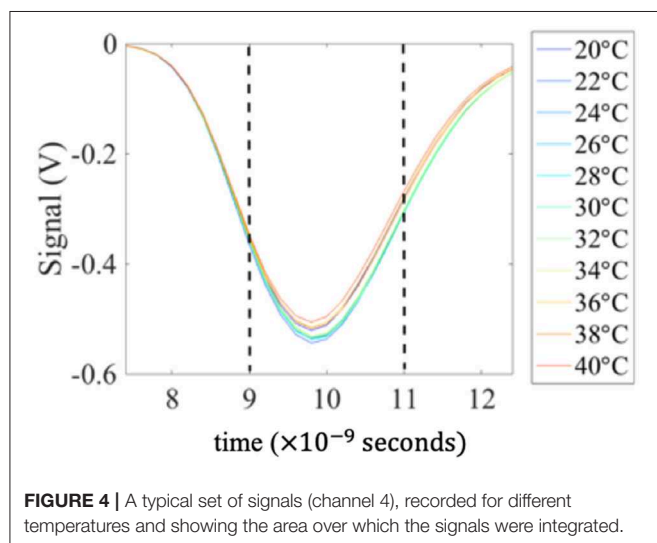


FIGURE 4 | A typical set of signals (channel 4), recorded for different temperatures and showing the area over which the signals were integrated.

temperatures dependent on the markers, hereafter called “predicted temperatures” (Equation 7).

$$T_{predicted} = (\text{gradient} \times \text{marker}) + \text{intercept} \quad (7)$$

where $T_{predicted}$ represents the predicted temperature estimated by a temperature marker. RMSTE values ($\pm^\circ\text{C}$) were calculated for the predicted temperature in comparison with the reference temperature values and used as a measure of the accuracy of temperature determination by the various markers.

Linear Combination Methods: Enhancing Temperature Predictions

Our spectrometer design enabled signals to be collected from all spectral channels simultaneously, hence the four temperature markers described in Equations (2–5) each contain independent information about temperature. In de Lima Ribeiro et al. (2019b) we proposed and evaluated a multiple linear regression model, which we will call the linear combination (LC) method, combining all four markers into one model to enhance temperature predictions according to Equation 8.

$$T_{predicted} = \beta_0 + \beta_1 \times two - color(\parallel) + \beta_2 \times two - color(\perp) + \beta_3 \times depol(A) + \beta_4 \times depol(B) + \varepsilon \quad (8)$$

where β_0 is an independent term, β_1 – β_4 are calibration terms generated by the model and correlated with each marker and are the residual errors. LC models for the set of “average markers” were constructed for each sample analyzed in this paper.

RESULTS AND DISCUSSION

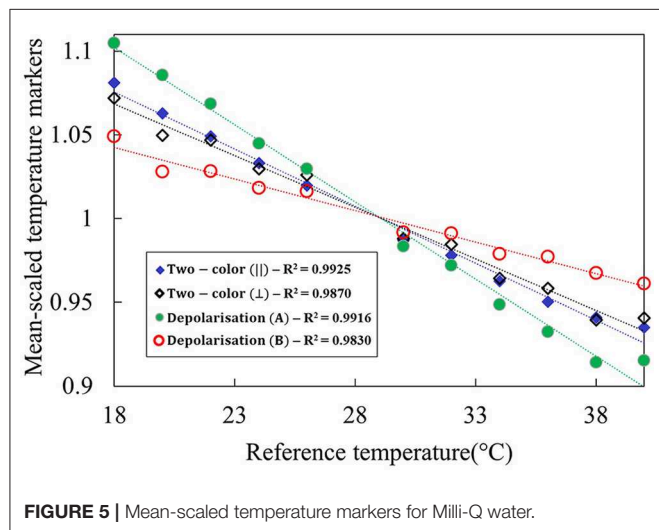
Milli-Q Water Analysis

In this section, we explore the temperature markers calculated from Raman signals retrieved by our blue multichannel RS for an ultrapure (Milli-Q) water sample. Specifically, we consider the accuracy of temperature predictions, markers sensitivities and % errors in the temperature markers. We consider that the Raman signals acquired from the ultrapure water sample are solely due to the interactions between the excitation light and water molecules

TABLE 2 | RMSTEs ($\pm^\circ\text{C}$), sensitivities (% change/ $^\circ\text{C}$), and absolute percentage errors in markers (%) for a Milli-Q water sample.

Temperature marker	Milli-Q water sample		
	RMSTE ($\pm^\circ\text{C}$)	Sensitivity (%/ $^\circ\text{C}$)	Marker % error (%)
Two-color() [Range]	0.5 [0.5–0.7]	0.68	0.04
Two-color(\perp) [Range]	0.7 [0.7–1.6]	0.62	0.12
Depolarisation(A) [Range]	0.5 [0.5–0.6]	0.92	0.09
Depolarisation(B) [Range]	3.2 [2.5–3.2]	0.38	0.07
Linear combination	0.3 [0.3–0.6]	-	-

Data in brackets is based on the analysis of four datasets; data without brackets is based on the "average markers" dataset. Refer to section Temperature Markers Calculations for details.

**FIGURE 5** | Mean-scaled temperature markers for Milli-Q water.

and will give rise to optimum performance of our RS. A summary with the main results found for ultrapure water analysis is shown in **Table 2**.

The mean-scaled value of each temperature marker is shown as a function of temperature in **Figure 5**. Their sensitivities extracted from the slope of each curve are summarized in **Table 2**.

Maximum sensitivities of 0.92%/°C were found for depolarisation(A) markers, significantly higher than the second best sensitivities found for two-color(||) (0.68%/°C). Additionally, these were the markers which exhibited lowest absolute % errors [0.04% for two-color(||) and 0.09% for depolarisation(A)] and the best RMSTEs of $\pm 0.5^\circ\text{C}$ were found for both markers. Sensitivity values were generally smaller than the 1%/°C reported by the authors of Chang and Young (1972) and Leonard and Caputo (1983), however, it is necessary to consider the impact of the spectral channels widths on the final sensitivities. The authors of Artlett and Pask (2015) evaluated the trade-offs between spectral channels and sensitivities by performing simulations with unpolarized Raman signals acquired from ultrapure (Reverse-Osmosis) water samples. The mean-scaled markers sensitivities calculated from two spectral channels of 250 cm^{-1} width exhibited values around 0.68%/°C; and sensitivities for channels widths around 150 cm^{-1} were

estimated to be around 1.03%/°C. Considering that the spectral channels used in our work had widths of 234 cm^{-1} and 137 cm^{-1} at the FWHM, the sensitivities found for both depolarisation(A) and two-color(||) markers were reasonably in agreement with the values proposed in Artlett and Pask (2015).

Two-color(\perp) and depolarisation(B) had inferior performance for all parameters analyzed, exhibiting lower sensitivities, higher absolute % errors and higher RMSTEs. This was particularly true for depolarisation(B) markers, with RMSTEs of $\pm 3.2^\circ\text{C}$, sensitivities of 0.38%/°C and % errors of 0.07%, indicating that the markers showed low efficiency when extracting temperature-dependent information from water Raman signals. LC methods resulted in an average improvement of 40% in RMSTEs for the Milli-Q water sample, showing it to be a valuable technique for enhancing accuracy of temperature prediction.

There is a lack of LIDAR-compatible studies in the Raman remote sensing of water temperature using blue lasers, restricting the discussion of the results from this article to comparisons with the reports of Leonard and Caputo (1983). In the occasion, the authors reported the use of a LIDAR-compatible custom-built RS integrated to a 470 nm laser (15 mJ per pulse, 2 kHz repetition rate) measuring water temperature in laboratory from depolarisation markers and finding accuracies of $\pm 0.5^\circ\text{C}$. These were the same accuracies found for our multichannel blue RS when measuring Milli-Q water temperature from depolarisation(A) information.

In de Lima Ribeiro et al. (2019b), we reported a multichannel LIDAR-compatible RS integrated to a 532 nm excitation laser (green) which configuration was similar to our multichannel LIDAR compatible RS integrated to a 473 nm laser (blue) presented in this work. The similarities between both systems include: (1) same number of collection channels; (2) simultaneous collection of both orthogonally-polarized components of the water Raman signal; (3) same methods of calculation for temperature markers. In de Lima Ribeiro et al. (2019b), RMSTEs as low as $\pm 0.4^\circ\text{C}$ were achieved for temperature predictions from two-color(||) markers, similar to the findings in this report ($\pm 0.5^\circ\text{C}$). Regarding sensitivities, maximum values for maximum sensitivity for the green multichannel RS were 0.68%/°C, whilst sensitivities for the blue multichannel RS reached values as high as 0.92%/°C. However, comparisons between RMSTEs and sensitivities achieved in this report and the findings in de Lima Ribeiro et al. (2019b) are limited by the following factors: (1) the laser power used for excitation in the abovementioned study was five times larger than the laser power used for excitation in this study; (2) channels widths for the green multichannel RS were twice as large as the channel widths used in the blue multichannel RS; and (3) there were differences in the central wavelength relative to the Raman spectra for the blue and green RS. Both RS, blue and green, allowed for temperature predictions equal or better than $\pm 0.5^\circ\text{C}$.

Natural Water Analyses

Natural water samples from Sydney Harbor were collected on various dates and analyzed with our blue multichannel RS. We start by acknowledging that comparisons between the results

obtained for the samples are somewhat limited, considering the presence of different (unquantified) concentration of optically active components in water for each natural sample. Our intention here was to use a range of authentic natural samples in our analyses rather than “fine-tune” our methods to one particular sample.

Accuracy of temperature predictions (RMSTEs), sensitivities and % errors in the temperature markers were calculated for each natural water sample and results for the fourth dataset (“average markers”) are summarized in **Table 3**. The range of RMSTEs found for all datasets (1, 2, 3, and “average markers”) is also indicated in the table.

We start by analyzing the temperature sensitivity for each marker in natural waters. For two-color(\parallel), two-color(\perp) and depolarisation(A) markers, sensitivities from all natural samples were smaller or marginally greater than the ones found for ultrapure water (0.68%/°C, 0.62%/°C, and 0.92%/°C, respectively). This is in agreement with the findings reported in de Lima Ribeiro et al. (2019b), where lower sensitivities were reported in natural waters due to the fluorescence of optically active constituents. Here, the main purpose of using excitation at 473 nm was avoiding Chl-a fluorescence at 680 nm, as the water Raman peak for blue excitation lies around 560 nm. However, constituents other than Chl-a exhibit fluorescence peaks around 560 nm, including DOM and other photosynthetic pigments (James et al., 1999; Lin, 1999, 2001; de Lima Ribeiro et al., 2019a), and it is virtually impossible to avoid overlapping between the water Raman peak and all possible signal sources in natural waters. In de Lima Ribeiro et al. (2019b), the presence of Chl-a fluorescence signals overlapping with the water Raman signals excited by green light (532 nm) led to higher signal counts and consequent higher SNRs, and lower % errors in the markers calculated for all-natural water sample. The same pattern was not so clearly identified in all natural water samples analyzed in the present study using blue excitation, indicating that signal counts were generally less impacted by the presence of fluorescence when using blue excitation. Comparisons between both studies, however, are limited due to the use of different natural water samples which will have particular optical characteristics. To allow for full comparison and reasoning regarding fluorescence impact in total signals, further investigations could be conducted in the future where the same natural sample is analyzed by both green (532 nm) and blue (473 nm) Raman spectrometers.

RMSTE values varied from $\pm 0.5^\circ\text{C}$ [two-color(\parallel), natural sample 4)] to $\pm 7.1^\circ\text{C}$ [depolarisation(B), natural water sample 1]. The two-color(\parallel) marker consistently delivered the best RMSTEs (± 0.5 to $\pm 0.7^\circ\text{C}$) for all samples. Next was the depolarisation(A) marker, which delivered RMSTEs ranging from ± 0.7 to $\pm 1.3^\circ\text{C}$. These were also the markers with highest temperature sensitivities found in this investigation. Depolarisation(B) exhibited consistent poor accuracies when predicting water temperature (RMSTEs higher than $\pm 2.2^\circ\text{C}$) and was also the marker with lowest sensitivities in all water samples. This indicates that the temperature marker is not effectively extracting temperature information from Raman signals, and its use should be re-evaluated in future investigations.

The LC analyses resulted in average improvements in temperature accuracies of 47% when compared to the best RMSTE obtained using a single marker. Final accuracies after the LC method were equal or better than $\pm 0.5^\circ\text{C}$ for all natural water samples under investigation, indicating the method was effective extracting meaningful temperature-dependent information from multiple markers.

Considering the Relative Merits of Spectrometers Using Blue and Green Excitation

The design of our multichannel LIDAR-compatible RS using blue excitation is conceptually similar to the RS reported in de Lima Ribeiro et al. (2019b), which used a green excitation laser. In practice, the two excitation lasers differed, most notably in pulse energy, and the band pass filters defining the spectral channels also differed in regard to their width and their positions relative to the Raman band. In this section we compare the prospects for predicting water temperature using blue and green excitation, and we also evaluate the potential benefits that blue excitation might have when combined with LIDAR depth-resolved measurements. **Table 4** summarizes the key characteristics of the blue and green excitation lasers used here and in de Lima Ribeiro et al. (2019b), respectively, along with the corresponding channel width, center positions and wavelength bands, as well as the key findings for temperature prediction in Milli-Q water and in natural waters.

We start our comparison by analyzing the accuracies achieved by each equipment measuring natural water temperature in the laboratory. Predictions performed by the green multichannel RS exhibited maximum accuracy of $\pm 0.4^\circ\text{C}$, marginally higher than the RMSTEs achieved by the blue multichannel RS ($\pm 0.5^\circ\text{C}$). In both cases, these accuracies were achieved by temperature predictions using two-color(\parallel) markers. Linear combination methods were effective in predicting temperature more accurately for both setups, with final accuracies of $\pm 0.2^\circ\text{C}$ being found for the blue RS and $\pm 0.3^\circ\text{C}$ for the green RS. These are the maximum accuracies ever reported for LIDAR-compatible Raman spectrometers predicting natural waters temperatures.

The key factors affecting RMSTEs are the intrinsic dependence of Raman spectra on temperature, and the errors and uncertainties associated with its measurement. In Milli-Q water, the measured sensitivities for the various markers reflect this dependence, plus the positions and widths of the spectral channels. According to simulations performed by Artlett and Pask (2015) for ultrapure (Reverse-Osmosis) water, an optimum trade-off between Raman signals strength and RMSTEs would be obtained for acquisition channels with spectral widths of around 200 cm^{-1} . Optimum spectral positions for such channels were explored using simulations in Artlett and Pask (2017), with the “low shift” channel central position at $3,200\text{ cm}^{-1}$ and the “high shift” channel central position at $3,600\text{ cm}^{-1}$. The availability of commercial Band Pass filters within these conditions is extremely limited, therefore the differences between spectral widths for channels collecting signals in the blue (254 and 136 cm^{-1})

TABLE 3 | RMSTEs ($\pm^{\circ}\text{C}$), sensitivities (% change/ $^{\circ}\text{C}$), and absolute percentage errors in markers (%) for natural water sample analyzed by two-color and depolarisation markers.

		Temperature markers				
		Two-color(I)	Two-color(L)	Depol(A)	Depol(B)	LC
Natural 1	RMSTE ($\pm^{\circ}\text{C}$)	0.70	1.50	1.30	7.20	0.4 [0.4–0.7]
	[Range]	[0.70–0.80]	[1.50–1.60]	[1.20–1.70]	[4.70–7.20]	
	Sensitivity (%/ $^{\circ}\text{C}$)	0.71	0.42	0.71	0.42	-
Natural 2	Marker % error (%)	0.05	0.12	0.42	0.07	-
	RMSTE ($\pm^{\circ}\text{C}$)	0.70	1.20	1.30	2.30	0.5 [0.5–0.7]
	[Range]	[0.70–1.0]	[1.20–2.0]	[1.10–1.70]	[2.30–5.60]	
Natural 3	Sensitivity (%/ $^{\circ}\text{C}$)	0.62	0.50	0.74	0.38	-
	Marker % error (%)	0.04	0.74	0.09	0.06	-
	RMSTE ($\pm^{\circ}\text{C}$)	0.70	0.90	0.80	4.90	0.3 [0.3–0.8]
Natural 4	[Range]	[0.50–1.10]	[0.90–1.50]	[0.80–1.00]	[3.70–5.6]	
	Sensitivity (%/ $^{\circ}\text{C}$)	0.71	0.51	0.85	0.38	-
	Marker % error (%)	0.03	0.09	0.09	0.06	-
Natural 4	RMSTE ($\pm^{\circ}\text{C}$)	0.50	0.80	0.70	2.20	0.2 [0.2–0.7]
	[Range]	[0.50–0.8]	[0.80–1.30]	[0.70–1.20]	[1.20–3.70]	
	Sensitivity (%/ $^{\circ}\text{C}$)	0.60	0.54	0.70	0.44	-
	Marker % error (%)	0.05	0.15	0.11	0.09	-

Data in brackets is based on the analysis of four datasets; data without brackets is based on the “average markers” dataset. Refer to section Temperature Markers Calculations for details.

and green (315 and 463 cm^{-1}) setups. Higher sensitivities for both setups were found for depolarisation(A) markers calculated from Raman signals scattered by Milli-Q water samples, with sensitivities of 0.92%/°C found in the blue setup and 0.59%/°C in the green. These values found in both setups are in agreement with was proposed by the simulations in Artlett and Pask (2015).

The errors and uncertainties associated with measurements performed on Milli-Q water originate from the SNR for each channel, and here the 5-times higher pulse energy of the green excitation laser, the higher Raman cross-section for blue excitation (Faris and Copeland, 1997) and the characteristics of the band pass filters all contribute. As can be seen in Table 4, despite the significant differences between the blue and green RS, the RMSTEs are remarkably similar for both cases. When it comes to natural waters, we can expect fluorescence signals arising from optically-active constituents such as DOM and photosynthetic pigments compromising the achievable RMSTE to some extent. As discussed earlier, the overlapping between the water Raman peak for this excitation and the chlorophyll-a peak at 680 nm is inevitable, reducing the accuracies that could be achieved by Raman signal analyses. Conversely, Raman photons from blue excitation have green wavelengths (550–575 nm), which exhibit good vertical transmission in water and do not overlap with the Chl-a peak; however, they are susceptible to other interactions with optically active constituents in water, such as DOM and phytoplankton.

The overlapping between the Raman peak for blue excitation and fluorescence from DOM has been previously assessed by other researchers (Dolenko et al., 2011; Vervald et al., 2015), who used Artificial Neural Networks (ANN) to solve for DOM fluorescence in water Raman spectra. The authors of Dolenko

et al. (2011) created a database of Raman spectra excited by a blue laser (488 nm) acquired from water samples at different temperatures, salinities and DOM concentrations, which was used as reference by the ANN model. In the occasion, accuracies of $\pm 0.8^{\circ}\text{C}$ were achieved for water temperature determination, and the model was able to neglect the overlapping between DOM and Raman peaks. Later, the authors of Vervald et al. (2015) conducted laboratory investigations of natural water samples using the same ANN model, achieving accuracies of up to $\pm 0.1^{\circ}\text{C}$. It is clear that ANN models are capable of minimizing the effect of the overlap between DOM fluorescence and Raman peaks acquired with blue excitation; however, this approach requires complex data manipulation and is not compatible with rapid, LIDAR methods. In de Lima Ribeiro et al. (2019a) we proposed a new technique for minimizing spectral baselines arising from fluorescence in natural waters named “correction by temperature markers.” In this method, Raman two-color markers are calculated for a “standard” water sample (i.e., a water sample without optically active constituents interacting with the excitation light) and compared with Raman markers calculated for same temperature from signals scattered by natural waters. The premise of the method is that the differences between the markers values are due to fluorescence from natural water constituents, and accuracies of up to $\pm 0.2^{\circ}\text{C}$ were achieved for temperature predictions in natural waters after the correction.

When it comes to considering the best excitation wavelength for combining our RS with LIDAR methods, there are additional facts to take into account. The number of Raman photons generated at a depth z and reaching the surface, $N_{\text{Raman}}(z)$ can be described by Equation 9, which is based and adapted from theory presented in

TABLE 4 | Technical overview of two multichannel LIDAR-compatible RS integrated to 473 nm (blue) and 532 nm (green) excitation lasers.

	Blue multichannel RS	Green multichannel RS [de Lima Ribeiro et al., 2019b]
Excitation wavelength (nm)	473	532
Laser energy (μJ/pulse)	5	25
Pulse duration at FWHM (ns)	1.5	0.9
Wavelength of Raman photons (nm)	550–575	630–660
Spectral channel widths (cm ⁻¹)	254	315
	136	463
Milli-q water		
Best sensitivity (%/°C) [marker]	0.92 [depolarisation(A)]	0.68 [depolarisation(A)]
Best RMSTE (±°C) [marker]	0.5 [Two-color(III)]	0.4 [Two-color(III)]
RMSTE (LC)	0.3	0.3
Natural water samples		
Best sensitivity (%/°C) [marker]	0.85 [depolarisation(A)]	0.59 [depolarisation(A)]
Best RMSTE (±°C) [marker]	0.5 [Two-color(III)]	0.4 [Two-color(III)]
RMSTE (LC)	0.2	0.3

Data in brackets is based on the analysis of 4 datasets; data without brackets is based on the “average markers” dataset. Refer to section Temperature Markers Calculations for details.

Leonard et al. (1979). For simplicity, we have overlooked Fresnel reflections into and out of the water and assumed solid angles of collection sufficiently small so that the Raman photons reach the surface at near-normal angles of incidence.

$$N_{Raman}(z) = N_{laser}(z) N_{scat}(z) \sigma_{Raman} \Delta R \frac{\Omega(z)}{n^2} T_{\lambda 1}(z) T_{\lambda 2}(z) \quad (9)$$

where $N_{laser}(z)$ is the number of excitation laser photons at a given depth (z);

N_{scat} is the density of water molecules interacting with the excitation light (molecules/m³);

σ_{Raman} is the Raman scattering cross-section per molecule per steradian (m²/molecule sr);

R is the minimum vertical range resolution, determined by the laser pulse duration (m);

$\Omega(z)$ is the solid angle of collection, dependent on the diameter of the telescope or other collection optics used (steradians) at a given depth;

n is the refractive index of seawater;

$T_{\lambda 1}(z)$ and $T_{\lambda 2}(z)$ are, respectively, the vertical transmission values for the excitation and Raman wavelengths in water (m⁻¹). These are functions of $T_{\lambda} = e^{-K_d z}$, where $K_d(\lambda)$ is the diffuse attenuation coefficient for light in water.

Modeling retrieval of Raman photons requires knowledge about the transmitter and receiver geometries and is beyond the scope of this paper. Here our purpose is to explore the relative benefit of using blue excitation, compared to green excitation. It is relatively straightforward to estimate the ratio of the expected Raman returns using blue or green excitation by considering only the terms in Equation 9 that are wavelength-dependent. The ratio is calculated assuming same pulse energy and duration for both excitation wavelengths (Equation 10).

$$\frac{N_{Raman}^{473}(z)}{N_{Raman}^{532}(z)} = \frac{\lambda^{473} \sigma_{Raman}^{473} e^{-((K_d^{473} + K_d^{568})z)}}{\lambda^{532} \sigma_{Raman}^{532} e^{-((K_d^{532} + K_d^{660})z)}} \quad (10)$$

The top section of **Table 5** provides typical values for the key LIDAR parameters (N_{laser} , ΔR , N_{scat} , σ_{Raman}) and the wavelength-dependent parameters used to calculate Equation 10. The bottom section of **Table 5** gives the calculated 1% extinction depths for blue and green excitation and the correspondent Raman wavelengths. These are calculated for three Jerlov water types. Jerlov water type I represents oceanic clear waters, and coastal waters were represented by types 1C (clear coastal water) and 7C (turbid coastal water). Raman cross-sections (σ_{Raman}) were calculated according to Faris and Copeland (1997) for collection channels centered at 568 nm (for blue excitation) and 660 nm (for green excitation). These “high shift” channels were chosen because attenuation increases with increasing wavelength.

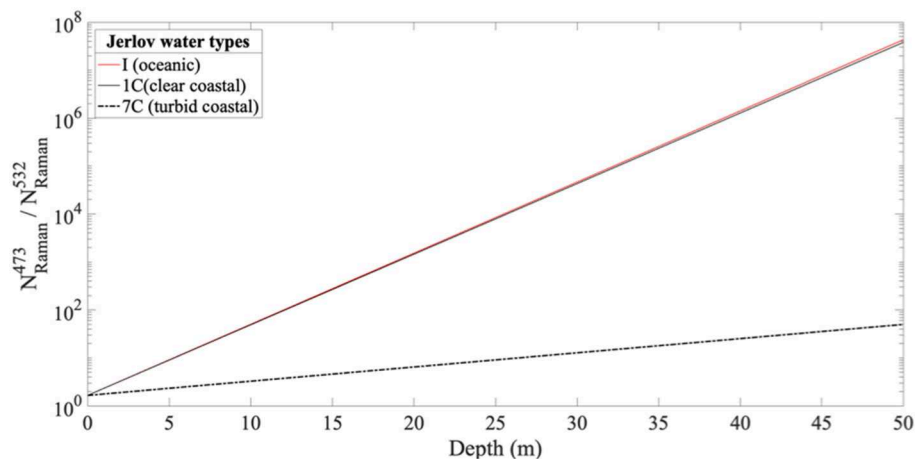
The transmissions of the excitation laser photons and returning Raman photons in the water column were estimated using the downwelling diffuse attenuation coefficient $K_d(\lambda)$. The values of $K_d(\lambda)$ for Jerlov water types I, 1C and 7C were obtained from Solonenko and Mobley (2015) and interpolated for the wavelengths of interest in our study.

The depths of extinction (1% of incident light) for excitation and Raman photons varied between different Jerlov water types. For excitation light, blue light exhibited better transmission in waters type I (oceanic clear) and 1C (coastal clear); in contrast, green light had better transmission in turbid coastal waters (type 7C) in comparison with blue. For Raman returns the depths of extinction of photons at 568 nm (for blue excitation) were always >660 nm (for green excitation). Bigger differences were found in type I (factor of 5), lesser differences in type 1C (factor of 3), and small differences in type 7C (factor of 2).

Figure 6 shows the ratio of expected Raman returns under blue vs. green excitation, as a function of depth. The ratio is always >1, due to the higher Raman cross-section when blue excitation is used (factor approaching two), and the ratio increases exponentially with increasing depth. Large and very similar ratios were calculated for types I and 1C, indicating big benefits to using blue excitation, mainly due to the combination of better excitation/Raman transmissions in water. The use of blue light, however, exhibited somewhat smaller advantages for type 7C, where the much higher transmission of Raman photons (568 vs. 660 nm) is offset by the higher transmission of green excitation

TABLE 5 | Input parameters for LIDAR modeling and outcomes for blue and green excitation lights in Jerlov water types I, 1C and 7C.

	Blue (473 nm)			Green (532 nm)		
N_{laser} (Photons/mJ)	2.38×10^{15}			1.34×10^{16}		
ΔR for typical 2 ns pulse (m)	0.5			0.5		
N_{scat} (molecules/m ³)	4.32×10^{20}			4.32×10^{20}		
σ_{Raman} (m ² /molecule sr)	9.62×10^{-30}			5.14×10^{-30}		
n	1.34			1.34		
Raman wavelength (nm)	568			660		
Coefficients of light attenuation in water (m ⁻¹)	I	1C	7C	I	1C	7C
K_d (excitation)	0.020936	0.141501	0.724552	0.056522	0.125776	0.454200
K_d (Raman)	0.067273	0.126629	0.363474	0.373014	0.481169	0.701930
Model outcomes						
Calculated 1% extinction depth for excitation laser (m)	>150	49	9.5	122.5	55	15
Calculated 1% extinction depth for Raman photons (m)	68.5	36.5	12.5	12.5	10	6.5

**FIGURE 6 |** The ratio given in Equation 10 is plotted as a function of depth (z) for Jerlov water types: oceanic type I, and coastal types 1C and 7C.

compared to blue. While this model is a rudimentary one, it clearly indicates the benefits of using blue excitation, predicting much greater Raman returns and therefore higher potential to determine subsurface water temperatures with reasonable accuracies. More sophisticated modeling would be required to calculate actual Raman returns and to predict the depth at which subsurface water temperature could be determined.

CONCLUSION

We have presented the design and performance of a custom-built multichannel Raman spectrometer integrated to a 473 nm pulsed laser, employing commercial optical filters to collect polarized Raman signals at spectral regions of interest

for the remote sensing of natural water temperature. Our spectrometer design is LIDAR-compatible and comprised of (1) a pulsed laser source with period ≤ 2 ns at the FWHM, to allow for depth resolutions better than 0.5 m; (2) collection of Raman signals at spectral regions highly sensitive to changes in temperature; (3) fast, sensitive detection by photomultipliers.

This was the first time that polarized Raman signals scattered from blue excitation (473 nm) were acquired in spectral channels for samples of natural waters and temperature was determined with accuracies as high as $\pm 0.5^\circ\text{C}$. The simultaneous acquisition of Raman signals in four channels at different polarization states and wavelength ranges allowed for calculation of different types of temperature markers. Two-color(||) (from parallel-polarized Raman

signals) and depolarisation(A) (calculated from signals of different polarization states) exhibited best performances when predicting water temperature, followed by two-color(\perp) and depolarisation(B). When all four markers were incorporated in the linear combination model, enhanced RMSTEs up to $\pm 0.2^\circ\text{C}$ were achieved. Those RMSTEs were similar to values reported in previous studies for green excitation (de Lima Ribeiro et al., 2019b).

Lastly, we have presented a simple model which predicts substantially higher Raman returns when blue excitation is used. The use of blue light is beneficial to our final goal of rapidly profiling the water column temperature by using a LIDAR-compatible system. The advantages over green light, traditionally used in oceanographic studies, include: (1) reduced spectral overlapping between Raman and fluorescence peak from chlorophyll-a at 680 nm; (2) higher Raman returns due to lower attenuation coefficients and higher Raman cross-sections.

Future work will entail field testing of the methodology presented in this paper. Particular focus needs to be given to implementing LIDAR to extract depth-resolved temperature information and strategies to mitigate the impact of fluorescence from optically active constituents.

REFERENCES

- Artlett, C. P., and Pask, H. M. (2015). Optical remote sensing of water temperature using Raman spectroscopy. *Opt. Express* 23:31844. doi: 10.1364/OE.23.031844
- Artlett, C. P., and Pask, H. M. (2017). New approach to remote sensing of temperature and salinity in natural water samples. *Opt. Express* 25:2840. doi: 10.1364/OE.25.002840
- Breschi, B., Cecchi, G., Pantani, L., Raimondi, V., Tirelli, D., and Valmori, G. (1992). Measurement of water column temperature by raman scattering. *EARSEL Adv. Remote Sens.* 1, 131–134.
- Brewin, R. J. W., de Mora, L., Billson, O., Jackson, T., Russell, P., Brewin, T. G., et al. (2017). Evaluating operational AVHRR sea surface temperature data at the coastline using surfers. *Estuar. Coast. Shelf Sci.* 196, 276–289. doi: 10.1016/j.ecss.2017.07.011
- Carey, D. M., and Korenowski, G. M. (1998). Measurement of the Raman spectrum of liquid water. *J. Chem. Phys.* 108:2669. doi: 10.1063/1.475659
- Chang, C. H., and Young, L. A. (1972). *Seawater Measurement From Raman Spectra*. Technical Report for Advanced Research Projects Agency, Naval Air Development Center, document AD-753, 481. doi: 10.21236/AD0753481
- Churnside, J. H. (2008). Polarization effects on oceanographic lidar. *Opt. Express* 16, 1196–1207. doi: 10.1364/OE.16.001196
- de Lima Ribeiro, A., Artlett, C., Ajani, P. A., Derkenne, C., and Pask, H. (2019a). Impact of fluorescence on Raman remote sensing of temperature in natural water samples. *Opt. Express* 27:22339. doi: 10.1364/OE.27.022339
- de Lima Ribeiro, A., Artlett, C., and Pask, H. (2019b). A LIDAR-compatible, multichannel raman spectrometer for remote sensing of water temperature. *Sensors* 19:2933. doi: 10.3390/s19132933
- Dickey, T. D. (2002). “A vision of oceanographic instrumentation and technologies in the early twenty-first century,” in *Oceans 2020*, eds J. G. Field, G. Hempl, and C. P. Summerhayes (Washington DC: Island Press), 209–254.
- Dolenko, T., Burikov, S., Sabirov, A., and Fadeev, V. (2011). Remote determination of temperature and salinity in presence of dissolved organic matter in natural

DATA AVAILABILITY STATEMENT

The datasets generated for this study are available on request to the corresponding author.

AUTHOR CONTRIBUTIONS

AL designed and assembled the multichannel, LIDAR-compatible Raman spectrometer integrated to a 473 nm (blue) laser and conducted the experiments which led to the results presented in the manuscript. AL was responsible for performing all analyses reported in the manuscript, and also responsible for writing much of the paper and prepared the figures for publication. The Raman spectra shown in **Figures 1B, 3** were acquired by C. Artlett. HP was responsible for supervising the experimental stage of this research, engaging in discussion regarding the results, and revising the manuscript.

ACKNOWLEDGMENTS

AL gratefully acknowledges receipt of Macquarie University iMQRES Ph.D. scholarship. HP gratefully acknowledges receipt of an Australian Research Council Future Fellowship (project number FT120100294).

- waters using laser spectroscopy. *EARSEL eProc.* 10, 159–165. Available online at: http://www.eproceedings.org/static/vol10_2/10_2_dolenko1.html
- Faris, G. W., and Copeland, R. A. (1997). Wavelength dependence of the Raman cross section for liquid water. *Appl. Opt.* 36:2686. doi: 10.1364/AO.36.002686
- Gordon, H. R. (1980). *Ed Ocean Remote Sensing Using Lasers*. NOAA Technical Memorandum ERL PMEL-18.
- Gordon, H. R. (1982). Interpretation of airborne oceanic lidar: effects of multiple scattering. *Appl. Opt.* 21, 2996–3001. doi: 10.1364/AO.21.002996
- IPCC (2014). *Summary for Policymakers*. Geneva, Switzerland
- James, J. E., Lin, C. S., and Hooper, W. P. (1999). Simulation of laser-induced light emissions from water and extraction of Raman signal. *J. Atmos. Ocean. Technol.* 16, 394–401. doi: 10.1175/1520-0426(1999)016<0394:SOLILE>2.0.CO;2
- Jerlov, N. G. ed. (1968). *Optical Oceanography, 1st Edn.* Amsterdam; London, UK; New York, NY: Elsevier.
- Leonard, D., a, Caputo, B., and Hoge, F. E. (1979). Remote sensing of subsurface water temperature by Raman scattering. *Appl. Opt.* 18, 1732–1745. doi: 10.1364/AO.18.001732
- Leonard, D. A., and Caputo, B. (1983). Raman remote sensing of the ocean mixed-layer depth. *Opt. Eng.* 22:223288. doi: 10.1117/12.7973107
- Lin, C. (1999). Tunable laser induced scattering from coastal water. *IEEE Trans. Geosci. Remote Sens.* 37, 2461–2468. doi: 10.1109/36.789642
- Lin, C. S. (2001). Characteristics of laser-induced inelastic-scattering signals from coastal waters. *Remote Sens. Environ.* 77, 104–111. doi: 10.1016/S0034-4257(01)00198-5
- Rees, W. G. (2001). *Physical Principles of Remote Sensing, 2nd Edn.* Cambridge: Cambridge University Press. doi: 10.1017/CBO9780511812903
- Solan, M., Germano, J. D., Rhoads, D. C., Smith, C., Michaud, E., Parry, D., et al. (2003). Towards a greater understanding of pattern, scale and process in marine benthic systems: a picture is worth a thousand worms. *J. Exp. Mar. Bio. Ecol.* 285–286, 313–338. doi: 10.1016/S0022-0981(02)00535-X
- Solonenko, M. G., and Mobley, C. D. (2015). Inherent optical properties of Jerlov water types. *Appl. Opt.* 54:5392. doi: 10.1364/AO.54.005392
- Soloviev, A., and Lukas, R. (2014). *The Near-Surface Layer of the Ocean*. Dordrecht: Springer Netherlands. doi: 10.1007/978-94-007-7621-0

- Vervald, A., Mazurin, E., and Plastinin, I. (2015). "Simultaneous determination of temperature and salinity of natural water by Raman spectra using artificial neural networks data analysis," in *1st Student Workshop on Ecology and Optics of the White Sea*. doi: 10.12760/02-2015-1-04
- Walrafen, G. E., Fisher, M. R., Hokmabadi, M. S., and Yang, W.-H. (1986). Temperature dependence of the low- and high-frequency Raman scattering from liquid water. *J. Chem. Phys.* 85, 6970–6982. doi: 10.1063/1.451384
- Whiteman, D. N., Walrafen, G. E., Yang, W. H., and Melfi, S. H. (1999). Measurement of an isosbestic point in the Raman spectrum of liquid water by use of a backscattering geometry. *Appl. Opt.* 38, 2614–2615. doi: 10.1364/AO.38.002614

Conflict of Interest: The authors declare that the research was conducted in the absence of any commercial or financial relationships that could be construed as a potential conflict of interest.

Copyright © 2020 de Lima Ribeiro and Pask. This is an open-access article distributed under the terms of the Creative Commons Attribution License (CC BY). The use, distribution or reproduction in other forums is permitted, provided the original author(s) and the copyright owner(s) are credited and that the original publication in this journal is cited, in accordance with accepted academic practice. No use, distribution or reproduction is permitted which does not comply with these terms.



Oceanids C2: An Integrated Command, Control, and Data Infrastructure for the Over-the-Horizon Operation of Marine Autonomous Systems

Catherine A. Harris^{1*}, Alvaro Lorenzo-Lopez¹, Owain Jones¹, Justin J. H. Buck², Alexandra Kokkinaki², Stephen Loch², Thomas Gardner² and Alexander B. Phillips¹

¹ Marine Autonomous and Robotic Systems, National Oceanography Centre, Southampton, United Kingdom, ² British Oceanographic Data Centre, National Oceanography Centre, Liverpool, United Kingdom

OPEN ACCESS

Edited by:

Leonard Pace,
Schmidt Ocean Institute,
United States

Reviewed by:

Adrian Tramallino,
Schmidt Ocean Institute,
United States
Philip Andrew McGillivray,
United States Coast Guard Pacific
Area, United States

*Correspondence:

Catherine A. Harris
cathh@noc.ac.uk

Specialty section:

This article was submitted to
Ocean Observation,
a section of the journal
Frontiers in Marine Science

Received: 15 November 2018

Accepted: 07 May 2020

Published: 08 June 2020

Citation:

Harris CA, Lorenzo-Lopez A, Jones O,
Buck JH, Kokkinaki A, Loch S,
Gardner T and Phillips AB (2020)
Oceanids C2: An Integrated
Command, Control, and Data
Infrastructure for the Over-the-Horizon
Operation of Marine Autonomous
Systems. *Front. Mar. Sci.* 7:397.
doi: 10.3389/fmars.2020.00397

Long-range Marine Autonomous Systems (MAS), operating beyond the visual line-of-sight of a human pilot or research ship, are creating unprecedented opportunities for oceanographic data collection. Able to operate for up to months at a time, periodically communicating with a remote pilot via satellite, long-range MAS vehicles significantly reduce the need for an expensive research ship presence within the operating area. Heterogeneous fleets of MAS vehicles, operating simultaneously in an area for an extended period of time, are becoming increasingly popular due to their ability to provide an improved composite picture of the marine environment. However, at present, the expansion of the size and complexity of these multi-vehicle operations is limited by a number of factors: (1) custom control-interfaces require pilots to be trained in the use of each individual vehicle, with limited cross-platform standardization; (2) the data produced by each vehicle are typically in a custom vehicle-specific format, making the automated ingestion of observational data for near-real-time analysis and assimilation into operational ocean models very difficult; (3) the majority of MAS vehicles do not provide machine-to-machine interfaces, limiting the development and usage of common piloting tools, multi-vehicle operating strategies, autonomous control algorithms and automated data delivery. In this paper, we describe a novel piloting and data management system (C2) which provides a unified web-based infrastructure for the operation of long-range MAS vehicles within the UK's National Marine Equipment Pool. The system automates the archiving, standardization and delivery of near-real-time science data and associated metadata from the vehicles to end-users and Global Data Assembly Centers mid-mission. Through the use and promotion of standard data formats and machine interfaces throughout the C2 system, we seek to enable future opportunities to collaborate with both the marine science and robotics communities to maximize the delivery of high-quality oceanographic data for world-leading science.

Keywords: marine autonomous systems, over-the-horizon operations, autonomous gliders, data curation, near-real-time data, human-robot interface, microservices architecture, software development

1. INTRODUCTION

Due to the scale and complexity of the extreme environment of the world's oceans, acquiring marine measurements at an optimal spatial and temporal resolution is very challenging. Traditional ship-based methods are often prohibitively expensive and only enable observation in the locality of the research ship, resulting in very limited snapshots of marine ecosystems. The Argo array of 4,000+ floats addresses this by providing coarse global coverage of temperature, salinity and velocity measurements (Roemmich et al., 2009), but are unable to provide spatially targeted measurements, measurements from the deep-ocean, sampling of seasonal ice zones, marginal seas, and boundary currents, due to the drifting nature of float technology (Roemmich and the Argo Steering Team, 2009).

Advances in long-endurance Marine Autonomous Systems (MAS) (Eriksen et al., 2001; Manley and Willcox, 2010; Furlong et al., 2012; Roper et al., 2017), piloted over-the-horizon, i.e., without an operator or research ship nearby, offer an opportunity to bridge the gap between research vessels and float technology, significantly reducing reliance on research ships, enabling multiple robotic vehicles to operate simultaneously in an area for an extended period of time and providing an improved composite picture of the marine environment. Underwater gliders in particular have been viewed as a critical component of future observing systems (Testor et al., 2010, 2019; Liblik et al., 2016), while Long Range Autonomous Underwater Vehicles (AUVs) are being considered for monitoring disperse decommissioned oil and gas infrastructure (Jones et al., 2019).

To facilitate access to marine measurement technologies, the UK's Natural Environment Research Council (NERC) funds the National Marine Equipment Pool (NMEP) hosted at the National Oceanography Centre (NOC). The NMEP is the largest centralized marine scientific equipment pool in Europe, providing scientific instruments and equipment capable of sampling from the sea surface to the deep ocean. It includes the Marine Autonomous and Robotic Systems (MARS) fleet of 40+ robotic platforms, comprising Autonomous Underwater Vehicles, Remotely Operated Vehicles (ROVs), Unmanned Surface Vehicles (USVs), and underwater gliders (see **Figure 1A**). To fulfill our obligations to the NERC Data Policy and to "ensure the continuing availability of environmental data of long-term value..."¹, scientific data collected from the MARS platforms is delivered and archived by the British Oceanographic Data Centre (BODC) (a data assembly center, DAC), where it is made available to the wider scientific community and the general public.

MARS vehicles are now routinely used in simultaneous single or multi-vehicle campaigns over geographically disparate locations (see **Figure 2**) and are involved in many large-scale national and international research programmes. Recent examples include: the use of underwater gliders to collect a continuous record of the full water-column within the Overturning in the Sub-polar North Atlantic Programme

(OSNAP) (Houpert et al., 2018); the acoustic harvesting of data from the RAPID array of trans-Atlantic moorings (Cunningham et al., 2007); deep ocean exploration in the Southern Ocean (Salavasidis et al., 2018; Garabato et al., 2019) and under the Filchner-Ronne ice shelf in Antarctica (McPhail et al., 2019) (see **Figure 1B**). The annual MASSMO (Marine Autonomous Systems in Support of Maritime Operations) deployments have seen heterogeneous fleets of USVs and underwater gliders operating in shelf and shelf-break locations to demonstrate the capabilities of MAS each year since 2014. In May 2017, MASSMO 4 saw eight vehicles collect oceanographic and passive acoustic data in the Faroe-Shetland Channel (see **Figure 1C**).

Whilst the popularity of MAS vehicles continues to grow, the further expansion of heterogeneous multi-vehicle operations is currently limited by a number of factors: firstly, MAS are typically highly specialized vehicles, each model of which operates using its own command interface, without cross-platform standardization; secondly, the data produced by each vehicle is typically in a custom format, making the automated ingestion of observational data for near-real-time analysis and subsequent data discovery very difficult, resulting in a time-consuming manual process; thirdly, the majority of MAS vehicles do not provide machine-to-machine interfaces, limiting the development and usage of multi-vehicle operating strategies and the automated delivery of data to end-users.

To ensure the MARS fleet is used to its full potential, the Oceanids Command and Control (C2) project is developing the required piloting tools and data services to streamline operation of MAS platforms operating over-the-horizon. In this paper, section 2 highlights the challenges for large scale over-the-horizon operation and section 3 reviews existing work addressing these issues. Section 4 describes the approach adopted and section 5 provides an overview of the C2 system. Section 6 addresses the C2 piloting infrastructure and section 7 describes the C2 data system. Section 8 describes ongoing developments and applications to real-world science deployments. Finally, section 9 presents conclusions from the work to date.

2. PROBLEM DEFINITION

Traditionally, deployments of marine autonomous systems (MAS) have consisted of a vehicle being launched from a support ship, performing a single pre-defined mission (lasting in the order of one day) and returning to the ship for recovery, data analysis, and redeployment on the next mission (German et al., 2008; McPhail, 2009). As a result of increases in battery and power technology, long-endurance vehicles such as underwater gliders are being deployed in increasingly large fleets for months at a time, without the need for a support ship. This paradigm shift has many implications for the piloting and operation of fleets of such long-endurance vehicles. In traditional deployments, a plan for a single vehicle would be constructed by highly-skilled pilots using prior knowledge of the environment ascertained from support ship observations of the deployment site. However, long-endurance vehicles perform multiple missions in a single deployment, periodically establishing communications with a

¹Natural Environment Research Council (NERC) data policy. Available online at: <https://nerc.ukri.org/research/sites/data/policy/data-policy/> (accessed November 12, 2018).

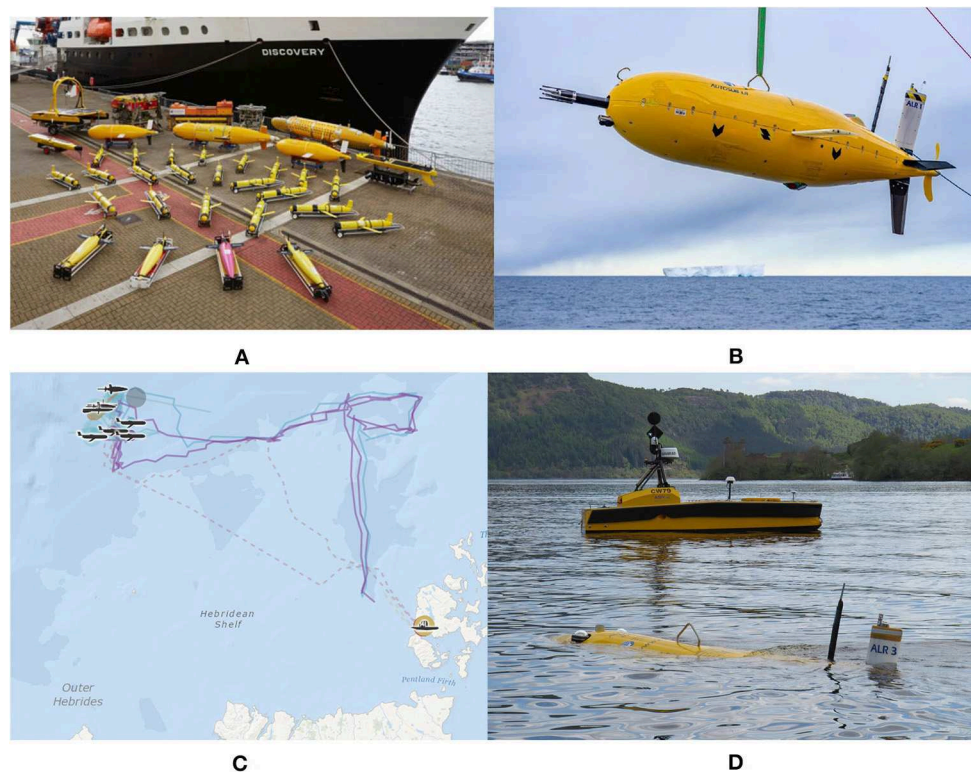


FIGURE 1 | Introduction to the MARS fleet at the National Oceanography Center: **(A)** MARS fleet, **(B)** Autosub long range, **(C)** MASSMO multi-vehicle operations, and **(D)** AUV/USV operations.

remote pilot via a satellite link. This is known as “over-the-horizon” piloting and requires highly-skilled pilots to be on-call throughout the day and night, to construct new plans based on ocean models and limited observations from the vehicle itself, and to respond to unexpected vehicle states, such as aborts and drifts in calibration. With the increasing frequency, duration, and complexity of MAS deployments, human piloting is becoming more intensive. New data streams from models, forecasts and live observations inform piloting decisions but also increase the time and piloting skills required to take them. The number of highly-skilled pilots cannot feasibly grow at the same rate as the number and duration of MAS operations, highlighting a future scalability problem. If unaddressed, this will limit the number of MAS vehicles which can be deployed simultaneously and may impact mission success rates.

In this section, we discuss the key factors which currently limit the operation of larger, heterogeneous fleets of MAS vehicles and consequently form the major design drivers for our C2 system. Key user interactions with the C2 system and operating modes of the long-range fleet are illustrated in **Figure 3**.

2.1. Diverse Platform Types

The majority of the MARS fleet are long-range platforms which can be piloted over-the-horizon. These can be classified into three distinct vehicle types:

1. **Underwater gliders**—vehicles which use a pump mechanism to make small changes to their buoyancy to move up and down through the water-column (Rudnick et al., 2004). Instead of using a power-hungry propeller, gliders have fixed wings which convert this vertical motion into forwards speed. The resulting sawtooth profile samples the ocean both vertically and horizontally, and requires very little power in comparison to a traditional propeller and motor. As a result, the range of a single glider deployment has been demonstrated as several 1,000 km. Gliders surface and communicate at irregular periods, determined by the dive depth. In shallow water this can be of the order of tens of minutes, whilst for deep-rated gliders diving to 6,000 m this can exceed 24 h.
2. **Long-range autonomous underwater vehicles (LRAUVs)**—are propeller-driven underwater robots which, unlike gliders, are able to move independently in the horizontal and vertical plane (Furlong et al., 2012; Hobson et al., 2012; Roper et al., 2017). This enables them to conduct more complex behaviors while submerged, such as benthic and geological surveys. As LRAUVs can spend days to months underwater without surfacing, opportunities for satellite communication with a remote pilot are highly dependent on the mission plan. Underwater communication channels, such as acoustic modems are very limited in range, with limited application to over-the-horizon operations. The use of Unmanned Surface Vehicles, acting as acoustic communications gateways to



LRAUVs is a promising area of ongoing research (German et al., 2012; Phillips et al., 2018) (see **Figure 1D**). However, the need for a second vehicle type increases piloting complexity and mission risk.

3. **Long-range unmanned surface vehicles (LRUSVs)**—such as Waveglider (Manley and Willcox, 2010), C-Enduro, and Autonaut, are able to maintain continuous satellite communication. As LRUSVs are on the surface constantly, they pose a collision risk to shipping traffic. As a result, LRUSVs are typically supervised constantly by a team of pilots in order to meet existing COLREGS.

In contrast to traditional single-vehicle deployments, MAS deployments are increasingly involving multiple vehicle-types, deployed simultaneously. These heterogeneous fleets have many benefits for data quality and coverage, providing a comprehensive view of both spatial and temporal variation within the operating environment. However, the different capabilities of these vehicle types adds significant piloting overheads, requiring pilots to be trained in the control and operation of multiple vehicles.

In addition to the complexity of multiple vehicle types, vehicles are manufactured by a range of commercial and academic developers. For example, underwater glider models include Seagliders (Eriksen et al., 2001) and Slocum Gliders (Schofield et al., 2007), both of which use the same underlying principles, implemented in significantly different ways. Differences in manufacturer design lead to a wide range of vehicle capabilities, constraints, procedures, and interfaces, even for vehicles of a common type. Many vehicle interfaces were designed considering traditional single-vehicle mission formats and, as a result, lack the interoperability needed to facilitate multi-vehicle operations.

2.2. Deployment-Specific Configurations

Each vehicle type has different sensor suite configurations, enabling the vehicle to be customized to meet the science requirements and energy constraints of the mission. This leads to complexity in the command, control and data processing associated with each vehicle, as different physical components have different commands, operating constraints, failure-modes and data formats. For instance, an altimeter on a glider enables the vehicle to measure its altitude above the seafloor, reducing the likelihood of collisions. However, the altimeter significantly increases power consumption, so to maximize vehicle endurance, pilots may be trained to switch the altimeter off whilst away from the seafloor. This creates complexity for the data and metadata systems, as the number of datastreams from the vehicle is not fixed throughout the mission. For the analysis of vehicle reliability, it is also important to record whether the loss of a datastream mid-mission was operator commanded, or as a result of a vehicle/sensor fault. The inclusion of the altimeter or other scientific sensors within the vehicle configuration also increases the number of components which may fail and thus should be routinely checked by the pilot throughout a deployment to ensure correct operation.

Consequently, piloting interfaces and procedures, as well as data and metadata formats, need to be adaptable and robust to changes in sensor suite.

2.3. Availability of Near-Real-Time Data Mid-Mission

As long-range vehicles are typically at sea for weeks to months at a time, pilots receive data throughout the mission as well as fully curated research-quality data-sets following recovery of the vehicle. Following the definitions of Roemmich et al. (2010), we refer to mid-mission data as “near-real-time” (NRT), as whilst there is a delay due to satellite communications only being possible whilst on the surface, this data is available significantly faster than with traditional devices, where data is only accessible on recovery of the instrument (referred to as “delayed-mode” data). Major advantages of NRT data include the ability to use this data to inform piloting and scientific decisions made mid-mission, for example in adjusting the location of survey locations, or the sampling parameters of on-board sensors etc to increase data quality.

The C2 system will allow the opportunities presented by NRT data to be fully exploited to benefit MAS deployment

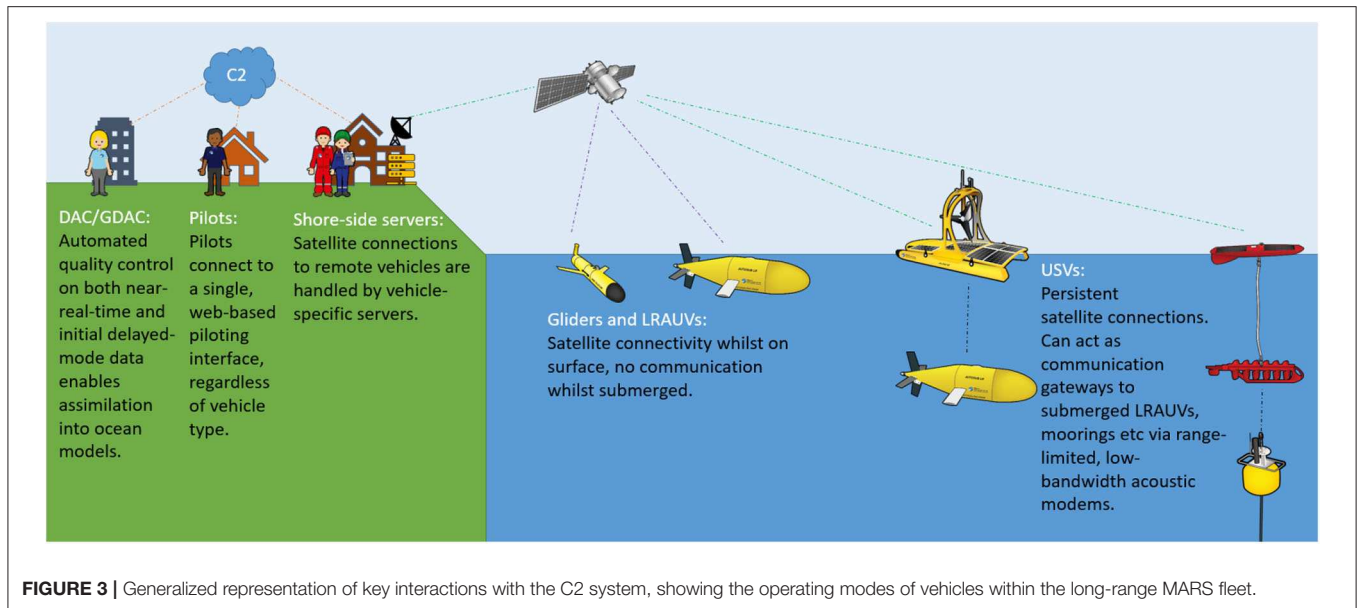


FIGURE 3 | Generalized representation of key interactions with the C2 system, showing the operating modes of vehicles within the long-range MARS fleet.

scientific objectives. The data pathway of the C2 system will automatically process both delayed-mode data and NRT data, with priority given to the processing of NRT data into standard scientific data formats. Historically, within BODC the bulk of the data in the archives is delayed-mode, and much effort has been spent to log and include the necessary metadata to ensure the data is discoverable. However, BODC also has experience of NRT data management which, in the case of Argo (Roemmich and the Argo Steering Team, 2009) dates back to 2001, and for gliders from 2011. The advent of the C2 data system with its emphasis on metadata assembly prior to deployment promises to revolutionize the role of the data center by: (1) significantly reducing the effort required from data center staff by, for example, automating the accessioning process, (2) speeding up processing and reducing time-to-delivery by two orders of magnitude or more, and (3) providing a highly automated processing service for scientists. In other words, users can expect to see calibrated and quality controlled data one or two minutes after the relevant MAS vehicle has surfaced.

DACs, such as BODC, submit data to Global data assembly centers (GDACs) and other end-users for ingestion and assimilation into models and data products. Such users may require the data to be delivered within a specific time-window for inclusion. For example, the World Meteorological Organization's Global Telecommunication System (which coordinates the collection, exchange and distribution of observation data for ocean and weather forecasting) requires data to be submitted within a 19 h window. As such, the data system within the C2 must be able to meet these time-constraints. There are also data quality levels to be considered—automated quality control methods can be applied to both NRT data and the initial delayed-mode data collected on recovery of the vehicle. This process enables a quality assurance that is sufficient for assimilation into operational ocean models.

2.4. Data Standardization

In order to maximize the exploitation of the data by end users, it is crucial that metadata and data are easily accessible and presented in a well-defined standard format. Without a standard, there is a significant learning curve for end-users to read and analyse a data set from a new vehicle or data provider, whilst also complicating the comparison of data between multiple platforms, or over different time periods. Therefore it is important that MAS missions are supported by an appropriate data management strategy that archives and disseminates collected data and associated metadata in a sustainable format that is exchangeable and discoverable between stakeholders. For underwater gliders the European community has recently standardized on the Everyone's Gliding Observatories (EGO) Network Common Data Form (NetCDF)² format (EGO gliders data management team, 2017) which documents the naming conventions and metadata content. However, adoption of a new format requires buy-in from all users and the time and resources to convert from existing processing methods, so further work is still required before this can be considered industry-standard. Whilst different standards have been defined within the US (IOOS) (U.S. IOOS National Glider Data Assembly Center, 2018) and Australian (IMOS) (Australian National Facility for Ocean Gliders, 2012) glider communities, these formats have many similarities with EGO NetCDF and there is ongoing communication between the communities to standardize into a global format. There are base standards such as NetCDF, Climate and Forecast (CF), Attribute Convention for Data Discovery (ACDD)³, and common vocabularies for metadata that underpin the common

²Network Common Data Form (NetCDF). Available online at: <https://www.unidata.ucar.edu/software/netcdf/> (accessed November 14, 2018).

³Attribute Convention for Data Discovery. Available online at: http://wiki.esipfed.org/index.php/Attribute_Convention_for_Data_Discovery (accessed November 14, 2018).

elements of interoperability between IMOS, IOOS, and EGO formats. Efforts to fully harmonize the formats will simplify access to users and the development of common software tools for working with ocean glider data. For metadata, applicable exchange formats are SeaDataNet Common Data Index (CDI)⁴ records, Marine Sensor Web Enablement⁵ profile SensorML (Open Geospatial Consortium, 2016) and Semantic Sensor Network (Haller et al., 2017). A recently introduced metadata standard is schema.org which will enable data discovery via Google dataset search. There are also community data access tools, such as ERDDAP⁶, that aid interoperability and data exchange. As LRAUVs are a relatively new technology that is still heavily under development, community standardized data formats have yet to emerge. Therefore, there is a requirement within our C2 system to ensure that data from LRAUVs sent to the DAC is in a suitably adaptable, modular format, to facilitate later adoption of a standard or unification with EGO NetCDF, for instance.

2.5. Scalability and Resilience

It is essential that the C2 system is resilient and scalable to increases in vehicle connections, data streams and vehicle types. The system must be resilient to failures or interruptions at any stage of the processing of data or piloting commands. As a result, critical services and databases, for example those which contain metadata and control information, must have failover in place. The architecture of the C2 system must be sufficiently modular, flexible and portable to support expansion and enable the potential use of Cloud resources where required.

2.6. Vehicle Reliability Requirements

Deploying and operating robots in the extreme environment of the world's oceans is very challenging. The inherent uncertainty of the highly dynamic operating environment adds significant risk to MAS deployments, both to the physical safety of the vehicle itself and to the successful delivery of the scientific data. If a vehicle is lost without first sending data back via satellite, any data which has been collected is also lost. Whilst this has clear implications for the delivery of the mission's scientific objectives, the loss of the engineering data also has significant impact for analysing the reliability of the fleet. If a vehicle is lost or experiences a fault whilst at sea, it is crucial that we analyse the available data in an attempt to identify the root cause, design effective mitigation, and ascertain whether the fault is common to other vehicles of that model or type. At present, human pilots are required to supervise the operation of complex vehicles throughout the day and night (constantly, in the case of LRUSVs). Under such working conditions, a degree of human error is inevitable (Stokey et al., 1999)—it is very easy within the

existing manual process for a pilot to fail to spot an emerging trend for example, or to fail to record key information whilst communicating with the vehicle under time pressure. To both increase the amount of engineering data available for reliability analysis and to reduce the emphasis on individual pilots to record key events and information, the new system should log all data and communications with the vehicle automatically. This data can then be analyzed in near-real-time by the server, with anomalous data brought to the user's attention.

2.7. Machine-to-Machine Interfaces

With the recent research focus and subsequent popularization of deep learning tools and the wider field of Artificial Intelligence (AI), there is the clear potential to apply such techniques to the remote piloting of MAS vehicles. At present, human pilots follow standard procedures of checks and manual optimization of vehicle performance. Some of these tasks, such as the regression of glider flight variables, are well-suited to AI and machine learning methods. Furthermore, the online availability of external data sets such as weather forecasts and ocean models, opens up the opportunity to use algorithms to perform larger-scale optimization across a wide-range of piloting tasks, from waypoint definition to minimize vehicle resource usage, to sensor parameter adjustment to optimize data quality. To enable the use of intelligent algorithms and automation programs, it is necessary to have well-defined machine-to-machine interfaces which:

- Allow bidirectional communications.
- Prioritize the safe operation of MAS vehicles, preventing the violation of vehicle, or mission constraints.
- Ensure secure access to remote vehicles and associated infrastructure.
- Follow industry standards, enabling software developers to quickly understand the interfaces they need to use to generate their applications.

However, many existing vehicles and associated piloting interfaces were designed for a human pilot to operate a single vehicle via a user interface, and as such there was never a previous need for interfaces to enable machine access and control. The development and standardization of machine-to-machine interfaces to unify piloting across different vehicle types is a key objective of the C2 project.

2.8. Range of Stakeholders

The Oceanids C2 project aims to serve a wide number of stakeholders as a UK national infrastructure. In **Table 1** we present the identified stakeholders.

3. LITERATURE REVIEW

3.1. Autonomous Ocean Sampling Networks

There have been multiple successful demonstrations of the potential for Autonomous Ocean Sampling Networks (AOSN) (Ramp et al., 2009; Leonard et al., 2010; Haworth et al., 2016). AOSN deployments typically consist of a heterogeneous fleet of MAS vehicles, ships, and/or sensor moorings, operating within

⁴SeaDataNet Common Data Index (CDI). Available online at: <https://www.seadatanet.org/Metadata/CDI-Common-Data-Index> (accessed November 11, 2018).

⁵Open Geospatial Consortium, Sensor Web Enablement. Available online at: <http://www.opengeospatial.org/domain/swe#initiative> (accessed November 14, 2018).

⁶ERDDAP. Available online at: <https://coastwatch.pfeg.noaa.gov/erddap/index.html> (accessed November 14, 2018).

TABLE 1 | Key users of the oceanids C2.

Stakeholder	Role
Principal investigator (PI)	Scientist/engineer who instigated the deployment and is ultimately responsible for designing missions to meet their scientific objectives.
Pilot	Highly-trained operator who sends commands to one or more vehicles to achieve the PI's mission. Concerned with the day-to-day operation and health of the vehicle.
Fleet manager	The person in charge of the use of the vehicles within an organization. Concerned with ensuring vehicles, sensors and pilots are able to meet the requirements of the PI. The Fleet Manager may also be a Pilot.
Data assembly centre (DAC) e.g., BODC	The data flow within the C2 data system is delivered by three stakeholders, the PI, Data assembly centre (DAC) and Global Data Assembly Centre (GDAC). The PI provides the data and all metadata to the DAC, where it is assembled into EGO-compliant files where it is forwarded to the GDAC to be made publicly available. Formerly for NERC funded deployments this has been a highly manual and time-consuming operation.
Global data assembly Centre (GDAC)	GDAC are the global data aggregation and community delivery centers that national data centers submit data to. The Ocean glider programme GDAC is hosted by Ifremer. Concerned with ingestion of data in standard accepted formats.
Scientist	Expert end-user of scientific data. May have PI's permission to access NRT data. Concerned with scientific data quality and coverage, metadata availability, standardization of data formats for ease of analysis.
Engineer	Expert end-user of engineering data. Responsible for the maintenance and operation of the MAS system at the vehicle's home institution. Concerned with engineering data quality and coverage, metadata availability, standardization of data formats for ease of analysis.
Reliability analyst	Expert end-user of engineering data. Typically concerned with identifying trends in vehicle reliability across deployments and/or vehicle types from delayed mode data, rather than NRT data from a single mission.
C2 Collaborator	Third-party software developer and end-user of C2 APIs, for example from academic or industrial partner. Concerned with ease of access, standardized formats and representative schemas.
Member of the Public	Under the NERC data policy, data collected by NERC vehicles is ultimately a public good. End-user of NERC data for a wide variety of reasons. Assumed to be non-expert concerned with ease of access and discovering information about data availability.
Policy maker	Requires data products suitable for decision making and regulatory monitoring

the same area of interest, providing significant advances in temporal and spatial resolution compared to traditional single vehicle or ship-based surveys. Ramp et al. (2009) deployed a wide range of gliders, AUVs, aircraft, and ships in Monterey Bay, assimilating NRT data from these platforms into ocean models. The models were then used to provide forecasts for the following day and inform the adaptation of planned survey strategies. The C2 seeks to ease the deployment and management of such large fleets by unifying the command, control and data infrastructure of MAS vehicles within the NMEP. Through well-defined application programming interfaces (APIs), web-based connectivity and quality control of NRT data, the C2 system will enable assimilation of data into ocean models for decision making mid-mission.

Paley et al. (2008) present experimental results of their Glider Co-ordinated Control System (GCCS), which generates waypoints using environmental models to coordinate a fleet of Slocum and Spray gliders. A remote I/O component handles communication to and from the vehicle shore-side servers, enabling a human pilot to monitor the status of a mission, and notifies the user of any software or operational issues. The GCCS was later used on the large scale Adaptive Sampling and Prediction field experiment, which continuously coordinated six gliders for 24 days (Leonard et al., 2010). Whilst this work has similarities with our C2 system, Paley et al. (2008) focused on lower-level control and the prediction of gliders motion, rather than on the development of a common piloting and data infrastructure. Through the development of an Automated Piloting Framework (see section 8.1), the C2 will enable external collaborators to integrate control algorithms which generate generic commands (such as waypoints) which are verified before

translation to vehicle-specific instructions and transmission to the shore-side server for execution on the vehicle. We seek to create a closed loop between data collection, quality control, model assimilation, and adaptive data-driven decision making. Through the definition of industry-standard APIs, we aim to enable the C2 to interface with a wide range of externally-hosted models and control systems developed by C2 collaborators.

3.2. Web-Based Piloting Infrastructure

It is becoming increasingly commonplace for organizations operating fleets of long-endurance MAS vehicles to display NRT data from these platforms via a public webpage, e.g., PLOCAN⁷, MARS⁸, GEOMAR⁹, and ANFOG¹⁰. Such portals are beneficial for both public and stakeholder engagement, enabling end-users to view NRT data and details about different vehicle types. However, it is unclear how many of these portals also enable pilots to interact with the remote vehicle via the web-browser.

The LSTS Toolchain (Pinto et al., 2013; Ferreira et al., 2017) was developed to support the control of heterogeneous fleets of maritime robots, from underwater through to aerial vehicles, communicating across multiple channels for a range of applications including oceanographic survey (Ferreira et al., 2019). The toolchain comprises: *Dune*, a framework for the

⁷PLOCAN Data Portal. Available online at: <http://obsplatforms.plocan.eu/vehicle/USV/test/> (accessed November 11, 2018).

⁸National Oceanography Centre - NMF vehicles. Available online at: <https://mars.noc.ac.uk/> (accessed November 11, 2018).

⁹GEOMAR Navigator. Available online at: <https://waveglider.geomar.de/navigator/> (accessed November 11, 2018).

¹⁰Australian National Facility for Ocean Gliders - ANFOG Glider Fleet. Available online at: <http://anfog.ecm.uwa.edu.au/index.php> (accessed November 11, 2018).

development of embedded software onboard the robot; *IMC*, a common control message format; and *Neptus*, a distributed command and control desktop application for mission planning, execution, monitoring and post mission analysis. In addition, Dias et al. (2006), Faria et al. (2014), and Pinto et al. (2017) describe a Cloud-based piloting server named Ripples, which acts as a communication hub, forwarding data and commands between disparate groups of deployed vehicles and maintaining a global state. The LSTS Toolchain shares the goal of the C2 to provide a common piloting interface to multiple vehicle types, enabling the operation of heterogeneous fleets of vehicles. However, the LSTS is built around a desktop piloting tool, Neptus, with the Ripples layer providing global situation awareness between multiple Neptus workstations and their associated vehicles. The C2 is a fully web-based microservice architecture, where all piloting is performed via a web-interface. The C2 assumes a many-to-many relationship between pilots and vehicles, which may be deployed for months at a time. The Norwegian University of Science and Technology Applied Underwater Laboratory have developed a Mission Control System (MCS) (Buadu et al., 2018) in collaboration with the LSTS toolchain. The main purpose of the MCS is to control formations of fleets of vehicles. MCS can either work in combination with or as a replacement for Neptus in the LSTS toolchain. In a similar way, MCS or similar systems which provide capabilities such as formation movement, could in theory be interfaced with the C2 via the third-party interfaces provided within the Automated Piloting Framework (discussed in section 8.1).

3.3. Ocean Data Delivery Systems

The data processing and delivery of ocean glider data builds on that of more established infrastructures and observation networks. The AtlantOS Strategy for knowledge management, protection and exploitation of results (Reitz et al., 2016) outlines the architecture and stakeholders within the marine community bordering the Atlantic. Buck et al. (2019) outline potential new data users and stakeholders along with the enabling technologies for data standardization. Rudnick et al. (submitted) describe the future vision for ocean glider data over the next decade including alignment of data delivery with the FAIR principles (Wilkinson et al., 2016) and across existing international infrastructures.

4. METHODOLOGY

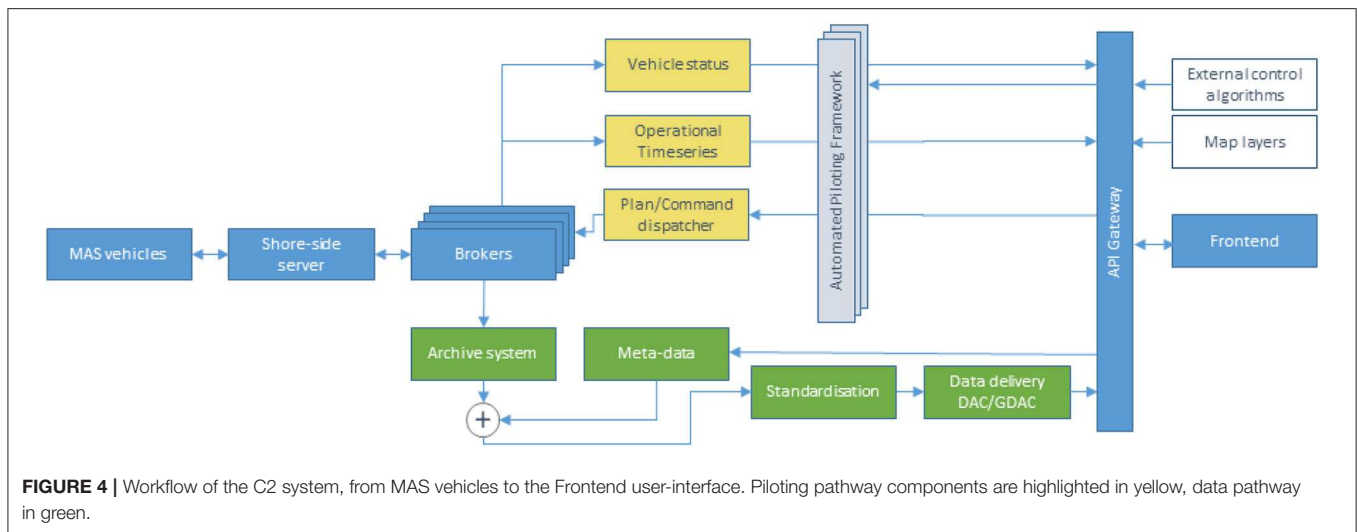
The development ethos of the C2 system centers around the need to capture the continually developing requirements of the diverse range of end-users and project stakeholders (see Table 1). To perform cutting-edge research at the forefront of marine science and maximize the use of the available observation technology, PIs and science users require MAS vehicles to be operated in new and innovative ways in increasingly challenging or remote environments. As a result, the development of the C2 system is a multi-institutional effort, in which the user and stakeholder community is engaged throughout the development of the system, using releases of the new system in parallel with existing piloting software and acting as “product owners” for

features relevant to their expertise. At the start of the project, whilst the need for a unified command, control and data system was clear (see section 2), the exact form of the optimal solution was not known. Consequently, the development of the C2 has followed agile software design principles, prioritizing modularity, and extensibility in architecture design, which has enabled us to welcome the evolution of user requirements throughout development and to prioritize features in response to the needs of both users and scheduled autonomous vehicle deployments. As a result, features and releases to-date have focused on underwater gliders and long-range autonomous underwater vehicles, rather than autonomous surface vessels (ASVs). Periodic release cycles enable the user community to benefit from additional functionality, e.g., web-based piloting tools, as soon as these are ready, which provides ongoing user feedback, additional requirements and maintains close communication with the stakeholder community. The C2 development ethos represents a significant shift, from standalone desktop piloting applications, designed for a one-to-one relationship between pilot and MAS vehicle, toward a software-as-a-service model in which the C2 forms a central common component in the operation of over-the-horizon MAS vehicles within the NMEP. This holistic view of MAS piloting and data infrastructure prioritizes maintainability and scalability through identifying and exploiting commonality between vehicle and data types. As an example, gliders from different manufacturers are controlled through different interfaces using different workflows. Whilst these vehicles have some key differences, they share the underlying principles and model of glider operation. Through the identification of shared concepts and the development of common design patterns, we seek to develop a single web-based piloting front-end user interface to enable a pilot to focus on making high-level control decisions to optimize operation of a heterogeneous fleet without first needing training in the many implementation differences between vehicle types. Likewise, data are harmonized from the variety of manufacturer prescribed formats to a single community EGO NetCDF and metadata to Marine SWE profile SensorML format. This simplifies user data access and enable interoperability of data and metadata.

To aid future collaboration with external software developers, e.g., the integration of a new decision making algorithm or data analysis tool, and ensure that users of the MARS fleet continue to benefit from advances in technology made within the wider marine, computing, and robotics communities, the C2 will use open standards, software, and APIs wherever possible.

5. SYSTEM OVERVIEW

Through the creation of well-defined APIs and associated microservices, the C2 infrastructure provides an abstraction on top of custom vehicle control systems, enabling a common web-based user-interface to be used for piloting across the MARS fleet, regardless of vehicle type. By creating a common piloting framework on top of the underlying machine-to-machine APIs, the C2 infrastructure will provide the necessary safeguards and constraints to allow the creation of multi-vehicle co-operative



survey strategies by collaborators and stakeholders, such as the wider robotics and marine science communities.

The solution implements the workflow illustrated in **Figure 4**. The system is an event-driven architecture, which reacts to connections from vehicles, inputs from users and internal/external systems e.g., scheduled data processing. For brevity, we discuss the workflow as initiated by the connection of a remote vehicle, e.g., a glider:

1. The vehicle connects to its associated shore-side server. Shore-side servers are typically manufacturer-provided and are responsible for communicating with the vehicle via its native protocol, which may be proprietary.
2. The brokers sit between the shore-side servers and the C2 infrastructure and provide a common interface to all shore-side servers. A key role of the broker is to distribute data streams, coming to and from the shore-side server, to relevant microservices within the wider C2 infrastructure.
3. The workflow then separates into two logical backend infrastructure “pathways” that appear to end-users as a single unified API gateway and web-based frontend. These pathways are:
 - **Piloting pathway**—encompasses all the infrastructure required for a user or external system to interact with the MAS vehicles and associated shore-side servers. The Vehicle Status service discretizes health information (e.g., battery and positional data) into a state representation for the vehicle reducing the complexity of decision making. The Operational Timeseries service stores the engineering and scientific data from the vehicle within a continuous time-indexed database. Finally, the Plan/Command Dispatcher generates vehicle-specific commands from abstract representations (e.g., waypoints, survey behaviors etc.), shared between vehicle types.
 - **Data pathway**—encapsulates the flow of data to the DAC (BODC). Data from scientific sensors is received from the piloting pathway (based on site at NOC Southampton),

standardized and fused with operational metadata (on site at NOC Liverpool). By developing the data pathway on site at the DAC, the data pathway is able to interface directly with BODC’s existing archive tools, ahead of dissemination to the relevant scientific communities and networks, e.g., via GDACs. Metadata are entered into the metadata system via web forms with values for terms based on controlled vocabularies on the NERC vocabulary server¹¹. The metadata are exposed to the web in SensorML and SSN formats, with snapshots of metadata exposed to the C2 data system in JSON format. Data are archived via a push to the API gateway by the piloting application and, after automated virus checking, are placed in a secure archive. Data are ingested to an intermediate internal NetCDF 4 format, named RXF, for subsequent delivery in a range of standard formats. Data are automatically pushed to the UK Met Office for operational assimilation if the data sets have an open data access policy. Data are delivered in a range of community formats (currently EGO with a desire to include SeaDataNet NetCDF later). Future delivery of data will include API endpoints such as ERDDAP and automated push of files to the Ocean Glider Programme.

5.1. Architecture and Back-End Infrastructure

As a multi-institution project supporting the national infrastructure of the NMEP, it was essential that components of the C2 could be easily portable and reconfigurable between partner institutions, scaling with the addition of new vehicles and data streams. For example, pilots from the Scottish Association of Marine Science (SAMS) control Seaglidors within the MARS fleet, so commands and data from the C2 system need to be sent to the Seaglider shore-side server at SAMS, and vice versa. It was considered that the easiest way to communicate between

¹¹NERC Vocabulary Server. Available online at: https://www.bodc.ac.uk/resources/products/web_services/vocab/ (accessed November 11, 2018).

institutions given their independently-managed IT networks was to develop a web-based system, as it is rare for outgoing web traffic to be blocked by institutional firewalls, thus lowering the barrier of entry for participating institutions.

5.2. Microservices

In contrast to traditional monolithic systems, the architecture of our C2 system is highly modular and extensible, comprising a collection of microservices which interact through HTTP REST APIs and the event-driven Advanced Message Queueing Protocol (AMQP) via RabbitMQ¹². Most of our microservices provide an API which can be consumed by anyone with access to a HTTP client and has the requisite permissions, while the event-driven component of the system (the “event-bus”) allows the microservices and external API consumers to listen for and react to specific events as soon as they happen, which is more reactive and efficient than polling the HTTP APIs for changes. One example of this is a service which sends SMS messages to pilots as soon as one of the vehicles connects to the system, allowing pilots to respond quickly to intermittent events when these occur, rather than having to constantly watch a computer. By exposing the event-bus using the EventSource (Hickson, 2015) and WebSocket standards (Fette and Melnikov, 2011), we have developed a web-based front-end to the system which can react to changes instantaneously.

Most microservices are running on top of the Docker containerization software, which creates a consistent and immutable environment for each service regardless of the host hardware and operating system used. Docker images are portable by nature, and allow third-party services to be easily included in the system, as many popular server software packages provide Docker images on Docker Hub¹³. This reduces the complexity of installing and configuring the constituent parts of the system and the supporting software, so that it is easier to port the system to different environments, such as different Cloud services. The Microservices architecture separates the system into small lightly-coupled, highly reconfigurable functional units. This provides a number of key advantages for the C2 system:

- **Increased portability**—Component microservices can be deployed to run either on the Cloud or on servers based within partner institutions (or a mixture of the two, known as Hybrid-Cloud). This is powerful for the C2 because it does not restrict the system to a particular infrastructure or service provider, enabling us to adapt to evolving technical and financial requirements. Cloud-based infrastructure has clear advantages in terms of power and maintenance: professional Cloud platforms such as Microsoft’s Azure and Amazon Web Services provide infrastructure at a scale generally not achievable by any single academic organization.
- **Increased scalability and resilience**—The division of functionality into microservices makes it straightforward to add or update component services without first having to take

other parts of the system down. This reduction in down-time is important as MAS operations take place around the clock throughout the year. The modularity of the microservices architecture also eases integration of the C2 with other external systems, as the system can be split across many processes which can be started and stopped independently of each other.

- **Increased flexibility**—As independent components of the system, microservices can make use of different underlying technologies, selected to best-suit their individual function rather than needing to be supported by, and relevant to, all components. For example, within the C2 system the Timeseries microservice uses the open-source Timescale extension¹⁴ to PostgreSQL, which optimizes the underlying database technology for indexing and searching large time-series datasets. However, due to the modularity of the microservice pattern, this database extension does not need to be used by all other services within the C2.
- **Ease of development**—The modularity of the microservice architecture is well-suited to distributed development teams, as is common within academic or research consortia such as the C2 project, because each service has a separate code-base and thus is smaller and easier to develop, debug and understand.

The majority of the C2 ecosystem is managed by the Kubernetes orchestration software¹⁵, which is responsible for managing resources given to each service, monitoring health and acting on service failures, providing an increased level of resilience to the system.

5.3. API Gateway

To reduce the apparent complexity of a growing collection of microservices, we utilize an API Gateway to present an end-user or external system with a single coherent access point to the C2. This pattern abstracts the user from the underlying architecture and technologies within the C2—reconfiguration and addition of microservices can occur without impacting the end-user and ensures the system remains portable, i.e., the user does not need to change their access route in response to a change to on-site or Cloud hosting. The gateway secures and controls access to different end-users, allowing them to see relevant parts of the system and to meet the needs of the NERC data policy¹⁶.

All APIs being served via the gateway have publicly available Swagger¹⁷ definitions. These definitions are independent of the code and allow both internal and external developers to see all available methods along with a list of the required and optional input variables. The definitions include notes on method implementation, descriptions of method inputs for both required and optional variables, and reason for HTTP status codes. We

¹²RabbitMQ - open source message broker. Available online at: <https://www.rabbitmq.com/> (accessed November 12, 2018).

¹³Docker Hub - Dev-test pipeline automation. Available online at: <https://hub.docker.com/> (accessed November 12, 2018).

¹⁴Timescale—Open-source time-series database powered by PostgreSQL. Available online at: <https://www.timescale.com/> (accessed November 12, 2018).

¹⁵Kubernetes. Available online at: <https://kubernetes.io/> (accessed November 14, 2018).

¹⁶Natural Environment Research Council (NERC) data policy. Available online at: <https://nerc.ukri.org/research/sites/data/policy/data-policy/> (accessed November 12, 2018).

¹⁷Swagger. Available online at: <https://swagger.io/> (accessed November 14, 2018).

have also used Swagger to model the JSON formatted data we pass around the C2 system.

5.4. Security

The design of the C2 system seeks to minimize the risk of external agents disrupting or interfering with either the vehicle, mission or data:

- *Security of the vehicle*—For commercially-designed MAS systems, the security of both onboard systems and the satellite link between the vehicle and its shore-side servers are often proprietary and limited to what is provided by the manufacturer or satellite provider. This creates challenges for securing the entire data chain from vehicle to data assembly center, as end-to-end encryption, for example, is not possible if not supported by the vehicle. We are currently investigating options to increase security at this point in the chain, for example by creating a VPN between the shore-side servers and the satellite service provider.
- *Integrity of the mission*—The C2 reduces the risk of unauthorized interference with the mission and control of the vehicle through authentication¹⁸ and authorization of users¹⁹. In addition, we are implementing different pilot user-profiles, which limit the access of the user to only the vehicles and commands they have been trained to use.
- *Security of data interfaces*—In order to ensure all transmitted data comes from a trusted source, the API gateway requires a token on all API calls for the pushing of data to the C2 system. These tokens are then decoded and stored as part of an audit trail allowing the system to link all incoming data to a user account. The same is true for the metadata APIs. All connections to the gateway are encrypted using industry-standard encryption certificates.

6. PILOTING PATHWAY

The piloting pathway facilitates interaction between the user, the vehicle shore-side server and the vehicle itself. The piloting pathway consists of multiple services which convert from vehicle-specific data formats to normalized abstract representations and vice versa. For example, Seaglidors and Slocums report their positions or accept waypoints in different vehicle-specific formats, but an event or plan within the C2 system captures that information in a generalized representation which is vehicle-agnostic. Farley et al. (2019) provides a comparison of the existing piloting workflows of Slocum gliders, Seaglidors, and Autosub Long Range, alongside their resulting unification into a single common workflow.

At the time of writing, there are 22 microservices within the C2 architecture providing APIs for piloting and data processing functionality. Of these, there are several which are crucial to the piloting pathway:

- **Vehicle status**—On receipt of communication streams from a remote vehicle via the brokers (see **Figure 4**), the Vehicle Status service extracts key information from these communications including: the vehicle's GPS position, the time according to its internal clocks, any engineering data provided by the vehicle and relevant information about vehicle behavior, e.g., the current waypoint, or mission state. This data stream is then discretized into vehicle events, representing a change in vehicle or connection state. For example, a vehicle connecting to the C2 or aborting whilst connected to the C2 would result in a change in Vehicle Status, whilst continuous changes to vehicle battery would not unless this fell below a pre-defined threshold, triggering a low-battery vehicle state. The formats and protocols containing vehicle communications differ for each type of vehicle: Iridium Short-Burst Data (SBD) messages are generally received via email, which contains the Iridium geolocation as well as the vehicle-specific formatted data, usually in a concise binary format; Slocum gliders output information in a continuous stream of text over a long-running satellite modem connection, where the order in which text is received is not fixed. Other devices attached to a vehicle, such as third-party GPS trackers, e.g., Argos²⁰, may present their information via other web APIs in more common formats such as JSON, CSV, or XML. The Vehicle Status service parses these disparate, heterogeneous streams of information as they arrive within the C2 and generates a timeline of communication events per vehicle in a normalized format. This can then be used by the rest of the system without having to decode the unique formats provided by different vehicle types. For instance, a position report will provide latitude, longitude, timestamp, and radius of GPS accuracy in the same format, regardless of which vehicle or communications medium the original message was sent from. Wherever possible engineering data is normalized across vehicle types.
- **Operational timeseries**—The Timeseries service provides an efficient database in which to store and query continuous numerical engineering and science data arriving from each vehicle, such as battery voltages, altimetry ranges and uncalibrated CTD data. Similar to the Vehicle Status service, the Timeseries accepts data files from the vehicles in their native format and normalizes observation points into PostgreSQL database rows, which can then be output by the API in whichever format is suitable for an end-user (such as comma-separated values, CSV)²¹. The raw data coming from the entire MARS fleet across all deployments has the potential to be stored in this database, allowing us to perform complex aggregate queries involving one or many variables across one or many vehicles. Whilst this service provides a similar functionality to the data pathway, it should be noted that as this service is designed to facilitate operational access to data mid-mission, it only stores the raw data from vehicles without

¹⁸ OAuth Community Site. Available online at: <https://oauth.net/> (accessed April 23, 2020).

¹⁹ Open Policy Agent. Available online at: <https://www.openpolicyagent.org/> (accessed April 23, 2020).

²⁰ Argos - Worldwide tracking and environmental monitoring by satellite. Available online at: <http://www.argos-system.org/> (accessed November 12, 2018).

²¹ Timescale - Open-source time-series database powered by PostgreSQL. Available online at: <https://www.timescale.com/> (accessed November 12, 2018).

delayed-mode data ingestion or quality-control pipelines in place. This service is useful for reacting to engineering and preliminary scientific data as soon as it is received from the vehicles, for quick access and analysis by pilots or to inform planning algorithms whilst the vehicle is still on the surface. The raw engineering data stored within Timeseries may also be used to inform reliability studies post-deployment.

- **Plan/Command dispatcher**—This is comprised of three services: a planner service stores vehicle-agnostic plans (abstract lists of behaviors, such as lists of waypoints or instructions to switch sensors on and off). The compiler service can then be used to convert these plans into the formats required by individual vehicle types. As microservices are designed to be stateless and provide individual functionalities, to manage the flow of execution required to first generate a plan and then send it to a vehicle, a third service, the Conductor, accesses these services in turn and sends the generated output to the data brokers. The data brokers then forward the vehicle-specific plans to the required shore-side servers. The Conductor monitors the state of the plan throughout creation and dispatch, informing users as each event takes place. The Conductor can halt and revert the process to an earlier step should an error occur at any point. This transforms a complex sequence of operations into what appears to external users as a single operation.

6.1. Piloting Frontend—User interface

At present, each of the different models of long-range vehicles within the MARS fleet are piloted with a different bespoke user-interface as provided by the vendor. These solutions range from proprietary desktop applications to sending modified files via FTP/SSH to shore-side servers. The significant variation in piloting interface results in a steep learning-curve for pilots. Consequently, a new pilot has to undergo training for each of the bespoke tools and operating procedures for each model of vehicle within the fleet.

The C2 system will unify piloting by implementing a single web-based user interface for the piloting of all over-the-horizon vehicles within the MARS fleet. Whilst each vehicle has different capabilities and modes of operation, preventing the use of an identical piloting interface for all platforms, we have identified commonality between vehicle workflows, developing design patterns to be used throughout the user interface and shared by all vehicles.

Where possible, we are following a user-interface design language, Material Design, developed by Google²² and used throughout their products including Google Maps, Docs, and Gmail. As these products are incredibly widely-used by the general public, the behavior and association of many user interface elements, from buttons and sidebars to icons and use of color, will already be very familiar to many users of the C2. Through this consistency with existing widely-used products, we aim to reduce the learning-curve associated with the C2 system, enabling trainee pilots to focus on learning the

technical operation and control of the vehicle itself, rather than how to navigate the website and interact with online forms, plots etc.

During deployments of MAS vehicles, pilots are on-call to check and ensure the safety of the platform at all times. Consequently, the ability to monitor mission progress from a mobile device was a requirement identified following engagement with pilot users. Material Design components scale and rearrange in consistent ways, familiar to users of Google apps, enabling use of the piloting interface on mobiles and tablets without the need for the development of a separate mobile-optimized front-end interface.

Due to the broad nature of the C2 web-based frontend as a portal for piloting, data discovery and analysis, there have been occasions where the existing Material Design standards did not cover our use-cases and therefore we have had to extend the principles. For example, we extended the concept of the top-level navigation bar to accommodate nested layers of navigation within different parts of the app. This is illustrated in **Figure 5**, where the second-level navigation bar represents functionality within the “Pilot” app, currently selected in the Top-level navigation bar. Equally, Material Design only provides a specification for simple in-browser pop-ups to notify the user of an event. However, as piloting is a high-risk activity requiring active user-engagement, our system needs to be able to interrupt the user in the event of an abort, for instance. Consequently, we have made use of native system notifications to notify the user of any events whilst the piloting interface is minimized or behind another application window (e.g., whilst the user is currently using a different application on their device). However, the underlying philosophy has been maintained and is in-line with the recent general broadening of the Material Design standard.

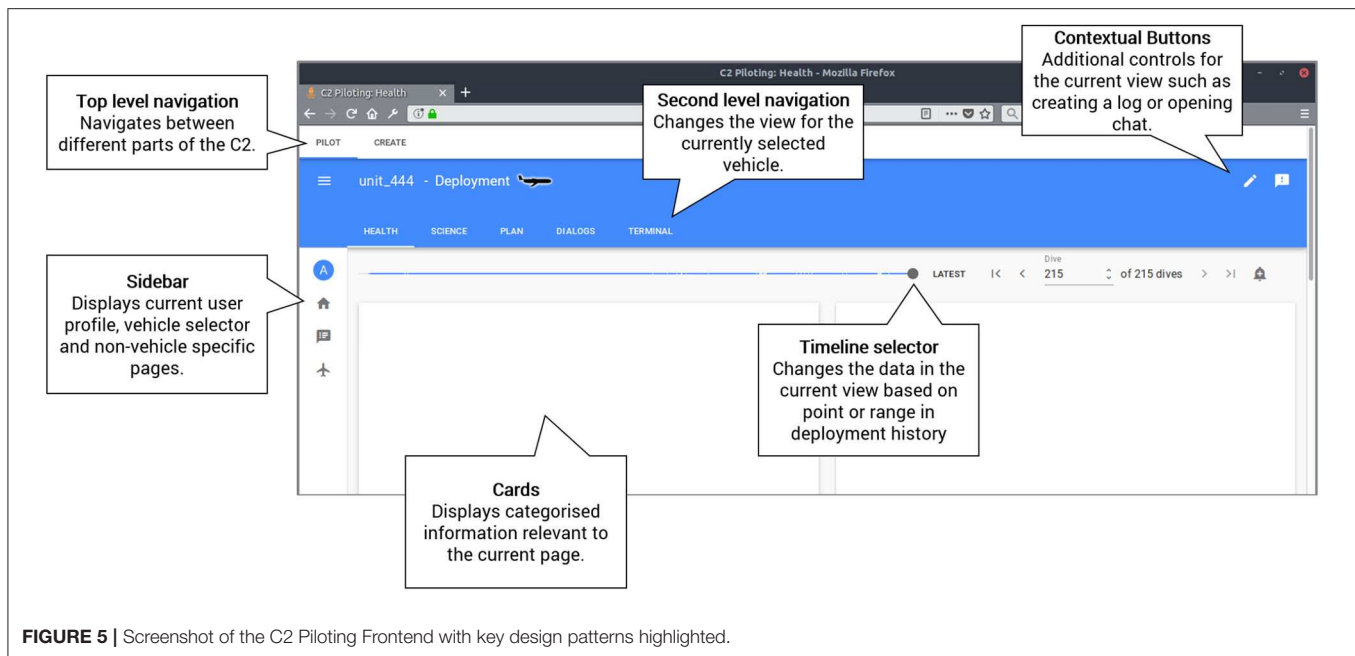
Figure 5 shows a labeled wireframe of the C2 user-interface, illustrating key design patterns, common to the piloting interfaces of all vehicles within the C2. In the remainder of this section, we discuss these key concepts in more detail.

6.2. Timeline

Whilst data collected by MAS vehicles is continuous and time-varying, vehicles typically connect to shore-side servers at discrete points in time. Within the C2, the continuous data from the vehicle is labeled according to these communication events, enabling a pilot to easily evaluate the data over the period since they last communicated with the vehicle, interpreting current health, and data quality.

To enable the pilot to explore data from earlier stages in the mission and to analyse trends across a period of data, the C2 front-end uses a Timeline design pattern (see **Figure 5**). The Timeline is a slider component allowing a user to move the state of the C2 to a particular point in time, or to specify a particular historic time range. This makes analysis of events and associated causality faster. Markers for specific events, such as changes in mission or platform errors, are also able to be added to the timeline.

²²Material Design. Available online at: <https://material.io/design/> (accessed November 11, 2018).



6.3. Piloting Navigation

Within the piloting interface for each vehicle, the user is presented with four tabs, the concept of which is common to all vehicle types—“Health,” “Science,” “Plan,” and “Dialogs”:

- **Health** displays Material Design cards which summarize and plot engineering data crucial to evaluating the current status of the vehicle, including battery voltage, device reports, and GPS position.
- **Science** comprises cards which display interactive plots of data from the science sensor suite onboard the vehicle. Some of these cards are common to all vehicles (e.g., CTD) whilst some will be vehicle or deployment specific.
- **Plan** is a dynamic interface which is customized to the vehicle type and capabilities but ultimately enables the user to alter waypoints or define new missions for the vehicle via a common mission planning and execution interface.
- **Dialogs** summarizes and displays the raw contents of human-readable communication from the vehicle. Whilst the health page provides a single-page overview for assessing the vehicle health, the dialogs page enables the pilot to review the specific details of each connection to further investigate faults.

In addition to the above tabs, displayed for all vehicle types, vehicle-specific tabs may be included where necessary. For instance, the piloting interface for the Slocum glider (Schofield et al., 2007) includes a “Terminal” tab, which implements a bidirectional command-line interface to the glider allowing an expert pilot to take full control of the glider when required. Integrating the terminal into the C2 removes the need for a second interface for interacting directly with the vehicle. However, such functionality is conditional upon user-permissions, so trainee glider pilots will not be able to send commands which may endanger the safety of the platform.

6.4. Map

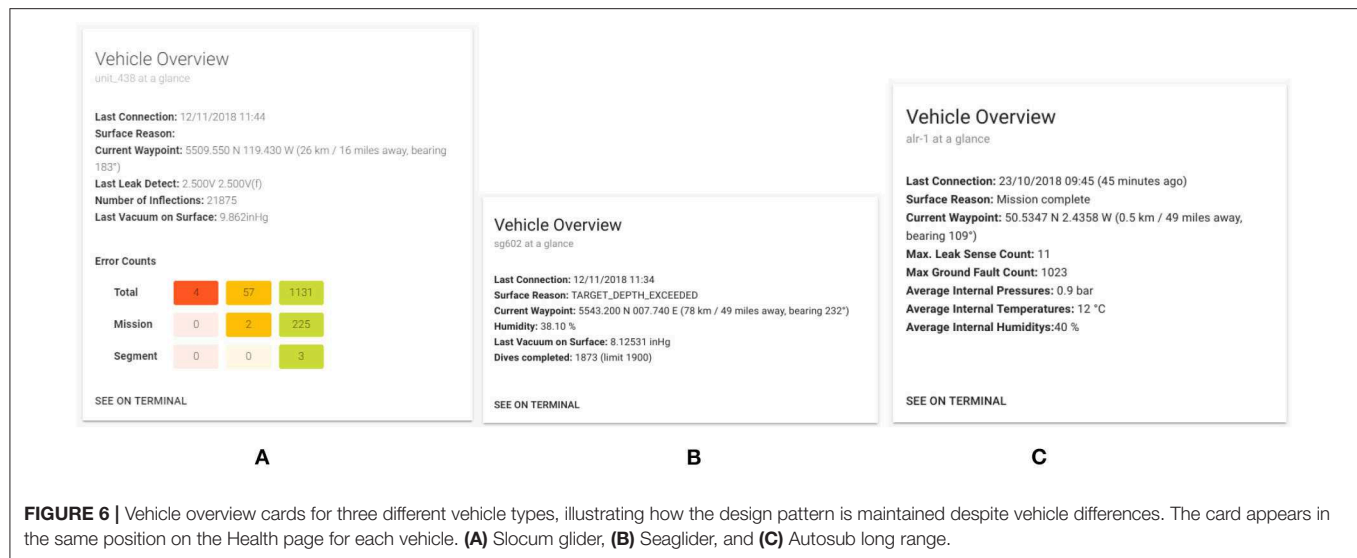
The map card consists of an interactive map implemented with Leaflet²³ which displays the current and previous positions of remote vehicles. Such data will automatically update when a vehicle sends its position to its shore-side server, enabling the pilot to keep track of progress or positioning amongst a fleet.

Users of the C2 are able to add and customize additional map layers to suit specific vehicle and mission requirements, including the uploading of image, video and Geographical Information System (GIS) layers and third-party TileLayers displaying Automatic Identification System (AIS) data. Users are able to set which layers are displayed by default such as isobaths or ice coverage layers depending on the area of operation. With such data sources available to the pilot, the map is also used for designing and verifying mission plans by allowing the pilot to annotate behaviors such as transit behaviors directly on the map before being compiled as a list of waypoints and sent to the vehicle.

6.5. Vehicle Overview Card

The Vehicle Overview card summarizes the most critical vehicle parameters, providing a concise snapshot of vehicle health (see Figure 6). The Vehicle Overview card appears in a consistent position within the piloting interface for each platform. The aim of the card is to alert the pilot to critical events such as water leaks and aborts, which need to be handled urgently. The other cards within the piloting interface then allow the pilot to further investigate the suspected cause of the critical event.

²³ Leaflet - an open-source JavaScript library for mobile-friendly interactive maps. Available online at: <https://leafletjs.com/> (accessed November 11, 2018).



6.6. Logs

The accurate logging of pilot actions and metadata associated with MAS deployments is essential for investigating vehicle faults and improving long-term reliability of the MARS fleet.

The creation of log entries needs to be quick and easy, as a pilot is likely to be under time pressure as a result of interacting with the vehicle at the same time, and may be under additional stress if a fault or leak has been identified. As a result, we have developed a consistent logging design pattern throughout the C2 interface, which consists of a button on all pages which opens a floating log entry alongside the current view. The user may continue to navigate between pages and pilot vehicles whilst the log entry is open, without losing the contents of a half-written log.

We are in the process of developing context-specific log functionality which will automatically suggest annotating the log entry with labels relating to the contents of the page the user is currently interacting with. For example, if a log entry is created on the Health tab for a glider whilst the vehicle is displaying an abort and a leak, the log entry will automatically be tagged with the vehicle name, ID, abort, and leak values. The user can then remove these tags with a single-click or add their own. At present, the body of the log-entry is a free-form text box. However, we intend to develop standard templates to prompt the user for key information and to ease subsequent quantitative analysis of log records.

6.7. Interactive Plots

To ensure the platform is navigating and collecting data correctly, pilots must monitor various engineering and scientific data sets that are sent back from the platforms. This can include: multiple flight parameters to allow for the correction of navigation behavior, science data samples to ensure the instruments are working correctly, and long-term engineering data to monitor deterioration in devices and calibrations.

Visualizing this data in plots allows pilots to efficiently analyse the data and make corrections quickly when necessary. However,

with deployments as long as six months, and data sampling as often as one sample every 15 s for as many as 20 variables, the amount of data needing to be visualized, especially while looking for long-term trends, can be very large. Such large datasets can be detrimental to the performance of a web application, especially on mobile browsers, requiring large loading and rendering times. To reduce the amount of data being sent to the client, data is windowed and aggregate statistics (such as 10 min averages) for each window are created for the requested time range. A pilot can then zoom in on narrower time ranges to download more detailed information for those particular ranges, as illustrated in Figure 7.

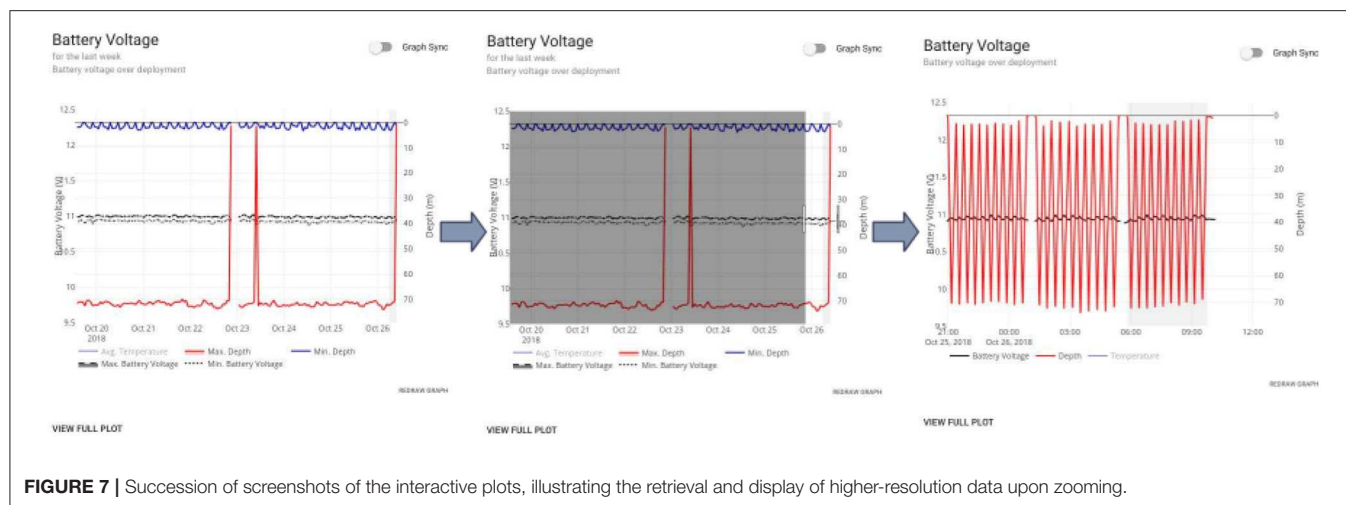
The `plotly.js` module²⁴ is used to build these plots in the C2 and allows for interaction with the data, such as extracting particular values or toggling the display of variables on the plots, to make analysis easier and reduce visual clutter. Graphs for specific platforms have been replicated in the C2 from existing piloting tools to make the transition to the C2 interface easier for existing users.

7. DATA PATHWAY

The data pathway within the C2 system is being jointly implemented by BODC and SAMS. In the same way as the piloting pathway, the data pathway is accessed via the common API gateway (see section 5.3) which enables the forwarding and delivery of both metadata and data from the vehicles and front-end user interface to the data-assembly center, BODC.

The requirements discussed in section 2 led to key architecture design decisions, namely: a target intermediate NetCDF4-based format devised for the data pathway called RXF, an archive system, exchange of metadata in JSON structures, and a scheduling algorithm to allow prioritization of the most pertinent

²⁴`plotly.js` - the open source JavaScript graphing library. Available online at: <https://plot.ly/javascript/> (accessed November 11, 2018).



data streams. RXF is a holding format used internally within BODC to allow for long-term stability regardless of updates and changes to external formats. RXF is flexible enough to support subsequent conversion to any required output format, such as EGO NetCDF. **Figure 4** highlights components of the C2 data system in green.

The workflow for the processing of both NRT and initial delayed-mode data is as follows:

1. Data are delivered from the shore-side servers to the archive system via the brokers throughout the mission, on the surfacing of the vehicle and completion of each mission.
2. On arrival at the archive system, the data are scanned by a virus checker. The archive system performs automated replication of the data to another site to enable cross-site data system redundancy and secure data archival.
3. Once data are registered in the archive they are ingested into the standardization system in RXF format.
4. On production of the RXF, the result is copied back to the archive to provide resilience. The RXF is built incrementally, with new data added to the existing file at each stage.
5. Once the RXF has been copied to the archive, an EGO file can be produced by the standardization system. This is not done incrementally but restarted for each update of the RXF. This is because EGO is a NetCDF3 format and would need to grow along more than one dimension, something that NetCDF3 does not allow.

Each element of the C2 data system will now be described in detail.

7.1. Metadata Service

The presence of sufficiently detailed metadata, and its subsequent availability on the web, is essential for data discovery and identification, for example by providing key information on sensor variables, units etc. At present, engineers and PIs (see **Table 1**) enter campaign and deployment information prior to the deployment of MAS vehicles, enabling automated data processing to begin when vehicles are at sea. However, the

longer-term aim is to extract metadata directly from both the MAS vehicles as well as NOC calibration and inventory management systems, removing the need for a user to enter this data, reducing error. Consequently, the C2 system has been designed to support this future automated acquisition of metadata and work has started on developing the necessary interfaces between the C2 and existing NOC systems.

The exposure of metadata to the web builds on a prototype developed by the European Commission supported SenseOCEAN project (Kokkinaki et al., 2016; Martínez et al., 2017) and is accessed according to open standards including World Wide Web Consortium (W3C) RDF/XML and the use of the Semantic Sensor Network (SSN) ontology (Haller et al., 2017) and Open Geospatial Consortium (OGC) SensorML (Open Geospatial Consortium, 2016) standard. Metadata exposure via SSN and SensorML is achieved using a database built using pre-existing ontologies and terms from the NERC vocabulary server 2.0 (NVS2) (Kokkinaki et al., 2016), ensuring consistency with other NERC data sources. Data will be delivered in EGO NetCDF format (EGO gliders data management team, 2017) and the OGC Observations and Measurements standard. Additional formats will be served by implementation of endpoints such as the NOAA ERDDAP tool²⁵.

7.2. Archive System

BODC is a ICSU World Data Systems accredited data center²⁶. When data is archived at BODC it is stored in duplicate with a checksum to ensure long-term data integrity within the BODC archive, with a third copy stored offsite as a backup.

Archive initiation is automatic and is triggered by the deployment of a MAS vehicle and the periodic arrival of mission data throughout the deployment. A security token enables data to be pushed to the archive from the shore-side server, via the

²⁵ERDDAP. Available at: <https://coastwatch.pfeg.noaa.gov/erddap/index.html> (accessed November 13, 2018).

²⁶ICSU World Data System. Available online at: <https://www.icsu-wds.org/services/certification> (accessed November 13, 2018).

brokers, and combined with metadata entered in advance of the deployment by the PI.

7.3. Standardization—EGO Production

Ingestion into the standardization system requires the creation of a mapping from vehicle-specific variable names to BODC's P01 vocabulary²⁷, which defines terms for observed properties, e.g., salinity. These mappings are encoded as JSON. To date, we have implemented mappings for both Slocum and Seagliders. Slocum data arrives in a proprietary binary format and is ingested after first being translated into ASCII. Seaglider data is already formatted as NetCDF and therefore no decompression or processing of raw data is required prior to ingestion.

Prior to the production of the EGO formatted data, all data in the RXF must be merged to a common, resolved time channel, as required by the EGO format. The current EGO specification requires NetCDF3 which, as mentioned previously, means that unlike the RXF, the EGO file cannot be grown incrementally. Following the intention of the EGO designers to make the file format largely self-sufficient, EGO contains an abundance of metadata (unlike RXF). Such information is communicated via JSON, utilizing the BODC vocabulary P06, which defines units of measurement²⁸. If variable units require scaling, this is also performed at this stage.

Production of EGO files within the C2 data system has been shown to be relatively fast, taking no more than 30 s for a 100 MB file using existing BODC server infrastructure. Given the slow speed of MAS vehicle missions (gliders and Autosub Long Range move at a slow walking pace) and the time taken to transmit data via Iridium, the time required for EGO production is considered negligible.

7.4. Data Delivery

The standardization of data delivery via the API gateway enables timely NRT data to be served to users of the C2, BODC users, and operational users²⁹. The use of open standards will also enable web interfaces to be rapidly built on the API gateway and the delivery of data to European research infrastructures that include aligned reference models for data infrastructure. The C2 data system contributes data and metadata directly to the OceanGlider (Testor et al., 2019) network which enables the data to be included in Copernicus³⁰ and EMODnet³¹ data products.

The combination of the C2 data system and the underlying database developed within the SenseOCEAN project (Martínez et al., 2017) is aligned with many of the FAIR principles (Wilkinson et al., 2016). Findability, accessibility, and interoperability of data will be archived via dissemination of data to the Ocean Glider Network where unique identifiers

will be assigned. Findability of metadata is partially archived with unique sensor/platform/deployment identifiers at the data centre level, pending the outcomes of the Research Data Alliance (RDA)³² working group on the persistent identification of instruments³³. Accessibility and re-usability of metadata is archived and exposed via the OGC Sensor Observation Service (Bröring et al., 2012). Interoperable metadata is achieved via the use of a the marine Sensor Web Enablement³⁴ profile for SensorML that includes use of the NERC vocabulary server for terms and values. Data reusability is partially obtained via the use of community standards and on-going work to develop a common data access policy.

At the time of writing, the C2 data system metadata is available via the 52° North GmbH variant³⁵ of the OGC SOS service. Future machine-to-machine services include making data available via the 52° North SOS server, addition of the data to an ERDDAP server, a W3C Linked-data data catalogue vocabulary (DCAT) exposure of data with a SPARQL endpoint, and exposure of metadata in W3C Semantic Sensor Network (SSN).

8. ONGOING AND FUTURE WORK

8.1. Automated Piloting Framework

Many aspects of long-range MAS piloting are routine, defined by standard-operating-procedures (SOPs), and require the pilot to check that various vehicle parameters are within the nominal range. Such checks would be straightforward to automate and would reduce the probability of human-error, particularly when piloting out-of-hours or in adverse environments, such as on a moving boat (Stokey et al., 1999). By automating these time-consuming and well-defined checks, we will increase the capacity of expert pilots to focus on meeting the science goals of the deployment and making more complicated fleet-level piloting decisions. By placing this autonomy on servers rather than on the vehicle itself, we enable the entire process to be monitored, interrupted and overridden by a human pilot as required. MAS vehicles will make contact with the C2 via satellite, as at present, receiving commands issued by either the automated piloting system or a human pilot.

Maintaining a level of human oversight and influence over the piloting process is crucial for the accountability of MAS operations. If, at any point, the status of the vehicle is determined to be outside the nominal range (as defined by the SOPs) the automated piloting system will escalate piloting decisions to the supervising human pilot and cease issuing commands. Once the human pilot is satisfied that the status of the vehicle has returned

²⁷NERC Vocabulary Server, P01. Available online at: <http://vocab.nerc.ac.uk/collection/P01/current/> (accessed November 13, 2018).

²⁸NERC Vocabulary Server, P06. Available online at: <http://vocab.nerc.ac.uk/collection/P06/current/> (accessed November 13, 2018).

²⁹OceanGlider Data Assembly Centre (DAC) for UK glider deployments. Available online at: https://www.bodc.ac.uk/data/bodc_database/gliders/.

³⁰Copernicus Marine Environment Monitoring Service. Available online at: <http://www.copernicus.eu/main/marine-monitoring> (accessed November 14, 2018).

³¹EMODnet. Available online at: <http://www.emodnet.eu/> (accessed November 14, 2018).

³²Research Data Alliance. Available online at: <https://www.rd-alliance.org/> (accessed November 14, 2018).

³³RDA Persistent Identification of Instruments working group. Available online at: <https://www.rd-alliance.org/groups/persistent-identification-instruments-wg> (accessed November 14, 2018).

³⁴Open Geospatial Consortium, Sensor Web Enablement. Available online at: <http://www.opengeospatial.org/domain/swe/initiative> (accessed November 14, 2018).

³⁵52° North Sensor Observation Service. Available online at: <https://52north.org/software/software-projects/sos/> (accessed November 14, 2018).

to normal, the human pilot may again delegate control back to the automated piloting system. We therefore require a mixed-initiative approach in which the human pilot may set the level of piloting responsibility to delegate to the automated system. We envisage the use of concepts such as user-adjustable autonomy, as presented by Ai-Chang et al. (2004) in their MAPGEN system for Mars rover missions.

To support the collaborative aims of the C2 development, the framework implements clear interfaces which third-party developers, scientists or engineers may use to develop and integrate their own automated piloting algorithms. The framework ensures that such mission plans created by third-party developers are compliant with regulatory requirements and NOC SOPs, keeping mission risk to within an acceptable level. If any constraints are violated by a proposed plan, the automated piloting framework alerts an expert pilot and ceases sending automated commands. Through these interfaces, additional capabilities such as intelligent COLREGS behaviors for LRUSVs, current-aware piloting algorithms and task scheduling approaches can be integrated into the C2.

We are also working to address the need for ongoing monitoring and detection of adverse performance trends, highlighted by Thieme and Utne (2017), who state that “Unanticipated faults and events might lead to loss of vessels, transported goods, collected scientific data, and business reputation. Hence, systems have to be in place that monitor the safety performance of operation and indicate if it drifts into an intolerable safety level,” a view shared by the Maritime Autonomous Surface Ships Industry Conduct Principles Code of Practice³⁶, section 8.8.1. In collaboration with University College London (UCL), we are currently developing and integrating two systems to address this need:

1. An automated system for determining the optimal flight parameters for Seaglidors (Anderlini et al., 2019), which present results to either a human pilot as a recommendation, or can be sent directly to the vehicle, depending on the user-defined level of autonomy. This will enable around the clock operations, reducing the substantial piloting overhead at the start of a mission and allowing more vehicles to be deployed simultaneously. We are planning to test the system at sea in Summer 2020.
2. A monitoring system for gliders in which the data provided by the C2 system is analyzed and compared to the glider flight model using statistical and machine learning methods to identify adverse conditions including biofouling and wing-loss (Anderlini et al., submitted). Early results from the approach have been very promising, with the detection of conditions which have previously been challenging for pilots to manually identify.

Investigating why the AUV community has yet to widely adopt adaptive mission planning, Brito et al. (2012) found uncertain

vehicle behaviors to be the largest concern (39.7%) of expert AUV operators. The second largest concern (20.7%) was that the technology is not understood, with the majority of respondents reporting that it has not been well explained. To address this concern and to build confidence in the automated piloting framework amongst both MAS pilots and stakeholders, decisions made by the system must be clearly communicated to the pilot at all times and fully logged. To this end, we are investigating the use of techniques such as explainable planning (Fox et al., 2017) and robot transparency (Wortham et al., 2017).

8.2. Risk and Reliability Modeling

By unifying the piloting interfaces and data flow across the long-range MARS fleet, the C2 offers an opportunity to record, quantify and analyse vehicle reliability on a scale that was previously impossible. Brito and Griffiths' (2009), Brito et al. (2010) previously created a risk model for the Autosub3 AUV. However, due to the lack of objective data and metadata on faults, mission success and vehicle performance, the model was constructed using expert subjective judgment. Whilst this work informed successful mitigation for under-ice work, the authors highlighted the difficulties associated with using expert judgment, stating that a panel of experts provided probabilities of a fault leading to vehicle loss that spanned three orders of magnitude. The C2 system will address this gap in objective data by automatically logging and monitoring vehicle connections, events, and constraint violations, reducing the need for the pilot to accurately record this information manually. The development of data-driven techniques and risk models to extend Brito and Griffiths' (2010) previous work is an active area of our ongoing research. By integrating context-specific logging functionality into the common piloting frontend (see section 6.6), rather than requiring the pilot to log-in to a separate system or resort to pen and paper, we are seeking to minimize the overheads associated with accurate fault and event recording, promoting uptake. Through the C2 APIs, we seek to aggregate vehicle and fault data with data from our inventory management and ship-programme systems, enabling a holistic identification and characterization of the elements involved in faults, such as planned maintenance, equipment history, and deployment location (Dopico-Gonzalez et al., 2019). Once we have sufficient data, we aim to incorporate real-time risk analysis and feedback into the piloting process, alerting the pilot, PI, or automated piloting algorithm when the planned mission is calculated to increase risk to the vehicle or its scientific data cargo.

8.3. Notable Ocean Deployments of the C2 System

To evaluate the design and usability of the Automated Piloting Framework, we created an external path-planning algorithm that uses AI techniques to calculate the optimal trajectory through an area of high-current, using the UK Met Office Forecast Ocean Assimilation Model (FOAM)³⁷ forecasts. This algorithm

³⁶Maritime Autonomous Surface Ships Industry Conduct Principles Code of Practice, Available online at: <https://www.maritimeuk.org/media-centre/publications/maritime-autonomous-surface-ships-industry-conduct-principles-code-practice/> (accessed April 27, 2020).

³⁷E.U. Copernicus Marine Service Information - Atlantic - European North-West shelf ocean physics analysis and forecast. Available online at: <https://tinyurl.com/y82gbodh> (accessed November 12, 2018).

connected to the C2 via the APIs, and was successfully used to command a glider on deployment in the North Sea in Spring 2019 alongside the AlterEco³⁸ project gliders. This deployment proved the concept of the Automated Piloting Framework and engaged with scientific stakeholders, allowing us to identifying areas for further development.

During the MASSMO 5 and Summer 2018 AlterECO deployments of Slocum gliders, the C2 data processing system was fully trialed, including the submission of delayed-mode data to the Ocean Glider Programme GDAC, and the submission of NRT data to the UK Met Office. During MASSMO 5, the EGO files produced by the C2 data processing system were visualized by project partners including Plymouth Marine Laboratory (PML) and SAMS. Feedback and lessons learnt during these trials were subsequently fed into requirements for future development.

9. CONCLUSIONS

As the popularity of MAS operations continues to grow, it is essential that factors which currently limit the scalability of piloting and data systems are addressed. Existing MAS piloting interfaces were typically custom-made for each vehicle by the manufacturer, assuming a one-to-one relationship between pilot and vehicle. This has resulted in a significant training overhead for pilots which, combined with limited cross-vehicle standardization, restricts the size and complexity of heterogeneous fleet operations. Likewise, data have historically been primarily “delayed-mode” i.e., available only on recovery of the MAS vehicle. However, advances in long-range MAS vehicles, capable of operating for months at a time, have created opportunities to automate the processing of NRT data, enabling assimilation into ocean models and delivery to the end-user throughout the mission.

³⁸ AlterEco - The National Oceanography Centre and the Natural Environment Research Council: <http://altereco.ac.uk/> (accessed July 25, 2018).

REFERENCES

- Ai-Chang, M., Bresina, J., Charest, L., Chase, A., Hsu, J. C. J., Jonsson, A., et al. (2004). Mapgen: mixed-initiative planning and scheduling for the Mars exploration rover mission. *IEEE Intell. Syst.* 19, 8–12. doi: 10.1109/MIS.2004.1265878
- Anderlini, E., Harris, C., Phillips, A. B., Lopez, A. L., Woo, M., and Thomas, G. (2019). Towards autonomy: a recommender system for the determination of trim and flight parameters for seaglidors. *Ocean Eng.* 189:106338. doi: 10.1016/j.oceaneng.2019.106338
- Australian National Facility for Ocean Gliders (2012). *Data Management User's Manual*. Technical report, University of Western Australia.
- Brito, M., Bose, N., Lewis, R., Alexander, P., Griffiths, G., and Ferguson, J. (2012). “The role of adaptive mission planning and control in persistent autonomous underwater vehicles presence,” in *Proceedings of IEEE/OES Autonomous Underwater Vehicles, AUV'12* (Southampton: Institute of Electrical and Electronic Engineers). doi: 10.1109/AUV.2012.6380748
- Brito, M., and Griffiths, G. (2009). “On the use of expert judgment elicitation for autonomous underwater vehicle risk prediction and management,” in *Proceedings of the European Safety and Reliability Conference, ESREL'09* (Prague: Taylor and Francis), 1221–1227. doi: 10.1201/9780203859759.ch169
- Brito, M. P., Griffiths, G., and Challenor, P. (2010). Risk analysis for autonomous underwater vehicle operations in extreme environments. *Risk Anal.* 30, 1771–1788. doi: 10.1111/j.1539-6924.2010.01476.x
- Bröring, A., Stasch, C., and Echtermhoff, J. (2012). *OGC Sensor Observation Service Interface Standard*. Technical report, Open Geospatial Consortium.
- Buadu, S., Schjølberg, I., and Mo-Bjørkelund, T. (2018). “Mission planner for multiple AUVs: verification procedures combining simulations and experiments,” in *2018 IEEE/OES Autonomous Underwater Vehicle Workshop (AUV)* (Porto), 1–6. doi: 10.1109/AUV.2018.8729793
- Buck, J. J. H., Bainbridge, S. J., Burger, E. F., Río Fernandez, J. d., Delory, E., Fischer, P., et al. (2019). Ocean data product integration through innovation-the next level of data interoperability. *Front. Mar. Sci.* 6:32. doi: 10.3389/fmars.2019.00032
- Cunningham, S. A., Kanzow, T., Rayner, D., Baringer, M. O., Johns, W. E., Marotzke, J., et al. (2007). Temporal variability of the Atlantic meridional overturning circulation at 26.5°N. *Science* 317, 935–938. doi: 10.1126/science.1141304
- Dias, P. S., Gomes, R. M., and Pinto, J. (2006). “Mission planning and specification in the Neptus framework,” in *Proceedings 2006 IEEE International Conference on Robotics and Automation* (Orlando, FL), 3220–3225. doi: 10.1109/ROBOT.2006.1642192
- In this paper, we have presented the Oceanids C2, a unified web-based system for the command, control and data management of MAS vehicles within the NMEP. Through the use of data, metadata, and API standards, and prioritizing the flexibility and scalability of the C2 system, we seek to enable future collaborations with both the marine science and robotics communities to revolutionize the use of long-range MAS vehicles and ultimately increase the delivery of high-quality oceanographic data for cutting-edge science.

AUTHOR CONTRIBUTIONS

CH is leading the Automated Piloting Framework and wrote the paper. AL-L oversaw technical development of the C2 Infrastructure and wrote the paper. OJ developed the backend. JB acted as product owner for the data pathway and wrote the paper. AK was the architect of the metadata system. SL oversaw development of the data standardization workflow and wrote the paper. TG built APIs and integrated the first gateway. AP oversaw the project and wrote the paper.

FUNDING

The development of the C2 infrastructure was funded by the UK's Industrial Strategy Challenge Fund (ISCF)—Natural Environment Research Council (NERC) Oceanids Capital investment in Marine Autonomous Systems.

ACKNOWLEDGMENTS

The authors would like to thank Ashley Morris, Jack Farley, Stephen Fraser, Kay Thorne, Malcolm Hearn, Matthew Cazaly, James Yannaros, Cieran Brazier, Karen Vickers, Jack Gee, Thomas Bailey, Maaten Furlong, Russ Wynn, Carolina Dopico Gonzalez, Paola Arce, Sam Jones, Matt Toberman, and Louise Darroch for their work on the Oceanids C2 project.

- Dopico-Gonzalez, C., Harris, C. A., and Phillips, A. B. (2019). "Risk and reliability management of marine autonomous systems within the UK's national marine equipment pool," in *OCEANS 2019* (Marseille), 1–9. doi: 10.1109/OCEANSE.2019.8867521
- EGO gliders data management team (2017). *Ego Gliders netcdf Format Reference Manual*. Technical report, Ifremer.
- Eriksen, C. C., Osse, T. J., Light, R. D., Wen, T., Lehman, T. W., Sabin, P. L., et al. (2001). Seaglider: a long-range autonomous underwater vehicle for oceanographic research. *IEEE J. Ocean. Eng.* 26, 424–436. doi: 10.1109/48.972073
- Faria, M., Pinto, J., Py, F., Fortuna, J., Dias, H., Martins, R., et al. (2014). "Coordinating UAVs and AUVs for oceanographic field experiments: challenges and lessons learned," in *2014 IEEE International Conference on Robotics and Automation (ICRA)* (Hong Kong), 6606–6611. doi: 10.1109/ICRA.2014.6907834
- Farley, J., Morris, A., Jones, O., Harris, C. A., and Lorenzo, A. (2019). "Marine science from an armchair: a unified piloting framework for autonomous marine vehicles," in *OCEANS 2019* (Marseille). doi: 10.1109/OCEANSE.2019.8867573
- Ferreira, A. S., Costa, M., Py, F., Pinto, J., Silva, M. A., Nimmo-Smith, A., et al. (2019). Advancing multi-vehicle deployments in oceanographic field experiments. *Auton. Robots* 43, 1555–1574. doi: 10.1007/s10514-018-9810-x
- Ferreira, A. S., Pinto, J., Dias, P., and de Sousa, J. B. (2017). "The LSTS software toolchain for persistent maritime operations applied through vehicular ad-hoc networks," in *2017 International Conference on Unmanned Aircraft Systems (ICUAS)* (Miami, FL), 609–616. doi: 10.1109/ICUAS.2017.7991471
- Fette, I., and Melnikov, A. (2011). *Rfc 6455: The WebSocket Protocol*. Technical report, IETF. doi: 10.17487/rfc6455
- Fox, M., Long, D., and Magazzeni, D. (2017). Explainable planning. *CoRR*, abs/1709.10256.
- Furlong, M. E., Paxton, D., Stevenson, P., Pebody, M., McPhail, S. D., and Perrett, J. (2012). "Autosub long range: a long range deep diving AUV for ocean monitoring," in *Autonomous Underwater Vehicles (AUV)*, 2012 IEEE/OES (Southampton), 1–7. doi: 10.1109/AUV.2012.6380737
- Garabato, A. C. N., Frajka-Williams, E. E., Spingys, C. P., Legg, S., Polzin, K. L., Forryan, A., et al. (2019). Rapid mixing and exchange of deep-ocean waters in an abyssal boundary current. *Proc. Natl. Acad. Sci. U.S.A.* 116, 13233–13238. doi: 10.1073/pnas.1904087116
- German, C. R., Jakuba, M. V., Kinsey, J. C., Partan, J., Suman, S., Belani, A., et al. (2012). "A long term vision for long-range ship-free deep ocean operations: persistent presence through coordination of autonomous surface vehicles and autonomous underwater vehicles," in *Autonomous Underwater Vehicles (AUV)*, 2012 IEEE/OES (Southampton), 1–7. doi: 10.1109/AUV.2012.6380753
- German, C. R., Yoerger, D. R., Jakuba, M., Shank, T. M., Langmuir, C. H., and Nakamura, K.-I. (2008). Hydrothermal exploration with the autonomous benthic explorer. *Deep Sea Res. Part I* 55, 203–219. doi: 10.1016/j.dsr.2007.11.004
- Haller, A., Janowicz, K., Cox, S., Phuoc, D. L., Taylor, K., and Lefrançois, M. (2017). *Semantic Sensor Network Ontology. w3c Recommendation*. Technical report, W3C.
- Haworth, C., Evans, J., McManamon, K., and McNally, K. (2016). "Combined USV/subsea-glider fleets for tidal mixing front tracking and monitoring," in *OCEANS 2016 MTS/IEEE* (Monterey, CA), 1–6. doi: 10.1109/OCEANS.2016.7761332
- Hickson, I. (2015). *Rec-Eventsource-2015020: Server-Sent Events*. Technical report, W3C.
- Hobson, B. W., Bellingham, J. G., Kieft, B., McEwen, R., Godin, M., and Zhang, Y. (2012). "Tethys-class long range AUVs-extending the endurance of propeller-driven cruising AUVs from days to weeks," in *Autonomous Underwater Vehicles (AUV)*, 2012 IEEE/OES, 1–8. Southampton: IEEE. doi: 10.1109/AUV.2012.6380735
- Houpert, L., Inall, M., Dumont, E., Gary, S., Johnson, C., Porter, M., et al. (2018). Structure and transport of the north Atlantic current in the eastern subpolar gyre from sustained glider observations. *J. Geophys. Res.* 123, 6019–6038. doi: 10.1029/2018JC014162
- Jones, D. O., Gates, A. R., Huvenne, V. A., Phillips, A. B., and Bett, B. J. (2019). Autonomous marine environmental monitoring: application in decommissioned oil fields. *Sci. Tot. Environ.* 668, 835–853. doi: 10.1016/j.scitotenv.2019.02.310
- Kokkinaki, A., Darroch, L., Buck, J., and Jirka, S. (2016). "Semantically enhancing SensorML with controlled vocabularies in the marine domain," in *Proceedings of GSWC 2016, Geospatial Sensor Webs Conference* (Munster).
- Leonard, N. E., Paley, D. A., Davis, R. E., Fratanoni, D. M., Lekien, F., and Zhang, F. (2010). Coordinated control of an underwater glider fleet in an adaptive ocean sampling field experiment in Monterey Bay. *J. Field Robot.* 27, 718–740. doi: 10.1002/rob.20366
- Liblik, T., Karstensen, J., Testor, P., Alenius, P., Hayes, D., Ruiz, S., et al. (2016). Potential for an underwater glider component as part of the global ocean observing system. *Methods Oceanogr.* 17, 50–82. doi: 10.1016/j.mio.2016.05.001
- Manley, J., and Willcox, S. (2010). "The wave glider: a persistent platform for ocean science," in *OCEANS 2010 IEEE* (Sydney), 1–5. doi: 10.1109/OCEANSSD.2010.5603614
- Martinez, S., Delory, E., del Rio, J., Jirka, S., Pearlman, J., D'Angelo, P., et al. (2017). *Deliverable d7.8 Policy Document - Sensor Development for the Ocean of Tomorrow*. Technical report, European Union Seventh Framework Programme.
- McPhail, S. (2009). Autosub6000: a deep diving long range AUV. *J. Bion. Eng.* 6, 55–62. doi: 10.1016/S1672-6529(08)60095-5
- McPhail, S., Templeton, R., Pebody, M., Roper, D., and Morrison, R. (2019). "Autosub long range AUV missions under the Filchner and Ronne ice shelves in the Weddell sea, Antarctica-an engineering perspective," in *OCEANS 2019* (Marseille), 1–8. doi: 10.1109/OCEANSE.2019.8867206
- Open Geospatial Consortium (2016). *Sensor Model Language (sensorml)*. Technical report. Available online at: Opengeospatial.org.
- Paley, D. A., Zhang, F., and Leonard, N. E. (2008). Cooperative control for ocean sampling: the glider coordinated control system. *IEEE Trans. Control Syst. Technol.* 16, 735–744. doi: 10.1109/TCST.2007.912238
- Phillips, A. B., Salavasidis, G., Kingsland, M., Harris, C., Pebody, M., Roper, D., et al. (2018). "Autonomous surface/subsurface survey system field trials," in *Autonomous Underwater Vehicles (AUV)*, 2018 IEEE/OES (Porto), 1–7. doi: 10.1109/AUV.2018.8729740
- Pinto, J., Dias, P., Ribeiro, M., Costa, M., and Sousa, J. (2017). "Networked vehicle systems: from vision to reality," in *OCEANS 2017* (Aberdeen), 1–6. doi: 10.1109/OCEANSE.2017.8084823
- Pinto, J., Dias, P. S., Martins, R., Fortuna, J., Marques, E., and Sousa, J. (2013). "The LSTS toolchain for networked vehicle systems," in *2013 MTS/IEEE OCEANS* (Bergen), 1–9. doi: 10.1109/OCEANS-Bergen.2013.6608148
- Ramp, S. R., Davis, R. E., Leonard, N. E., Shulman, I., Chao, Y., Robinson, A., et al. (2009). Preparing to predict: the second autonomous ocean sampling network (AOSN-II) experiment in the Monterey Bay. *Deep Sea Res. Part II* 56, 68–86. doi: 10.1016/j.dsr2.2008.08.013
- Reitz, A., Visbeck, M., and Fritz, J.-S. (2016). *AtlantOS Exploitation Plan*. Technical Report, European Union Horizon 2020.
- Roemmich, D., Boehme, L., Claustre, H., Freeland, H., Fukasawa, M., Goni, G., et al. (2010). Integrating the ocean observing system: mobile platforms. *Proc. OceanObs* 9:33. doi: 10.5270/OceanObs09.pp.33
- Roemmich, D., Johnson, G. C., Riser, S., Davis, R., Gilson, J., Owens, W. B., et al. (2009). The Argo program: observing the global ocean with profiling floats. *Oceanography* 22, 34–43. doi: 10.5670/oceanog.2009.36
- Roemmich, D., and the Argo Steering Team (2009). Argo: the challenge of continuing 10 years of progress. *Oceanography* 22, 46–55. doi: 10.5670/oceanog.2009.65
- Roper, D. T., Phillips, A. B., Harris, C. A., Salavasidis, G., Pebody, M., Templeton, R., et al. (2017). "Autosub long range 1500: an ultra-endurance AUV with 6000 km range," in *OCEANS 2017* (Aberdeen: IEEE), 1–5. doi: 10.1109/OCEANSE.2017.8084928
- Rudnick, D. L., Davis, R. E., Eriksen, C. C., Fratanoni, D. M., and Perry, M. J. (2004). Underwater gliders for ocean research. *Mar. Technol. Soc. J.* 38, 73–84. doi: 10.4031/002533204787522703
- Salavasidis, G., Munafò, A., Harris, C. A., Prampart, T., Templeton, R., Smart, M., et al. (2018). Terrain-aided navigation for long-endurance and deep-rated autonomous underwater vehicles. *J. Field Robot.* 36, 447–474. doi: 10.1002/rob.21832
- Schofield, O., Kohut, J., Aragon, D., Creed, L., Graver, J., Haldeman, C., et al. (2007). Slocum gliders: robust and ready. *J. Field Robot.* 24, 473–485. doi: 10.1002/rob.20200

- Stokey, R., Austin, T., von Alt, C., Purcell, M., Forrester, N., Goldsborough, R., et al. (1999). "AUV bloopers or why Murphy must have been an optimist: a practical look at achieving mission level reliability in an autonomous underwater vehicle," in *Proceedings of the Eleventh International Symposium on Unmanned Untethered Submersible Technology* (Durham, NC), 32–40.
- Testor, P., de Young, B., Rudnick, D. L., Glenn, S., Hayes, D., Lee, C. M., et al. (2019). Oceangliders: a component of the integrated GOOS. *Front. Mar. Sci.* 6:422. doi: 10.3389/fmars.2019.00422
- Testor, P., Meyers, G., Pattiaratchi, C., Bachmayer, R., Hayes, D., Pouliquen, S., et al. (2010). "Gliders as a component of future observing systems," in *OceanObs'09* (Venice). doi: 10.5270/OceanObs09.cwp.89
- Thieme, C. A., and Utne, I. B. (2017). Safety performance monitoring of autonomous marine systems. *Reliabil. Eng. Syst. Saf.* 159, 264–275. doi: 10.1016/j.ress.2016.11.024
- U.S. IOOS National Glider Data Assembly Center (2018). *Ngdac Netcdf File Format Version 2*. Technical report, Integrated Ocean Observing System.
- Wilkinson, M. D., Dumontier, M., Aalbersberg, I. J., Appleton, G., Axton, M., Baak, A., et al. (2016). The FAIR guiding principles for scientific data management and stewardship. *Sci. Data* 3:160018. doi: 10.1038/sdata.2016.18
- Wortham, R. H., Theodorou, A., and Bryson, J. J. (2017). "Improving robot transparency: real-time visualisation of robot AI substantially improves understanding in naive observers," in *IEEE RO-MAN 2017* (Lisbon). doi: 10.1109/ROMAN.2017.8172491

Conflict of Interest: The authors declare that the research was conducted in the absence of any commercial or financial relationships that could be construed as a potential conflict of interest.

Copyright © 2020 Harris, Lorenzo-Lopez, Jones, Buck, Kokkinaki, Loch, Gardner and Phillips. This is an open-access article distributed under the terms of the Creative Commons Attribution License (CC BY). The use, distribution or reproduction in other forums is permitted, provided the original author(s) and the copyright owner(s) are credited and that the original publication in this journal is cited, in accordance with accepted academic practice. No use, distribution or reproduction is permitted which does not comply with these terms.



Multi-Decadal Humpback Whale Migratory Route Fidelity Despite Oceanographic and Geomagnetic Change

Travis W. Horton^{1*}, Alexandre N. Zerbini^{2,3,4,5}, Artur Andriolo^{4,6}, Daniel Danilewicz^{4,7,8} and Federico Sucunza^{4,6,9}

¹ Te Kura Aronukurangi – School of Earth and Environment, University of Canterbury, Christchurch, New Zealand, ² Joint Institute for the Study of the Atmosphere and Ocean (JISAO), University of Washington & Marine Mammal Laboratory, Alaska Fisheries Science Center, National Marine Fisheries Service, NOAA, Seattle, WA, United States, ³ Cascadia Research Collective, Olympia, WA, United States, ⁴ Instituto Aqualie, Juiz de Fora, Brazil, ⁵ Marine Ecology and Telemetry Research, Seabeck, WA, United States, ⁶ Laboratório de Ecologia Comportamental e Bioacústica, ICB, Universidade Federal de Juiz de Fora, Juiz de Fora, Brazil, ⁷ Grupo de Estudos de Mamíferos Aquáticos do Rio Grande do Sul, Osório, Brazil, ⁸ Universidade Estadual de Santa Cruz, Jaboticabal, Brazil, ⁹ Grupo de Estudos de Mamíferos Aquáticos do Rio Grande do Sul (GEMARS), Rua Bento Gonçalves, Torres, Brazil

OPEN ACCESS

Edited by:

Eric Delory,
Oceanic Platform of the Canary
Islands, Spain

Reviewed by:

Peter Corkeron,
New England Aquarium,
United States
Jan Straley,
University of Alaska Southeast,
United States

*Correspondence:

Travis W. Horton
travis.horton@canterbury.ac.nz

Specialty section:

This article was submitted to
Ocean Observation,
a section of the journal
Frontiers in Marine Science

Received: 13 April 2019

Accepted: 12 May 2020

Published: 24 June 2020

Citation:

Horton TW, Zerbini AN,
Andriolo A, Danilewicz D and
Sucunza F (2020) Multi-Decadal
Humpback Whale Migratory Route
Fidelity Despite Oceanographic
and Geomagnetic Change.
Front. Mar. Sci. 7:414.
doi: 10.3389/fmars.2020.00414

Understanding how organisms respond to environmental change is one of the most pressing grand challenges of organismal biology. In the vast oceans that cover 71% of Earth's surface, remote sensing technologies have created unprecedented opportunities to create new knowledge and deliver integrated understandings of marine organism-environment interactions via long-term monitoring. Using historic whaling records and >15 years of satellite-derived data, we show that movement parameters associated with long-distance humpback whale migrations, including utilization of a south-southeast directed migratory corridor, migration path straightness, direction, timing, and velocity, have not significantly changed during a period of dynamic oceanographic and geomagnetic conditions. These findings reveal an apparent paradox: humpback whale migrations do not change in a changing ocean. Geophysical analyses of the same humpback whale movements demonstrate that these whales maintained prolonged migratory fidelity to a limited suite of spatiotemporal trajectories through gravitational coordinates, raising the possibility that migratory decisions are relatively insensitive to changing oceanographic and geomagnetic conditions. Our findings highlight the importance of filling the knowledge gaps that currently limit our ability to understand and anticipate organismal responses to rapidly changing Earth system conditions.

Keywords: satellite telemetry, remote sensing, humpback whale, migration, navigation, South Atlantic Ocean, geomagnetism, environmental change

INTRODUCTION

Migratory animals face an uncertain future (Cotton, 2003; Wilcove and Wikelski, 2008; Hazen et al., 2013; Hof et al., 2017; Cohen et al., 2018). Global change, climate change, development, resource extraction, habitat fragmentation, and other human-induced perturbations combine to present unprecedented challenges to the sustainability of migratory populations and the ecosystem services they provide (Peñuelas et al., 2002; Harris et al., 2009, 2018; Roman and McCarthy, 2010; Thackeray et al., 2016; van Doren et al., 2017). Ensuring that sustainable populations of migratory animals

persist into the future requires knowledge of how migrants respond to Earth system dynamics (Schwenk et al., 2009; Bowlin et al., 2010).

It is widely agreed that addressing the challenges inherent to a dynamic Earth system requires long-term monitoring delivered through integrated interdisciplinary research approaches (Schwenk et al., 2009; Bowlin et al., 2010; Hays et al., 2016; Urban et al., 2016; Miloslavich et al., 2018). At present, models intending to predict the effects of Earth system dynamics on the biosphere suffer from both a lack of data and a limited understanding of the dominant biological mechanisms through which adaptations occur, including: phenology and demography; physiology; range dynamics; evolutionary potential; species interactions; and organismal responses to environmental variability (Urban et al., 2016). Robust prediction of future scenarios requires monitoring of the relevant variables at appropriately matched spatial and temporal scales (Hazen et al., 2013; Pereira et al., 2013; Urban et al., 2016; Miloslavich et al., 2018). Although significant progress in remote monitoring has occurred, relatively few studies integrate long-term datasets of both organismal behavior and the dynamic environments they inhabit (Sprogis et al., 2018; Abrahms et al., 2019). The primary goal of this research was to explore gaps in our knowledge regarding how humpback whale (*Megaptera novaeangliae*) long-distance migrations respond to oceanographic and geomagnetic change through long-term remote ocean monitoring.

Environmental changes should evoke biological responses, including habitat shifts in marine organisms (e.g., Hoegh-Guldberg and Bruno, 2010; Hazen et al., 2013), and large whales are no exception (Santora et al., 2020). For example, recent research suggests that ocean circulation dynamics in the North Atlantic have forced changes in right whale (*Eubalaena glacialis*) foraging patterns (Record et al., 2019), and in the North Pacific, humpback whale feeding behavior has been shown to respond to oceanographic conditions, including sea surface temperature, upwelling, and biomass (Fleming et al., 2016). Along the coast of California, habitat compression associated with the 2014–2016 marine heatwave likely contributed to an order of magnitude increase in annual humpback whale entanglement rate (Santora et al., 2020). In the South Pacific, Oceania's changing climate is predicted to cause distribution shifts in endangered humpback whales (Derville et al., 2019). In the Southwest Atlantic, environmental variables, including ocean currents and sea surface temperatures, were found to be strong predictors of humpback whale distribution in the Abrolhos Bank breeding area (Bortolotto et al., 2017). Ocean water temperature has also been linked to changes in humpback whale foraging behavior in the Southern Ocean (Owen et al., 2019). Although the literature clearly establishes that large whale distribution and behavior are sensitive to environmental conditions in their breeding and feeding areas, the cues and conditions that inform long-distance migratory behavior remain largely unknown.

Current evidence suggests that whale movement decisions are likely informed by some combination of magnetic, oceanographic, and gravitational cues. For example, integrating magnetic cues into whale behavior research has led to novel insights into whale stranding and navigation (Kirschvink et al.,

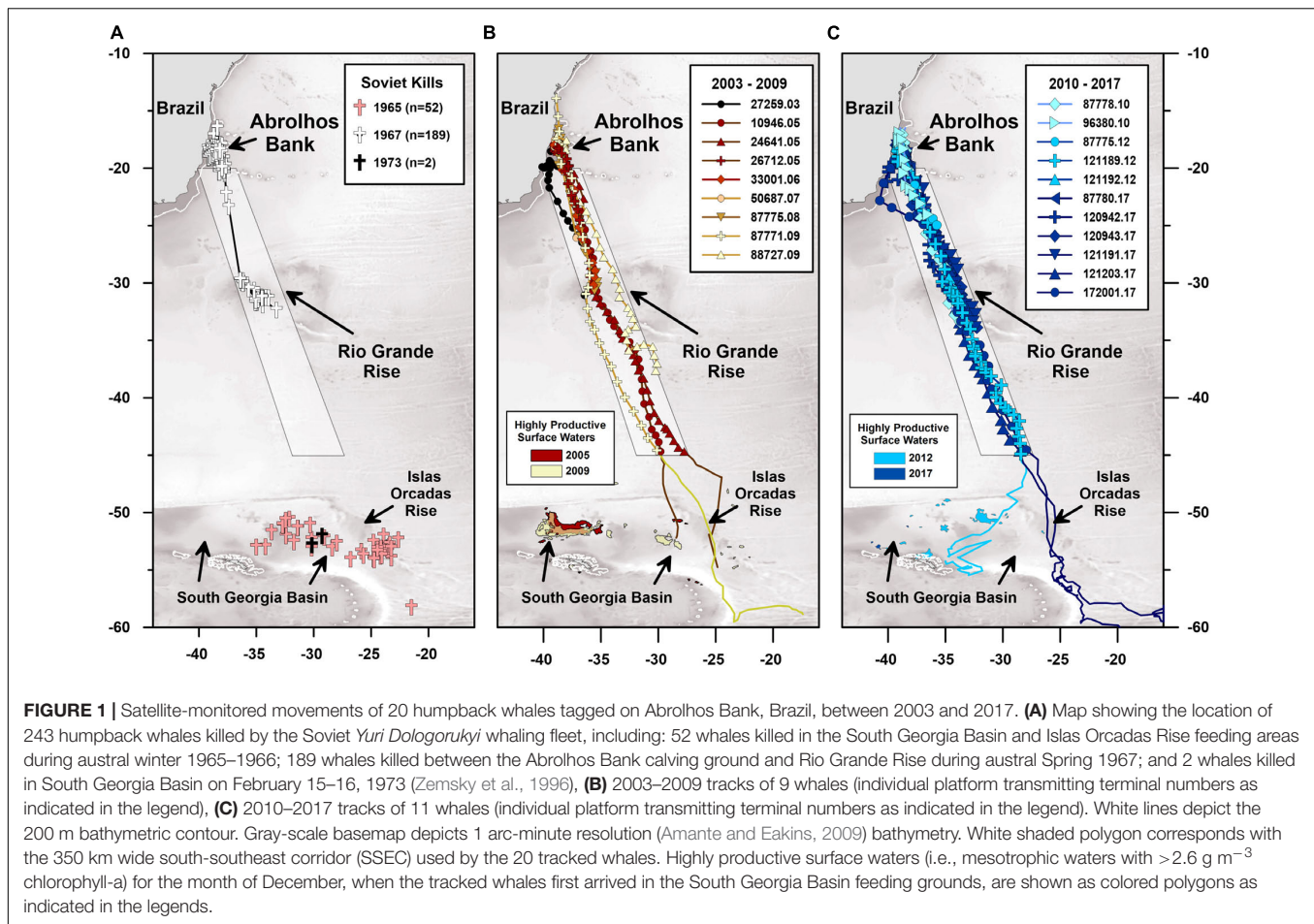
1986; Horton et al., 2017). Oceanographic conditions, including temperature, productivity, and currents, are known to be key variables in whale distribution (e.g., Horton et al., 2011; Hazen et al., 2013; Fleming et al., 2016; Derville et al., 2019; Owen et al., 2019), and gravity is an inescapable driver of whale buoyancy and movement behavior (e.g., Clarke, 1978; Horton et al., 2017).

Yet, oceans are highly dynamic, and in the Southwest Atlantic magnetic and oceanographic cues are anything but constant. Sophisticated long-term analyses of satellite-derived oceanographic observations of the southwest Atlantic's subtropical gyre, where the Malvinas (10–88 Sv) and Brazil (5–22 Sv) currents converge, demonstrate that oceanographic conditions throughout the region, including water transport, eddy kinetic energy, sea height anomaly, sea surface temperature, and ocean current circulation patterns, are extremely variable throughout the region (Goni et al., 2011; Wu et al., 2012; Marcello et al., 2018). With respect to magnetism, the South Atlantic Anomaly (SAA) is the most rapidly changing feature in Earth's magnetic field over the past 400 years (Hartmann and Pacca, 2009). In marked contrast, latitude and bedrock dependent gravitational cues are relatively stable despite the presence of pronounced gravitational anomalies, like the Rio Grande Rise (Mohriak et al., 2010).

Because the Southwest Atlantic is known to be dynamic with respect to oceanographic and magnetic conditions, but stable with respect to gravity, it is an ideal region in which to explore possible correlations between movement behaviors and oceanographic and geophysical cues, including gravity. By integrating long-term humpback whale satellite tracking and historic whaling datasets with satellite-derived oceanographic, magnetic, and gravitational monitoring and mapping datasets, our research illuminates one of biology's most pressing questions: How do animal migrants respond, if at all, to environmental dynamics?

MATERIALS AND METHODS

We present satellite-monitored essential biodiversity and ocean variables during a multi-decadal period of humpback whale migratory route fidelity in the Southwest Atlantic Ocean. Our study integrates published whaling records with several satellite-derived remote sensing datasets, including: (1) the latitude, longitude, and date on which 243 humpback whales were killed by the Soviet *Yuri Dologorukiy* fleet in the Southwest Atlantic Ocean between 1965 and 1973 (Zemsky et al., 1996; **Figure 1A**); (2) platform transmitting terminal (PTT) satellite telemetry data that document the spatial and temporal locations of 20 humpback whales as they migrated through a <350 km wide and >3000 km long south-southeast corridor (SSEC) in the South Atlantic Ocean between 2003 and 2018 (**Figures 1B,C**); (3) magnetic field parameters determined using the Swarm satellite derived Enhanced Magnetic Model (Chulliat et al., 2015); (4) Terra satellite derived Moderate Resolution Imaging Spectroradiometer (MODIS) estimates of near-surface temperature (NASA, 2018) and chlorophyll-a concentrations (NASA, 2018); (5) Ocean Surface Current Analysis Real-time (OSCAR) estimates of near-surface ocean



currents based on data collected by Jason-1/Jason-2 and Gravity Recovery and Climate Experiment (GRACE) satellites (ESR, 2009); (6) latitude and bedrock dependent gravitational acceleration data derived, in part, from TOPEX/Poseidon satellite observations (Balmino et al., 2012; Götze, 2014). We integrated these datasets through geospatial and time-series analyses that collectively reveal how humpback whales respond, and fail to respond, to changing Earth system conditions. The specific hypothesis we tested was: Southwest Atlantic humpback whale migratory movements describe systematic and highly reproducible sinusoidal trajectories when plotted in spatiotemporal gravitational coordinates (Horton et al., 2017).

Humpback Whale Locations and Movement Variables

As part of a long-term monitoring program, 138 PTT tags were deployed on humpback whales seasonally residing off the coast of Brazil between 2003 and 2018 (Zerbini et al., 2006, 2011; this study). Humpback whales were tracked using published methods (Zerbini et al., 2006, 2011; Horton et al., 2011, 2017). In brief, SPOT radio-frequency PTT satellite tags (Wildlife Computers, Redmond, WA, United States) were transdermally implanted into the upper flank of each whale near the base of the dorsal fin using a carbon-fiber pole or a modified pneumatic

line-thrower. In all references to PTT tag numbers in the current study, the two digits to the right of the decimal point correspond with the abbreviated Julian calendar year in which the tag was deployed.

Raw humpback whale location estimates were assigned a location class (i.e., 3, 2, 1, 0, A, B, Z) by the Argos-CLS system based on the estimated location error and the number of messages received (Argos-CLS, 2016). All locations that passed a 20 km h^{-1} velocity filter were used in this study. Velocity-filtered locations were combined to determine single average daily locations for each whale using PAST (v. 3.26; Hammer et al., 2001) to ensure that individual tracks were uniformly distributed with respect to time. The humpback whale tracking research we report was performed in accordance with research approvals granted by the Brazilian Environmental Agency (IBAMA), permit #009/02/CMA/IBAMA and process #02001.000085/02-27.

The date and location of 243 humpback whales killed by the Soviet *Yuri Dologorukiy* fleet between 1965 and 1973 were derived from the records reported by Zemsky et al. (1996; see also: Zerbini et al., 2006). Our understanding is that the *Yuri Dologorukiy* fleet humpback whale kills we report were hidden, in hard copy form, in the potato cellar of Dimitry Tomorsov until the end of the Cold War.

Humpback whale movement variables, including movement direction, distance traveled, straightness index, and movement velocity, were determined using the equations (1–4) as reported below. Movement direction was determined by:

$$\alpha = \arctan \left(\frac{(\lambda_2 - \lambda_1)}{\ln \left(\tan \left(\frac{\pi}{4} + \frac{\varphi_2}{2} \right) \times \left(\frac{1 - e \sin \varphi_2}{1 + e \sin \varphi_2} \right)^{\frac{e}{2}} \right) - \ln \left(\tan \left(\frac{\pi}{4} + \frac{\varphi_1}{2} \right) \times \left(\frac{1 - e \sin \varphi_1}{1 + e \sin \varphi_1} \right)^{\frac{e}{2}} \right)} \right) \quad (1)$$

where: α is the whale's movement direction in degrees; λ_1 and φ_1 are the whale's longitude and latitude, respectively, in decimal degrees at location 1; λ_2 and φ_2 are the whale's longitude and latitude, respectively, in decimal degrees at location 2; e is the eccentricity of the spheroid (i.e., 0.081819791). Distance traveled was determined by:

$$S = a \times \sec \alpha \left[\left(\left(1 - \frac{1}{4} e^2 \right) \times (\varphi_2 - \varphi_1) \right) - \left(\frac{3}{8} e^2 (\sin 2\varphi_2 - \sin 2\varphi_1) \right) \right] \quad (2)$$

where: S is the distance traveled between locations; a is the length of the major semiaxis in km (i.e., 6378.137 km); α is the whale's movement direction in degrees; e is the eccentricity of the spheroid (i.e., 0.081819791); φ_1 is the whale's latitude in decimal degrees at location 1; φ_2 is the whale's latitude in decimal degrees at location 2. Since the Argos-CLS system provides point locations rather than movement paths, the distance traveled data are minimum estimates of the true distance traveled between sequential locations. Straightness index was determined by:

$$SI = \frac{D}{L} \quad (3)$$

where: SI is the straightness index as defined by Batschelet (1981); D is the finite rhumb line distance between a starting location and an end location; L is the length of path followed between the starting location and the end location. Movement velocity was determined by:

$$v = \frac{S}{(t_2 - t_1)} \quad (4)$$

where: v is the velocity; S is the distance traveled (see: equation 2); $t_2 - t_1$ is the time it took for the whale to travel from location 1 to location 2. Since S is necessarily a minimum estimate of the true distance traveled, the movement velocity values we report will also be minimum estimates of true movement velocity. Kernel density estimation (Silverman, 1986) was used to determine the number of modes present in the humpback whale movement velocity data distribution.

Spatiotemporal, Geophysical, and Astronomical Variables

Spatiotemporal, geophysical, and astronomical variables were determined for the humpback whale locations we report. The time at which each whale initiated its continuous southward migration away from Abrolhos Bank was determined via piecewise linear regression breakpoint analysis (PLR-BPA) using the 'segmented' package in [R] (Muggeo and Muggeo, 2017).

We used PLR-BPA, rather than state-space switching models, as PLR-BPA enables quantification of the time at which movement behavior likely changed between sequential PTT locations. These piecewise linear regression breakpoint analyses allowed us to determine both when and where major changes in humpback whale movement behavior occurred, including: (1) migratory departures, represented in the tracking data as the time and place where each whale initiated continuous directional movement; (2) migratory stop-overs; (3) migratory re-starts following stop-overs.

Geomagnetic field parameters, including inclination (I) and intensity (F) at each PTT location, were determined using the Enhanced Magnetic Model (Chulliat et al., 2015). Latitude and bedrock dependent gravitational accelerations at each PTT location were determined using the International Gravity Formula (Götze, 2014) and spherical harmonic analysis of the Earth's topography-bathymetry ETOPO1 (Amante and Eakins, 2009) dataset up to degree and order 10,800 as reported in the International Gravimetric Bureau's 2×2 arc-min (i.e., $\sim 3.7 \times \sim 3.7$ km) World Gravity Map (Balmino et al., 2012). Astronomical variables, including moon illumination, Earth-moon distance, and lunar declination, were calculated using astronomical algorithms (Meeus, 1991). The magnitude of the tidal gravity vector at the Abrolhos Bank migratory departure site of PTTs 24641.05, 121203.17, and 120942.17 were determined using ETIDE (Fisahn et al., 2012, 2015).

Using these geophysical data we determined the latitude and bedrock dependent gravitational accelerations experienced by each whale. We then normalized the sum of these two spatially dependent gravitational cues to the gravitational acceleration present at the individual humpback whale migratory departure sites identified using PLR-BPA. This departure site normalization was done by:

$$\text{Normalized Gravity (\%)} = \left[\frac{(g_L + g_B)}{(g_{Ld} + g_{Bd})} \right] \times 100 \quad (5)$$

where: g_L is the latitude dependent gravitational acceleration at the whale's location; g_B is the bedrock dependent acceleration (i.e., Bouguer gravity anomaly); g_{Ld} is the latitude dependent gravitational acceleration at the whale's migratory departure site identified by PLR-BPA; g_{Bd} is the bedrock dependent gravitational acceleration at the same migratory departure site for which g_{Ld} was determined. We plotted these departure site-normalized gravity data against moon illumination, a temporally dependent visual and gravitational cue. We analyzed the resulting migratory trajectories using PAST's (v. 3.26; Hammer et al., 2001) sinusoidal regression. In this study, we restricted our least-squares regression analyses to a single sinusoid of the general form,

$$a \times \cos \left[\left(2\pi \frac{(g_L + g_B) - (g_{Ld} + g_{Bd})}{\Lambda} \right) - \Phi \right] \quad (6)$$

where: a is the amplitude of the sinusoid, which we did not restrict to the natural range in moon illumination values (i.e., 0 to 1); g_L , g_{Ld} , g_B , and g_{Bd} are the same as in equation (5);

Λ is the sinusoidal period; Φ is the sinusoidal phase. PAST minimizes the residual sum of squares via an ordinary least squares regression process by adjusting the fitted sinusoid's amplitude, period and phase.

Oceanographic Variables

Oceanographic variables, including sea surface temperatures, ocean currents, and Chlorophyll-a concentrations, were extracted from satellite monitored raster datasets at humpback whale locations using ArcGIS Desktop (ESRI, 2011). Sea surface temperature and chlorophyll-a concentration rasters (4 km pixel size) were obtained from the Goddard Space Flight Center (NASA, 2018); zonal and meridional ocean surface currents (1/3° pixel size) were estimated using the ocean surface current analysis real-time (OSCAR) model provided by JPL Physical Oceanography DAAC and developed by Earth and Space Research (ESR, 2009). In order to determine if any significant trends were present in the oceanographic conditions the tracked whales experienced, we performed Mann-Kendall trend tests (Gilbert, 1987), a non-parametric test for the presence of significant temporal trends in time-series data, on equally spaced sea-surface temperatures in the SSEC, total areal extent of mesotrophic ocean surface waters (i.e., $>2.6 \text{ g m}^{-3}$ chlorophyll-a concentration) in the southwest Atlantic/Southern Ocean basin, and ocean surface current direction within the SSEC every December during the 2002–2017 satellite tracking period. Mann-Kendall trend tests were also performed on the 2003–2018 humpback whale movement parameters: straightness, swimming direction, date of migration onset, and swimming velocity.

RESULTS

The data we report include six primary findings. First, the historic Soviet whaling and satellite telemetry data demonstrate that Southwest Atlantic humpback whales have utilized a spatially restricted ~ 1.0 million km^2 migratory corridor (i.e., SSEC) for >50 years (Figure 1). Second, fidelity to the SSEC manifests as relatively constant movement parameters, including straightness (Batschelet, 1981), movement direction, timing, and velocity when analyzed with respect to time. Third, humpback whale movement velocities in the SSEC was bimodal. Fourth, orientation cues derived from Earth's magnetic field changed significantly ($p < 0.05$) during the 2003–2018 monitoring period. Fifth, essential oceanographic variables (Miloslavich et al., 2018), including sea surface temperature, ocean current direction, and productivity, were highly variable during the 2003–2018 monitoring period. Sixth, the humpback whale migrations we report describe highly significant and reproducible sinusoidal gravitational coordinate (i.e., g-space) trajectories.

Soviet Whaling and Humpback Whale Satellite Telemetry

Between 1965 and 1973 the Soviet *Yuri Dologorukiy* fleet killed 243 humpback whales in the Southwest Atlantic Ocean (Zemsky et al., 1996). Fifty-two of these whales were killed on their feeding grounds in the South Georgia Basin during the austral

summer of 1965–1966. Not long after, during a 2-week period between 31 October and 13 November, 1967, the same fleet killed 189 humpback whales on the Abrolhos Bank calving grounds or within the SSEC (Figure 1A). Prolonged utilization of this same south-southeast directed migratory corridor (i.e., SSEC) is confirmed by the 2003–2018 humpback whale tracking dataset reported below.

The humpback whale tracking dataset we analyzed includes 45 PTT tags (i.e., 33% of all tags) that successfully recorded the onset of individual southward migrations away from the continental shelf and migratory movement south of -24°S latitude. Of these 45 migratory movements, 20 whales followed open-ocean paths that fell within the 350 km wide and 3000 km long SSEC located between -20°S and -45°S latitude (Figures 1B,C). Of the 20 whales that utilized the SSEC, only 6 were successfully tracked south of -45°S latitude and into the population's feeding grounds within and adjacent to the South Georgia Basin (Figures 1B,C). Satellite telemetry tracking data for 5 of these 20 whales (PTTs: 27259.03; 10946.05; 26712.05; 24641.05; 87771.09) have been published previously (Zerbini et al., 2006, 2011; Horton et al., 2011).

The PTT satellite tracking data demonstrate that 44% of migrating whales (i.e., 20 of 45 tracked whales) utilized less than 10% of the available ocean area during a >15 year-long period, consistent with the finding that multiple species of marine megafauna are capable of prolonged spatial and temporal fidelity to well-defined migratory domains (Horton et al., 2017). Movement parameters, including straightness (Figure 2A), swimming direction (Figure 2B), the timing of migratory onset (Figure 2C), and swimming velocity (Figure 2D), for the 20 whales migrating through the SSEC, showed no significant trends through time ($p > 0.05$; non-parametric Mann-Kendall trend test).

However, kernel density estimation revealed that the swimming velocity data distribution was bimodal (Figure 3), with a slow mode peaking at 3.23 km h^{-1} and a fast mode peaking at 4.54 km h^{-1} . The swimming velocities we report are consistent with PTT derived humpback whale swimming velocities reported by others, including: (1) 3.4 and 3.6 km h^{-1} in the Southwest Pacific Ocean (Hauser et al., 2010; Riekkola et al., 2018); (2) 3.6 km h^{-1} in the Indian Ocean (Trudelle et al., 2016); (3) 4.1 km h^{-1} in the North Atlantic (Kennedy et al., 2014); (4) 4.5 and 6.25 km h^{-1} in the North Pacific (Mate et al., 1998). Due to the bimodal distribution we observed, we classified individual whales as either slow ($<4.0 \text{ km h}^{-1}$) or fast ($\geq 4.0 \text{ km h}^{-1}$), based on their average migratory swimming velocities (Table 1).

The bimodal swimming velocity distribution is likely real, and not an artifact of the potential PTT underestimation of true swimming velocity, because of the straightness of the migratory paths followed by these whales (Table 1 and Figures 1, 4). To demonstrate this point, we calculated the cumulative migratory distance traveled, using both raw Argos PTT location estimates and our interpolated whale locations, for both a slow (PTT 87775.08) and a fast (PTT 121203.17) whale during the first $\sim 1000 \text{ km}$ of their southward migrations (Figure 4C). As expected, the more frequent Argos PTT location estimates yielded higher

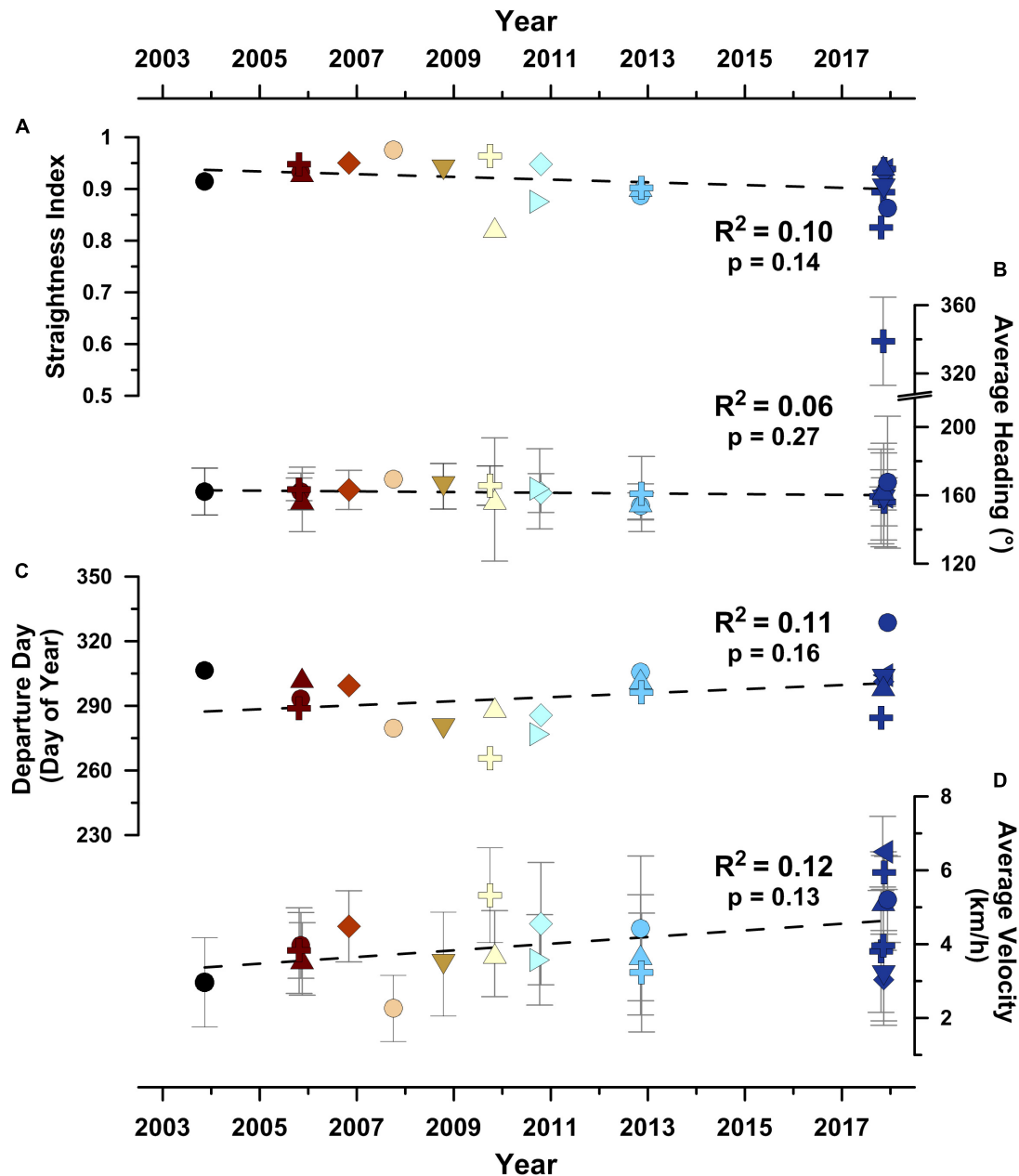
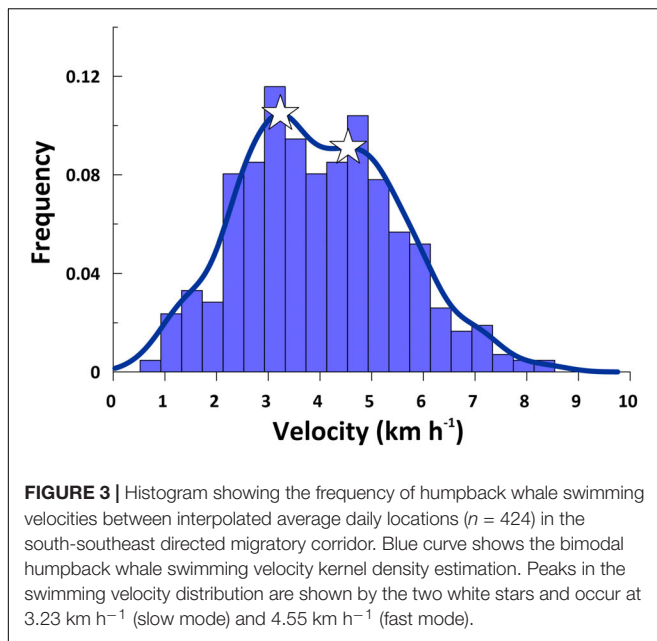


FIGURE 2 | Movement parameters for the 20 humpback whales migrating through the south-southeast migratory corridor (i.e., SSEC) across the 2003–2018 year satellite tracking campaign. **(A)** Movement straightness index (see section “Materials and Methods”; Batschelet, 1981), **(B)** average swimming direction heading, **(C)** day of departure from Abrolhos Bank wintering grounds, and **(D)** average swimming velocity. Symbols as shown in Figure 1. Gray whiskers show $\pm 1\sigma$ error bars in **(B,D)**. Least-squares linear regression correlation coefficients are shown alongside non-parametric Mann-Kendall trend test (Gilbert, 1987) probabilities (i.e., p -values) that a significant (i.e., $p < 0.05$) temporal trend is present.

cumulative distances traveled at any point in time during the satellite monitored migratory movements. However, there is an extremely significant difference ($p < 0.05$; t -test on the linear regression slopes) between the fast and the slow swimming velocities for both the raw Argos PTT data and the interpolated daily locations. Although interpolation of higher temporal resolution PTT location estimates minimizes movement distances and velocities, these effects do not

obscure significant differences in movement parameters in directional long-distance migration data. Noad and Cato (2007) demonstrate that singing humpbacks swim significantly slower than non-singing humpbacks during long-distance migration, suggesting a potential sex-related or behavioral driver for the bimodal swimming velocity distribution we report, and further investigation of the role acoustics play in long-distance movement behaviors is warranted.



Piecewise linear regression breakpoint analysis identified significant breakpoints associated with migratory departures for 15 of the whales that migrated through the SSEC (**Figure 5A**). The satellite tracking data for the remaining 5 whales that used the SSEC did not include significant breakpoints associated with the onset of southward migration because either: (1) the whale was already migrating southward when its PTT tag was deployed (e.g., **Figure 5B**); or (2) the PTT dataset included a >3 day-long gap spanning the onset of continuous southward movement (e.g., **Figure 5C**).

Humpback whale PTT 120942.17 was the only whale to perform a multi-day stop-over with associated decisions to stop and (re)start directed migratory movements (**Figure 5A**). The complexity of 120942.17's track is noteworthy as it demonstrates spatiotemporal fidelity to a well-defined migratory path at the ecological expense of both time and energy. Following ~ 15 days and >1700 km of continuous south-southeast (159°) directed swimming away from Abrolhos Bank, 120942.17 stopped over above Rio Grande Rise. Unexpectedly, 120942.17 resumed continuous directed swimming several days later along an overall north-northwest bearing (339°), antithetical to its initial south-southeast directed movement (**Figure 2B** and **Table 1**). Following ~ 10 days and ~ 1000 km of swimming along this "reverse" trajectory, 120942.17 again stopped its directed swimming for a single overnight period, only to return to its original south-southeast directed migration 2 h (± 1 h) before sunrise on 11 November, 2017.

In total, PLR-BPA identified 20 significant changes in latitudinal time-series for the 20 whales migrating through the SSEC. Of these significant changes in movement behavior, 15 occurred within ± 4.5 h of sunrise and 5 occurred within ± 5 h of sunset (**Figure 5D**). A significant local peak in the data distribution ($p = 0.0007$, two-tailed exact binomial probability), centered on dawn twilight, includes nine of the twenty

breakpoints identified. Our breakpoint analyses demonstrate that crepuscular navigation is a common component of humpback whale movement behavior.

Geomagnetic and Oceanographic Conditions

In contrast to the prolonged stability of the humpback whale movement parameters, the magnetic field these whales swam through changed significantly during the study period. For example, geomagnetic inclination (I) significantly changed ($p < 0.05$; non-parametric Mann-Kendall trend test) by $>12.5\%$ at the humpback whale wintering grounds on Abrolhos Bank between October 2003 and October 2017 (**Figure 6A**).

The relationship between this significant change in geomagnetic coordinates and geographic coordinates is notable. Magnetic inclination angles, equivalent to those present at Abrolhos Bank in 2003, were located >340 km to the northwest and >130 km inland of the Brazil coast by 2017.

Secular variation in magnetic orientation cues were more severe at the southern end of the SSEC where equivalent magnetic inclinations (I) shifted >400 km to the west between 2003 and 2017. Equivalent magnetic field intensity-inclination polar bi-coordinate locations (Lohmann et al., 1999; Brothers and Lohmann, 2018) present in 2003 no longer existed in 2017. The severity of these temporal changes in the magnetic field are due to the South Atlantic Anomaly (SAA), the most rapidly changing feature in Earth's magnetic field over the past 400 years (Hartmann and Pacca, 2009).

In addition to a changing magnetic field, the whales we tracked also experienced dynamic oceanographic conditions. Although no significant trend was detected ($p > 0.05$; non-parametric Mann-Kendall trend test), between November 2003 and November 2017, average sea surface temperatures in the SSEC increased by approximately 0.3°C (**Figure 6B**), roughly three times larger than the contemporaneous global trend (Hausfather et al., 2017).

It is not surprising that the humpback whales we tracked through the SSEC experienced dynamic ocean surface currents, annually varying across a $>90^\circ$ range of predominantly head-currents during late austral spring humpback whale migration period (**Figure 6C**). Such considerations are important as animals moving through a flowing medium, such as air or ocean, are affected by the direction and magnitude of currents, and these currents have the potential to impact animal movement trajectories (Gaspar et al., 2006; Chapman et al., 2011). To consider this possibility, we analyzed both uncorrected and current-corrected (Gaspar et al., 2006) humpback whale tracks. Our analyses demonstrate that: 1) uncorrected and current-corrected humpback whale locations were not significantly different (average drift = 9.2 km day^{-1} ; paired two-tailed t -test, $p > 0.05$; see: **Supplementary Figures S1, S2**), there is no significant difference between uncorrected and current-corrected humpback whale movement trajectories (two-tailed paired t -test, $p > 0.05$; see: **Supplementary Figure S2**). Despite the dynamic nature of near-surface ocean currents in the SSEC, our analyses demonstrate that these currents have

TABLE 1 | Satellite telemetry data summary.

ID Number (PTT)	Start longitude (°)	Start latitude (°)	Start date	SSEC end longitude (°)	SSEC end latitude (°)	SSEC end date	SSEC distance traveled (km)	Straightness index	Average velocity $\pm 1\sigma$ (km h ⁻¹)	Motif (Fast/Slow)	Average heading $\pm 1\sigma$ (°)
27259.03	-39.38	-19.52	4 November 2003	-36.43	-31.06	23 November 2003	1407	0.91	2.9 (± 1.2)	Slow	162.2 (± 13.7)
10946.05	-38.66	-18.65	21 October 2005	-29.69	-45.41	23 November 2005	3222	0.93	4.1 (± 0.9)	Fast	162.2 (± 10.8)
26712.05	-37.88	-21.34	22 October 2005	-36.87	-24.52	26 October 2005	371	0.96	4.1 (± 1.5)	Fast	163.4 (± 6.61)
24641.05	-38.91	-18.39	25 October 2005	-27.35	-45.04	4 December 2005	3405	0.90	3.5 (± 1.0)	Slow	157.5 (± 18.8)
33001.06	-38.09	-19.16	27 October 2006	-35.62	-30.18	8 November 2006	1291	0.95	4.4 (± 0.9)	Fast	163.1 (± 11.4)
50687.07	-38.34	-18.32	23 September 2007	-37.13	-26.03	11 October 2007	880	0.98	7.0	Fast	169.3
87775.08	-38.69	-19.74	6 October 2008	-35.55	-30.70	21 October 2008	1303	0.94	3.4 (± 1.4)	Slow	165.2 (± 13.3)
87771.09	-38.89	-13.90	14 September 2009	-29.37	-45.69	13 October 2009	3706	0.96	5.3 (± 1.2)	Fast	165.6 (± 11.5)
88727.09	-35.09	-9.14	16 October 2009	-30.23	-37.65	21 November 2009	3754	0.85	4.3 (± 1.5)	Fast	157.5 (± 36.0)
96380.1	-38.78	-17.49	3 October 2010	-36.52	-24.02	12 October 2010	804	0.91	3.4 (± 1.3)	Slow	163.8 (± 23.4)
87778.1	-38.76	-15.31	7 October 2010	-33.71	-33.39	27 October 2010	2128	0.95	4.4 (± 1.4)	Fast	161.3 (± 11.3)
121189.12	-39.12	-18.98	22 October 2012	-28.37	-45.59	4 December 2012	3309	0.90	3.1 (± 1.5)	Slow	160.7 (± 21.9)
121192.12	-39.07	-18.28	28 October 2012	-33.70	-31.58	13 November 2012	1580	0.94	4.1 (± 1.4)	Fast	156.1 (± 10.5)
87775.12	-37.67	-21.46	4 November 2012	-35.77	-24.95	8 November 2012	438	0.89	4.4 (± 1.9)	Fast	153.7 (± 7.73)
120942.17 (Stage 1)	-38.98	-18.15	9 October 2017	-34.84	-28.30	24 October 2017	1766	0.79	3.5 (± 1.5)	Slow	159.2 (± 27.7)
120942.17 (Stage 2)	-34.84	-28.30	24 October 2017	-35.24	-30.23	31 October 2017	388	0.64	2.2 (± 0.5)	Slow	207.0 (± 63.8)
120942.17 (Stage 3)	-35.24	-30.23	31 October 2017	-37.62	-22.23	10 November 2017	1057	0.89	4.0 (± 1.0)	Fast	338.8 (± 25.7)
120942.17 (Stage 4)	-37.56	-22.25	11 November 2017	-35.91	-25.71	14 November 2017	296	0.94	5.9 (± 0.4)	Fast	156.1 (± 14.0)
121203.17	-38.49	-19.56	24 October 2017	-28.23	-45.67	18 November 2017	3101	0.95	5.0 (± 1.3)	Fast	163.1 (± 11.7)
120943.17	-39.30	-17.99	26 October 2017	-32.26	-33.88	22 November 2017	1993	0.89	2.9 (± 1.2)	Slow	162.1 (± 28.3)
121191.17	-38.62	-18.80	27 October 2017	-32.41	-33.85	22 November 2017	1953	0.86	3.0 (± 1.2)	Slow	157.3 (± 27.4)
87780.17	-38.09	-19.99	28 October 2017	-34.89	-27.86	4 November 2017	937	0.94	5.9 (± 1.6)	Slow	159.2 (± 5.68)
172001.17	-38.97	-18.08	22 November 2017	-26.93	-45.40	21 December 2017	3541	0.87	5.0 (± 1.2)	Fast	167.6 (± 38.6)

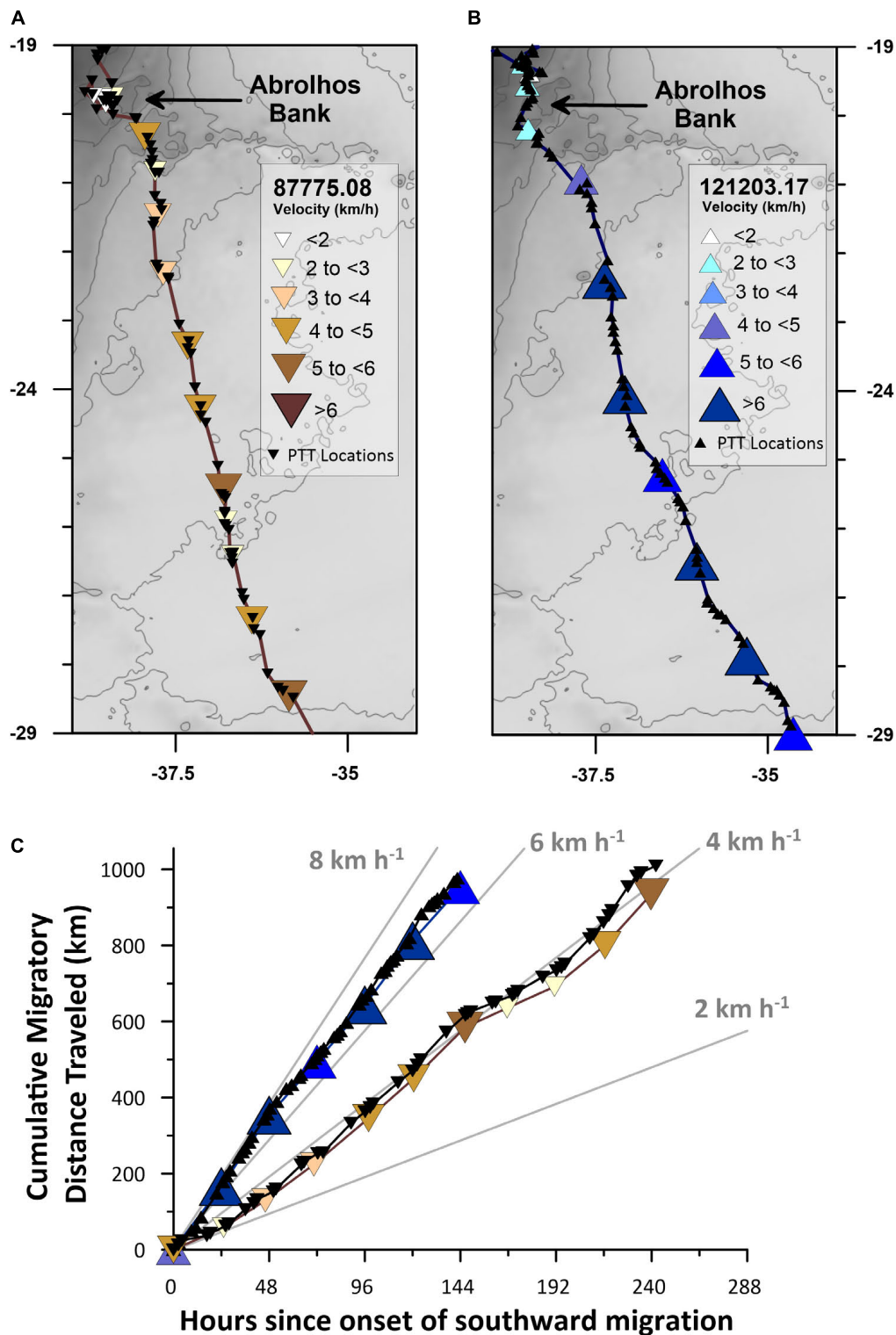


FIGURE 4 | Satellite track maps and cumulative migratory distance traveled time-series for the first ~1000 km of a slow (PTT 87775.08) and a fast (PTT 121203.17) humpback whale's directional long-distance migrations. **(A)** Raw Argos PTT location estimates (black inverted triangles) and interpolated daily location estimates (colored inverted triangles classified by velocity; see legend) for humpback whale PTT 87775.08. **(B)** Raw Argos PTT location estimates (black triangles) and interpolated daily location estimates (colored triangles classified by velocity; see legend) for humpback whale PTT 121203.17. **(C)** Cumulative migratory distance traveled time-series plot of the raw Argos PTT and interpolated daily location estimates shown in **(A,B)**. Gray-scale basemap depicts contoured (50 mGal interval) bedrock derived Bouguer Gravity Anomaly values (Balmino et al., 2012).

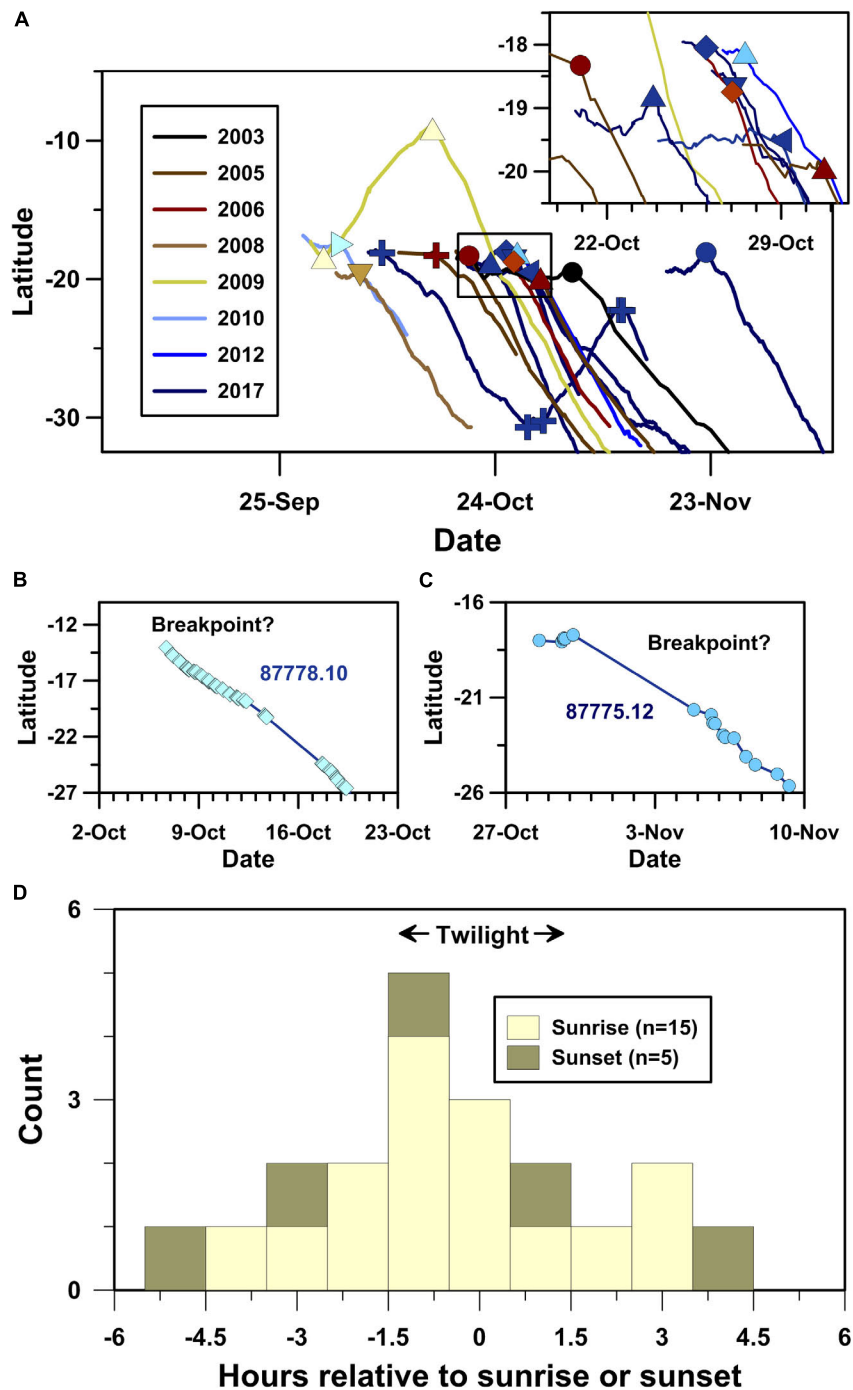


FIGURE 5 | Timing of humpback whale movement decisions identified using piecewise-linear regression breakpoint analysis (PLR-BPA). **(A)** Latitude time-series plot showing locations of migratory departure points identified using PLR-BPA (symbols as in **Figure 1**), **(B)** humpback whale PTT 87778.10's latitude time-series profile, wherein no significant breakpoint was detected due to continuous southward movement, **(C)** humpback whale 87775.12's latitude time-series profile, wherein no significant breakpoint was detected due to a multi-day gap in the satellite telemetry dataset, and **(D)** histogram showing the temporal distribution of the 20 significant breakpoints identified using PLR-BPA relative to sunrise (light shading) and sunset (dark shading).

relatively minor effects on migrating humpback whale trajectories due to the factor 10 difference between average current velocity (0.43 km h^{-1}) and average whale movement velocity (4.6 km h^{-1}).

With respect to feeding, the primary motivation of poleward humpback whale migrations, the areal extent of highly productive (i.e., $>2.6 \text{ g m}^{-3}$ chlorophyll-a) surface water decreased significantly ($p < 0.05$; non-parametric Mann-Kendall trend test)

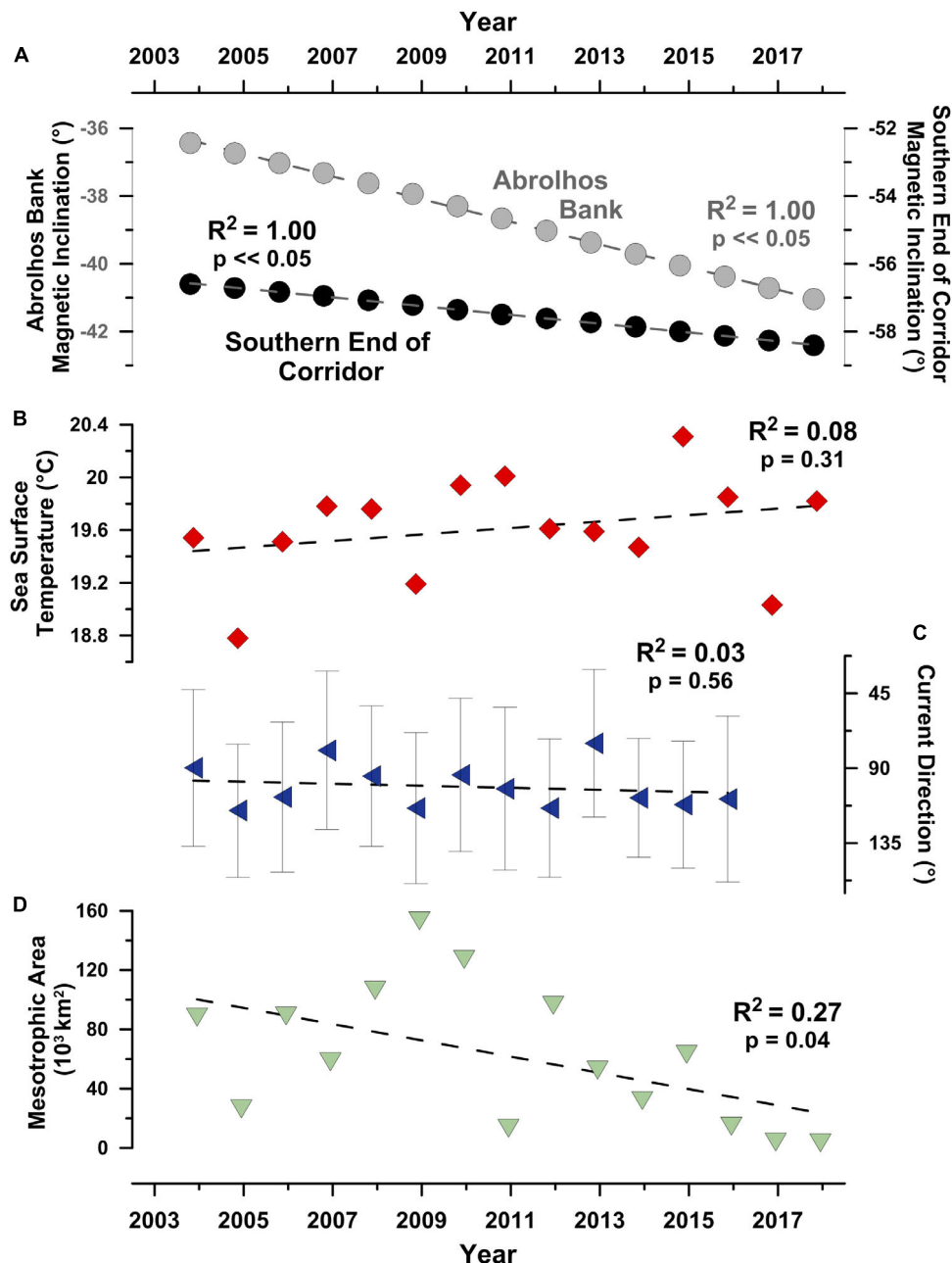


FIGURE 6 | Geomagnetic and oceanographic conditions the 20 tracked humpback whales experienced during their south-southeast directed migrations.

(A) Geomagnetic inclination angles at the northern and southern ends of the south-southeast migratory corridor (i.e., SSEC), **(B)** average sea surface temperature in the SSEC, **(C)** average ocean surface current direction in the SSEC, and **(D)** total area of highly productive mesotrophic surface water (i.e., chlorophyll-*a* concentration $> 2.6 \text{ g m}^{-3}$) in the southwest Atlantic/Southern Ocean basin during the month of December. Gray whiskers in **(C)** show $\pm 1\sigma$ error bars.

over the past decade from a high of $\sim 160,000 \text{ km}^2$ in December 2008 to lows of $< 15,000 \text{ km}^2$ in December 2015, 2016, and 2017 (**Figure 6D**).

Movements in Gravitational Coordinates

A central goal of this research was to test the hypothesis that humpback whale migratory movements describe highly

significant sinusoidal gravitational coordinate (i.e., g-space) trajectories. The results of these analyses demonstrate that humpback whales utilizing the SSEC followed a limited range of temporally modulated gravitational coordinate trajectories (**Figure 7**). These highly significant sinusoidal correlations (sinusoidal regression; *F*-test; $\alpha = 0.05$; $p < 0.05$) support the hypothesis as posed and suggest that the observed g-space trajectories are a non-random consequence of navigational

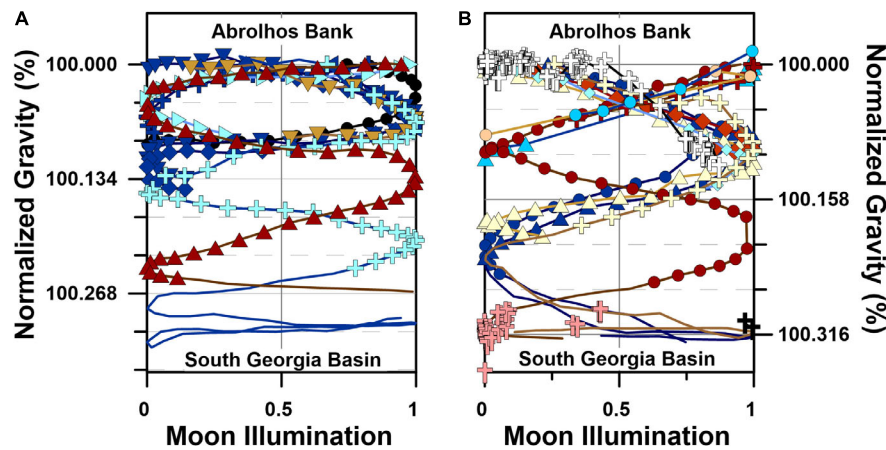


FIGURE 7 | Humpback whale movements in gravitational coordinates (i.e., g-space). **(A)** g-space trajectories for slow swimming (i.e., $<4 \text{ km h}^{-1}$) humpback whales ($n = 9$, symbols as in **Figure 1**), **(B)** g-space trajectories for fast swimming (i.e., $>4 \text{ km h}^{-1}$) humpback whales ($n = 11$) and the 243 Southwest Atlantic humpback whales killed by the Soviet Yuri Dologorukyi fleet (Zemsky et al., 1996) between 1965 and 1973 (symbols as in **Figure 1**). Normalized gravity values in **(A,B)** were determined by dividing the sum of the latitude dependent gravity (Götze, 2014) and the bedrock dependent gravity (Balmirio et al., 2012) at each whale location by the value present at each individual's Abrolhos Bank migratory departure site. Moon illumination depends solely on time, and it cyclically evolves from no illumination (i.e., New Moon, 0) to full illumination (i.e., Full Moon, 1) to no illumination (i.e., New Moon, 0) over a 29.5 day average period (i.e., synodic month).

behavior (**Figure 7**). Although the twenty whales that migrated through the SSEC followed distinct geographic-Julian calendar coordinate paths (e.g., **Figure 5A**), these same movements describe overlapping temporally phased trajectories when plotted in gravitational coordinates (**Figure 7**). Yet, two different motifs, consistent with the two modes in the humpback whale movement velocity distribution, are apparent in the g-space trajectories: a slow motif (**Figure 7A**) and a fast motif (**Figure 7B**).

The slow motif includes 9 whales that swam through the SSEC at an average swimming velocity of $3.6 \pm 0.9 \text{ km h}^{-1}$, whereas the 11 whales in the fast motif swam significantly faster ($p = 0.008$; two-tailed t -test), at an average velocity of $4.8 \pm 0.9 \text{ km h}^{-1}$ (**Table 1**). The data demonstrate that eight of nine whales in the slow motif initiated their southward migrations in the days immediately prior to first-quarter or last-quarter moons (**Figure 7A**), while the ninth whale in the slow motif, PTT 27259.03, initiated its migration 2 days after first-quarter moon. In contrast, the eleven whales in the fast motif initiated their southward migrations near full or new moons (**Figure 7B**). Both the slow and fast motifs include significant in-phase and out-of-phase sinusoidal correlations between departure site-normalized gravitational acceleration and moon illumination (**Figure 7**), similar to significant correlations present in the g-space trajectories followed by diverse megafaunal species, including white sharks (*Carcharodon carcharias*) and northern elephant seals (*Mirounga angustirostris*) (Horton et al., 2017). Based on these results, we accept the hypothesis that humpback whale migratory movements describe highly significant sinusoidal g-space trajectories.

The results we report demonstrate that, despite changing oceanographic and geomagnetic conditions, humpback whale long-distance migrations in the Southwest Atlantic Ocean are characterized by prolonged (i.e., >50 years) fidelity to a heavily utilized south-southeast directed migratory corridor connecting

calving grounds on the Abrolhos Bank to feeding grounds in the South Georgia Basin. When analyzed in spatiotemporal gravitational coordinates, these same humpback whale migratory movements describe richly patterned and highly reproducible trajectories in either a fast or a slow motif. Thus, the historic Soviet whaling and humpback whale satellite telemetry data we report reveal an apparent paradox: humpback whale long-distance migrations do not change in a changing ocean.

DISCUSSION

Understanding organismal responses to environmental change remains one of the most pressing challenges in ecology (Schwenk et al., 2009), and as relatively high trophic level predators, it is particularly important to determine how large whales respond to dynamic oceanographic conditions given the role cetaceans play in circulating marine nutrients, trophic architecture, trophic cascades, and carbon turn-over rates (e.g., Croll et al., 2006; Roman and McCarthy, 2010; Witteveen and Wynne, 2016). In this context, it is somewhat surprising that Southwest Atlantic humpback whale movements do not appear to have responded to a significant decrease in the areal extent of mesotrophic surface waters and dynamic oceanographic and geomagnetic conditions over a period of several years. This paradox of migratory fidelity despite environmental change raises important questions, including: (1) How do humpback whales maintain migratory stability despite oceanographic and geomagnetic change? (2) What cues and rules inform humpback whale migratory decisions? One possible answer to both questions invokes the spatially and temporally dependent, yet stable, gravitational cues ubiquitous to the Earth system (Horton et al., 2017).

The recurrent pattern of phased gravitational coordinate trajectories in our long-term satellite tracking dataset supports

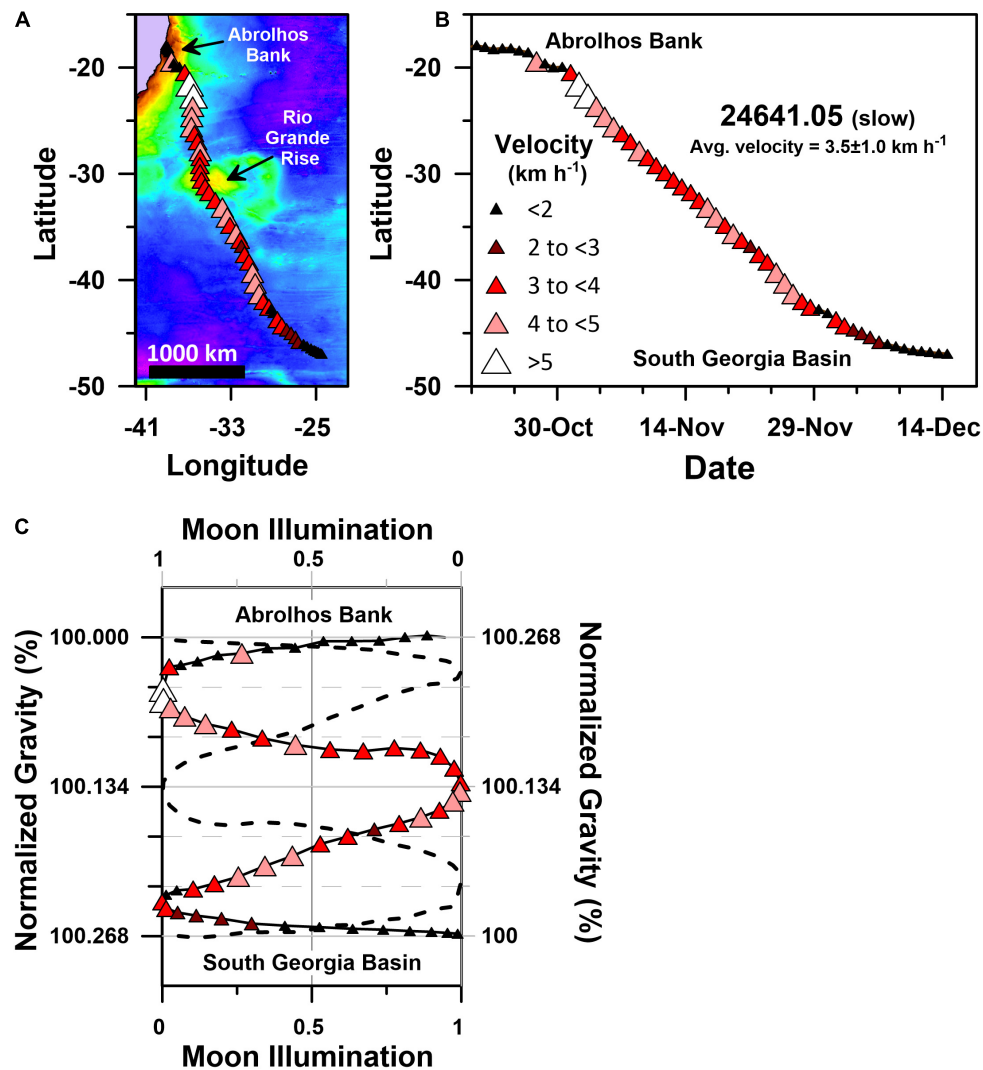


FIGURE 8 | Geographic and gravitational coordinate migratory trajectories of PTT 24641.05's slow motif humpback whale migration (average migratory velocity = $3.5 \pm 1.0 \text{ km h}^{-1}$). **(A)** Geographic coordinate (plate-carée projection) track map of 24641.05's single stage south-southeast directed migration, **(B)** latitude time-series plot for 24641.05's geographic coordinate Julian calendar migratory trajectory, **(C)** g-space trajectory of 24641.05's migration track, including the actual and mirror image g-space trajectories. The mirrored trajectory (dashed black curve) is plotted on the reverse direction moon illumination and normalized gravity axes. Actual migratory trajectories in **(A–C)** are shown as red-hued triangles that are color-coded and sized according to 24641.05's average daily velocity as shown in the legend. Normalized gravity values in **(C)** were determined by dividing the sum of the latitude dependent gravity (Götze, 2014) and the bedrock dependent gravity (Balmino et al., 2012) at each average daily location by the value present at 24641.05's Abrolhos Bank migratory departure site. Colored basemap in **(A)** depicts bedrock gravity anomalies across a 150 to 660 mGal range.

the interpretation that humpback whale migrations are both stable and non-randomly distributed in space and time (e.g., Figure 7). In the following sections, we discuss three separate examples from our tracking dataset that describe the conditions under which different humpback whales were able to maintain migratory fidelity to a limited range of spatiotemporal trajectories through gravitational coordinates.

Slow Migration: PTT 24641.05

Humpback whale PTT 24641.05's south-southeast directed migration was relatively slow, averaging $3.5 \pm 1.0 \text{ km h}^{-1}$ (Table 1 and Figure 8). Like other slow motif whales, 24641.05

started its migration when the lunar disk was $\sim 50\%$ illuminated (i.e., last quarter moon on 25 October 2005), and it continued its non-stop and highly directional (straightness index = 0.90; average heading $157 \pm 18.8^\circ$; Table 1) swimming for $\sim 3400 \text{ km}$ over ~ 1.5 months, ending its migration around 7 December 2005 within 24 h of first-quarter moon (Table 1 and Figure 8C).

Several rare conditions were met during 24641.05's migration that collectively determined the gravitational accelerations it experienced. First, 24641.05 initiated its migration away from Abrolhos Bank on a quarter moon neap tide, when: (1) the tidal gravity vector achieved an anomalously low daily range in acceleration values ($\sim 100 \mu\text{Gal}$; Supplementary Figure S3);

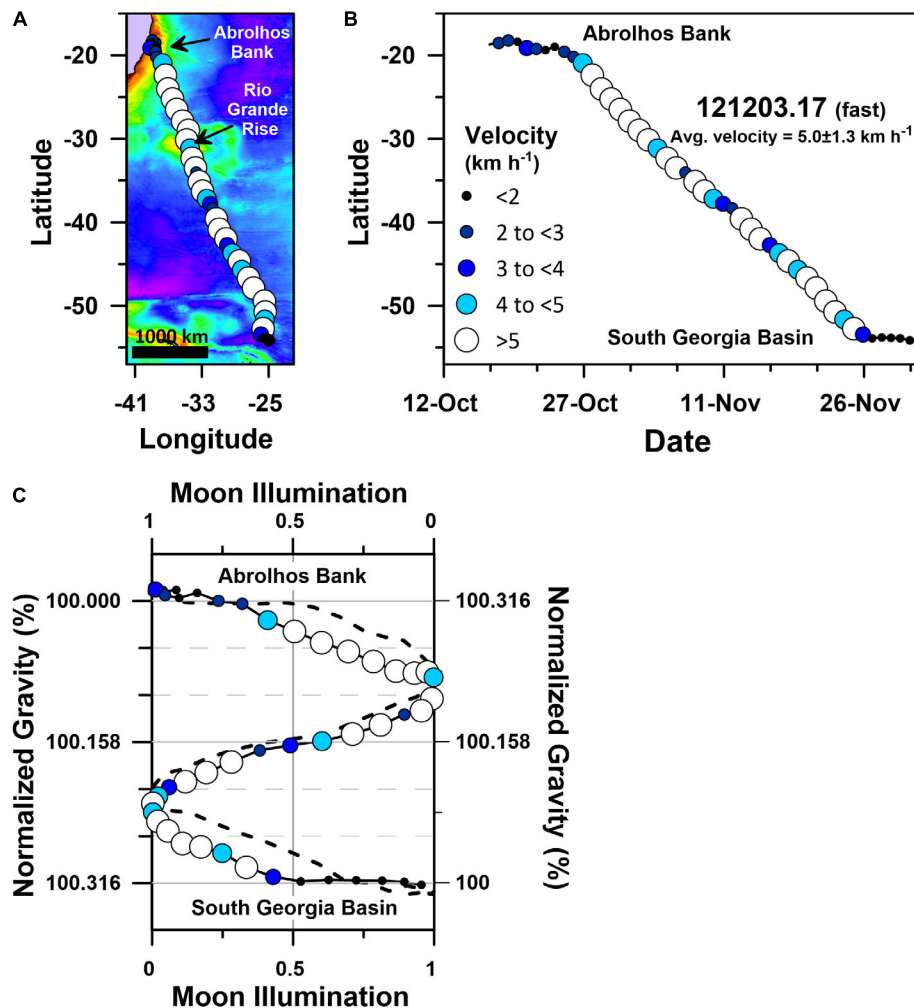


FIGURE 9 | Geographic and gravitational coordinate migratory trajectories of PTT 121203.17's fast motif humpback whale migration (average migratory velocity = $5.0 \pm 1.3 \text{ km h}^{-1}$). **(A)** Geographic coordinate (plate-carée projection) track map of 121203.17's single stage south-southeast directed migration, **(B)** latitude time-series plot for 121203.17's geographic coordinate Julian calendar migratory trajectory, **(C)** g-space trajectory of 121203.17's migration track, including the actual and mirror image g-space trajectories. The mirrored trajectory (dashed black curve) is plotted on the reverse direction moon illumination and normalized gravity axes. Actual migratory trajectories in **(A–C)** are shown as blue-hued triangles that are color-coded and sized according to 121203.17's average daily velocity as shown in the legend. Normalized gravity values in **(C)** were determined by dividing the sum of the latitude dependent gravity (Götze, 2014) and the bedrock dependent gravity (Balmino et al., 2012) at each average daily location by the value present at 121203.17's Abrolhos Bank migratory departure site. Colored basemap in **(A)** depicts bedrock gravity anomalies across a 150 to 660 mGal range.

(2) the moon was within 72 h of its quasi-monthly (i.e., the 27.32 day duration lunar sidereal month; **Supplementary Figure S3**) lunar declination maximum of $\sim 28^\circ$; (3) the moon was within 24 h of its quasi-monthly (i.e., the 27.55 day duration anomalistic month; **Supplementary Figure S3**) apogee of $\sim 404,000 \text{ km}$. Second, 24641.05's migration describes a highly symmetrical gravitational coordinate trajectory with mirror planes through both the gravitational midpoint of its migration (i.e., 100.134% of its departure site's gravitational acceleration; **Figure 8C**) and the 29.5 day duration synodic month's 50% moon illumination position. Maintenance of this highly symmetrical trajectory required 24641.05 to swim both faster and slower when it experienced relatively higher or lower bedrock derived gravity anomalies, respectively (**Figure 8A**). Third, 24641.05 ended its

south-southeast migration, on a neap tide first-quarter moon, as it approached 46°S latitude in the end of the first week of December, 2005. Similar patterns are present in the gravitational coordinate trajectories of all 9 slow motif humpback whales (**Figure 7A**), irrespective of the year in which the migration occurred or the prevailing geomagnetic and oceanographic conditions (**Figure 6**).

Fast Migration: PTT 121203.17

Humpback whale PTT 121203.17's south-southeast directed migration was relatively fast, averaging $5.0 \pm 1.3 \text{ km h}^{-1}$ (**Table 1** and **Figure 9**). Like the 10 other fast motif whales, 121203.17 started its migration in the days surrounding new or full moon, and it continued its non-stop and highly directional (straightness

index = 0.95; average heading $161 \pm 11.7^\circ$; **Table 1**) swimming for ~ 3900 km during a ~ 1.25 month long period. Humpback whale 121203.17 ended its migration on 26 November 2017 within 24 h of first-quarter moon (**Figure 9C**) as it approached 54°S latitude (**Figure 9B**).

As was the case for PTT 24641.05, several rare conditions were met during 121203.17's relatively fast and highly directional migration that collectively determined the gravitational accelerations 121203.17 experienced. First, PLR-BPA suggests 121203.17 initiated its migration on 24 October 2017: (1) when the moon was $<25\%$ illuminated and the tidal gravity vector achieved a relatively moderate $\sim 180 \mu\text{Gal}$ daily range (**Supplementary Figure S4**); (2) within 24 h of the sidereal month's lunar declination minimum of -19.4° (**Supplementary**

Figure S4); (3) within 24 h of the moon's anomalistic month's apogee (i.e., $\sim 405,000$ km; **Supplementary Figure S4**). Second, 121203.17's migration describes a highly symmetrical gravitational coordinate trajectory with mirror planes through both the gravitational midpoint of its migration (i.e., 100.158% of its departure site's gravitational acceleration; **Figure 9C**) and the synodic month's 50% moon illumination (i.e., neap tide) position. As was the case with 24641.05, maintenance of this highly symmetrical trajectory required 121203.17 to swim both faster and slower when it experienced relatively higher or lower bedrock derived gravity anomalies, respectively (**Figure 9A**). Similar patterns are present in the gravitational coordinate trajectories followed by all 11 whales in the fast motif (**Figure 7B**), irrespective of the year in which the migration

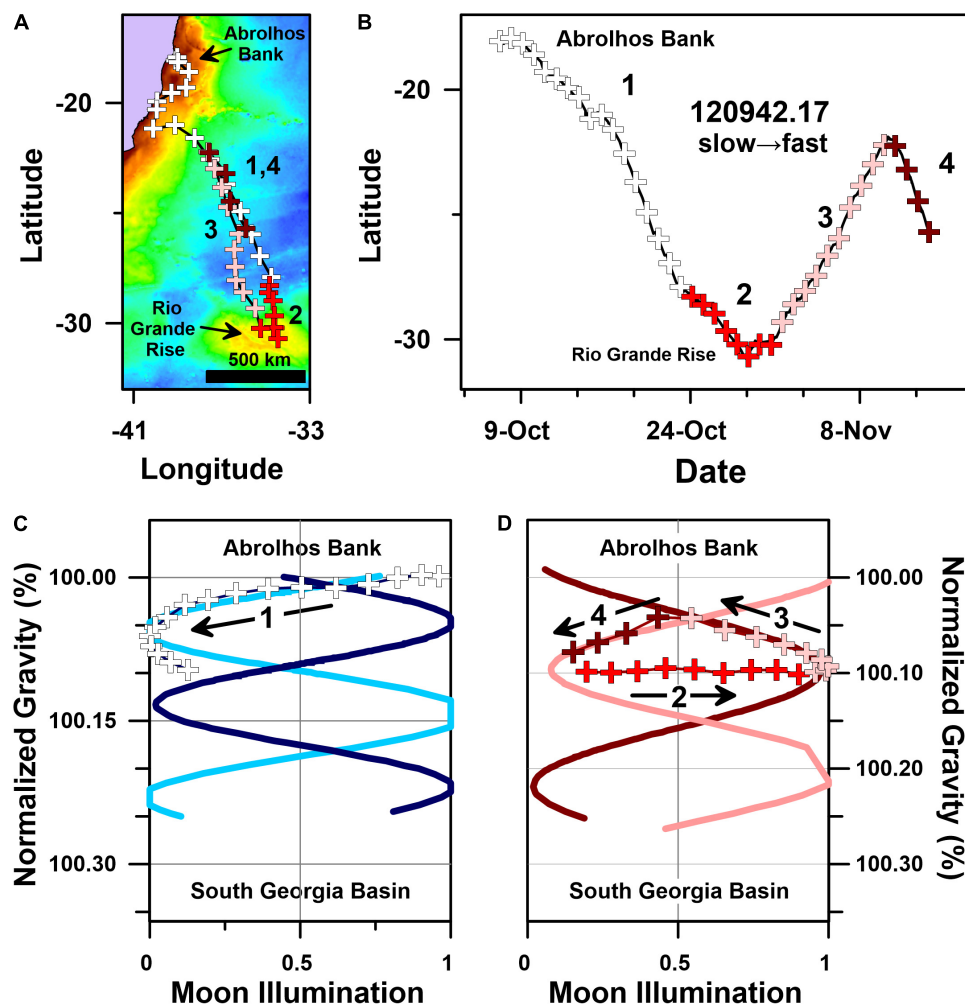


FIGURE 10 | Geographic and gravitational coordinate migratory trajectories of a dynamically paced humpback whale migration (PTT 120942.17). **(A)** Geographic coordinate (plate-carée projection) track map of whale 120942.17's multi-stage migration, **(B)** latitude time-series plot for 120942.17's geographic coordinate Julian calendar migratory trajectory (bold numbers correspond with stages 1–4 of 120942.17's migration, see text), **(C)** g-space trajectory for stage 1 (white addition symbols) of humpback whale 120942.17's migration track (black arrow indicates trajectory direction through time), and **(D)** g-space trajectory for stage 2 (red addition symbols), stage 3 (pink addition symbols) and stage 4 (dark red addition symbols) of whale 120942.17's migration track (black arrows indicate the movement trajectory through time). Colored basemap in **(A)** depicts bedrock gravity anomalies across a 150 to 660 mGal range. Blue sinusoids in **(C)**, and red sinusoids in **(D)**, depict sinusoidal regression fits to the satellite tracking data presented in **Figure 6A** (i.e., 9 slow motif whales) and **Figure 6B** (i.e., 11 fast motif whales), respectively. All four sinusoidal regression fits are highly significant (i.e., $p < 0.05$).

occurred or the prevailing geomagnetic and oceanographic conditions (Figure 6).

Dynamically Paced Migration: PTT 120942.17

The migratory movements of one of the whales we tracked, PTT 120942.17, were particularly anomalous. Our results indicate that 120942.17 was the only whale in our PTT dataset to both: (1) perform a multiple day-long migratory stop-over; and (2) retrace its migration route with north-northwest swimming over a ~10 day-long period (Figure 10). PTT 120942.17 is also the only whale to clearly shift from one velocity motif (slow) to the other (fast) during its staged southward migration (Table 1).

Humpback whale PTT 120942.17's movements can be divided into four separate stages (Figure 10). Stage 1 includes its initial south-southeast directed migration from Abrolhos Bank to the northern flank of Rio Grande Rise (Figures 10A,C). Stage 2 includes its stop-over above Rio Grande Rise, where ocean floor altitudes ~550 m below sea level are ~4000 m higher than adjacent abyssal plains (Amante and Eakins, 2009). Stage 3 includes 120942.17's reverse north-northwest directed migration back toward Abrolhos Bank (Figures 10B,D), and stage 4 includes 120942.17's recovery of its initial south-southeast directed migration path (Figures 10B,D).

Despite the anomalous and staged structure of 120942.17's movements, the g-space trajectories described by these movements coincide with the phased sinusoidal trajectories followed by several other whales that also migrated through the SSEC at distinctly different times between 2003 and 2017 (Figures 7, 10). Specifically, stage 1 of 120942.17's migration (Figure 10C) initially coincides with the phased movements of other whales in the slow motif (Figure 7A), including the g-space trajectory followed by PTT 24641.05, approximately 12 years earlier (Figure 8C). Despite initially following a g-space trajectory similar to the one followed by PTTs 24641.05 and 96380.10 (Figure 7A), 120942.17 subsequently departs from this slow motif trajectory as it approaches Rio Grande Rise and transitions into stage 2 of its migration (Figures 10A–C).

Importantly, PTT 120942.17 continued in an overall southward direction during stage 2 of its migration (Figure 10A). Yet, the gravitational acceleration 120942.17 experienced during this ~10 day period did not change (Figure 10D). This apparent discrepancy between 120942.17's geographic and gravitational coordinate movements is easily explained. Although 120942.17 continued swimming southward (Figure 10B), the gravitational effects of this continued southward movement were counter balanced by local changes in gravity associated with the bedrock underlying Rio Grande Rise (Figure 10A). These facts resulted in 120942.17 experiencing a constant gravitational acceleration throughout stage 2 of its migration (Figure 10D). As a direct consequence of its movement behavior during stage 2 of its migration, 120942.17 is moving in geographic coordinates, but not moving in gravitational coordinates for precisely one-half of a tidal gravity cycle (i.e., from new moon to full moon; Figure 10D).

Stage 3 of 120942.17's migration includes an anomalous north-northwest directed 'reverse' migration back toward Abrolhos Bank (Figures 10A,B). When plotted in g-space, this north-northwest directed stage 3 movement coincides with the phased sinusoidal trajectory followed by 6 other southward migrating whales in the fast motif (PTTs: 33001.06, 87771.09, 88727.09, 87778.10, 121203.17, 172001.17; Figures 7B, 10D).

Finally, stage 4 of 120942.17's migration begins in the dawn twilight on a last-quarter moon. The associated g-space trajectory for stage 4 coincides with the phased sinusoidal trajectories followed by the remaining 5 whales in the fast motif (PTTs: 10946.05, 26712.05, 50687.07, 87775.12, 121192.12; Figures 7B, 10D).

Despite making multiple movement decisions that both delayed its southward migration by more than 24 days and added more than 2000 km of swimming distance, 120942.17's migration describes highly symmetrical and phased gravitational coordinate trajectories that coincide with segments of the g-space trajectories followed by 13 of the other 19 whales that migrated through the SSEC. The symmetrically patterned and reproducible structure of these gravitational coordinate trajectories implies that the benefits of swimming through a well-defined and heavily utilized spatiotemporal corridor outweigh the energetic and temporal costs of swimming farther for longer periods. The risks associated with such a strategy are not minor and include exposure to changing oceanographic conditions, shifts in prey availability (e.g., Figures 1, 6), heightened competition, and predictability.

Indeed, the predictability of the humpback whale migrations we report may have already hurt the population (Rosenbaum et al., 2009). The fact that Soviet whale ships killed humpback whales at the southeast corner of Abrolhos Bank, within the SSEC, and above Rio Grande Rise but crucially not elsewhere, over a 2-week period suggests there has been >50 years of spatiotemporal fidelity to the migratory corridor revealed by our satellite tracking research despite dynamic oceanographic and geomagnetic conditions. Plotting the time and location of the Western South Atlantic Soviet humpback whale kills in gravitational coordinates supports this interpretation: the 1967 Soviet whaling kills coincide with the sinusoidal gravitational trajectories followed by the humpback whales we tracked between 2003 and 2018 (Figure 7B).

CONCLUSION

Using long-term satellite remote sensing data, our research provides empirical support for what several models have predicted: changes in Earth system conditions will challenge the sustainability of some populations of marine megafauna (MacLeod, 2009; Barbraud et al., 2011; Hazen et al., 2013; Silber et al., 2017). The prolonged spatiotemporal fidelity of humpback whale movements, despite contemporaneous oceanographic and geomagnetic change, suggests humpback whale movement decisions include mechanistic responses to stable and predictable exogenous cues, including gravity.

The relative stability of gravitationally derived cues helps explain the apparent paradox of humpback whale migratory fidelity despite pronounced oceanographic and geomagnetic change. Yet, the extent to which dynamic oceanographic conditions evoke changes in marine megafaunal long-distance migratory movement decisions, and the environmental and biogeophysical thresholds that trigger specific movement behaviors, remain unknown. Navigation during long-distance migration is likely to be informed by a diverse suite of cues, and if we are to ever truly know how whales navigate, all reasonable mechanisms must be considered as part of inclusive and integrated research on diverse species across a variety of environmental and biogeophysical contexts over prolonged periods. Documenting the extent to which animal migration routes, destinations, and movement decisions change, or perhaps fail to change, in a changing environment is essential to preserving biodiversity and sustainably managing diverse ecosystems and the services they provide.

DATA AVAILABILITY STATEMENT

All datasets generated for this study are included in the article/**Supplementary Material**.

ETHICS STATEMENT

Humpback whale tracking was performed in accordance with approvals granted by the Brazilian Environmental

Agency (IBAMA), permit #009/02/CMA/IBAMA and process #02001.000085/02-27.

AUTHOR CONTRIBUTIONS

TH conceived the study, compiled all satellite remote-sensing data, prepared the figures, performed the geophysical, astronomical, and statistical analyses, and wrote the initial manuscript. AZ, AA, DD, and FS performed all of the field research, including satellite tag preparation, deployment, and data management. All authors contributed to the writing and revision of the initial manuscript. The scientific results and conclusions, as well as any views or opinions expressed herein, are those of the author(s) and do not necessarily reflect those of NOAA or the US Department of Commerce.

FUNDING

Funding from Shell Brasil and CGG Brasil supported collection of the humpback whale satellite telemetry data we report.

SUPPLEMENTARY MATERIAL

The Supplementary Material for this article can be found online at: <https://www.frontiersin.org/articles/10.3389/fmars.2020.00414/full#supplementary-material>

REFERENCES

- Abrahms, B., Hazen, E. L., Aikens, E. O., Savoca, M. S., Goldbogen, J. A., Bograd, S. J., et al. (2019). Memory and resource tracking drive blue whale migrations. *Proc. Natl. Acad. Sci. U.S.A.* 116:201819031. doi: 10.1073/pnas.1819031116
- Amante, C., and Eakins, B. W. (2009). *ETOPO1 1 Arc-Minute Global Relief Model: Procedures, Data Sources and Analysis*. NOAA Technical Memorandum NESDIS NGDC-24. Silver Spring, MA: NOAA.
- Argos-CLS (2016). *Argos User's Manual*. Milton Keynes: Argos.
- Balmino, G., Vales, N., Bonvalot, S., and Braias, A. (2012). Spherical harmonic modelling to ultra-high degree of Bouguer and isostatic anomalies. *J. Geodesy* 86, 499–520. doi: 10.1007/s00190-011-0533-4
- Barbraud, C., Rivalan, P., Inchausti, P., Nevoux, M., Rolland, V., Weimerskirch, H., et al. (2011). Contrasted demographic responses facing future climate change in Southern Ocean seabirds. *J. Anim. Ecol.* 80, 89–100. doi: 10.1111/j.1365-2656.2010.01752.x
- Batschelet, E. (1981). *Circular Statistics in Biology*. Cambridge, MA: Academic press, 388.
- Bortolotto, G. A., Danilewicz, D., Hammond, P. S., Thomas, L., and Zerbini, A. N. (2017). Whale distribution in a breeding area: spatial models of habitat use and abundance of western South Atlantic humpback whales. *Mar. Ecol. Prog. Ser.* 585, 213–227. doi: 10.3354/meps12393
- Bowlin, M. S., Bisson, I. A., Shamoun-Baranes, J., Reichard, J. D., Sapir, N., Marra, P. P., et al. (2010). Grand challenges in migration biology. *Integrat. Comp. Biol.* 50, 261–279.
- Brothers, J. R., and Lohmann, K. J. (2018). Evidence that magnetic navigation and geomagnetic imprinting shape spatial genetic variation in sea turtles. *Curr. Biol.* 28, 1325–1329.
- Chapman, J. W., Klaassen, R. H., Drake, V. A., Fossette, S., Hays, G. C., Metcalfe, J. D., et al. (2011). Animal orientation strategies for movement in flows. *Curr. Biol.* 21, R861–R870.
- Chulliat, A., Alken, P., Nair, M., Woods, A., and Maus, S. (2015). *The enhanced Magnetic Model 2015-2020*. Asheville, CA: National Centers for Environmental Information.
- Clarke, M. R. (1978). Buoyancy control as a function of the spermaceti organ in the Sperm Whale. *J. Mar. Biol. Assoc. U. K.* 58, 27–71. doi: 10.1017/s0025315400024395
- Cohen, J. M., Lajeunesse, M. J., and Rohr, J. R. (2018). A global synthesis of animal phenological responses to climate change. *Nat. Clim. Change* 8, 224–228. doi: 10.1038/s41558-018-0067-3
- Cotton, P. A. (2003). Avian migration phenology and global climate change. *Proc. Natl. Acad. Sci. U.S.A.* 100, 12219–12222. doi: 10.1073/pnas.1930548100
- Croll, D. A., Kudela, R., and Tershy, B. R. (2006). "Ecosystem impact of the decline of large whales in the North Pacific," in *Whales, Whaling and Ocean Ecosystems*, eds A. James, J. A. Estes, D. P. DeMaster, D. F. Doak, R. L. Brownell, and T. M. Williams (Berkeley, CA: University of California Press), 202–214. doi: 10.1525/california/9780520248847.003.0016
- Derville, S., Torres, L. G., Albertson, R., Andrews, O., Baker, C. S., Carzon, P., et al. (2019). Whales in warming water: assessing breeding habitat diversity and adaptability in Oceania's changing climate. *Global Change Biol.* 25, 1466–1481. doi: 10.1111/gcb.14563
- ESR (2009). *OSCAR third Degree Resolution Ocean Surface Currents*. Available at: <http://dx.doi.org/10.5067/OSCAR-03D01> (accessed May 22, 2018)
- ESRI (2011). *ArcGIS Desktop. "Release 10." Documentation Manual*. Redlands, CA: Environmental Systems Research Institute.
- Fisahn, J., Klingel, E., and Barlow, P. (2015). Lunar gravity affects leaf movement of *Arabidopsis thaliana* in the International Space Station. *Planta* 241, 1509–1518. doi: 10.1007/s00425-015-2280-x
- Fisahn, J., Yazdanbakhsh, N., Klingel, E., and Barlow, P. (2012). *Arabidopsis thaliana* root growth kinetics and lunisolar tidal acceleration. *New Phytol.* 195, 346–355. doi: 10.1111/j.1469-8137.2012.04162.x

- Fleming, A. H., Clark, C. T., Calambokidis, J., and Barlow, J. (2016). Humpback whale diets respond to variance in ocean climate and ecosystem conditions in the California Current. *Global Change Biol.* 22, 1214–1224. doi: 10.1111/gcb.13171
- Gaspar, P., Georges, J. Y., Fossette, S., Lenoble, A., Ferraroli, S., and Le Maho, Y. (2006). Marine animal behaviour: neglecting ocean currents can lead us up the wrong track. *Proc. R. Soc. B Biol. Sci.* 273, 2697–2702. doi: 10.1098/rspb.2006.3623
- Gilbert, R. O. (1987). *Statistical Methods for Environmental Pollution Monitoring*. New York, NY: Van Nostrand Reinhold.
- Goni, G. J., Bringas, F., and DiNezio, P. N. (2011). Observed low frequency variability of the Brazil Current front. *J. Geophys. Res. Oceans* 116:C10037.
- Götze, H.-J. (2014). “International gravity formula,” in *Encyclopedia of Solid Earth Geophysics*, ed. H. K. Gupta (Dordrecht: Springer), 611–612. doi: 10.1007/978-90-481-8702-7_102
- Hammer, Ø., Harper, D. A. T., and Ryan, P. D. (2001). PAST: paleontological statistics software package for education and data analysis. *Palaeontol. Electron.* 4, 1–9.
- Harris, G., Thirgood, S., Hopcraft, J. G. C., Cromsigt, J. P. G. M., and Berger, J. (2009). Global decline in aggregated migrations of large terrestrial mammals. *Endanger. Species Res.* 7, 55–76. doi: 10.3354/esr00173
- Harris, L. R., Nel, R., Oosthuizen, H., Meyer, M., Kotze, D., Anders, D., et al. (2018). Managing conflicts between economic activities and threatened migratory marine species toward creating a multiobjective blue economy. *Conserv. Biol.* 32, 411–423. doi: 10.1111/cobi.12992
- Hartmann, G. A., and Pacca, I. G. (2009). Time evolution of the South Atlantic magnetic anomaly. *Anais Acad. Brasil. Ciên.* 81, 243–255. doi: 10.1590/s0001-3762009000200010
- Hauser, N., Zerbini, A. N., Geyer, Y., Heide-Jørgensen, M. P., and Clapham, P. (2010). Movements of satellite-monitored humpback whales, *Megaptera novaeangliae*, from the Cook Islands. *Mar. Mamm. Sci.* 26, 679–685.
- Hausfather, Z., Cowtan, K., Clarke, C. D., Jacobs, P., Richardson, M., Rohde, R., et al. (2017). Assessing recent warming using instrumentally homogeneous sea surface temperature records. *Sci. Adv.* 3:e1601207. doi: 10.1126/sciadv.1601207
- Hays, G. C., Ferreira, L. C., Sequeira, A. M. M., Meekan, M. G., Duarte, C. M., Bailey, H., et al. (2016). Key questions in marine megafauna movement ecology. *Trends Ecol. Evol.* 31, 463–475.
- Hazen, E. L., Jørgensen, S., Rykaczewski, R. R., Bograd, S., Foley, D. G., Jonsen, I. D., et al. (2013). Predicted habitat shifts of Pacific top predators in a changing climate. *Nat. Clim. Change* 3:234. doi: 10.1038/nclimate1686
- Hoegh-Guldberg, O., and Bruno, J. F. (2010). The impact of climate change on the world's marine ecosystems. *Science* 328, 1523–1528. doi: 10.1126/science.1189930
- Hof, A. R., Rodríguez-Castañeda, G., Allen, A. M., Jansson, R., and Nilsson, C. (2017). Vulnerability of subarctic and arctic breeding birds. *Ecol. Appl.* 27, 219–234. doi: 10.1002/eap.1434
- Horton, T. W., Hauser, N., Zerbini, A., Francis, M. P., Domeier, M. L., Andriol, A., et al. (2017). Route fidelity during marine megafauna migration. *Front. Mar. Sci.* 4:422.
- Horton, T. W., Holdaway, R. N., Zerbini, A. N., Hauser, N., Garrigue, C., Andriol, A., et al. (2011). Straight as an arrow: humpback whales swim constant course tracks during long-distance migration. *Biol. Lett.* 7, 674–679. doi: 10.1098/rsbl.2011.0279
- Kennedy, A. S., Zerbini, A. N., Vásquez, O. V., Gandilhon, N., Clapham, P. J., and Adam, O. (2014). Local and migratory movements of humpback whales (*Megaptera novaeangliae*) satellite-tracked in the North Atlantic Ocean. *Can. J. Zool.* 92, 9–18. doi: 10.1139/cjz-2013-0161
- Kirschvink, J. L., Dizon, A. E., and Westphal, J. A. (1986). Evidence from strandings for geomagnetic sensitivity in cetaceans. *J. Exp. Biol.* 120, 1–24.
- Lohmann, K. J., Hester, J. T., and Lohmann, C. M. F. (1999). Long-distance navigation in sea turtles. *Ethol. Ecol. Evol.* 11, 1–23. doi: 10.1080/08927014.1999.9522838
- MacLeod, C. D. (2009). Global climate change, range changes and potential implications for the conservation of marine cetaceans: a review and synthesis. *Endanger. Species Res.* 7, 125–136. doi: 10.3354/esr00197
- Marcello, F., Wainer, I., and Rodrigues, R. R. (2018). South Atlantic subtropical gyre late twentieth century changes. *J. Geophys. Res. Oceans* 123, 5194–5209. doi: 10.1029/2018jc013815
- Mate, B. R., Gisiner, R., and Mobley, J. (1998). Local and migratory movements of Hawaiian humpback whales tracked by satellite telemetry. *Can. J. Zool.* 76, 863–868. doi: 10.1139/z98-008
- Meeus, J. H. (1991). *Astronomical Algorithms*. Richmond, VA: Willmann-Bell, Incorporated.
- Miloslavich, P., Bax, N. J., Simmons, S. E., Klein, E., Appeltans, W., Aburto-Oropeza, O., et al. (2018). Essential ocean variables for global sustained observations of biodiversity and ecosystem changes. *Global Change Biol.* 24:16–2433.
- Mohriak, W. U., Nóbrega, M., Odegard, M. E., Gomes, B. S., and Dickson, W. G. (2010). Geological and geophysical interpretation of the rio grande rise, south-eastern Brazilian margin: extensional tectonics and rifting of continental and oceanic crusts. *Petrol. Geosci.* 16, 231–245. doi: 10.1144/1354-079309-910
- Muggeo, V. M., and Muggeo, M. V. M. (2017). Package ‘segmented’. *Biometrika* 58, 525–534.
- NASA (2018). *Goddard Space Flight Center, Ocean Ecology Laboratory, Ocean Biology Processing Group. Moderate-resolution Imaging Spectroradiometer (MODIS) Aqua {Aqua MODIS Sea Surface Temperature, Monthly, 4 km} Data*. Greenbelt, MD: NASA.
- Noad, M. J., and Cato, D. H. (2007). Swimming speeds of singing and non-singing humpback whales during migration. *Mar. Mamm. Sci.* 23, 481–495. doi: 10.1111/j.1748-7692.2007.02414.x
- Owen, K., Jenner, K. C. S., Jenner, M. N. M., McCauley, R. D., and Andrews, R. D. (2019). Water temperature correlates with baleen whale foraging behaviour at multiple scales in the Antarctic. *Mar. Freshw. Res.* 70, 19–32.
- Peñuelas, J., Filella, I., and Comas, P. (2002). Changed plant and animal life cycles from 1952 to 2000 in the Mediterranean region. *Global Change Biol.* 8, 531–544. doi: 10.1046/j.1365-2486.2002.00489.x
- Pereira, H. M., Ferrier, S., Walters, M., Geller, G. N., Jongman, R. H. G., Scholes, R. J., et al. (2013). Essential biodiversity variables. *Science* 339, 277–278.
- Record, N., Runge, J., Pendleton, D., Balch, W., Davies, K., Pershing, A., et al. (2019). Rapid climate-driven circulation changes threaten conservation of endangered north atlantic right whales. *Oceanography* 32, 162–169.
- Riekkola, L., Zerbini, A., Andrews, G., Andrews-Goff, V., Baker, C. S., and Childhouse, S. (2018). Application of a multi-disciplinary approach to reveal population structure and Southern Ocean feeding grounds of humpback whales. *Ecol. Indic.* 89, 455–465. doi: 10.1016/j.ecolind.2018.02.030
- Roman, J., and McCarthy, J. J. (2010). The whale pump: marine mammals enhance primary productivity in a coastal basin. *PLoS One* 5:e13255. doi: 10.1371/journal.pone.0013255
- Rosenbaum, H. C., Pomilla, C., Mendez, M., Leslie, M. S., Best, P. B., Findlay, K. P., et al. (2009). Population structure of humpback whales from their breeding grounds in the South Atlantic and Indian Oceans. *PLoS One* 4:e7318. doi: 10.1371/journal.pone.0007318
- Santora, J. A., Mantua, N. J., Schroeder, I. D., Field, J. C., Hazen, E. L., Bograd, S. J., et al. (2020). Habitat compression and ecosystem shifts as potential links between marine heatwave and record whale entanglements. *Nat. Commun.* 11, 1–12.
- Schwenk, K., Padilla, D. K., Bakken, G. S., and Full, R. J. (2009). Grand challenges in organismal biology. *Integrat. Comp. Biol.* 49, 7–14. doi: 10.1093/icb/icp034
- Silber, G. K., Lettrich, M. D., Thomas, P. O., Baker, J. D., Baumgartner, M., Becker, E. A., et al. (2017). Projecting marine mammal distribution in a changing climate. *Front. Mar. Sci.* 4:413. doi: 10.3389/fmars.2017.00413
- Silverman, B. W. (1986). *Density Estimation for Statistics and Data Analysis*. London: Chapman & Hall.
- Sprogis, K. R., Christiansen, F., Wandres, M., and Beijder, L. (2018). El Niño Southern Oscillation influences the abundance and movements of a marine top predator in coastal waters. *Global change Biol.* 24, 1085–1096.
- Thackeray, S. J., Henrys, P. A., Hemming, D., Bell, J. R., Botham, M. S., Burthe, S., et al. (2016). Phenological sensitivity to climate across taxa and trophic levels. *Nature* 535, 241–245. doi: 10.1038/nature18608
- Trudelle, L., Cerchio, S., Zerbini, A. N., Geyer, Y., Mayer, F.-X., Jung, J.-L., et al. (2016). Influence of environmental parameters on movements and habitat utilization of humpback whales (*Megaptera novaeangliae*) in the Madagascar breeding ground. *R. Soc. Open Sci.* 3:160616. doi: 10.1098/rsos.160616
- Urban, M. C., Bocedi, G., Hendry, A. P., Mihoub, J. B., P'er, G., Singer, A., et al. (2016). Improving the forecast for biodiversity under climate change. *Science* 353:aad8466.

- van Doren, B. M., Horton, K. G., Dokter, A. M., Klinck, H., Elbin, S. B., Farnsworth, A., et al. (2017). High-intensity urban light installation dramatically alters nocturnal bird migration. *Proc. Natl. Acad. Sci. U.S.A.* 114, 11175–11180. doi: 10.1073/pnas.1708574114
- Wilcove, D. S., and Wikelski, M. (2008). Going, going, gone: is animal migration disappearing. *PLoS Biol.* 6:e188. doi: 10.1371/journal.pbio.0060188
- Witteveen, B. H., and Wynne, K. M. (2016). Trophic niche partitioning and diet composition of sympatric fin (*Balaenoptera physalus*) and humpback whales (*Megaptera novaeangliae*) in the Gulf of Alaska revealed through stable isotope analysis. *Mar. Mamm. Sci.* 32, 1319–1339. doi: 10.1111/mms.12333
- Wu, L., Cai, W., Zhang, L., Nakamura, H., Timmermann, A., Joyce, T., et al. (2012). Enhanced warming over the global subtropical western boundary currents. *Nat. Clim. Change* 2, 161–166. doi: 10.1038/nclimate1353
- Zemsky, V. A., Berzin, A. A., Mikhaliyev, Y. A., and Tormosov, D. D. (1996). *Soviet Antarctic whaling Data (1947–1972)*, 2nd Edn. Moscow: Center for Russian Environment Policy.
- Zerbini, A. N., Andriolo, A., Heide-Jørgensen, M. P., and Moreira, S. (2011). Migration and summer destinations of humpback whales (*Megaptera novaeangliae*) in the western South Atlantic Ocean. *J. Cetacean Res. Manag.* 3, 113–118.
- Zerbini, A. N., Andriolo, A., Heide-Jørgensen, M. P., Pizzorno, J. L., Geyer, Y., VanBlaricom, G. R., et al. (2006). Satellite-monitored movements of humpback whales *Megaptera novaeangliae* in the Southwest Atlantic Ocean. *Mar. Ecol. Prog. Ser.* 313, 295–304. doi: 10.3354/meps313295

Conflict of Interest: The authors declare that the research was conducted in the absence of any commercial or financial relationships that could be construed as a potential conflict of interest.

Copyright © 2020 Horton, Zerbini, Andriolo, Danilewicz and Sucunza. This is an open-access article distributed under the terms of the Creative Commons Attribution License (CC BY). The use, distribution or reproduction in other forums is permitted, provided the original author(s) and the copyright owner(s) are credited and that the original publication in this journal is cited, in accordance with accepted academic practice. No use, distribution or reproduction is permitted which does not comply with these terms.

Advantages of publishing in Frontiers



OPEN ACCESS

Articles are free to read
for greatest visibility
and readership



FAST PUBLICATION

Around 90 days
from submission
to decision



HIGH QUALITY PEER-REVIEW

Rigorous, collaborative,
and constructive
peer-review



TRANSPARENT PEER-REVIEW

Editors and reviewers
acknowledged by name
on published articles

Frontiers

Avenue du Tribunal-Fédéral 34
1005 Lausanne | Switzerland

Visit us: www.frontiersin.org

Contact us: frontiersin.org/about/contact



REPRODUCIBILITY OF RESEARCH

Support open data
and methods to enhance
research reproducibility



DIGITAL PUBLISHING

Articles designed
for optimal readership
across devices



FOLLOW US

@frontiersin



IMPACT METRICS

Advanced article metrics
track visibility across
digital media



EXTENSIVE PROMOTION

Marketing
and promotion
of impactful research



LOOP RESEARCH NETWORK

Our network
increases your
article's readership